SLAC – 316
UC – 34C
(T/E)

SLAC--316

DE88 010766

PROCEEDINGS OF THE WORKSHOP ON ELECTRONUCLEAR PHYSICS WITH INTERNAL TARGETS STANFORD LINEAR ACCELERATOR CENTER JANUARY 5–8, 1987

Edited by R. G. Arnold and R. C. Minehart

Stanford Linear Accelerator Center
Stanford University
Stanford, California 94305

May 1987

Prepared for the Department of Energy
under contract number DE-AC03-76SF00515

Printed in the United States of America. Available from the National Technical Information Service, U.S. Department of Commerce, 5285 Port Royal Road, Springfield, Virginia 22161. Price: Printed Copy A11, Microfiche A01.

Workshop Organizing Committee

R. G. Arnold, Chairman	American University
K. Van Bibber	LLNL
F. S. Dietrich	LLNL
T. W. Donnelly	MIT
A. K. Kerman	MIT
S. E. Koonin	CalTech
S. Kowalski	MIT
R. D. McKeown	CalTech
R. C. Minehart	University of Virginia
E. Moniz	MIT
B. E. Norum	University of Virginia
S. E. Rock	American University
J. E. Spencer	SLAC
J. P. Vary	Iowa State University

Forward

The Workshop on Electronuclear Physics with Internal Targets was held at SLAC on January 5-8, 1987. The idea for this workshop grew out of interest among physicists at SLAC and MIT/Bates who have been exploring the possibilities for internal targets in the PEP ring at SLAC and in a proposed stretcher ring at MIT/Bates. The aim of the workshop was to bring together physicists from these groups and from other laboratories and universities to discuss the new physics that could be made accessible with internal targets, and to share information on recent developments in internal target technology, on the impact of internal targets on ring operation, and on the detector requirements. The workshop was sponsored by NPAS, the program of Nuclear Physics at SLAC, and it was attended by more than 100 physicists from the U.S., Canada, Europe, and Japan.

The workshop sessions began with two days of invited talks followed by two days of shorter presentations organized by the chairmen of four Working Groups. Written versions of all the plenary talks and all but four of the Working Group talks are presented here. The table of contents closely follows the meeting agenda. One talk on the agenda was not presented orally, but the written version by J. Fay and M. Macri is included here. Also included are two papers contributed for the proceedings that were not on the agenda.

Use of low density internal gas targets in high current circulating electron beams offers a number of unique features that would open up several new areas for electronuclear physics research. A primary advantage is the possibility for detection of multiple particles in the final state using large acceptance detectors. In addition a variety of nuclei can be produced in the form of polarized gas with high polarization and sufficient density and purity to give useful counting rates in high current circulating beams. Polarized targets will allow unique measurements of the spin dependence in a variety of electromagnetic interactions, and large acceptance detectors will make possible a large class of measurements of nuclear structure and reaction mechanisms not practical with external beams and thick targets. Finally it may also be possible to produce beams of polarized electrons and arrange for longitudinal polarization at the target. With polarized electrons and polarized targets, a number of fundamental measurements of nuclear and nucleon spin structure might be possible that would otherwise be impossible using external beams.

Future developments of the internal target method for electron beams will benefit from and be stimulated by work planned or under way for numerous other internal and external beams around the world. At the workshop we heard about previous internal target work for the proton beams at Fermilab and CERN. The requirements for the large acceptance detectors will be similar to other detector systems in use today or planned, for example, at CEBAF. The unique physics made accessible by this technique will be complementary to that now under investigation or planned for fixed target beams at SLAC, MIT/Bates, Fermilab, CERN, and CEBAF. There was considerable interest expressed at the workshop in pursuing future work on ideas for internal target experiments at electron

rings. It is possible that if these developments continue there will emerge a new subfield of experimental research exploring a wide range of topics in nuclear and nucleon structure.

We would like to express our thanks to all the speakers and authors of the papers presented here for their efforts in advancing our understanding of these topics. We also want to thank those people who helped organize the meetings and produce the proceedings: the Organizing Committee and the Working Group Chairmen for arranging the speakers and planning the program; Lynn Hanlon, Lesia Machicao, and Nina Adelman, the Conference Secretariat, who worked behind the scenes and smoothly operated the front desk; Kevin Johnston and Lucy Yuen who masterfully converted the manuscripts into this proceedings.

R. G. Arnold R. C. Minehart
May 1987

Contents

Session IV

Chairman: C. F. Williamson

Working Group I

Physics with Multi-Arm Detectors and Nucleon Targets
Chairmen: R. G. Arnold and S. J. Brodsky

Working Group II

Physics with Multi-Arm Detectors and Nuclear Targets
Chairmen: S. E. Rock and J. P. Vary

Working Group III

Physics with 4π Detectors

Chairmen: S. E. Koonin and K. Van Bibber

Working Group IV

Physics with Polarized Beams and Targets

Chairmen: T. W. Donnelly and B. E. Norum

Contributed Papers

FROM THE HADRONIC PHOTON AT $Q^2=0$ TO HARD SCATTERING AT SPACE-LIKE Q^2

T. Sloan

University of Lancaster
Physics Department
Lancaster, LA1 4YB, England

Introduction

Real photons ($Q^2=0$) show much larger cross sections for the production of hadrons than would be expected if they interacted only electromagnetically. In contrast the scaling behaviour in deep inelastic scattering shows that the space like virtual photons scatter from point like nucleon constituents (quarks) without any form factor effects. Thus space-like virtual photons behave as pure electromagnetic probes whereas real photons behave more like hadrons.

In real photoproduction ($Q^2=0$) a large cross section for the production of ρ^o mesons is observed which is ~9 times the cross section for ω meson production. These observations led to the formulation of the vector meson dominance model (VMD) for the interactions of real photons[1]. In this model the cross section for the photoproduction of vector mesons V is written as;

$$\left(\frac{d\sigma}{dt}\right)_{\gamma p \to Vp} = f_V^2 \left(\frac{d\sigma}{dt}\right)_{Vp \to Vp}$$

where f_V represents the coupling constant between the photon and vector meson and $\left(\frac{d\sigma}{dt}\right)_{Vp \to Vp}$ is the elastic scattering cross section for the vector meson V. The ratio of the coupling constants is expected to be

$$f_\rho^2 : f_\omega^2 : f_\phi^2 : f_{J/\psi}^2 : f_\upsilon^2 = 9:1:2:8:2$$

from SU(3) symmetry (quark charges).

Clearly there is a substantial difference between the behaviour of real photons and that of virtual photons at higher Q^2. In this paper, I shall attempt to trace the evolution of the hadron-like behaviour of the photon at $Q^2=0$ to its electromagnetic behaviour at larger space like Q^2.

Exclusive Vector Meson Production at High Energies

Exclusive vector meson production is the process

$$\gamma^* + p \to V + p$$

where γ^* is a real ($Q^2=0$) or a virtual (finite negative Q^2) photon in electron or muon deep inelastic scattering. Experimental data at high energies are available on exclusive ρ^o and ϕ^2 and J/ψ production[3]. Figure 1 shows the total cross sections as a function of Q^2. It can be seen from this figure that the ratio of $\sigma_\rho : \sigma_\phi : \sigma_{J/\psi}$ is tending towards the values 9:2:8 as Q^2 increases i.e. the values expected from the photon coupling to the quark charges.

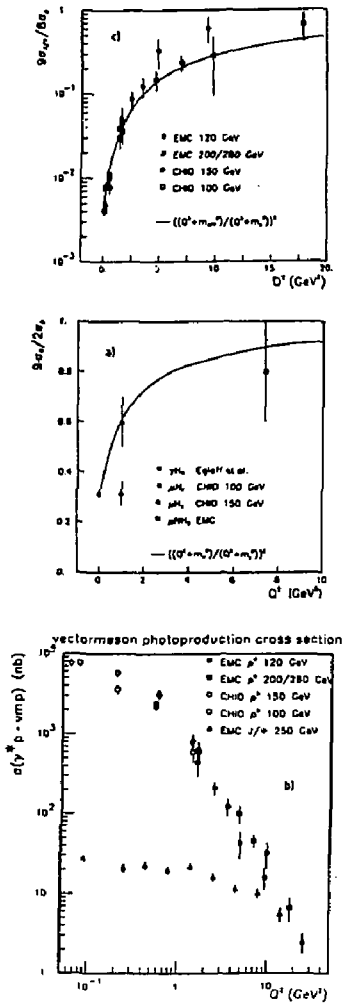

Fig. 1

a) The ratio $9\sigma(\phi)/2\sigma(\rho)$, b) The cross sections sections for elastic ρ^o and J/ψ production.
c) The ratio $9\sigma(J/\psi)/8\sigma(\rho)$ as a function of Q^2.

In the generalised vector dominance model[1], assuming ρ^o dominance and neglecting off diagonal terms, the cross section for exclusive ρ^o production at higher Q^2 should follow the form

$$\sigma(Q^2) = \sigma(Q^2=0)\ \frac{m_\rho^4}{(Q^2+m_\rho^2)^2}\ [1+\varepsilon\xi^2\frac{Q^2}{m_\rho^2}] \qquad (1)$$

where m_ρ is the mass of the ρ^o meson, ε is the ratio of the longitudinal to transverse virtual photon fluxes and $\xi^2Q^2/m_\rho^2=R$, the ratio of the production cross sections of longitudinally and transversely polarised virtual photons ($R=\sigma_L/\sigma_T$).

In real photoproduction ($Q^2=0$) of ρ^o mesons s channel helicity is observed to be conserved[1], i.e. transverse photons produce ρ^o's in a helicity ± 1 state in the s channel frame (which gives a pure $\sin^2\theta$ angular distribution of the decay pions). If s channel helicity were conserved at higher Q^2 any longitudinal photon contribution would give a $\cos^2\theta$ component to the angular distribution. The EMC observed[2] that the ρ^o's are produced with almost a pure $\cos^2\theta$ angular distribution at high Q^2, and that the $\sin^2\theta$ component falls rapidly with Q^2. From fits to the angular distribution assuming s channel helicity conservation this group deduce that the parameter ξ^2 should be 0.4 ± 0.1. Figure 2 shows the measured cross section for exclusive ρ^o production as a function of Q^2. The solid curve (dashed curve) shows the generalised vector dominance model prediction (eqn. 1) with $\xi^2=0.4$ ($\xi^2=0.0$). It is clear that the data prefer the value $\xi^2=0.0$ and exclude the value $\xi^2=0.4$. Thus generalised vector meson dominance with s channel helicity conservation does not describe the data at high Q^2.

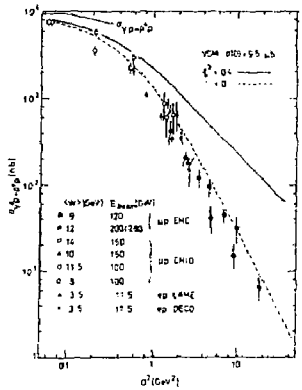

Fig. 2

ρ^o photoproduction cross section versus Q^2. The smooth curves show the VMD predictions (equation 1) with $\xi^2=0$ and $\xi^2=0.4$.

The EMC have measured independently (from the incident muon energy dependence) the value of $R=\sigma_L/\sigma_T=0.4^{+0.9}_{-0.4}$ by combining their data with the measurements of the CHIO group, each extrapolated to $Q^2=2$ GeV^2. This shows that exclusive ρ^o production is mainly by transversely polarised virtual photons. Projecting out the observed $\sin^2\theta$ and $\cos^2\theta$ components from the decay pion angular distributions would imply a value $R=2.7\pm0.5$ at $Q^2=2$ GeV^2 if s channel helicity were conserved. Comparing these two values of R one concludes that s channel helicity is no longer conserved at larger Q^2 i.e. exclusive ρ^o photoproduction occurs mainly from transverse (helicity $\pm$ 1) photons and the ρ^o's are produced mainly in a helicity 0 state.

Could the generalised vector meson dominance picture work with s channel helicity flip? Equation (1) shows that as Q^2 becomes large the expected cross section ratio $\sigma_\rho:\sigma_\phi:\sigma_{J/\psi}$ (large Q^2) $= \sigma_\rho m_\rho^4 : \sigma_\phi m_\phi^4 : \sigma_{J/\psi} m_{J/\psi}^4$ $(Q^2=0)=9:1:0.75$. The value of these ratios observed at $Q^2=15$ GeV^2 are $9:1.6\pm0.4:5.6\pm1.0$ and are inconsistent with this picture. Thus the generalised vector dominance model with or without s channel helicity conservation fails to describe the data at higher Q^2. However, the observed ratios are tending to the values expected (9:2:8) from the electromagnetic coupling of the virtual photon to the quark charges.

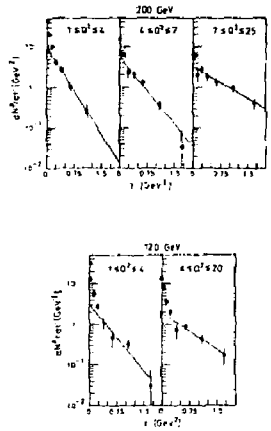

Fig. 3

The exclusive ρ^o yields as a function of $t'=|t-t_{min}|$ in different Q^2 bins from an ammonia (mainly nitrogen) target

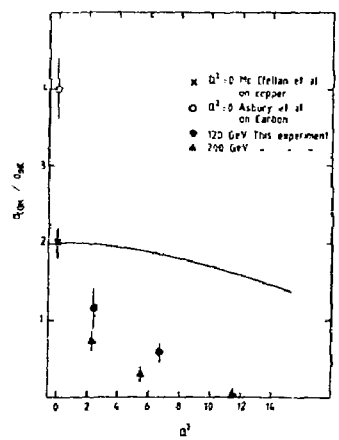

Fig. 4

The ratio of the total coherent to incoherent cross sections from nitrogen as a function of Q^2. The smooth curve shows the expected decrease due to the increase of t_{min} with Q^2.

Figure 3 shows the measured $t'(=t-t_{min})$ dependence[2] for exclusive ρ^o production from an ammonia (mainly nitrogen) target. The sharp peak at small t is due to coherent production smeared by experimental resolution. The smooth curves are fits of the form $e^{-bt'}$ outside the coherent region ($t'<0.2$). Figure 3 shows that the value of b decreases rapidly with Q^2. This indicates that at higher Q^2 exclusive ρ^o production is dominated by a hard scattering mechanism. The exponentials in fig. 3 were extrapolated under the coherent peak to measure the ratio of the coherent to incoherent cross sections. Figure 4 shows that this ratio decreases with Q^2. Such behaviour can be understood from the failure of s channel helicity conservation at high Q^2. In the forward direction, by angular momentum conservation, the helicity flip of the ρ^o implies that the nucleon spin must also flip. Such spin flip amplitudes cannot contribute to coherent production since the final state of the nucleus changes.

The coherent cross section ratio decreases approximately as $1/Q^2$. Presumably such a cross section is due to the residual diffractive (i.e. vector meson dominance type) behaviour. A $1/Q^2$ dependence indicates that such behaviour is a higher twist mechanism.

Nuclear Shadowing of Photons[4]

This is studied by measuring the A dependence of the total hadronic photoabsorption cross section $\sigma_{\gamma A}$ where A is the atomic mass number. For any nucleus we define

$$A_{eff} = \frac{A\sigma_{\gamma A}}{(Z\sigma_{\gamma p}+N\sigma_{\gamma n})}$$

where $\sigma_{\gamma p}$ and $\sigma_{\gamma n}$ are the free proton and neutron cross sections and Z and N are the number of protons and neutrons in the nucleus. This is parameterised by

$$\frac{A_{eff}}{A} = A^{\epsilon}$$

Such a parameterisation fits imperfectly the pion-nucleus cross section variation with a value $\epsilon\sim-0.14$. However, it will suffice for the less precise photon data.

For real photons ($Q^2=0$) of energy $\nu\geq 10$ GeV, ϵ is found to be approximately independent of ν with a value of about -0.07. This indicates partial shadowing of real photons. The data are well represented by a model which assumes that the photon has a point-like cross section as well as a part interacting as in the vector meson dominance model[5].

There are several experiments with have contributed data on shadowing at finite Q^2 in charged lepton scattering[6,10]. Splitting these data into different Q^2 ranges and plotting ϵ as a function of $x=Q^2/2M\nu$, trends appear in the measurements. Here x is the fraction of the momentum of the nucleon carried by a struck parton in the quark parton model. Figure 5 shows ϵ as a function of x for the low Q^2 range[6,7] ($Q^2<1$). The measurements show that shadowing turns off smoothly as x increases (i.e. ν decreases) as would be expected in the model used to describe the real photoproduction data. Figure 6 shows the ratio of $Aeff/A$ ($=\sigma_{\gamma A}/A\sigma_{\gamma N}$, where N is the average of the proton and neutron cross sections) for carbon and iron or copper for intermediate Q^2[8], $Q^2<4$ GeV^2 and high Q^2[10] $Q^2>2$ GeV^2. The data of [9] has been omitted from this plot because the two experiments neither agree with each other or with the other measurements[8] in the same Q^2 range. At $x>0.1$ the ratio decreases with x. This effect is known as the EMC effect. For $x<0.1$ the ratio decreases and tends to show shadowing i.e. the ratio tends to a value <1.

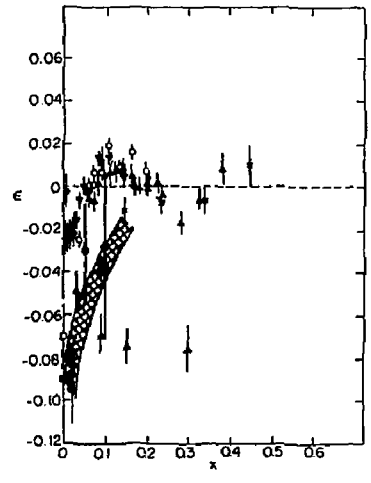

Fig. 5

The parameter ϵ as a function of x for low Q^2 data the hatched region shows the range of variation of the data of[6] and the points are the data of [7].

Many theoretical models exist to explain the EMC effect at high x[11]. There are three models of the contributing mechanisms in the region $x\lesssim 0.2$. The model of Brodsky, Close and Gunion[5] predicts that shadowing occurs at small x, but that it dies uniformly with Q^2. This model does not predict antishadowing at $x\sim 0.15$, as indicated by the data.

The presence of pions in the nucleus has been used to predict the antishadowing excess at $x\sim 0.15$[12]. In this model the nucleon structure function in the nucleus is given by

$$F_2^A(x) = \int_x^A f_N(z)\, F_2^N(\tfrac{x}{z})dz + \int_x^A f_\pi(z)\, F_2^\pi(\tfrac{x}{z})dz$$

where F_2^N and F_2^π are the structure functions and f_N, f_π are the fractional momentum distributions of the nucleon and pion in the nucleus respectively. The increase of the ratio in fig. 6 above unity at $x\sim 0.15$ is ascribed to the excess pion content and the decrease below unity at large x to momentum conservation. The shadowing at small x is not predicted and is ascribed to a separate process e.g. the Brodsky, Close and Gunion mechanism.

A parton model of shadowing and antishadowing was developed by Nicholaev and Zacharov[13]. They postulate that soft partons (e.g. gluons) can fuse to produce harder partons. Thus the tiny x region, $x\gtrsim A^{-1/3}\, m_\pi/m_N$ (where m_π and m_N are the pion and nucleon

masses), in deep inelastic scattering is depleted as there are fewer soft partons which accrete at x~0.15, giving an excess in this region. In this model the ratios will be approximately Q^2 independent.

At present the data are too few and too imprecise to separate these two pictures. It will be necessary to measure the Q^2 dependence of the ratio in fig. 6 in the tiny x region to understand the detailed mechanisms in the shadowing region.

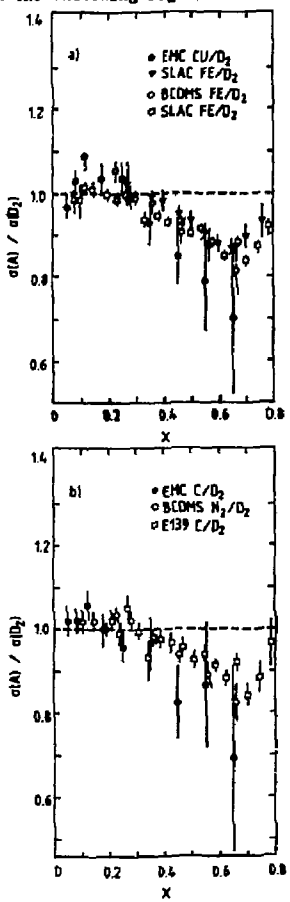

Fig. 6

The ratio of the cross section for deep inelastic scattering per nucleon from a) iron or copper b) carbon to that from deuterium at high and intermediate values of Q^2

Conclusions

In exclusive vector meson production in deep inelastic scattering, the vector meson dominance picture dies away and the production mechanism becomes a hard scattering process at $Q^2 \geq 1$ GeV^2. The virtual photon has been demonstrated to behave as a pure electromagnetic probe. In shadowing in nuclei there are indications for the electromagnetic behaviour of the photon but the picture is still somewhat confused. There is a need to measure the Q^2 dependence of the shadowing region at very small x in order to better understand the processes involved.

I would like to thank the organisers of the HPAS Workshop at SLAC for their hospitality. I should also like to thank Per Grafström for helpful discussions.

References

1. For a review see T.H. Bauer, R.D. Spital, D.R. Yennie and F.M. Pipkin, Rev. Mod. Phys. 50, 261 vol. 2 (1978).
2. CHIO, W.D. Schambroom et al., Phys. Rev. D26, 1 (1982);
   EMC, J.J. Aubert et al., Phys. Lett. 161B, 203 (1985);
   EMC, K. Mönig, Diplom Thesis, Univ. of Wuppertal WUD 86-10.
3. BFP, T. Markiewicz, Ph.D. Thesis (Lawrence Berkeley Laboratory);
   EMC, J.J. Aubert et al., Nucl. Phys. B213, 1 (1983).
4. For a review, see G. Grammer Jr. and J.D. Sullivan, Electromagnetic Interactions of Hadrons, vol. 2 edited by A. Donnachie and G. Shaw (Published by Plenum Press, 1978).
5. S.J. Brodsky, F.E. Close and J. Gunion, Phys. Rev. D6, 177 (1972).
6. J. Franz et al., ($.08<Q^2<1$ GeV^2) Z. Phys. C10, 105 (1981);
   G. Huber et al., ($.075<Q^2<1.$ GeV^2) Z. Phys. C2, 279 (1979);
   J. Bailey et al., ($0.1<Q^2<0.3$ GeV^2) Nucl. Phys. B151, 367 (1979).
7. J. Eickmeyer et al., (Q^2~0.1 GeV^2) Phys. Rev. Letts. 36, 289 (1976).
8. S. Stein et al., Phys. Rev. D12, 1884 (1975);
   W.R. Ditzler et al., Phys. Letts. 57B 201 (1975)
9. M. May et al., Phys. Rev. Letts. 35 407 (1975);
   M. Miller et al., Phys. Rev. D24, 1 (1981).
10. SLAC-E139, R.G. Arnold et al., Phys. Rev. Letts. 52, 722 (1984).
    EMC, P.R. Norton, Talk at 23rd Int. Conf. on High Energy Physics, Berkeley, 1986.
    BCDMS CERN preprint EP/87-13.
    BCDMS G. Bari et al., Phys. Lett 163B, 282, (1985).
11. O. Nachtmann, Proc. 11th Int. Conf. on Neutrino Physics and Astrophysics, Nordkirchen, Dortmund, (1984) p.405;
    N.N. Nikolaev, Oxford University preprint TP 58/84 (1984);
    C.H. Llewellyn-Smith, Proc. FAMIC, Heidelberg 1984 eds. B. Povh and G.zu Putlitz, Nucl. Phys. A434 35c (1985);
    A. Krzywicki, Proc. 11th Europhysics Conf. "Nuclear Physics with Electromagnetic Probes", Paris 1985 eds. A. Gerard and C. Samour, Nucl. Phys. A446 135c (1935).
    J. Dias de Deus, Int. Conf. on High Energy Physics, Bari 1985 eds. L. Nitti and G. Preparata p.571.
12. E. Berger, ANL-HEP-CP-86-103 (ANL Preprint).
13. N.N. Nicholaev and V.I. Zacharov, Phys. Lett. 55B 397 (1975).

TESTING QUANTUM CHROMODYNAMICS IN ELECTROPRODUCTION*

STANLEY J. BRODSKY

Stanford Linear Accelerator Center
Stanford University, Stanford, California 94305

Introduction

Deep inelastic lepton nucleon scattering has been one of the key testing grounds of QCD over the past two decades. Measurements of the nucleon and nuclear structure functions have not only tested the short-distance properties of the theory, (such as the scaling properties of structure functions and their logarithmic evolution with momentum transfer), but they have also illuminated the nonperturbative bound state structure of the nucleon and nuclei in terms of their quark and gluon degrees of freedom. For the most part, this information has been obtained from single-arm inclusive experiments where only the recoil lepton was detected.

One of the important potential advantages of an internal target facility in an electron storage ring as discussed in this workshop is that the entire final state of electroproduction can be measured in coincidence with the scattered electron with close to 4π acceptance. In the case of the PEP ring ($E(e^{\pm}) \sim 15$ GeV), measurements can be performed above the onset of Bjorken scaling. Both polarized and unpolarized hydrogen and nuclear targets may be feasible, and eventually even polarized electron beams may be available. High precision comparisons between electron and positron scattering would allow the study of higher order QED and electroweak interference effects. The asymmetry in the cross sections for $e^{\pm}p \to e^{\pm}\gamma X$ can be sizeable,[1] providing a sum rule for the cube of the charges of the quarks in the target.

At the most basic level, Bjorken scaling of deep inelastic structure functions implies the production of a single quark jet, recoiling against the scattered lepton. The spectator system—the remnant of the target remaining after the scattered quark is removed—is a colored $\bar{3}$ system. (See fig. 1.) According to QCD factorization, the recoiling quark jet, together with the gluonic radiation produced in the scattering process, produces hadrons in a universal way, independent of the target or particular hard scattering reaction. This jet should be identical to the light quark jets produced in e^+e^- annihilation. In contrast, the hadronization of the spectator system depends in detail on the target properties. Unlike the quark jet, the leading particles of the target spectator system do not evolve and thus should not depend on the momentum transfer Q^2 [at fixed $W^2 = (q+p)^2$]. At present we do not have a basic understanding of the physics of hadronization, although phenomenological approaches, such as the Lund string model, have been successful in parameterizing many features of the data.

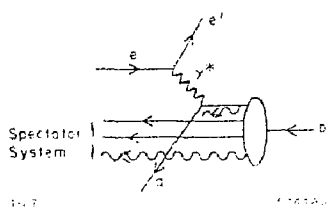

Fig. 1. Struck quark and spectator systems in electroproduction.

At a more detailed level, the features of the standard leading twist description are modified by coherent or nonperturbative effects. For example, higher twist–power-law suppressed contributions arise when two or more quarks recoil against the scattered lepton. At high energies, the quark jet does not change its state or hadronize over a distance scale proportional to its energy. Thus inelastic or absorptive processes cannot occur inside a nucleus—at least for the very fast hadronic fragments. We will discuss this target length condition[2,3] in more detail below. Nevertheless, a nuclear target can provide an essential tool for studying the detailed features of jet hadronization since the fast fragments are expected to scatter elastically in the nuclear medium, and the slow particles can interact inelastically and shower inside the nucleus. A review of the QCD predictions for jet hadronization can be found in Berger's contribution[4] to this workshop.

Many of the novel features expected in QCD are also apparent in QED. It is thus often useful to keep a QED analog in mind, replacing the target by a neutral atom such as positronium. Even in QED where there is no confinement, one expects in certain kinematic regions significant corrections to the Bjorken scaling associated with positron or electron knockout, in addition to the logarithmic evolution of the QED structure functions associated with induced photon radiation. For example, at low Q^2, the interference between amplitudes where different constituents are struck become important. Near threshold, where charged particles emerge at low relative velocities, there are strong Coulomb distortions, as summarized by the Sommerfeld[5] factor. In QCD these have their analog in a phenomena called "jet coalescence"[6] which we discuss in a later section. The Coulomb distortion factor must be included if one wants to maintain duality between the inelastic continuum and a summation over exclusive channels in electroproduction.

My main emphasis is this talk, however, is in the study of exclusive channels in electroproduction. It is clearly interesting to study how the summation of such channels yields the total inelastic cross section. More important, each individual exclusive channel can provide detailed information on basic scattering mechanisms in QCD and how the scattered quarks and gluons recombine into hadrons. In certain cases such as Compton scattering and meson electroproduction, we can study new aspects of the light cone expansion for the product of two currents, thus extending the renormalization group analysis into a new domain.[7] The diffractive production of vector mesons at high Q^2 can test the basic composition of the Pomeron in QCD. Further, as we discuss in the next section, measuring exclusive reactions inside a nuclear target allows the study of "color transparency",[8,9] the "formation zone"[2] and other novel aspects of QCD.

Exclusive Channels in Electroproduction

In high momentum transfer inclusive reactions, the underlying quark and gluon scattering processes lead directly to jet production in the final state, To leading order in $1/Q^2$, the cross sections and jet hadronization can be understood at the probabilistic level. In contrast, in *exclusive* electroproduction processes, one studies quark and gluon scattering and their reformation into hadrons at the *amplitude* level. Exclusive reactions thus depend in detail on the composition of the hadron wavefunctions themselves.

* Work supported by the Department of Energy, contract DE-AC03-76SF00515.

There is now an extensive literature, both experimental and theoretical, describing the features of large momentum transfer exclusive reactions. The QCD predictions are based on a factorization theorem[10-14] which separates the non-perturbative physics of the hadron bound states from the hard scattering amplitude which controls the scattering of the constituent quarks and gluons from the initial to final directions. This is illustrated for the proton form factor in fig. 2. Electroproduction of exclusive channels provides one of the most valuable testing ground of this QCD formalism, since the incoming photon provides a probe of variable spacelike mass directly coupling to the hard-scattering amplitude.

It has been known since 1970 that a theory with underlying scale-invariant quark-quark interactions leads to dimensional counting rules[15] for large momentum transfer exclusive processes; e.g. $F(Q^2) \sim (Q^2)^{1-n}$ where n is the minimum number of quark fields in the hadron. QCD is such a theory; the factorization formula leads to nucleon form factors of the form:[16]

$$G_M(Q^2) = \left[\frac{\alpha_s(Q^2)}{Q^2}\right]^2 \sum_{n,m} a_{nm} \left(\ell n \frac{Q^2}{\Lambda^2}\right)^{-\gamma_n-\gamma_m} \times \left[1 + O(\alpha_s(Q)) + O\left(\frac{1}{Q}\right)\right]$$

The first factor, in agreement with the quark counting rule, is due to the hard scattering of the three valence quarks from the initial to final nucleon direction. Higher Fock states lead to form factor contributions of successively higher order in $1/Q^2$. The logarithmic corrections derive from an evolution equation[10,16] for the nucleon distribution amplitude. The γ_n are the computed anomalous dimensions, reflecting the short distance scaling of three-quark composite operators. The results hold for any baryon to baryon vector or axial vector transition amplitude that conserves the baryon helicity. Helicity non-conserving form factors should fall as an additional power of $1/Q^2$. Measurements of the transition form factor to the $J = 3/2$ $N(1520)$ nucleon resonance are consistent with $J_z = \pm 1/2$ dominance, as predicted by the helicity conservation rule.[17] It is very important to explicitly verify that $F_2(Q^2)/F_1(Q^2)$ decreases at large Q^2. The angular distribution decay of the $J/\Psi \to p\bar{p}$ is consistent with the QCD prediction $\lambda_p + \lambda_{\bar{p}} = 0$.

The normalization constants a_{nm} in the QCD prediction for G_M can be evaluated from moments of the nucleon's distribution amplitude $\phi(x_i, Q)$. There are extensive on-going theoretical efforts computing constraints on this nonperturbative input directly from QCD. The pioneering QCD sum rule analysis of Chernyak and Zhitnitskii[12] provides constraints on the first few moments of $\phi(x, Q)$. Using as a basis the polynomials which are eigenstates of the nucleon evolution equation, one gets a model representation of the nucleon distribution amplitude, as well as its evolution with the momentum transfer scale.

The QCD sum rule analysis predicts a surprising feature: strong flavor asymmetry in the nucleon's momentum distribution. The computed moments of the distribution amplitude imply that 65% of the proton's momentum in its 3-quark valence state is carried by the u-quark which has the same helicity as the parent hadron. (See fig. 3.) A recent comprehensive re-analysis by King and Sachrajda[18] has now confirmed the Chernyak and Zhitnitskii form in its essential details. In addition, Dziembowski and Mankiewicz[19] have recently shown that the asymmetric form of the CZ distribution amplitude can apparently be derived from a rotationally-invariant CM wavefunction transformed to the light cone using a Melosh-type boost of the quark spinors. The transverse size of the valence wavefunction is found to be significantly smaller than the mean radius of the proton–averaged over all Fock states. This was predicted in ref. 10. Dziembowski and Mankiewicz also show that the perturbative QCD contribution to the form factors dominates over the soft contribution (obtained by convoluting the non-perturbative wave functions) at a scale $Q/N \approx 1$ GeV, where N is the number of valence constituents. Similar criteria were also derived in ref. 20. Results of the similar Jacob and Kisslinger[21] analysis of the pion form factor are shown in fig. 4. Claims[22] that a simple overlap of soft hadron wavefunctions could fit the form factor data were based on wavefunctions which violate rotational symmetry in the CM.

A detailed phenomenological analysis of the nucleon form factors for different shapes of the distribution amplitudes has been given by Ji, Sill, and Lombard-Nelsen.[23] Their results show that the CZ wavefunction is consistent with the sign and

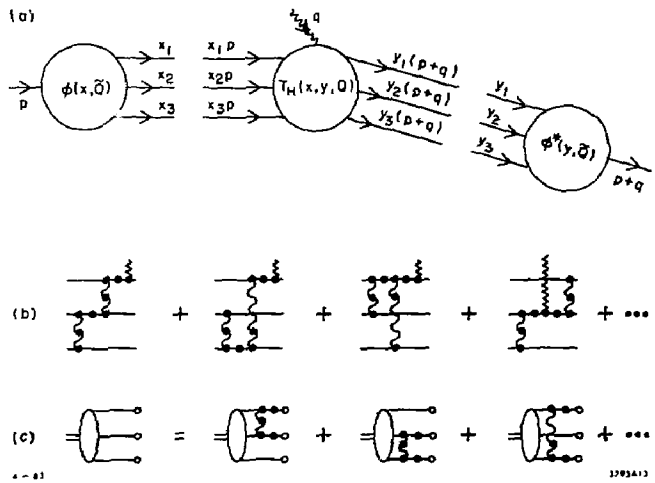

Fig. 2. Factorization of the nucleon form factor at large Q^2 in QCD.

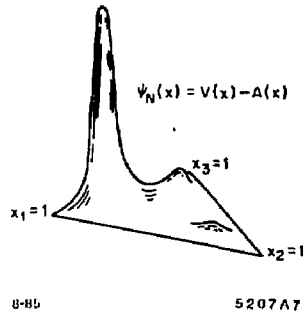

Fig. 3. QCD sum rule prediction for the proton distribution amplitude.

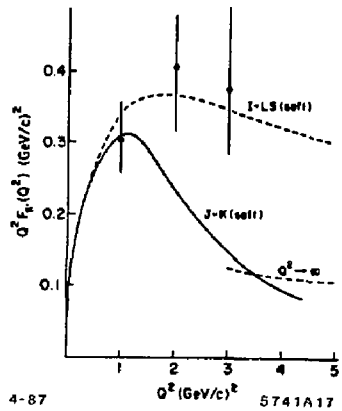

Fig. 4. Models for the "soft" contribution to the pion form factor. The Isgur-Llewellyn-Smith prediction[22] is based on a wavefunction with Gaussian fall-off in transverse momentum but power-law falloff at large x. The Jacob-Kisslinger prediction[21] is based on a rotationally symmetric form in the center of mass frame. The perturbative QCD contribution calculated with CZ[12] distribution amplitudes is consistent with the normalization and shape of the data for $Q^2 > 1$ GeV^2.

magnitude of the proton form factor at large Q^2 as recently measured by the American University/SLAC collaboration.[24] (See fig. 5.) The fact that the correct normalization emerges is a non-trivial test of the distribution amplitude shape; for example, the if the proton wavefunction has a non-relativistic shape peaked at $x_i \sim 1/3$ then one obtains the wrong sign for the nucleon form factor. Furthermore symmetrical distribution amplitudes predict a much too small magnitude for $Q^4 G_M^2(Q^2)$ at large Q^2. Gari and Stefannis[25] have developed a useful model for the nucleon form factors which incorporates the CZ distribution amplitude predictions at high Q^2 together with VMD constraints at low Q^2. Their analysis predicts sizeable values for the neutron electric form factor at intermediate values of Q^2. (See fig. 6.)

Measurements of the two-photon exclusive processes $\gamma\gamma \to \pi^+\pi^-$ and K^+K^- are in excellent agreement with the perturbative QCD predictions. The data[26] (see fig. 7) extend out to invariant mass squared 10 GeV^2, a region well beyond any significant contribution from soft contributions.

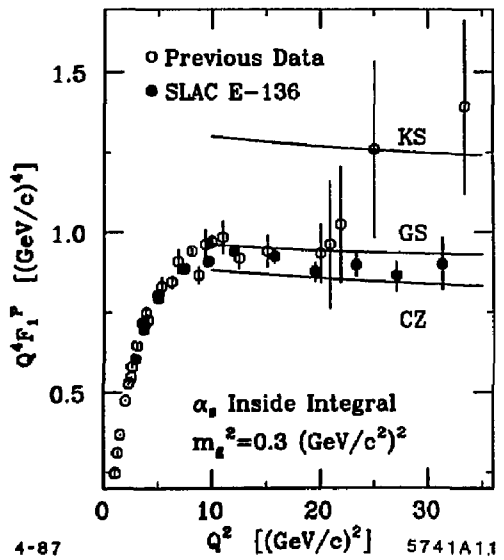

Fig. 5. Comparison of perturbative QCD predictions and data for the proton form factor. The calculation, based on the CZ QCD sum rule distribution amplitude, is from ref. 23. The prediction depends on the use of the running coupling constant as a function of the exchanged gluon momentum. The data are from ref. 24.

Nevertheless, one can question[22] with the consistency of the perturbative QCD analysis, particularly for baryon reactions at moderate momentum transfer:

1. The perturbative analysis of the baryon form factor and large angle hadron-hadron scattering depends on the suppression of the endpoint regions $x_i \sim 1$ and pinch singularity contributions. This suppression occurs automatically in QCD due to Sudakov form factors, as has been shown by Mueller[11] based on the all-orders analysis of the vertex function by Sen.[27] Since these analyses require an all-orders resummation of the vertex corrections, they cannot be derived by standard renormalization group analysis. In this sense the baryon and large angle scattering results are considered less rigorous than the results from analysis of the meson form factor and the $\gamma\gamma$ production of meson pairs.[28]
2. The magnitude of the proton form factor is sensitive to the $x \sim 1$ dependence of the proton distribution amplitude, where non-perturbative effects could be important. The CZ asymmetric distribution amplitude, in fact, emphasizes contributions from the large x region. Since non-leading corrections are expected when the quark propagator scale $Q^2(1-x)$ is small, relatively large Q^2 is required to clearly test the perturbative QCD predictions. A similar criterion occurs in the analysis of corrections to QCD evolution in deep inelastic lepton scattering. Dziembowski and Mankiewicz[19] claim that one can consistently fit low energy phenomena (the nucleon magnetic moments), the measured high momentum transfer hadron form factors, and the CZ distribution amplitudes with a self-consistent ansatz for the quark wavefunctions.

A complete derivation of the nucleon form factors at all momentum transfers would require a calculation of the entire set of hadron Fock wavefunctions. (See fig. 8.) This is the

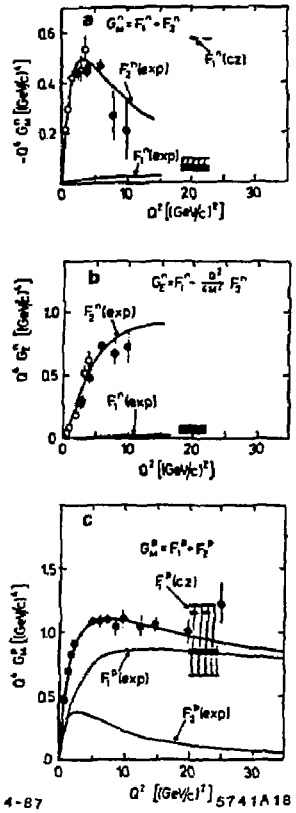

Fig. 6. Predictions for the nucleon form factors assuming VMD at low Q^2 and perturbative QCD at high Q^2. From ref. 25.

goal of the "discretized light-cone quantization" approach[29] for finding the eigen-solutions of the QCD Hamiltonian quantized at equal light cone time $\tau = t + z/c$, using a discrete basis. Thus far results have been obtained for the spectrum and wavefunctions for QED and Yukawa field theories in one-space and one-time dimension. The structure function of the lowest mass bound state in QED(1+1) as a function of a scaled coupling constant is shown in fig. 9.

Color Transparency

The QCD analysis of exclusive processes depends on the concept of a Fock state expansion of the nucleon wavefunction, projected onto the basis of free quark and gluon Fock states. The expansion is done at equal time on the light-cone and in the physical light-cone gauge. At large momentum transfer the lowest particle-number "valence" Fock component with all the quarks within an impact distance $b_\perp \leq 1/Q$ controls the form factor at large Q^2. Such a Fock state component has a small color dipole moment and thus interacts only weakly with hadronic or nuclear matter.[8,9] Thus if elastic electron-scattering is measured as a quasi-elastic process inside a nucleus, one predicts negligible final state interactions in the target as Q becomes large. Integrating over Fermi-motion, one predicts[30] that the differential cross section is additive in the number of nucleons in the nucleus. A test of this novel effect, "color transparency", has recently been carried out at

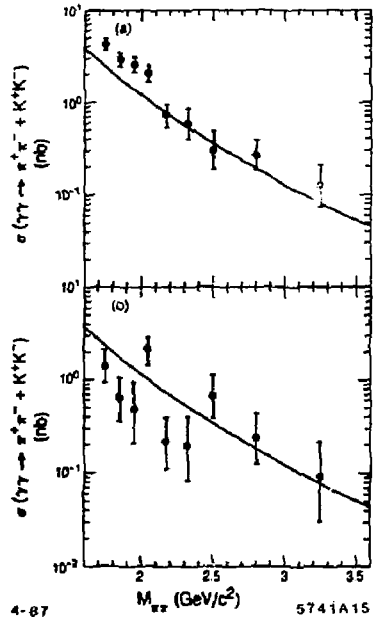

Fig. 7. Measurements[26] of exclusive two-photon reactions compared with the perturbative QCD predictions of ref. 28. The predictions are nearly independent of the shape of the meson distribution amplitudes.

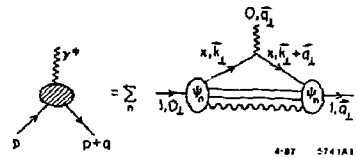

Fig. 8. Representation of electoweak hadron form factors in the light-cone formalism. The sum is over all charged quark lines and all Fock states ψ_n.

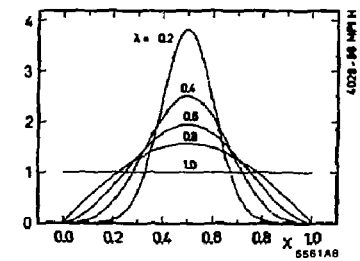

Fig. 9. The structure function of the lowest mass bound state for QED in 1+1 space-time dimensions, as calculated in the DLCQ formalism.[30]

Brookhaven for large momentum transfer elastic pp scattering in nuclear targets by a BNL-Columbia collaboration.[31] The initial results are consistent with diminished absorptive cross sections at large momentum transfer. If these preliminary results are verified they could provide a striking confirmation of the perturbative QCD predictions.

The strong spin-asymmetries seen in elastic p-p scattering[32] and the oscillations of the data modulating the predicted dimensional counting rule power-law fall-off[33] suggest possible resonant interference effects with the perturbative amplitude. [See also ref. 34.] These features evidentially cannot be explained in terms of the simplest QCD perturbative contributions.[35] (See fig. 10.) It is interesting to speculate whether one is observing an interference with pinch singularity contribution[34] or di-baryon resonances associated with the "hidden color" degrees of freedom of the six-quark state.[36] Since the resonant contributions are not coupled to small valence Fock states, one could expect significant final state corrections at energies where the resonances are important. Thus color transparency can be used to distinguish mechanisms for hadron scattering.

In the case of nucleon transition form factors measurable in inelastic electron nucleon scattering, the magnitude of the final state interactions should depend on the nature of the excited baryon. For example final state resonances which are higher orbital qqq states should have large color final state interactions.

Perhaps the most dramatic application of color transparency is to the QCD analysis of the deuteron form factor at large momentum transfer.[20,43] A basic feature of the perturbative QCD formalism is that the six-quark wavefunction at small impact separation controls the deuteron form factor at large Q^2. Thus even a complex six-quark state can have negligible final state interactions in a nuclear target–provided it is produced in a large momentum transfer reaction. One thus predicts that the "transparency ratio" $\frac{d\sigma}{dt}[eA \to ed(A-1)] / \frac{d\sigma}{dt}[ed \to ed]$ will increase with momentum transfer. The normalization of the effective number of deuterons in the nucleus can be determined by single-arm quasi-elastic scattering.

Other experimental tests of the reduced amplitude formalism are discussed in a later section.

Diffractive Electroproduction Channels

As a further example of the richness of the physics of exclusive electroproduction consider the "diffractive" channel $\gamma^* p \to \rho^0 p$. At large momentum transfer, QCD factorization for exclusive amplitudes applies, and we can write each helicity amplitude in the form:[10]

$$\mathcal{M}_{\gamma^* p \to \rho^0 p}(s,t,q^2) = \int \prod dx_i \; T_H(x_i, p_T^2, \theta_{cm}, q^2)$$

$$\times \; \phi^\dagger_{\rho^0}(x_i, p_T)\phi^\dagger_p(x_i, p_T)\phi_p(x_i, p_T) \; .$$

This represents the convolution of the distribution amplitudes $\phi(x,Q)$ for the ingoing and outgoing hadrons with the quark-gluon hard scattering amplitude $T_H(\gamma^* + (qqq)_p \to (q\bar{q})_{\rho^0} + (qqq)_p)$ for the scattering of the quarks from the initial to final hadron directions. Since T_H involves only large momentum transfer, it can be expanded in powers of $\alpha_s(Q^2)$. The distribution amplitudes $\phi(x_i, p_T)$ only depend logarithmically on the momentum transfer scale, as determined from the meson and baryon evolution equations. As we discussed above, the functional dependence of the meson and baryon distribution amplitudes can be predicted from QCD sum rules. A surprising feature of the Chernyak and Zhitnitsky analysis[12] of the distribution amplitude of helicity-zero mesons is the prediction of a double-hump shape of $\phi_M(x,Q)$ with a minimum at equal

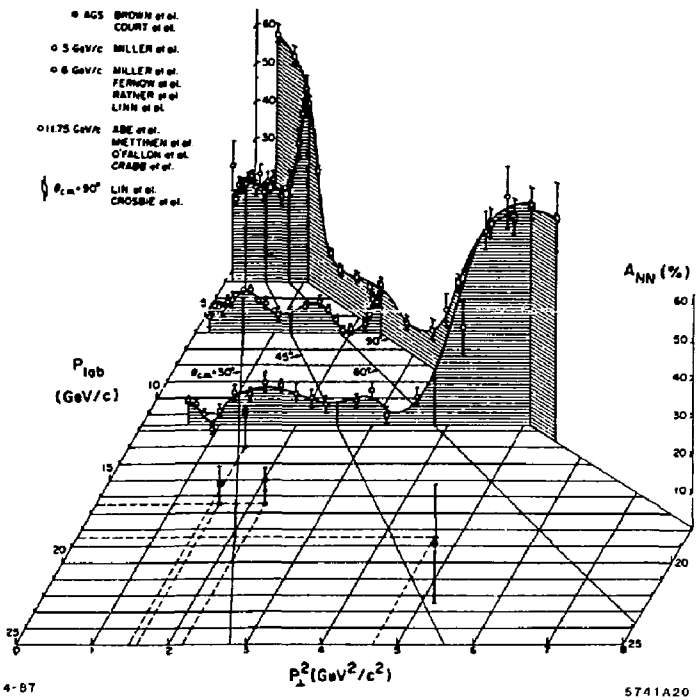

Fig. 10. Spin asymmetry for polarized pp elastic scattering. From ref. 32.

partition of the light-cone momentum fractions. (See fig. 11.) This result has now been confirmed in a lattice gauge theory calculation of the pion distribution amplitude moments by Martinelli and Sachrajda.[37] Similar conclusions also emerge from the wavefunction ansatz of Dziembowski and Mankiewicz.[19]

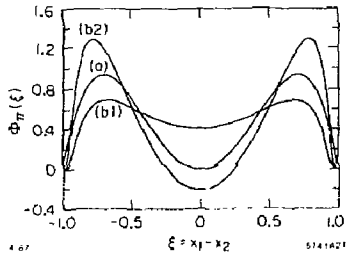

Fig. 11. Theoretical predictions for the pion distribution amplitude.

The main dynamical dependence of the electroproduction amplitude is determined by T_H. To leading order in $\alpha_s(p_T^2)$, T_H can be calculated from minimally-connected tree graphs; power counting predicts

$$T_H = \frac{c\alpha_s^3(p_T^2)}{(p_T^2)^5} f\left(\theta_{cm}, \frac{Q^2}{p_T^2}\right)$$

and thus

$$\frac{d\sigma}{dt}(\gamma^* p \to \rho p) \sim \frac{\alpha\alpha_s^6(p_T^2)}{(p_T^2)^7} F\left(\theta_{cm}, \frac{Q^2}{p_T^2}\right)$$

to leading order in $1/p_T^2$ and $\alpha_s(p_T^2)$. This prediction is consistent with the dimensional counting rule $d\sigma/dt \sim s^{2-n} f(\theta_{cm})$ where $n = 9$ is the total number of initial and final fields. The scaling laws hold for both real and virtual photons. As shown in fig. 12, the data[38] for $\gamma p \to \pi^+ n$ are consistent with the QCD scaling law prediction.

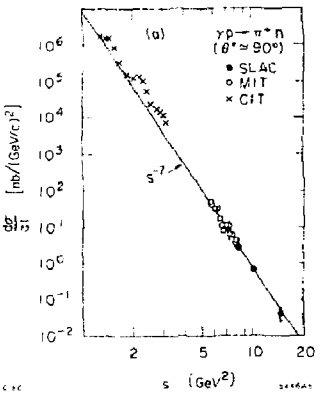

Fig. 12. Comparison of pion photoproduction data[38] at $\theta_{cm} = \pi/2$ with the quark counting rule prediction.

The leading contributions at large momentum transfer in QCD satisfy hadron helicity conservation[17]

$$\lambda_p = \lambda_{p'} + \lambda_\rho \ .$$

This selection rule is an important test of the vector coupling of the gluon in QCD. The result is independent of the photon helicity! Furthermore, the leading behavior comes from the "point-like" Fock component of the photon. The vector-meson-dominance contribution corresponds to the $q\bar{q}$ state where the constituent momenta are restricted to be collinear to the photon. This region gives a power-law suppressed $(1/p_T^2)^8$ contribution to the cross section at fixed θ_{cm}.

The dependence on the photon mass in exclusive electroproduction amplitudes in QCD occurs through the scaling variable Q^2/p_T^2. Thus for $Q^2 \ll p_T^2$, the transverse photon electroproduction amplitudes are predicted to be insensitive to Q^2. This is in striking consequence to the vector meson dominance picture, which predicts a universal $1/(1 + Q^2/m_\rho^2)$ dependence in the amplitude. Furthermore, since only the point-like component of the photon is important at large p_T, one expects no absorption of the initial state photon as it penetrates a nuclear target. The reaction $\gamma^* n \to \pi^- p$ is a particularly interesting test of color transparency since the dependence on photon mass and momentum transfer can be probed.

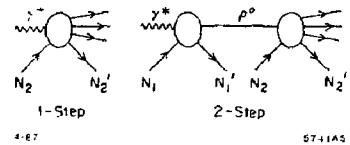

Fig. 13. Conventional description of nuclear shadowing of low Q^2 virtual photon nuclear interactions. The 2-step amplitude is opposite in phase to the direct contribution on nucleon N_2 because of the diffractive vector meson production on upstream nucleon N_1.

The conventional theory[39] of shadowing of photon interactions is illustrated in fig. 13. At large Q^2 the two-step amplitude is suppressed and the shadowing effect becomes negligible. This is the basis for a general expectation that shadowing of nuclear structure functions is actually a higher-twist phenomena, vanishing with increasing Q^2 at fixed x. [A recent analysis on shadowing in electroproduction by Qiu and Mueller[40] based on internucleon interactions in the gluon evolution equation in a nucleus suggests that shadowing is a higher twist effect, but decreases slowly as Q^2 increases.] Thus we predict simple additivity for exclusive electroproduction in nuclei

$$\overline{\frac{d\sigma}{dt}}(\gamma^* A \to \rho^0 N(A-1)) = A \frac{d\sigma}{dt}(\gamma^* N \to \rho^0 N)$$

to leading order in $1/p_T^2$. (The bar indicates that the cross sections are integrated over the nucleon Fermi motion.) This is another application of color transparency. What is perhaps surprising is that the prediction holds for small Q^2, even $Q^2 = 0$! Note that the leading contribution in $1/p_T^2$ (all orders in $\alpha_s(p_T^2)$) comes from the $\gamma \to q\bar{q}$ point-like photon coupling in T_H where the relative transverse momentum of the $q\bar{q}$ are of order p_T. Thus the "impact" or transverse size of the $q\bar{q}$ is $1/p_T$, and such a "small" color dipole has negligible strong interactions in a nucleus. The final state proton and ρ^0 also couple in leading order to Fock components which are small in impact space, again having minimal initial or final state interactions. If this additivity and absence of shadowing is verified, it will also be important to explore the onset of conventional shadowing and absorption as p_T^2 and Q^2 decrease.

Electroproduction of Diffractive Channels

Exclusive processes such as virtual Compton scattering, $\gamma^* p \to \gamma p$ and ρ^0 electroproduction $\gamma^* p \to \rho^0 p$ play a special role in QCD as key probes of "pomeron" exchange and its possible basis in terms of multiple-gluon exchange.[7] At large photon energy, the diffractive amplitudes are dominated by $J = 1$ Regge singularities.

Recent measurements of $\gamma^* p \to \rho^0 p$ by the EMC group[41] using the high energy muon beam at the SPS show three unexpected features: (1) The ρ^0 is produced with zero helicity at $Q^2 \geq 1$ GeV^2; (2) the falloff in momentum transfer becomes remarkably flat for $Q^2 \geq 5$ GeV^2; and (3) the integrated cross section falls as $1/Q^4$.

The most surprising feature of the EMC data is the very slow fall-off in t for the highest Q^2 data. (See fig. 14.) Using the parameterization $e^{bt'}$, $t' = |t - t_{min}|$, the slope for $7 \leq Q^2 \leq 25$ GeV^2, $E_L = 200$ GeV data is $b \sim 2$ GeV^{-2}. If one assumes Pomeron factorization, then the fall-off in momentum transfer to the proton should be at least as fast as the square of the proton form factor,[42] representing the probability to keep the scattered proton intact. (See fig. 15(b).) The predicted slope for $|t| < 1.5$ GeV^2 is $b \sim 3.4$ GeV^{-2}, much steeper than the EMC data. The background due to inelastic effects is estimated by the EMC group to be less than 20% in this kinematic domain.

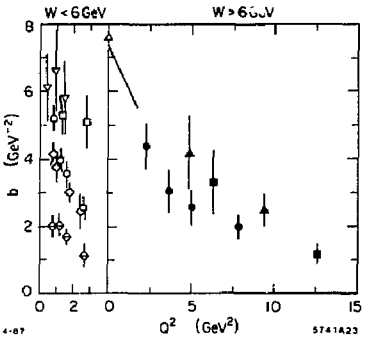

Fig. 14. The slope parameter b for the form $d\sigma/dt = Ae^{bt'}$ fit to the EMC data (ref. 41) for $\mu p \to \mu \rho^0 p$ for $|t'| \leq 1.5$ GeV^2.

In the vector meson dominance picture one expects: (1) dominantly transverse ρ polarization (s-channel helicity conservation); (2) fall-off in t similar to the square of the proton form factor (Pomeron factorization); and (3) a $1/Q^2$ asymptotic fall-off when longitudinal photons dominate.

The physics of electroproduction is quite different in QCD. At large $Q^2 \gg p_T^2$ diffractive channels take on a novel character.[7] (See fig. 15(c).) The transverse momentum k_T in the upper loop connecting the photon and ρ^0 is of order the photon mass scale, $k_T \sim Q$. (Other regions of phase space are suppressed by Sudakov form factors). Thus just as in deep inelastic inclusive scattering, the diffractive amplitude involves the proton matrix element of the product of operators near the light-cone. In the case of virtual Compton scattering $\gamma^* p \to \gamma p'$, one measures product of two electromagnetic currents. Thus one can test an operator product expansion similar to that which appears in deep inelastic lepton-nucleon scattering, but for non-forward matrix elements. In such a case the upper loop in fig. 15(c) can be calculated using perturbative methods. The ρ enters through the same distribution

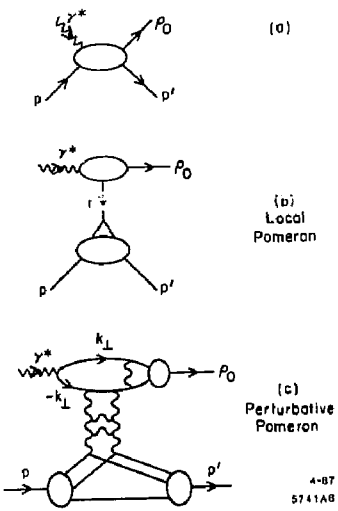

Fig. 15. (a) Diffractive electroproduction of vector mesons. (b) Local pomeron contribution coupling to one quark. (c) Perturbative pomeron contribution. For large transverse momentum $k_i^2 \approx Q^2$ two-gluon exchange contributions are dominant.

amplitude that appears in large momentum transfer exclusive reactions. Since the gauge interactions conserve helicity, this implies $\lambda_\rho = 0$, $\lambda_p = \lambda_{p'}$ independent of the photon helicity. The predicted canonical Q^2 dependence is $1/Q^4$, which is also consistent with the EMC data.

Since the EMC data is at high energy ($E_\gamma = 200$ GeV, $s \gg p_T^2$) one expects that the vector gluon exchange diagrams dominate quark-exchange contributions. One can show that the virtuality of the gluons directly coupled to the $\gamma \to \rho$ transition is effectively of order Q^2, allowing a perturbative expansion. The effect is a known feature of the higher Born, multi-photon exchange contributions to massive Bethe Heitler processes in QED.[6]

The dominant exchange in the t-channel should thus be the two-gluon ladder shown in fig. 15(c). This is analogous to the diagrams contributing to the evolution of the gluon structure function. If each gluon carries roughly half of the momentum transfer to different quarks in the nucleon, then the fall-off in t can be significantly slower than that of the proton form factor, since in the latter case the momentum transfer to the nucleon is due to the coupling to one quark. This result assumes that the natural fall-off of the nucleon wavefunction in transverse momentum is Gaussian rather than power-law at low momentum transfer.

In the case of quasi-elastic diffractive electroproduction in a nuclear target, we expect neither shadowing of the incident photon nor final state interactions of the outgoing vector meson at large Q^2 (color transparency).

Thus ρ^0 electroproduction and virtual Compton scattering can give essential information on the nature of diffractive (pomeron exchange) processes. Data at all energies and kinematic regions are clearly essential.

Exclusive Nuclear Processes in QCD

One of the most elegant areas of application of QCD to nuclear physics is the domain of large momentum transfer exclusive nuclear processes. Rigorous results have been given by Lepage, Ji and myself[43] for the asymptotic properties of the

deuteron form factor at large momentum transfer. The basic factorization is shown in fig. 16. In the asymptotic $Q^2 \to \infty$ limit the deuteron distribution amplitude, which controls large momentum transfer deuteron reactions, becomes fully symmetric among the five possible color-singlet combinations of the six quarks. One can also study the evolution of the "hidden color" components (orthogonal to the np and $\Delta\Delta$ degrees of freedom) from intermediate to large momentum transfer scales; the results also give constraints on the nature of the nuclear force at short distances in QCD. The existence of hidden color degrees of freedom further illustrates the complexity of nuclear systems in QCD. It is conceivable that six-quark d^* resonances corresponds to these new degrees of freedom may be found by careful searches of the $\gamma^* d \to \gamma d$ and $\gamma^* d \to \pi d$ channels.

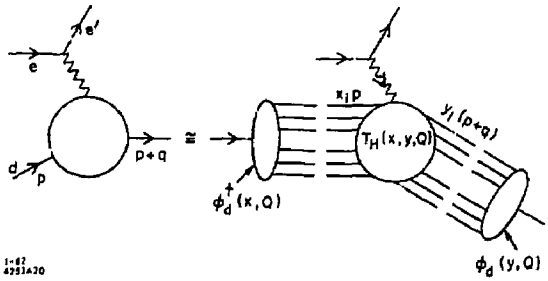

Fig. 16. Factorization of the deuteron form factor at large Q^2.

The QCD analyses suggests a consistent way to eliminate the effects of nucleon compositeness in exclusive nuclear reactions.[20,44] The basic observation is that for vanishing nuclear binding energy $\epsilon_d \to 0$, the deuteron can be regarded as two nucleons sharing the deuteron four-momentum. The $\gamma^* d \to np$ amplitude then contains two factors representing the probability amplitude for the proton and neutron to remain intact after absorbing momentum transfers

$$\hat{t} = (p_p - \tfrac{1}{2} p_d)^2 \quad \text{and} \quad \hat{u} = (p_n - \tfrac{1}{2} p_d)^2 \,.$$

The "reduced" amplitude

$$m_r(\gamma^* d \to np) = \frac{M(\gamma^* d \to np)}{F_{1N}(\hat{t}) F_{1N}(\hat{u})}$$

is predicted to have the same fixed angle scaling behavior as $\gamma^* M \to q\bar{q}$; i.e., the nucleons are reduced to point particles. We thus predict

$$\frac{\frac{d\sigma}{d\Omega_{cm}}(\gamma^* d \to np)}{F_{1N}^2(\hat{t}) F_{1N}^2(\hat{u})} \sim \frac{f(\Omega_{cm})}{(p_T^2)^2}$$

to leading order in $1/p_T^2$.

The analogous analysis (see fig. 17) of the deuteron form factor as defined in

$$\frac{d\sigma}{dt}(\ell d \to \ell d) = \left.\frac{d\sigma}{dt}\right|_{point} |F_d(Q^2)|^2$$

yields a scaling law for the reduced form factor

$$f_d(Q^2) \equiv \frac{F_d(Q^2)}{F_{1N}\left(\frac{Q^2}{4}\right) F_{1N}\left(\frac{Q^2}{4}\right)} \sim \frac{1}{Q^2}$$

i.e., the same scaling law as a meson form factor. As shown in fig. 18, this scaling is consistent with experiment for $Q^2 = p_T^2 \gtrsim 1$ GeV^2. There is also evidence for reduced amplitude scaling for $\gamma d \to pn$ at large angles and $p_T^2 \gtrsim 1$ GeV^2. (see fig. 19). We thus expect similar precocious scaling behavior to hold for $\bar{p}d \to \pi^- p$ and other $\bar{p}d$ exclusive reduced amplitudes. In each case the incident and outgoing hadron and nuclear states are predicted to display color transparency, i.e. the absence of initial and final state interactions if they participate in a large momentum transfer exclusive reaction.

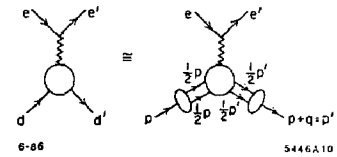

Fig. 17. Application of the reduced amplitude formalism to the deuteron form factor at large momentum transfer.

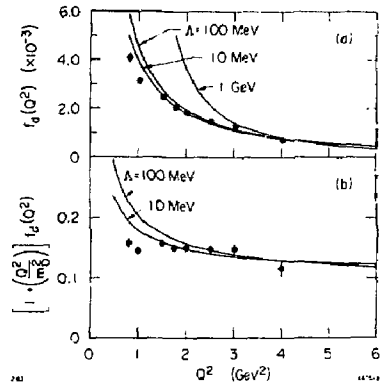

Fig. 18. Scaling of the deuteron reduced form factor. The data are summarized in ref. 20.

Electroproduction: A General View

The factorization formula[45]

$$\frac{d\sigma(AB \to CX)}{d^3p_c/E_c} \cong \sum_{ab,cd} \int_0^1 dx_a \int_0^1 dx_b \int_0^1 \frac{dx_c}{x_c^2}$$

$$\times G_{a/A}(x_a,Q) G_{b/B}(x_b,Q) \widetilde{G}_{C/c}(x_c,Q)$$

$$\times \delta(s' + t' + u') \frac{s'}{\pi} \frac{d\sigma}{dt'}(ab \to cd)$$

for the inclusive production processes $AB \to CX$ has general validity in gauge theory. The systems A, B, C can be leptons, photons, hadrons, or nuclei. The primary subprocess in electroproduction is $eq \to eq$. The electron structure function $G_{e/e}(x,Q)$ automatically provides the (leading logarithmic) QED radiative corrections. The energy distribution of the beam itself plays the role of the non-perturbative or initial structure function. (See fig. 20(b).) The subprocess $\gamma^* q \to gq$ corresponds to photon-induced two-jet production. (See fig. 20(a).) This subprocess dominates reactions in which

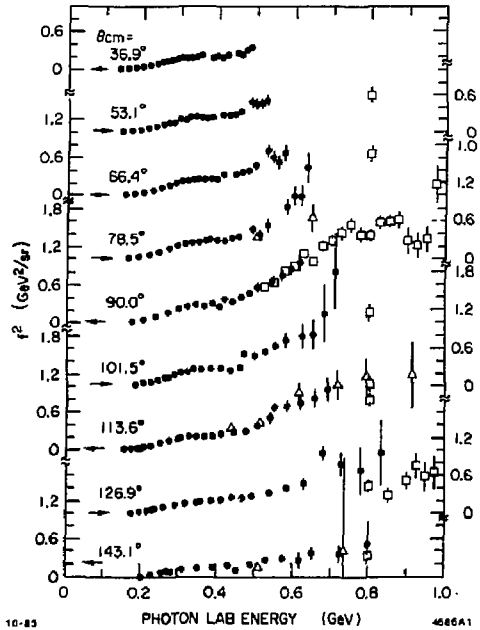

Fig. 19. Scaling of the reduced amplitude for deuteron electrodisintegration. The data are summarized in ref. 44.

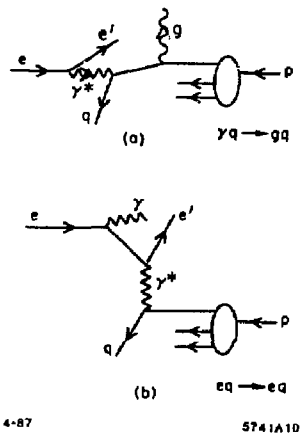

Fig. 20. Application of gauge theory factorization to electroproduction. (a) The $\gamma q \to gq$ subprocess produces hadron jets at high p_T. (b) The $eq \to eq$ produces one quark jet and one recoil electron jet at high p_T. The QED radiative corrections are incorporated into the electron and photon QED structure functions.

the large transverse momentum trigger is a hadron rather than the scattered lepton. Thus one sees that conventional deep inelastic $eq \to eq$ scattering subprocess is just one of the several modes of electroproduction.

The dominant contribution to the meson semi-inclusive cross section is predicted by QCD factorization to be due to jet fragmentation from the recoil quark and spectator diquark jets. When the momentum transfer is in the intermediate range $1 \lesssim Q^2 \lesssim 10$ GeV^2, several other contributions for meson production are expected to become important in $eN \to e'MX$. These include:

(1) Higher twist contributions to jet fragmentation:

$$\frac{dN_\pi}{dz} = D_{\pi/q}(z,Q^2) \cong A(1-z)^2 + \frac{C}{Q^2} \qquad (z \to 1)\ .$$

The scaling term reflects the behavior of the pion fragmentation function at large fractional momentum ($z \to 1$) as predicted by perturbative QCD (one-gluon exchange). (See fig. 21(a).) The C/Q^2 term[46] is computed from the same perturbative diagrams. For large z where this term dominates, we predict that the deep inelastic cross section will be dominantly longitudinal rather than transverse $R = \sigma_L/\sigma_T > 1$.

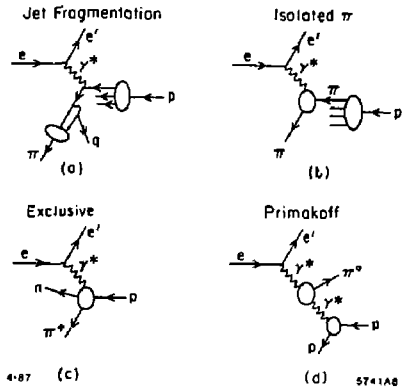

Fig. 21. QCD contributions to pion electroproduction. (a) Jet fragmentation, including leading and $1/Q^2$ higher twist contributions. (b) Isolated pion contributions at order $1/Q^4$. (c) Exclusive production. (d) Primakoff contribution.

(2) "Direct" meson production. Isolated pions may also be created by elastic scattering off of an effective pion current: (See fig. 21(b).)

$$\frac{d\sigma}{dQ^2 dx_\pi} = G_{\pi/p}(x_\pi)\ \left.\frac{d\sigma}{dQ^2}\right|_{e\pi\to e\pi}$$

$$\left.\frac{d\sigma}{dy dQ^2}\right|_{e\pi\to e\pi} = \frac{4\pi\alpha^2}{(Q^2)^2}\ |F_\pi(Q^2)|^2(1-y)\ .$$

Here $y = q\cdot p/p_e\cdot p$. In the case of a nuclear target, one can test for non-additivity of virtual pions due to nuclear effects, as predicted in models[47] for the EMC effect[41] at small x_{Bj}. Jaffe and Hoodbhoy[48] have shown that the existence of quark exchange diagrams involving quarks of different nucleons in the nucleus invalidates general applicability of the simplest convolution formulae conventionally used in such analyses. The $G_{\pi/p}(x,Q)$ structure function is predicted to behave roughly as $(1-x)^5$ at large x, as predicted from spectator quark counting rules.[15,45] Applications of these rules to other off-shell nucleon processes are discussed in refs. 20 and 49.

(3) Exclusive Channels. (See fig. 21(c).) The mesons can of course be produced in exclusive channels; e.g. $\gamma^* p \to \pi^+ n$, $\gamma^* p \to \rho^0 p$. Pion electroproduction extrapolated to $t = m_\pi^2$ provides our basic knowledge of the pion form factor at spacelike Q^2. With the advent of the perturbative QCD analyses of

large momentum transfer exclusive reactions, predictions can be given over the whole range of large t and Q^2. We discussed some of the features of ρ^0 electroproduction above.

(4) Another possible meson production channel is Primakoff production $\gamma^*\gamma \to \pi^0$, etc., identifiable from very low target recoil events. (See fig. 21(d).) Such measurements would allow the determination of the $\gamma \to \pi^0$ transition form factor. This quantity, combined with the QCD analysis of the pion form factor leads to a method to determine the QCD running coupling constant $\alpha_s(Q^2)$ solely from exclusive measurements.[28]

The above examples make it clear that complete final state measurements are necessary for separating the various production channels; detailed study of meson electroproduction can yield valuable information concerning basic issues in QCD.

Higher Twist Contributions to Deep Inelastic Scattering

One of the most difficult aspects of electroproduction phenomenology is the separation of logarithmic scaling violations predicted by QCD evolution from the scale violations induced by power law corrections. The lack of a full understanding of these higher twist terms has prevented the extraction of reliable values of the QCD scale Λ_{QCD} from the data. As we have noted above, shadowing behavior in nuclei is likely associated with higher twist contributions. In addition, it is not clear whether ordinary Regge behavior of the inelastic lepton scattering cross section, which is a valid parameterization at fixed Q^2, persists into the scaling region or whether it is associated with higher twist dynamical effects. The fact that the non-singlet structure functions obey additive sum rules suggests that Regge behavior is absent in leading twist.

In some cases the higher twist effect corresponds to coherent many-particle processes which potentially could be identified by study of the final state. As an example, consider the processes illustrated in fig. 22. At intermediate Q^2 and $x = x_{Bj} \sim 1$ the cross section has the simplified form

$$\frac{d\sigma}{dQ^2 dx} \simeq \frac{4\pi\alpha^2}{Q^4}\left[A(1-x)^3 + B(1-x)\left(\frac{1}{Q^2}\right)^2 + C(1-x)^{-1}\left(\frac{1}{Q^2}\right)^4\right].$$

The three terms correspond to lepton scattering off of one, two, or three quarks, respectively. The power in $1/Q^2$ increases with the number of active quarks: $(Q^2)^{2(n_A-1)}$ The power in $(1-x)$ counts the number of spectators required to stop as $x \to 1$: $(1-x)^{2n_s-1}$. The "diquark" term gives a large σ_L contribution.[46] The analogous structure in the pion structure function has been confirmed in the Drell-Yan reaction $\pi N \to \mu^+\mu^- X$ at large x.[46] The relative normalization of the power-law suppressed terms is uncertain, although the model calculations based on tree-graph gluon exchange diagrams performed by Blankenbecler, Gunion, and Nason[50] suggests very large coefficients B and C. If this is true for the physical situation, then the existence of such terms would make it very difficult to isolate the logarithmic corrections to scaling, except at very high momentum transfers–where unfortunately the sensitivity to the numerical value of Λ_{QCD} is small. Internal target experiments may be able to confirm the different contributions by studies of the recoil and spectator systems as functions of Q^2 and x together with separation of σ_L and σ_T.

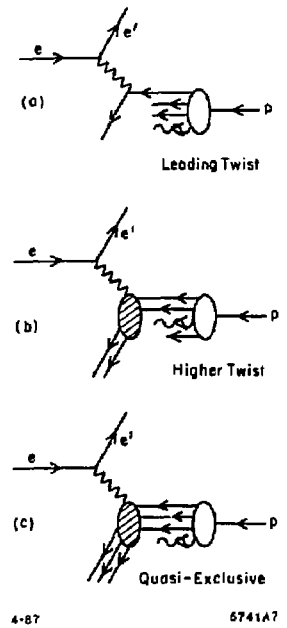

Fig. 22. Leading and higher twist contributions to deep inelastic lepton scattering due to multiparticle hard scattering subprocesses.

Formation Zone Phenomena in Deep Inelastic Scattering

One of the remarkable consequences of QCD factorization for inclusive reactions at large p_T is the absence of inelastic initial or final state interactions of the high energy particles in a nuclear target. Since structure functions measured in deep inelastic lepton scattering are essentially additive (up to the EMC deviations), factorization implies that the $q\bar{q} \to \mu^+\mu^-$ subprocesses in Drell-Yan reactions occurs with equal effect on each nucleon throughout the nucleus. At first sight this seems surprising since one expects energy loss from inelastic initial state interactions.

In fact, potential inelastic reactions such as quark or gluon bremsstrahlung induced in the nucleus which could potentially decrease the incident parton energy (illustrated in fig. 23) are suppressed by coherence if the quark or gluon energy (in the laboratory frame) is large compared to the target length:

$$E_q > \mu^2 L_A$$

Here μ^2 is the difference of mass squared that occurs in the initial or final state collision. This phenomenon has its origin in studies of QED processes by Landau and Pomeranchuk. The QCD analysis is given by Bodwin, Lepage and myself.[2] Elastic collisions, however, are still allowed, so one expects collision broadening of the initial parton transverse momentum. Recent measurements of the Drell-Yan process $\pi A \to \mu^+\mu^- X$ by the NA-10 group[51] at the CERN-SPS confirm that the cross section for muon pairs at large transverse momentum is increased in a tungsten target relative to a deuteron target. (See fig. 24). Since the total cross section for lepton-pair production scales linearly with A (aside from relatively small EMC-effect corrections), there must be a corresponding decrease of the ratio

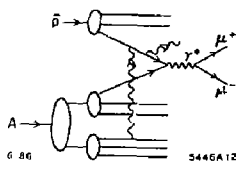

Fig. 23. Induced radiation from the propagation of an anti-quark through a nuclear target in massive lepton production. Such inelastic interactions are coherently suppressed at parton energies large compared to a scale proportional to the length of the target.

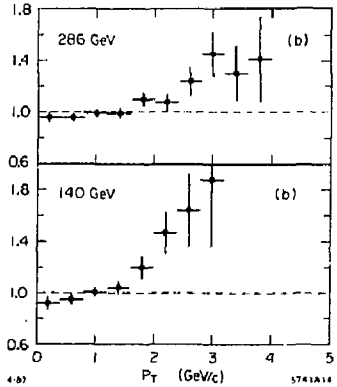

Fig. 24. The ratio $\sigma(\pi^- W \to \mu^+\mu^- X)/\sigma(\pi^- D \to \mu^+\mu^- X)$ as a function of the pair transverse momentum. From ref. 51.

of the differential cross section at low values of the di-lepton transverse momentum. This is also apparent in the data.

These results have striking implications for the interaction of the recoil quark jet in deep inelastic electron-nucleus scattering. For the quark (and gluons) satisfying the length condition, there should be no extra radiation induced as the parton traverses the nucleus. Thus gluon radiation of the type illustrated in fig. 25 should be suppressed. However, low energy gluons, emitted in the deep inelastic electron-quark collision, can suffer radiative losses, leading to cascading of soft particles in the nucleus. It is clearly very important to study this phenomena as a function of recoil quark energy and nuclear size.

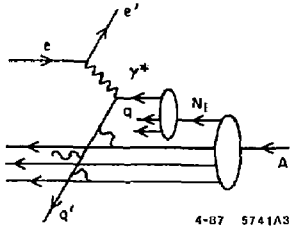

Fig. 25. Propagation of the struck quark through a nuclear target. Induced gluon radiation (inelastic final state interactions) is suppressed at high quark energies. Elastic scattering in the final state however is not suppressed.

It should be emphasized that the absence of inelastic initial or final state collisions for high energy partons does not preclude collision broadening due to elastic initial or final state interactions. The elastic corrections are unitary to leading order in $1/Q$ and do not effect the normalization of the deep inelastic cross section. Thus we predict that the mean square transverse momentum of the recoil quark and its leading particles will increase as $A^{1/3}$.

The transverse momentum of the recoil quark reflects the intrinsic transverse momentum of the nucleon wavefunction. The EMC effect[41] implies that quarks in a nucleus have smaller average longitudinal momentum than in a nucleon. (See fig. 26.) Independent of the specific physical mechanism underlying the EMC effect, the quarks in a nucleus would also be expected to have smaller transverse momentum. This effect can counteract to a certain extent the collision broadening of the outgoing jet.

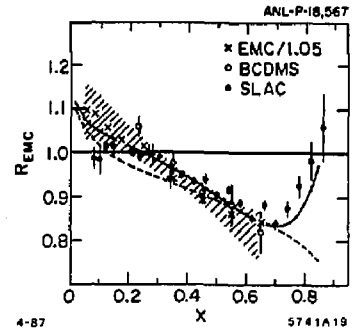

Fig. 26. Ratio of nuclear and nucleon structure functions. The theoretical curves are from the pion current calculation of Berger and Coester, ref. 47.

Unlike the struck quark the remnant of the target system does not evolve with the probe momentum Q. However, since the quantum numbers of the spectator system is $\bar{3}$ in color, nonperturbative hadronization must occur. Since the transverse momentum of the leading particles in the spectator jet is not affected by the QCD radiative corrections, it more closely reflects the intrinsic transverse momentum of the hadron state.

It is also interesting to study the behavior of the transverse momentum of the quark and spectator jets as a function of x_{Bj}. For $x_{Bj} \sim 1$, the 3-quark Fock state dominates the reaction. If the valence state has a smaller transverse size[10] than that of the nucleon, averaged over all of its Fock components, then we expect an increase of $\langle k_1^2 \rangle$ in that regime. Evidence for a significant increase of $\langle k_1^2 \rangle$ in the projectile fragmentation region at large quark momentum fractions has been reported by the SFM group[52] at the ISR for $pp \to$ dijet $+X$ reactions.

Diffraction Channels and Nuclear Structure Function Non-Additivity

One unusual source of non-additivity in nuclear structure functions (EMC effect) are electroproduction events at large Q^2 and low x which nevertheless leave the nucleus completely intact $x < (1/ML_A)$. In the case of QED, analogous processes such as $\gamma^* A \to \mu^+\mu^- X$ yield nuclear-coherent contributions which scales as $A_{eff} = Z^2/A$. (See fig. 27(a).) Such processes contribute to the Bjorken-scaling, leading-twist cross section.[53] In QCD we expect[54] the nuclear dependence to be less than additive for the analogous gluon exchange contributions (see fig. 27(b)) because of their diffractive coupling to the nucleus. One can identify nuclear-coherent events contributions by observing a rapidity gap between the produced particles and the

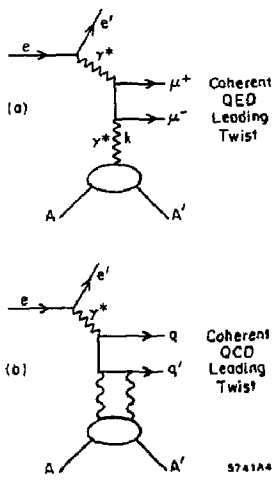

Fig. 27. Leading twist contributions to deep inelastic lepton-nucleus scattering that leave the target intact. (a) QED example. (b) QCD example.

recoiling target. An interesting question is how the gluon momentum fraction sum rule is modified by the diffractive contributions.

Studying "Jet-Coalescence" in Electroproduction

What happens if two jets overlap in phase-space? Certainly independent fragmentation of the jets will fail because of coherent effects. For example, in QED there are strong final state interactions when two charged particles are produced at low relative velocity. In the case of particles of opposite charge $Z_1e, -Z_2e$, the QED Born cross sections are corrected by the factor[5] :

$$\sigma = \sigma_0 \frac{2\pi Z_1 Z_2 \alpha/v}{1 - exp(2\pi Z_1 Z_2 \alpha/v)}$$

which increases the cross section dramatically at low relative velocity v. We expect similar effects in QCD when two jets can coalesce to attractive color channels ($Z_1 Z_2 \alpha \to C_F \alpha_s$ for $q\bar{q}$ color singlets). In the case of electroproduction, the low relative velocity enhancements provide a simple estimate of the increase of the $ep \to eX$ cross section at low values of $W^2 = (q+p)^2$, beyond that given by simple duality arguments.

Gunion, Soper and I[6] have recently proposed this jet coalescence mechanism as an explanation of the observed leading particle correlations seen in charm hadroproduction experiments and the anomalously large cross section[55] observed at the SPS for $\Sigma^- N \to A^+(esu)X$ at large x_L. [The hyperon momentum was 135 GeV/c.] In the case of heavy quark electroproduction *e.g.* $\gamma^* g \to s\bar{s}, c\bar{c}$, one predicts an enhancement of the cross section when the produced quark is at low rapidity relative to the target fragmentation region. The correction to the rate, integrated over relative rapidity, is found to vanish only as a single inverse power of the heavy quark mass, and thus may give significant corrections to charm production rates and distributions.

Summary

Electroproduction at intermediate energies on an internal target in a storage ring such as PEP could allow the study of many fundamental phenomena in QCD:

(a) A primary goal is the channel-by-channel reconstruction of the final state in electroproduction in order to understand in detail the final state hadronization of both the quark and nucleon spectator jets in a regime where Bjorken scaling is manifest. Such studies can also provide checks on the effect of the higher-twist coherent contributions to electroproduction cross sections. The hadronization of the target jet is a still largely unexplored phenomenon.

(b) The dynamics of individual exclusive electroproduction amplitudes can be probed as a function of all kinematic energy and angle variables including the virtual photon's mass and polarization. As we have discussed here, such processes can often be analyzed systematically in perturbative QCD, providing detailed checks on both QCD dynamics and hadron wavefunctions. The diffractive reactions also allow the study of the non-forward matrix elements of the same operator product entering the near the light-cone analysis of deep inelastic structure functions.

(c) A nuclear target provides a unique probe of short-distance QCD dynamics. The basic subprocesses can be studied in a background nuclear field. In particular, one wants to study the sources of nonadditivity in the nuclear target channel by channel. This includes tests of various shadowing mechanisms, effects of modification of mesonic degrees of freedom, the predicted "color transparency" of quasi-exclusive amplitudes at large momentum transfer inside a nucleus, and the propagation of quark jets through the nuclear medium. Further, as discussed in ref 20, one can use large x measurements to probe nuclear matter in the far off-shell domain. We also note that exclusive channels which involve the scattering of light nuclei at high momentum transfer probe the NN interaction at short distances.

(d) Given sufficient luminosity, internal target experiments could allow the study of strange and charm particle electroproduction near threshold. By comparing electron and positron beam experiments, one can probe[1] virtual Compton scattering; the sum of the quark charges cubed can be obtained from the ratio of the $e^{\pm}p \to e^{\pm}\gamma + X$ cross sections. Polarized proton and nuclear targets allow the study of detailed effects of spin via correlations with final state properties. The combination of polarized target and polarized electron beams allow measurements of the spin dependent structure functions and their sum rules,[56] checks of helicity selection rules, and the separation of different electroproduction channels.

Although there has been extensive of many aspects of electroproduction over the past decade, there are still many phenomena not fully explored. The distinction between logarithmic and power-law scale breaking effects is still in a confused state. Shadowing, diffraction, the interrelation with vector meson dominance, the structure of the (non-evolved) spectator jet system, Regge behavior in non-singlet structure functions, and other phenomena at the boundary between perturbative and non-perturbative effects, all are central topics in hadron and nuclear dynamics, ideally studied in electroproduction.

References

1. S.J. Brodsky, J.F. Gunion and R.L. Jaffe Phys. Rev. **D6**, 2487 (1972).
2. S.J. Brodsky, G.T. Bodwin and G.P. Lepage, in the Proc. of the Volendam Multipart. Dyn. Conf., 1982, p. 841; Proc. of the Banff Summer Inst., 1981, p. 513. This effect is related to the formation zone principle of L. Landau and I. Pomeranchuk, Dok. Akademii Nauk SSSR **92**, 535,735 (1953).
3. G.T. Bodwin, Phys. Rev. **D31**, 2616 (1985); G.T. Bodwin, S.J. Brodsky and G.P. Lepage, ANL-HEP-CP-85-32-mc (1985), presented at 20th Rencontre de Moriond, Les Arcs, France, March 10-17, 1985.
4. E. Berger, ANL-HEP-PR-87-45 and references therein.

5. A. Sommerfeld, *Atombau and Spektallinen* (Vieweg, Braunschweig, 1939).
6. S.J. Brodsky, J.F. Gunion and D. Soper, SLAC-PUB-4193 (1987).
7. S.J. Brodsky and A.H. Mueller, in preparation.
8. A.H. Mueller, Proc. of the Moriond Conf., 1982.
9. S.J. Brodsky, XIII Int. Symp. on Multiparticle Dynamics, 1982.
10. G.P. Lepage and S.J. Brodsky, Phys. Rev. **D22**, 2157 (1980); G.P. Lepage, S.J. Brodsky, T. Huang and P.B. Mackenzie, CLNS-82/522, published in the Proc. of the Banff Summer Institute, 1981.
11. A.H. Mueller, Phys. Rept. **73**, 237 (1981).
12. V.L. Chernyak and I.R. Zhitnitskii, Phys. Rept. **112**, 1783 (1984); Xiao-Duang Xiang, Wang Xin-Nian and Huang Tao, BIHEP-TH-84, 23 and 29 (1984).
13. A.V. Efremov and A.V. Radyushkin, Phys. Lett. **94B**, 245 (1980).
14. S.J. Brodsky, Y. Frishman, G.P. Lepage and C. Sachrajda, Phys. Lett. **91B**, 239 (1980).
15. S.J. Brodsky and G.R. Farrar, Phys. Rev. Lett. **31**, 1153 (1973); Phys. Rev. **D11**, 1309 (1975).
16. S.J. Brodsky and G.P. Lepage, Phys. Rev. **D23**, 1152 (1981); S.J. Brodsky, G.P. Lepage and S.A.A. Zaidi, Phys. Rev. **D23**, 1152 (1981).
17. S.J. Brodsky and G.P. Lepage, Phys. Rev. **D24**, 2848 (1981).
18. I.D. King and C.T. Sachrajda, SHEP-85/86-15 (1986), p. 36.
19. Z. Dziembowski and L. Mankiewicz, Warsaw University preprint (1986).
20. S.J. Brodsky and B.T. Chertok, Phys. Rev. Lett. **37**, 269 (1976); Phys. Rev. **D114**, 3003 (1976).
21. O.C. Jacob and L.S. Kisslinger, Phys. Rev. Lett. **56**, 225 (1986).
22. N. Isgur and C.H. Llewellyn Smith, Phys. Rev. Lett. **52**, 1080 (1984).
23. C-R Ji, A.F. Sill and R.M. Lombard-Nelsen, SLAC-PUB-4068 (1986).
24. R.G. Arnold *et al.*, SLAC-PUB-3810 (1986).
25. M. Gari and N. Stefanis, Phys. Lett. **B175**, 462 (1986), M. Gari and N. Stefanis, preprint RUB-TPII-86-21 (1986).
26. J. Boyer *et al.*, Phys. Rev. Lett. **65**, 207 (1986).
27. A. Sen, Phys. Rev. **D24**, 3281 (1981).
28. S.J. Brodsky and G.P. Lepage, Phys. Rev. **D24**, 1808 (1981). The next to leading order evaluation of T_H for these processes is given by B. Nezic, Ph.D. Thesis, Cornell Univ. (1985).
29. H.C. Pauli and S.J. Brodsky, Phys. Rev. **D32**, 1993 (1985); Phys. Rev. **D32**, 2001 (1985).
30. T. Eiler, H.C. Pauli and S.J. Brodsky, Phys. Rev. **D35**, 1493 (1987).
31. S. Heppelmann, DPF Meeting, Salt Lake City (1987).
32. A.D. Krisch, UM-HE-86-39 (1987).
33. A.W. Hendry, Phys. Rev. **D10**, 2300 (1974).
34. J.P. Ralston and B. Pire, Phys. Rev. Lett. **57**, 2330 (1986).
35. S.J. Brodsky, C.E. Carlson and H.J. Lipkin, Phys. Rev. **D20**, 2278 (1979); H.J. Lipkin, private communication.
36. C.-R. Ji and S.J. Brodsky, Phys. Rev. **D34**, 1460; **D33**, 1951; **D33**, 1406; **D33**, 2653 (1986); Phys. Rev. Lett. **55**, 2257 (1985).
37. G. Martinelli and C.T. Sachrajda, CERN-TH-4637/87 (1987). The results are based on the method of S. Gottlieb and A.S. Kronfeld, Phys. Rev. **D33**, 227 (1986); A.S. Kronfeld and D.M. Photiadis, Phys. Rev. **D31**, 2939 (1985).
38. R.L. Anderson *et al.*, Phys. Rev. Lett. **30**, 627 (1973).
39. S.J. Brodsky and J. Pumplin, Phys. Rev. **182**, 1794 (1969); S.J. Brodsky, F.E. Close and J.F. Gunion, Phys. Rev. **D6**, 177 (1972).
40. A.H. Mueller and J. Qui, Nucl. Phys. **B268**, 427 (1986); J. Qui, preprint CU-TP-361.
41. J.J. Aubert *et al.*, Phys. Lett. **123B**, 275 (1983); For a recent review see E.L. Berger and F. Coester, ANL-HEP-PR-87-13 (to be published in Ann. Rev. of Nucl. Part. Sci.).
42. A. Donnachie and P.V. Landshoff, Phys. Lett. **185B**, 403 (1987).
43. S.J. Brodsky, C.-R. Ji and G.P. Lepage, Phys. Rev. Lett. **51**, 83 (1983).
44. S.J. Brodsky and J.R. Hiller, Phys. Rev. **C28**, 475 (1383).
45. J.F. Gunion, S.J. Brodsky and R. Blankenbecler, Phys. Rev. **D8**, 287 (1973); Phys. Lett. **39B**, 649 (1972); D. Sivers, S.J. Brodsky and R. Blankenbecler, Phys. Reports **23C**, 1 (1976). Extensive references to fixed angle scattering are given in this review.
46. E.L. Berger and S.J. Brodsky, Phys. Rev. **D24**, 2428 (1981).
47. E.L. Berger and F. Coester, ANL-HEP-PR-87-13 (1987).
48. P. Hoodbhoy and R.L. Jaffe, Phys. Rev. **D35**, 113 (1987); R.L. Jaffe, CTP #1315 (1985).
49. L.A. Schmidt and R. Blankenbecler, Phys. Rev. **D15**, 3321 (1977).
50. J.F. Gunion, P. Nason and R. Blankenbecler, Phys. Rev. **D29**, 2491 (1984); Phys. Lett. **117B**, 353 (1982).
51. K. Freudenreich, Zurich, NA-10 collaboration.
52. H.G. Fischer, presented at the Leipzig Conference, 1984.
53. G. Alexander, E. Gotsman and U. Maor, Phys. Lett. **161B**, 384 (1985).
54. S.J. Brodsky and M. Soldate, unpublished.
55. S.F. Biagi *et al.*, Z. Phys. **C28**, 175 (1985).
56. R.L. Jaffe, MIT-CTP-1445 (1987).

A SPACE-TIME ANALYSIS OF MUO-PRODUCED HADRONIC SHOWERS

Jorge G. Morfín
Fermi National Laboratory
Batavia, IL 60510

Abstract

Hadron showers, produced by high energy muons interacting on various targets, have been analysed for evidence of a space-time structure of parton fragmentation by the European Muon Collaboration. Target-dependent multiplicity ratios and Bose-Einstein interference phenomena both yield information on this subject

Introduction

What I will be discussing in this presentation is the latest step in the process which has taken the concept of partons from being a theoretical explanation[1] for a surprising experimental result to a particle in its own right. While it is true that the unconfined parton has not yet been detected, the characteristics of the parton have been fairly well defined through experimentation[2]. By studying the space-time development of a high energy muo-produced hadron shower, we are trying to answer two more fundamental questions about the nature of the quark. First, what is the quark-nucleon crosssection? Second, when does the struck quark start fragmenting into hadrons? Since the relevant distances and time intervals will turn out to be relatively large we will have opportunity to briefly look at the problem of quark confinement. Furthermore, we will see that a study of nuclear effects becomes not only very intriguing but crucial to answering the above two questions. As experimental references I will concentrate on the results of the European Muon Collaboration (EMC), which used muons of energy 100 - 300 GeV on various targets, and the Tevatron Muon Experiment[3] (TMC), scheduled to start running this spring at Fermi National Laboratory with 600 GeV muons. It is not coincidental that the primary goal of the TMC is a high statistics analysis of these nuclear effects.

Experimentally we are trying to determine what happens between the time a muon is detected as entering the experimental target and a shower of hadrons emerges. The process can be divided into three stages:

1. The muon transfers a fraction of its energy to a parton.
2. The parton travels through the nuclear medium and hadronizes.
3. The hadrons continue the passage through the target material and emerge.

Stage 1 covers such topics as the hadronic nature[4] of the photon which mediates the deep inelastic interactions (to be covered in these proceedings by T. Sloan) and the measurement of the nucleon structure function[5]. These results tell us the probability with which we will interact with a quark of a given flavor and what fraction of the total nucleon's momentum will be carried by the quark. Stage 3 has been studied for many years and is covered well by references[6] dealing with the passage of a particle through matter. Naturally stage 3 phenomena also includes hard final state scatters which would take us back to stage 2 ... etc.

Kinematics

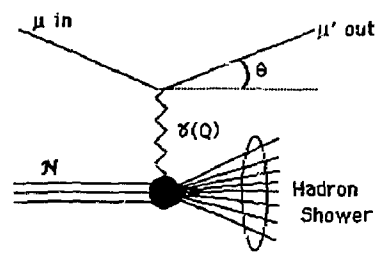

Fig 1. Feynman Graph representation of deep inelastic muon scattering

In discussing the phenomena of deep inelastic scattering, there are standard kinematic variables that are most helpful in characterising the interaction. If the incoming muon has energy E

while the scattered muon has energy E' and scattering angle θ then the amount of 4-momentum transferred to the struck quark is:

$$Q^2 = 4EE'\sin^2\theta/2 = -q^2$$

and the transferred energy is

$$\upsilon = E - E' .$$

The ratio of the 4-momentum transferred to the energy transferred is a measure of the fraction of the total nucleon momentum carried by the struck quark, as first formulated by Bjorken:

$$x_{Bj} = Q^2 / 2M\upsilon.$$

The hadronic shower is described by the effective mass of the shower

$$W^2 = M^2 + 2M\upsilon - Q^2,$$

and individual hadrons within the shower are characterized by the ratio of the hadron's energy to the total energy transferred to the hadron system

$$z = p / p_{max} = E_h / \upsilon.$$

Finally, Feynman-x relates a hadron's 3-momenta to the 3-momentum of the photon propagator, and the rapidity of a hadron is a measure of it's direction relative to the photon propagator's direction:

$$x_F = \frac{P_L^*}{(P_L^*)_{max}}$$

$$Y = 0.5 \ln \frac{E + P_L}{E - P_L}$$

Survey of Theoretical Ideas: A-Dependent Multiplicity Distributions

The significance of a space-time analysis of high energy processes as well as the basic ideas were summarized by Bjorken[7] in several fundamental reports from the mid 70's. He pointed out the importance of long time intervals and large distances which had been hinted at earlier by Landau and colleagues[8]. At the time, the emission of hard hadrons was postulated to be a tail effect of a bremsstrahlung-type process of soft hadron emission. In this case, the distance required for the hadron to form in the lab is simply the time/distance for the quark to fragment to the hadron in the quark rest frame - a distance of $\approx 1/m_h$ - boosted by its Lorentz factor (E_h / m_h) into the lab. This hypothesis was consistent with the observed[9] absence of intra-nuclear cascading of high energy hadrons since if E_h / m_h^2 > nuclear size, the hadron is **formed outside of the nuclear matter.**

A series of increasingly complex models followed these early concepts. They attempt to describe the behavior of leading hadrons with large z (or x_F):

Dar and Takagi[10] -- postulated that the leading quark either escapes completely or is entirely absorbed in a single interaction. With a quark-nucleon cross section (σ_{qN}) of 13 mb they were able to successfully describe the existing data as shown in Fig 2.

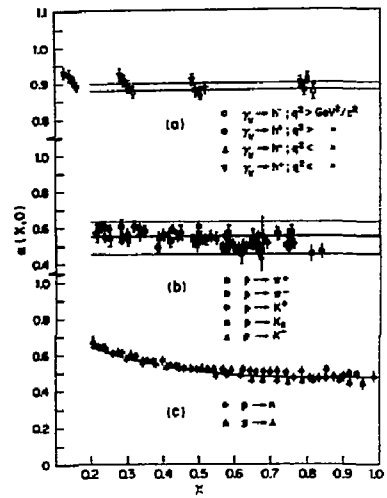

Fig. 2 The predictions of reference 10 (solid lines) compared to various experimental results.

Nilsson, Andersson and Gustafson[11] -- The quark can interact more than once, transferring energy to a nucleon each time, before finally fragmenting. They needed a value of σ_{qN} = 20 mb to fit the data as in Fig 3.

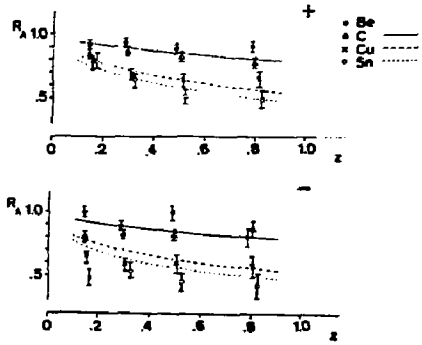

Fig. 3 The predictions of reference 11 compared to the positive and negative particles from the data of reference 17.

Bialas and Bialas[12] -- This model was relatively sophisticated in that it contained multiple elastic and inelastic quark - nucleon scattering. A separate analysis of the longitudinal and transverse hadron momentum spectra yielded information on σ_q^{inel} and σ_q^{tot} respectively.

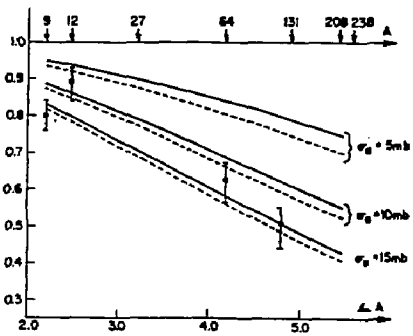

Fig. 4 The A-dependence of the ratio of hadronic yields from nuclei and H_2 for different values of the total quark-nucleon cross section. The data are from reference 17.

Bialas[13] -- This was the first model to stress the simple idea of measuring the A-dependence of the multiplicity of *different* leading hadrons. If it is the same, the intermediate state which escapes the nucleus is a quark. Bialas also stressed the importance of the interplay between σ_q and the formation length τ_q --> h.

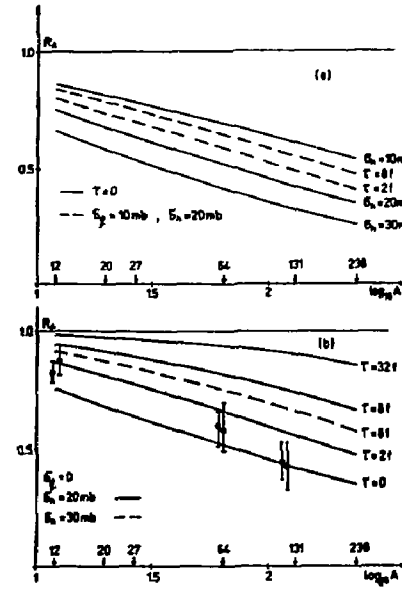

Fig. 5 The ratio of multiplicities from nucleus A versus H_2 for various values of the formation length and the quark nucleon cross section. The data are from reference 17.

Nikolaev[14] -- A very sophisticated model which uses a nuclear transport equation combined with the concept of formation length to predict multiplicity distributions for deep inelastic and photoproduced hadron showers.

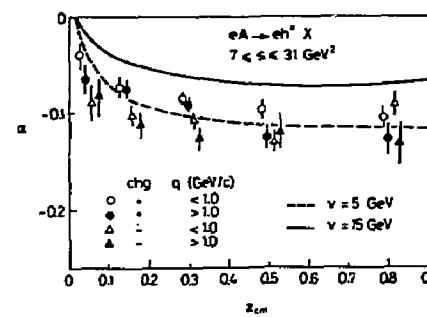

Fig. 6 The predicted behavior of α, the exponent of A^{α}, vs z in the cm system and compared to the data of reference 17.

Bialas and Chmaj[15] -- Introduced an alternative definition of formation length by postulating that fragmentation may be similar to the decay of the quark into a hard hadron. In this case, the formation length is $\tau = \upsilon / m_q^2$ where the quark life-time has been assumed to be $\approx 1 / m_q$. If this is the case, then the formation length should be Q^2 dependent. Fig. 7.

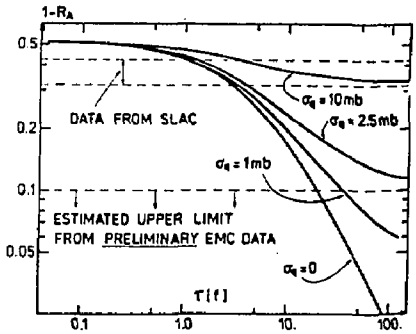

Fig. 7 The ratio of hadrons produced on copper and H_2 versus the formation length for various values of the quark nucleon cross section. The data are from reference 17 and early EMC results.

QCD Models[16] -- The application of QCD to the space-time development of hadron showers does not appreciably change the basic scale invariant parton model predictions we have just outlined.

One common thread which binds all of the models which we have discussed and which has guided our planning of the Tevatron Muon Collaboration is that

To determine the validity of the various ideas contained in these models, a measurement of the A-DEPENDENCE of the hadron shower characteristics is crucial!!

Experimental Results: A-Dependent Multiplicity Distributions

The EMC experiment was not the first to study leptoproduced hadron showers. There have been electron and neutrino as well as earlier muon experiments which have studied lepton-nucleus scattering. However, the earlier experiments were handicapped by a lack of statistics and/or a low and limited energy range. Except for the SLAC results[17] using a 20.5 GeV electron beam with statistics of 10000 events per target, the earlier experiments were limited to 600 ($\langle E_\upsilon \rangle \approx 20$ GeV) and 3100 ($\langle E_\upsilon \rangle \approx 200$ GeV) event neutrino[18,19] experiments and an 88 event muon ($E_\mu = 150$ GeV) emulsion experiment[20].

The European Muon Collaboration, running without a vertex detector, took data with Carbon and Copper targets[21] and compared it with earlier data[22] using a hydrogen target. The main thrust of this phase of the experiment was to study the ratios of multiplicity distributions of hadrons produced off of these different nuclei. Examined was the ratio of differential multiplicity distributions

$$R_{A_1/A_2}(z) = \left(\frac{1}{N_\mu}\frac{dn}{dz}\right)_{A_1} / \left(\frac{1}{N_\mu}\frac{dn}{dz}\right)_{A_2}$$

and, to emphasize any nuclear effects on the leading hadrons, the ratio of integrated z distributions

$$\bar{R}_{A_1/A_2}(z_{min}) = \int_{z_{min}}^{1.0} dz \left(\frac{1}{N_\mu}\frac{dn}{dz}\right)_{A_1} / \int_{z_{min}}^{1.0} dz \left(\frac{1}{N_\mu}\frac{dn}{dz}\right)_{A_2}$$

Kinematic Cuts and Data Sample

To keep acceptance corrections small and consistent for the different nuclear runs, the following kinematic cuts were made on all samples:

$$Q^2 > 5.0 \text{ GeV}^2$$
$$\upsilon > 50.0 \text{ GeV}$$
$$x_{Bj} > 0.02$$
$$W^2 > 25.0 \text{ GeV}^2$$
$$p_{had} > 6.0 \text{ GeV}$$

After these cuts had been made, the following sample sizes were used in the final analysis:

Nucleus	E_μ	Events	$\langle W^2 \rangle$	$\langle \upsilon \rangle$	$\langle Q^2 \rangle$	$\langle x \rangle$
Hydrogen	120 GeV	9.0 K	121 GeV^2	71 GeV	12 GeV^2	.10
Hydrogen	280	9.8 K	174	108	29	.15
Carbon	200	13.9 K	186	110	21	.11
Copper	200	10.4 K	188	112	21	.11

The differences between the hydrogen and heavier nuclei samples arose since the Carbon and Copper runs were performed at a different time with a somewhat altered spectrometer.

Analysis

Since the analysis concentrates on the ratios of hadronic distributions from the three targets, it is the *differences* in the corrections which are crucial. For the acceptance corrections it was determined that at high z the acceptance during hydrogen running was twice as high as for the heavy nucleus runs. For the radiative corrections, the C and Cu data had to be corrected for coherent radiative processes in addition to the corrections which had been applied to the hydrogen sample. This amounted to, at most, a 5% correction to the Cu data in the lowest x range. The only other correction required to account for the difference between hydrogen and the heavier nuclei is a compensation for hadronic interactions with other nuclei of the target. Absorption or the creation of secondaries modified produced multiplicities. Using Monte Carlo techniques the maximum correction was found to be < 5%. **Note that after this correction the results correspond to zero target length.**

Results

The overall average multiplicities are 1.58 ± .02 for Carbon and 1.69 ±.02 for Copper. This represents an increase of 7% ± 2%(statistical) ± 3%(systematic) which is hardly significant. A more detailed look at the multiplicities is shown in the following figure. Even at this level there is no difference between the carbon and copper data.

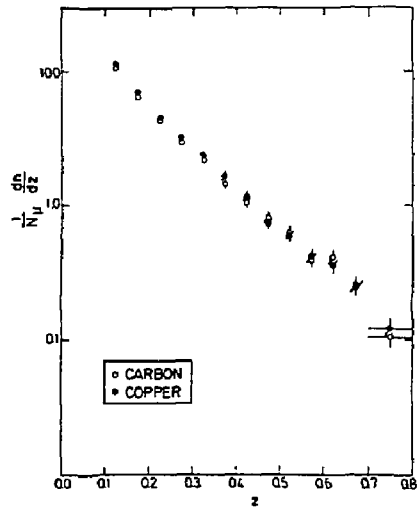

Fig. 8 shows the charged hadron multiplicity as a function of z for C and Cu.

To see if the multiplicities are dependent on the energy transferred to the struck parton, the data has been divided into three υ bins; 50 < υ < 70 GeV, 70 < υ < 90 GeV, and υ > 90 GeV. The results are shown in Fig. 9.

The average multiplicity ratios for leading (z>0.5) hadrons in the three υ bins is:

Ratio	50<υ<70	70<υ<90	υ>90 GeV
Cu/C	.78±.13±.05	1.27±.20±.10	1.04±.12±.14
C/H_2	1.07±.13±.17	0.77±.12±.11	1.16±.12±.20
Cu/H_2	0.84±.12±.14	0.97±.14±.13	1.20±.12±.20

The overall trend of the υ-dependence is a depletion of leading hadrons and an overall broadening of hadron showers at low υ in Cu compared to C and H_2.

There is a similar although statistically less significant effect when we look at the x_{Bj} dependence of the multiplicities. We find a depletion of leading hadrons and a broadening of the hadron showers at large x. Since $x = Q^2/2M\upsilon$ we are probably seeing a reflection of the previously mentioned υ dependence in the x-distribution.

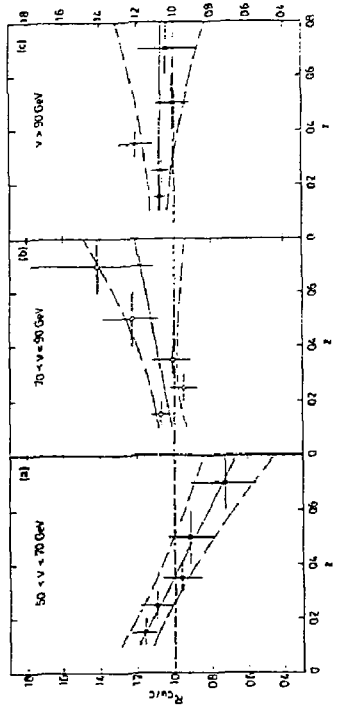

Fig. 9 The ratio of copper and carbon multiplicities as a function of z in three different virtual gamma energy bins. The solid lines are linear fits to the data and the dashed lines are the 1 sd limits.

We can combine these EMC results with the earlier SLAC[17] results for 3 <υ <17 GeV.

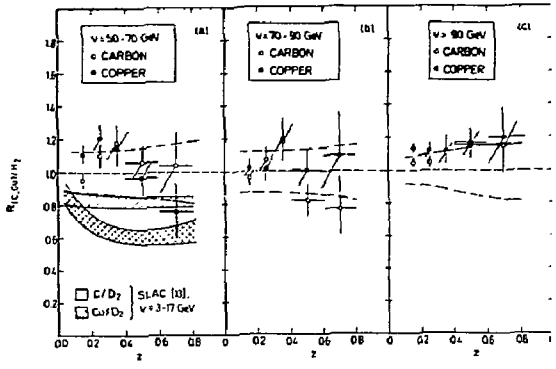

Fig. 10 The ratio of multiplicity distributions from EMC and the low energy SLAC results plottec together.

The nuclear effects are much more pronounced at the low SLAC values of υ. Assuming that the effect depends only on υ (not on Q^2), the model of Bialas[13] can be used to fit the two υ ranges (roughly 3 < υ < 180 GeV) of the SLAC and EMC results. Using the measured ratios of C:Cu <1.25 (2 s.d) by EMC at <υ> ≈ 100 GeV and C:Cu > 1.17 by the SLAC group at <υ> = 8 GeV, and expressing the formation length τ as

$$\tau(\text{fm}) = \delta(\text{fm/GeV}) * \upsilon(\text{GeV})$$

then Fig. 11 shows the region in the δ-σ_{qN} plane allowed by the two results.

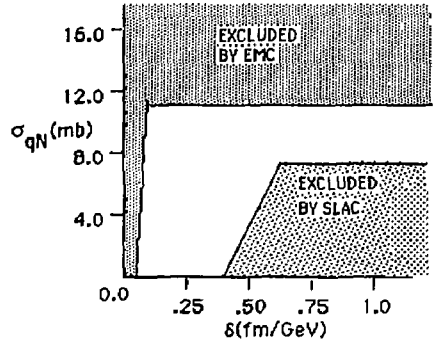

Fig. 11 Allowed region in the δ-σ_{qN} plane by both the SLAC and EMC results using Bialas' model.

It can be seen that the SLAC results favor smaller values of δ while the EMC results exclude δ = 0. Cross sections larger than ≈ 10 mb are excluded by the EMC results. It should be quite obvious that much more exact data at all values of υ are necessary before further model dependent interpretation is possible.

Conclusions: A-Dependent Multiplicity Distributions

There is a depletion of leading particles and a broadening of hadron jets at low υ with increasing A of the target. Analysis of the EMC and SLAC results in terms of the Bialas model implies that τ, the formation length, is υ dependent and comparable to the size of the nucleus (r_C = 2.7 fm and r_{Cu} = 4.8 fm) and the quark-nucleon cross section would have to be less than 10 mb.

Improvements expected from the Tevatron Muon Experiment

Following is a list of the major improvements we expect from the upcoming Tevatron experiment on nuclear targets compared to the recently completed EMC heavy target experiment:

1. Increase statistics by an order of magnitude
2. Improved acceptance for high-z particles.
3. Various A targets will be exposed in the same run to the same muon energy distribution resulting in reduced systematic errors.
4. There will be a factor > 2 larger kinematic range which should allow finer binning in υ and a measurement of the Q^2 dependence of the formation length τ.
5. Much better particle identification (i.e. K/π separation from 1 to 120 GeV) should improve the chance of measuring τ and σ_{qN} for different hadrons.

The Bose-Einstein Effect: Introduction

I am sure we all recall studying the difference between Fermi statistics and Bose-Einstein statistics in Quantum Mechanics and, perhaps, thinking that this will never apply to much that we would be doing professionally. This next method for studying the development of a hadron shower is a vindication of the hours invested in studying Bose-Einstein!

A method to use Bose-Einstein interference to determine the spatial extent of an object was first proposed by Hanbury-Brown and Twiss[23] in the mid 50's to determine the diameter of stellar objects using photon interferometry. Several years later, and unaware of the Hanbury-Brown Twiss work, G. Goldhaber and colleagues[24] noticed a distinct difference between the rate of like-charge and unlike-charge pion pairs as a function of the opening angle between the pions. After a month of contemplation they interpreted this result in terms of the Bose-Einstein effect for pions and were able to obtain a quantitative fit to their data by symmeterizing the two pion wave functions for like pions. In the intervening years the analysis has become much more sophisticated[25] and high statistics experiments now use correlation densities to extract the effect. Defining the one and two particle densities

$$\rho(p_1) = \frac{1}{\sigma}\frac{d\sigma}{dp_1}$$

$$\rho(p_1,p_2) = \frac{1}{\sigma}\frac{d^2\sigma}{dp_1 dp_2}$$

respectively, the two body correlation coefficient is given by

$$C_2 = \frac{\rho(p_1, p_2)}{\rho(p_1)\,\rho(p_2)}$$

To remove kinematic and dynamic correlations not associated with the Bose-Einstein effect, ratios are taken between a like-sign experimental density and a reference sample density which should not have any Bose-Einstein correlations,

$$R_0^{Like} = \frac{\rho(p_1, p_2)}{\rho_0(p_1, p_2)}$$

The quantity $(R_0{}^{Like} - 1)$ is the **Fourier transform of the space-time distribution of the particle source.**[26]

The important thing for experimentalists is that the consequences of the Bose-Einstein effect should be an enhancement of n(>1) identical boson final states compared to a final state composed of n dissimilar bosons. Using the parameterization chosen by the EMC collaboration[27], if $\Delta p = p_i - p_j$ is the difference of the 4-momenta of two like sign pions, then the ratio of like-sign pairs to non-interfering pairs can be expressed as

$$I = 1 + \lambda \exp(-\tilde{M}^2 R^2)$$

with $\tilde{M}^2 = -(\Delta p)^2$ the square of the difference of the pions 4-momenta and R **is the rms size of the pion source!** The factor λ is necessary to compensate for coherently produced pions.

The Bose-Einstein Effect: EMC Results

The European Muon Collaboration's full spectrometer (with streamer chamber and associated vertex detectors) was used to study the Bose-Einstein effect in muoproduced hadronic showers. Using 280 GeV muons on a H_2 target, a sample of events was collected which survived the

following kinematic cuts;

$Q^2 > 4$ GeV^2
$4 < W < 20$ GeV
$20 < \upsilon < 260$ GeV
$y < 0.9$
$\theta_{\mu'} > 0.75°$

After further resolution associated cuts, the final sample consisted of 17,343 events.

Since only 50% of the hadrons were identified, it was assumed that all negative hadrons were pions. This was justified by the Lund Monte Carlo results which showed that the ratio $\pi : K : P$ was 80 : 9 : 11. Furthermore, within the hadronic shower all particles had to have momentum measurements with $\Delta P/P < 20\%$ and, most significantly, all accepted tracks had to be measurable in the streamer chamber. This last requirement effectively limited the particles to $x_F < 0.2$ which is relatively low momentum particles. Under these conditions the following combinations were found

126,000 $(\pi^+\pi^-)$ combinations

60,000 $(\pi^+\pi^+)$ combinations
38,300 $(\pi^-\pi^-)$ combinations
98,300 like sign pion pairs

Results

The most difficult task in the analysis is separating the Bose-Einstein Effect from elementary kinematic and dynamic correlations. The standard technique, mentioned above, is to form ratios of the like-sign pairs--$\rho(p_1,p_2)$--to pairs where the Bose-Einstein effect should be absent--$\rho_0(p_1,p_2)$. In the EMC analysis three reference groups were formed;

REF 1 — $(\pi^+\pi^-)$ combinations from the same event in which a like-sign pair was found,

REF 2 — $(\pi^+\pi^-)$ combinations from the same event but with transverse momentum from random pions within the event,

REF 3 — LIKE combinations constructed from random tracks from various events.

The LIKE/REF ratios as a function of $\tilde{M}^2$ are shown in Fig. 12a. There is an increase in the ratio as $\tilde{M}^2$ approaches 0, but there is an inconsistency in the shapes as well as the overall normalization of the three curves. This is an indication that there are still dynamical or kinematical correlations that remain uncompensated in the ratios. The next step in eliminating these non-interfering correlations involves the use of the Lund Monte Carlo[28] which does not contain interference effects. Subjecting the Monte Carlo events to the same cuts as the data the ratio LIKEMC/REFMC is formed. Again it is seen--Fig. 12b--that there is a disagreement in shape and normalization between the three ratios which must arise from residual dynamic and/or kinematic correlations. In an attempt rid the sample of these correlations, a "ratio of ratios" is formed resulting in the curves shown in Fig. 12c.

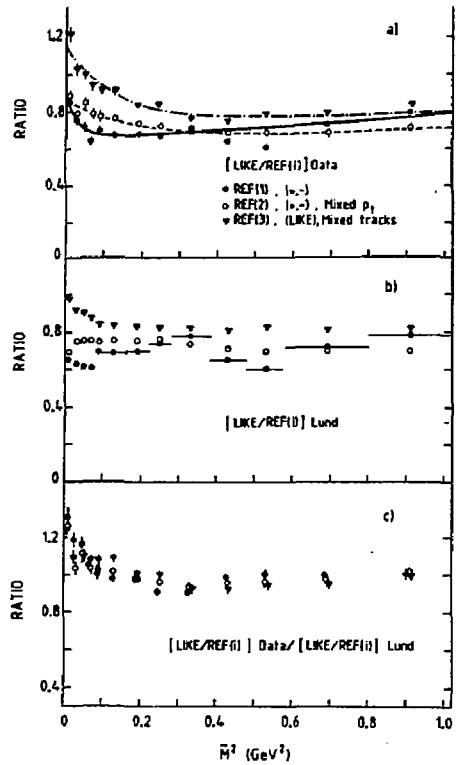

Fig. 12 Ratios as a function of the difference in the 4-momenta of the pion pairs. a) ratio of LIKE to REF(i) as defined above, b) the same ratios when using the Lund Monte Carlo results and c) the ratio of ratios a) and b).

The results now show a trend which is similar in both shape and magnitude indicating that the non-interfering correlations have been more successfully removed. A fit to $\tilde{M}^2$ and λ yields the following values, using the double ratios, for the three reference samples

	R(fm)	λ	χ^2 (12 DF)
REF 1	0.84 ± 0.03	1.08 ± 0.10	12.4
REF 2	0.66 ± 0.01	0.60 ± 0.06	12.2
REF 3	0.46 ± 0.03	0.73 ± 0.06	20.3

The results still depend on the reference sample which indicates that there are some correlations that have not been removed from the LIKE sample. Berger and his colleagues have shown[29] how intertwined the Bose-Einstein and resonance correlations can be.

Conclusion

The EMC analysis continues in an attempt to extract the shape of the pion emission region and the details can be found in reference 27. The EMC group comes to the conclusions that:

1. The Bose-Einstein interference effect has been seen in muoproduced like-sign pion pairs,
2. The results are consistent with a spherically shaped pion emission region, and
3. The radius of the emission region is **0.46 < R < 0.84 fm** and the suppression factor is $0.6 < \lambda < 1.0$.

These results are approximately consistent with almost every other experiment, regardless of energy or target, which has attempted the analysis. This, as well as the *spherical* nature of the emission region, tends to go against intuition and might indicate that there is something not consistent with either the method and/or the interpretation of the results of the Bose-Einstein analysis.

Critique

No one doubts the validity of Bose-Einstein statistics so that there should indeed be an interference effect that would enhance the number of "similar" bosons. However, aside from the difficulty of extracting the signal due to interference from the non-interfering correlations, the question of interpretation of the result is quite crucial.

The method used by the EMC and others, which involves describing the pion emission region with a single spatial variable R, is realistic in only a very few situations[30]. There is obviously no directional information in R so the data can only be described by this form if the source density of the emission region depends only on the length of the 4-vector difference between the two pions. Furthermore, and most telling, the 4-momentum difference of any pair of pions as well as the "shape" of the source has to depend on the frame in which they are being evaluated. Fig. 13 illustrates this by indicating a pair of pions which have identical 4-vectors in a frame where the current and target fragment sources are moving in opposite directions with respect to each other. Upon boosting to the lab they are no longer "identical pions". This, of course, implies that if lab momenta are used to search for identical pion pairs, there is no way that the resulting pion source size can be a measure of the **total emission (current + target fragments) region!** It is, at best, a measure of the spatial extent of either current fragment sources or target fragment sources. Even this interpretation is not necessarily correct if there is an ordered momentum/space-time correlation, as postulated by Bjorken and incorporated by the successful Lund Monte Carlo, so that particles with similar momentum have been emitted at **neighboring** space-time points in the evolution of the hadronic shower!

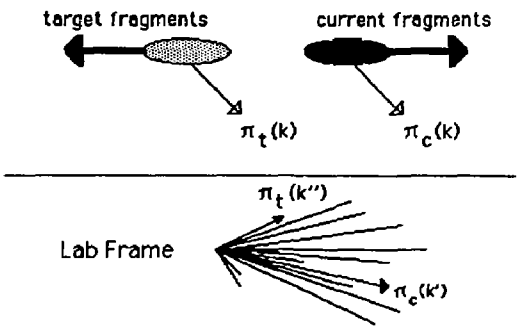

Fig. 13 Identical pion in one frame are not identical pions in all frames.

There have been attempts[30,31], particularly in the interpretation of e^+e^- Bose-Einstein analyses, to determine whether currently acceptable hadronization models, such as the Lund-type string model, might yield the results found by almost all Bose-Einstein analyses including the EMC result. Both of the references find consistency between string model predictions and the experimental results that the emission region is "spherical" and the associated length is of the order of 1 fm. However, this length has little to do with the spatial extent of the source of all particles in the shower.

The TMC will take a much more critical look at the method and interpretation of Bose-Einstein interference effects. Much improved particle identification, improved momentum resolution and increased kinematical range should allow Bose-Einstein analyses in more than one reference frame and off various targets.

Overall Conclusion

The topic of the space-time development of a hadron shower, although of fundamental importance, has barely progressed beyond the most elementary level of experimental investigation. The concepts of quark-nucleon cross sections and hadron formation lengths are still more philosophical than scientific quantities. There is a need for carefully controlled, high statistics measurements of hadron multiplicities off a variety of nuclear targets and over a wide kinematic range before a quantified knowledge of the space-time structure of a hadronic shower can be claimed. This need will be answered by the upcoming Tevatron Muon Collaboration which will begin taking data at Fermilab in the very near future. A second experiment, preferably covering lower energies than this Tevatron experiment, would be extremely useful in answering the questions posed in this presentation.

References

1. R. P. Feynman, Photon-Hadron Interactions, W. A. Benjamin, New York, 1972.
2. T. Sloan, Recent Results in Deep Inelastic Scattering, CERN EP/86-111, August, 1986.
3. Muon Scattering with Hadron Detection at the Tevatron, Fermilab Experiment 665.
4. T. Sloan, Recent Results in Deep Inelastic Scattering, CERN EP/86-111, August, 1986.
5. J. J. Aubert et al., Nucl. Phys B272 , 158 (1979).
6. E. Segrè, Nuclei and Particles, W. A. Benjamin, New York, 1964.
7. J. D. Bjorken, SLAC-PUB-1756, May 1976.
8. L. D. Landau, Izv. Acad. Nauk. SSSR 17, 31 (1953).
9. W. Busza, Acta Phys. Pol. B8 , 333 (1977).
10. A. Dar and F. Takagi, Phys. Rev. Lett. 44, 768 (1980).
11. G. Nilsson, B. Andersson and G. Gustafson, Phys. Lett. 83B, 379 (1979).
12. A. Bialas and E. Bialas, Phys. Rev. D21, 675 (1980).
13. A. Bialas, Acta Phys. Pol. B11, 475 (1980).
14. N. N. Nikolaev, Z. Phys. C 5, 291 (1980).
15. A. Bialas and T. Chmaj, Phys. Lett. 133B, 241 (1983).
16. S. J. Brodsky, SLAC-PUB-2970, September 1982. A. H. Mueller, Topics in High Energy Perturbative QCD Including Interactions with Nuclear Matter, Proc. XVIIth Rencontre de Moriond, Les Arcs, 1982.
17. L. S. Osborne et al., Phys. Rev. Lett. 40, 1624 (1978).
18. J. P. Berge et al., Phys. Rev. D18, 3905 (1978).
19. H. Deden et al., Nucl. Phys. 198B, 365 (1982).
20. L. Hand et al., Z. Phys. C 1, 139 (1979).
21. A. Arvidson et al., Nucl. Phys. B246, 381 (1984).
22. J. J. Aubert et al., Phys. Lett. 114B, 373 (1982).
23. R. Hanbury-Brown and R. Q. Twiss, Philos. Mag. 45, 663 (1954).
24. G. Goldhaber et al., Phys. Rev. Lett. 3, 181 (1959).
25. G. Goldhaber, LBL Preprint 19417 (1985).
26. G. Goldhaber et al., Phys. Rev. 120, 300 (1960).
27. M. Arneodo et al., CERN-EP/86-42, April 1986.
28. G. Ingelman et al., Nucl. Phys. B206, 239 (1982).
29. E. L. Berger et al., Phys. Rev. D15, 206 (1977).
30. M. G. Bowler, Z. Phys. C 29, 617 (1985).
31. B. Andersson and W. Hofmann, Phys. Lett. 169B, 1986)

THE NUCLEAR RESPONSE AT MEDIUM ENERGY*

T. W. Donnelly†

Center for Theoretical Physics
Laboratory for Nuclear Science
and Department of Physics
Massachusetts Institute of Technology
Cambridge, Massachusetts 02139 U.S.A.

Abstract

The use of internal targets to investigate the nuclear response at medium energies is discussed with emphasis being placed on what can be learned by employing polarized targets to study "electromagnetic spin physics." The importance of having longitudinally polarized electrons is stressed. Both single-arm and coincidence reactions are discussed and contrasted with similar studies involving final-state polarimetry using external beams and targets. Conclusions are drawn concerning practical implications for polarized internal target experiments.

Introduction

The discussions here center around what can be learned about the nuclear response at medium energy by exploiting polarization degrees of freedom: polarized electrons, polarized targets and measurement of final-state polarizations. As we shall see in the closing comments, there are only a very few special cases in which it is practical to use polarized targets with external beams of electrons, whereas with the extremely high current which can be obtained in electron storage/stretcher rings it becomes feasible to contemplate using (low density) *internal polarized targets.* Consequently, the main focus in the present context is placed on reactions of this sort, with or without having polarized electrons as well. In certain cases, the same or possibly complementary information can be obtained using unpolarized targets but measuring some final-state polarization; these are noted in the following discussions.

Two classes of reactions are considered, the first being single-arm (inclusive) studies of the type

$$e + \vec{A} \rightarrow e' + X$$
$$\vec{e} + \vec{A} \rightarrow e' + X \ ,$$

in which a (possibly polarized) electron is scattered from a polarized target and the scattered electron is detected. The products of the reaction, X, are presumed not to be detected. Of course, from the kinematics of the electron scattering it is possible to specify the total energy of the final state and, when this is a discrete nuclear level (such as the ground state itself

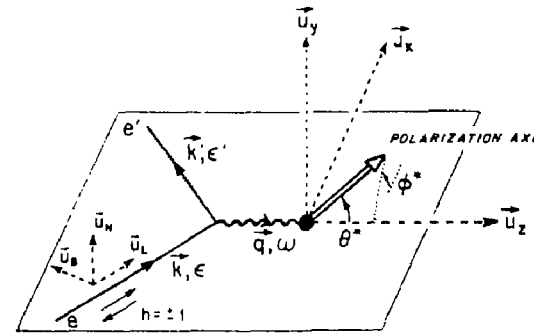

Fig. 1: Single-arm electron scattering from polarized targets including the possibility of having longitudinally polarized electrons (helicity $h = \pm 1$), $\vec{A}(\vec{e}, e')$. The target polarization axis is specified by the angles (θ^*, ϕ^*) as shown.

in elastic scattering), the word "exclusive" is frequently used. However, here we presume no knowledge of the final-state polarization, no knowledge of the final-state decay branching (even for a discrete state it can, say, γ-decay with several branches) and no knowledge of the specifics of how the various open channels are populated when above particle emission threshold (for example, the relative weightings of proton knockout, neutron knockout, two-nucleon knockout, pion production, etc.).

The second class of reactions considered here are then the more exclusive coincidence reactions, for instance of the type

$$e + \vec{A} \rightarrow e' + x + X$$
$$\vec{e} + \vec{A} \rightarrow e' + x + X \ ,$$

where, in addition to detecting the scattered electron, a particle x in the final state is also detected. Again, the rest, X, is not detected. These particular cases can be termed exclusive-1 reactions (or alternatively semi-inclusive reactions). There are also exclusive-2, -3, $\cdots$ reactions in which 2, 3, $\cdots$ particles are detected in coincidence with the scattered electron; here we restrict our attention only to the simplest class of exclusive-1 or double-arm coincidence reactions.

For either of the two general classes we may or may not assume that the electron is polarized. The kinematics are specified in Fig. 1. Here, an electron with 3-momentum $\vec{k}$ and energy ϵ is scattered through an angle θ_e to be detected with 3-momentum $\vec{k}'$ and energy ϵ'. The 3-momentum transfer is

*This work is supported in part by funds provided by the U. S. Department of Energy (D.O.E.) under contract # DE-AC02-76ER03069.

†Alexander von Humboldt Foundation Senior U.S. Scientist Award holder.

Typeset in TEX by Roger L. Gilson.

$\vec{q} = \vec{k} - \vec{k}'$ with magnitude $q = |\vec{q}|$ and the energy transfer is $\omega = \epsilon - \epsilon'$. The 4-momentum transfer $q_\mu q^\mu = \omega^2 - q^2$ is space-like (≤ 0). In general, we may consider coordinate systems fixed by the electron momenta so that $\vec{u}_L$ is along $\vec{k}$, $\vec{u}_N$ is normal to the electron scattering plane and $\vec{u}_S = \vec{u}_N \times \vec{u}_L$, with a similar form labelled L', N', S' going with the scattered electron. Here $L \leftarrow$ longitudinal, $N \leftarrow$ normal, $S \leftarrow$ sideways (as used in hadron scattering). The cross section may be broken down into specific projections, $\sigma^{P'P}$, where $P = L, N$ or S and $P' = L', N'$ or S'. We are specifically interested in the Extreme Relativistic Limit (ERL) in which $\gamma = \epsilon/m_e >> 1$ and $\gamma' = \epsilon'/m_e >> 1$ and so where terms of order γ^{-1} or γ'^{-1} can safety be neglected (*i.e.* in all but a few very specific circumstances such as when $\theta_e < \gamma^{-1}$). In the ERL we find that[1]

$$\sigma^{P'P} \sim \begin{cases} O(1) & \text{for } P'P = L'L, \\ O(\gamma^{-1} \text{ or } \gamma'^{-1}) & \text{for } P'P \neq L'L \end{cases} ,$$

and so we practically only need to consider *longitudinally polarized electrons* having helicities $h = \pm 1$ and $h' = \pm 1$. Furthermore, the scattering process is *helicity conserving* to $O(\gamma^{-1} \text{ or } \gamma'^{-1})$, $h' = h$ and so the information obtained using an incident longitudinally polarized electron beam is the same as that obtained by measuring the longitudinal polarization of the scattered electron. We only consider the former as they are trivially related.

The polarized electron cross section in this case may be written

$$\sigma^h = \Sigma + h\Delta \ , \tag{1}$$

where the helicity averaged cross section

$$\Sigma = \frac{1}{2}\left(\sigma^{+1} + \sigma^{-1}\right) \tag{2a}$$

is obtained using unpolarized beams and where determination of the helicity difference cross section

$$\Delta = \frac{1}{2}\left(\sigma^{+1} - \sigma^{-1}\right) \tag{2b}$$

requires the use of longitudinally polarized electrons. There are then two general classes of responses to be addressed. Note that in the very low energy case (electron energy $\sim m_e$; or equivalently muon energy $\sim m_\mu$, which may have some application for muon scattering), when terms of $O(\gamma^{-1}$ or $\gamma'^{-1})$ are also considered, then transverse polarizations and helicity flips become accessible and Eq. (1) needs to be extended.[1] The practical implications of requiring longitudinally polarized electrons for internal target studies are important and will have a non-negligible impact on the facility requirements (see the talk by B. Norum at this workshop).

We may now proceed with a discussion of the nuclear response itself. The general situation involves a treatment of cross sections labelled Σ_{fi} and Δ_{fi}, where "f" and "i" signify specific polarizations for the final and initial nuclear states involved. We shall usually focus on the more restricted category involving only polarized targets and so responses labelled Σ_{fi} and Δ_{fi}, where f indicates that no final-state polarization information is presumed to be known. The target polarization is referred to a polarization axis which may be oriented in an arbitrary direction specified by the angles (θ^*, ϕ^*) as shown in Fig. 1. We begin with a discussion of single-arm (inclusive) scattering.

Single – Arm Scattering

Recently,[1] the subject of single-arm (inclusive) electron scattering from polarized targets has been discussed in some depth and applied to a variety of nuclear structure examples (see also Refs. [2]-[5]). Here only the most salient features are extracted for presentation, together with a few specific (interesting) examples to illustrate the basic ideas involved.

Unpolarized Electrons

Let us begin by discussing the scattering of unpolarized electrons from polarized targets, $\vec{A}(e,e')$. Only the cross section Σ_{fi} is then accessible. Using the known properties of the electron-photon part of the problem (just pure quantum electrodynamics), we may decompose this into four basic classes of response:[1]

$$\Sigma_{fi} = \sigma_0\{v_L W_{fi}^L + v_T W_{fi}^T + \cos\phi^* v_{TL} W_{fi}^{TL} + \cos 2\phi^* v_{TT} W_{fi}^{TT}\} \ , \tag{3}$$

where σ_0 is the elementary cross section (proportional to the Mott cross section) and the v's are factors involving the electron kinematics (L, $T \leftarrow$ longitudinal and transverse projections with respect to $\vec{q}$):

$$\begin{aligned} v_L &= \lambda^2 \\ v_T &= \frac{1}{2}\lambda + \tan^2\frac{\theta_e}{2} \\ v_{LT} &= -\frac{1}{\sqrt{2}}\lambda\sqrt{\lambda + \tan^2\frac{\theta_e}{2}} \\ v_{TT} &= -\frac{1}{2}\lambda \ , \end{aligned} \tag{4}$$

where $\lambda \equiv -q_\mu q^\mu/q^2$ so that $0 \leq \lambda \leq 1$. These factors together with σ_0 contain the entire dependence on θ_e for fixed q and ω. The entire dependence on the azimuthal polarization angle ϕ^* (see Fig. 1) is contained in the factors $\cos\phi^*$ and $\cos 2\phi^*$ and so by varying θ_e and ϕ^* it is possible to extract the four nuclear response functions W_{fi}^L, W_{fi}^T, W_{fi}^{TL}, and W_{fi}^{TT} in what might be termed a "super-Rosenbluth" decomposition. Each response still depends on (q,ω) and the polar angle of polarization θ^* (see Fig. 1). This latter dependence may also be made explicit[1] yielding a decomposition into *reduced response functions* which contain the dependence on q (and ω, which we take to be fixed to study some specific excitation):

$$W_{fi}^L = F_L^2(q) + \sum_{\substack{J\geq 2 \\ \text{even}}} f_J^{(i)} P_J(\cos\theta^*) W_J^L(q)_{fi} \tag{5a}$$

$$W_{fi}^T = F_T^2(q) + \sum_{\substack{J\geq 2 \\ \text{even}}} f_J^{(i)} P_J(\cos\theta^*) W_J^T(q)_{fi} \tag{5b}$$

$$W_{fi}^{TL} = \sum_{\substack{J\geq 2 \\ \text{even}}} f_J^{(i)} P_J^1(\cos\theta^*) W_J^{TL}(q)_{fi} \tag{5c}$$

$$W_{fi}^{TT} = \sum_{\substack{J\geq 2 \\ \text{even}}} f_J^{(i)} P_J^2(\cos\theta^*) W_J^{TT}(q)_{fi} \ . \tag{5d}$$

The first terms in Eqs. (5a) and (5b) involve the familiar longitudinal and transverse form factors and are present whether or not the target is polarized:

$$F_L^2(q) = \sum_{J\geq 0} F_{CJ}^2(q) \tag{6a}$$

$$F_T^2(q) = \sum_{J\geq 1} \left\{F_{EJ}^2(q) + F_{MJ}^2(q)\right\} \tag{6b}$$

These involve only incoherent sums of squares of Coulomb (C), Electric (E) and Magnetic (M) form factors. For example, suppose the ground state has $J_i^{\pi_i} = \frac{3}{2}^-$ and we consider only electro-excitation to a state having $J_f^{\pi_f} = \frac{5}{2}^+$. The allowed multipoles are $C1/E1$, $M2$, $C3/E3$ and $M4$, and we have

$$F_L^2 = F_{C1}^2 + F_{C3}^2$$
$$F_T^2 = F_{E1}^2 + F_{M2}^2 + F_{E3}^2 + F_{M4}^2 \ .$$

Clearly, we cannot isolate the individual multipoles if we only have F_L^2 and F_T^2; this is the frustration we are faced with in studying unpolarized electron scattering. However, with polarized targets, more information is present in general. In Eqs. (5) the terms involving the sums occur only when the target is polarized. The factors $f_I^{(i)}$ contain all the information on how the target M-states are populated (these are the Fano tensors, see Ref. [1]) and are presumed to be known. The entire θ^*-dependence is now displayed in the (associated) Legendre polynomials. Thus we have sets of reduced nuclear response functions as observables which may be obtained by controlling the direction of target polarization. Importantly, the sums in Eqs. (5) are finite: $2 \le I \le 2J_i$, with I = even only. If $J_i = 0$, clearly none of the sums occur and we have only $W_{fi}^L = W_{fi}^L = F_L^2$, $W_{fi}^T = W_{fi}^T = F_T^2$, $W_{fi}^{TL} = W_{fi}^{TT} = 0$, yielding for Eq. (3) just the familiar Rosenbluth formula for unpolarized electron scattering (indicated ff). Note that the same is true when the target has spin-$\frac{1}{2}$; in this case we cannot form any even-rank tensors except for the $I = 0$ ones which constitute the unpolarized form factors F_L^2 and F_T^2. Thus, lacking polarized electrons (see below) there is no point in going to the trouble of polarizing spin-$\frac{1}{2}$ targets for studies of inclusive electron scattering.

The first interesting case is that of electron scattering from a polarized spin-1 target, such as $^2\vec{H}$. For instance, for elastic scattering there are three basic form factors, $C0$, $M1$ and $C2$ (see Refs. [1] and [3]). The unpolarized cross section involves the longitudinal and transverse form factors,

$$F_L^2 = F_{C0}^2 + F_{C2}^2$$
$$F_T^2 = F_{M1}^2 \ ,$$

but the $C0$ and $C2$ contributions are summed incoherently and no relative phase information is available. The additional reduced response functions which are accessible with polarized targets are[1,3,6]

$$W_2^L = -2\sqrt{3}F_{C2}\left(F_{C0} + \frac{1}{2\sqrt{2}}F_{C2}\right)$$
$$W_2^T = -\frac{1}{2}\sqrt{\frac{3}{2}}F_{M1}^2$$
$$W_2^{TL} = \frac{3}{\sqrt{2}}F_{M1}F_{C2}$$
$$W_2^{TT} = \frac{1}{4}\sqrt{\frac{3}{2}}F_{M1}^2 \ .$$

Clearly with this polarization information it is possible to separate the individual multipole form factors. Thus, the prime use of polarization in single-arm electron scattering emerges, namely as a *"Multipole Meter"*. This is more generally true, for higher spin situations and for inelastic scattering, where additional *interference information* (for example, the $F_{C2}F_{C0}$ or $F_{M1}F_{C2}$ interferences above) becomes available.

In passing, a special circumstance should be mentioned: for elastic scattering and for light nuclei it is possible to obtain the same information with polarized targets or by measurement of the final-state recoil polarization. An example is provided by the recent experiment at Bates involving a measurement of the recoil tensor polarization in elastic scattering from deuterium.[7] It should be remarked, however, that inelastic excitations are not generally accessible with the final-state polarization measurements (since the final states generally decay too fast, although the reaction $(e, e'\gamma)$ can be a powerful alternative tool here and can be related directly to the present polarization discussions[8]) and that all but the lightest targets are probably impractical (since the slow recoil is usually too hard to handle).

Polarized Electrons

Now let us extend the above ideas to include the scattering of polarized electrons from polarized targets, $\vec{A}(\vec{e}, e')$. In this case the cross section Δ_{fi} becomes accessible together with Σ_{fi}. The analog to Eq. (3) is

$$\Delta_{fi} = \sigma_0 \left\{ v_{T'} W_{fi}^{T'} + \cos\phi^* v_{TL'} W_{fi}^{TL'} \right\} \ , \qquad (7)$$

and so we have two more classes of responses, giving six in general: L, T, TL, TT, T' and TL'. The two new electron kinematical factors are[1]

$$v_{T'} = \sqrt{\lambda + \tan^2\frac{\theta_e}{2}}\tan\frac{\theta_e}{2}$$
$$v_{TL'} = -\frac{1}{\sqrt{2}}\tan\frac{\theta_e}{2} \ . \qquad (8)$$

Furthermore, analogous to Eqs. (5) we now have

$$W_{fi}^{T'} = \sum_{\substack{I\ge 1\\ \text{odd}}} f_I^{(i)} P_I(\cos\theta^*) W_I^{T'}(q)_{fi} \qquad (9a)$$

$$W_{fi}^{TL'} = \sum_{\substack{I\ge 1\\ \text{odd}}} f_I^{(i)} P_I^1(\cos\theta^*) W_I^{TL'}(q)_{fi} \ , \qquad (9b)$$

where the sums are restricted to odd tensors only with $1 \le I \le 2J_i$.

For $J_i = 0$ these electron helicity difference responses are zero. In obtaining this fact we have assumed that the scattering process is purely electromagnetic and so is parity conserving. However, at the level of the weak interaction there are interferences between the γ-exchange and Z^0-exchange (neutral current) diagrams which can occur which lead to non-zero polarization asymmetries.[9,10] An experiment at Bates involving the elastic scattering of polarized electrons from ^{12}C is in the final stages of preparation.

For $J_i = \frac{1}{2}$ we saw above that the Σ_{fi} cross section contained only the familiar unpolarized responses involving the form factors F_L^2 and F_T^2:

$$\Sigma_{fi} = \sigma_0 \left\{ v_L F_L^2 + v_T F_T^2 \right\} \ . \qquad \left[\text{spin-}\frac{1}{2}\right] \qquad (10a)$$

The helicity difference cross section is now not zero but contains interesting information since rank–1 responses can be obtained ($1 \le I \le 2J_i \Longrightarrow I = 1$ for $J_i = \frac{1}{2}$):

$$\Delta_{fi} = f_1^{(i)}\sigma_0\{\cos\theta^* v_{T'} W_1^{T'}(q)_{fi} + \sin\theta^*\cos\phi^* v_{TL'} W_1^{TL'}(q)_{fi}\} \ . \qquad (10b)$$

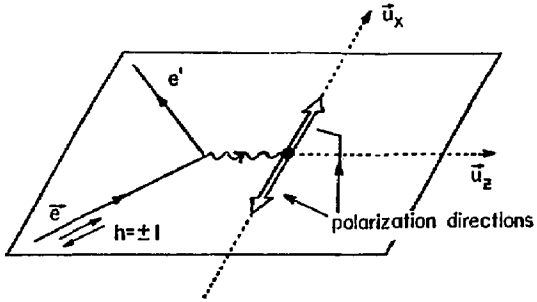

Fig. 2: Special choice of polarization directions for use with polarized spin-$\frac{1}{2}$ targets (see text).

Note that the $W_1^{TL'}$ response in the helicity difference cross section can be isolated by placing the target polarization in the special directions shown in Fig. 2. Thus for inclusive scattering of polarized electrons from polarized spin-$\frac{1}{2}$ targets there are four observables that are accessible: F_L^2, F_T^2, $W_1^{T'}$ and $W_1^{TL'}$. The general character of these responses is discussed in Ref. [5] while here we only consider two special cases

First, consider elastic scattering in which F_{C0} and F_{M1} form factors occur (equivalently, we can use G_E and G_M for the nucleon). The unpolarized cross section involves $F_L^2 = F_{C0}^2$ and $F_T^2 = F_{M1}^2$ which can in principle be separated by making a Rosenbluth decomposition of Eq. (10a). In practice, however, one may be dominant (as occurs for some values of q for the nucleon) and it may be very difficult to extract the smaller from the larger. For example, at all but the lowest values of q the present information on G_E^n comes from unpolarized electron scattering using deuterium as perhaps the simplest target containing neutrons. But at low-to-intermediate values of q, $|G_E^n| << |G_M^n|$ and the separation is very poorly defined. Now suppose this polarized electron/polarized target information is added. We have[1,3,6]

$$W_1^{T'} = -\sqrt{2}F_{M1}^2$$
$$W_1^{TL'} = -2\sqrt{2}F_{C0}F_{M1} \ .$$

The former just involves F_T^2 again, whereas the latter is the one of interest for the present purposes: it involves the *interference* between the two form factors and, when one is small in magnitude and the other large, it provides a much more sensitive way to extract one from the other. Note that this is the contribution which is isolated by using the special polarization orientation shown in Fig. 2. The specific measurements which are of high priority here are $\vec{p}(\vec{e},e')p$ (to extract G_E^p from G_M^p; even this is interesting for some values of momentum transfer) and ${}^3\vec{H}(\vec{e},e')$ or ${}^3\vec{H}e(\vec{e},e')$ in the region where the process corresponds best to quasi-free scattering from a nucleon (to extract G_E^n from G_M^n and to check the approximations involved by extracting G_E^p and G_M^p as well).

Next consider inelastic scattering for the transition $\frac{1}{2}^{\pm} \rightarrow \frac{3}{2}^{\pm}$ in which F_{M1}, F_{C2} and F_{E2} form factors occur. The four accessible responses here are[1]

$$F_L^2 = F_{C2}^2$$
$$F_T^2 = F_{M1}^2 + F_{E2}^2$$
$$W_1^{T'} = \frac{1}{\sqrt{2}}\left(F_{M1}^2 - F_{E2}^2 - 2\sqrt{3}F_{M1}F_{E2}\right)$$
$$W_1^{TL'} = -\sqrt{2}F_{C2}\left(F_{M1} + \sqrt{3}F_{E2}\right)$$

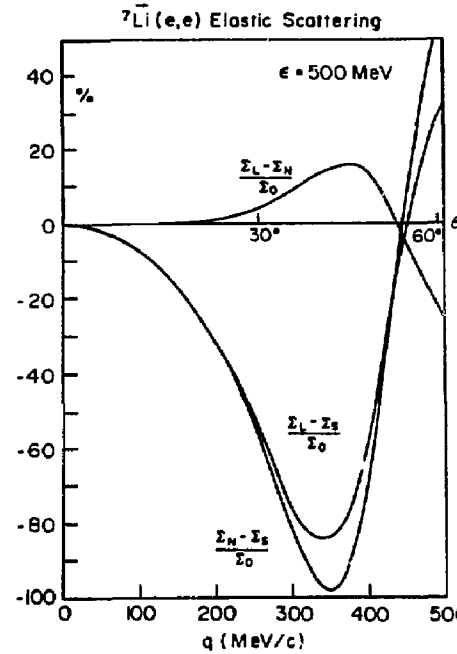

Fig. 3: Elastic electron scattering from the $\frac{3}{2}^-$ ground state of polarized ^{7}Li. The polarization asymmetries displayed correspond to taking the target to be 100% polarized along the L, N and S directions in Fig. 1 and then forming differences and dividing by the unpolarized cross section Σ_0.

A specific situation is the $N \rightarrow \Delta$ transition, say in $\vec{p}(\vec{e},e')\Delta$. To the extent that other channels than the $\frac{3}{2}^+$ final state can be neglected, we have the above responses. For the $N \rightarrow \Delta$ transition the $M1$ contribution is dominant and the $C2/E2$ pieces, which reflect the baryon deformations, are small. Again, a straightforward Rosenbluth separation of the unpolarized cross section yields F_L^2 and F_T^2 where the former is very small compared to the latter (and furthermore, where the latter contains two contributions, one very large and the other very small). The polarization responses involve interferences and especially the $W_1^{TL'}$ contribution is interesting, since it can only be non-zero when $F_{C2} \neq 0$. Moreover, the $W_1^{TL'}$ response is linearly proportional to F_{C2}, whereas F_L^2 involves the square F_{C2}^2.

Our conclusions from this simple analysis have important practical implications: to obtain new information particularly of the type involving interesting interferences using single-arm electron scattering to study spin-$\frac{1}{2}$ targets, it will be necessary to have polarized targets *and* longitudinally polarized electrons.

Finally, to set the scale of the asymmetries which are typical for studies of nuclear structure, let us extract some of the results from Ref. [1] for scattering of electrons (polarized or unpolarized) from polarized ^{7}Li. Two transitions are considered, elastic scattering from the $\frac{3}{2}^-$ ground state and inelastic scattering to the first excited state at 0.478 MeV, $\frac{3}{2}^- \rightarrow \frac{1}{2}^-$. The resulting polarization effects are displayed in Figs. 3—6.

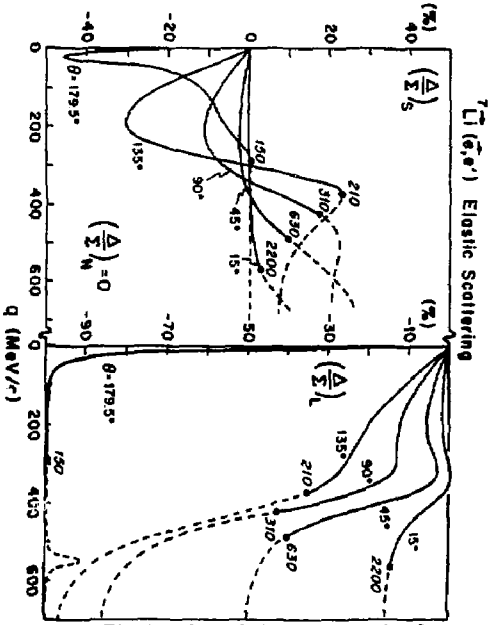

Fig. 4: Elastic polarized electron scattering from the $\frac{3}{2}^-$ ground state of polarized ^{7}Li. The polarization ratios Δ/Σ are given for the situations where the target is 100% polarized along the L, N and S directions in Fig. 1. Solid lines correspond to unpolarized cross sections above $10^{-33}\,\mathrm{cm^2\,sr^{-1}}$ and dashed lines to smaller cross sections. The incident electron energy in MeV at which $10^{-33}\,\mathrm{cm^2\,sr^{-1}}$ is reached for a given scattering angle is indicated near the dot on each line. (Figure shown sideways.)

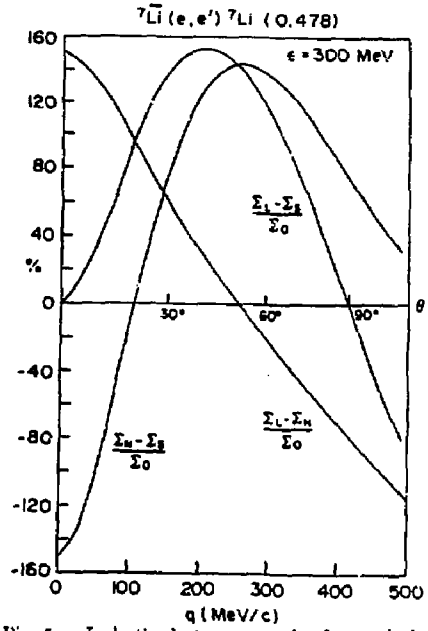

Fig. 5: Inelastic electron scattering from polarized ^{7}Li involving the transition $\frac{3}{2}^-$ (g.s.) $\rightarrow \frac{1}{2}^-$ (0.478 MeV). The asymmetries are defined as in Fig. 3.

The main observations to be drawn here are (1) the cross sections are $\gtrsim 10^{-33}\,\mathrm{cm^2\,sr^{-1}}$ over an interesting range of momentum transfers (this will have implications for the relevant range of luminosities, as discussed in the last section), and (2) the polarization asymmetries are typically large and vary significantly as q is changed or as the polarization direction is changed.

Coincidence Reactions

Let us now turn briefly to the exclusive-1, $(e,e'x)$ coincident reactions in Figs. 7 and 8. We consider two situations, the first without polarized targets but where the polarization of the particle x in the final state is measured (Fig. 7) and the second where the target is polarized but no final-state polarization is measured (Fig. 8). In both cases the electrons may or may not be longitudinally polarized. The former situation is pertinent for external beams and targets and requires the use of a polarimeter to measure the polarization of particle x (this is usually a limitation, since polarimeter efficiencies are typically quite low); the latter is pertinent for internal (polarized) target studies, just as for inclusive scattering (see above and the last section).

The decomposition made above into the six major classes of response (L, T, TL, TT with electrons unpolarized; T', TL' with polarized electrons) is quite general and applies here as well. The form of Eq. (1) is valid for the electron helicity dependence of the cross section in the ERL and, as above, two sets of responses may be separated using this dependence (see Eqs. (2)):

$$\Sigma \sim v_L R^L + v_T R^T + v_{TL} R^{TL} + v_{TT} R^{TT} \qquad (11a)$$

$$\Delta \sim v_{T'} R^{T'} + v_{TL'} R^{TL'} \ , \qquad (11b)$$

in parallel with Eqs. (3) and (7) for inclusive scattering. The six responses here depend on (q,ω), the energy and angles for the outgoing particle x (E_x, θ_x, ϕ_x; see Figs. 7 and 8) and the polarization angles. For the case of the reaction $A(\vec{e},e'\vec{x})$ in Fig. 7, these are the angles (θ_x^*, ϕ_x^*) as shown; for the case of the reaction $\vec{A}(\vec{e},e'x)$ in Fig. 8, these are the target polarization angles (θ^*, ϕ^*) where ϕ^* is now measured relative to the plane with azimuthal angle ϕ_x. The dependence on the azimuthal angle ϕ_x can be isolated:[5,11]

$$R^{TL} \equiv \cos\phi_x W^{TL} + \sin\phi_x \tilde{W}^{TL} \qquad (12a)$$

$$R^{TT} \equiv \cos 2\phi_x W^{TT} + \sin 2\phi_x \tilde{W}^{TT} \qquad (12b)$$

$$R^{TL'} \equiv \sin\phi_x W^{TL'} + \cos\phi_x \tilde{W}^{TL'} \qquad (12c)$$

$$R^L,\ R^T,\ R^{T'} : \text{ independent of } \phi_x \ ,$$

and so at this stage there are nine basic classes to consider in general.

Let us specialize first to a discussion of inclusive-1 electron scattering with only the electron possibly being polarized, $A(e,e'x)$ and $A(\vec{e},e'x)$. Then it can be shown[5,11] that $\tilde{W}^{TL} = \tilde{W}^{TT} = R^{T'} = \tilde{W}^{TL'} = 0$. In the completely unpolarized situation, $A(e,e'x)$, there are the four familiar responses to consider (R^L, R^T, W^{TL} and W^{TT}), which may be separated using the θ_e- and θ_x-dependences displayed above.

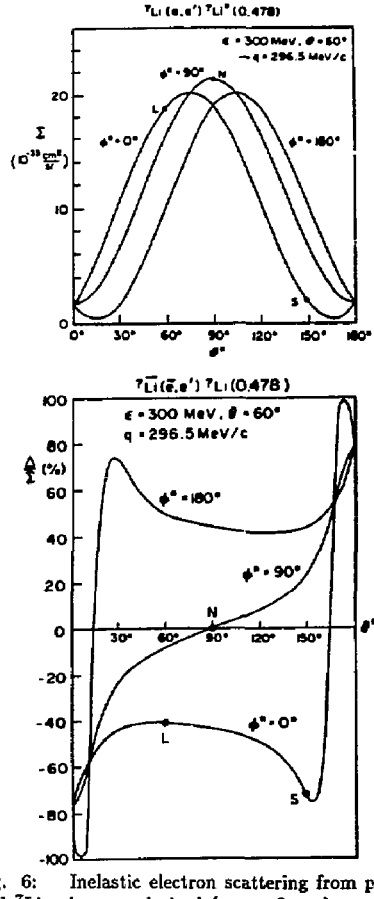

Fig. 6: Inelastic electron scattering from polarized ^{7}Li using unpolarized (upper figure) or polarized (lower figure) electrons for the same transition as that in Fig. 5. For specific electron scattering kinematics the quantities Σ and Δ/Σ are shown as functions of the target polarization angles θ^* and ϕ^* (see Fig. 1). The points corresponding to the L, N and S directions in Fig. 1 are indicated.

Having polarized electrons and studying the electron helicity-difference cross section for $A(\vec{e},e'\vec{x})$ yields another, the so-called "fifth" response function $W^{TL'}$ (note that this requires an out-of-plane measurement because of the factor $\sin\phi_x$ in Eq. (12c)). In contrast to single-arm scattering with polarized electrons but unpolarized targets, this fifth response function is non-zero in general even when parity is conserved. Thus only the helicity-difference cross section in $A(\vec{e},e')$ is likely to be practical for studies of electroweak parity violating effects: such effects would usually be overwhelmed by the non-zero parity conserving asymmetries. The TL' fifth response function and the usual TL response have similar structures:

$$W^{TL} \sim \mathrm{Re}(T^*L)$$
$$W^{TL'} \sim \mathrm{Im}(T^*L) \ ,$$

where T^*L represents the appropriate (*i.e.* determined by the dynamics of the specific problem of interest) bilinear combination of (transverse)*×(longitudinal) matrix elements. The

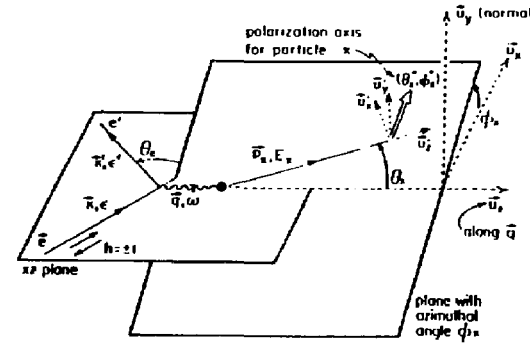

Fig. 7: Coincidence electron scattering from unpolarized targets including the possibility of having longitudinally polarized electrons and of detecting the polarization of the outgoing particle x, $A(\vec{e},e'\vec{x})$. The direction of the particle x is specified by the angles (θ_x,ϕ_x) referred to the xyz coordinate system as shown. Furthermore, the polarization of the particle x is specified by the angles (θ_x^*,ϕ_x^*), but now referred to the $x'y'z'$ coordinate system where z' is along $\vec{p}_x$, y' is orthogonal to $\vec{q}$ and $\vec{p}_x$ (along $\vec{q}\times\vec{p}_x$), and x' is orthogonal to both of these (along $\vec{u}_{y'}\times\vec{u}_{z'}$ and so is in the plane containing $\vec{q}$ and $\vec{p}_x$).

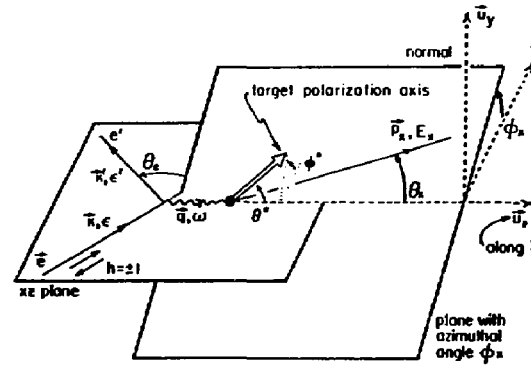

Fig. 8: Coincidence electron scattering from polarized targets including the possibility of having longitudinally polarized electrons, $\vec{A}(\vec{e},e'x)$. The direction of the particle x is specified by the angles (θ_x,ϕ_x) as in Fig. 7 and the target polarization directions is specified by (θ^*,ϕ^*) where θ^* is as in Fig. 1 and ϕ^* is measured relative to the plane with azimuthal angle ϕ_x.

same combinations occur in the two responses; the only difference is that one has the real part and the other the imaginary part. Now, if the reaction proceeds through a channel in which a single phase dominates for all projections of the current ($T \sim |T|e^{i\delta}$, $L \sim |L|e^{i\delta}$, with the same δ), the T^*L is real and, while W^{TL} is non-zero in general, $W^{TL'}$ vanishes.

Moreover, it happens that $W^{TL'}$ also vanishes in the absence of final-state interactions. Therefore, if $W^{TL'} \neq 0$, then interesting effects must be coming into play. For example, in the Δ-region coincidence electron scattering will be driven to a large degree by the 33-amplitude with a single phase, δ_{33}, and, while $W^{L,T,TL,TT}$ may all be non-zero, $W^{TL'}$ may be expected to vanish. To the extent that it does not vanish, we will be able to access information concerning interferences of the 33-amplitude with amplitudes for other channels which are usually too weak to be studied directly.

The L, T, TL and TT (unpolarized) responses on the one hand and the TL' (polarized electrons, but otherwise unpolarized) response on the other may be characterized by their time-reversal properties, even and odd, respectively. Time-reversal even responses are always real parts of bilinear products involving the currents, while time-reversal odd responses involve imaginary parts (as for TL and TL' above, respectively). The specific responses discussed so far where the electron was the only particle whose polarization was presumed to be known are members of larger sets of responses all of which may be characterized as time-reversal even or odd. These extended sets become accessible when target polarizations and/or final-state polarizations (other than the scattered electron) are presumed to be known. This polarization information may be organized into spherical tensors characterized by rank I, where I may be even or odd with $I = 0$ corresponding to the unpolarized cross sections above. When target polarizations are considered, this is the same type of tensor decomposition that we encountered earlier for single-arm scattering; when the polarization of particle x in $(e, e'\vec{x})$ and $(\vec{e}, e'\vec{x})$ is measured, then I labels the tensor polarization measured in some second scattering experiment. The general break-down into time-reversal even and odd responses is as follows:[12]

		I = even	I = odd
Σ	L	TRE	TRO
{electron unpolarized}	T	TRE	TRO
	TL	TRE	TRO
	TT	TRE	TRO
Δ	T'	TRO	TRE
{electron polarized}	TL'	TRO	TRE

where TRE (TRO) refers to time-reversal even (odd).

Let us consider a more specific situation to help clarify these ideas. Suppose the target is unpolarized and we consider reactions of the sort $(e, e'p)$, $(\vec{e}, e'p)$, $(e, e'\vec{p})$ and $(\vec{e}, e'\vec{p})$, where in fact the proton $(x = p)$ could be any spin-$\frac{1}{2}$ particle as far as the characterization of the cross section is considered. Since the particle whose polarization may be detected in the final state has spin-$\frac{1}{2}$, the only allowed values of I are 0 and 1 ($I = 0$ corresponds to the unpolarized cross sections discussed above, the first two in this list; $I = 1$ corresponds to measurements of the vector polarization of the out-going proton, the last two in this list). So for the $I = 0$ pieces we have the previous results:

$$
\begin{aligned}
(e, e'p): \quad & R^L_{I=0} = R^L_{\text{unpol.}} \\
& R^T_{I=0} = R^T_{\text{unpol.}} \\
& R^{TL}_{I=0} = \cos\phi_p W^{TL}_{\text{unpol.}} \\
& R^{TT}_{I=0} = \cos 2\phi_p W^{TT}_{\text{unpol.}} \qquad (13) \\
(\vec{e}, e'p): \quad & R^{T'}_{I=0} = 0 \\
& R^{TL'}_{I=0} = \sin\phi_p W^{TL'}_{\text{unpol.}} \ ,
\end{aligned}
$$

where the first four are time-reversal even and the fifth response function is time-reversal odd. For the $I = 1$ pieces we have

$$
\begin{aligned}
R^K_{I=1} = a_p \{ & \cos\theta^*_p R^K_{\text{pol.}}(\ell') + \sin\theta^*_p \cos\phi^*_p R^K_{\text{pol.}}(s') \\
& + \sin\theta^*_p \sin\phi^*_p R^K_{\text{pol.}}(n') \} \ ,
\end{aligned} \qquad (14)
$$

where a_p is the vector polarization of the proton, $-1 \leq a_p \leq 1$ and where we have decomposed the responses $R^K_{I=1}$, $K = L$, T, TL, TT, T' and TL', into components involving the ℓ', s' and n' directions, *i.e.* the z', x' and y' directions in Fig. 7 (see Refs. [12] and [13]). In this case, the following ϕ_p-dependences are found for the $I = 1$ responses (Cf. Eqs. 12)):

		ℓ'	s'	n'
$(e, e'\vec{p})$:	L	0	0	1
	T	0	0	1
	TL	$\sin\phi_p$	$\sin\phi_p$	$\cos\phi_p$
	TT	$\sin 2\phi_p$	$\sin 2\phi_p$	$\cos 2\phi_p$
$(\vec{e}, e'\vec{p})$:	T'	1	1	0
	TL'	$\cos\phi_p$	$\cos\phi_p$	$\sin\phi_p$

(15)

where the first four classes are time-reversal odd and the last two are time-reversal even. Thus, for example, the entire L response is

$$
\begin{aligned}
R^L &= R^L_{I=0} + R^L_{I=1} && \text{(16a)} \\
&= R^L_{\text{unpol.}} + a_p \sin\theta^*_p \sin\phi^*_p R^L_{\text{pol.}}(n') && \text{(16b)}
\end{aligned}
$$

and the entire TL response is

$$
\begin{aligned}
R^{TL} &= R^{TL}_{I=0} + R^{TL}_{I=1} && \text{(17a)} \\
&= \left\{ \cos\phi_p W^{TL}_{I=0} + \sin\phi_p \tilde{W}^{TL}_{I=0} \right\} \\
&\quad + \left\{ \cos\phi_p W^{TL}_{I=1} + \sin\phi_p \tilde{W}^{TL}_{I=1} \right\} && \text{(17b)} \\
&= \left\{ \cos\phi_p W^{TL}_{\text{unpol.}} \right\} \\
&\quad + a_p \left\{ \cos\phi_p \left(\sin\theta^*_p \sin\phi^*_p W^{TL}_{\text{pol.}}(n') \right) \right. && \text{(17c)} \\
&\quad \left. + \sin\phi_p \left(\cos\theta^*_p W^{TL}_{\text{pol.}}(\ell') + \sin\theta^*_p \cos\phi^*_p W^{TL}_{\text{pol.}}(s') \right) \right\} \ ,
\end{aligned}
$$

and so on for the other cases. There are 18 responses to be separated in this way; nine are time-reversal even and nine are time-reversal odd. The former are obtained using the reactions $(e, e'p)$ and $(\vec{e}, e'\vec{p})$; the latter use $(\vec{e}, e'p)$ and $(e, e'\vec{p})$.

A specific set of measurements of this sort which may require the determination of several of these responses is the following. One way to obtain information on G^n_E is to use an unpolarized deuteron target and study the (TRE) polarization transfer reactions $^2H(\vec{e}, e'\vec{p})n$ or $^2H(\vec{e}, e'\vec{n})p$ in the quasi-free region where final-state interactions are supposed to be weak enough to permit the (small) effects which are proportional to G^n_E to be isolated. An important question will be: How important are the final-state interaction uncertainties in confusing the G^n_E determination? A possible answer may lie in measuring one of the time-reversal odd responses using $^2H(\vec{e}, e'p)n$ or $^2H(e, e'\vec{p})n$ (or $p \leftrightarrow n$) which are sensitized to these effects as discussed above.

A similar structure occurs for exclusive-1 reactions involving polarized targets, $\vec{A}(e, e'x)$ and $\vec{A}(\vec{e}, e'x)$. The general TRE/TRO decomposition involving I = even and odd tensors pertains as well. In fact, for spin-$\frac{1}{2}$ targets the same characterization given above for $(e, e'p)$ also works, now with angles (θ^*_p, ϕ^*_p) replaced by (θ^*, ϕ^*), the angles specifying the

target polarization direction. For targets with spin ≥ 1, however, the response structure is richer. For example, for the reactions ${}^2\vec{H}(e,e'p)$ and ${}^2\vec{H}(\vec{e},e'p)$ with polarized deuterium, I may be 0, 1 or 2. The first two are classified just as above, while 15 *new* $I = 2$ responses have the following breakdown:[12] $L(3\mathrm{TR}\,E)$, $T(3\mathrm{TR}\,E)$, $TL(3\mathrm{TR}\,E, \sim \cos\phi_p)$, $TT(3\mathrm{TR}\,E, \sim \cos 2\phi_p)$, $T'(0)$, $TL'(3\mathrm{TR}\,E, \sim \sin\phi_p)$. Using polarized targets there are then 33 responses available in this example.

The formalism for the general problem with any spins with/without electron, target or outgoing coincident particle polarizations now exists;[12] our current efforts are directed towards specific problems of interest to evaluate the relative merits of using external unpolarized targets but presuming that an outgoing particle polarization is measured and of using polarized internal targets without requiring final-state polarization determinations.

To end these discussions, let us conclude with one very explicit example to illustrate the content of the many responses a little more concretely. Let us consider the reactions $p(e,e'p)X$, $p(\vec{e},e'p)X$, $p(e,e'\vec{x})X$ and $p(\vec{e},e'\vec{p})X$ (or equivalently for the last two, $\vec{p}(e,e'p)X$ and $\vec{p}(\vec{e},e'p)X$). The general decomposition is given in Eqs. (13) and (15). Let us first specialize to co-planar geometry where $\phi_p = 0$; then we have four $\mathrm{TR}E$ $I = 0$ responses, no $\mathrm{TR}O$ $I = 0$ responses (Eqs. (13), four $\mathrm{TR}O$ $I = 1$ responses, all of n' character and four $\mathrm{TR}E$ $I = 1$ responses, two of ℓ' character and two of s' character (Eqs. (15)). Such measurements are made easier by not having to place a proton spectrometer out of the electron scattering plane (Cf. Figs. 7 and 8). Let us be even more specific and consider parallel kinematics where $\theta_p = 0$ so that the proton is detected along $\vec{q}$ (see Fig. 9). Now the TT response vanishes and we are left with the following behavior:[12]

$$R^L = R^L_{\mathrm{unpol.}} = N^2|S|^2 \tag{18a}$$

$$R^T = R^T_{\mathrm{unpol.}} = N^2|T|^2 \tag{18b}$$

$$R^{TL} = a_p \sin\theta^*_p \sin\phi^*_p W^{TL}_{\mathrm{pol.}}(n') = -a_p \sin\theta^*_p \sin\phi^*_p N^2 2\,\mathrm{Im}\,(S^*T) \tag{18c}$$

$$R^{TT} = 0 \tag{18d}$$

$$R^{T'} = a_p \cos\theta^*_p W^{T'}_{\mathrm{pol.}}(\ell') = a_p \cos\theta^*_p R^T \tag{18e}$$

$$R^{TL'} = a_p \sin\theta^*_p \cos\phi^*_p W^{TL'}_{\mathrm{pol.}}(s') = a_p \sin\theta^*_p \cos\phi^*_p N^2 2\,\mathrm{Re}\,(S^*T) \tag{18f}$$

where N^2 is an overall kinematic factor and where

$$S \equiv \frac{1}{\sqrt{2}} \sum_\ell \left\{ \ell^2 S_{\ell-} + (\ell+1)^2 S_{\ell+} \right\} \tag{19a}$$

$$T \equiv \frac{1}{2} \sum_\ell \{ (\ell+1)(\ell+2) E_{\ell+} - \ell(\ell-1) E_{\ell-} + \ell(\ell+1)\,[M_{\ell+} - M_{\ell-}] \} \ , \tag{19b}$$

using the multipole notation familiar from studies of pion electroproduction. These are for the reactions where the outgoing proton polarization is possibly measured. For the corresponding situation where the proton target is polarized, it is necessary only to change (θ^*_p, ϕ^*_p) into (θ^*, ϕ^*) and to replace a_p by $-\sqrt{2} f_1^{(i)}$.

Suppose only the $M1$ piece of the $N \to \Delta$ transition is important. Then M_{1+} is non-zero, but all other multipoles may be neglected. Then we would have

$$R^L = R^{TL} = R^{TT} = R^{TL'} = 0$$

$$R^T = N^2|M_{1+}|^2$$

$$R^{T'} = a_p \cos\theta^*_p R^T \ .$$

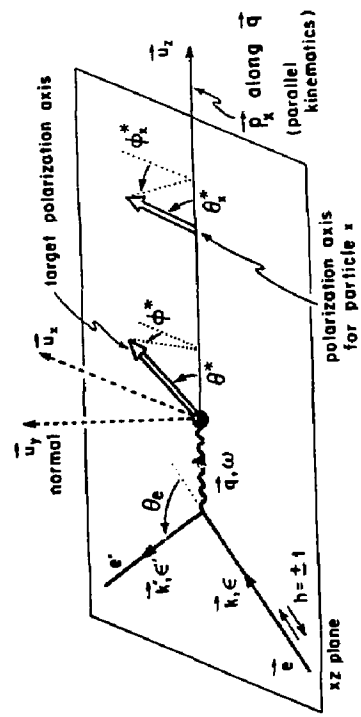

Fig. 9: Specialization of Figs. 7 and 8 to the situation where $\vec{p}_x$ is along $\vec{q}$ (parallel kinematics). (Figure shown sideways.)

If, on the other hand, the $C2/E2$ multipoles are also non-zero (Cf. discussion of inclusive scattering above), then we would have

$$R^L = N^2 8|S_{1+}|^2$$

$$R^T = N^2|M_{1+} + 3E_{1+}|^2$$

$$R^{TL} = -a_p \sin\theta^*_p \sin\phi^*_p N^2 4\sqrt{2}\,\mathrm{Im}\,\left(S^*_{1+}(M_{1+} + 3E_{1+})\right)$$

$$R^{TT} = 0$$

$$R^{T'} = a_p \cos\theta^*_p R^T$$

$$R^{TL'} = a_p \sin\theta^*_p \cos\phi^*_p N^2 4\sqrt{2}\,\mathrm{Re}\,\left(S^*_{1+}(M_{1+} + 3E_{1+})\right) \ .$$

The TL and TL' responses in particular are interesting, since they involve the imaginary and real parts of the interference $S^*_{1+}(M_{1+} + 3E_{1+})$, respectively. For fixed θ^*_p, as the angle ϕ^*_p varies the proportions of these two contributions also vary (weighted by $-\sin\phi^*_p$ and $\cos\phi^*_p$, respectively.

Of course, the analysis can be continued to include other partial waves and multipoles in the final state. Furthermore, relatively simple expressions are also obtained[12] for reactions involving deuterium instead of the proton, except that now there are differences when the outgoing proton's polarization is measured versus when the deuterium target is polarized. The former class of reaction has responses which involve an interference between amplitudes containing singlet and triplet partial waves, but only rank 0 and 1 information; no such interferences occur for the latter class, but additional rank 2 information is now present.

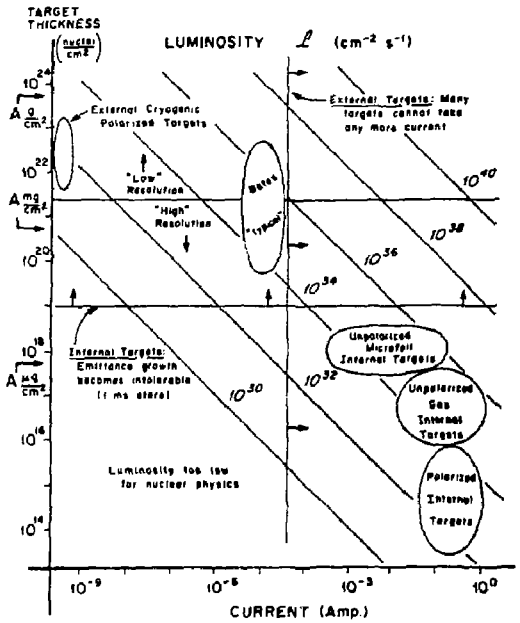

Fig. 10: Luminosity as a function of target thickness and electron current. The former is given in units of nuclei/cm^2 with the specific values of Ag/cm^2, mg/cm^2 and μg/cm^2 indicated as well. The various regions are discussed in the text

Summary and Practical Implications

What has been presented here is a brief overview of some of the highlights of "spin physics" in electron scattering. Interesting interference effects become accessible when polarization degrees of freedom can be controlled. For inclusive (single-arm) scattering the general case requires that polarized targets be available, with studies involving the detection of final-state polarizations comprising a more limited range of possibilities. For exclusive (coincidence) reactions there are interesting processes to explore in both cases, with targets polarized and when a specific particle in the final state is detected together with its polarization. In many cases, it is important (or essential, such as with single-arm scattering from polarized spin-$\frac{1}{2}$ targets) to have longitudinally polarized electrons available.

The practical implications are severe. For detection of final-state polarizations, a polarimeter is required and these are usually devices with limited efficiencies. For polarized target studies the problem is to obtain significant luminosities and still have feasible experiments. This is illustrated in Fig. 10 where luminosity is given for ranges of target thicknesses and electron currents. To be practical for nuclear physics studies it must be possible in general to obtain luminosities above, say, $10^{30}\,\mathrm{cm}^{-2}\,\mathrm{s}^{-1}$ (and frequently considerably above this). To have good resolution capability in general requires that the target not be too thick. Typical external cryogenic polarized targets cannot withstand more than a few $\times$ 1 nAmp before depolarizing and so to reach the desired range of luminosity requires a very thick target. In fact, with such targets the degree of polarization is usually rather low and so the effective luminosity is actually quite a bit smaller than the nominal value. With internal targets using a circulating electron beam the current can be very high (Bates is designed for 80 m Amp internal current, for example[14]). The implications here are clear: for such studies in the region indicated in the figure, it is necessary to have internal polarized target densities lying above 10^{14} nuclei/cm^2.

References

1. T. W. Donnelly and A. S. Raskin, *Ann. Phys.* **169**, 247 (1986).
2. T. W. Donnelly, "Considerations of Polarization in Electron Scattering," at the Workshop *Perspectives in Nuclear Physics at Intermediate Energies*, Trieste (1983).
3. T. W. Donnelly and I. Sick, *Rev. Mod. Phys.* **56**, 461 (1984).
4. T. W. Donnelly, "Polarized Electron Scattering from Polarized Nuclei," at the 6th Seminar *Electromagnetic Interactions of Nuclei at Low and Medium Energies*, Moscow (1984).
5. T. W. Donnelly, "Polarization Degrees of Freedom in Electron Scattering from Nuclei," at the Summer School *New Vistas in Electro-Nuclear Physics*, Banff, Canada (1985).
6. R. G. Arnold, C. E. Carlson and F. Gross, *Phys. Rev.* **C23**, 363 (1981).
7. M. E. Schultze *et al.*, *Phys. Rev. Lett.* **52**, 597 (1984).
8. T. W. Donnelly, A. S. Raskin and J. F. Dubach, (to be published).
9. J. D. Walecka, *Nucl. Phys.* **A285**, 349 (1977).
10. T. W. Donnelly and R. D. Peccei, *Phys. Rep.* **50**, 1 (1979).
11. T. W. Donnelly, "Electron Scattering and Neutrino Reactions in Nuclei," in the proceedings of *Nuclear and Subnuclear Degrees of Freedom and Lepton Scattering*, Erice, Sicily (1984).
12. A. S. Raskin, Ph.D. Thesis (M.I.T., 1987, unpublished).
13. A. Picklesimer, J. W. Van Orden and S. J. Wallace, *Phys. Rev. C* **32**, 1312 (1985); A. Picklesimer and J. W. Van Orden, *Phys. Rev. C* **35**, 266 (1987).
14. Proposal for a CW Upgrade of the William H. Bates Linear Accelerator Center (June, 1984).

Storage Rings, Internal Targets and PEP*

J. E. Spencer
Stanford Linear Accelerator Center
Stanford University, Stanford, CA 94305

Prologue

Most of the talks here will be on physics from accelerators and storage rings rather than the physics of such systems since the "physics" is hard enough without having to worry about the beams or how you get them. As a result, this remains transparent to the user via an equipartition of effort worthy of a business school. This is especially debatable for colliding beam storage rings and leads to the corollary that most rings will be born, live and die as dedicated systems. SPEAR is a notable exception while PEP is not – even though PEP seems to provide more unique opportunities over a broader spectrum of physics. Examples include one and two photon physics with real and virtual photons to make all J^{PC} quark combinations as well as high luminosity QCD confinement studies with internal targets as discussed at this workshop. Some related possibilities include external beams of high energy photons; single-pass, free-electron lasers and x-ray synchrotron radiation which could all be the highest energy, resolving power, intensity and brilliance anywhere. From the viewpoint of accelerator physics, such examples fall into three categories: colliding beam physics, internal and external target physics.

How unique such possibilities are, whether they are truly possible e.g. what modifications might be required and questions of compatibility are discussed. Some systematic accelerator physics studies are suggested with implications for this and other proposed projects. As a fan of Gary Larson, I begin with Fig.1 showing his perspective of the PEP tunnel relevant to this occasion. Figure 2 is about reinventing the wheel(or ring in this case) with a lot of people trying to figure out what it is and how you use it. While one can't be sure what they'll come up with it's certain to be "interesting". However, because there have been several proposals for dedicated rings with properties which seem no better than PEP, perhaps Evelyn Waugh should have the last word here: *"If politicians and scientists were lazier, how much happier we should* all *be."*

1. Introduction

The goal is to describe storage rings with internal targets using PEP as example. Although fixed-target experiments were suggested some twenty-five years ago[1] little work of this kind has been done[2]. The differences between electrons and heavier particles such as protons, antiprotons or heavy ions is significant and is also discussed because it raises possibilities of bypass insertions for more exotic experiments. Finally, I compare PEP to other rings, in various contexts, while examining and verifying the statements made in the prologue e.g. that it is an ideal ring for many fundamental and practical applications that can be carried on simultaneously.

A. Some History and Perspective

In a sense, the SLAC linac was built to provide space-like photons[3] for deep inelastic scattering experiments on few nucleon systems. Such experiments demonstrated the basic underlying parton structure of the nucleon. In direct contrast, the subsequent development of SPEAR provided highly time-like photons via the (e^+, e^-) annihilation process shown in Fig. 3(b) which led to the first observations of resonant production of charmed quark pairs$(q_c, \bar{q}_c)$ as well as the heavy, electron-like particle called the tau. Related work is still being done at SPEAR together with a considerable amount of synchrotron radiation research.

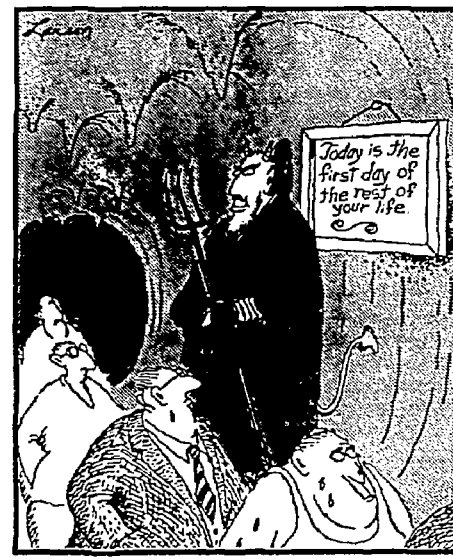

Fig. 1: Perspective of the PEP tunnel.

* Work supported by the Department of Energy, contract DE-AC03-76SF00515.

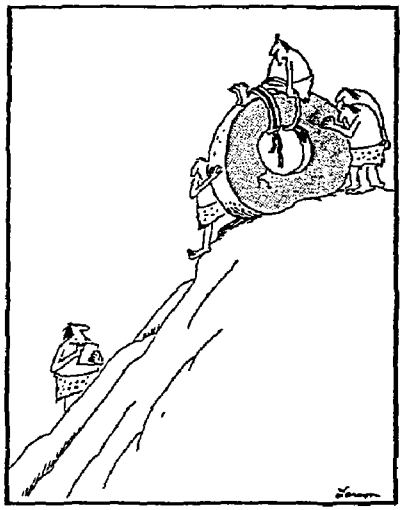

Fig. 2: Early experiments in transportation

With the higher energies available at PEP, higher-order processes become important with the space-like photon production processes of Fig. 3(c) being dominant. This two photon reaction is the main production channel for C-even particles with the physics at the internal vertices in diagrams such as Fig. 3(f) where $X \equiv f\bar{f}$. In all diagrams except Fig. 3(c), the cross sections fall with energy predominately as $1/s$ whereas 3c increases[3,4] in such a way that the crossover between it and processes such as 3b occur at beam energies above $\sqrt{s}/2 = 1\text{GeV}$ depending on the mass m_f.

Concerning internal targets, the first experimental work at SLAC will be discussed at this workshop. My own interest in this area began in 1981 with the question[5]: "Is it possible to use internal foils to reduce phase space and simultaneously serve as a scattering target for an external, high-resolution spectrometer?" With dispersion at the target and the low ring emittance, this would be a consistent and significant improvement in SLAC's capabilities. Unfortunately, the answer to both questions was no unless the foil was a scraper or stripper which was neither new nor very interesting.

More recently, the subject was again considered[4] at an high energy e^+-e^- workshop on PEP because of new developments in polarized gas targets[6]. In this context, the results were quite positive and led to simple scaling relations for internal target luminosity. Furthermore, this option was just one of several to obtain higher luminosities with alternative incident channels: 1) e-γ, 2) γ-γ, and 3) e-A and γ-A. Using high current, stored bunches to produce the primary photon beam which is Compton converted to high energy by backscattering on a high current, high energy linac beam appeared to be an excellent way to upgrade the effective energy and luminosity of existing storage rings. Reaction rates would be improved because photoproduction cross sections are larger than electroproduction and higher current densities are possible by eliminating the conventional beam-beam interaction. While the primary and secondary photon beams would be a significant new research tool, only the e-A option will be discussed further here.

B. A Short History and Description of PEP

Figure 4 shows a schematic layout of the Positron-Electron Project, PEP, as used for colliding beam physics up to 1986. The ring has sixfold symmetry and divides into 12 regions of alternating arcs and long straight sections for experiments called insertions. The odd-numbered regions are the arcs which are subdivided into 19 FODO cells containing a Focusing quad(F), bending magnets with little or no focusing(O) and a Defocusing quad(D). Insertions for injection, extraction or experiments are so labelled because they perturb the otherwise simply periodic structure of identical FODO or unit cells introducing what are called superperiods into the structure. Individual particles can be thought of as oscillators under these focusing forces with frequencies that depend on particle energy.

A good description, including initial operating results and funding history, is available elsewhere[7]. In brief, formal ground breaking took place in June 1977, the ring was completed by April 1980 and delivered $\mathcal{L} > 10^{30} cm^{-2} s^{-1}$ at 11GeV by June.

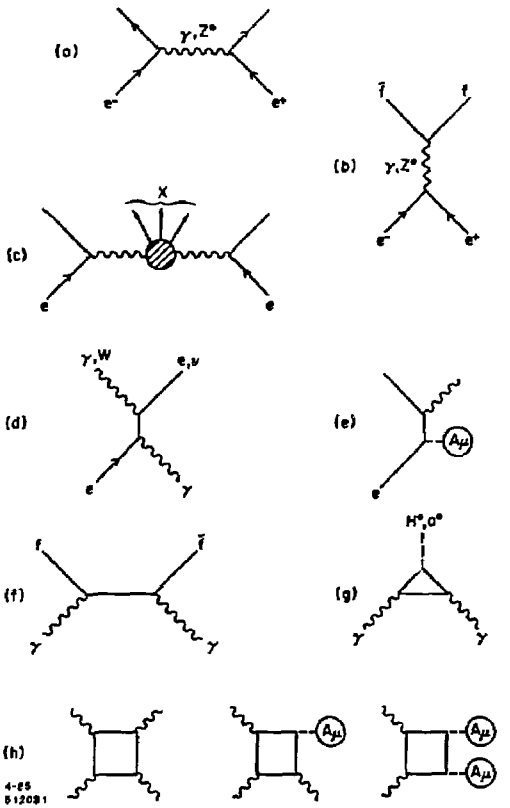

Fig. 3: Low order diagrams in the standard model for: (a,b) elastic, electroweak scattering; (b) electron-positron annihilation into elementary fermions $f = e, \mu, \tau \ldots q_u, q_d, q_t \ldots \nu_{e,\mu,\tau} \ldots$ as well as elementary bosons ($W^{\pm}, Z^{\circ} H^{\circ}, H^{\pm 2}$); (c) two-boson, electro-weak production; (d) Compton scattering or conversion ($\gamma \rightarrow W^{\pm}$); (e) potential bremsstrahlung; (f) two-photon annihilation to fermions; (g) two-photon annihilation to bosons; and (h) photon-photon scattering, inverse photon bremsstrahlung (harmonic production) and Delbrück scattering.

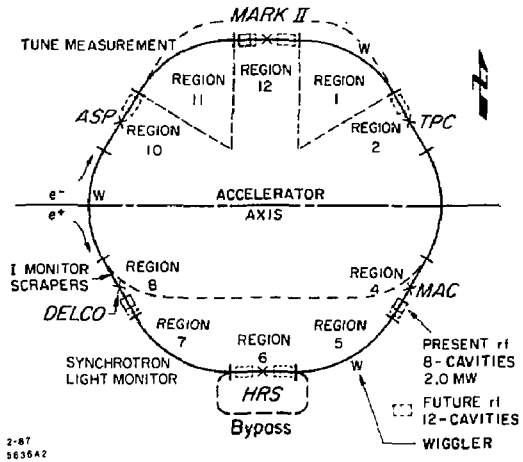

Fig. 4: Schematic layout of PEP showing some characteristics of interest here.

Typical values circa 1984 with all interaction regions active with good detector deadtimes and beam lifetimes at 14.5GeV were $\mathcal{L} \approx 3-4 \times 10^{31}$ giving integrated luminosities per IR of

$$\int_{Day} \mathcal{L}dt \approx 1500 \text{ nb}^{-1} \quad \text{or} \quad \bar{\mathcal{L}} \approx 1.8 \times 10^{31}\ cm^{-2}s^{-1}\ .$$

This implies reaction rates on the order of 1 event per picobarn of cross section per day.

The different detectors then were an upgraded MarkII from SPEAR which will be used on SLC next. At 2 o'clock was the Time Projection Chamber which can track and identify all particles such as pions, kaons, protons etc. At 4 o'clock was the MAgnetic Calorimeter for measuring total, final state hadron energy including neutrons and K^0_L followed by the High Resolution Spectrometer at 6 o'clock which had significantly better mass resolution than the other detectors. The Direct Electron Counter identified all final state electrons and the Assymetric Photon search was a supersymmetry experiment looking for new particles like the photino. MAC was also used for these experiments because PEP provided an ideal operating range for them.

Such experiments demonstrated the ability to measure cross sections on the order of tens of femtobarns(10^{-39}cm^2) with storage rings which is an impressive achievement. Notice that the basic annihilation cross ection is

$$R = \frac{4}{3}\pi\alpha^2/s = 86.8/E_{cm}(TeV)^2 \text{ fb}$$

for processes such as Fig. 1(b) which is independent of mass m_f.

Some other elements in PEP besides those shown in Fig. 4 include beam position monitors and vacuum hardware around the ring, a tune measuring setup as well as transverse and longitudinal feedback hardware. Table I updates the more important parameters and capabilities of PEP which will be discussed in more detail after we motivate and define some terms.

2. The View From Mt. Hamilton

This section is a description of storage rings for physicists. The first problem is how to confine high intensity bunches of charged particles in stable 3-dimensional potential wells for long periods of time. In the rest frame of the bunch, a transverse electric potential results from transverse magnetic fields and the longitudinal well results from the RF field required to replace energy lost to synchrotron(and bremsstrahlung) radiation. The relativistic equation of motion of charged particles in an electromagnetic field in Hamiltonian form i.e. the total energy as a function of canonical variables q and p is:

$$H\Psi = i\dot{\Psi} = (H_{rad} + H_{part} + H_{int})\Psi$$

$$H_{rad} = \frac{1}{8\pi}(E^2 + B^2)\delta v; \quad H_{part} + H_{int} = \sum_i H_i$$

$$H_i(p,q) = e_i\phi(\vec{r}_i) + [(\vec{p}_i - e_i\vec{A}(\vec{r}_i))^2 + m_i^2]^{1/2}$$

where $A = (\phi, \vec{A})$ is the external field from the magnets, atoms, or lasers as well as the fields produced by the charges themselves. H_{rad} is the field energy and H_i is the total particle energy in the field.

Table I: Some Representative Storage Ring Parameters for PEP

Characteristic	Value
Nominal Maximum Energy per Beam[a]	17 GeV
Nominal Minimum Energy per Beam[a]	2 GeV
Maximum Current per Beam at 15GeV[b]	46 mA
Number of Particles per Beam at 15GeV	2.1×10^{12}
Maximum Colliding Bunches per Beam	3
Design Luminosity per Interaction Region $\mathcal{L}_{GB}$(Below 15 GeV)	$10^{32}(E/15)^2$ cm^{-2} sec^{-1}
Number of Interaction Regions	6
$\mathcal{L}_{IT}$ (Constant τ_l and I)[c]	$10^{34}/Z(Z+1)$ cm^{-2} sec^{-1}
Average Vacuum in Ring	10^{-9} Torr
Energy Spread (σ_E/E)	$6.7 \times 10^{-5}E$(GeV)
Natural Emittance (ϵ_x)[d]	$5.5E(\text{GeV})^2$ Å
Length of Each Straight IR Insertion	120 m
Available Free Length for Experiments	15 m
Circumference	2200 m
Symmetry	6
RF Power Installed[e]	6.0 MW
Number of Accelerating Sections	24
Number of 0.5 MW Klystrons[e]	12
RF Frequency	353.2 MHz
Harmonic Number	2592

a This energy has not been well defined as discussed in the text.
b For single beam operation this scales up as the number of beams.
c Assumes lifetime τ_l = 2h, current I=100mA for atomic number Z.
d This can be significantly reduced as discussed in the text.
e Commercial klystrons are now available with twice this power.

Spin terms are ignored together with the whole question of beam polarization because our concern is with the classical dynamics of motion which should not be influenced by spin effects even for the "small" emittances of interest here. However, if such effects were to be emphasized, superconducting or permanent magnet storage rings would be an ideal place for them.

Retaining only first degree terms in $\vec{A}_o$, in the rest frame, gives

$$H_{oi} - m_i = (\vec{p}_{oi} - e_i\vec{A}_o(\vec{r}_{oi}))^2/(2m_i) + e_i\phi(\vec{r}_{oi}) + V \ .$$

For a pure electrostatic field ($\vec{A} = 0$) this gives the familiar non-relativistic expression for the energy. Neither H nor H_i includes interaction between particles unless we add a term such as V with subscripts ij, ijk etc. which then gives coupled equations. If we are interested in such beam dynamics as coherent effects within a beam bunch, or various excitation modes in a laser medium, crystal lattice, atom or "elementary" particle we must include such terms.

The fields $\vec{A}$ and ϕ are generally nonlinear due to magnet errors and end fields, the sinusoidal character of the RF and the fields induced by the beam through self forces(e.g. the so-called ponderomotive potentials) or wake fields(interaction with the rest of the external world exclusive of guide fields). Such fields can couple the degrees of freedom of the single particle e.g. provide transverse-transverse (x-y) and transverse-longitudinal (x-z) coupling. Furthermore, since wake fields can be either transverse or longitudinal as well as fast or slowly decaying ($\tau \lesssim 1/\omega_s$ or $1/\omega_{x,y}$ for fields with Fourier components $\omega \lesssim c/L$), one expects that both single and multibunch instabilities will be possible.

Even assuming only one beam and one bunch, there are a number of current dependent effects which can cause beam blowup and subsequent particle loss by leakage out of the well. A good general reference for single-particle effects is Ref's. 8& 9. Collective effects have been discussed in Ref. 10. They may be broken down into coherent and incoherent depending on whether there are phase relations between individual particles or not. Where there are, one can think of modes of motion like that of the incompressible liquid drop of Bohr and Mottelson i.e. one has dipole and quadrupole motion that can be quite dramatic. There are many ways to both induce and cure such coherent effects. Thus, as the bunch oscillates, the potential well dynamically distorts which can produce an oscillating force back on the beam that can either drive or damp it. Similarly, the external potential well can be made to act the same way – usually via negative electronic feedback that senses and then feeds back to damp an instability. One can also add harmonic cavities to statically distort the potential well for various reasons[11] such as bunch length control or power consumption.

The canonical position, q, can be understood to represent the transverse displacement x and y from the equilibrium orbit and is a function of time, the independent variable, or equivalently, the distance along the central orbit s (or z). The momentum, $p \approx \gamma m q'$ where $q' = dq/ds$ so the important Liouville invariant is

$$\int pdq = m\int \gamma q' dq \equiv m\gamma\epsilon \equiv m\epsilon_n$$

for any particle with ϵ its area in transverse phase space. A beam of particles has a distribution function in phase space which convention describes by

$$\epsilon_n \equiv \gamma\sigma\sigma' = \gamma\frac{\sigma^2}{\beta}$$

where ϵ_n defines the normalized, "invariant", transverse emittance in any direction with σ, σ' the rms size and divergence and β the focusing or betatron function of the cells in that coordinate(x,y). It is also called a Twiss parameter[8].

The phase space trajectory of a representative particle that defines the rms beam envelop can be expressed[8,9] as

$$q = \sqrt{\epsilon\beta(s)}\cos(\phi(s) - \phi_0)$$

$$q' = -\sqrt{\frac{\epsilon}{\beta}}\left[\sin(\phi(s) - \phi_0) - \alpha\cos(\phi(s) - \phi_0)\right]$$

where $\alpha = \beta'/2$ and the phase

$$\phi(s) = \int_0^s \frac{ds}{\beta(s)}$$

with $\phi(0) = 0$ and $\phi(s)$ is another twiss parameter. Integrated around the ring, it gives the tune or betatron number

$$\nu = \frac{1}{2\pi}\int_0^L \frac{ds}{\beta(s)} = \frac{1}{2\pi}\oint \frac{ds}{\beta} \ .$$

The transformation of $\{q\} = (q, q')$ from one place to another, $\{q_2\} = R\{q_1\}$, is derivable from these expressions in a number of ways[8] e.g. using two linearly independent solutions such as $\phi_0 = 0, \frac{\pi}{2}$ giving:

$$R_{11} = \sqrt{\frac{\beta_2}{\beta_1}}\left[\cos\Delta\phi + \alpha_1\sin\Delta\phi\right]$$

$$R_{12} = \sqrt{\beta_1\beta_2}\sin\Delta\phi$$

$$R_{21} = \frac{1}{\sqrt{\beta_1\beta_2}}\left[(\alpha_1 - \alpha_2)\cos\Delta\phi - (1 + \alpha_1\alpha_2)\sin\Delta\phi\right]$$

$$R_{22} = \sqrt{\frac{\beta_1}{\beta_2}}\left[\cos\Delta\phi - \alpha_2\sin\Delta\phi\right]$$

where $\Delta\phi = \phi_2 - \phi_1$. These expressions are the first order transformations for the transverse motion of the Hamiltonian system and allow tracking with nonlinear perturbations etc. More importantly we have defined most of the terms used in Table I and needed for a more detailed study of rings such as PEP.

3. Three Kinds of Luminosity

A good place to begin is to define some different kinds of luminosity and what I mean by high and low luminosity and thick and thin targets etc. Conventional colliding beam luminosity which I will call $\mathcal{L}_{CB}$ has been discussed in detail[9,4].

A. Colliding Beam Luminosity

The incoherent beam-beam interaction between colliding bunches produces strong, nonlinear forces on the bunches which limit the operation of present rings. The leading-order, linear focusing force for head-on $e^{\pm}$ collisions, expressed as a tune perturbation per crossing, is[9]

$$\Delta\nu_{x,y} = \frac{r_e N_e \beta^*_{x,y}}{2\pi\gamma\sigma^*_{x,y}(\sigma^*_x + \sigma^*_y)}$$

where σ is the rms bunch size, N_e is the number of particles per bunch and β^* is the beta function at the crossing point or IR. For protons one would use the classical proton radius, r_p. Notice that γ for 20 TeV SSC protons is the same as for 10 GeV PEP electrons. The limiting magnitude of this number for most electron rings is $\Delta\nu^*_{x,y} \lesssim 0.05$.

With internal targets, this number can serve as a benchmark to compute the allowable number of ions replacing N_e with $-sgn(\frac{q}{z})N_i$, depending on whether we use an $e^{\pm}$ beam, before a clearing field is needed. The expressions are otherwise the same i.e. higher energy beams are preferred. Constraints from the operation of the target are generally more stringent i.e. depolarization and replenishment rates that are possible but multi-bunch instabilities with electron beams also have to be considered.

Although the above expression can be identified with the average, small amplitude tune shift for gaussian bunches it is best thought of as the tune *spread* in the core of the bunch[9]. At some limiting value of this tune spread ($\Delta\nu^*$) or bunch current (N^*_e) the bunch cross-section ($\sigma^*_x\sigma^*_y$) increases, luminosity fails to increase and may decrease and the lifetime may well decrease. *If this limit is made the same in both transverse* directions by making $\beta^*_y/\beta^*_x \simeq K(\equiv \epsilon_y/\epsilon_x)$, the tune independent, x-y coupling in the machine), one expects the maximum achievable luminosity when $\sigma^*_x \gg \sigma^*_y$ to be:

$$\mathcal{L}_{max} = \frac{(N^*_e)^2}{4\pi\sigma^*_x\sigma^*_y} f n = (\Delta\nu^*)^2(\frac{\gamma}{r_e})^2\frac{\epsilon_x}{\beta^*_y} f n$$

where $\epsilon_x = \pi\sigma^2_x/\beta_x$, f is the revolution frequency and n is the number of bunches per beam. Table II for PEP and SPEAR shows they are both near their limits of $10^{31} < \mathcal{L}_{CB} < 10^{32}$.

B. External Target Luminosity

For resolutions of order 20-50 keV at energies typical of Bates or LAMPF one must use target thicknesses of $t_t \approx$10–50mg/cm^2. Typical currents with a consistent phase space and energy spread are $I_b \approx$50–100μA. Translating these numbers into an equivalent luminosity gives:

$$\mathcal{L}_{ET} = (\frac{I_b}{e})N_A(\frac{\rho x}{A}) = 3.1\times10^{35}[\frac{I_b}{100\mu A}][\frac{t_t}{10mg/cm^2}][\frac{12}{A}]$$

where N_A is Avogadro's number, A the gram-molecular weight and A the atomic mass number in carbon units. This is a good benchmark for comparison to other facilities.

Table II: Some current operating parameters for the SPEAR and PEP storage rings for both colliding and single beams. These numbers do not involve the use of wigglers except during PEP injection at 5 GeV.

Energy(GeV)	2 SPEAR	5 PEP	10 PEP	15 PEP	
Beam Current, I_b^{Max}	100	30(?)	120(?)	92	mA
Beam Current, I_b^{Col}	25	5	20	46	mA
Coupling, $K \equiv \epsilon_y/\epsilon_x$	6.3	6.3	7.6	7.6	%
Emittance, $\epsilon_x \equiv \sigma^2_x/\beta_x$	0.195	0.0138	0.055	0.124	mm-mr
Emittance, $\epsilon_y \equiv \sigma^2_y/\beta_y$	12.2	0.866	4.19	9.43	μm-mr
Energy Spread, σ_E/E	0.048	0.033	0.067	0.10	%
Damping Time, $\tau_{x,y}$	28.3	100	27.5	8.2	msec
Revolution Time, T_o	0.78	7.34	7.34	7.34	μsec
IR Beta, β^*_x	0.9/20	3.0/15	3.0/15	3.0/15	m
IR Beta, β^*_y	0.03/35	0.12/0.6	0.12/0.6	0.12/0.6	m
IR Size, σ^*_x	0.42/1.97	0.20/0.45	0.41/0.91	0.61/1.36	mm
IR Size, σ^*_y	.019/0.65	.010/.023	.022/.050	.034/.075	mm
Divergence, σ^*_x	.465/.099	.068/.030	.136/.061	.203/.091	mr
Divergence, σ^*_y	.638/.019	.085/.038	.187/.084	.280/.125	mr
Energy Loss/Turn	0.110	0.333	5.33	27.0	MeV
Peak RF Voltage, V_p	0.495	0.650	6.49	39.1	MV
Bunch Length, σ_z	3.5	2.8	2.3	2.0	cm

C. Internal Target Luminosity

One can write the internal target luminosity in terms of the target thickness, n_t, as

$$\mathcal{L}_{IT} = (\frac{I_b}{e})N_A(\frac{\rho x}{A}) = 6.2\times10^{32}[\frac{I_b}{100mA}][\frac{n_t}{10^{15}/cm^2}]\ cm^{-2}s^{-1}.$$

One will find that luminosities on the order of 10^{33} are possible without significant effects on the beam. Targets on the order of $n_t \sim 10^{15}/cm^2$ or *tens of* ng/cm^2 *are very thin but the* currents are greater than for $\mathcal{L}_{ET}$ because of the more than 10^5 traversals per second in the ring. Such thicknesses appear *ideal* for optically pumped, *polarized* targets because of depolarizing *effects due to beam heating in solid targets. Furthermore,* there appears[7] to be a large range of (A,Z) available including H^1, D^2 and He^3 i.e. the 3, 6 and 9 quark systems.

Because $\mathcal{L}$ does not depend on the beam cross-section, one can operate in a mini-maxi β configuration with small angular spreads at the target and small $\mathcal{L}_{CB}$. Considerably thicker targets are also possible through the use of "target scrapers" and a better understanding of dynamic aperture.

There could also be a tune perturbation as mentioned above and the same limit $\Delta\nu^*$ can be used as a guideline. Such questions are interesting and should be studied. An appropriately designed target would also allow study of, wake fields, plasma lenses and their control of β^* as well as various tune modulation and feedback effects just to mention a few possibilities.

4. Luminosity Limitations

A. Colliding Beams

Increasing the frequency via superconducting magnets, or the number of bunches or the energy i.e. stiffening the beam are all expected to improve luminosity. Unfortunately, increasing the number of bunches (and duty factor) produces multibunch instabilities and other problems when the total number of bunches exceeds the number of IR's. Thus, one seldom sees a linear increase in luminosity with n unless $\Delta\nu < \Delta\nu^*$. Decreasing either β_y^* or increasing the horizontal emittance ϵ_x reduces the beam-beam force but is difficult because this increases the sensitivity to transverse instabilities. Decreasing β_y^* also implies shorter bunches which increases the sensitivity to transverse-longitudinal couplings i.e. synchrobetatron resonances. Using wigglers in existing rings to increase ϵ_x with *decreasing* energy[12] is now well established and relatively benign but the reverse is not true. In PEP, the wigglers are used to both decrease damping time and increase emittance.

Evidence from many rings has shown[13] that $\Delta\nu^* \lesssim 0.05$ and that it is difficult to keep this matched in both directions with increasing beam currents. Nevertheless, this number can presumably be increased in a variety of ways e.g. by increasing damping by going to higher bend fields (and thus also increasing f) or by incorporating more wigglers. However, because the multipole expansion of the beam-beam interaction goes to high order and these multipoles can't be reduced by simply increasing the aperture as for quadrupoles it is clear that the linear description of the beam-beam interaction is not adequate. At the same time, it is not at all clear how to deal with such nonlinearities or even to simulate them in a self-consistent way. Furthermore, very little effort has gone into this and related questions such as multibunch instabilities.

I will not go into the many attempts to compensate or cancel $\Delta\nu$ except to mention the charge-neutralization scheme of the Orsay Group[14] using 4 beams and double rings. It was hoped this approach would provide an improvement in $\mathcal{L}_{max}$ of two-orders of magnitude but so far has not been made to work. The Stanford single-pass collider (SLC) represents the opposite extreme where it seeks to maximize $\Delta\nu^*$ with high bunch current and low-emittance to enhance luminosity through a pinch effect. Another attitude we have taken is to avoid the beam-beam problem[3,4] through conversion of the charged particles into photons. The limits in this case are presumably the maximum, single bunch currents which a linac can provide and a storage ring can store with good stability and emittance. This can be limited by many external effects before internal space-charge becomes important but again there is very little systematic information available on this question. The "external" photon beam from this technique would also be a unique resource for fixed target experiments.

B. Internal Targets

The current limits discussed above apply here as well. In addition, there is the beam lifetime and emittance due to internal target density. The PEP handbook shows the expected lifetimes due to various sources of loss in PEP. While this implies the importance of three different processes over the range of energies of interest, the most important one for our purposes is atomic bremsstrahlung since we assume the Touschek effect will only be important near the IR's and that the particle density can easily be varied by the required factor of two or so. This same factor of two might also be obtainable by manipulating $(\beta^*_{min}, \beta^*_{max})$ in a mini-maxi beta scheme. This is clearly not a problem but bremsstrahlung from "residual-gas" is – because the differential probability for radiation loss is roughly constant up to the full electron energy for the electron energies of interest here.

Integrating Rossi's expression[15] for the differential radiation probability per unit radiation length gives:

$$\int_{(\frac{k}{\gamma})_{RF}}^{1} \Psi_{rad}(x)dx = [\frac{4}{3}\ln(\frac{\gamma}{\delta\gamma})_{RF} - \frac{5}{6}]$$

where x is the fractional photon energy, ω/ϵ. The fractional particle loss is then

$$\frac{dN_b}{N_b} = -[\,]\frac{\rho}{X_o}dx \longrightarrow \frac{1}{\tau} = [\,]\frac{c\rho}{X_o}$$

assuming a simple target unifo distributed around the ring like residual gas. Here $1/X_o \equiv \mathcal{N}\sigma_{rad}/A$ with σ_{rad} the total bremsstrahlung cross section per nucleus or atom and x is the lineal thickness. In terms of both ring and target components, the expression is

$$\frac{1}{\tau} = [\,][\sum_i \frac{c\rho_i^{STP}}{X_{oi}}(\frac{P_i}{760}) + \sum_j \frac{c\rho_j^{STP}}{X_{oj}}(\frac{l_t}{l_R})(\frac{P_j}{760})(\frac{273}{T_j})]$$

where l_t/l_R is the ratio of target length to ring circumference. Including both the atomic bremsstrahlung cross section for electrons and nucleus so that $\sigma^i_{rad} = 4\alpha Z_i(Z_i+1)r_e^2[\ln 183/Z_i^{1/3} + \frac{1}{18}]$ but ignoring all but one target component (i.e. considering only the partial lifetime due to the target) in an otherwise perfect vacuum gives:

$$\frac{T_o}{\tau_t} \simeq [\,]4\sigma_o Z(Z+1)\ln(183/Z^{1/3})[\frac{N_A}{A}\rho^{STP}l_t(\frac{P}{760})(\frac{273}{T})].$$

The last factor in brackets is just the target thickness n_t (#/unit area), $\sigma_o \equiv \alpha r_e^2$ and T_o is the revolution time around the ring (see Table II). For hydrogen, $\rho^{STP}_{H_2} = 0.090\ kG/m^3$ so for $l_t = 10$ cm

$$n_t = \frac{2N_A}{A_{H_2}}\rho^{STP}_{H_2}l_t(\frac{P_t}{760}) = 5.38\times10^{20}(\frac{P_t}{760})[atoms/cm^2].$$

For $n_t = 10^{14}/cm^2$, this implies $P_t = 1.4\times10^{-4}$ Torr or a required differential pumping rate of $\sim 10^{-5}$ Torr at room temperature which is reasonable. One wants this differential rate to roughly correspond to the l_t/l_R factor ($\simeq 4.5\times10^{-5}$ in PEP) since the two main, residual gas components observed with mass analyzers are hydrogen and carbon monoxide.

Because the RF capture bucket width can be $\delta\epsilon_e/\epsilon_e \gtrsim \pm 1\%$ in both SPEAR and PEP, the corresponding partial lifetime for a $10^{14}/\mathrm{cm}^2$, hydrogen target is:

$$\frac{\tau_\ell^H}{T_o} \simeq (5.31 \times 4 \times 0.58mb \times 10.42 \times 10^{14})^{-1}$$

$$= 7.8 \times 10^{10} \begin{cases} 159 \text{ hrs} & \text{(PEP)} \\ 16.9 \text{ hrs} & \text{(SPEAR)} \end{cases}$$

This indicates these experiments can be done on both SPEAR and PEP without requiring dedicated operation with $\mathcal{L} \gtrsim 10^{33}$ $\mathrm{cm}^{-2}\mathrm{s}^{-1}$ using state-of-the-art polarized gas targets! This is independent of beam energy and valid for all energies of current interest ($\epsilon \gtrsim 1.5$ GeV) as well as elements with $\alpha Z \ll 1$. PEP, with its large radius and large energy range, would seem to be an ideal system for these experiments especially when multibunch operation with higher duty factor and current is developed. These operating conditions are ideally matched to simultaneous synchrotron radiation operation.

C. Accelerator Physics Studies

Systematic machine physics studies on PEP with a single beam that are relevant to these questions include bunch cross-section measurements versus all of the following: bunch current (N_b); bunch number (n_b) and distribution; both high and low $\beta^*_{x,y}$; ν_s, σ_ϵ, σ_ℓ and V_{RF}; and $\nu_{x,y}$. These should be done at a couple of energies e.g. a low (5 GeV), intermediate (10 GeV) and high energy (15-17 GeV). Any instabilities observed should be characterized by their threshold behavior (N_{th}) versus these parameters including possible differences between electrons and positrons.

5. PEP Capabilities

Designing storage rings for a specific process in Fig. 3 might emphasize energy spread for Fig. 3(b) and electron polarization for Fig. 3(c) but the most important parameters characterizing both accelerators and storage rings are the energy range (C-M) and the beam current or luminosity available over this range. While the primary goal is to reach higher energies, it also seems important to improve the luminosity and range of capabilities of existing facilities. The PEP storage ring, with its large, single-beam energy range ($E_b \sim 2 - 17(25)$ GeV) in conjunction with the SLAC high energy, high current, low emittance linac beam provides some unique opportunities. Here we will discuss some of the factors each application wants and try to show how PEP can supply them.

A. Synchrotron Radiation

Figure 5 compares the synchrotron light spectra available from the cell bending magnets for a number of existing and proposed facilities. While most of these have wigglers which enhance such spectra, these comparisons appear to be easily biased and also change rapidly. Nonetheless, PEP has some unique possibilities here as well e.g. it has 5m symmetry straight sections midway between interaction regions which already have 2T wigglers as shown in Fig. 4. In addition, I have shown some bypass possibilities in Fig. 4 and from Table I and Figs. 4 and 6 one sees there are already several long, straight insertions with lengths up to 120m which could be used for coherent undulators. Because there are also a number of new, low emittance configurations possible for PEP[16], some of which are shown in Table III, such options seem inevitable.

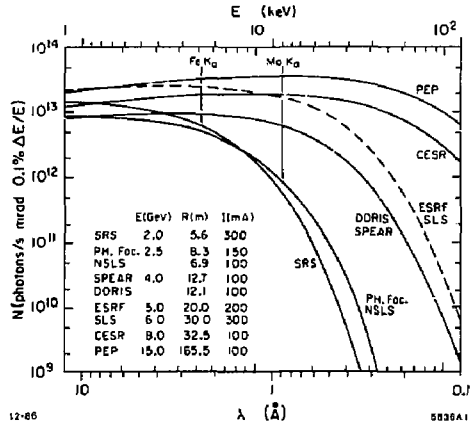

Fig. 5: Comparison of PEP's synchrotron radiation spectrum with a number of existing and proposed rings such as the European Synchrotron Radiation Facility and the Argonne Synchrotron Light Source.

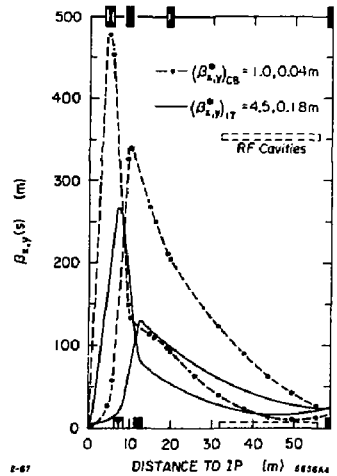

Fig. 6: Beta functions for the new colliding beam configuration of Table III around the Interaction Region(IR) and RF cavities.

For high brightness you need low emittance. Let's compare to SLS whose design emittance[17] at 6 GeV is $\epsilon = 65$Å compared to PEP's 45Å. This can also be improved[18] by at least another factor of two by using Robinson wigglers to increase the horizontal damping partition, J_x. It seems almost too good to be true but higher brightness also requires high current capability at the lower energies which is discussed in the next section.

Table III: Some New Operating Configurations for use at PEP.

	Mini-Beta 1-Fold	Low Emittance 6-Fold	Low Emittance 1-Fold	
Hor. Tune, ν_x	21.28	29.28	29.28	
Vert. Tune, ν_y	18.22	13.20	13.20	
Mom. Comp., α	0.00255	0.000986	0.000973	
$\epsilon_x/E(GeV)^2$	5.49	1.39	1.27	λ-GeV^{-2}
$(\sigma_E/E)/E(GeV)$	0.00666	0.00666	0.00666	%-GeV^{-1}
β_x^*	1.00	67.9	54.0	m
β_y^* IR	0.04	100.0	356.6	m
η^*	-0.093	-2.0	0.0	cm
β_x	22.6	20.6	20.2	m
β_y Cell	36.8	43.0	44.0	m
η	1.23	0.55	0.51	m
β_x	32.3	26.0	26.4	m
β_y S.P.	5.5	5.7	5.3	m
η	1.49	0.62	0.53	m
β_x^*	4.50		79.3	m
β_y^* 5 IR's	0.18		96.6	m
η^*	0.004		0.0	cm

B. Internal Targets

PEP, with its large radius ($2\pi\bar{R}$ = 2.20 km) and large energy range would also seem to be an ideal system for these experiments especially when multibunch operation with higher duty factor and current is developed. The beam lifetime was shown to be the product of three terms, relating to the RF capture bucket, the electron-nuclear bremstrahlung cross-section and the target thickness. The log factors can each be approximated by 5, so one has:

$$\mathcal{L}_{IT} = \left(\frac{I_b}{100mA}\right)\left(\frac{2}{\tau(h)}\right)\left(\frac{T_o(\mu s)}{7.34}\right)\left(\frac{1}{Z(Z+1)}\right) \times 10^{34}\ cm^{-2}s^{-1}.$$

Such conditions are ideally matched to simultaneous synchrotron radiation operation so long as there is no significant increase in emittance. The lifetime due to single coulomb scattering goes as $E^2A_s^2/Z^2\beta_t\beta_s n_t$ and is orders of magnitude larger than for bremstrahlung so that setting the aperture (or scrappers) at $\pm A_s$ allows an analytic approach to emittance growth and indicates no growth at PEP for bremstrahlung limited target densities. This also allows experiments when an internal target with variable n_t is available. Lower emittance (higher tune) configurations than used in Table I for colliding beam operation are clearly possible at lower energies because the goals are reversed. At some point emittance growth could become a problem but only at the lowest energies where currents are also a problem. Similarly, the harmonic number of the ring is $h = 2592$ but only three bunches per beam have been seriously studied.

A major limitation on the total and single-bunch currents is the impedance of the ring which is dominated by limiting apertures such as the RF cavities shown in Figs. 4 and 6 and, of course, any gas cell – especially one that is poorly designed. A considerable amount of work has gone into the design of the PEP vacuum and RF system[19] and this has undergone several changes[20] based on optics changes and measurements of the limiting currents observed[21]. Figure 7 shows the latest calculations for PEP based on Table I and the new colliding beam configuration[22] in Table III. Figure 6 shows $\beta_{x,y}$ in the vicinity of the cavities. This distribution is clearly not optimal and never was which explains why the previous single-bunch, fast, head-tail threshold was roughly consistent[21] with the PEP transverse cavity impedance.

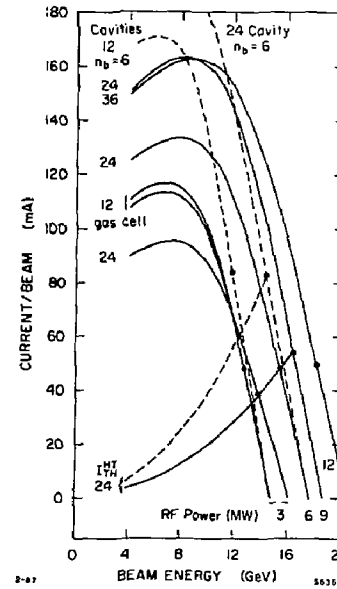

Fig. 7. Some representative RF limited current characteristics for PEP. Currently it runs with three bunches per beam with 24 cavities and 6 MW (Table I). Solid curves assume 3 bunches and dashed 6 bunches per beam. The intersection of these curves with the predicted current limits from the single-bunch, fast head-tail effect are shown as dots marking the dominance of these two regimes.

A number of different possibilities are considered in Fig. 7 such as adding and removing cavities, increasing the number of bunches and running with a single gas cell such as the one described in Ref. 23 with conditions where the effects should be most evident. A properly terminated cell of this type does not influence the beam significantly but the reverse may not be true. Although the beam will tend to drop some energy in it, this should be small in the practical domain of operation. The limit will be determined by multibunch instabilities and could cause depolarization. This is another area for study and testing.

One predicts from Fig. 7 that the current becomes RF limited below the dots on each curve i.e. at higher energies. The dots represent the threshold for dominance of the the transverse mode coupling instability or fast, head-tail effect[20,21]. To my knowledge there is no evidence for multi-bunch instabilities in PEP except for those associated with colliding beam operation. N-bunch, single beam operation can be thought of

as N coupled oscillators with N normal modes which require N-independent tuning knobs which are available from the RF cavities around the ring. The present distribution is not optimal for this but could certainly be improved. Several points can now be made. First, higher energies are best, both from the maximum single bunch limit and for multi-bunch operation i.e. we don't want to simply remove our sources of pickup and feedback and also that the bunch spacing and harmonic number are so large in PEP that it is certainly possible to use feedback to deal with such problems. Also, while one expects coupled bunch instabilities and other problems, a stable, single bunch current of $\approx$ 1 mA at 4.5 GeV has been verified so we have used very conservative numbers for the beam currents at the lower energies in the various Tables. Concerning higher energies, Fig. 8 shows a typical magnetization cycle that every cell dipole magnet was subjected to and measured along. While the current supplies will only go to about 17 GeV the magnets go much higher and the character of the curves imply reasonably simple operation from $2 < E(\text{GeV}) < 25$. Several systematic machine physics studies on PEP are clearly suggested by such questions.

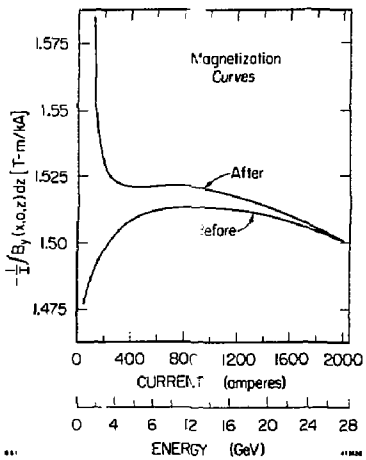

Fig. 8. Field integrals measured before and after subjecting a virgin PEP bending magnet to a magnetization cycle. Every PEP magnet was measured in this way with data taken from 1-27 GeV.

Other questions also include various polarization effects. The scattering of circularly polarized light by $e^{\pm}$ can be used to measure polarization of the $e^{\pm}$ and can also be used to induce it but with poor efficiencies at these energies. A low-energy, polarized electron beam can be used in a similar way to the photon beam to measure the polarization of a stored electron beam or to polarize photons via Compton scattering. Implementing longitudinal polarization with the new, efficient, tensor polarized gas targets could then provide an absolutely unique facility for nuclear QCD studies from 2-17(25) GeV that would allow high luminosity $\vec{e}+\vec{\gamma}$ and $\vec{e}+\vec{A}$ and $\vec{\gamma}+\vec{A}$ studies etc. A number of alternative insertions to provide longitudinal polarization in one or more interaction regions are possible in PEP but IR 6 appears best.

6. Compatibilities

Table IV is a "truth" table showing some possible operating modes and how they interrelate to one another. No doubt everyone would like an IR hall for detectors, spectrometers, bypasses or future possibilities. While SR is produced everywhere, the IR and symmetry straight sections are the most popular for them as well. Typically, the dispersion functions are minimal near the IR and maximal at the SP so the wigglers in SP 1, 5 and 9 improve luminosity below 15 GeV by increasing emittance while putting them near the IR would have the reverse effect. Their roles for luminosity would reverse above 15 GeV. The use of dispersion at the IT implies one is using dispersion matching to achieve higher energy resolution e.g. even though PEP has a very low energy spread compared to the linac, it can still be improved to do high resolution spectrometer studies at much higher energies than Bates or LAMPF. I won't discuss the various uses of wigglers implied in the Table but leave this as a topic for future discussion among interested parties.

Table IV: Operational compatibilities between Colliding Beam physics[CB], Internal Target physics[IT] and Synchrotron Radiation physics[SR]. "D" stands for experiments requiring Dispersion, "SP" stands for Symmetry Point, "IR" for Interaction Region, "U" for Undulator, "W" for standard Wiggler and W_R is a Robinson wiggler located at high η e.g. at the SP.

E(GeV)	5	10	15	20
CB	W_{SP}	W_{SP}		W_{IR},W_R
IT	Any	Any	Any	Any
ITD	U	U	U	U
SRSP	U,W_R	U,W_R	U,W_R	U,W_R
SRIR	U,W	U,W	U,W	U,W

7. A Few Conclusions (and Possibilities)

There are a remarkable number of possibilities available that can be arranged into an interesting, long-range program with well defined stages. First on the list is the new mini-beta upgrade which allows a variable mini-maxi scheme as shown in Table III. This will be tested this fall. Variable density targets, in conjunction with wigglers could improve low-energy, colliding beam operation by providing independent control over longitudinal and transverse phase space. Implementing longitudinal polarization with the new, efficient, tensor polarized gas targets could then provide an absolutely unique facility for nuclear QCD studies from 2-17(25) GeV. Multi-bunch operation in a dedicated mode of operation or even CB mode could provide high duty factors whose magnitude needs to be studied. It seems clear that an energy closer to 15 than 5 is preferred on most grounds.

Implementing a high energy photon facility would augment the internal target program as well as the high energy physics studies since one wants to use such beams near their source even though good external photon beams will naturally arise. There are many interesting research and development projects here such as the study of high current, high density bunches;

development of highly segmented, fast, efficient photon detectors and the development of long, combined function undulators to name a few. An injection IR is clearly preferred for this work which would allow high luminosity $\vec{e}+\vec{\gamma}$ and $\vec{\gamma}+\vec{A}$ studies as well as $\vec{\gamma}+\vec{\gamma}$ over a large energy range.

There are many interesting accelerator physics studies e.g. we don't really understand the low energy limits of the ring such as the fundamental limits on single and multi-bunch beams as a function of energy or operating configuration. How should one use the various wigglers, bunch lengthening cavities, higher order multipoles, internal targets and various types of feedback to control or optimize current and aperture limitations? It is interesting that a long list of such projects for PEP compiled in 1982 has gone virtually untouched even though they might have justified PEP as a national test facility.

Some of the things discussed here could be started now and when PEP resumes operation and probably should because they impact longer range planning and funding. Samuel Butler viewed "progress" as a form of generic cancer when he said: *All progress is based on a universal innate desire on the part of every organism to live beyond its means.* A possible antidote to this is better long range planning for proposed uses and funding commitments. Past parochialism or specialization in both areas is neither efficient nor effective and this seems a good place to try something different.

Acknowledgements

I should thank many people for their interest and suggestions but particularly Karl Bane, Stan Brodsky, Phil Morton, Albert Hofmann, Ewan Patterson, Ron Ruth and Perry Wilson. I should also mention Elliot Bloom who is studying the CB possibilities, George Brown and Herman Winick with whom I've discussed the SR interests and especially S.G. Popov for bringing me up to date on the Russian IT work that has been done on the VEPP rings.

References

1. W.C. Barber, G.K. O'Neill, W.K.H. Panofsky and B. Richter, "Experimental Test of QED, Proposal to U.S.A.E.C.," May 1958.
2. V.F. Dmitriev, D.M. Nikolenko, S.G. Popov, I.A. Rachek, Yu.M. Shatunov, D.K. Toporkov, E.P. Tsentalovich, Yu.G. Ukraintsev, B.B. Voitsekhovskii and V.G. Zelevinsky, "First Measurement of Asymmetry in Electron Scattering by a Jet Target of Polarized Deuterium Atoms," Phys. Lett. 157B (1985) 143.
3. I assume a natural metric for four-vectors with $p \equiv (\epsilon, \vec{p})$ and $\hbar = c = 1$ so $s = (\omega_1 + \omega_2)^2 - (\vec{k}_1 + \vec{k}_2)^2 \equiv 4\omega_1\omega_2$ for collinear collisions between real photons. For a discussion of the various processes in Fig. 3, see J.E. Spencer and S.J. Brodsky, IEEE Trans. Nucl. Sci. NS-32 (1985) 3431 and Ref. 4 below.
4. J.E. Spencer, "Higher Luminosities via Alternative Incident Channels," SLAC-PUB-3645, April 1985.
5. J.E. Spencer, "Storage Rings, Internal Targets and Such," Argonne Workshop on High Resolution Spectrometers, PEP-PTM-366, Sept. 1981.
6. R.J. Holt, "Polarized Gas Targets in Electron Rings," CEBAF Workshop, June 1984.
7. J.M. Paterson, Proc. XI-th Int'l. Conf. on High Energy Accelerators, CERN, July 1980; J.R. Rees, IEEE Trans. Nucl. Sci. NS-28 (1981) 1989; R.H. Helm *et al.*, IEEE Trans. Nucl. Sci. NS-30 (1983) 2001.
8. E. Courant and H. Snyder, Ann. Phys. 3 (1958) 1.
9. M. Sands, "The Physics of Electron Storage Rings – An Introduction," SLAC-121, 1970.
10. C. Pellegrini, Lectures at Varenna Summer School, June 15-30, 1969.
11. R. Gram and P. Morton, "Advantages of Second Harmonic RF Cavities," SLAC-TN-30, Dec. 1967; A. Hofmann and S. Myers, "Beam Dynamics in a Double RF System," XI-th Int'l. Conf. on High Energy Accelerators, CERN, July 1980.
12. J.M. Paterson, J.R. Rees and H. Wiedemann, PEP-Note-125 (1975); W. Brunk, G. Fischer and J. Spencer, IEEE Nucl. Sci. 26 (1979) 3860.
13. See for example: H. Wiedemann, SLAC-PUB-2320, 1979.
14. J.E. Augustin *et al.*, VII-th Int'l. Conf. on High Energy Accelerators, Vol. 2 (1969) 113.
15. B. Rossi, "High Energy Particles," Prentice Hall, Inc. (1952).
16. M. Donald, L. Rivkin and A. Hofmann, "Low Emittance Configuration for PEP," PEP-PTM-257, Oct. 1985.
17. Y. Cho *et al.*, "Conceptual Design of the Argonne 6 GeV Synchrotron Light Source," IEEE Trans. Nucl. Sci. NS-32 (1985) 3383.
18. A. Hofmann, Private Communication.
19. P.B. Wilson, "Stored Current in PEP Using the Measured Ring Impedance," PEP-PTM-216, March 1980; K.L.F. Bane, "RIPPLES," PEP-PTM-125, Nov. 1975.
20. P.B. Wilson and L. Rivkin, "Threshold Current for the Transverse Single-Bunch Instability in PEP," PEP-NOTE-374, Aug. 1982; R.D. Ruth, "Single Bunch Instabilities in an SSC".
21. P.L. Morton and PEP Group, "Correlation Between Experimental and Theoretical Results for the Fast Head-Tail Instability in PEP," SLAC-PUB-3175, July 1983.
22. M. Donald and D. Helm, private communication.
23. R.G. Milner, R.D. McKeown and C.E. Woodward, "Study of Spin Relaxation by a Charged Particle Beam in a Polarized ^{3}He Gas Target," Nucl. Instrum. Methods, to be published.
24. J.E. Spencer, "Harmonic Strengths of the PEP Dipoles and Some Related Effects and Lessons," PEP-PTM-367, Sept. 1981.

Polarized Electrons for Internal Target Experiments

Blaine E. Norum
Department of Physics
University of Virginia
Charlottesville, VA 22901

Abstract

Stated briefly, the problem is to maintain polarized electrons in a storage ring such that at a particular point in the ring the direction of polarization is parallel to the beam momentum. At other points in the ring the polarization must be oriented to ensure that the magnitude of the polarization of the stored electrons is maintained at as high a level as possible. Possible solutions for the PEP storage ring and the proposed MIT-Bates storage ring will be discussed.

Introduction

Two basic processes must be considered in order to understand the behavior of electron polarization in a storage ring. First, the evolution of the electron spin vector in the presence of a magnetic field $\vec{B}$ is described by the Bargmann-Michel-Telegdi[1] (BMT) equation:

$$\dot{\vec{s}} = \hat{s} \times \left(\frac{e}{7m_e} \right) \left[(1 + a\gamma) \vec{B}_t + (1 + a) \vec{B}_l \right]$$

where: e is the electron charge,

g is the electron energy divided by its rest mass,

$a = (g-2)/2 = 0.00116$ and g is the electron gyromagnetic ratio, and

$B_t(B_l)$ = is the component of $\vec{B}$ perpendicular (parallel) to the electron momentum $\vec{p}$.

The corresponding equation of motion for the electron is:

$$\dot{\vec{p}} = \hat{p} \times \left(\frac{e}{7m_e} \right)$$

Thus, an axial field does not affect the momentum but does produce a precession of the spin about the momentum, $\vec{p}$. The angle of precession is given by:

$$\theta_s[\text{rad}] = \frac{0.30}{E[\text{GeV}]} B_l L[\text{T-m}]$$

where L is the length of the trajectory in the field $\vec{B}$

A transverse field affects not only the spin, but also the momentum:

$$\frac{d}{dt} \left[\hat{s} \cdot \hat{p} \right] = \left(\frac{ea}{m_e} \right) \hat{s} \cdot \hat{p} \times \vec{B}_t$$

Thus, the spin precesses about $\vec{B}_t$. The magnitude of the precession is given by:

$$\theta_s = 2.27\ E[\text{GeV}]\ \theta_B = \frac{E[\text{GeV}]}{0.44065}\ \theta_B$$

where θ_s is the angle between the spin and the momentum and θ_B is the angle through which the electron is deflected. Note that an electron with an energy of n x 0.44065 GeV will have its spin aligned in the same direction after each time it is bent through 360°. For electrons with any other energy, the spins will be pointing in some other direction after deflection through 360°.

The second phenomenon which must be considered is that of radiative polarization.[2] Asymmetry in the polarization of the synchrotron radiation emitted by an electron as it is deflected tends to make the electron spins align themselves with the deflecting field. In the case of a storage ring where the guide field is vertical this effect causes a buildup of the polarization in the vertical direction. The asymmetry in the radiation is relatively small, so this process does not lead to unit polarization. Rather, in an ideal storage ring where the circulating electrons encounter only vertical fields the maximum attainable polarization is 92.4%.

Radiative polarization has been observed in electron storage rings at Orsay, Novosibirsk (VEPP-2, VEPP-4), SLAC (SPEAR), Cornell (CESR), and DESY (PETRA).[3] An important observation to be drawn from the SPEAR results in particular is that the observed polarization properties were very accurately described using matrix methods (a la TRANSPORT) developed by A. Chao.[4] Subsequent refinements and improvements of the methods give one confidence that

these effects can be accurately computed.[5]

The development of the polarization is generally slow, approaching its limiting value P_0 exponentially:

$$P(t) = P_0 \{ 1 - \exp(t/\tau_p) \}$$

where the time constant τ_p is given approximately by:

$$\tau_p[s] = 16 \times \frac{C[m]\ \rho[m]^2}{E[GeV]^5}$$

where C is the circumference and ρ is the magnetic radius. Clearly, these times are strongly energy-dependant. Table I contains representative polarization times for several electron storage rings being considered for use with internal targets by the nuclear physics community. The storage times that one may hope for are at most a few hours, so it is readily apparent that radiative effects may be of concern only at PEP.

TABLE I

Radiative Polarization Rates

PEP:		
$\tau_p = 1.2 \times 10^5$ s ≃	34 h @	6 GeV
$= 9.5 \times 10^3$ s ≃	3 h @	10 GeV
$= 1.8 \times 10^3$ s ≃	30 m @	14 GeV
$= 5.0 \times 10^2$ s ≃	8 m @	18 GeV
MIT-Bates:		
$\tau_p = 1.6 \times 10^7$ s ≃	6 m @	0.5 GeV
$= 5.1 \times 10^5$ s ≃	6 d @	1.0 GeV
Saskatchewan Accelerator Laboratory:		
$\tau_p = 1.8 \times 10^8$ s ≃	5 y @	0.1 GeV
$= 7.2 \times 10^5$ s ≃	8 d @	0.3 GeV

The absence of significant radiative polarization at MIT-Bates and Saskatchewan dictates that the beam injected into these storage rings must be polarized. Since there are no immediate plans to install a polarized electron source at Saskatchewan, further discussion will be limited to the proposed MIT-Bates storage ring and the PEP storage ring.

The situation at PEP is more complicated than at MIT-Bates (see Figure 1). At the lowest energies (below 6 GeV) the polarization time is long compared to anticipated storage times so radiative polarization effect can be ignored. At higher energies τ_p is sufficiently short that radiative polarization will cause a buildup of polarization parallel to the vertical guide field over times comparable to the storage times. Above about 12-14 GeV the rate is fast enough to be useful as a means of obtaining polarized electrons; below, it is not. Consequently, as at MIT-Bates the injection of polarized electrons will be required.

The existence of a dynamic mechanism forcing the polarization into the vertical direction suggests that it would be desirable to keep the polarization oriented vertically throughout most of the ring and to rotate it into the horizontal direction just before the internal target and to rotate it back into the vertical direction just after. In this way, the radiative polarization can be useful in either enhancing the polarization of the injected beam or, at least, in helping to compensate for the loss of polarization due to other mechanisms. Various techniques of rotating the spins will be discussed.

Depolarization

Any process which causes the electron spins to point in a direction other than the desired one constitutes a depolarizing effect. These effects can be divided into two groups: non-resonant and resonant.

In the non-resonant group two effects are of major importance, one which does not involve radiation and one which does. However, both arise from imperfections and misalignments of the elements of the storage ring. In a real ring the guide field encountered by each electron is not uniformly oriented vertically. Even particles near the nominal orbit experience a random sequence of (hopefully small) vertical and horizontal fields. Consequently, their spins will precess differently and, after a large number of revolutions of the machine, may point in significantly different directions. This "diffusion" of the spins sets a limit on the ability of a ring operating at energies at which radiative effects play no role to maintain polarization.

Under conditions when radiative effects do play a role, the small "kicks" due to field irregularities play an added role. When an electron undergoes a kick it radiates and tends to align its spin along the field generating the kick. Consider the case where the nominal polarization direction is vertical. Horizontal kicks are generally not a serious problem in this regard; since the ring has a closed orbit the sum of the spurious leftward deflections must equal the sum of the rightward ones. If radiation emitted during the rightward deflections tends to polarize the beam upward

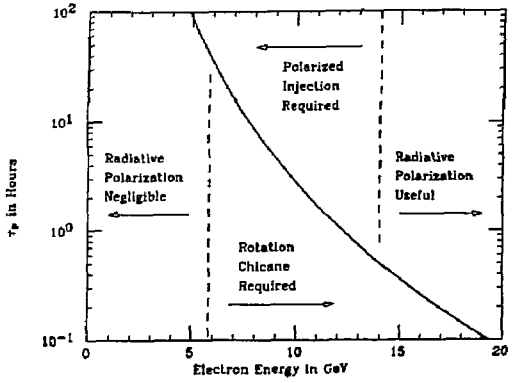

Figure 1.
Polarization Time in PEP

then that during the leftward kicks will tend to polarize it downward and the two effects will (roughly) cancel. On the other hand, vertical kicks arising from horizontal fields are particularly destructive. When an electron is deflected in the vertical plane it radiates and tends to orient its spin in the horizontal direction, to the left or the right. Either way, it generates a loss in vertical polarization.

Figure 2 (taken from Reference 6) shows the results of a calculation of the asymptotic polarization (P_0) in PEP as a function of electron energy. Note that for no energy does value of P_0 reach the ideal value of 92.4%.

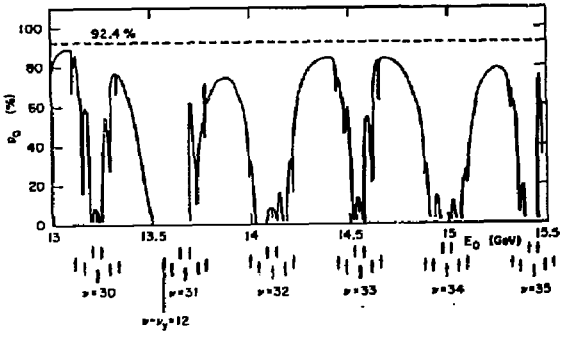

Figure 2.
Asymptotic Polarization in PEP

Resonant depolarization occurs when the rate of precession of the spins as the electron circles the ring is in resonance with the rate of other motions of the electron. The condition defining the three strongest and most damaging resonances is:

$$\left[\frac{g-2}{2}\right]\gamma = \nu + n_y\nu_y + n_s\nu_s$$

where ν, n_y, and n_s are integers and ν_y and ν_s are the vertical betatron tune and synchrotron tune respectively. The term ν corresponds to an "imperfection" resonance which depends only upon the energy of the stored beam. It occurs whenever:

$$E_\gamma = n \times 0.44065 \text{ GeV}$$

Note in Fig. 2 the zeroes in the polarization whenever this condition is satisfied.

The term containing n_y corresponds to an "intrinsic" resonance whereby the precession of the electron spins couples to the vertical betatron oscillations. Similarly, the term containing n_s corresponds to a "synchrotron" resonance. Both of these resonances can be avoided by varying the tunes of the ring.

The depolarizing effects presented here do not preclude the storage of polarized electrons but they do provide a stringent set of constraints to be satisfied by any possible solution.

Possible Solutions

Resonant Energies

The simplest solution is to operate a planar ring at energies $E_\gamma = n \times 0.44065$ GeV. At these energies, an electron with a properly aligned longitudinal spin on one pass will have the spin similarly aligned on subsequent passes. However, first electrons with slightly different energies will have their spins diverge from the nominal on successive passes since the required condition is not met. Moreover, these energies correspond to conditions for the imperfection resonance discussed earlier. Hence, their use is not viable.

Siberian Snake of the First Kind

First suggested by Ya. Derbenev and A.M. Kondratenko in 1976,[7] the Siberian Snake will, in principle, enable a storage ring to store longitudinally polarized electrons of any energy. In particular, a first order calculation shows it to be extremely stable with respect to deviations in the electron energy; the degree to which the polarization is maintained in the longitudinal direction (at the target) is proportional to

only fourth and higher powers of the energy deviation.

The basic concept is illustrated in Figure 3. A solenoid which precesses the spin of an electron with an energy E_0 through 180° about the electron momentum is placed opposite the target. An electron of energy E_0 which is longitudinally polarized at the target will be pointed in a direction ϕ (a function of E_0) at the solenoid. After the solenoid it will be at the same angle but on the other side of the momentum direction. The ensuing 180° bend will return it to the longitudinal direction at the target.

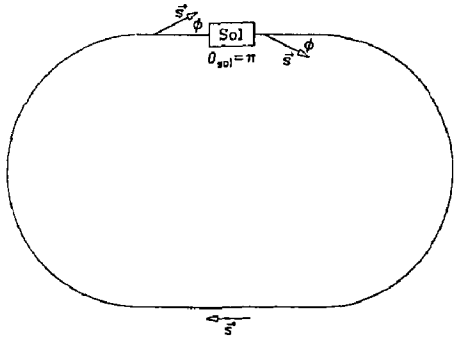

Figure 3.
Siberian Snake of the First Kind

A ring with a Siberian Snake operates, essentially, atop an imperfection resonance. However, the solenoid stabilizes it against perturbations. For example, assume that an electron receives a vertical kick such that its spin has a +y component when it reaches the solenoid. The 180° precession results in a -y component of equal magnitude. When the electron receives the vertical kick on the next revolution it cancels this -y component.

The nominal direction of the polarization in the Siberian Snake is always in the horizontal plane. As a result, it is ill-suited for use under conditions where radiative polarization plays a significant role. However, for the MIT-Bates application this would not pose a problem.

Another problem is that the scheme requires solenoids of very high fields. These introduce strong focussing and coupling between the horizontal and vertical betatron oscillations. Stringent demands are thus placed on both the tuning and dispersion control in ring.

A version of the Snake which avoids the problem of the solenoid can be constructed using an alternating sequence of horizontal and vertical bends to achieve the 180° precession. The severe problem with this scheme is that a given sequence of dipoles would provide the *correct precession for only one energy*. Thus, to operate the ring at different energies would involve physically reconfiguring the machine, clearly not an attractive prospect.

Siberian Snake of the Second Kind

A scheme similar to the previous one can be constructed using a 180° precession about not the momentum direction but about the horizontal direction perpendicular to the momentum (see Figure 4). However, this precession can only be achieved using a sequence of horizontal and vertical bends so the scheme suffers from the same flaw discussed above.

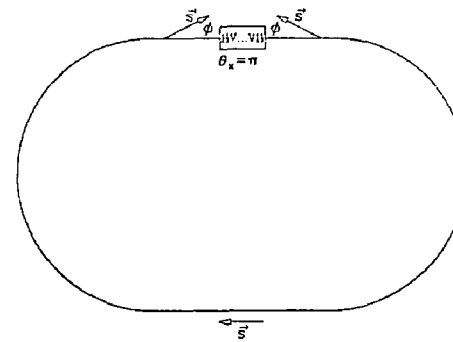

Figure 4.
Siberian Snake of the Second Kind

Figure 8

This novel solution to the problem can be considered a rather gross distortion of the Siberian Snake. Instead of precessing the spin on the side opposite the target so that the effect of the second 180° bend cancels the effect of the first, the direction of the second bend is reversed to achieve the same result (see Figure 5). The scheme has the dual adv ntages of working for all energies and of not requiring strong solenoids.

Unfortunately, it also has severe problems. First, its shape makes it useless as a scheme for retrofitting PEP; similarly, its shape makes it inappropriate for use

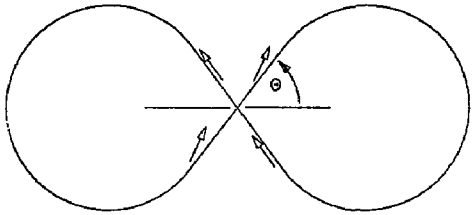

Figure 5.
Figure 8 Scheme

as a pulse stretcher which is to be the primary function of the proposed MIT-Bates ring. Moreover, like the original Siberian Snake it essentially operates atop an imperfection resonance but unlike the Siberian Snake it is a purely planar scheme. Consequently, it has no "restoring force" to control vertical excursions of the spin. The beam would therefore depolarize rapidly due to vertical kicks caused by extraneous horizontal magnetic fields.

Resonant Snake

Since the Siberian Snake already operates by construction atop an imperfection resonance, little harm is done by operating at a resonance energy (E_r = n x 0.44065 GeV). In these cases it has been shown[8] that a much weaker solenoid will suffice to maintain the polarization. For the first resonant energy, 0.44065 GeV, a solenoid capable of precessing the spin through only 5° is sufficient to maintain the polarization at the target within 1% of the stored beam polarization (for a beam with an energy spread of 10^{-3}). For the second resonant energy it still requires only a precession angle of 10° (see Figure 6).

For higher energies the required precession angle grows rapidly (45° for E_r = 3.965 GeV) until the scheme has no significant advantages over the regular Siberian Snake. It also retains the weakness of the Siberian Snake with regards radiative polarization. As a result, it is a useful possibility for the MIT-Bates storage ring but not for PEP.

When considering schemes which are useful when radiative polarization plays a role one is inexorably drawn toward the schemes wherein the spin is maintained parallel to the (vertical) guide field as much as possible. By so doing, the radiative effects in a large

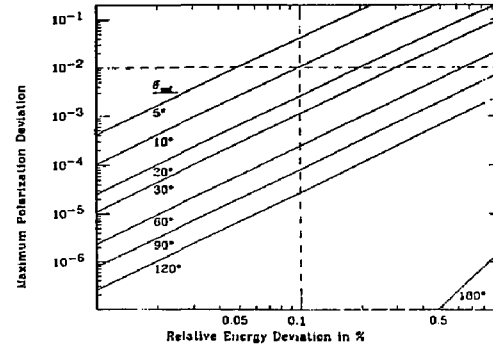

Figure 6.
Resonant Snake

part of the ring help to increase the polarization rather than decrease it. Only near the region of the target are the spins precessed into the longitudinal direction and then back into the vertical. The schemes to be considered now differ only in the technique used to perform these rotations.

Richter-Schwitters (R-S) Scheme

The scheme originally proposed in conceptual form by R. Schwitters and B. Richter[9] has two striking advantages. First, it has the spins aligned vertically throughout most of the ring. Second, it involves only bends in a single plane. Conceptually, it consists of a series of vertical bends inserted into a straight section of an otherwise planar ring (see Figure 7). The electrons are deflected first up then down so they approach the target at an angle θ to the horizontal. A mirror image sequence returns the electrons to the ring midplane and their spins to the vertical direction.

The shortcoming of this method is that it works exactly for only one energy or, more precisely, one energy modulo 0.44065 GeV x $2\pi/\theta$. For any reasonable value of θ, this means a single energy. This is however not such a serious problem as the system is stable for a broad range of energies. The only loss in operating at an energy different from the nominal design energy is that the degree of longitudal polarization at the target is reduced relative to polarization of the stored beam by a factor T given by:

$$T = \sin\left(\frac{E}{E0} \times \frac{\pi}{2}\right)$$

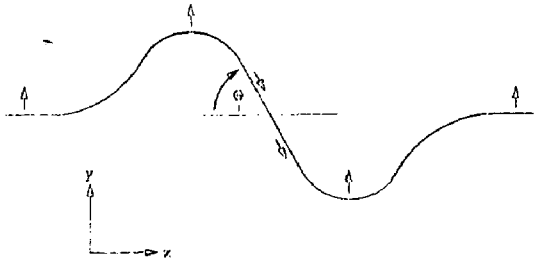

Figure 7.
Richter-Schwitters Scheme

where E0 is the nominal design energy. In the case of PEP a scheme with a nominal design energy of 10 GeV would have $\theta \simeq 4°$ and T would exceed 0.8 for all energies between 6 GeV and 14 GeV.

A remaining shortcoming of this design is the large number of magnets that are required in the area of the target. These would severely limit the space available for detectors. A simplified version of the scheme that would involve fewer magnets would have the shape of an inverted V. The beam would simply be bent upwards through an angle $+\theta$ as before and the target would be placed in the sloped straight section. After the target an angle of -2θ would direct the beam back down to the ring midplane where a second bend of $+\theta$ would return it to the horizontal direction.

Solenoid Spin Rotator

Another way[10] of precessing a vertical spin into the longitudinal direction is first to precess it into the horizontal direction perpendicular to the beam and then precess it into the longitudinal direction by passing it through a horizontally bending dipole (see Figure 8, taken from Ref. 10). A mirror image system located after the target returns the spin to the vertical direction.

The system has the same shortcomings as the R-S scheme in that it works ideally only at one energy. Moreover, it requires two very strong solenoids, the combined strength of which equals that required by a Siberian Snake at the same energy. On the positive side, the energy limitation of the R-S scheme was seen to be minimal. Furthermore, the angle through which the electrons are bent while their spins are not parallel to the guide field is half that of the R-S scheme (for the same nominal energy E0) so the resultant depolarizing effects are reduced by a factor of two.

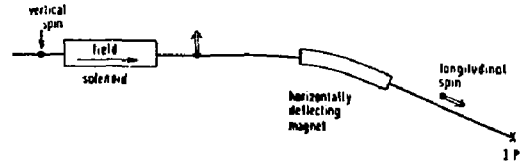

Figure 8.
Solenoid Spin Rotator

Applying this scheme to PEP would require modifications to the main lattice, not just the (straight) insertion where the target would be located. A straight section long enough to accomodate the requisite solenoid and associated quadrupoles would be needed prior to the last two dipoles before the insertion. The beam line in the insertion would therefore be parallel to the present beam line, but would be displaced outwards.

It is an idea which merits serious study.

Mini-Rotator

In 1983 K. Steffen proposed[11] a scheme for the HERA storage ring which would precess the electron spins from the vertical to the longitudinal (and back) by means of a series of small horizontal and vertical bends. The scheme has several promising features, among them the fact that no strong solenoids are required. However, it suffers from a narrow energy acceptance which can be improved only by repositioning magnets. Furthermore, compared to the R-S or Solenoid Rotator schemes electrons in this scheme pass through significantly more magnetic field wherein their spins are not aligned parallel to that field. This increases the rate of radiative depolarization. Similarly, for energies other htan the nominal energy the equilibrium direction for the spins in the main ring magnets is not quite vertical; this also increases the rate of depolarization. It was for these latter reasons that work on the Solenoid Rotators was initially pursued.

Conclusions

The problem of obtaining longitudinally polarized electrons in the proposed MIT-Bates ring and in PEP appears solvable; not easy, but solvable. In the case of the MIT-Bates ring a Siberian Snake or a derivative such as the Resonant Snake appear to be viable

alternatives. In the case of PEP, the R-S Scheme, the Solenoid Rotator, and the Mini Rotator all appear possible. Each has its stengths and should be pursued to determine the costs and limitations.

Finally, I would like to point out that with the possible exception of the highest energies possible at PEP, the degree of polarization that will be possible is limited to that of the injected beam. Consequently, it is of equal importance that attempts be made to increase the polarization obtainable from the sources used in the linac injectors.

References

1) V. Bargmann, L. Michel, and V.L. Telegdi, Phys. Rev. Lett. 2 (1959) 435.
2) A.A. Sokolov and I.M. Ternov, Sov. Phys. Dokl. 8 (1964) 1203.
3) R. Schwitters, Proc. of Workshop on Polarized Electron Acceleration and Storage, Hamburg, West Germany (1982).
4) A. Chao, Nucl. Instrum. Meth. 180 (1981) 29.
5) J. Kewisch, DESY Report 83-32 (1983).
6) A.W. Chao, PEP Report 263 (1978).
7) Ya.S. Derbenev and A.M. Kondratenko, Novosibirsk Preprint 76-84 (1976).
8) B.E. Norum, Longitudinally Polarized Electrons for Internal Target Experiments, CEBAF Report (1984).
9) R. Schwitters and B. Richter, PEP Note 87 (1974).
10) D.P. Barber et al., DESY Report 84-102 (1984).
11) K. Steffen, DESY Report PET 78/11 (1978).

USE OF INTERNAL TARGETS AT THE PROPOSED MIT/BATES RING

J. B. Flanz and the Bates Staff
MIT-Bates Linear Accelerator Center
Middleton, Massachusetts 01949

Introduction

The construction of a ring at the MIT/Bates Accelerator Center has been proposed since 1984. It would operate as a Pulse Stretcher Ring (PSR), providing near CW electron beams of up to 1 GeV to the existing experimental apparatus at Bates. The proposal also includes a unique facility for conducting experiments using internal targets (IT). The present layout of Bates is shown in Fig. 1. The machine, as shown, produces a beam whose quality is summarized by the parameters in Table I. The laboratory currently supports three experimental halls with five main beam lines. On the "B" line exists three spectrometers with characteristics that make them well suited for coincidence measurements [1]. However, at present as listed in Table I, the duty factor available is limited to one percent. the proposed additions to the laboratory are shown in Fig. 2. The pulsed beam from the accelerator would be injected into the ring in a short straight section on the right side. The CW beam would be extracted from the upper long straight section. Also included is an energy compressor system to reduce the effective energy spread of the beam. The resulting beam parameters after the proposed additions are also summarized in Table I.

An experimental hall is provided for internal target experiments on the lower long straight section. The internal target hall is currently envisioned as being 12.2 m x 15.25 m (40' x 50'). There appears to be sufficient room in the ring for optical inserts that may be useful for internal target experiments. It is workshops such as this one that are important for defining the detailed requirements of such a facility. In fact, we hope to obtain from this meeting a better feeling for the needs of an IT hall and the possible optical inserts that may be useful.

TABLE I

BATES BEAM PARAMETERS FOR PROPOSED UPGRADE

		Single Pass	Simultaneous Recirculation	Head-Tail Recirculation
Energy	(MeV)	50-500	400-1060	400-1060
Peak I	(mA)	< 40	< 5	< 40
Average I	(μA)	< 100	< 100	< 100
Pulse Width	(μS)	< 20	< 20	2.6
PPS	(Hz)	< 1000	< 1000	< 1000
Duty	(%)	< 1	< 1	< 0.26/86
ΔE/E	(%)	< 0.3/.04	< 0.3/.04	< 0.6/.04
Δφ	(Deg)	3°/45°	3°/45°	/45°
ε/π	(mm-mr)	10/π	10/π	30/π

Beam Properties

The beam quality available from the Bates Linac is important in the consideration of the possible experiments that might be undertaken. Both the transverse and longitudinal phase space are very small, especially for a pulse machine. In normal operation, the longitudinal phase space is characterized by a 3° bunch width and is contained within 0.3% in energy spread. The transverse phase space is, for example, .01π mm-mr at 500 MeV. This allows sub millimeter beam size with reasonable strength quads at reasonable distances from a target. In this way, the monochromatic spot size at the target of the energy loss spectrometer has enabled the spectrometer to resolve better than 5×10^{-5} in energy.

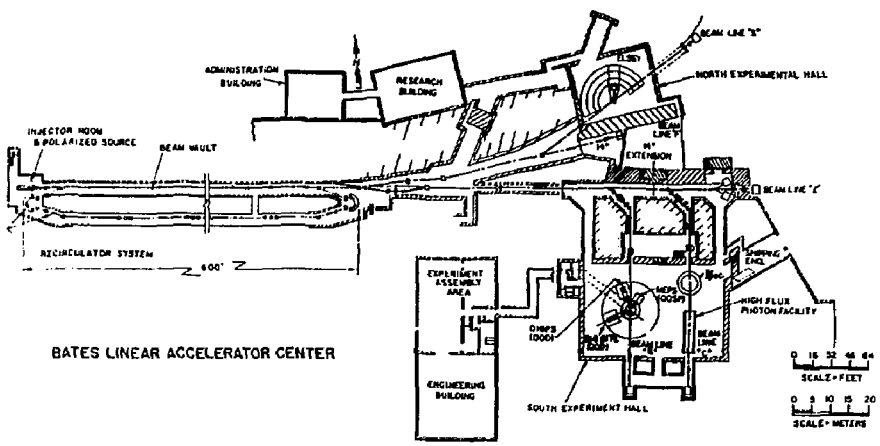

Figure 1

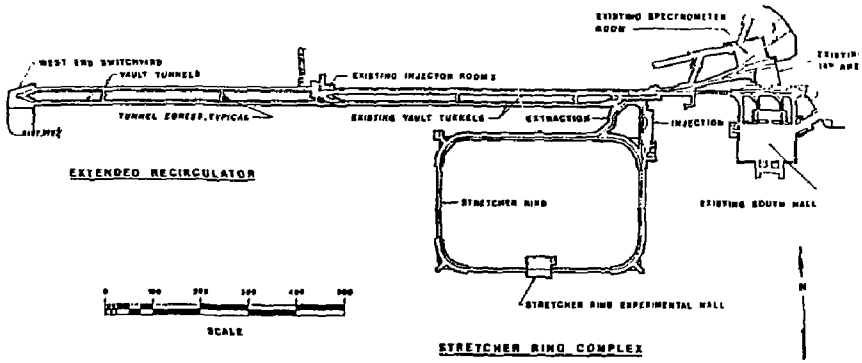

Figure 2 Bates Linear Accelerator Center CW upgrade facilities plan.

The spacial stability of the beam is another contribution to the effective transverse emittance. Measurements have shown the beam jitter to be less than 0.2 mm rms (locked to 60 Hz) at a position where the beam size is near 1 mm (equivalent to a beta of approximately 30 m).

The Linac energy has been increased over the past few years by a variety of methods, and is continuing to be upgraded. First, a recirculation system was installed to nearly double the single pass energy by sending the beam through the accelerator twice. This system can be seen in Fig. 1. The design constraints included maintaining the 1% duty capability of the accelerator and, therefore, required long pulse simultaneous recirculation. For optical reasons, this limits the peak current (while recirculating) to less than 5 mA. In order to quickly fill a ring with electrons, it is helpful to maximize the peak current and minimize the pulse length. Therefore, 40 mA will be accelerated. Recirculation will be done in the head-to-tail scheme with an extended recirculator so that the pulse length will be 2.6 μsec. The turns of injection into the 1.3 μsec ring will provide 80 mA of circulating current, and 100 μA of extracted current at a 1 KHz cycling rate. Preliminary tests of the head-to-tail recirculation method with 40 mA of peak current were successfully conducted. An increase in both the longitudinal and transverse phase space was observed. There was no attempt to adjust the source parameters at this increase current operation. Therefore, for the purposes of the proposed ring, we assume a beam with 0.6% energy spread injected into the energy compressor and approximately double the usual transverse emittance.

The second method used to increase the energy has been the addition of a sixth modulator system, thus bringing the RF equipment complement up to that requested in the original proposal for the construction of Bates. Finally, the klystron power will be increased in the near future from 4 MW peak to over 5 MW peak to allow a recirculated beam energy up to 1 GeV.

The proposed facility includes an energy compression system (ECS). This will trade the longitudinal phase extent for energy spread. Given the small phase width, a factor of 15 can be expected in the energy spread reduction or a final energy spread of .04%. The University of Saskatoon accelerator has already demonstrated an improvement in beam energy spread of over factor of 10 with their new ECS. Other laboratories have enjoyed similar benefits when with such systems.

The "numbers" discussed above are very useful for estimating experiment parameters. However, we are currently investigating the limitations of these "numbers". For example, in principle, the energy spread on the microbunch level, considering only the phase width, should be an order of magnitude smaller than the average energy spread that is measured. The discrepancy could be due to RF fluctuations or ramps whose time constant might be on the order of the beam pulse width. If that is the case, the beam centroid energy can be tagged during an experiment and effectively reduce the beam energy spread and effective spectrometer resolution in the non-dispersion matched spectrometers.

With regard to emittance, measurements of the beam halo are in progress, in collaboration with J. Calarco (UNH) for preparation of a coincidence experiment in the giant resonance region[2]. This experiment requires the use of solid state detectors in the scattering chamber and is very sensitive to background caused by beam halo. Measurements made with the medium energy pion spectrometer (MEPS) of the counting rates for a variety of targets with different hole sizes, as well as empty target frames of different sizes, have been taken.

Although the beam emittance is small, the final focus is not strong (3 mm beam equivalent to a beta of approximately 100 m), and there are small tails which are not measurable during normal emittance measurements which consider only 68% to 90% of the beam. These tails may effect the outcome of the experiment and provide a limit on the beam size, including over 99.9% of the beam, especially if target frames of limiting apertures are used. As seen in Fig. 3, with some tuning one can achieve a situation with 0.8% of the beam outside of a 1 cm hole and less than $.5 \times 10^{-5}$ outside a 4 cm diameter. On the same figure, the fraction of a guassian beam outside a particular radius is also plotted. The difference between the two curves can be considered the beam halo. Better

conditions have also been achieved with more considerable tuning. The above situation is sufficient to allow detection of giant resonance protons and alphas in coincidence with scattered electrons. The detectors were located 20 cm from the beam, and the target frame was 2000 times thicker than the target.

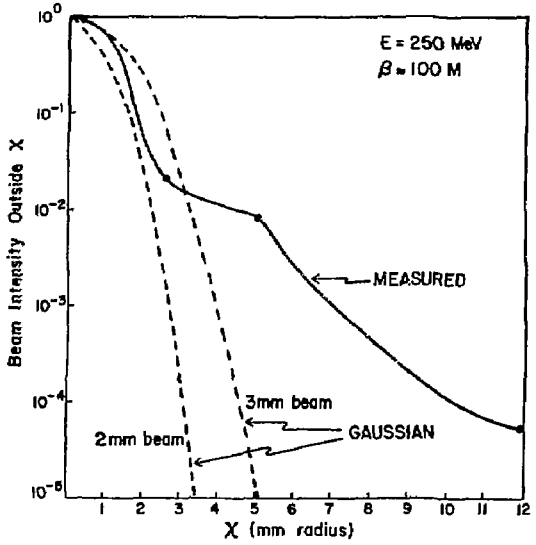

Figure 3. Beam "Halo" Measurements

Ring Description

The layout of the proposed ring lattice is shown in Fig. 4. The basic rectangular shape is made up of four 90° bend regions which are connected by four straight sections. The short sections are 42.3 m long and the two long sections are 92.6 m long. The ring circumference is 390.5 m.

The ring is composed of six basic cell types. These include bend cells (12); FODO cells (7, (5)) on the long straight sections; FODO cells on the short straight sections; matching cells (4) to match the higher beta function of the long straight section to the bend section; an extraction cell (1), to provide a higher than average beta for extraction; and an internal target cell (0, (1)) to provide a lower than average beta for internal target work. The machine functions are shown in Fig. 5 with the dashed line that of an internal target optics cell.

The basic criteria and considerations which affect the design of the PSR are summarized briefly:

- The operating energy range is 300-1060 MeV;
- Two-turn injection is planned which will fill the ring with 80 mA of circulating current;
- The bend cells, in combination with the short straight sections, are designed to be second order achromats with symmetry corrected second order centroid shift aberrations. This ensures that the geometric aberrations can be controlled and the chromaticity of the ring can be adjusted without affecting the desired geometric aberrations.

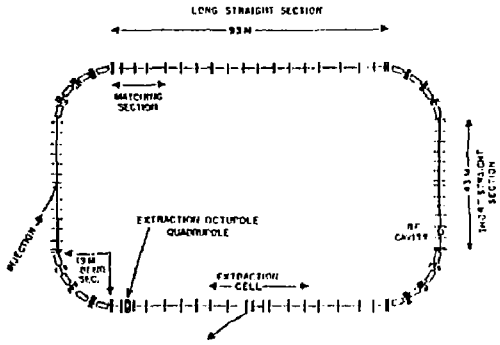

Figure 4. Layout of Pulse Stretcher Ring

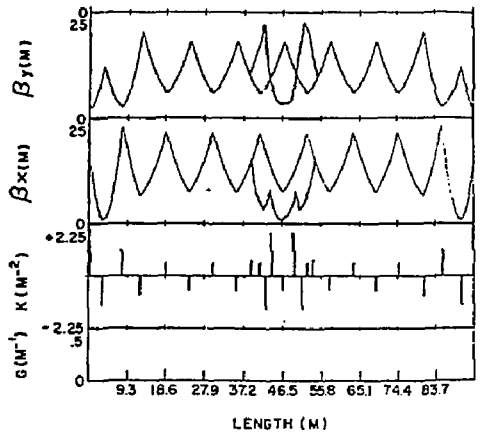

Figure 5. Long Straight Section with Internal Target

- There will be a high beta region (beta = 30 m) for extraction to minimize septum heating and decouple the extraction from the rest of the ring. It also provides a convenient place for providing collimation to clean up the emittance growth when an internal target is placed in the ring.
- An injection beta = 9 m minimizes the injector kicker strength and prevents extracted beam from hitting the injection septum.
- A lower than average beta = 1 m for internal targets will allow for slower emittance growth.
- The bending radius must be large enough to allow linear operation over the dynamic range and synchrotron losses are minimized, along with a minimized synchrotron oscillation period needed for extraction. This minimizes the RF requirements, however, it does increase the damping times.

Table II summarizes some of the interesting ring operating parameters. Given 80 mA of circulating current, the possible luminosity attainable in the proposed ring can be found in Fig. 6 for a range of internal targets.

TABLE II

RING PARAMETERS

Circumference	390.5 m
Length	131.0 m
Width	80.9 m
Bending Radius	9.1 m
Momentum Compaction	0.014
RF (Max)	2K kev @ 2856 MHz (350 sec. between hand)

Energy	250	440	880	1000
Damping Time (Sec)	9.6	1.6	0.196	0.13
Damped Emittance (mm mr)/π	0.0045	0.0147	0.0586	0.0757
Damped Energy Spread (%)	0.007	0.013	0.025	0.029

	Horizontal	Vertical
Tune	Extraction 10.46 Internal ~ 10.2	10.60 10.6
Chromaticity		
Uncorrected	- 16	- 13
Correctable to	0	0

Beta Functions		Min.	Max.	Min.	Max.
Bend	β	3.6	13.9	2.6	6.1
	η	0	3.8		
Extraction Long Straight		1.0	32.0	2.6	20.3
Mini Beta Straight		1.0	13.7	3.6	24.5

Instabilities - Transverse Multi-Bunch ~ 50 msec (.1 mm rms for extraction)
for IT @ β = 1 ~ 10^2 - 10^3 msec

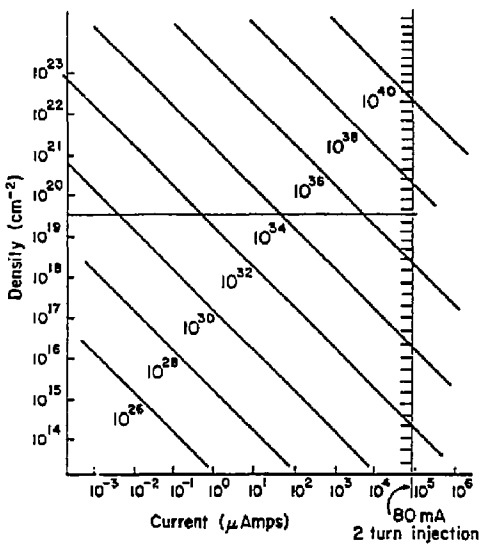

Figure 6. Luminosity in ring as a function of beam current and target density.

Ring Parameters Relevant to Internal Target Use

Vacuum Considerations

There are a few types of targets that have been discussed. They include jet-type targets and bottle targets. The vacuum requirements of the ring include long term storage, as well as an ion density low enough to produce small tune changes over the range of current of ring operation. This vacuum level is on the order of 10^{-9} torr. Consider an internal target in the ring with a density of from 10^{14} to 10^{15} atoms/cm^2. This converts to a local pressure of from 10^{-4} to 10 torr. Table III shows the nearby vacuum assuming differential pumping speeds of 60,000 l/s per chamber and conductance limiters of 1 cm and 5 mm. Note that at least two conductance limiters are needed with these available pumps for the highest target density.

For the case of cluster jet target, pollution of the ring vacuum can come from collisions within the gas, evaporation of the clusters, and evaporation induced by ionization. The approximate total loss can be 10^{-3} of the gas. Assuming thermal velocity and a 1 cm jet thickness, this corresponds to a leakup rate of .1 torr l/sec. This leakup rate also requires a conductance limiter device (at least one, probably two). It may be possible to reduce the vacuum constraints if the storage time is not important. This may be an important tradeoff since it is advantageous to reduce the mass in the region of the internal target.

In Fig. 7, some internal target sources which have been used in rings are compared with the ring vacuum resulting from having introduced these targets.[3] Included on the graph is the region that proposed

TABLE III

IT VACUUM CONSIDERATIONS

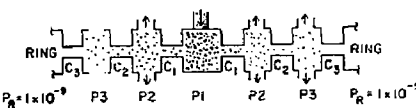

Target cm⁻²	P1 Torr	C1 ℓ/s	P2 Torr	C2 ℓ/s	P3 Torr	C3 ℓ/s	P4 Torr
10^{14}	10^{-4}	4	7(-8)				
10^{15}	10^{1}	4	7(-4)	4	4(-4)	4	< 10^{-9}
10^{14}	10^{-4}	.5	8(-10)				
10^{15}	10^{1}	.5	8(-5)	.5	7(-9)		

Assumptions - 60,000 ℓ/sec pumping capacity each cell
4 ℓ/sec conductance - 1 cm diameter pipe
0.5 ℓ/sec conductance - 0.5 cm diameter pipe

Conclusion - At least one if not two conductance limiters on each side.

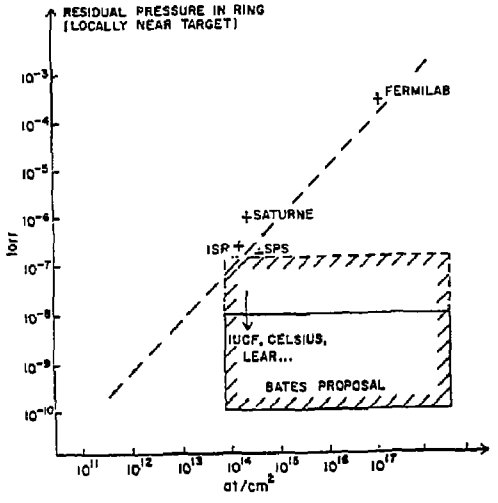

Figure 7. Pressure near IT in ring.

Bates facility hopes to operate. It should be noted that the operational vacuum measurement is near the target and not an average measurement of the entire ring. However, it is also interesting to note that in the estimated leakup, rates are generally an order of magnitude below the actual rates. We will, therefore, assume that there will be at least one 1 cm aperture on each side of the target.

Apertures

The locations in the ring that restrict the nominal aperture include:

1. RF cavity (4 cm diameter)
2. Injection septum (12 mm from closed orbit)
3. Extraction septum (8 mm from closed orbit)
4. Internal target region target conductance limitation (1 cm diameter))
5. Other energy and emittance limiting apertures)

The RF cavity aperture is fixed and unchangeable. The septa could be retracted for internal target usage, although it would be nice, once they are adjusted, to allow them to remain untouched. The horizontal phase space contains most of the limiting apertures and optics.

The horizontal phase space coordinates at the internal target location, with the small beta region, are plotted in Fig. 8. Also on Fig. 8 are the projected admittance limitations for the items discussed above. In an expanded view of the phase space, (Fig. 9), various possible circulating beam phase spaces are shown for comparison purposes. The smallest represents one turn of on-axis injection. The largest represents the normal phase space filled for extraction. The intersecting parabolas depict the boundary between stable and unstable oscillation of a particle in the ring. This is used for extracting in the pulse stretching mode. The intermediate case represents two turn injection with a minimum of phase space filled. This is defined by allowing the minimum of room required for the injected beam to cleanly pass by the injection septum.

To safely contain the beam within the ring and enable an internal target experiment, the beam emittance must be contained within some quantity, for example, the admittance. The emittance will grow in most cases, and one must provide a means to catch the

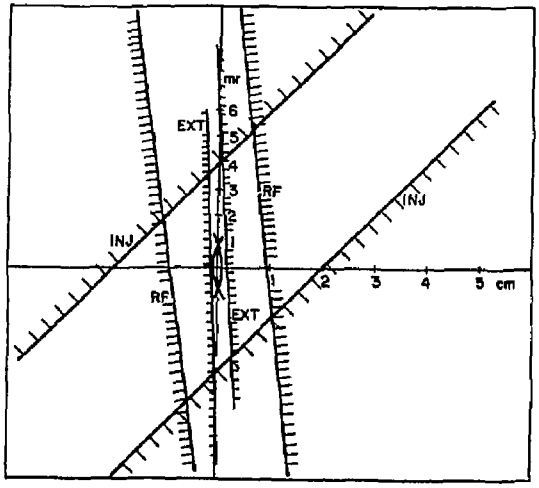

Figure 8. Ring Admittance with restricting apertures

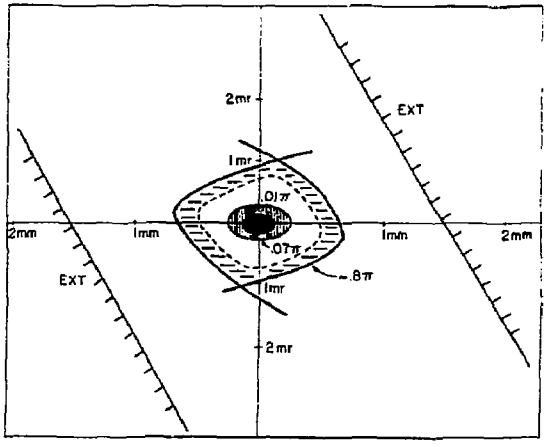

Figure 9. Expanded view of Beam Phase Snace and Ring Admittance.

beam that is outside of the acceptible boundaries safely. the most logical place in this ring is at the extraction cell where the beta is 30 m. Therefore, if one wants to restrict the admittance to that defined by the septum, then a collimator of 16 mm diameter is necessary. If the septum is retracted, then the next aperture is the RF, in which case, a collimator of 6 cm diameter would be necessary at the extraction location. Note that collimators in this location maximize the necessary aperture for restricting the admittance. It (they) are also located on the opposite side of the ring from the target.

Operating Conditions

In the most straightforward injection schemes, a pulse of 2.6 (1.3) μsec of 40 mA fills the ring in two (one) turns with 80 (40) mA. this can be repeated as often as every 1 msec. Given this current capability, one can infer from Fig. 6 the luminosity that the ring is capable of providing for internal targets. This beam can be extracted if the phase space at the extraction location is filled as in Fig. 9.

At this time the ring RF will support 80 mA of stored current. If necessary, if would be possible to store more current as in other storage rings, however, that would involve more RF power for this mode. The damping time, important for storing more current, ranges from 130 msec at 1 GeV, to over a second. Thus, filling times will be seconds. The beam would have to be stored long, relative to this, for useful efficiency or the tradeoffs more carefully examined. Even without question of more current than 80 mA, the storage time question is still useful to discuss.

The ring can be filled every msec. To fill less often would save linac power. However, if one is anticipating using the linac pulsed beam elsewhere during that time, beam sharing techniques which allow recovery of machine parameters quickly, when it was time to refill would be necessary. Finally, there is the possibility of parasitic experiments that can run while the beam is being extracted, without damaging the extraction beam.

It is useful to consider some of the mechanisms which affect the beam quality and ultimately determine the experiments which are feasible. This will also yield information on the possible modes of operation of the ring. The mechanisms include the effects of the target on the beam, the effect of the ring on the beam, and the effects of the beam on the target. Some of these are summarized below.

Effects of Target on the Beam

- Emittance Growth Mechanisms
  - Multiple, single, and plural scattering
  - Wakefield effects from target and collimators
- Energy Loss Mechanisms
  - Bremsstrahlung
  - Wakefield effects from target and collimators

Effects of Ring on the Beam

- Emittance Affecting Mechanisms
  - Damping (antidamping)
  - Quantum fluctuations
  - Instabilities

Effects of Beam on the Target

- Dissociation
- Depolarization

Consideration of the above mechanisms can be used to establish the operational limits of the various operational modes mentioned above. In particular, the conditions for use of the different modes of operation are summarized below.

Modes and Conditions

Any mode:

a. background manageable
b. sufficient luminosity
c. beam emittance acceptable
d. target density/polarization acceptable

Storage mode (any current):

a. Emittance does not grow beyond detector limitations for i) resolution or ii) track reconstruction. For i), $e < 4\pi$ mm mrad.

b. Emittance does not grow so as to have halo hit target aperture, producing backgrounds. Since the aperture may be 100,000 times thicker than the target, that means that the emittance in this case implies that part of the beam containing more than $1.-^{5}$ of the beam. At $\beta = 1m$, $e < 0.5\pi$ mm mrad.

c. Emittance does not grow beyond admittance. With extraction septum $e < 4\pi$. Without extraction septum, $e < 40\pi$ mm mrad.

Parasite Mode

a. Emittance does not grow more than 10%

b. Experiment can stand extracted beam tail which contains up to .1% of beam up to a radius of 1 mm.

Beam Loss Mechanisms

Scattering

Of the emittance growth mechanisms discussed above, the most talked about and the most serious is that due to scattering. Maloney, Craft and Williamson, Crannell, and Norum, have all shown that this effect is tolerable over an acceptable range of parameters. There have been three approaches to this subject. Craft and Williamson showed the relationship between passing through an internal target once and many times within a ring, thus allowing analytical calculations based on multiple scattering[4] through a thicker target. This was compared with simulations of a particle traced through a ring undergoing single scattering with each target passage, and the agreement was found to be very good. Crannell used the approximate form for multiple scattering, while Norum used the single scattering form and included damping effects in the ring. To calculate the emittance growth for present Bates design, the approximate form was used, including a factor of .75 which yielded better results for the rms scattering angle agreement with the results of Nigam et al. The calculation also includes the effect of damping in the proposed ring.

Wakefields

Another potentially important effect is the transverse charge dependent kick that is possible when a beam crosses a transition in pipe diameter. In this case, the magnetic field lags behind the electric field caused by the beam image charges. This mismatch causes a transverse force on the beam, proportional to

the charge. This is, therefore, a spread in the angles and an increase in emittance, following Bane and Morton.[5]

The magnitude, and therefore the spread of the force, can be reduced by tapering the edges of the transitions. For the collimators considered, the effect is very small in comparison to the scattering effect, even considering the fact that actual wake forces in rings generally tend to be over an order of magnitude more than expected from calculations.

Figures 10 and 11 show the results for 440 and 880 MeV. With a beta equal to one meter at the internal target region, all reasonable operating conditions listed above are limited to an emittance growth under $1.^{-6}$. It is interesting that for long storage times (seconds), the effect of damping is important. Figures 12 and 13 compare the effects of long storage times with and without damping.

The horizontal lines on Figs. 10-13 represent the limits imposed by the constraints discussed above for the different modes of operation. By noting the time it takes to reach those lines, the plot of storage times in Fig. 14 can be formed. Each line in Fig. 14 represents a different condition as described earlier.

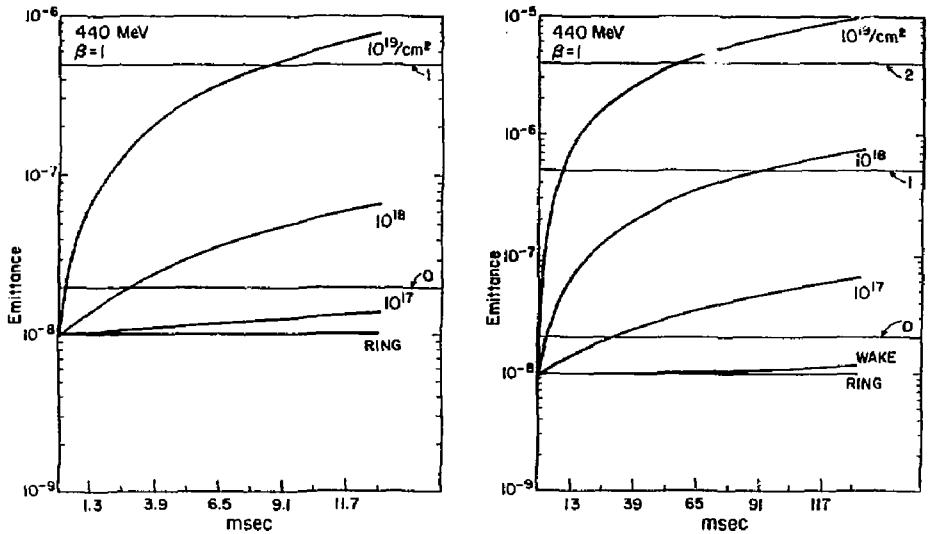

Figure 10. Emittance growth with different target thicknesses of a 440 MeV beam during the above two time scales.

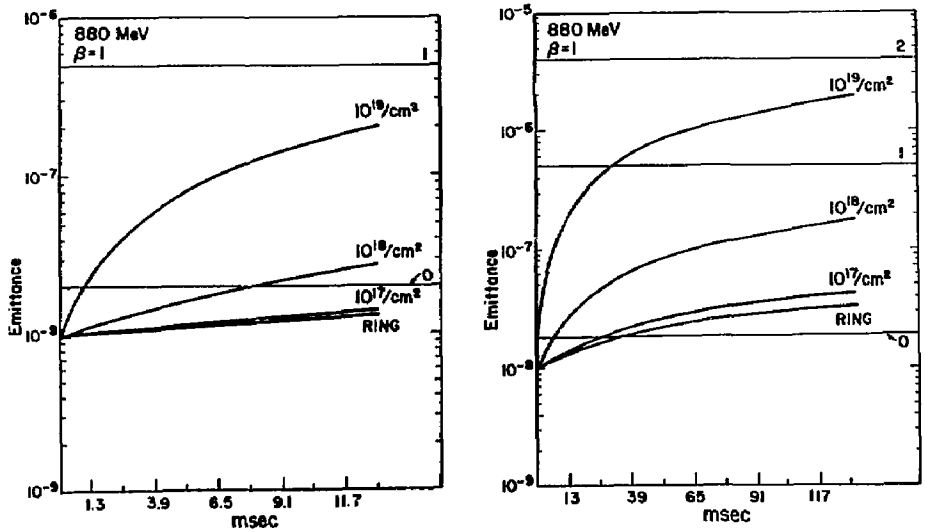

Figure 11. Emittance growth with different target thicknesses of a 880 MeV beam during the above two time scales.

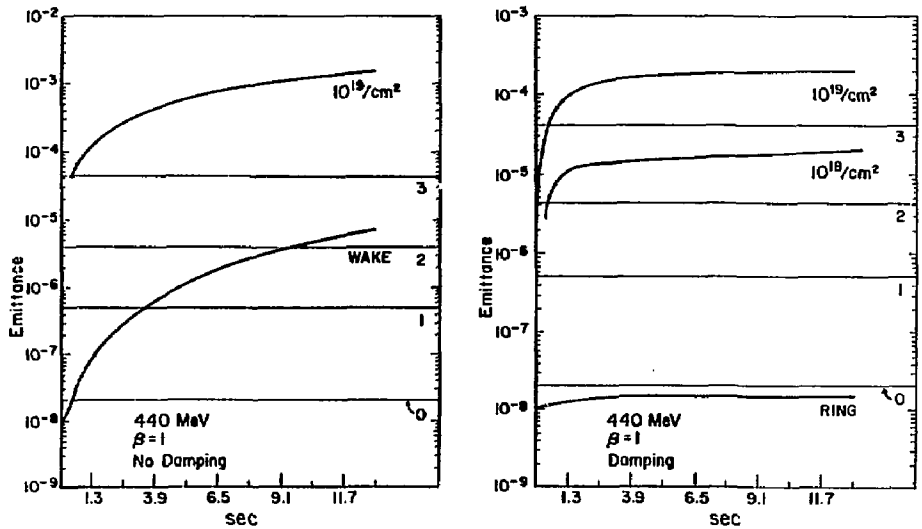

Figure 12. Emittance growth over a long time scale comparing the effects of damping with that when no damping is included for a 440 MeV beam.

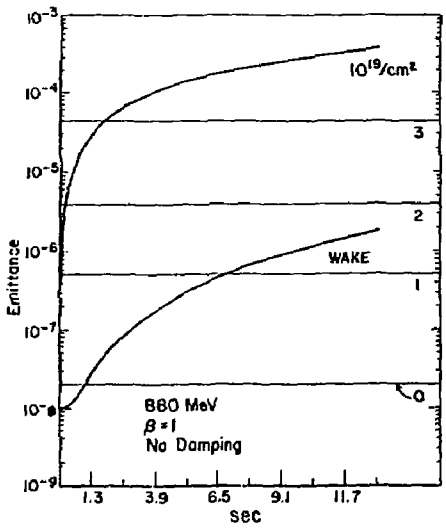

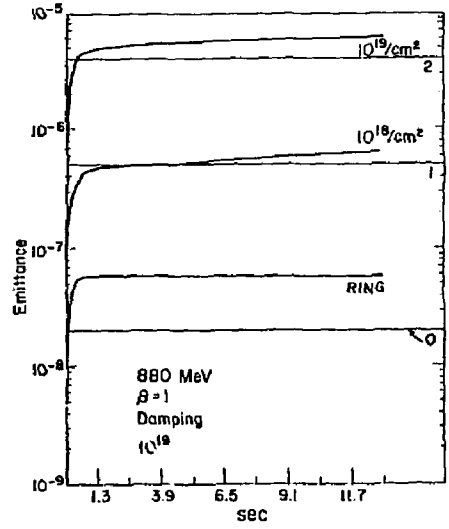

Figure 13. Emittance growth over a long time scale comparing the effects of damping with that when no damping is included for a 880 MeV beam.

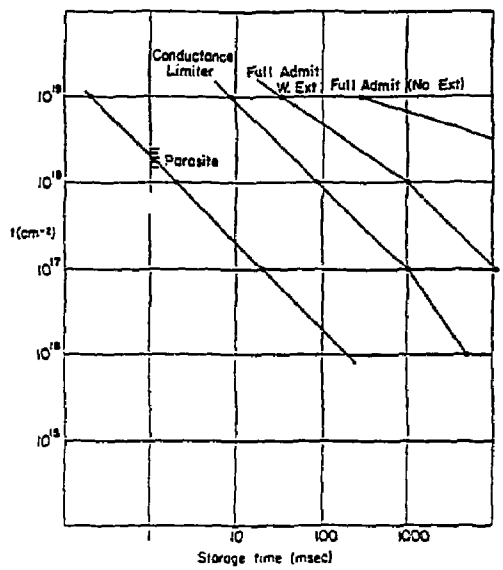

Figure 14. Storage times for different internal target densities and different conditions.

Longitudinal Phase Space

The admittance in longitudinal phase space is restricted by the RF power available. There is room in the RF bucket for 0.08% in energy. This is compared to the expected .04% to be injected. The physical limitation comes about at the point of largest dispersion which is 3.8 cm/%. Given a beam pipe size of 7.6 cm this converts to a ring acceptance of 2% in energy without any reduced apertures. Synchrotron and parasitic losses are made up with the RF. The energy lost by most of the beam going through the internal target is negligible.

Wakefields

Another source of loss is that from those collimators which were used as conductance limiters and emittance protectors. The wakefields from these discontinuities in the vacuum pipe effect the energy of the beam as a function of beam position and charge. The curve in Fig. 15 shows a beam bunch traversing a target cell. The wakefields are seen not to be perpendicular, the longitudinal component causes energy change. Figure 16 shows the wake function for that case per picoCoulomb. Given a bunch with 28 picoCoulombs the maximum energy spread incurred by this transition is 200 volts. The wake shape is reminiscent of an RF source shifted in phase by approximately the radius of the small aperture. Its voltage is too small to cause the beam to shift out acceptance of the main source of RF. Note, however, in the figure the dependence of the wakefield amplitude on taper of the collimator edge. With four collimators in the ring, this is doubled. Compared to other sources, however, this is still small. Judicious design of collimators is still prudent, considering the general discrepancies between calculated and measured ring impedances.

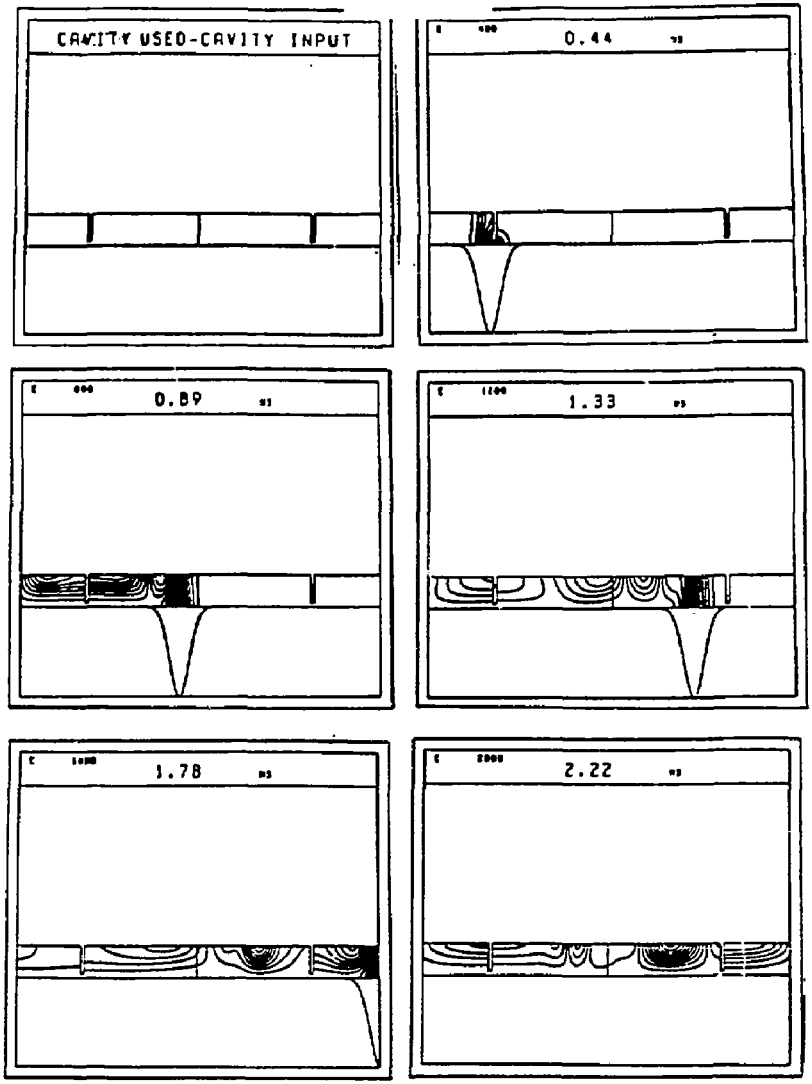

Figure 15. Electric field lines induced by gaussian beam bunch traveling through internal target at time indicated in figure (ns).

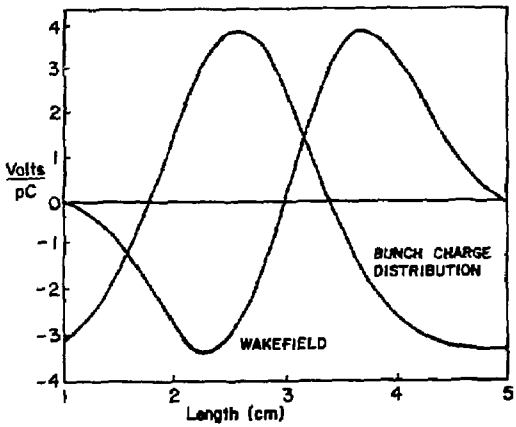

Figure 16. Wakefields of a collimator for given band bunch distribution.

Bremsstrahlung

There is some fraction of the beam that loses energy via bremsstrahlung. Some of this is lost near the target and will be treated later. Some of it, continues through the ring and would pass through the target. If one tried to limit the energy aperture to the injected energy spread of .04%, an aperture of the highest dispersion location of 1.5 mm would be necessary. This is not possible. However, it would seem that the fraction of loss is small enough so as not to affect an experiment.

Backgrounds

The above described emittance growth mechanisms become loss mechanisms. Two issues are important for ring operation. First, the collimators designed for cleaning purposes must be able to handle the power of the lost beam. Second, the losses nearest the internal target need to be investigated for background production. Sources of the latter include:

- Emittance growth halo hitting target aperture;
- Multiple and single scatterings hitting nearby beam pipe and ring elements;
- Bremsstrahlung losses coupling the energy dependence of quadrupole focussing (e/xδ) causing overfocussing after the first quad near the internal target.

Assuming the first effect is controlled by limiting the lifetime in the ring, the other effects are independent of the lifetime and still must be considered.

Three sources of background are treated as shown in Fig. 17. Since the first quad is 2.5 m from the target, any beam scattered between 15.2 mr to 50 mr will hit the pipe and the surface of the quad. Due to the strength of the nearby quad, any beam having lost more than 25% of its energy will strike the pipe between the first and second quad. Table IV summarizes the fraction of beam lost in these areas. Also in the table is the corresponding beam lost in electrons assuming 80 mA circulating current in the ring.

TABLE IV

BACKGROUNDS

- Scattering Hitting Ring Chamber and Elements
- Energy Loss Coupled to Energy Dependent Focussing of Quads

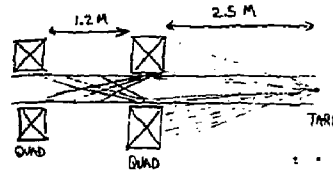

Figure 17

(After 1,000 turns) $\ell = 10^{15}/cm^2$ $\mathcal{E} = 440$ MeV $E = 880$ MeV

Fraction Hitting Pipe	1.8(-6)	4.4(-7)
Fraction Hitting Quad + Pipe	6.3(-5)	1.6(-5)
Fraction Hitting After Quad	4.9(-4)	4.9(-4)

Note: 80 mA = 6.5 x 10^{14} electrons

1 x 10^{-5} x 6.5 x 10^{14} electrons ~ = 18 x 10^{12} neutrons/sec per 1,000 turns

Figure 18 is a sketch of the beam line within the proposed internal target experimental hall. It is provided for your imagination. No cutout pieces provided.

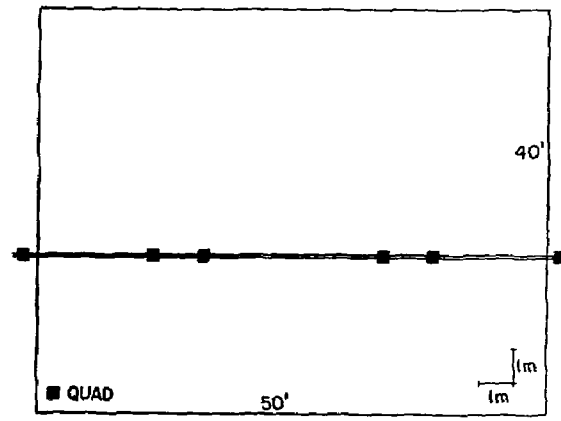

Figure 18. Beam line inside IT hall.

Conclusions

The calculations described indicated that a wide range of operational modes are possible in the proposed ring. Given the fast refill time possible, targets as thick as 10^{15} cm^{-2} are feasible, and targets as thick as 10^{18} are possible in a parasitic mode. It is also possible to store beam for many seconds and possibly longer (depending upon ring behavior) with thinner targets.

Consideration of vacuum requirements leads to the conclusion that conductance limiters near the internal target will be important for the thicker targets, as well as cleanup apertures located at the high beta region in the ring. Design of these apertures should take into account the wakefield production and have tapers near 30° for reduced wakefield effects.

The ring being proposed for Bates has several advantages for internal target work. They include:

1. Large admittance
2. Flexibility high beta and low beta
3. High space/element ratio
4. Excellent beam quality

The budget for this facility includes the cost of solenoidal magnets to contain longitudinal polarization of the electron beam in the ring as described by B. Norum (U.Va.) in this workshop.

At present, no facility for photon tagging is planned. The Bates staff is currently evaluating the experimental needs for the planned internal target hall. Figure 18 shows the internal target hall and beam line as presently planned. Input from potential users would be helpful at this stage.

I would like to thank several people who helped in the preparation of this talk. Particularly Claude Williamson and Michel Garcon for contributing details of their related work. I also would like to thank Ken Jacobs for his calculations of the longitudinal wakefields. Finally, thanks to Jim Spenser, Phil Morton, and Karl Bane for conversations relevant to this workshop.

This work was supported in part by DOE and MIT.

References

1. G. Nixon, Editor, Bates Annual Report, 1984.

2. J. Calarco, private communication.

3. M. Garcon, private communication.

4. P. Maloney, "Internal Targets in Electron Storage Rings", Master's Thesis, U.Va., 1983.

   B. Craft and C. Williamson, "A Study of Effects of Internal Targets in a 1.0 GeV Electron Storage Ring", Bates Internal Report #83-03, (1983).

   H. Crannell, CEBAF 1985 Summer Study, #12-95, (1985).

   B. Norum, CEBAF 1985 Summer Study, #12-70, (1985).

   B. P. Nigam et al., Phys Rev. 115, 491 (1959).

5. K. Bane and P. Morton, SLAC Pub-3983, May 1986.

INTERNAL TARGET PHYSICS AT 1 GeV

S. Kowalski

Bates Linear Accelerator Center
Laboratory for Nuclear Science and Department of Physics
Massachusetts Institute of Technology
Cambridge, MA 02139

Abstract

The use of internal targets operating at high luminosity in an electron storage ring in the energy range 0.3-1.0 GeV is discussed. Examples are presented of fundamental physics problems which would be ideally suited to such a unique new capability. Special emphasis is placed on the use of polarized targets to measure spin observables and thus provide a *"Multipole Meter"* for separating individual form factor multipoles. The combination of laser technology with optical pumping now makes possible the polarization of a broad class of nuclear species to useful densities. The importance of longitudinally polarized electrons for studying nuclear structure is also discussed.

I. Introduction

The electromagnetic probe is an important tool as a precise microscope in unraveling the structure of nucleons and nuclei. It involves a fundamental well understood weak interaction (QED) with unmatched specificity. Modern facilities have exploited high resolution electron scattering to probe distances of much less than 1 fm with great precision. A new generation of medium energy CW accelerator facilities, 0.3 - 4 GeV, are being developed to expand our present capabilities; particularly those for coincidence experiments and those emphasizing the measurement of spin observables.

The proposed Bates upgrade involves the use of a storage ring which would make possible experiments with very thin internal targets at high luminosity. The description of this pulse stretcher ring is summarized in a contribution to this conference by Flanz. Key parameters for internal target operation are:

Energy	0.3 - 1.0 GeV
$\Delta E/E$	~0.04%
Current	40 mA/turn
Duty Factor	100%
Emittance (1-turn)	.01π mm•mr
Beam Polarization	~40%
Vacuum	10^{-9} torr
Internal Targets	$< 10^{19}$/A nuc/cm^2

There has developed a strong interest over the past few years for such an internal target facility that could provide a unique capability for addressing fundamental problems in nuclear physics. The combination of ultra-thin targets ~10^{17}/cm^2 and large circulating currents ~80mA results in high effective luminosities ~5×10^{34}cm^{-2}s^{-1}. This is competitive with luminosities generally used with external beams. In addition the low target density opens up entirely new fields of study.

One important area involves experiments detecting relatively low energy, highly ionizing reaction products. Such studies would include electrofission, giant resonances and threshold pion production. In all cases there will be an emphasis on exploiting our ability to map out the (q,ω) plane for the reaction process as well as to isolate contributing multipoles.

Polarized electrons and/or polarized targets have up to now played only a minor role in nuclear physics. At high energies the SLAC parity violation experiment[1] involving the scattering of longitudinally polarized electrons from quarks provided a crucial test of our understanding of electro-weak processes. Other experiments[2] using polarized electrons and polarized H studied the spin structure function of the proton. Parity violating electro-weak experiments in the nuclear physics regime are underway at both MAINZ and MIT.

It is now clear that spin measurements can play a much broader role in nuclear physics than simply searching for parity violation. Recent theoretical studies[3] have shown that the capabilities of polarized electrons and polarized targets will provide a unique opportunity for addressing some long standing physics problems. They would allow in principle a complete experimental determination of the form factor multipole structure. Such a decomposition represents the most complete characterization possible of the electromagnetic structure of nucleons and nuclei. Electron scattering can achieve this in a model independent way.

The full power of the electromagnetic probe is realizable only with the measurement of spin observables: polarized targets, polarized beam and recoil polarizations. In such measurements one can exploit the interference nature of an asymmetry to measure small but important amplitudes. Fundamental physics problems include the deuteron t_{20}, neutron charge form factor and the deformation of the delta. More speculative weak interaction studies may also be possible.

Developing laser technology has made possible the polarization of a broad class of nuclear species to interesting densities (10^{14-16}nuc/cm^2). Combining a storage cell geometry with the high circulating current of a storage ring would make spin measurements in electromagnetic physics for the first time practical.

In this review we will present examples of the kinds of physics problems that could be studied in the near future with the development of internal target facilities. These include experiments in nuclear spectroscopy, those involving ionizing recoils, some fundamental measurements on nucleons and few-body systems and weak interaction studies.

II. Internal Targets

An important practical consideration for carrying out an effective internal target program is the question of luminosity. Comparing typical

luminosities for both external and internal beams we have:

External Beam:

$I \sim 25\mu A$

$t \sim (1\text{-}100) mg/cm^2$

$L_{ext} = 10/A \times 10^{34\text{-}36} cm^{-2} s^{-1}$

Internal Beam:

$I \sim 80mA$

$t \sim 10^{14\text{-}16}$ nuc/cm^2 (polarized targets)
$> 10^{17}$ nuc/cm^2 (unpolarized jets or microfoils)

$L_{int} = 5 \times 10^{31\text{-}34} cm^{-2} s^{-1}$

Although the internal target luminosities are in general smaller, such luminosities are more than sufficient to carry out a broad program of electronuclear studies. Experiments detecting low energy highly ionizing reaction products, such as those resulting from electro-fission or threshold pion production, require the use of very thin targets.

A very important class of experiments for an internal target program involves the use of polarized targets. The standard techniques used to produce dense polarized targets in nuclei such as H and D involve low temperatures and very high magnetic fields. Such targets have limited usefulness. For example, polarized deuterium targets which are used in external beams are limited to a few nA of current due to beam heating and radiation damage. The effective luminosity is substantially reduced.

The use of laser driven optical pumping and spin exchange techniques opens the possibility of polarizing a broad class of nuclear species. When combined with internal beams, such targets with densities of $10^{14\text{-}15}$ nucl/cm^2 give high luminosities. They have, in addition, much higher polarization resulting in a better overall figure-of-merit. Since the internal targets can operate at low magnetic fields the spin orientation is easily controlled and rapid spin reversal for control of systematic errors is a relatively straight forward operation.

There is presently extensive activity in constructing polarized gas targets of useful densities for nuclear physics studies. A tensor polarized deuterium target and a polarized ^{3}He target are under development at ANL[4] and Cal Tech,[5] respectively. Further, as techniques are advanced, for both polarized and unpolarized targets one sees potential experimental advantages involving high accuracy and low background operation.

Various target geometries have been considered for use in storage rings. An important requirement is to provide adequate clearance for the circulating beam and to maintain low vacuums outside of the target region. The most promising target configurations are gas jets and storage cells. These are illustrated in Figure 1.

GAS JET TARGET

- TARGET MATERIAL UNDER HIGH PRESSURE
- SPECIALLY DESIGNED NOZZLES
- GAS COLLECTION/PUMPING

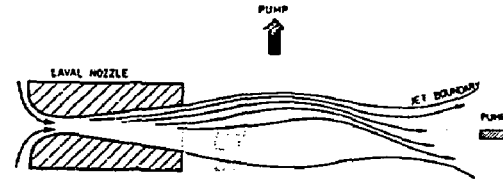

STORAGE CELL TARGET

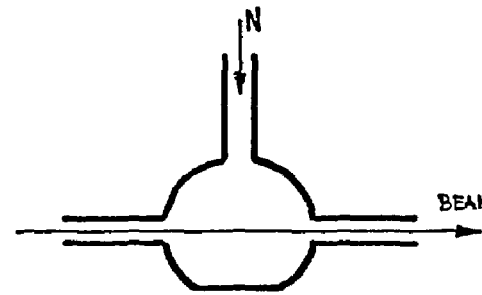

Fig. 1: Schematic gas jet and storage cell internal target geometries.

Another important consideration in the use of internal targets involves the beam-target interaction. Important issues include:

- energy loss
- emittance growth
- pumping apertures
- target depolarization.

A complete discussion of these and other targeting problems in the proposed Bates 1-GeV ring is reviewed in the contribution to this conference by Flanz.

III. Nuclear Spectroscopy

High resolution single-arm electron scattering is the source of much of our precise and detailed information on the electromagnetic structure of complex nuclei. An example which emphasizes both the specificity and shortcomings of this simple process is ^{17}O. The data[6] for the transverse form factor of the ^{17}O ground state in the effective momentum transfer range $0.5 < q_{eff} < 2.8$ fm^{-1} are shown in Figure 2.

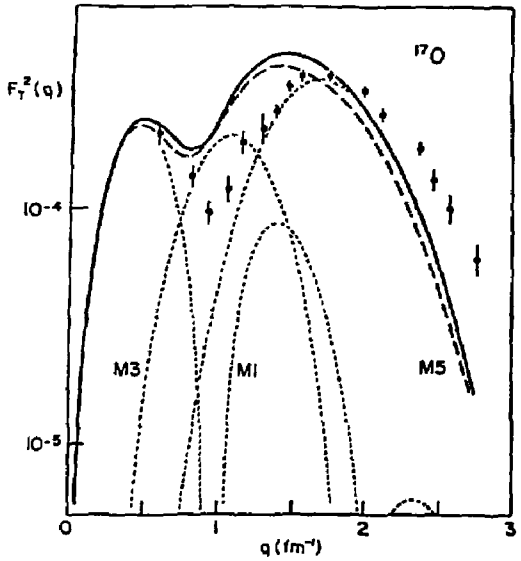

Fig. 2: The ^{17}O data of Hynes et al., are compared to the prediction of the extreme single-particle model calculation using a harmonic oscillator wave function (solid curve and dotted curves for individual multipoles). The dashed curve is calculated using a Woods-Saxon radial wave function.

In the simplest picture of ^{17}O a $d_{5/2}$ neutron is bound to a possibly deformed ^{16}O core. Both the longitudinal and transverse form factors have contributions from several multipoles.

$$F_L^2 = F_{C0}^2 + F_{C2}^2 + F_{C4}^2$$
$$F_T^2 = F_{M1}^2 + F_{M3}^2 + F_{M5}^2$$

These incoherent combinations of multipoles cannot be separated in a model independent way without polarization information. Single particle calculations using HO wave functions indicate that there is a sizeable suppression of the M3 component. Neither core-polarization nor meson exchange effects can account for the observations.

The detailed discussion of the nuclear structure information made accessible through the use of polarized targets and longitudinally polarized electrons is summarized in a recent review by Donnelly and Raskin.[3] The "*Multipole Meter*" aspect of spin observables is demonstrated by examples involving elastic and inelastic scattering in complex nuclei. All show the detailed sensitivity that these new techniques provide for separating the nuclear structure information into the maximal fundamental information that is allowed by a measurement of the individual electromagnetic form factors.

As a specific example we will consider elastic electron scattering from $^{39}K(I=3/2)$. This nucleus can be described in the extreme single-particle model as a $1d_{3/2}$ proton hole relative to ^{40}Ca using simple harmonic oscillator wavefunctions. The effects of core polarization and meson exchange currents are included in the characterization of the measured[7] transverse form factors (Figure 3).

In Figure 4 are shown the predicted results for the asymmetries. The plotted asymmetries are:

$$A_{NS} = (\Sigma_N - \Sigma_S)/\Sigma_0$$
$$A_{LN} = (\Sigma_L - \Sigma_N)/\Sigma_0$$
and
$$A_{LS} = (\Sigma_L - \Sigma_S)/\Sigma_0$$

where the Σ_i are the respective polarization cross sections and Σ_0 is the unpolarized cross section and i = L, N and S refer to the usual[8] target polarization directions with respect to the incident electron direction. The polarization ratio $(\Delta/\Sigma)_i$, calculated for specific orientations of the target polarization, is shown in Figure 5.

The results show significant variations for both the asymmetries and polarization ratios as a function of momentum transfer. These variations result from a complicated interference between the contributing form factors and are particularly emphasized when any of

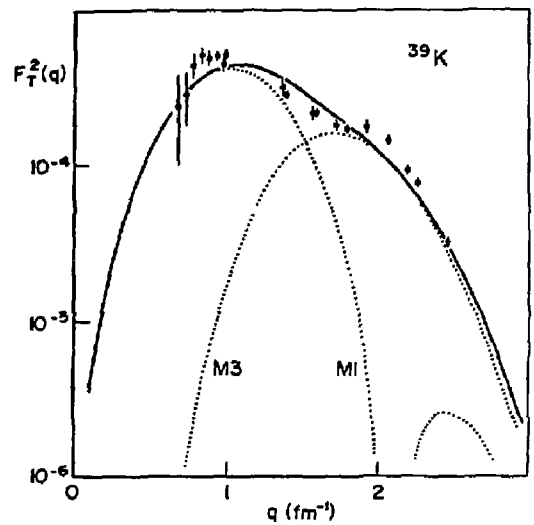

Fig. 3: The ^{39}K data of DeJager et al., are compared to a phenomenological fit made using $d_{3/2}^2$ and $f_{7/2}^2$ matrix elements and a harmonic oscillator radial wave function.

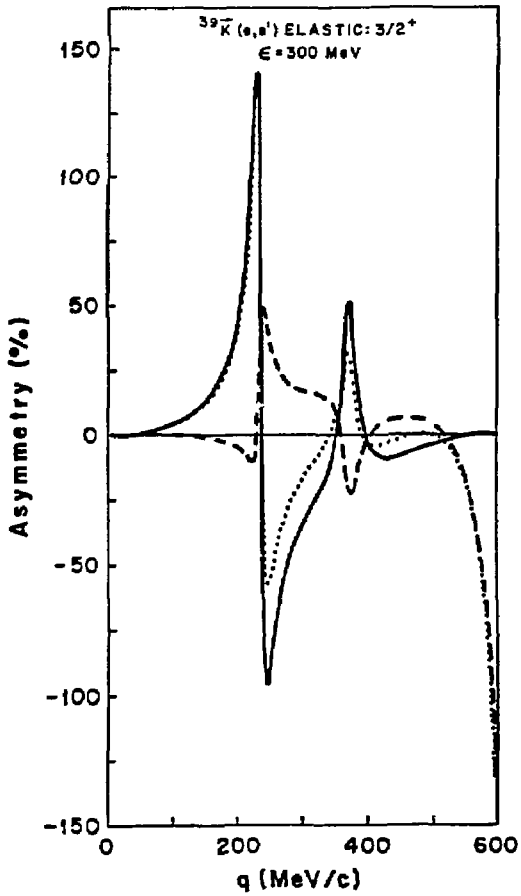

Fig. 4: Elastic electron scattering from polarized ^{39}K. The polarization asymmetries correspond to taking the target to be 100% polarized along the L, N, and S directions and forming the differences and dividing by the unpolarized cross section Σ_o.

the individual form factors goes through zero. Precise measurements of cross sections and asymmetries when combined with the usual longitudinal-transverse separation using unpolarized targets will allow a complete separation of the four form factors which contribute in this case.

IV. Ionizing Recoils

Internal targets will also offer a unique capability for studies of the nuclear continuum. Experiments requiring the detection of highly ionizing reaction products are in many cases severely limited by targeting requirements in external beams. Gas jet

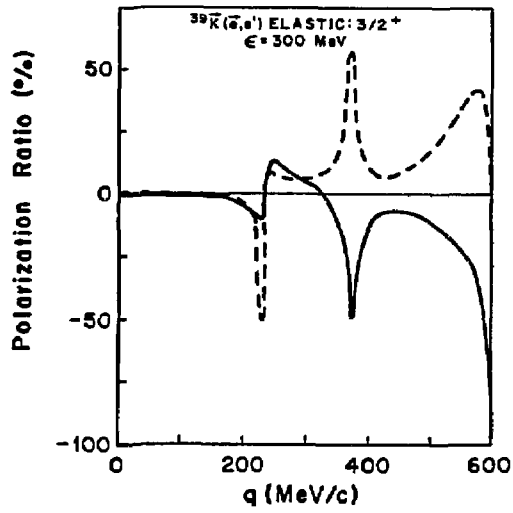

Fig. 5: Elastic longitudinally polarized electron scattering from polarized ^{39}K. The polarization ratios $(\Delta/\Sigma)_L$ (solid line), and $(\Delta/\Sigma)_S$ (dashed line) are calculated for a 100% polarized target.

while at the same time allowing for in-vacuum coupling between the detector and target.

Examples of areas of research which could benefit from the use of internal targets include:

- Electrofission
- Giant Resonance
- Pion Electroproduction

1. Electrofission

Reactions such as $^{24}Mg(e,^{12}C\ ^{12}C)e'$ have been studied using CW accelerators. Several sharp structure resonances were discovered[8] in the GR region of ^{24}Mg and ^{28}Si. They exhausted a significant fraction of the E2 and E0 sum rules and decayed primarily into "exotic" channels such as binary or near binary fission. The nuclear structure of these resonances still remains a puzzle. It would be very interesting to do a complete (q,ω) map of the process by detecting the scattered electron in coincidence. Such experiments appear to be practical only with internal targets.

In the HEPL experiments using 400μA average currents on targets of 3μg/cm^2 the luminosity was $3\times10^{32}cm^{-2}sec^{-1}$ for ^{24}Mg. An internal target could in principle be four times thicker and with the large circulating current the resulting luminosity would be higher by more than two orders of magnitude. It would be sufficient to carry out a full coincidence program.

2. Giant Resonance

The objective of much of the current work in giant resonance studies is to separate modes of different multipolarity and to carry out a spatial mapping of the coupling to various decay channels. Luminosities for both external and internal target experiments are similar. There are, however, other advantages offered by the use of thin internal targets.

One can achieve better energy resolution in (e,e'x) experiments where target thickness is a serious limiting factor. The use of thin targets, either gas jets or very thin foils, allows the study of rare (and/or expensive) nuclear species.

One final important consideration is that internal targets allow the detection of very heavy and highly ionizing recoil particles. For example, experiments such as (e,e'n), which are difficult to do otherwise, could be carried out by detecting the recoiling residual nucleus if it is sufficiently stable. The study of $^{13}C(e,e'n)$ by detecting ^{12}C and measuring its energy is one possibility. Other interesting examples of light nuclei include ^{4}He, ^{7}Li, ^{11}B, ^{13}C, ^{15}N, etc... Recoil species such as ^{11}C, ^{15}O, ^{19}Ne are sufficiently long lived as well. A real advantage would be the study of (e,e'p) and (e,e'n) in the same apparatus.

Figure 6 shows a typical apparatus of a coincidence GR experiment[9] in the Novosibirsk ring and some results for the $^{16}O(e,e'\alpha_0)$ decay channel. This was a relatively low energy (130 MeV) experiment using a gas jet target.

3. Threshold Electroproduction of Pions

A special type of experiment which requires thin targets and high luminosity is the study of pion electroproduction from nuclei near threshold. The standard technique involves pion detection in reactions of the type $_{Z}{}^{A}(e,e'\pi^{-})_{Z+1}{}^{A}$.

One could alternatively measure the recoiling daughter nuclei in the reactions $_{Z}{}^{A}(e,e'_{Z\mp1}{}^{A})\pi^{\pm}$. The very thin targets required to detect heavy recoils combined with the high circulating current provide the necessary luminosities. Predicted cross sections are very small.

Coincidence experiments such as these would involve a complete mapping of the (q,ω)-plane for which the relative energy of the pion daughter-nucleus system is near threshold. The (γ,π) reaction only studies the process where $q=\omega$. Reaction kinematics shows a one-to-one relationship between pion angle in the CM frame and residual nucleus kinetic energy in the laboratory frame. The nucleus energy distribution yields a measurement of the pion angular distribution. An accurate spectrum measurement would allow a separation of s- and p-wave components for the process.

Motivations for such studies include:

- Measure for virtual photons to compliment real photon results.
- Measure the spatial distribution of the pion wavefunction and use it to decide on the correct form of the π-nucleus optical potential at low energies.
- Study π^{+} and π^{-} production between analog states. Coulomb interaction modifies the strong interaction and could provide a measure of where the strong interaction distortion is turned on and off.
- Study the production amplitude as final state CM energy is increased from threshold. At higher energies the leading Kroll-Ruderman $\vec{\sigma} \cdot \vec{\epsilon}$ term is modified by the addition of momentum dependent terms.

V. Fundamental Measurements

The high luminosity of a stretcher ring will make practical the precise measurement of spin observables in nucleon and few nucleon systems using polarized electrons and/or polarized targets. Some of the most fundamental of such studies which now appear feasible include the separation of the deuteron charge monopole and quadrupole form factors, the neutron charge form factor and the deformation of the delta.

1. Deuteron Form Factors

The deuteron is our simplest bound nuclear system. All of its static properties have been

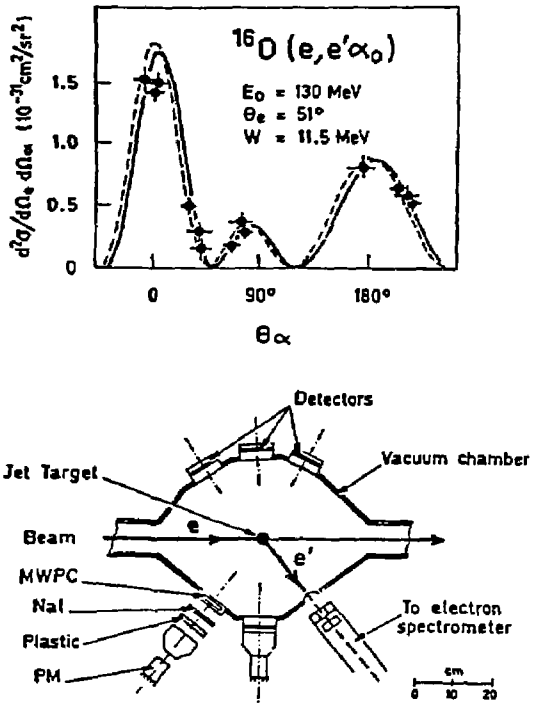

Fig. 6: Data and schematic experimental layout for an $^{16}O(e,e'\alpha_0)$ measurement using internal targets in the VEPP-2 ring at Novosibirsk.

precisely measured. Electron-deuteron scattering provides important information on the short range behavior of the deuteron wavefunctions as well as a measure of non-nucleonic degrees of freedom such as isobar and meson exchange currents. Quark degrees of freedom are expected to contribute at large q^2.

A complete description of the electromagnetic properties of the deuteron (J=1) requires a measurement of three form factors: charge monopole (F_C), charge quadrupole (F_Q) and magnetic dipole (F_M) as a function of an extensive range in momentum transfer.

The unpolarized e-d elastic cross section is usually written as:

$$\frac{d\sigma}{d\Omega} = \sigma_M \left\{ A(q^2) + B(q^2) \tan^2 \theta/2 \right\}$$

where

$$A(q^2) = F_C^2(q^2) + \frac{8}{9}\eta^2 F_Q(q^2) + \frac{2}{3}\eta F_M(q^2)$$

$$B(q^2) = \frac{4}{3}\eta(\eta+1)F_M^2(q^2)$$

$$\eta = \frac{q^2}{4M_D^2}$$

The two structure functions $A(q^2)$ and $B(q^2)$ have been measured to high q^2 and are separated using the usual Rosenbluth method. Such an angular distribution provides a measure of F_M but F_C and F_Q cannot be separated in a model independent manner. The location of a zero in the charge monopole contribution is important to our understanding of the validity of different potential models as well as providing a measure of two body currents.

The measurement of a spin observable in principle allows the complete separation of the individual multipole contributions. Electron scattering from a tensor-polarized deuterium target is sensitive to additional interfering bilinear combinations of deuteron form factors. The t_{20} component of the tensor polarization,

$$t_{20} = -\sqrt{2}\sigma_M \left[\frac{4}{9}\eta^2 F_Q^2 + \frac{4}{3}\eta F_C F_Q + \frac{1}{3}\eta F_M^2 \left[\frac{1}{2} + (1+\eta)\tan^2\frac{\theta}{2} \right] \right] / \frac{d\sigma}{d\Omega} .$$

The most important contribution to t_{20} in the momentum transfer range $q^2 < 1.2(GeV/c)^2$ comes from the interference term $F_C F_Q$. This provides the additional handle which allows a separation of the multipole contributions.

In a recent Bates experiment,[10] the tensor polarization was determined by measuring the polarization of the recoil deuterons (electron beam and target unpolarized) in coincidence with the scattered electrons. Such an experiment involves a second analyzing scattering of known sensitivity to tensor polarized deuterons. In this case the reaction $\vec{d}(^3He,p)$ was used. The extracted values of t_{20} are compared with theoretical predictions of several realistic potential model calculations in Figure 7.

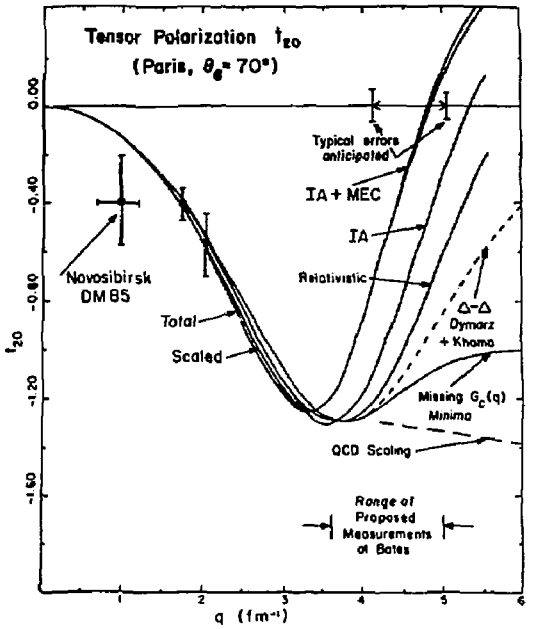

Fig. 7: Comparison between different theoretical predictions for deuteron t_{20} including QCD scaling, Δ-Δ admixtures and the effect implied by the filling in of the minima in $G_C(q)$. The Novosibirsk and Bates experimental data are shown as well as the q-range and anticipated sensitivity of the proposed new measurements.

Extensions of these measurements to regions of momentum transfer Q~1GeV/c are under way[11] and involve some very interesting physics. The potential model dependences are sizeable and perturbative QCD predictions are completely at variance with the potential model results. These new measurements do not involve the use of polarized targets but rely on the use of a polarimeter whose properties and performance must be accurately known.

An alternative approach involves measuring the asymmetry in elastic electron-deuteron scattering from a tensor polarized target. Such measurements are currently underway at the Bonn synchroton where 1nA beams of electrons are incident on a tensor polarized liquid ND_3 target. A Q^2 up to 0.7 GeV^2/c will be probed and in the future extended to $Q^2 > 1$ GeV^2/c on the ELSA ring.

Holt[4] at ANL is developing a tensor polarized deuterium target for use as a gas jet internal to the Aladdin 1 GeV storage ring. A target density of $\sim 10^{14}$ atoms/cm^2 in a circulating current of 100 mA results in luminosities of the order of $10^{32} cm^{-2} s^{-1}$. Such a

high density of polarized deuterium nuclei is obtained by using optically-pumped polarized alkali atoms which transfer polarization to deuterium atoms by atomic spin exchange. Densities in excess of 10^{15} atoms/cm^2 appear feasible with present-day techniques.

2. Neutron Electric Form Factor

The elastic scattering of unpolarized electrons from unpolarized nucleons (J_1=1/2) involves a measurement of the cross section

$$\frac{d\sigma}{d\Omega} = \sigma_M f_{rec}^{-1}\left[G_{EN}^2(Q^2)+\tau G_{MN}^2(Q^2)\left\{1+2(1+\tau)\tan^2\frac{\theta}{2}\right\}\right]$$

where

$$\tau = -Q^2/4M_N^2$$

The electric and magnetic form factors, $G_{EN}(Q^2)$ and $G_{MN}(Q^2)$, respectively, are related to the $F_L(Q)$ and $F_T(Q)$ by

$$\sqrt{4\pi}F_L = (1+\tau)G_{EN} \text{ and } \sqrt{4\pi}F_T = \sqrt{2\tau(1+\tau)}G_{MN}.$$

A Rosenbluth separation of the form factors allows for reasonable accuracy only when the two amplitudes are comparable. In the nucleon case the magnetic form factor dominates over the electric one at high momentum transfer. As a result only the magnetic form factor is relatively well known over an extended range in momentum transfer.

The electric form factor is directly related to the charge distribution of the nucleon and is a fundamental quantity whose knowledge is important for the detailed understanding of both nucleon and nuclear structure. For the proton, reasonable knowledge of G_{Ep} exists only up to 4(GeV/c)^2. In the case of the neutron, which is charge neutral, G_{En} is very small and as a result is very poorly known for all q, except for q=0.

The usual method of measuring G_{En} involves the Rosenbluth decomposition of electron-deuteron elastic and quasi-elastic scattering. Interpretation of the results is plagued with both model dependence and large systematic errors. The available body of data for G_{En} up to q^2~1.5(GeV/c)^2 are shown in Figure 8.

For the nucleon case (J_1=1/2) polarized targets without polarized electrons yields no new information. The polarization cross section for scattering from polarized nucleons is

$$\Delta_{fi} = -\Sigma_o\left\{\sqrt{2}F_T^2(q)v_{T'}\cos\vartheta^* + 2\sqrt{2}F_L(q)F_T(q)v_{TL'}\sin\vartheta^*\cos\phi^*\right\}/\sqrt{2}F^2$$

where

$$F^2(q) = v_L F_L^2(q) + v_T F_T^2(q).$$

A measurement of the polarization ratio Δ_{fi}/Σ_o (asymmetry) or equivalently that of the recoil nucleon polarization by means of a second scattering involves

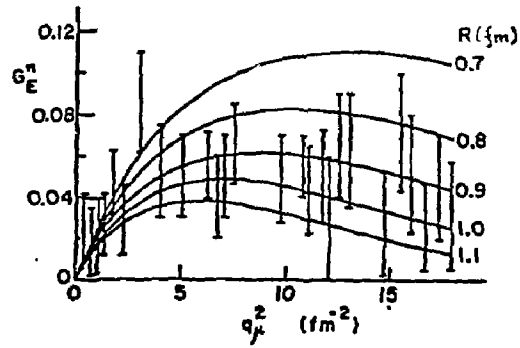

Fig. 8: Neutron electric form factor for different bag radii and existing experimental data.

the interference term $F_L(q)\,F_T(q)$ which is directly sensitive to the small form factor and to their relative sign. The simple Rosenbluth separation is insensitive to the small amplitudes

Possible experiments which can be exploited to measure the neutron electric form factor G_{En}, include:

$^2\vec{H}(\vec{e},e'n)p$ exclusive

$^2\vec{H}(\vec{e},e')x$ inclusive

$^2H(\vec{e},e'\vec{n})p$

$^3\vec{He}(e,e')x$ inclusive.

The sensitivity of the polarized-electron polarized-deuteron experiment to G_{En} has recently been calculated by Cheung and Sloshyn.[12] The results for the cross section and polarization asymmetry at an electron energy of 1 GeV are shown in Figure 9. The deuteron is polarized in the scattering plane at 45° to the incident electron direction. The neutron electric form factor has been parametized by:

$$G_{En}(Q)^2 = \frac{-\mu_n\tau}{(1+\eta\tau)\left[1+\frac{Q^2(\text{GeV})^2}{0.71}\right]^2}$$

with $0 < \eta < \infty$. The asymmetry shows large sensitivity to G_{En} and appears to be measurable.

The sensitivity to G_{En} has also been calculated[13] for scattering from polarized ^{3}He. In the simplest picture of ^{3}He the protons have opposite spins, and their contributions to spin-effects should essentially cancel. The spin-dependent effects are then primarily due to the neutron and the results for inclusive scattering are shown in Figure 10. The same parameterization was used for the neutron electric form factor and β is the angle in the scattering plane between the polarization axis of ^{3}He and the incident electron direction.

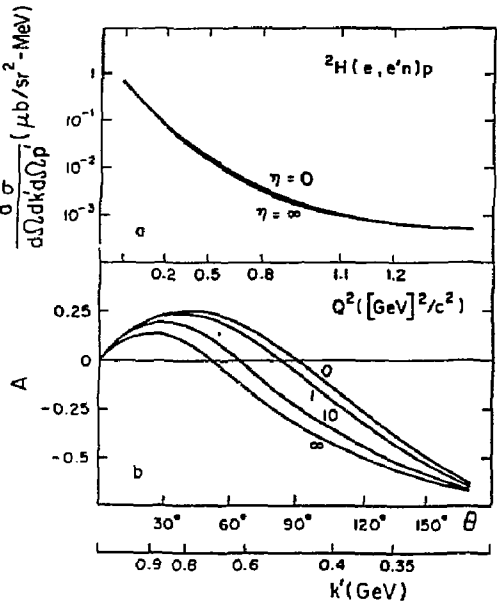

Fig. 9: Exclusive cross section for $^2\vec{H}(\vec{e},e'n)p$ at quasi-free kinematics for different neutron electric form factors using 1 GeV incident electrons. Asymmetry with respect to change in the electron longitudinal polarization for different neutron electric form factors. The deuteron is polarized at 45° to the incident electron direction.

An experiment to measure G_{En} using polarized electrons and a recoil neutron polarization measurement is being planned at MIT-Bates.[14] Future experiments involving polarized targets will require internal target capabilities at the new electron stretcher ring facilities now under development. The present technology for polarized targets needs the high luminosity of an internal target to make such experiments realistic. Such facilities are likely to provide our most precise measurements of G_{En} over an extended range in q.

3. N → Δ Transition

The N→Δ transition involves the lowest spin-isospin excitation of the nucleon. Angular momentum and parity considerations allow three form factors F_{M1}, F_{E2} and F_{C2}. In a naive spherically symmetric quark model the nucleon and delta are each made up of three 1s-quarks. The transition then corresponds to a pure M1 spin-isospin flip of a 1s quark with no quadrupole contribution. Non-spherical admixtures to the Δ arising from a tensor quark-quark interaction would allow for L=2 contributions as well.

Quark models have been used to estimate the quadrupole C2 contribution. In such models a nucleon s-quark makes a transition to a d-quark in the delta.

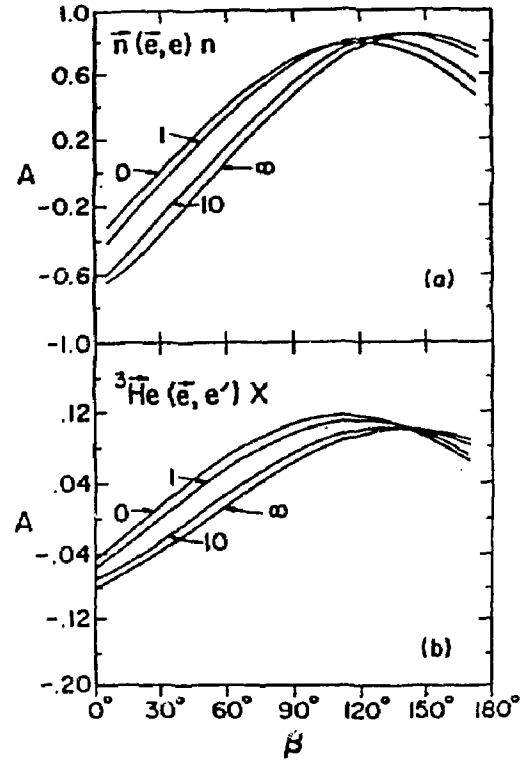

Fig. 10: Asymmetries as a function of target polarization angle β for a) polarized electron-polarized neutron scattering, b) inclusive polarized electron scattering from polarized ^{3}He at the quasi-free peak. Incident 1.5 GeV electrons are scattered at 60° for different choices of the neutron electric form factor.

A precise measurement of the C2 amplitude could shed some light on a possibly deformed delta.

The polarization cross section for a I/2 → 3/2 transition on polarized nucleons is given by

$$\Delta = 4\pi\sigma_M f_{rec}^{-1}\left\{v_T,\cos\theta^*\left[F_{M1}^2 - F_{E2}^2 - 2\sqrt{3}F_{M1}F_{E2}\right]/\sqrt{2}\right.$$

$$\left. - \sqrt{2}\, v_{TL},\sin\theta^*\cos\phi^*\left[F_{C2}(F_{M1} + \sqrt{3}F_{E2})\right]\right\}$$

and the spin-averaged cross section

$$\Sigma = 4\pi\sigma_M f_{rec}^{-1}\left\{v_L F_{C2}^2 + v_T\left[F_{M1}^2 + F_{E2}^2\right]\right\}$$

Previous experiments have tried to make the usual Rosenbluth separation to determine F_{C2}. The results[15] are shown in Figure 11. The small longitudinal contribution is poorly known and is consistent with zero.

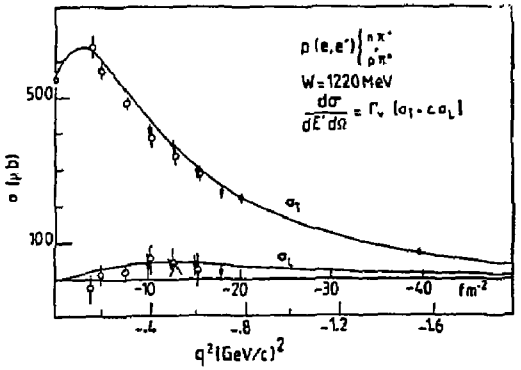

Fig. 11: Longitudinal and transverse response for p(e,e')Δ through the resonance region.

Experiments involving polarized electrons on polarized nucleon targets would be directly sensitive to the interesting $F_{C2}F_{M1}$ interference term and provide a measure of F_{C2}. Possible experiments include:

$$^1\vec{H}(\vec{e},e')\Delta \quad \text{and} \quad ^3\vec{He}(\vec{e},e')\Delta$$

The combination of both experiments would allow for a separation of neutron and proton contributions to the transition.

VI. Weak Interaction Physics

A more speculative ("Science-Fiction") experiment involving the use of internal targets would be a measurement of the charge changing weak interaction process such as

$$^3He(e^-,{}^3H)\nu_e.$$

This reaction, although not as fundamental as the single-nucleon process $p(e^-,n)\nu_e$, involves a charged final state making it more amenable to experiment. The basic process is illustrated in Figure 12 for which cross section predictions have been made by Donnelly.[16]

The cross sections ($\sim 10^{-40}cm^2sr^{-1}$) are very small and include contributions from vector and axial-vector terms which could in principle be separated. Combined with elastic electron scattering results this would provide a test of CVC. Based on the standard model with massless left-handed neutrinos, the cross section should be zero for right-handed electrons. A non-zero measure would indicate the presence of non-standard contributions.

The counting rates are low and would require a large acceptance detector system. Reaction kinematics show a strong correlation between recoil

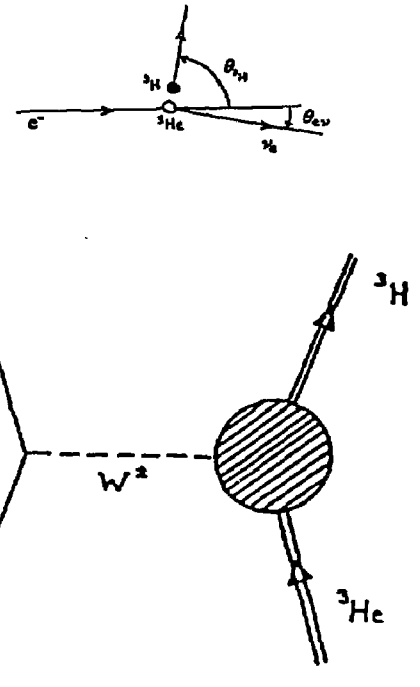

Fig. 12: $^3He(e^-,{}^3H)\nu_e$ charge-changing weak interaction physics.

angle and triton energy. This would need to be exploited to reject background events. With a circulating current of 100mA, a solid angle of 0.5sr and a target of 10^{19}atoms/cm² the event rate is approximately 2/hr.

The experiment, however, involves serious background problems. First, the kinematics are identical to elastic scattering. Since this is 12-14 orders of magnitude greater, the ^3He target must be ultrapure; the ^3H component must be less than 10^{-14}. Target walls must be far removed to reduce recoiling ^3He charge exchange reactions which would mask the tritons. Charge-sensitive detectors could help to overcome this problem.

This type of experiment is highly demanding but offers an exciting opportunity to measure a weak interaction form factor. It may be impractical. It should, however, be looked at as an interesting example of the kinds of "exotic" but very exciting experiments which may be possible using internal targets.

VII. Summary

We have tried to show in this brief review, using a few select examples, a glimpse of the new physics that would be made possible using internal targets at

a 1-GeV storage ring. The ability to measure accurately small amplitudes and interfering processes over an extended region in (q,ω) space would be an important new tool for electromagnetic nuclear physics. A basic program using spin observables to address a broad range of fundamental problems would be possible for the first time.

To make the proposed experiments a reality will require a nominal investment in the upgrade of existing accelerator facilities. The accelerator technology is well understood and only a modest investment in research equipment would be needed for carrying out many of the first interesting experiments.

There is currently much activity in the development of optically pumped polarized targets. The results look very promising.

Worldwide, the storage ring at Novosibirsk has been used for internal target nuclear physics studies. Plans are underway for possible experiments at the new Saskatoon Pulse Stretcher Ring just beginning operation. It has a maximum energy capability of up to 300 MeV. In the US, the ANL group has designed a deuteron t_{20} experiment for the Aladdin storage ring. The proposed Bates CW upgrade would provide a unique facility for such studies over an extended energy range of 0.3 - 1.0 GeV. *With timely funding such a facility could be operational in a few years.*

References

1. C.Y. Prescott et al., Phys. Lett. B77, 347 (1978).
2. M.J. Alguard et al., Phys. Rev. Lett 41, 70 (1978).
3. T.W. Donnelly and A.S. Raskin, Annals of Physics, 169, 247 (1986).
4. Holt, R., Proceedings of the Conference on Intersections Between Particle and Nuclear Physics, Steamboat Springs, edited by R.E. Mischke, AIP 123, 499 (1984).
5. R. McKeown and R.G. Milner, proceedings to this conference.
6. M.V. Hynes et al., Phys. Rev. Lett. 42, 1444 (1979).
7. K. DeJager et al., quoted by L. Lapikas, Proc. Conf. Nucl. Phys. Electrom. Int., Mainz, Lecture Notes in Physics 108, 41 (1979).
8. A.M. Sandorfi et al., Phys. Rev. Lett. 45, 1615 (1980).
9. S.G. Popov, Proc. of Workshop on the Use of Electron Rings for Nuclear Physics Research, Lund 1982, p150. D.M. Nikolenko et al., Europhysics Conference Abstracts 90, 242 (1985).
10. M.E. Schulze et al., Phys. Rev. Lett. 52, 597 (1984).
11. J. Cameron et al., Bates Proposal (1984).
12. C.Y. Cheung and R.M. Woloshyn, Phys. Lett. 127B, 149 (1983).
13. B. Blankleider and R.M. Woloshyn, Phys. Rev. C29, 538 (1984).
14. R. Madey and S. Kowalski, Bates Proposal (1985).
15. W. Bartel et al., Phys. Lett. 35B, 181 (1971).
16. T.W. Donnelly et al., Research Program at CEBAF, Report of the 1985 CEBAF Summer Study Group.

VECTOR DOMINANCE REVISITED BY A QUARK THEORIST

C.E.Carlson
Physics Department
College of William and Mary
Williamsburg, VA 23185, USA

Abstract: We examine from the viewpoint of QCD some topics that are often treated at lower energies by other means, particularly vector meson dominance, VMD. We would like to see why the older methods worked well enough to be pursued and what limits QCD says they should tend toward at higher energies.

I. Introduction

We will examine a trio of "old" topics, which have often been analyzed using vector meson dominance[1], from the viewpoint of a modern theorist who likes to analyze in terms of quarks and quantum chromodynamics. The three topics selected are the electromagnetic N-Δ transition form factors (where we don't mention VMD), the nucleon form factors, and Compton scattering from a proton target.

We will try to see either why VMD gave decent results in some situations or what contraints QCD will set upon putative models that one uses when a simple (i.e., coupled with perturbation theory) QCD won't work because the energy is too low. The latter of course is the problem. When an adequate calculation beginning from QCD is intractable, we use models like VMD that use some experimental data to say for example that there exist bound states with certain masses, that have the same coupling constants in a variety of situations, etc. In addition to seeing why VMD worked we would like to establish its domain of validity and see if it agrees with QCD in kinematic regions where perturbative QCD is applicable. We will in turn examine our three subjects and then make some closing remarks.

II. N-Δ transitions

The goal here is to compare expectations at high Q^2 and low Q^2, particularly regarding spin observables such as the E2/M1 ratio, and to see how the underlying theory gives high Q^2 trends and helps interpret the data.

E2/M1 ratio. At low Q^2 it is natural to analyze reactions in terms of multipole amplitudes, which we could well call multipole form factors. For N-Δ electromagnetic transitions with the photon off shell, there are two electric quadrupole amplitudes called E2 and C2 and a magnetic dipole amplitude M1. If the N and Δ both have spherically symmetric spatial wave functions and recoil is neglected, then the E2 and C2 amplitudes are both zero and the M1 dominates[2].

At high Q^2, because the quarks are loathe to flip their helicity, it is more natural to analyze in terms of helicity amplitudes[3]. The three helicity amplitudes are illustrated in Fig. 1, where we always give the incoming nucleon helicity +½ and label the amplitude by the helicity of the incoming photon.

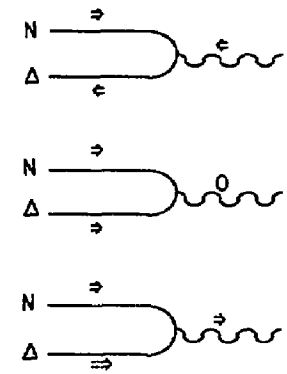

Fig. (1)

Notice that amplitude G_+ requires no quarks to flip helicity, G_0 requires at least one quark helicity flip, and G_- requires at least two quarks to flip helicity. Since each quark helicity flip costs a factor of $O(m/Q)$, where m is some relevant mass scale, we learn that G_- is smaller than G_+ at high Q^2 by a factor of $O(m^2/Q^2)$. Translating into helicity amplitudes,

$$G_- = \sqrt{\pi}\,(-\sqrt{3}\,F_{M1} + F_{E2}),$$
$$G_+ = \sqrt{\pi}\,(F_{M1} + \sqrt{3}\,F_{E2}). \qquad (1)$$

where we have followed Donnelly et al's notation[4]. The cancellation necessary for the asymptotic G_-/G_+ result leads to[5]

$$\begin{cases} F_{E2}/F_{M1} = \sqrt{3} & \text{Donnelly et al}^{4}, \\ E_{1+}/M_{1+} = 1 & \text{Many authors}^{6}, \\ E2/M1 = -\sqrt{5} & \text{Durand, DeCelles, and Marr}^{7}, \end{cases} \qquad (2)$$

where we have quoted the same result in several different conventions. The result is in great constrast

to the low Q^2 expectation. The data at 3 GeV^2 is still consistent with zero[8] and it will be interesting to see what happens just a few GeV^2 higher.

Q^2 falloff of leading form factor. The data on the high Q^2 falloff of the leading N-Δ form factor is usually quoted in terms of a form factor G_M^* which is defined operationally[9] from the cross section for $eN \to e\pi N$ and plotted compared to the dipole form. We show this in Fig. (2a) where

$$\frac{G_M^*(Q^2)}{G_D(Q^2)} = \frac{G_M^*(Q^2)}{G_M^*(0)\ \left(1 + Q^2/0.71\text{GeV}^2\right)^{-2}} \qquad (3)$$

is squared and shown plotted vs. Q^2. $G_M^*(Q^2)$ clearly falls faster with Q^2 than the dipole form.

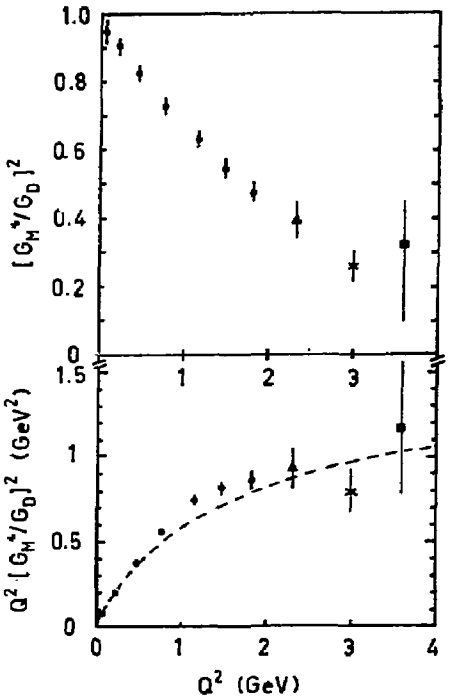

Fig. (2)

However, we must also consider what QCD would teach us to expect. By direct calculation or dimensional analysis of the lowest order perturbation theory diagram for G_+, Fig. (3), one can show at high Q^2 that

$$G_+ \propto 1/Q^3. \qquad (4)$$

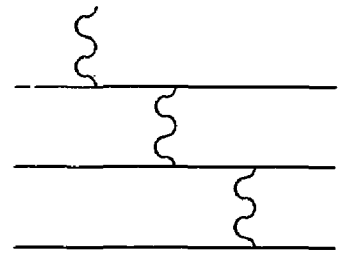

Fig. (3)

Chasing down the kinematic factors one discovers that[5]

$$G_M^* = (m_N^2\sqrt{8}/Q^2)\,G_+ \sim 1/Q^5 \qquad (5)$$

at high Q^2. Hence one expects that G_M^* will fall faster with Q^2 that the nucleon elastic form factors. One should really plot $Q^2[G_M^*/G_D]^2$ vs. Q^2 as in Fig. (2b) before interpreting any difference of behavior with Q^2 between the N-Δ transition form factor and the elastic nucleon form factor.

III. VMD and nucleon form factors

VMD can be implemented in several ways. How does it get the right Q^2 falloff and why can it fit the data so well? We will see how Iachello, Jackson, and Lande[10] (IJL) did it in 1973 and how Gari and Krümpelmann[11] (GK) did it in 1985. Those two treatments are similar enough to be discussed together but are by no means unique, as one can learn by examining Höhler et al[12] or Körner and Kuroda[13], for examples.

Basic implementation of VMD. To begin, one doesn't do the most naive thing, illustrated on the next page in Fig. (4a). Here there is just a vector meson connecting the photon to the nucleon so

$$F(Q^2) \propto \frac{1}{Q^2 + m_V^2}\ F_{VNN}(Q^2) \qquad (6)$$

Data (even before QCD!) show a $1/Q^4$ falloff so that giving F_{VNN} a monopole falloff implied the correct high Q^2 form. (This is one of the arguments for using monopole forms for the meson-nucleon-nucleon form factors as is often done in nuclear force calculations.) But even with the correct high Q^2 form, the fit to the

data is not good enough at all Q^2.

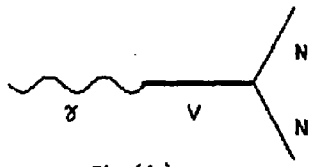

Fig. (4a)

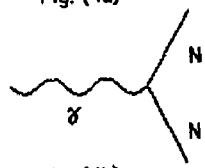

Fig. (4b)

Instead, IJL and GK add a "direct term," Fig. (4b), as well as the VDM term, Fig. (4a). For the isovector and isoscalar dirac form factors including just the ρ and ω vector mesons, they have

$$F_{1V}(Q^2) = (\tfrac{1}{2})g(Q^2)\,[\,1 - \beta_\rho + \beta_\rho m_\rho^2/(m_\rho^2 + Q^2)\,]$$

$$F_{1S}(Q^2) = (\tfrac{1}{2})g(Q^2)\,[\,1 - \beta_\omega + \beta_\omega m_\omega^2/(m_\omega^2 + Q^2)\,] \qquad (7)$$

The "intrinsic form factor" is given by

$$g(Q^2) = (1 + \lambda Q^2)^{-2} \qquad (8)$$

(Actually IJL give several choices for the intrinsic form factor, but with hindsight we should only consider the one that gives the asymptotic falloff predicted by QCD.) Note that

(i) We have the right falloff at high Q^2 but it comes form the extra intrinsic form factor and the direct coupling.

(ii) The VMD term is not significant at high Q^2. (Also, the argument given parenthetically above that F_{VNN} has a monopole form is no longer valid.)

(iii) From fitting data

$$\beta_\rho = \begin{cases} 0.4 & \text{GK} \\ 0.7 & \text{IJL } (\Gamma_\rho{=}0 \text{ choice, below}) \end{cases} \qquad (9)$$

so that the VMD terms are not in fact <u>dominant</u> for any $Q^2 > 0$.

<u>Asymptotic VMD contribution</u>. What does QCD say about the high Q^2 behavior of γ-nucleon couplings via vector mesons. The relevant diagram is drawn in Fig. (5).

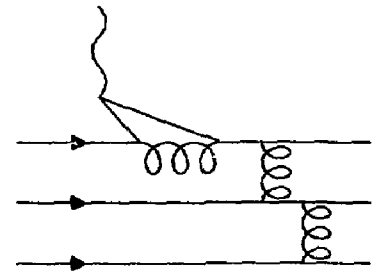

Fig. (5)

There are three extra propagators as compared to the intrinsic form factor diagram, which is identical to Fig. (3). The two extra quark propagators are absorbed into the vector meson wave function, and the loop integral is over the momentum fractions and relative transverse momenta carried by the quarks of the vector meson. The only extra Q^2 dependence is a $1/Q^2$ from the extra gluon propagator. Hence the entirety of Fig. (5) gives a $1/Q^6$ contribution to the form factor[14] which is exactly what is used.

Thus, by coincidence or otherwise, the asymtotic Q^2 dependence of both the direct and vector dominance terms are correct in these fits to the nucleon form factors, and clearly the vector dominance term has a pole in the right location, so one can understand why the fits to the form factors can be good.

<u>Asymptotic neutron/proton ratio</u>. IJL and GK give rather different values for the ratio F_{1n}/F_{1p} at high Q^2 and we would like to understand why this is so. The answer has to do with differing ways of accounting for the width of the ρ meson.

In a preliminary way, let us quote that at high Q^2 the form factor F_1 falls like $1/Q^4$ and will dominate the cross section unless it is unusually small and the form factor F_2 fall like $1/Q^6$. This means that at sufficiently high Q^2, F_1 and G_M are identical. We can also give a brief catalog of what is firmly known about the neutron form factors:

(a) $F_{1n}(0) = 0$ and $F_{2n}(0) = \kappa_n = -1.913$.

(b) From scattering of thermal neutrons off atomic electrons[15],

$$\frac{dG_{En}}{dQ^2}(0) = \frac{dF_{1n}}{dQ^2}(0) - \frac{\kappa_n}{4m_n^2} = 0.510 \pm 0.007 \text{ GeV}^{-2}$$

$$\frac{dF_{1n}}{dQ^2}(0) = -.0031 \pm 0.007 \text{ GeV}^{-2} \qquad (10)$$

Thus the slope of F_{1n} is small.

(c) The ratio of differential cross sections σ_n/σ_p is measured[16] at Q^2 = 2.5, 4, 6, 8, and 10 Gev^2 at one scattering angle. The ratio is about 1/4 at 10 GeV^2 which allows us to state

$$|G_{Mn}/G_{Mp}| \leq 1/2 \qquad (11)$$

at 10 GeV^2 and the upper limit is falling betweeen 5 and 10 GeV^2.

So if

$$F_{1n} = \frac{1}{2} g(Q^2) \left[\beta_\omega - \beta_\rho - \frac{\beta_\omega m_\omega^2}{m_\omega^2 + Q^2} + \frac{\beta_\rho m_\rho^2}{m_\rho^2 + Q^2}\right] \qquad (12)$$

and $m_\rho \approx m_\omega$ then forcing $F_{1n}' \approx 0$ at low Q^2 makes $F_{1n} \approx 0$ at all Q^2. But the ρ has a large width and we should account for it, for example following, as IJL do, Frazier and Fulco[17]. Using labels $f_{1,2}$ for convenience below we make a replacement for the ρ propagator in the preceding formula,

$$f_1 = \frac{m_\rho^2}{m_\rho^2 + Q^2} \Rightarrow$$

$$f_2 = \frac{m_\rho^2 + 8\Gamma_\rho m_\pi/\pi}{(m_\rho^2+Q^2) + (4m_\pi^2+Q^2)\Gamma_\rho A(Q^2)} \qquad (13)$$

with

$$A(Q^2) = \frac{2}{\pi}\sqrt{\frac{Q^2+4m_\pi^2}{Q^2}}\ln\left[\frac{\sqrt{Q^2+4m_\pi^2}+Q}{2m_\pi}\right] \qquad (14)$$

After this replacement, we still have $F_{1n}(0) = 0$, but

$$\frac{df_1}{dQ^2}(0) = -\frac{1}{m_\rho^2} \qquad (15)$$

whereas

$$\frac{df_2}{dQ^2}(0) = -\frac{1 + 8\Gamma_\rho/3\pi m_\pi}{m_\rho^2 + 8\Gamma_\rho m_\pi/\pi} \approx -\frac{2}{m_\rho^2} \qquad (16)$$

thus upsetting the balance between β_ρ and β_ω when the slope of F_{1n} is fit. One then gets the asymptotic result

$$\lim_{Q^2\to 0} \frac{F_{1n}}{F_{1p}} = \begin{cases} -4.40 & \text{IJL } (\Gamma_\rho \neq 0) \\ -0.028 & \text{GK } (\Gamma_\rho = 0) \end{cases} \qquad (17)$$

(More accurately, GK do say they account for the width of the ρ but in a way that doesn't have any affect on their fitting of the β's.)

The result seems unfair. The width of the ρ is large and should be taken into account, but the result IJL got by doing so is incompatible with the high Q^2 neutron data subsequently obtained. The result of GK fits the cross sections well.

IV. Proton Compton scattering

The elastic reaction $\gamma p \to \gamma p$ rpovides another check of vector meson dominance. We separate discussion of the high momentum transfer and low momentum transfer regions. At fixed large scattering angle in the center of mass, using QCD and direct coupling of the photons to the quarks in the proton illustrated in Fig. (6a) we have

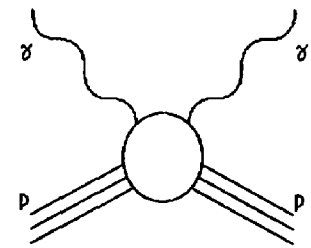

Fig. (6a)

a rule which follows from dimensional counting[18] which we quote and then use, (18)

$$\frac{d\sigma_{\gamma p\to\gamma p}}{dt} \propto s^{2-n_A-n_B-n_C-n_D} = s^{-6}$$

Here s is the c.m. energy squared, t is the momentum transfer squared, and n_A is the number of elementary fields in particle A.

If we mix QCD with vector meson dominance, then Fig. (6b) pertains and VMD tells us that

$$\frac{d\sigma_{\gamma p\to\gamma p}}{dt} = \sum_V \frac{e^2}{f_V^2} \frac{d\sigma_{Vp\to Vp}}{dt} \qquad (19).$$

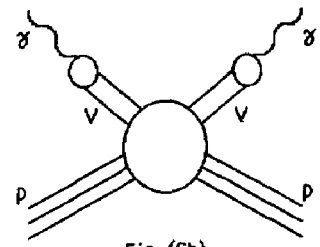

Fig. (6b)

Since there are now two extra elementary fields involved in the actual scattering,

$$\frac{d\sigma}{dt}_{\gamma p \to \gamma p} \propto s^{-8} \qquad (20).$$

Data from Shupe et al[19] is shown in Fig. (7), and it is clear that the s^{-6} behavior is more compatible with the data than s^{-8}. The direct coupling dominates.

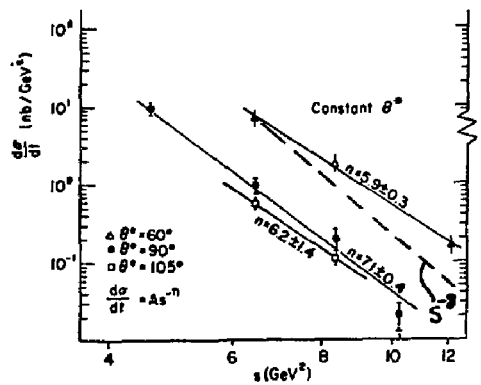

Fig. (7)
Compton scattering cross sections at constant c.m. scattering angle θ*. The straight lines are fits to the data.

On the other hand for total cross sections, the VMD relation[1]

$$\sigma_{\gamma p \to \gamma p} = \sum_V \frac{e^2}{f_V^2} \sigma_{Vp \to Vp} \qquad (21)$$

works to at least the 80% level with just V=ρ, ω, and φ. The total cross section of course is dominated by low momentum transfer processes, so the result seems to say that VMD gives a good result for low momentum transfer processes but not for high momentum transfer processes.

V. Concluding Remarks

Vector meson dominance is an approximation technique to be used when QCD calculations are intractable.

There are places where it works well. One example is the total Compton cross section, another is the fit to nucleon electromaagnetic form factor data inspired if not dictated by vector meson dominance. Still another not mentioned earlier is the agreement among vector meson coupling constants obtained from different reactions such as $\rho \to e^+e^-$, $\rho \to \pi^+\pi^-$, $\gamma p \to \rho p$, etc. (J.J. Sakurai published in 1966 a Physical Review Letter[20] with the fine title, "Eight ways of determining the ρ-meson coupling constant.") Let me also recommend examining Dr. Sloan's lecture in these proceedings.

However, as we have seen from some examples, VMD with a finite number of vector mesons does not give the high momentum transfer trends correctly. It might be commented that with an umlimited number of ever more massive vector mesons, it seems that high momentum transfer trends can be accomodated[21], but a detailed look at the demonstrations of this shoes that the arguments amount in the end to dimensional analysis. In any case, as a practical matter VMD is not useful if one has to use a large number of vector mesons, so its utility domain is an intermediate one where the energy is high enough so that time dilations allow any vector meson that the photon fluctuates into to live longer than a transit time across a nucleon or nucleus[1], but not so high a momentum transfer that direct couplings of the photon to quarks dominate the VMD contributions.

Acknowledgement

I thank the organizers for this fine conference and the NSF for financial support.

References and Footnotes

1. I learned much from the review article of T.H. Bauer, R.D. Spital, D.R. Yennie, and F.M. Pipkin, Rev. Mod. Phys. 50, 261 (1978). Historically, vector meson dominance has beginnings in both nuclear physics and particle physics. In the latter field, vector mesons were suggested to explain the nucleon electromagnetic form factors, for example by Y. Nambu, Phys. Rev. 106, 1366 (1957) [then using the name ρ^0 for what is today called the ω^0] and J.J. Sakurai, Ann. Phys. (N.Y.) 11, 1 (1960). In the former field, vector mesons were involved in the $\vec{L}\cdot\vec{S}$ terms in the nuclear force and one can examine G. Breit, Phys. Rev. 120, 287 (1960) [this article, incidentally, is

partly based on the thesis calculations of K. Lassila].
2. See for example H.J. Weber and M. Weyrauch, Phys. Lett. 178, 13 (1986).
3. S.J. Brodsky and G.P. Lepage, Phys. Rev. D 24, 2848(1981).
4. T.W. Donnelly and A. Raskin, Ann. Phys. (N.Y.) 169, 247 (1986).
5. C.E. Carlson, Phys. Rev. D 34, 2704 (1986).
6. E.g., F. Foster and G. Hughes, Rep. Prog. Phys. 46, 1445 (1983).
7. L. Durand, P.C. DeCelles, and R.B. Marr, Phys. Rev. 126, 1882 (1962).
8. Foster and Hughes, Ref. 6, and V. Burkert in "Research Program at CEBAF (II): Report of the 1986 Summer Study Group" (Continuous Electron Beam Accelerator Facility, Newport News, V. Burkert et al, editors, 1987).
9. W.W. Ash etal, Phys. Lett. 28B, 148 (1967) and S. Stein etal, Phys. Rev. D 12, 1884 (1975).
10. F. Iachello, A.D. Jackson, and A. Lande, Phys. Lett. 43B, 191 (1973).
11. M. Gari and W. Krümpelmann, Z. Phys. A 322, 689 (1985) and Phys. Lett. B173, 10 (1986).
12. Höhler etal.
13. J.G. Körner and M. Kuroda, Phys. Rev. D 16, 2165 (1977).
14. I thank S.J. Brodsky for a comment on this point.
15. L. Koester, W. Nistler, and W. Waschkowski, Phys. Rev. Lett. 36, 1021 (1976); V.E. Krohn and G.R. Ringo, Phys. Rev. 148, 1303 (1966).
16. S. Rock et al, Phys. Rev. Lett. 49, 1139(1982).
17. W.R. Frazier and J.R. Fulco, Phys. Rev. 117, 1609 (1960).
18. G.P. Lepage and S.J. Brodsky, Phys. Rev. D 22, 2157(1980); S.J. Brodsky and G.R. Farrar, Phys. Rev. Lett. 31 1153 (1973) and Phys. Rev. D 11, 1309 (1975); V.A. Matveev, R.M. Muradyan, and A.V Tavkheldize, Lett. Nuovo Cimento 7, 719 (1973).
19. M.A. Shupe etal, Phys. Rev. D 19, 1921 (1979).
20. J.J. Sakurai, Phys. Rev. Lett. 17, 1021 (1966).
21. S.J. Brodsky and J. Pumplin, Phys. Rev. 182, 1794 (1969).

SEMI-INCLUSIVE INELASTIC ELECTRON SCATTERING FROM NUCLEI

Edmond L. Berger
High Energy Physics Division
Argonne National Laboratory
Argonne, IL 60439

Abstract

A survey is presented of the physics of the electroproduction of hadrons from nuclear targets, $eA \to e'hX$. Variables and structure functions are specified. The parton model description of electroproduction is summarized; fragmentation functions are defined and their properties are listed. Specific measurements are suggested. Predictions of the pion exchange model are presented for the nuclear dependence of $eA \to e'hX$, including a discussion of the special subprocess $e\pi \to e'\pi$ in which scattering occurs from the pion constituents of nuclei.

1. Introduction

This workshop was organized to identify aspects of the structure of nucleons and nuclei which might be studied profitably with internal targets principally at the PEP electron positron storage ring at the Stanford Linear Accelerator Center. The energy of the incident electron (positron) beam would be limited initially to the "intermediate energy" range, $E \lesssim 15$ GeV.

A considerable literature has developed on nuclear dependence[1] of deep inelastic *inclusive* (or *single-arm*) lepton scattering, $eN \to e'X$, prompted by the observation[2,3,4] of intriguing differences between the inclusive structure functions of nucleons and nuclei (the "EMC" effect). In $eN \to e'X$, e and e' denote the initial and final electron, and N may be a free nucleon or a nucleus. Symbol X represents an inclusive sum over all final states. The data show directly that the quark momentum distribution of a nucleus differs significantly from that of a free nucleon. It is natural to inquire whether more differential measurements would shed further light on the dynamics underlying nuclear dependence. In this paper, I will focus on the theory and phenomenology of *semi-inclusive* (or *two-arm coincidence*) measurements: $eN \to e'hX$; h labels a specific final state hadron (e.g. π, K, p,...) whose momentum is measured.

My intent is *not* to present a comprehensive review of the electroproduction of hadrons. Rather, I will define variables and cross sections, raise some issues pertinent to nuclear dependence, provide references, and try to communicate a particle physicist's perspective on semi-inclusive processes to an audience composed primarily of nuclear physicists. One indication of the gulf that has developed between our disciplines is that we have developed different dialects and symbols: coincidence measurements and $(e, e'\pi)$ are the translations of semi-inclusive measurements and $eN \to e'\pi X$. Summaries of many general properties of the distribution of final state hadrons from leptoproduction experiments may be found in the review by Schmitz[5] and in numerous papers from the European Muon Collaboration.[6]

In Section 2, I define the five independent kinematic variables and four independent structure functions, $H_i^{N,h}$, necessary to specify the process $eN \to e'hX$. Next, in Section 3, the parton model description of inclusive and semi-inclusive inelastic electon scattering is reviewed.[7,8,9] Fragmentation functions are defined, some of their properties are listed, and measurements are suggested for determining specific fragmentation functions and their A dependence. In Section 4, I discuss a particular high twist contribution[10,11] to the quark fragmentation function.[10] Section 5 includes statements concerning the nuclear (A) dependence of $eA \to e'hX$ based on the pion exchange model[12] used to explain the nuclear dependence of the inclusive process $eA \to e'X$. In Section 6, I present predictions for the contribution of the elastic scattering process $e\pi \to e'\pi$ to $eA \to e'\pi X$, where the initial π in $e\pi \to e'\pi$ is a pion bound in nucleus A. A summary is found in Section 7.

2. Kinematics, Definitions, Cross Sections, and Structure Functions

I begin with the fully inclusive scattering of an electron or muon from either a nucleon N or a nuclear target A, sketched in Fig. 1(a). This process is usually denoted $\ell A \to \ell' X$, where symbol X represents an inclusive sum over all final states. The initial four-momenta of the lepton and the target are denoted by k and p. The four-vector q is the momentum transfer from the initial lepton to the target; that is, it is the difference between the four-momenta of the initial and final leptons. The laboratory energies of the initial and final leptons are E and E'; ν is the energy transfer, $E - E'$, in the laboratory frame. It is conventional to define $Q^2 = \mathbf{q}^2 - \nu^2 = -q^2 > 0$, and two dimensionless variables x and y, $x = Q^2/2M_N\nu$, $y = \nu/E$, where M_N is the mass of the nucleon. (Boldface symbols represent Euclidean three-vectors.)

The deep-inelastic domain is that in which the energy transfer is large compared to the four-momentum transfer,

$$\nu^2/Q^2 \equiv Q^2/(2M_N x)^2 \gg 1. \tag{1}$$

Light-front components $p^\pm$ of any four-vector p are defined by

$$p^\pm \equiv p^0 \pm \mathbf{n}\cdot\mathbf{p}, \tag{2}$$

where $\mathbf{n}$ is a unit vector chosen in the direction of the momentum transfer, $\mathbf{n} = -\mathbf{q}/|\mathbf{q}|$. For deep-inelastic scattering, $q^- \approx 2\nu$, $q^+ \approx 0$, $p\cdot q \approx \frac{1}{2}p^+q^- \approx p^+\nu$. Light-front momentum *fractions* are defined as ratios of plus-components (or of minus-components) of momenta and are thus invariant under longitudinal boosts.

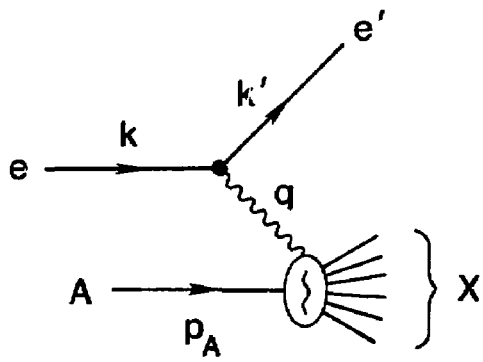

(a)

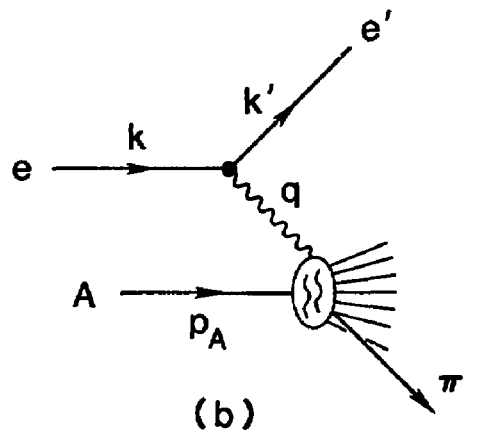

(b)

Figure 1: Sketches of a) inclusive reaction $eA \rightarrow e'X$ and b) semi-inclusive reaction $eA \rightarrow e'\pi X$.

In the one photon exchange approximation, the differential cross section for inclusive inelastic scattering of a *charged lepton* ($eA \rightarrow e'X$ or $\mu A \rightarrow \mu' X$) by any target is proportional to tensors $f_{\lambda\rho}(q,k)$ and $F^{\lambda\rho}(q,p)$ that depend respectively on the properties of the lepton and the target only:

$$\frac{d^2\sigma}{dx\,dy} = \frac{4\pi\,\alpha^2\,2M_N\,y}{Q^4} F^{\lambda\rho} f_{\lambda\rho}. \tag{3}$$

The tensor $F^{\lambda\rho}$ is a linear combination of "structure functions", invariant functions of Q^2 and $p\cdot q$, multiplied by universal covariant functions of p and q. In the case of the scattering of unpolarized particles, there are two structure functions for the conserved electromagnetic current: $F_i(x',Q^2)$, $x' \equiv Q^2/(2p\cdot q) = x(M_N\nu/p\cdot q)$.

In the deep-inelastic approximation,

$$F_N^{\lambda\rho} f_{\lambda\rho} = E\left\{(1-y)F_2^N(x',Q^2) + 2x' F_1^N(x',Q^2)(y^2/2)\right\}/y, \tag{4}$$

for scattering by a nucleon, and

$$F_A^{\lambda\rho} f_{\lambda\rho}/A = E\left\{(1-y)F_2^A(x'_A,Q^2) + 2x'_A F_1^A(x'_A,Q^2)(y^2/2)\right\}/y, \tag{5}$$

for a nucleus. Note that the nucleon number A is used as a label to identify the nucleus. In Eq. (5) for the nucleus, variable x'_A, which is a multiple of x', is defined by $x'_A \equiv Q^2A/(2p_A\cdot q)$. If the nucleus is at rest, x'_A is approximately equal to x: $x'_A = xAM_N/M_A \approx x$. The ranges allowed kinematically for x' of the nucleon and for x'_A are (0,1) and (0,A) respectively. The structure functions F_1^A and F_2^A are structure functions *per nucleon*.

In Eqs. (3)-(5) the momentum of the target enters only through the variable x'. This means that for a collection of incoherent free nucleons the *momentum averaged cross section* is related to *momentum averaged structure functions* in the same manner as the cross section per nucleon of the nucleus is related to the structure functions of the nucleus per nucleon. The momentum average is called *Fermi smearing*.

To separate the contributions of F_1^A and F_2^A at fixed x and Q^2 it is necessary to study the cross section as a function of $y = \nu/E = Q^2/(2M_NE)$, i.e., as a function of energy E. If the Callan-Gross relation is imposed, i.e. $[(F_2 - 2xF_1)/2xF_1] = \sigma_L/\sigma_T \simeq 0$, then the cross section per nucleon may be expressed in terms of $F_2^A(x,Q^2)$ alone:

$$\frac{d^2\sigma}{dx\,dy} = \frac{4\pi\alpha^2 M_N E}{Q^4}\left[1+(1-y)^2\right] F_2^A(x'_A,Q^2). \tag{6}$$

In the *semi-inclusive* or two-arm coincidence process, $eA \rightarrow e'hX$, sketched in Fig. 1(b), four momenta k, k', and p_h of the initial and final lepton and of hadron h are measured, but an inclusive sum is otherwise made over all possible final states X allowed kinematically. For a fixed total energy, five independent kinematic variables are necessary to specify the final state. Two of these variables, x and Q^2 are determined by the incident and outgoing lepton. They are identical to those of the fully inclusive case. The remaining three variables specify the final hadron h. I'll work with a set which has become standard in particle physics: z, $|\vec{p}_T|$, ϕ. Here, z is a ratio of dot products of four vectors:

$$z = \frac{p_h\cdot p_A}{q\cdot p_A}; \tag{7}$$

$\vec{p}_T$ is the component of the final hadron's three-momentum transverse to the direction specified by q; and ϕ is an azimuthal angle:

$$\cos\phi = (-\mathbf{q}\times\mathbf{k})\cdot(-\mathbf{q}\times\mathbf{p}_h)/|\mathbf{q}\times\mathbf{k}||\mathbf{q}\times\mathbf{p}_h|. \tag{8}$$

I note that in the deep-inelastic approximation, z is the ratio of the minus-component of the momentum p_h to that of q:

$$z \cong p_h^-/q^-. \tag{9}$$

In the one photon exchange approximation, the spin-averaged cross section per nucleon for $eA \to e'hX$ may be expressed in terms of *four* independent structure functions which I denote $H_i^{A,h}(x, Q^2, z, p_T^2)$. In the deep inelastic limit, the cross section becomes

$$\frac{d\sigma^{A,h}}{dx\,dy\,dz\,dp_T^2\,d\phi} = \frac{4\pi\alpha^2 2M_N E}{Q^4}\Bigg[xy^2 H_1^{A,h} + (1-y)H_2^{A,h} + \left(\frac{2p_T}{Q}\right)(2-y)(1-y)^{1/2}\cos\phi H_3^{A,h} + \frac{p_T^2}{Q^2}(1-y)\cos 2\phi H_4^{A,h}\Bigg]. \quad (10)$$

Note that it is necessary to study ϕ dependence in order to isolate $H_3^{A,h}$ and $H_4^{A,h}$. Furthermore, y dependence (i.e. E dependence at fixed x, Q^2) must be measured in order to separate the four structure functions.

After integrating the cross section over ϕ, which eliminates dependence on H_3 and H_4, and over p_T^2, one obtains an expression in terms of only two independent dimensionless functions, denoted $\bar{H}_i(x, Q^2, z)$:

$$\frac{d\sigma^{A,h}}{dx\,dy\,dz} = \frac{4\pi\alpha^2 2M_N E}{Q^4}\Big[xy^2\bar{H}_1^{A,h}(x, Q^2, z) + (1-y)\bar{H}_2^{A,h}(x, Q^2, z)\Big]. \quad (11)$$

In terms of its dependence on y, this expression has the same structure as Eq. (4) or (5). If $R \equiv \sigma_L/\sigma_T \simeq 0$ in the semi-inclusive case, either because it is measured to be such or because the simple parton model is invoked, then $\bar{H}_2 \simeq 2x\bar{H}_1$, and Eq. (11) collapses to

$$\frac{d\sigma^{A,h}}{dx\,dy\,dz} = \frac{4\pi\alpha^2 M_N E}{Q^4}\left[1 + (1-y)^2\right]\bar{H}_2^{A,h}(x, Q^2, z). \quad (12)$$

For any inclusive process, conservation of four-momentum specifies that

$$\sum_h \int d^3\mathbf{p}\, p^\mu \frac{d\sigma^h}{d^3\mathbf{p}} = P^\mu \sigma_{\rm tot}. \quad (13)$$

Here P^μ is the total four-momentum, and p^μ is the four-momentum of a hadron of species h. When this equation is applied to the *difference* $(E_h - p_{L,h})$, where E_h is the energy, and $p_{L,A}$ is the longitudinal component of $\mathbf{p}_h$ along the current-target axis, a relationship is obtained between the semi-inclusive functions, $\bar{H}_i^{A,h}(x, Q^2, z)$, and the fully inclusive structure functions, $F_i^A(x, Q^2)$. For each value of i,

$$\sum_h \int_0^1 dz\, z\bar{H}_i^{A,h}\left(x, Q^2, z\right) = F_i^A\left(x, Q^2\right). \quad (14)$$

In the next section I discuss expectations for the x, Q^2, and z dependences of $\bar{H}_i^A(x, Q^2, z)$ based on the parton model.

3. Parton Model Description

Probabilities $q_f^A(\xi, Q^2)$, $\bar{q}_f^A(\xi, Q^2)$, and $G^A(\xi, Q^2)$ are defined which represent the quark, antiquark, and gluon number densities in a *nucleus*, A. These are densities *per nucleon*, just as are $F_{1,2}^A(x, Q^2)$, meaning that a factor of A has been removed. (These densities "per nucleon" should *not* be assumed to be the parton densities of "nucleons within nuclei".) Subscript f on q_f and $\bar{q}_f$ labels the flavor of the quark or antiquark: u, d, s, c, b, t. Variable ξ is the light front fraction of the momentum of the target A carried by a parton of a given type.

In the parton model,[7,8] ξ, $q_f^A(\xi, Q^2)$, $\bar{q}_f^A(\xi, Q^2)$, and $G^A(\xi, Q^2)$ are measurable quantities. Indeed, $\xi \equiv x$, with x determined from the lepton kinematics, as defined above. Furthermore, the observable F_2^{eA} measures the fraction of the momentum of the target A, *per nucleon*, carried by quarks and antiquarks, weighted by the squares of the fractional quark charges e_f:

$$F_2^{eA}(x, Q^2) = \sum_f e_f^2 x\left[q_f^A(x, Q^2) + \bar{q}_f^A(x, Q^2)\right]. \quad (15)$$

3.1 Quark Fragmentation Region

Turning now to the semi-inclusive process $eA \to e'hX$, let's ask what $\bar{H}_2^A(x, Q^2, z)$ measures. Recall, $z = p_h{\cdot}p_A/q{\cdot}p_A$, Eq. (7). The answer to this question involves a discussion of what happens[7,8] to the struck quark after it absorbs the energy and momentum of the virtual photon. If quarks or gluons could be liberated, then, for sufficiently large Q^2, a free quark or free gluon would emerge from the target along the direction of the momentum of the exchanged photon. However, quarks and gluons are confined; they are not observed as asymptotic states. Thus, a spray of hadrons is observed in the final state, hadrons said to be "fragments of the struck quark". For sufficiently large ν and Q^2 this spray is a collimated "jet", well separated from the debris of the spectator partons in the target. This fragmentation process is described by a *fragmentation function*, $D_{h/f}(z, Q^2)$. (At sufficiently large Q^2, there will be a discernable gluon jet or jets in the final state in addition to the quark jet. Gluon fragmentation is also described by a fragmentation function, $D_{h/G}(z, Q^2)$. In this paper I will restrict my remarks to quark fragmentation.)

I define two regions of physical interest, distinguished by the magnitude of p_h. In the first region, the dot product $p_h{\cdot}p_A$ is finite, whereas $q{\cdot}p_A$ grows in proportion to Q^2. The final hadron h moves with small momentum in the rest frame of the target. Hadron h is said to be in the "target fragmentation region", where typical long-distance hadron physics governs the dynamics. Correspondingly, no specific parton model statements can be made about the z dependence of $\bar{H}_2^A(x, Q^2, z)$, and the concept of a fragmentation function does not apply in this region. However, one does expect scaling, i.e. approximate Q^2 independence, at fixed x.

In the second region, $p_h{\cdot}p_A$ grows in proportion to Q^2, $0 < z < 1$. It is in this region that hadron h is said to be a "frag-

ment of the quark" or antiquark struck by the virtual photon in the deep inelastic collision. If the separation in momentum of the struck quark from the target spectators is large enough, it is natural to assume that *fragmentation* of the quark into hadrons is independent of *production* of the quark. Fragmentation should therefore be described by a function of z, be independent of x, and be *independent of the process in which the quark was produced* (i.e. whether deep inelastic lepton scattering, electron-positron annihilation, hadron-hadron scattering, etc.).

After absorbing the virtual photon, the struck quark carries the same minus-component of momentum as the incident virtual photon, $q^- \simeq 2\nu$. Therefore, Eq. (9) allows us to interpret z as the fraction of the (light-front) momentum of the struck quark carried by h.

A word of caution is in order concerning the applicability of the concept of distinct regions of *target fragmentation* and *quark fragmentation*. Observably distinct regions require large enough separation in momentum of quark and target fragments. Rapidity is a useful variable for examining this issue.

The rapidity y_h of final state hadron h in $eA \to e'hX$ is defined as

$$y_h = \frac{1}{2} \ln \left[\frac{E_h + p_{h,L}}{E_h - p_{h,L}} \right], \tag{16}$$

where $E_h, p_{h,L}$ are the energy and longitudinal component of momentum of hadron h. (Longitudinal is defined by the direction of the momentum q.) The full range of y_h allowed kinematically is $Y = \ln W_X^2 = \ln(Q^2(1-x)/x)$; W_X is the invariant mass of the system X in the fully inclusive $eA \to e'X$.

It has been established[13] experimentally that the typical hadronic correlation length in rapidity is $\Delta y_h \simeq 2$. Therefore, if the dynamics of quark fragmentation is to be studied independently of "contamination" from target fragmentation, it is necessary that $Y \gtrsim 4$, or, equivalently, that

$$W_X = \left[\frac{Q^2(1-x)}{x} \right]^{1/2} \gtrsim 7.4\text{GeV}. \tag{17}$$

Studies of hadrons produced by neutrino interactions on protons[5] confirm that the separation of quark and target fragmentation products is apparent for $W_X > 8$ GeV but not for $2 < W_X < 4$ GeV. The values of W_X accessible in the CERN EMC[6] and Fermilab E-665 experiments extend high enough to satisfy Eq. (17). However, it appears doubtful that large enough values can be obtained at SLAC with $E \gtrsim 15$ GeV.

If the inequality Eq. (17) is satisfied, it should be possible to measure fragmentation functions $D(z, Q^2)$ over essentially the full range of z, $0 < z < 1$. Somewhat smaller values of W_X may be adequate if attention is restricted to the large z region. As Y is increased above 2, or

$$W_X \gtrsim 3 \text{ GeV}, \tag{18}$$

the quark and target fragmentation regions begin to separate. As long as $Y \gtrsim 2$, the hadrons with the largest values of z are most likely quark fragments. Data[14] from $e^+e^- \to hX$ show that a distinct function $D(z)$ may have developed for $z \gtrsim 0.5$ at $W = 3$ GeV. The region extends to $z \simeq 0.2$ for $W = 4.8$ GeV, and to $z \simeq 0.1$ for $W = 7.4$ GeV. For $z > 0.3$, fragmentation functions have been obtained from data[15] on $ep \to e'\pi^\pm X$ at $E = 11.5$ GeV, with $3 < W_X < 4$ GeV.

At low values of Q^2, where the target and quark fragmentation regions overlap in momentum space, the concept of distinct production and fragmentation processes may not be relevant for the description of hadron formation in $eA \to e'hX$. This means, in particular, that nuclear A dependence observed in $H_2^A(x, Q^2, z)$ at modest values of Q^2 could not be attributed cleanly to nuclear dependence of the fragmentation process.

3.2 Quark Fragmentation Functions

In the region $0 < z < 1$ a function $D_{h/f}(z, Q^2)$ is defined which is the probability for a quark of flavor f to fragment into hadron h in an interval dz about z. In other words, $D_{h/f}(z, Q^2)$ is the *number density* in the quark of flavor f of hadrons of type h which carry a fraction z of the (light-front) momentum of the quark.

In the simple parton model $D(z, Q^2)$ is independent of Q^2, just as is $q_f(x, Q^2)$. Gluonic radiation in QCD generates logarithmic dependence[9] on Q^2 in both $D(z, Q^2)$ and $q_f(x, Q^2)$. Neither the full x dependence of $q(x, Q^2)$ nor the full z dependence of $D(x, Q^2)$ can be calculated as yet from first principles in quantum chromodynamics. At small values of z one expects[7] $D(z, Q^2)$ to be proportional to $1/z$, whereas at large z constituent counting rules and spin considerations may be used to specify[16,17,10] the power p in an expansion of the form $zD(z, Q^2) \propto (1-z)^p$.

In addition to Q^2 dependence of $q_f(x, Q^2)$ and $D(z, Q^2)$, gluonic radiative contributions in QCD generate a finite longitudinal structure function $\bar{H}_L(x, Q^2, z) = \bar{H}_2(x, Q^2, z) - 2x\bar{H}_1(x, Q^2, z)$ as well as finite contributions[18] proportional to H_3 and H_4 in Eq (10). In $eA \to e'hX$, intrinsic transverse momenta[19] of the partons in the initial hadron A and final hadron h are also a source of finite H_3 and H_4 contributions, as are higher twist effects.[10]

The statement of factorization plus the definition of fragmentation functions, $D(z, Q^2)$ for quarks and $\bar{D}(z, Q^2)$ for antiquarks, result in the following expression for the semi-inclusive structure function $\bar{H}_2(x, Q^2, z)$, valid in the quark fragmentation region, $z > 0$:

$$\bar{H}_2^{A,h}(x, Q^2, z) = \sum_f e_f^2 x \left[q_f^A(x, Q^2) D_{h/f}(z, Q^2) + \bar{q}_f^A(x, Q^2) \bar{D}_{h/f}(z, Q^2) \right], \tag{19}$$

with

$$\sum_h \int_0^1 dz\, z D_{h/f}(z, Q^2) = \sum_h \int_0^1 dz\, z\, \bar{D}_{h/f}(z, Q^2) = 1. \tag{20}$$

Combining Eqs. (6), (12), (15), and (19), we may observe that *when* $\sigma_L/\sigma_T \simeq 0$,

$$\frac{1}{\sigma_{\rm tot}}\frac{d\sigma(eA \to e'h\,X)}{dz} \equiv \frac{\dfrac{d\sigma(eA \to e'h\,X)}{dx\,dy\,dz}}{\dfrac{d\sigma(eA \to e'\,X)}{dx\,dy}} = \frac{\sum_f e_f^2\left[q_f^A(x,Q^2)D_{h/f}(z,Q^2) + \bar{q}_f^A(x,Q^2)\bar{D}_{h/f}(z,Q^2)\right]}{\sum_f e_f^2\left(q_f^A(x,Q^2) + \bar{q}_f^A(x,Q^2)\right)}. \tag{21}$$

This equation simplifies considerably the case of a nucleus with an equal number of protons and neutrons *and* $x \gtrsim 0.3$. (For $x \gtrsim 0.3$, antiquark densities as well as the strange quark density may be ignored.) Thus,

$$\left.\frac{1}{\sigma_{\rm tot}}\frac{d\sigma(eA \to e'h\,X)}{dz}\right|_{\substack{x \gtrsim 0.3 \\ \text{isoscalar} \\ \text{target}}} = \frac{1}{5}\left[4D_{h/u}(z,Q^2) + D_{h/d}(z,Q^2)\right]. \tag{22}$$

The number of independent fragmentation functions is limited by isospin and charge conjugation invariance. For example, for pion production,

$$D_{\pi^+/u} = D_{\pi^-/\bar{d}} = \bar{D}_{\pi^+/\bar{d}} = \bar{D}_{\pi^-/u}. \tag{23}$$

$$D_{\pi^+/\bar{d}} = D_{\pi^-/u} = \bar{D}_{\pi^+/u} = \bar{D}_{\pi^-/\bar{d}}. \tag{24}$$

$$D_{\pi^+/s} = D_{\pi^-/\bar{s}} = \bar{D}_{\pi^+/\bar{s}} = \bar{D}_{\pi^-/s}. \tag{25}$$

$$D_{\pi^+/f} + D_{\pi^-/f} = 2D_{\pi^0/f}. \tag{26}$$

Data on *differences* of π^+ and π^- spectra obtained in studies with *isoscalar* targets may be used to isolate specific fragmentation functions. Using Eq. (22), together with Eqs. (23) and (24), I obtain

$$D_{\pi^+/u}(z,Q^2) = \frac{4}{3}\frac{1}{\sigma_{\rm tot}}\frac{d\sigma(eA \to e'\pi^+ X)}{dz} - \frac{1}{3}\frac{1}{\sigma_{\rm tot}}\frac{d\sigma(eA \to e'\pi^- X)}{dz} \tag{27}$$

and

$$D_{\pi^-/u}(z,Q^2) = \frac{4}{3}\frac{1}{\sigma_{\rm tot}}\frac{d\sigma(eA \to e'\pi^- X)}{dz} - \frac{1}{3}\frac{1}{\sigma_{\rm tot}}\frac{d\sigma(eA \to e'\pi^+ X)}{dz}. \tag{28}$$

Relationships (23) and (24) may be used to obtain a very simple expression for the *sum* of the π^+ and π^- yields from a nucleus with an *arbitrary neutron/proton ratio*. Ignoring the contributions from strange, charm, and heavier quarks and antiquarks (but retaining the contributions from the up and down antiquarks), we may show that

$$\frac{1}{\sigma_{\rm tot}}\left[\frac{d\sigma(eA \to e'\pi^+ X)}{dz} + \frac{d\sigma(eA \to e'\pi^- X)}{dz}\right] = D_{\pi^+/u}(z,Q^2) + D_{\pi^-/u}(z,Q^2) = D_{\pi^+/\bar{d}}(z,Q^2) + D_{\pi^-/\bar{d}}(z,Q^2). \tag{29}$$

Equation (29) should be valid as long as it is safe to ignore the strange quark and antiquark densities, i.e. for $x \gtrsim 0.1$.

Note that the fully inclusive and semi-inclusive measurements provide *different* information. Inclusive scattering cross sections determine the quark and antiquark densities of the target, Eq. (15). Semi-inclusive cross sections determine fragmentation functions, Eqs. (22), (27)–(29). In rough terms, inclusive measurements provide data on constituent behavior in the initial state, *before* scattering occurs, whereas semi-inclusive measurements yield insight into the final state evolution of the scattered constituents into hadrons.

It has been suggested[20] that semi-inclusive data may be a source of information on the x dependence of quark and antiquark densities of nuclei. Equation (21) shows that extracting information on $q_f^A(x,Q^2)$ and $\bar{q}_f^A(x,Q^2)$ from semi-inclusive measurements is possible only if the fragmentation functions are known fairly precisely.

To appreciate the property of process independence of fragmentation functions, it is useful to examine briefly the description of hadron production in electron-positron annihilation at large Q^2, $e^+e^- \to h\,X$. In the one-photon approximation (ignored are effects associated with the Z^0), the cross section differential in z and angle θ is

$$\frac{d\sigma^h}{dz\,d\cos\theta} = \frac{3}{8}(1+\cos^2\theta)\frac{d\sigma_T^h(z,Q^2)}{dz} + \frac{3}{4}(1-\cos^2\theta)\frac{d\sigma_L^h(z,Q^2)}{dz}. \tag{30}$$

In this case $z = 2p_h \cdot q/Q^2$ and, in the e^+e^- center of mass frame, θ is the polar angle of hadron h with respect to the e^+e^- collision axis. The variable $\cos\theta$ replaces the variable y defined for $eA \to e'\pi\,X$. In the parton model, as extended by QCD,

$$\frac{d\sigma_T^h(z,Q^2)}{dz} = 3\sigma_0\sum_f e_f^2\left[D_{h/q}(z,Q^2) + \bar{D}_{h/q}(z,Q^2)\right], \tag{31}$$

where $\sigma_0 = 4\pi\alpha^2/3Q^2$. Through $O(\alpha_s)$, the total cross section for $e^+e^- \to X$ is

$$\sigma_{\rm tot}(Q^2) = 3\sigma_0\sum_f e_f^2\left(1 + \frac{\alpha_s(Q^2)}{\pi}\right), \tag{32}$$

where the term proportional to the strong coupling strength $\alpha_s(Q^2)$ is due to $\sigma_L^h(z,Q^2)$ in Eq. (30). Note the relative simplicity of Eq. (31) when compared with Eq. (19). Because quark and antiquark structure functions are absent from Eq. (31), the e^+e^- data permit a more direct measurement of the fragmentation function, albeit averaged over contributions from all flavors of quarks and antiquarks.

Data on the properties of fragmentation functions from e^+e^- annihilation experiments may be found in Refs. 14 and 21 *and from leptoproduction experiments in Refs. 15, 22, and 23.* An example is shown in Fig. 2.

3.3 Nuclear Dependence of Fragmentation Functions?

It may be noted that I have used the notation $D_{h/f}(z,Q^2)$, implicitly suggesting that this function does not depend on the target A. Should the fragmentation functions $D_{h/f}(z,Q^2)$ and $\bar{D}_{h/f}(z,Q^2)$ in Eq. (19) depend on A?

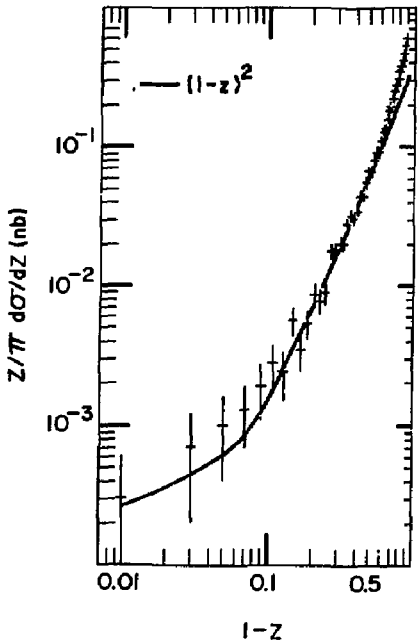

Figure 2: Fragmentation function $D(z,Q^2)$ from $e^+e^- \to \pi X$ at $Q^2 = (29\ \text{GeV})^2$, Ref. 21.

If the statement of factorization is correct, then $D_{h/f}(z,Q^2)$ must be independent of A because factorization is the assertion that this function is a process independent property of hadron h. In QCD, there can be gluon exchanges between the active quark and the spectator partons in either A or h. To demonstrate the validity of factorization one must show that these gluon interactions cancel. A proof exists[24] for the Drell-Yan process $hA \to \gamma^* X$, but no proof of factorization in QCD has yet been attempted for the crossed process of interest here, $\gamma^* A \to hX$. Presumably a "target-length condition" would emerge from such a proof, analogous to the relationship between Q^2 and A necessary for factorization in the Drell-Yan case: $Q^2 \gtrsim cA^{1/3}$.

Intuitively one would expect factorization to hold only if the separation in momentum of the struck quark from the target spectators is large enough. In a heavy nucleus, even in the quark fragmentation region, it is plausible that hadron production may be modified with respect to that observed in deuterium due to reinteraction effects of either the fragmenting quarks or the hadrons as they propagate through the nuclear medium. It is often assumed that fragmentation takes place within a limited interval in space-time.[8,25] Because of Lorentz dilation, the process will occur over a distance which increases as ν, the energy of the struck quark, increases. *For large enough ν, fragmentation would then occur outside the nucleus.* In this case the main effect on fragmentation would be the size of the quark cross section in nuclear matter. At large Q^2 this virtual quark is expected to have a small interaction probability.[20]

To explore these issues, it is of obvious interest to study possible nuclear A dependence of fragmentation as a function of ν, z, and Q^2. The dependence on all these variables is important. Equations (22), (27), (28), and (29) show that fragmentation functions, or combinations thereof, could be extracted from experiments done on different nuclei. The ratios of these results, $D^A(z,Q^2)/D^{D_2}(z,Q^2)$, should be independent of A if there is no nuclear dependence. If the ratios approach unity at large ν, the expectation of a small cross section for quark interaction in nuclear matter would be confirmed.

Available data on nuclear dependence of fragmentation are of limited statistics.[27-31] Effects of quark and/or hadron reinteraction are seen at low ν, but there is no evidence for such effects for $\nu > 70$ GeV. I will not discuss further here physical processes which may be important at low ν where the characteristic quark fragmentation length is comparable to or less than the radius of the nucleus. Treatments may be found in Refs. 8, 25, and 26.

4. High-Twist Contribution

High twist terms[10,11] in the structure functions, $q_f(x,Q^2)$, and fragmentation functions, $D(z,Q^2)$, are contributions which decrease in proportion to an inverse power of Q^2 relative to the leading scaling term. They arise from subprocesses in which more than one constituent in a given hadron is active in the hard scattering process. Sharing of the large momentum among several active constitutents requires that more than the minimum number of constituents be off-shell by $\sim Q^{-2}$. The presence of additional gluon or quark propagators supplies the additional inverse powers of Q^2 in the hard scattering amplitude.

In this section I call attention to a particular high-twist contribution to the fragmentation function[10] $D_{\pi/q}(z,Q^2)$. It is of interest in its own right and quantitatively important for the range of values of Q^2 accessible in $eA \to e'hX$ experiments at SLAC. Moreover, it is an important "background" to the coherent $e\pi \to e'\pi$ signal, discussed in Section 6, where the initial π is bound in the nucleus.

Consider the diagram for $\gamma^* q \to \pi q$ sketched in Fig. 3. The initial quark is a constituent of a target nucleon or nucleus. The final pion is represented by its minimum Fock space component $|q\bar{q}\rangle$. For "favored" fragmentation processes such as $u \to \pi^+ X$ or $d \to \pi^- X$, this diagram permits one to calculate both the expected large z form of the scaling term in $D(z,Q^2)$ and a Q^{-2} contribution appropriate at large z. Higher components, including gluons or additional $q\bar{q}$ pairs, are present and would supply terms suppressed by added powers of Q^2.

Extracting a fragmentation function from Fig. 3, one obtains[10,32]

$$D_{\pi/q}(z,Q^2) = A\left[(1-z)^2 + \frac{1}{3}F_\pi(Q^2)\right], \qquad (33)$$

where A is a normalization constant discussed below, and $F_\pi(Q^2)$

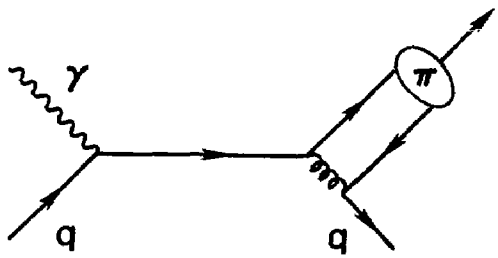

Figure 3: Diagram illustrating a higher-twist subprocess which contributes to $\gamma^* q \to \pi X$.

is the electromagnetic form factor of the pion. In the scaling limit, $Q^2 \to \infty$, Eq. (33) shows that $D_{\pi/q}(z)$ should fall off as $(1-z)^2$ as $z \to 1$. However, for finite Q^2, the function $D_{\pi/q}(z)$ is predicted to approach a finite value as $z \to 1$ whose magnitude decreases as Q^{-2}.

Information on the z dependence of $D(z,Q^2)$ at large z comes from $e^+e^- \to \pi X$. An example is shown in Fig. 2. A fit to $(1-z)^n$ for $z > 0.5$ yields[21] $n = 2.08 \pm 0.21$ compatible with the expectation of $n = 2$. The value of Q^2 for these data, $Q^2 = (29\ \mathrm{GeV})^2$, is so large that the high twist term is essentially absent.

Within the context of the approximations made in Ref. 10, the relative normalization between the two terms in Eq. (33) is specified. The overall normalization of the scaling term, $(1-z)^2$, is not fixed, but data[21] at large z can be used to determine a value of A in Eq. (33). Doing so, I find values in the range $1 \lesssim A \lesssim 2$.

For large z, the cross section corresponding to Fig. 3 has the form[10]

$$\frac{d\sigma(x,Q^2,z)}{dx\,dy\,dz} \propto \frac{1}{2}\left[1+(1-y)^2\right](1-z)^2 + \frac{4}{9}(1-y)F_\pi(Q^2). \tag{34}$$

Note that the high twist term discussed here contributes only to the structure function $\bar{H}_2$. A test of Eq. (34) requires examining data on $eN \to e'\pi X$ for large z and verifying whether there is a contribution to $\sigma(x,Q^2,z)$ which is proportional to $(1-y)/Q^2$. Tests made with neutrino and antineutrino data have shown encouraging results,[34-36] but much higher statistics are desirable over a broad range of Q^2.

5. Nuclear Dependence of $H_i^{A,h}(eA \to e'hX)$

Models[1] have been proposed to explain the nuclear (A) dependence of the fully inclusive structure functions $F_i^A(x,Q^2)$. In all approaches deep inelastic scattering occurs from quark and antiquark constituents. The approaches differ in the manner in which the constituents are grouped into color singlet degrees of freedom within a nucleus. These models provide expectations for the A dependence of the quark and antiquark densities, $q^A(x,Q^2)$ and $\bar{q}^A(x,Q^2)$.

If factorization is invoked, then *all* of these models of the nuclear dependence of $F_2^A(x,Q^2)$ lead to the expectation that at sufficiently large Q^2 the A dependence of the semi-inclusive structure function is expressed as

$$H_2^{A,h}(x,Q^2,z) = \sum_f e_f^2 x\left[q_f^A(x,Q^2)D_{h/f}(z,Q^2) + \bar{q}_f^A(x)\bar{D}_{h/f}(z,Q^2)\right]. \tag{35}$$

The only dependence on A resides in $q^A(x,Q^2)$ and $\bar{q}^A(x,Q^2)$ which are the measured parton densities of a nucleus.

In the remainder of this section I will comment briefly on further implications of the pion exchange model developed at Argonne.[12] It begins with the basic hypothesis that a nucleus is a *bound system of A nucleons plus an indefinite number of mesons.* The mesons are associated with nuclear binding. The structure functions (and hence the quark distributions) of the nucleons and mesons are not affected by the nuclear medium. They are the same as those measured on free nucleons and mesons.

The many-body bound state wave function of the nucleus is expressed in terms of the light-front momenta of the constituent nucleons and mesons. Fractions of the light-front momentum of the nucleus carried by nucleons and mesons are defined. These are fractions per nucleon, denoted x_π for π's, and x_N for nucleons. Number densities per nucleon of mesons and nucleons are also defined, $f_\pi^A(x_\pi)$ and $f_N^A(x_N)$, and computed from the bound state wave function. The mean number of pions per nucleon is given by the integral $\int f_\pi^A(x_\pi)\,dx_\pi = \langle n_\pi^A \rangle$. Use of light-front dynamics guarantees that the number densities are invariant under longitudinal Lorentz boosts.

In the pion exchange model, the fully inclusive structure function of a nucleus, per nucleon, $F_2^A(x,Q^2)$ is expressed in terms of the structure functions $F_2^N(x,Q^2)$ and $F_2^\pi(x,Q^2)$ measured on unbound nucleons and pions:

$$F_2^A(x,Q^2) = \int_x f_\pi^A(x_\pi)F_2^\pi\left(\frac{x}{x_\pi},Q^2\right)dx_\pi + \int_x f_N^A(x_N)F_2^N\left(\frac{x}{x_N},Q^2\right)dx_N. \tag{36}$$

Analogous expressions may be derived for the quark and antiquark densities per nucleon, $q^A(x,Q^2)$ and $\bar{q}^A(x,Q^2)$, as well as for the gluon density $G^A(x,Q^2)$. For example,

$$q^A(x,Q^2) = \int_x f_\pi^A(x_\pi)q^\pi\left(\frac{x}{x_\pi},Q^2\right)dx_\pi + \int_x f_N^A(x_N)q^N\left(\frac{x}{x_N},Q^2\right)dx_N. \tag{37}$$

According to the pion exchange model calculations, $\langle n_\pi^{Fe}\rangle = 0.095$, meaning that in an Fe nucleus, there are on average 5 to 6 pions from which deep inelastic scattering occurs. The mean momentum per nucleon carried by those pions is $\langle x_\pi^{Fe}\rangle = 0.052$. The "books are balanced" in the sense

that momentum lost to nucleons through binding, $\langle x_N^A \rangle < 1$, is carried by exchange pions. The average nucleon momentum $\langle x_N^A \rangle = 1 - \langle x_\pi^A \rangle \simeq 0.95$. This average nucleon momentum may be related to the mean one-nucleon separation energy observed in the reaction $(e, e'p)$. As shown in Fig. 4, the pion exchange model provides a unified description of $R_{\rm EMC}(x)$ for all x. The value of $\langle n_\pi^A \rangle$ controls the size of the enhancement of $R_{\rm EMC}(x)$ above unity at small x, whereas $\langle x_\pi^A \rangle$ controls the shape and size of the depression below unity for intermediate x. In the model, there is a modest change of $\langle n_\pi^A \rangle$ with A. For Al, Fe, and Au, $\langle n_\pi^A \rangle = 0.089, 0.095$, and 0.114.

Without further approximations, the pion exchange model may be used to obtain a convolution formula for semi-inclusive structure functions per nucleon:

$$\bar{H}_i^{A,h}(x,Q^2,z) = \int_{x_\pi > x} dx_\pi f_\pi^A(x_\pi) \bar{H}_i^{\pi,h}\left(\frac{x}{x_\pi}, Q^2, z\right) + \int_{x_N > x} dx_N f_N^A(x_N) \bar{H}_i^{N,h}\left(\frac{x}{x_N}, Q^2, z\right). \quad (38)$$

This equation expresses the semi-inclusive structure function of a nucleus as the incoherent sum of the semi-inclusive structure functions of the nucleon and pion constituents of the nucleus. The pion and nucleon densities, $f_\pi^A(x_\pi)$ and $f_N^A(x_N)$ are unchanged from the fully inclusive case.

Structure functions $\bar{H}_i^{N,h}(x,Q^2,z)$ are those measured on a deuteron target. The structure functions $\bar{H}_i^{\pi,h}(x,Q^2,z)$ would require experiments on a pion target: $e\pi \to e'hX$. In the fully inclusive case, it was possible to construct the functions $q^\pi(x,Q^2)$ and $F_2^\pi(x,Q^2)$ used in Eqs. (36) and (37) from measurements of pion induced massive lepton pair production $\pi N \to \mu\bar{\mu}X$. I know of no similarly direct way to obtain the function $\bar{H}^{\pi,h}(x,Q^2,z)$ which enters Eq. (38). Therefore, in order to extract specific predictions from Eq. (38), the x and z dependences of $\bar{H}^{\pi,h}$ would have to be modeled. In this sense, Eq. (38) is less predictive than Eq. (36).

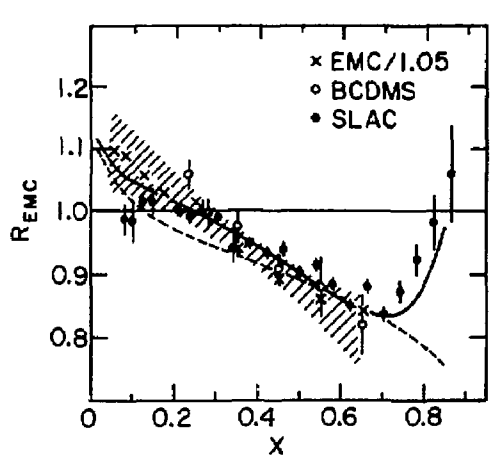

Figure 4: A compilation of data published prior to 1986 on the ratio of structure functions $R_{\rm EMC}(x,Q^2) \equiv F_2^{Fe}(x,Q^2)/F_2^D(x,Q^2)$ for deep inelastic electron and muon scattering. Shown are published results from the EMC Collaboration (Ref. 2), divided by 1.05, as well as data from the BCDMS Collaboration (Ref. 4), and from SLAC experiments (Ref. 3). The shaded band indicates the EMC group's estimate of experimental systematic uncertainties. The solid curve is calculated from the pion exchange model of Ref. 12. The dashed curve shows the expectation of Q^2 rescaling (Ref. 37) with $Q^2 = (200x + 10)$ GeV^2 appropriate for the kinematics of the EMC data.

One particularly interesting contribution to $eA \to e'\pi X$ is associated with elastic scattering from pions bound in the nucleus. This term is described in the next section.

6. Special Term $e\pi \to e'\pi$

In this section I consider briefly the possibility of elastic scattering from a constituent pion in the nucleus.[38,39] In the deep-inelastic limit, this subprocess provides the following specific contributions[39] to $\bar{H}_i^A$:

$$\bar{H}_1^{A,\pi}(x,Q^2,z) = 0 \quad (39)$$

$$\bar{H}_2^{A,\pi}(x,Q^2,z) = \delta(1-z)F_\pi^2(Q^2)\int_{x_\pi > x} dx_\pi f_\pi^A(x_\pi)\delta\left(\frac{x}{x_\pi} - 1\right) \quad (40)$$

$$= \delta(1-z)x f_\pi^A(x) F_\pi^2(Q^2).$$

Since the pion electromagnetic form factor, $F_\pi(Q^2)$, falls as Q^{-2} at large Q^2, this special contribution to $eA \to e'\pi X$ decreases as Q^{-4}. However, if it could be identified it would allow a direct measurement of the pion momentum density $xf_\pi(x$ in nuclei. The characteristic signatures of the contribution are the delta function, $\delta(1-z)$, in Eq. (40) and the Q^{-4} dependence.

If Eq.(40) is integrated over x, one obtains

$$\int \bar{H}_2^{A,\pi}(x,Q^2,z) = \delta(1-z)\langle x_\pi^A \rangle F_\pi^2(Q^2). \quad (41)$$

Recall that $\langle x_\pi^A \rangle$ is the mean momentum per nucleon carried by constituent pions in the nucleus.

A high twist Q^{-4} contribution of the form of Eq. (40) is also expected for scattering from a free proton, $ep \to e'\pi X$, and is therefore included in the function $\bar{H}_2^{N,\pi}(x,Q^2,z)$ which appears in Eq. (38). To proceed experimentally towards the identification of the special term in Eq.(40), it would be necessary to begin with precise measurements with a deuteron target to determine the full Q^2 dependence of $\bar{H}_2^{N,\pi}(x,Q^2,z)$ at large z. The special term in Eq.(40) could then be determined from the difference

$$\bar{H}_2^{A,\pi}(x,Q^2,z) - \int_{x_N > x} dx_N f_N^A(x_N)\bar{H}_2^{N,\pi}\left(\frac{x}{x_N}, Q^2, z\right).$$

Of practical concern for the identification of the special term are:

i. Since the pion must exit the nucleus without being absorbed, does the term survive?

ii. Is the term large enough to stand out above various backgrounds?

The concept of "color transparency"[20,40,41] suggests that the final pion will indeed emerge unscathed from the nucleus at large enough Q^2. Exclusive reactions such as $e\pi \to e'\pi$ are dominated at large Q^2 by contributions from the valence Fock state of the pion, $|q\bar{q}\rangle$. The valence state has small transverse separation of the constituents and therefore negligible hadronic interactions. Correspondingly, a large momentum transfer exclusive reaction can occur deep within a nuclear target without any elastic or inelastic initial or final state interaction. In addition to $e\pi \to e'\pi$, aother example would be $\pi A \to \pi p(A'-1)$. To obtain a rough estimate of the expected background to $e\pi \to e'\pi$, I adopt Eq.(19) for the contribution to single pion electroproduction from "conventional sources". Since the $e\pi \to e'\pi$ signal is prominent only at large z, Eq.(33) can be used for the fragmentation function, with $A = 1$. Summing over the charges of pions, and integrating over all x and $0.9 < z < 1$, I obtain

$$\int_0^1 dx \int_{0.9}^{1.0} dz \bar{H}_2^{A,\pi}(x,Q^2,z) = \frac{1}{3}\int_0^1 F_2^A(x,Q^2)dx \int_{0.9}^{1.0} dz F_\pi(Q^2), \tag{42}$$

valid for values of Q^2 such that the high twist term in Eq.(33) is dominant at large z. Since $\int F_2^A(x,Q^2)dx \simeq 0.5(5/18)$, I derive a signal to background ratio of

$$r^A \equiv \frac{\sigma(\text{special term})}{\sigma(\text{background})} \simeq 200\langle x_\pi^A\rangle F_\pi(Q^2). \tag{43}$$

The mean momentum per nucleon carried by pions is computed[12] to be $\langle x_\pi^{Fe}\rangle \simeq 0.05$, and I approximate[33] $F_\pi(Q^2)$ by $F_\pi(Q^2) \simeq (1+Q^2/0.4\ \text{GeV}^2)^{-1}$. Correspondingly, $r^{Fe} > 1$ for $Q^2 \lesssim 3\ \text{GeV}^2$.

This computation indicates that when an integral is made over all x, the contribution of the special term exceeds that of conventional sources of single pions as long as $Q^2 \lesssim 3\ \text{GeV}^2$. An experiment therefore looks feasible. However, at least two reservations should be stated. First, the restriction $Q^2 \lesssim 3\ \text{GeV}^2$ is in conflict with the assumption of the deep inelastic limit. A more thorough computation of the structure functions, Eqs. (39) and (40) should be made with non-asymptotic terms retained in the kinematics. Second, since experiments are done at fixed z or over a limited interval in x, a more relevant estimate of the signal to background ratio would be obtained by comparing Eqs. (19) and (40) at fixed x rather than after an integral is done over all x.

7. Summary and Conclusions

Some of the points made in this paper include:

- There are four independent structure functions for $eA \to e'hX$. To separate them at fixed x and Q^2, it is necessary to study the ϕ, p_T, and $y(=\nu/E)$ dependences of the cross section.
- Values of $W_X^2 = Q^2(1-x)/x \gtrsim 50\ \text{GeV}^2$ are required for clean separation of quark and target fragmentation effects in the data and unambiguous extraction of fragmentation functions $D(z,Q^2)$ for the full range of z. Values of $W_X \gtrsim 5$ GeV may be adequate if attention is restricted to $z \gtrsim 0.2$.
- In the region $z > 0$, factorization is the statement that the structure functions may be expressed as a sum of terms each having the form $q(x,Q^2)D(z,Q^2)$.
- Study of the nuclear A dependence of fragmentation as a function of Q^2, ν, x, and z will provide information on the breaking of factorization and on the dynamics of parton and hadron interactions in nuclear matter.
- Interesting high twist contributions to the quark fragmentation function $D_{\pi/q}(z,Q^2)$ may be extracted by studying the behavior of $D_{\pi/q}(z,Q^2)$ at large z and modest Q^2.
- The pion exchange model developed to interpret the A dependence of inclusive structure functions, $F_2^A(x,Q^2)$, leads to specific convolution formulas for the semi-inclusive structure functions $\bar{H}_2^{A,h}(x,Q^2,z)$.
- A special term, $e\pi \to e'\pi$, in which scattering occurs coherently from pions bound in nuclei provides a distinct contribution to $eA \to e'\pi X$. Identification of this contribution would allow a direct measurement of the pion momentum distribution in nuclei, $f_{\pi/A}(x)$.

Acknowledgment

I have benefitted from numerous discussions with Dr. Fritz Coester at Argonne.

References

1. For a recent review of data and interpretations, see E. L. Berger and F. Coester, Argonne report ANL-HEP-PR-87-13, to be published in Ann. Rev. of Nucl. Part. Sci. **37**, (1987).
2. J. J. Aubert *et al.*, Phys. Lett. **123B**, 275 (1983).
3. A. Bodek *et al.*, Phys. Rev. Lett. **50**, 1431 (1983), and **51**, 534 (1983); R. G. Arnold *et al.*, Phys. Rev. Lett. **52**, 727 (1984).
4. G. Bari *et al.*, Phys. Lett. **163B**, 282 (1985); A. C. Benvenuti *et al.*, CERN-EP/87-13, Phys. Lett., to be published.
5. N. Schmitz, Acta Phys. Pol. **B11**, 913 (1980).
6. European Muon Collaboration, M. Arneodo *et al.*, Z. Phys. **C31**, 1 (1986); J. J. Aubert *et al.*, Z. Phys. **C31**, 175 (1986); M. Arneodo, *et al.*, Nucl. Phys. **B258**, 249 (1985); M. Arneodo *et al.*, Z. Phys. C , (1987).
7. R. P. Feynman, *Photon-Hadron Interactions* (W. A. Benjamin, Reading, Mass., 1972).

8. J. D. Bjorken, Lectures at International Summer Inst. on Theoretical Physics, Hamburg, 1975, *Current Induced Reactions*, edited by J. G. Körner, G. Kramer, and D. Schildknecht (Springer-Verlag, 1976), p. 93.

9. G. Altarelli, R. K. Ellis, G. Martinelli, and S.-Y. Pi, Nucl. Phys. **B160**, 301 (1979).

10. E. L. Berger, Phys. Lett. **89B**, 241 (1980) and Z. Phys. **C4**, 289 (1980).

11. E. L. Berger, S. J. Brodsky, and G. P. Lepage in *Proceedings of the Drell-Yan Workshop*, Fermilab, 1982, edited by E. L. Berger, P. Malhotra, R. Orava, and H. Thacker, (Fermilab, 1982) p. 187. See also E. L. Berger and S. J. Brodsky, Phys. Rev. **D24**, 2428 (1981).

12. E. L. Berger, F. Coester, and R. Wiringa, Phys. Rev. **D29**, 398 (1984); E. L. Berger and F. Coester, Phys. Rev. **D32**, 1071 (1985); E. L. and Coester, F. in *Quarks and Gluons in Particles and Nuclei*, ed. by Brodsky, S. and Moniz, E. (World Scientific, Singapore, 1986), p. 255.

13. See, for example, E. L. Berger, Nucl. Phys. **B85**, 61 (1975).

14. J. L. Siegrist *et al.*, Phys. Rev. **D26**, 969 (1982); G. Hanson *et al.*, Phys. Rev. **D26**, 999 (1982).

15. DESY-Cornell Collaboration, G. Drews *et al.*, Phys. Rev. Lett. **41**, 1433 (1978).

16. R. D. Field and R. P. Feynman, Nucl. Phys. **B136**, 1 (1978).

17. R. Blankenbecler and S. J. Brodsky, Phys. Rev. **D10**, 2973 (1974); S. J. Brodsky and J. F. Gunion, Phys. Rev. **D17**, 848 (1978).

18. H. Georgi and H. D. Politzer, Phys. Rev. Lett. **40**, 3 (1978).

19. R. Cahn, Phys. Lett. **78B**, 269 (1978).

20. See, for example, A. Harindranath, K. Lassila, and J. Vary, Iowa State University report, 1986.

21. M. Derrick *et al.*, Phys. Lett. **164B**, 199 (1985); D. Bender *et al.*, Phys. Rev. **D31**, 1 (1985).

22. European Muon Collaboration, J. J. Aubert *et al.*, Phys. Lett. **160**, 417 (1985); M. Arneodo *et al.*, Phys. Lett. **150B**, 458 (1985); M. Arneodo *et al.*, Phys. Lett. **145B**, 156 (1984).

23. FNAL-Serpukhov-Moscow-Michigan Collaboration, J. P. Berge *et al.*, Nucl. Phys. **B203**, 1 (1982).

24. G. T. Bodwin, Phys. Rev. **D31**, 2616 (1985); J. C. Collins, D. E. Soper, and G. Sterman, Nucl. Phys. **B261**, 104 (1985).

25. A. Bialas and T. Chmaj, Phys. Lett. **133B**, 241 (1983); A. Bialas, Z. Phys. **C20**, 301 (1984); A. Bialas, Acta Phys. Polon. **B11**, 475 (1980); A. Bialas and E. Bialas, Phys. Rev. **D21**, 675 (1980) and Phys. Rev. **D20**, 2854 (1979).

26. A. H. Mueller in *Quarks, Leptons, and Supersymmetry*, Proceedings of the XVII Rencontre de Moriond, 1982, edited by J. Tran Thanh Van (Editions Frontieres, France), p. 13.

27. European Muon Collaboration, A. Arvidson *et al.*, Nucl. Phys. **B246**, 381 (1984).

28. MIT-SLAC collaboration, L. S. Osborne *et al.*, Phys. Rev. Lett. **40**, 1624 (1978).

29. J. P. Berge *et al.*, Phys. Rev. **D18**, 3905 (1978).

30. H. Deden *et al.*, Nucl. Phys. **B198**, 365 (1982).

31. Fermilab-Cracow-Michigan State-Univ. of Washington collaboration, L. Hand *et al.*, Acta Phys. Polon. **B9**, 1087 (1978).

32. To obtain Eq. (33), I begin with Eq. (6) of the first paper cited in Ref. 10. I then set $\langle p_T^2 \rangle = 0.4$ GeV^2. Noting next that the pion's electromagnetic form factor $F_\pi(Q^2)$ is measured (Ref. 33) to be approximately $(1 + Q^2/0.4 \text{ GeV}^2)^{-1}$, I replace $\langle p_T^2 \rangle / Q^2$ by $F_\pi(Q^2)$. For further discussion of the normalization of the high twist contribution to the longitudinal structure function in terms of $F_\pi(Q^2)$, see Ref. 11.

33. C. J. Bebek, *et al.*, Phys. Rev. **D13**, 25 (1976).

34. BEBC-WA59 Collaboration, P. J. Fitch *et al.*, Z. Phys. **C31**, 51 (1986).

35. M. Haguenauer *et al.*, Phys. Lett. **100B**, 185 (1981).

36. D. Allasia *et al.*, Phys. Lett. **124B**, 543 (1983).

37. F. E. Close, R. G. Roberts, and G. C. Ross, Phys. Lett. **129B**, 346 (1983).

38. F. Güttner, G. Chanfray, H. J. Pirner and B. Povh, Nucl. Phys. **A429**, 389 (1984).

39. E. L. Berger and F. Coester, in preparation.

40. G. Bertsch, S. J. Brodsky, A. S. Goldhaber, and J. G. Gunion, Phys. Rev. Lett. **47**, 297 (1981).

41. S. J. Brodsky, XIII International Symposium on Multiparticle Dynamics, 1982, edited by W. Kittel, W. Metzger, and A. Stergiou (World Scientific, 1982), 963.

EXPERIENCE WITH A WARM GAS JET TARGET FOR NUCLEAR PHYSICS

Andrew S. Hirsch, Physics Department, Purdue University,
West Lafayette, IN 47907

Abstract: A room temperature pulsed internal gas jet target has been used in the main ring at both FNAL and the Brookhaven AGS in order to study proton-nucleus collisions. We have produced ultra-thin targets in the range of 1-100 ng/cm^2 using a variety of pure and mixed gases.

Introduction

The viability of a gas jet target situated in the main accelerator ring has been demonstrated in a series of experiments conducted at both FNAL and the AGS at BNL. Our primary objective in these experiments has been to study proton-nucleus collisions, and to this end we have used a variety of noble gas targets mixed with molecular hydrogen. This paper summarizes our several thousand hours of experience with the gas jet.

In 1975, a feasibility study of a room temperature gas jet target for use in Fermilab's main ring was undertaken by Frank Turkot and Paul Mantsch.[1] A gas jet target built in the U.S.S.R. by the Dubna Laboratory had been in use in the Internal Target Area at FNAL since 1972. This target utilized liquid He both to cool the gas injected into the vacuum chamber and to cryopump the gas after it had passed through the beam. It was hoped that in developing a room temperature gas target, many of the complexities encountered in operating the cooled jet could be avoided.

From the experimental point of view, several features were deemed important: 1) a variable range of target thickness from 1 ng/cm^2 to 100 ng/cm^2, 2) a jet pulsing time at least 10% or 300 msec of the acceleration period, 3) a transverse dimension of the jet approximately equal to the horizontal size of the beam, 4) a density of gas not in the jet proper 1/1000 of that in the jet, 5) good access to the interaction region for detectors, 6) continuous operation with good reliability, 7) a design which permitted the installation of a spare nozzle in about 1 hour. Of course, accelerator operation imposes constraints on any potential gas jet target situated in the main ring. Scheduled access is usually limited to once per week at most. The attenuation of the beam must be small (< .1%) per jet pulse, and the extraction efficiency of the beam from main ring unaffected by the jet operation.

The de Laval Nozzle

The nozzle chosen for use at Fermilab was a 100 μm diameter de Laval nozzle (fig. 1) When a gas initially at rest in the entrance chamber under pressure escapes through such a nozzle, in general, two possibilities arise. The first is that the pressure in the flow decreases in the converging entry section up to the throat and increases in the diverging exhaust section of the nozzle. The flow remains subsonic throughout. This occurs when the receiver pressure remains above a certain value, P_2 (fig. 2).

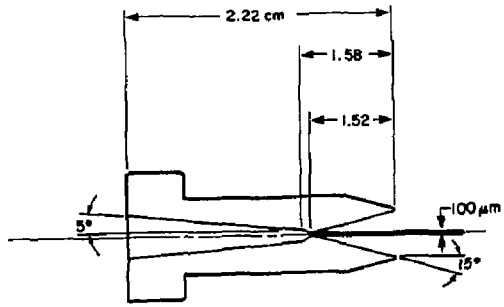

Fig. 1: de Laval Nozzle

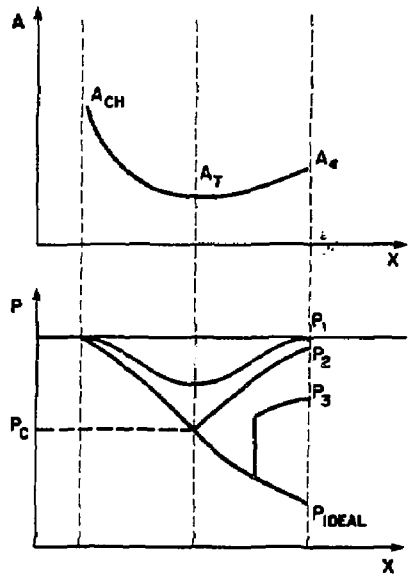

Fig 2: Area and Pressure as a function of distance along the nozzle

At P_2, the pressure at the throat achieves its critical value and is given by

$$P_c = P_1\left(\frac{2}{\gamma+1}\right)^{\frac{\gamma}{\gamma-1}} \qquad (1)$$

where γ is the ratio of specific heats and P_i is the inlet pressure. When the receiver pressure falls below the value P_2, the other possibility occurs; the pressure in the flow decreases up to the throat, as before, but now becomes just sonic at the throat. The flow up to the throat is not affected by further decreasing the receiver pressure. In the diverging exhaust section of the nozzle, the pressure continues to drop. If ideal flow is to be achieved, the receiver pressure must be matched to the pressure in the flow at the nozzle exit. Otherwise, the adjustment to the receiver pressure is made via a shock front. This behavior is summarized in figure 2. Under proper conditions, the adjustment to the receiver pressure will occur several centimeters outside the nozzle. This is the regime in which the nozzle was operated in our experiments.

Approximating the flow using a one-dimensional gas dynamics model that assumes an ideal gas in steady-state isentropic flow, we can find a relation among the parameters of interest, namely the density in the jet when its radius is R, the radius r, of the nozzle at its throat, the pressure, P_i, at the inlet, and the temperature, T_o of the gas at the inlet. (fig. 3)

$$\rho = \left(\frac{r}{R}\right)^2 \left(\frac{P_i M}{C\,T_o}\right)\left(\frac{2}{\gamma+1}\right)^{\frac{1}{\gamma-1}}\left(\frac{\gamma-1}{\gamma+1}\right) \qquad (2)$$

M is the molecular weight of the gas and C is the molar gas constant. The gas flow through the nozzle is given by

$$Q = \pi r^2 P_i \left(\frac{2}{\gamma+1}\right)^{\frac{1}{\gamma-1}} \left(\frac{2\gamma}{\gamma+1}\right)\left(\frac{C}{MT_o}\right)T_t \qquad (3)$$

where T_t is the temperature of the gas in the target box. We have measured the throughput of both a 100 and 150 μm nozzle by injecting a known quantity of helium gas into the nozzle. As shown in figure 4, the agreement with eq. (3) is quite satisfactory.

Measurement of the density profile of the jet can be made using the technique of hot wire anemometry. This technique, when used to measure a single component gas, gives reasonable agreement with the predicted results based on eq. (2). Typically, the measured values are about 70% of the predicted. Measurements performed on a 100 μm de Laval nozzle gave a linear relation between the jet full width at half maximum (fwhm), 2R, and the distance Z from the nozzle. At inlet pressures above about 40 psia using hydrogen, the FWHM is independent of the the inlet pressure and is approximated by

$$2R = 0.16Z + 0.4 \qquad (4)$$

where both R and Z are in mm. At pressures below 40 psia, there is a transition to a wider profile. At 35 psia,

$$2R = 0.38Z + 0.25 \qquad (5)$$

The target thickness, $2R\rho$, can now be expressed in terms of the inlet pressure and the distance from the nozzle.

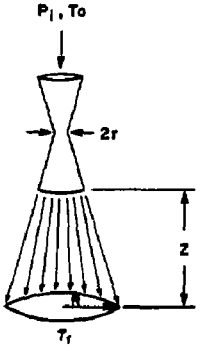

Fig. 3: de Laval Nozzle Schematic

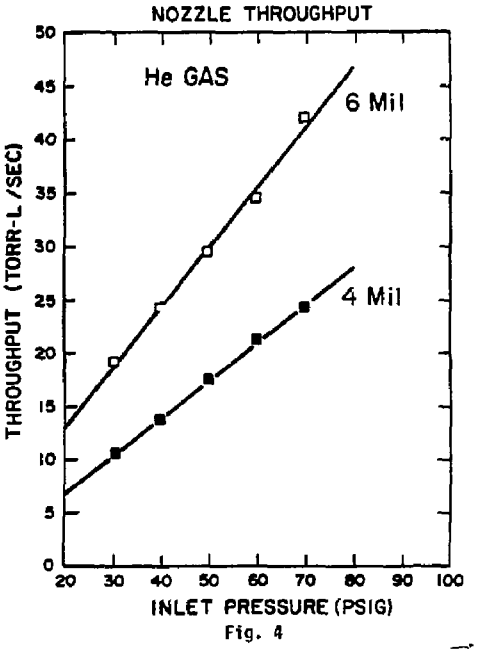

Fig. 4

The Jet Housing and Target Box

The de Laval nozzle was contained within a jet housing, shown in figure 5, which was situated above the target chamber. The housing was isolated from the target box by means of a 12 in. vacuum gate valve. During operation, the nozzle was positioned via remote control in both the vertical and horizontal planes by maximizing the beam-jet interaction as measured by the p-p elastic scattering from the hydrogen component of the target gas. At BNL, the nozzle opening was 3.8 cm above the nominal beam center line. Horizontal motion of the jet was ±0.5 in. along a line at 45° with respect to the incident beam direction. Inlet gas pressure was typically about 25 psig for all gases used. At pressures much lower, a suitable jet was not formed, whereas at higher pressures, radiative beam losses became a problem. The inlet valve shown in figure 5 was actually an electrically operated solenoid located inside the vacuum immediately before

the nozzle. When the solenoid opens, the gas is forced through the nozzle and forms a conically shaped jet within 10 ms. When the solenoid is closed to end the jet firing cycle, a small amount of gas is left between the valve and the nozzle. To aid in producing a sharp end to the jet and to help main ring vacuum recover, a small 75 liter buffer volume at 1 μm Hg was connected to the nozzle through a second 'exhaust' solenoid valve. This valve was opened 20 ms after the inlet valve closed and remained open for 200 ms in order to remove the residual gas.

A collection cone with an opening diameter of 5.0 cm was located below the jet and approximately 3.8 cm below the nominal beam position. Approximately 80% of the gas in the jet was captured by the cone which led to a 1000 liter buffer volume maintained at high vacuum by two unbaffled 5600 l/s oil diffusion pumps (DP). The remaining 20% of the gas escaped into the main ring target box and was pumped away by the main ring vacuum system, discussed below.

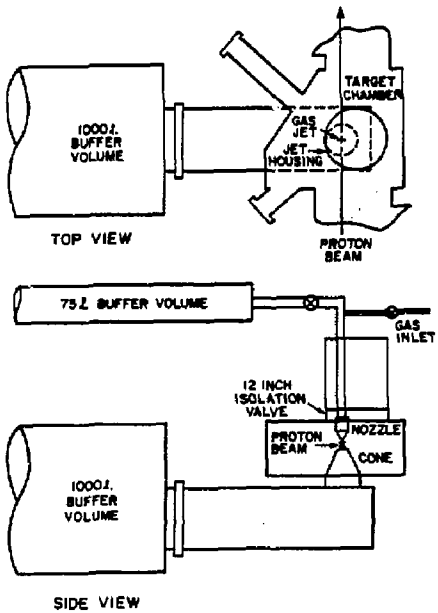

Fig. 5: Target box and Housing Jet

The Vacuum System and Jet Gating Electronics

The pressure rise due to the 20% of the gas which escaped capture by the buffer volume posed a threat to both the circulating beam and to our detectors. Hence, it was essential to contain the pressure fluctuations each time the jet was fired, and to return quickly to ambient vacuum levels.

At FNAL, the long straight sections facilitated the installation of the target box and additional pumps along the beam line. The layout at FNAL is shown in figure 6. Two 10 in. DPs, each 4000 l/s, were located on the target box. Additionally, there were three upstream and two downstream DPs on the main ring and at the ends of the straight section there were two ion pumps upstream and one ion pump downstream. Table 1 indicates the maximum pressures encountered at each pump during a typical pulse and compares these values with the corresponding ambient vacuum readings.

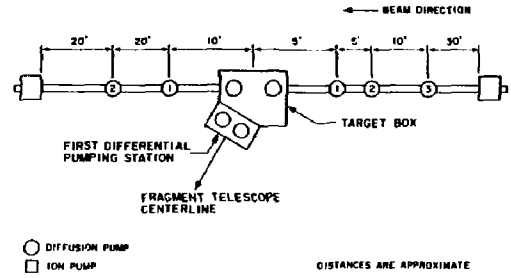

Fig. 6: FNAL Beam Line

Table 1
Pressure fluctuations at various locations in the FNAL vacuum system (see Fig. 6).

Location	Peak (Torr)	Recovery (Torr)
IP downstream	2×10^{-8}	6×10^{-9}
2nd DP downstream	1×10^{-7}	5×10^{-8}
1st DP downstream	4×10^{-6}	1×10^{-7}
Buffer Volume	3.5×10^{-4}	1×10^{-7}
Target Box	1.5×10^{-6}	5×10^{-7}
1st DP upstream	2.5×10^{-6}	1×10^{-7}
2nd DP upstream	7×10^{-7}	1×10^{-7}
3rd DP upstream	9×10^{-8}	6×10^{-8}
IP upstream	1×10^{-8}	4.5×10^{-9}

Installing the jet at the AGS required that all of the up and downstream pumping be accomplished within the eight feet between bending magnets. To this end, up and downstream of the central target chamber two end boxes of 200 l total volume were added (fig. 7) Each end box was pumped on by a 5600 l/s 10 in. DP with a cold water baffle. This cut the

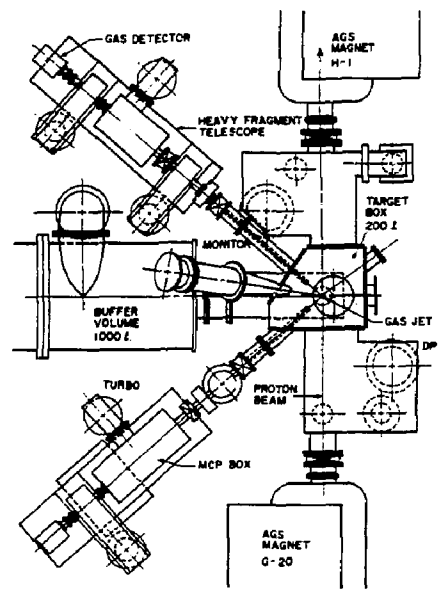

Fig. 7: BNL Detector Schematic

effective pumping speed in half but kept oil out of the main ring. Each end box was followed by a differential pumping chamber which further reduced the pressure rise as it travelled down the main ring beam pipe. Each differential chamber was pumped on by two baffled 750 l/s 6 in. DPs. Any gas getting past the differential pumping chambers entered the main ring vacuum system. During normal pulsing, the pressure fluctuation was damped to normal after about 40 feet. Table 2 contains the vacuum levels for a typical pulse at the AGS.

Table 2
Pressure fluctuations at various locations in the AGS vacuum system (see Fig. 7).

Location	Peak (Torr)	Recovery (Torr)
Upstream target box	5×10^{-6}	1.3×10^{-6}
Downstream target box	7×10^{-6}	7×10^{-7}
Central target box	4×10^{-5}	9×10^{-6}
Buffer volume	1×10^{-7}	2.8×10^{-7}
TEL1 1st DP	5.2×10^{-6}	5.2×10^{-6}
TEL1 MCP Box	3.8×10^{-7}	3.8×10^{-7}
TEL3 1st DP	1×10^{-7}	1×10^{-7}
TEL3 MCP Box	7×10^{-7}	7×10^{-7}

The entire vacuum system was monitored via cold cathode discharge gauges (DG) on all high vacuum boxes ($<10^{-5}$ Torr) and by thermocouple gauges (TC) located on each fore and rough pump and on the foreline on the low pressure side of each DP. All gauge readings were displayed in the operations trailer. Each gauge controller had trip sets which were fed into a central interlock box. In the event the vacuum rose above the trip point, the appropriate valves would be closed, DPs shut down, and the jet turned off.

The operation of the jet and vacuum systems was conducted from the operations trailer some 40 m away from the internal target. The jet was positioned, first vertically, then horizontally, by means of digital counter-comparators to some nominal preset position. A "jet scan" could then be performed by changing the horizontal position until the maximum p-p elastic counting rate was found. The timing of the jet firing was referenced to a clock signal provided by the accelerator. This signal, referred to as T_o represents the start of the acceleration cycle. Figure 8 shows schematically the gating electronics with times for a typical accelerator cycle. The gating signals were displayed on a CRT along with the beam intensity, the magnetic field ramp, the target box vacuum, and the horizontal and vertical beam position. A typical display is shown in figure 9. The jet timing parameters used during data acquisition are summarized in table 3.

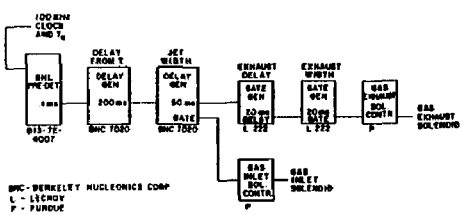

Fig. 8: Gating Electronics

Table 3
Typical times for the operation of the gas jet at FNAL and BNL.

Occurrence	Time after T_o at FNAL	Time after T_o at AGS (ms)
Gas valve opens	2.00	200
Gas valve closes	3.00	250
Evacuation valve opens	4.05	270
Evacuation valve closes	5.05	470

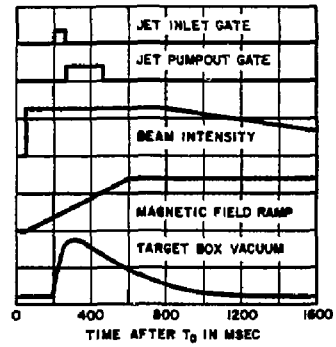

Fig. 9: CRT Display of Gating Signals

The Monitor Telescope and Jet Density Profile

Our primary objective has been the study of proton-nucleus collisions. In particular, we have been interested in the production of heavy nuclear fragments which emergy from the interaction between high energy (>1 GeV) protons and heavy nuclear targets, such as neon, argon, krypton, and xenon. One might expect that a supersonic jet target could be made from each of these gases. This is true, except that as the atomic weight of the gas increases, the input pressure must be increased in order to form a jet which has a reasonable profile. At the same time, the target thickness becomes so high that it causes significant beam losses. For this reason we used mixtures of molecular hydrogen and the above noble gases. These mixtures are presented in table 4. The use of the mixed gas target allowed us to normalize the heavy fragment data using the proton-proton elastic cross section.

The kinematics of p-p elastic scattering gives the following result for the relation between the recoil kinetic energy and the angle between this proton and the incident beam direction:

$$T(\theta) = \frac{2Mc^2\cos^2\theta}{((E+Mc^2)/(E-Mc^2)) - \cos^2\theta} \qquad (6)$$

where E is the total energy of the incident proton and M is the mass of the proton. The appropriate choice of θ will give recoil energies in a range that is manageable for silicon surface barrier detectors. At both FNAL and the AGS, θ was close to 85°. Over the incident energy range at the AGS, the recoil energy given by eq. (6) necessitated two two monitor arrays. These were located at 84.8° and inclined out of the plane defined by the AGS main ring by 30° and 34°. These telescopes were designated M4 and M5 respectively. The detector thicknesses were chosen to cover the range of 5 to 18 MeV in M4 and 8 to 28 MeV

Table 4
Target gas mixtures at FNAL and BNL

FNAL target gases	BNL target gases
10% xenon-90% hydrogen	1% xenon-99% hydrogen
10% krypton-90% hydrogen	3% xenon-97% hydrogen
20% krypton-80% hydrogen	100% hydrogen
25% argon-75% hydrogen	
60% neon-40% hydrogen	
100% methane	
100% hydrogen	

in M5. All detectors had an active area of 50 mm^2 with thicknesses listed in table 5. Because the passage of the beam through the jet caused both visible and ultra-violet radiation to be emitted from the jet, a 2.2 cm diameter 1360 $\mu g/cm^2$ nickel foil was placed between each monitor telescope and the jet to shield the detectors. The visible light was a useful indicator that the jet was working and was monitored by a TV camera stationed at a quartz window on the target chamber.

Table 5
Monitor silicon surface barrier detector thickness at BNL

Detector	Thickness (μm)
M4DE	200
M4E	2000
M4V	1000
M5DE1	500
M5DE2	2000
M5E	2000
M5V	1000

The monitor telescope housing was isolated from the target box by a gate valve. This enabled the monitor to be let up to atmosphere without disturbing the target box vacuum.

In figure 10, we display data from the high energy monitor M5, for incident beam momentum 13.9 < P_{inc} < 15.1 GeV/c, and a 50 ms jet of H_2 at 25 psig. The p-p elastic cross section in this region varies slowly with beam energy and is about 6.5 mb/sr at 84.8°. In order to extract the target thickness of hydrogen, we have modeled the jet density distribution as a Gaussian,

$$\rho(X) = \rho_o e^{-(X-X_o)^2/2\sigma_x^2} \qquad (7)$$

where ρ_o is the peak density and the parameter X_o is the displacement of the jet centroid from the nominal beam-jet intersection point. Since, according to eq. (6), to each recoil kinetic energy there corresponds a unique scattering angle, one can treat each energy bin of the recoiling proton as sampling a different portion of the jet density distribution, as shown in figure 11. Thus, the density distribution becomes

$$\rho(\phi) \propto e^{-(\phi-\phi_o)^2/2(\sigma_\phi/\cos\phi_o)^2} \qquad (8)$$

where, $\phi = \frac{\pi}{2} - \theta$, $\sigma_\phi/\cos\phi_o = \sigma_x/D$ and D is the -jet detector distance.

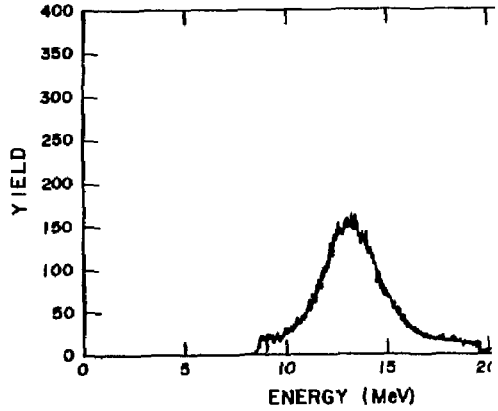

Fig 10a: p-p Elastic Peak

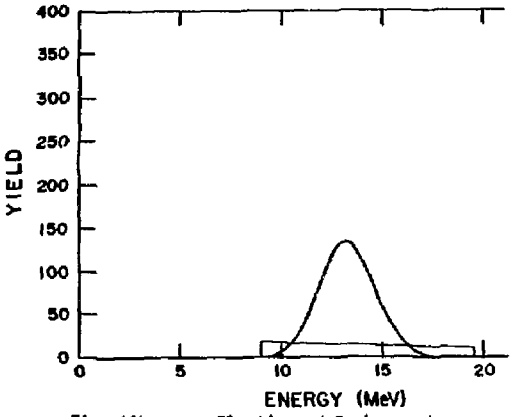

Fig. 10b: p-p Elastic and Background Contributions

In addition to the jet profile, we have added an empirical background contribution to account for scattering from residual gas in the target box of the form

$$A + BT + CT^2 \qquad (9)$$

where T is the detected proton's kinetic energy. We have fit the data according to the above procedure and show both the total fit and the separate contributions of the jet and background in figure 10. The target thickness is found by integrating eq. 7 over the variable X. After correcting the data for multiple scattering losses, about 20%, this yields a target thickness of $(2.5 \pm 0.2) \times 10^{15}$ atoms/cm^2 and a fwhm of 11.8 ± 0.1 mm. These results lie in between those predicted on the basis of eqs. (2), (4), and (5) with Z = 38 mm. This is quite reasonable since at 25 psig we have not yet made the transition to the narrow jet profile. Further details concerning the monitor array and fitting procedures can be found in references 2 and 3.

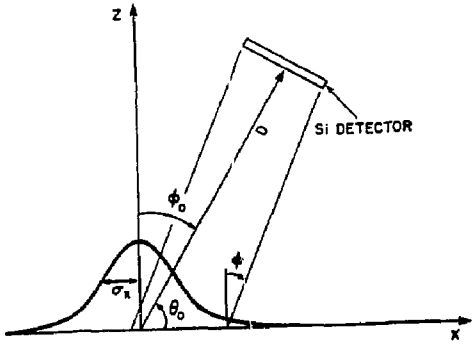

Fig. 11: p-p Elastic Geometry

The Fragment Telescopes

Heavy nuclear fragments emerging from high energy p-nucleus collisions typically have energies between 1 and 2 MeV per nucleon. Reaction products extend down to virtually zero kinetic energy. Thus, it is important that one use a thin target in order to limit the energy lost via ionization. In addition, one must design a low mass fragment detection telescope in order to determine the mass, charge, and energy over a wide range of fragment types and energies.

The fragment telescope at FNAL, shown schematically in figure 12, was located at a scattering angle of 34° and was attached to the first differential pumping station. Micro-channel plates, MCP, were used to provide fast timing signals, following the design of Zebelman, et al.[4] Since these detectors require a vacuum of less than 5×10^{-5} Torr to ensure their long-term operation, they were housed in aluminum boxes which could be vacuum isolated from the rest of the system. A turbomolecular pump (450 l/s) maintained the vacuum in this portion of the detector telescope.

The telescope terminated in a gas ionization chamber. An unsupported 3/4 in. diameter polypropylene window, 80 $\mu g/cm^2$ thick separated the aluminum boxes at high vacuum from the interior of the gas detector which was at 20 Torr. The flight path though the gas, P-10, was 11.11 cm. There was enough diffusion of the gas through the thin window so that it was necessary to have a diffusion pump between the gas detector window and the last MCP. A fast closing valve was inserted as well to protect the timing detectors in the event of a window rupture. The experimental apparatus was operated for several thousand hours during the course of testing and data acquisition. No catastrophic failures occurred and no detectors were lost due to vacuum system failure.

The fragment telescope was supported by an aluminum frame which was attached at its back end to a remotely controlled mechanical driving mechanism. In addition, a pivot point employing a flexible vacuum coupling located in the front of the telescope near the target box enabled the telescope to move horizontally and vertically ±2 in. Once the jet position had been established by maximizing the counting rate in the monitor telescope, the fragment telescope was then driven until its counting rate was maximized.

As an example of the data acquired with this

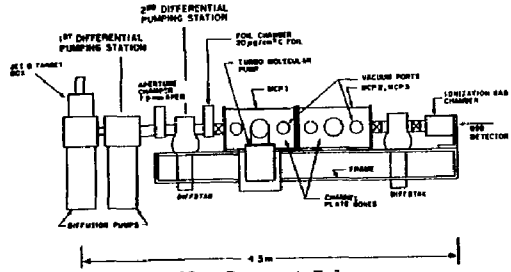

Fig. 12: Fragment Telescope

apparatus[5], we show the aluminum masses in figure 13. The flight of the fragments was between the first MCP (START) and the surface barrier detector (STOP) in the ionization chamber. Corrections were made for the energy and multiple scattering losses. The excellent mass resolution permitted the measurement of fragment kinetic energy spectra to quite low energies. Some typical spectra are shown in fig. 14.

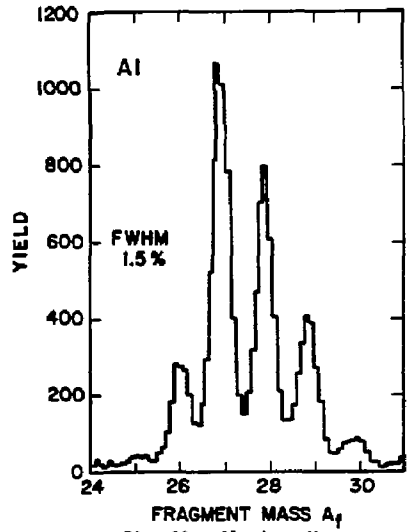

Fig. 13: Aluminum Masses

Conclusion

We have described the operation of a supersonic gas jet which has been used in several experiments at different national laboratories. The internal target has been proven to be flexible enough to permit adaptation to the different physical constraints encountered. The unique feature of the gas jet is its operation in the accelerator's main ring, where multiple traversals by the beam result in an effective target thickness comparable to that of a foil target. The ability to pulse the jet over the entire acceleration cycle, allows one to measure the energy dependence of the cross section of interest, while the ability to pulse mixed gases makes normalization of the data possible.

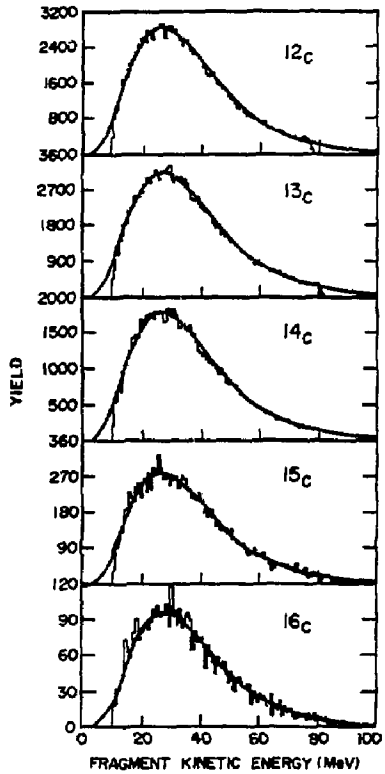

Fig. 14

References

1. D. Gross, P. Mantsch, and F. Turkot, FNAL Report TM-534-0710.0 (January 1975). P. Mantsch and F. Turkot, FNAL Report TM-582-0170.0 and FNAL Report TM-586-0710.0 (June 1975).

2. T. C. Sangster, Ph. D. Thesis, Purdue University (1986).

3. M. Mahi, Ph. D. Thesis, Purdue University (1986).

4. A. M. Zebelman, et al., Nucl. Instr. and Meth. 141, 443 (1977).

5. J. E. Finn, Ph. D. Thesis, Purdue University (1982).

POSSIBILITIES FOR POLARIZED INTERNAL TARGETS

R. D. McKeown
W. K. Kellogg Radiation Laboratory
California Institute of Technology
Pasadena, CA 91125

An important feature of experiments with internal targets in storage rings is the possibility of using thin polarized gas targets. Various methods of polarizing different nuclei are under development, and suitable target thicknesses appear quite feasible. A survey of techniques is presented with a discussion of advantages, disadvantages and possible problems that will need to be addressed.

Introduction

Many experiments in electronuclear physics benefit from the use of polarized targets. Often there are amplitudes that cannot be extracted by other methods, and the existence of interference effects in spin dependent quantities allows better access to small amplitudes. These features of polarized targets have been discussed by others at this workshop, so I will concentrate on the target technology itself.

The use of polarized targets in electron scattering experiments was pioneered at SLAC[1], and improvements in the technique have been recently reported by the Bonn group[2]. These polarized hydrogen targets contain hydrogen (or deuterium) in beads of alcohol or ammonia at low temperature (≈ 0.1°K). A large magnetic field (typically 5 Tesla) is applied to produce electronic polarization. Application of microwaves at a resonant frequency induces polarization of the protons (or deuterons). The protons become highly polarized, but tensor polarization of deuterium is low. Although the protons are highly polarized, only a small fraction (< 20%) of the nucleons in the target are actually polarized due to the presence of heavier nuclei in the beads. This reduces the measured asymmetry which makes the experiments correspondingly more difficult. The high magnetic field causes problems in deflecting the incident and/or scattered particles. (The detailed extraction of small amplitudes requires accurate determination of scattering angles and careful alignment of the spin direction with respect to particle momenta.) In addition, the targets become radiation damaged when the incident beam current is greater than a few nanoamperes, so that the full beam intensity cannot be utilized.

In contrast, the internal targets are of high purity, high polarization, and will not suffer from radiation damage. The holding field is usually in the range of 10-100 Gauss, which simplifies the problem of particle deflection. The type and degree of polarization is easily varied so that, for example, tensor polarization is as easy as vector polarization to achieve. Of course, the main disadvantage is the very thin target thickness, but this can be offset by the use of a storage ring with high circulating current.

Table I summarizes the basic beam parameters of the two facilities most likely to be utilized in the near future. Also included in the table is the estimated maximum target thickness allowed in the ring. Note that a thin ($10\mu g/cm^2$) carbon foil corresponds to $6 \times 10^{18}/A$ atoms/cm^2, so we should consider windowless, differentially-pumped gas targets.

For definiteness, I will consider the nucleon cross-section at $Q^2 = 1(\mathrm{GeV/c})^2$ as a reference cross-section for rate estimates. (This cross-section is at the boundary between the PEP energy range and the MIT-Bates range.) Then we roughly find that the cross-section per nucleus is given by

$$\frac{d\sigma}{d\Omega} \lesssim 2.5 \times 10^{-33} E^2 A \frac{\mathrm{cm}^2}{\mathrm{sr}}, \qquad (1)$$

where E is the incident beam energy. For a solid angle of 10 msr (0.01 sr) at $E = 2$GeV the cross-section becomes

$$\sigma \lesssim 1 \times 10^{-34} A \mathrm{cm}^2. \qquad (2)$$

To obtain a rate of 0.1 Hz (10^4 counts per day) then requires a luminosity of $L \gtrsim 10^{33}/A$ cm^2/sec, and assuming a beam current of 40mA the target thickness must be

$$n_t \gtrsim 4 \times 10^{15}/A \,\mathrm{atoms/cm}^2. \qquad (3)$$

I will use the reference value of 10^{15}cm^{-2} as a goal for target thickness. Of course, some experiments will require more or less, but this is usually within an order of magnitude of the requirements for experiments that have been considered recently.

I will survey the development of hydrogen and ^{3}He targets. Certainly other targets will be feasible (such as optically pumped alkali vapors), but these are the ones of most common interest and have a broader range of applicability in the field.

Table I. Relevant Storage Ring Parameters

		PEP	Bates PSR
Energy (GeV)		4–18	0.3–1.0
Current (mA)		> 20	40
Max. Target Thickness	$A \leq 6$	$6 \times 10^{15}/A$	$10^{19}/A$
(atoms/cm^2)	$A = 40$	6×10^{13}	2×10^{17}

Hydrogen Targets

I will discuss three types of polarized hydrogen targets which are relevant to internal target designs. Each could be used as either a proton or deuteron target.

The first technique has been under development for many years: the atomic beam[3]. A schematic is shown in fig. 1. A dissociator is used to form an atomic beam of H atoms, which is passed through a sextupole magnet yielding atomic (but not nuclear) polarization in a strong magnetic field. Polarization is transferred to the nucleus by inducing RF transitions of various types. The resulting beam of $\sim 5 \times 10^{11}$/cm^3 could be used to form a target by intersection with the electron beam

Figure 1. Polarized hydrogen atomic beam apparatus

of $n_t \sim 5 \times 10^{12}/\mathrm{cm}^2$. This falls short of our goal by about a factor of 100, and two methods are being explored to try to increase the density: (a) cooling the H beam[4], and (b) storing the H atoms in a bottle[5]. Cooling the beam slows the atoms so they spend more time in the path of the electron beam and increases the acceptance of the sextupole magnet. Cooling to 20°K should give about a factor of 50 improvement in density, but this has not been achieved in practice. The storage bottle is being developed at the Univ. of Wisconsin and they have had some success recently. The problem is that after several wall collisions, an H atom is likely to be depolarized or recombine to form a molecule. In order to reach $n_t \sim 10^{15}/\mathrm{cm}^2$ one will need to develop wall coatings that allow 10^3–10^4 wall collisions without loss of polarization. The Wisconsin group has recently achieved 120 bounces and hopes for further improvements[6].

Another technique which is currently under development at Argonne[7] is the spin-exchange method, shown schematically in fig. 2. Dissociated hydrogen is introduced to a cell containing a small amount (~ 1%) of potassium. The potassium is polarized by optical pumping with a dye laser, and transfers polarization to the hydrogen by spin-exchange collisions. The Argonne group expects to achieve a polarization rate of $\sim 5 \times 10^{16}$/sec with 100 milliwatts of laser power. This feed rate is equivalent to the best atomic beam available, and one could expect to increase the laser power to several watts. If this is achieved, the demand on the wall coatings could be reduced to the point where the existing coatings may be sufficient. The present status is that the Argonne group has just observed a polarization signal for the first time[8], and is proceeding to make improvements.

An interesting new technique has been proposed by Kleppner[9], and is being used to develop a target for the AGS at Brookhaven. The basic idea is sketched in fig. 3. Dissociated ultra-cold H (0.5°K) is expelled by a very large (~ 8Tesla) magnetic field. The resulting beam would be well focussed and monochromatic, with an estimated output density about a factor of 100 greater than a conventional atomic beam. RF transitions would then be used to create high nuclear polarization. The technique requires quite a bit of cryogenic equipment and a superconducting magnet, but certainly looks quite promising at the moment.

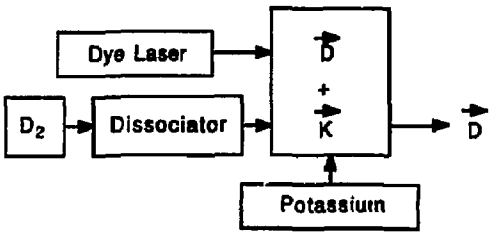

Figure 2. Polarized deuterium using spin exchange

^{3}He Targets

A polarized ^{3}He target can be used essentially as a polarized neutron target. The two protons are predominantly coupled to spin zero, so that the nuclear spin is primarily the neutron spin. Thus, measurement of a spin observable selects the neutron with only small corrections for the protons, which can be calculated accurately with Fadeev techniques[10]. Two techniques are employed to polarize ^{3}He, and both have been improved markedly in the last few years.

The first method is being developed by Chupp at Harvard and McDonald at Princeton[11], and is shown in fig. 4. The ^{3}He is in a cell with a small amount of rubidium and about 20% nitrogen. The rubidium is optically pumped with a dye laser and transfers spin to ^{3}He by spin exchange collisions. The Rb is optically thick to facilitate efficient angular momentum transfer, but this causes the phenomenon of "radiation trapping",

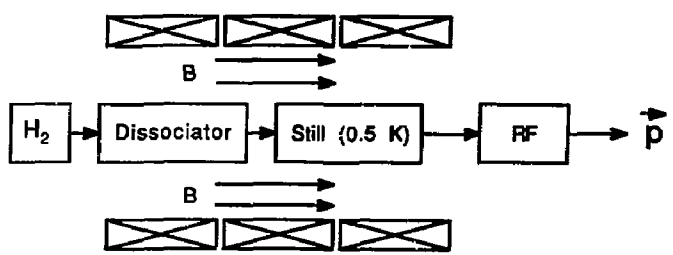

Figure 3. Ultracold polarized hydrogen apparatus

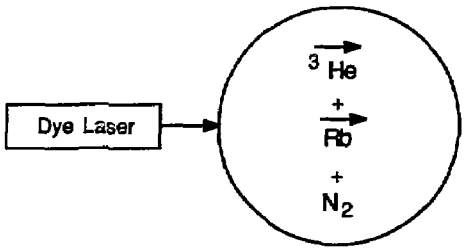

Figure 4. Polarized ^{3}He by spin exchange with Rb.

where re-emitted photons are absorbed leading to saturation of polarization at low values (the absorbed secondary photons depolarize atoms on the way out). The cure is to add the nitrogen as a buffer gas so that the Rb collisionally de-excites, eliminating the secondary photons. The presence of nitrogen is again a nuisance as it was for external hydrogen targets, but perhaps this is a soluble problem. In addition, the feed rate is low, but this may also be improved. Note that no bottle problem exists for ^{3}He since, being a noble gas, wall collisions are not severely depolarizing.

Another technique, shown in fig. 5, has been developed by Leduc and Laloe at L'Ecole Normale Superieur in Paris[12]. Our group at Caltech is presently adapting this technique to build realistic targets for use in electronuclear physics experiments[13]. In this technique, a small population of metastable triplet state ^{3}He atoms is optically pumped by a laser. The pumped atoms collide with ground state atoms and exchange electronic states leaving a polarized nucleus in an atomic ground state. Gradually, angular momentum is transferred to completely polarize the ground state population. The polarization rate with present laser technology is $\sim 10^{17}$/sec, and the ^{3}He is pure. This appears at present to be a very appropriate method for internal target use.

The Bottle and Effects of the Electron Beam

Most of the target designs discussed above require the use of a storage bottle to hold the gas in order to generate the appropriate target density. The typical bottle is shown in fig. 6. It consists of a 10 cm long cell with gas at 10^{14}/cm^3 and two long tubes (length l and radius a) to provide an impedance to gas flow and allow the beam to pass through. In the molecular flow limit (mean free path long compared to a) one can express the tube conductance, F, as[14]

$$F = \frac{5 \times 10^{16}/\text{sec}}{10^{14}/\text{cm}^2}, \\ = \frac{K\bar{v}}{4}\pi a^2, \tag{4}$$

where $K \approx \frac{8}{3}\frac{a}{l}$, $\bar{v} = 1.5 \times 10^4 \sqrt{T/A}$ cm/sec (thermal velocity), and we have assumed a feed rate of 10^{17} atoms/sec into the bottle which is at temperature T degrees Kelvin. For typical values of $A = 3$, $l = 30$cm, and $T = 300°$, one computes that the tube radius must be $a = 0.36$cm. The tube radius is the sensitive parameter, as the conductance goes as a^3. One can also estimate the mean holding time in the bottle as 0.01-0.1 sec which yields the number of wall collisions as $10^3 - 10^4$.

I will consider two possible sources of depolarization by the electron beam: ionization and magnetic field effects. The ionization rate is easily computed for minimum ionizing particles at 40mA intensity by assuming $\sim$ 30eV/ionized atom is required. This yields the result 1.5×10^{14}/sec, which is much less than the typical feed rates of $\sim 10^{17}$. This does not seem to be a problem.

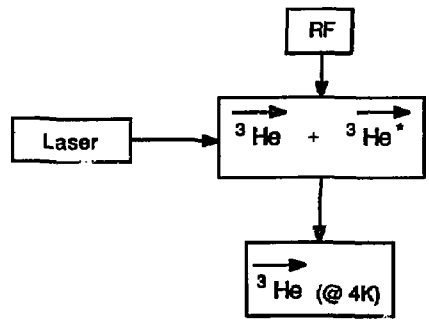

Figure 5. Polarized ^{3}He by Optical Pumping of Metastables

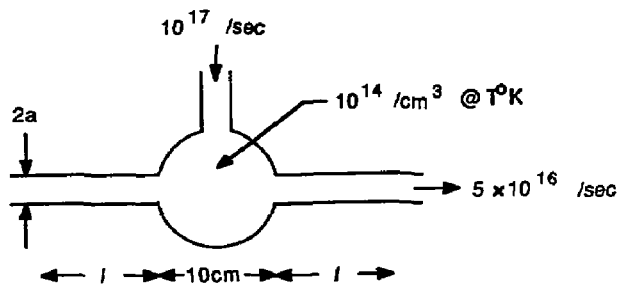

Figure 6. Bottle design for polarized gas target

The magnetic field of the beam is a rather subtle issue. We consider a hydrogen target, and a pulsed beam structure with pulse length τ and peak current I_p. The peak magnetic field in the vicinity of the beam is B_p and occupies about 10^{-4} of the target volume (this gives the number of affected atoms). If

$$B_p \gtrsim B_0 \tag{5}$$

(B_0 is the holding field) *and*

$$\tau \gtrsim (\gamma_B B_p)^{-1} \tag{6}$$

(γ_B is the Bohr frequency 1.7×10^7rad/G/sec), then there can be significant depolarization. The atoms will precess about the randomly oriented B_p by many radians within the affected volume. Thus the target will be depolarized in $\sim 10^4$ beam pulses. If $B_p \ll B_0$, the spins will only precess about B_0 with little depolarization. If $\tau \ll (\gamma_B B_p)^{-1}$, then an atom only precesses a small amount during the beam pulse, and then precesses about B_0, so a random walk takes place, and the depolarization is not severe.

At PEP with 40 mA beam, $B_p \sim 5$kG and $\tau \sim 10^{-10}$sec, so that a hydrogen target would be depolarized in $\sim 10^{-3}$sec (this calculation assumes 3 bunch operation). If the beam is spread out in hundreds of bunches, the peak magnetic field is reduced by ~ 100 and the target will retain its polarization. At Bates, where one only encounters the microstructure, the beam pulse is short compared to a rotation time so very little depolarization will occur. For noble gas targets such as ^{3}He, the frequency of spin precession is a factor of ~ 2000 smaller and these effects are not anticipated to be a problem.

Summary

In summary, it appears that several viable target technologies can be applied to the polarized internal target problem. Densities of 10^{15}/cm^2 seem quite feasible by several methods for H, D, ^{3}He, and other types of polarized targets. Many experimental groups are presently working on the construction of realistic targets and it seems likely that in the next year or two they will achieve the goals outlined here.

The depolarization due to the electron beam can be a problem when peak currents are high for long beam pulses. However, it appears that by spreading the beam over many bunches, the problem can be handled adequately. Nevertheless, one should consider these effects carefully in designing specific experiments.

Finally, it seems that with the anticipated target technology developments outlined here, and the very important physics issues that can be addressed by using that technology, more consideration should be given to the availability of appropriate facilities. The Bates PSR upgrade proposal explicitly provides for generation and maintenance of longitudinal polarization of the electrons at the interaction region in the ring. A detailed study of the requirements for a similar facility at PEP has not been carried out. B. Norum has worked on various schemes for maintenance of longitudinal polarization[15], but more work and some engineering need to be done to really assess the feasibility of these experiments at PEP. I hope that this issue will be addressed in the near future so that optimal utilization of these various target designs can become a reality at both facilities.

References

1. V. W. Hughes and J. Kuti, Ann. Rev. Nucl. Part. Sci. **33**, 611(1983).

2. K. H. Althoff *et al.*, "Radiation Resistance of Ammonia at 1 Kelvin and 2.5 Tesla" in *Proceedings of the 4th International Workshop on Polarized Target Materials and Techniques*, 1984, pp. 23-32.

3. W. Haeberli, AIP Conf. Proc. No. 128, American Institiute of Physics (New York) 1985, p. 251.

4. W. Gruebler, "Polarized Atomic Beams for Targets", in the *Proceedings of the Workshop on Polarized Targets in Storage Rings*, 1984, pp. 223-248.

5. W. Haeberli, Helvetica Physica Acta **59**, 597(1986).

6. W. Haeberli, private communication.

7. M. C. Green, "Design of a Tensor Polarized Deuterium Target Polarized by Spin Exchange with optically pumped Na", in the *Proceedings of the Workshop on Polarized Targets in Storage Rings*, 1984, pp. 307-342.

8. R. Holt, private communication.

9. D. Kleppner, AIP Conf. Proc. No. 80, American Institiute of Physics (New York) 1982, p. 138.

10. B. Blankleider and R. M. Woloshyn, Phys. Rev **C29**, 538 (1984).

11. T. Chupp, private communication.

12. M. Leduc *et al.*, Nuclear Science Appl. **1**, 1 (1983).

13. R. G. Milner, R. D. McKeown, and C. E. Woodward, to be published in Nucl. Instr. Meth.; R. G. Milner, in these proceedings.

14. S. Dushman and J. M. Lafferty, *Scientific Foundations of Vacuum Technique*. New York: J. S. Wiley and Sons, 1962, ch. 2, p. 91.

15. B. Norum, in these proceedings.

A LARGE ACCEPTANCE MAGNETIC SPECTROMETER FOR CEBAF

Bernhard A. Mecking

CEBAF
12070 Jefferson Avenue
Newport News, Virginia 23606

Abstract

A large acceptance magnetic spectrometer for the investigation of electron- and photon-induced nuclear reactions at CEBAF is described.

I. Introduction

The scientific program for the CEBAF 4 GeV electron accelerator aims at studying the structure and the motion of the nuclear constituents. The experimental equipment that has been proposed consists of focusing magnetic spectrometers with relatively small acceptances ($\Delta\Omega \simeq 10^{-3}$-$4\pi$, $\Delta p/p \simeq 10\%$) but high momentum resolution ($\Delta p/p \leq 10^{-4}$) and a large acceptance spectrometer. In the following report, the physics motivation for a large acceptance detector, the general design criteria and technical details of the detector will be discussed.

II. Physics Motivation

Electron scattering experiments have provided most of what we know about the structure of nuclei. However, our knowledge is limited to the electromagnetic structure of ground states and excited states of nuclei (explored in (e,e') experiments) and to some aspects of the nuclear single-particle structure (explored in (e,e'p) experiments). Very little is known about the many-body aspects of the nucleus, like e.g. the structure of bound nucleons, the origin of short-range correlations or the propagation of meson or nucleon resonances in the nuclear medium. The reason for this limitation is largely due to the technical features of the available experimental facilities:

a) The low duty-cycle of existing electron accelerators limits coincidence experiments to a narrow kinematical region where a sufficient signal-to-noise ratio can be achieved. It also makes the operation of large acceptance detectors inefficient because their counting rates are limited by the instantaneous background rates.

b) High accuracy in charged particle detection can only be achieved in small acceptance magnetic spectrometers.

Important technical developments have changed this picture

a) Electron accelerators with 100% duty-cycle are being built.

b) The quality and versatility of large acceptance detectors has improved dramatically.

A large acceptance detector will be required for the detection of multiple particle final states and for measurements at limited luminosity. Examples will be given for these experiments:

1. Multiple Particle Final States

For reactions involving several particles in the final state, high detection efficiency and a model-free analysis of the data can only be achieved by using a detector with a wide coverage of the angular and energy range for all outgoing particles. Examples for reactions which are of special interest for CEBAF are:

a) Hadronic final states in inclusive electron scattering off nuclei. Single arm electron scattering and (e,e'p) coincidence experiments have generated puzzles which can only be solved by a detailed investigation of the hadronic final state. Using a large acceptance detector, a bias-free investigation can be carried out by triggering on the scattered electron only. In the off-line analysis, the inclusive scattering cross section can then be decomposed into its hadronic channels. With increasing energy loss for the electron, the following phenomena can be studied:

(1) Electron scattering at large negative y (y= momentum component of the struck nucleon parallel to the direction of the virtual photon $\vec{q}$) yields higher cross sections than expected from standard nuclear models. The excess cross section can be explained by high momentum components in the nuclear wave function (→ emission of a single nucleon) or by interaction of the virtual photon with quark clusters[1] (→ emission of nucleon pairs or nucleon clusters like deuterons etc.). These two possibilities can be distinguished by detecting the hadronic final state.

(2) Quasi-free electron scattering off bound nucleons (requiring the hadronic final state to contain a recoiling nucleon around the direction of $\vec{q}$). A long-standing problem is the failure of the Coulomb sum rule to account correctly for the number of protons in the nucleus. This has been interpreted as a change of the nucleon form factor in the nuclear medium or as evidence for a direct interaction of the virtual photon with a six-quark bag.

(3) Multi-nucleon emission (requiring the hadronic final state to contain ≥2 nucleons). Two nucleon emission is assumed to be responsible for filling the dip between the quasi-free peak and the Δ-peak; there should also be strength in the Δ-region due to Δ-excitation with subsequent Δ-N interaction.

(4) Production and propagation of non-strange (Δ and higher nucleon resonances) and strange (Λ, Σ and their excited states) 3-quark objects in nuclei (requiring the hadronic final state to be a πN, ηN, ππN, KΛ etc. system in the appropriate mass range). Modifications of the properties of these resonances in the nuclear medium can be studied.

(5) Deep inelastic electron scattering. The aim of this program is to study the hadronisation of the struck quark in the region of large momentum and energy transfer and to understand how the inclusive cross section is built up out of individual hadronic channels.

Good particle identification for multiple particle final states down to very small angles ($\theta \leq 5°$) is important for this program.

b) Photo- and electro-excitation of the higher nucleon resonances. The harmonic oscillator quark model with QCD motivated additions (like a one-gluon exchange term) predicts, in addition to the known nucleon resonances, many states which have not been observed. A plausible explanation[2] is that these states decouple from the πN elastic channel and can, therefore, not be observed in elastic πN scattering. Since, on the other hand, the photocoupling is still strong, photoexcitation becomes the only available formation mechanism. Promising decay channels are:

$$\gamma N \to N^* \to \pi \Delta \to \pi\pi N$$
$$N^* \to N \rho \to \pi\pi N$$
$$N^* \to N \omega \to \pi\pi\pi N$$

c) Photo- (and electro-) excitation of vector mesons: $\gamma N \to V N$
($V = \rho, \omega, \phi$). An important goal of this program is to measure the γ-V coupling constant to get information on the hadronic content of the photon[3] and its variation with Q^2. In addition, the vector meson coupling to the nucleon can be determined. In boson exchange models of the nucleon-nucleon interaction, this quantity is of fundamental importance for the short range part of the NN-interaction.

d) Hyperon production and interaction: $\gamma N \to K \Lambda (\Sigma)$
The basic cross sections and coupling constants for these reactions have to be known for the analysis of the electromagnetic excitation of hypernuclei. Using the outgoing kaon to determine the Λ kinematics, a tagged low intensity hyperon beam can be generated. The production rates are large enough so that the decay and the interaction of the produced hyperon can be studied in the reactions:

(1) $\Lambda p \to \Lambda p$ (elastic scattering)
Because of its short decay length, the interaction of low momentum Λ's is best studied in the production target. Using the $\gamma p \to K^+\Lambda$ reaction for Λ production, about 500 Λ scattering events can be observed per day in a large acceptance spectrometer.

(2) $\gamma d \to K^+ \Lambda n$
This reaction allows also to study the ΛN interaction. Especially interesting is the search for long-lived S=-1 dibaryons; the masses of these objects have been predicted to be around the Σ-cusp[4].

(3) Radiative hyperon decay: $\Lambda^*(1520) \to \gamma \Lambda$ and $\Lambda^*(1520) \to \gamma \Sigma$.
Using a tagged photon beam, about $5 \cdot 10^5$ $\Lambda^*(1520)$ can be produced per day. The radiative decay width yields a sensitive test of the quark structure of the system.

e) Exclusive photoreactions on few-body systems

$$\gamma d \to N N \pi \qquad \gamma\, {}^3\mathrm{He} \to p p n$$
$$\to \Delta\Delta \to N N \pi\pi \qquad \to \pi \text{ (3N)}$$

The basic properties of bound 3-quark systems are best studied in few-body nuclei because the nuclear structure can be calculated exactly (at least in the framework of a non-relativistic potential model). Interesting questions are the off-shell behavior of the γNN^* vertex, the structure of the N^*N interaction, the existence of dibaryons[4] and of 3-body forces[5] in ^{3}He.

f) Interaction parameters of unstable particles.
The measurement of the A-dependence of total production cross sections for unstable particles will determine their total hadronic cross sections. In contrast to hadronic production reactions, the electromagnetic production offers the big advantage that the interaction of the incident projectile is so weak that the A-dependence of the cross section can be interpreted directly in terms of the interaction of the produced particle. Especially interesting is a comparison of the hadronic interaction of the $\eta(549)$ and $\eta'(958)$ which are supposed to be different mixtures of the same SU(3) states. The large η' mass is attributed to a sizeable exotic (gluonic or hybrid) component; this should show up as a difference in the hadronic behavior of η and η'[6].

A comprehensive study of the reactions b) - e) requires the use of polarized beams (longitudinally polarised electrons, linearly and circularly polarised photons) and polarised targets (polarised protons, vector- and tensor-polarised deuterons).

2. Limited Luminosity

The luminosity (target density * beam intensity) limitation can be due to the target or due to the beam.

a) Limitation due to the beam intensity.
Experimental programs using secondary particle beams (real γ, μ, π, K) need large acceptance coverage to collect sufficient count rate, independent of the number of particles in the final state. Especially important are tagged photon beam experiments where the intensity has to be limited to $\approx 10^7$ tagged γ/sec to keep accidental coincidences small.

b) Limitation due to the use of a polarised target.

(1) Polarised solid state hydrogen and deuterium targets.
For present solid state polarised targets (ammonia or deuterated ammonia) the luminosity has to be kept low ($\approx 10^{33} cm^{-2} sec^{-1}$ for tensor-polarised deuterium, $\approx 10^{35} cm^{-2} sec^{-1}$ for polarised hydrogen) in order to avoid a reduction of the polarisation due to beam heating and radiation damage.

(2) Polarised gas targets.
The disadvantages of polarised solid targets (high magnetic fields, nuclear background, low temperatures, limited to hydrogen and deuterium) can, in principle, be avoided by using a low density polarised gas target in combination with a high intensity electron beam. A dedicated electron storage ring would clearly be ideal for this program. However, the rapid progress in gas target technology will make experiments in the CEBAF external electron beam possible.

Compared to a storage ring, polarised gas target experiments in an external beam will have lower luminosity. However, there are also some important advantages:

a) No difficulties to achieve longitudinal electron polarisation.
b) Modest vacuum requirements → less differential pumping will be required.
c) Greater flexibility in the arrangement of the experimental apparatus.
d) Since the beam passes through the target only once, small beam losses are acceptable → thin

windows or very small diameter openings for bottle targets can be used.

These features should also make it possible to achieve higher target density than in a storage ring. A minimum density of $\simeq 10^{15}$ atoms/cm^2 is necessary to give reasonable counting rate. At this luminosity ($\simeq 10^{33}$cm^{-2}sec^{-1}), the combination of a polarised gas target and a large acceptance spectrometer will be useful for the investigation of reactions induced by quasi-real photons.

For ^{3}He, the densities already reached [8),9)] give a luminosity of several 10^{32}cm^{-2}sec^{-1}. This luminosity is high enough to allow for an extensive nuclear physics program especially with a large acceptance detector. Polarised ^{3}He targets can be used to investigate the structure of the 3-body system or as a source of polarised neutrons. The following experiments are of special interest:

(a) $^3\vec{He}(\vec{e},e'n)pp$ to determine the electric form factor of the neutron G_e^n.

(b) $^3\vec{He}(\vec{e},e'\Delta^0)pp$ to determine the C2/M1 ratio for the $n\rightarrow\Delta^0$ transition.

III. General Design Considerations

A large acceptance detector that is suitable for a broad range of photonuclear experiments using electron and photon beams should have the following properties:

1. Homogeneous coverage of a large angular and energy range for charged particles (magnetic analysis), photons (total absorption counters) and possibly neutrons.

2. Good momentum and angular resolution (→ magnetic analysis for charged particles).

3. Good particle identification properties in the momentum range of interest (→ combination of magnetic analysis and time-of-flight).

4. No transverse magnetic field at the beam axis (to avoid sweeping e$^+$e$^-$-pairs into the detector).

5. No magnetic field in the target region to provide for the installation of polarised (solid state or gaseous) targets requiring their own guiding field or other complicated equipment (cryogenic or track sensitive targets, vertex detectors etc.).

6. Symmetry around the beam axis to facilitate triggering and event reconstruction.

7. Large $\int B\cdot dl$ for forward going particles to account for the Lorents-boost.

8. High luminosity and count rate capability. The detector should operate in the difficult background environment encountered in electron scattering experiments. The background caused by a tagged bremsstrahlung photon beam ($N_\gamma \simeq 10^7$/sec) is much lower and will give no additional constraints.

9. Open geometry for the installation of a long time-of-flight path for neutron detection.

The consequences of these requirements for the choice of the magnetic field configuration have been studied. Transverse dipole, longitudinal solenoidal and toroidal fields have been considered. In all cases, the target has been assumed to be inside the magnetic field volume. The results are summarised in table I. To fulfill requirements #2 and #3, a large $\int B\cdot dl$ and a long time-of-flight (ToF) path is necessary. This can be achieved by all field configurations. The transverse dipole field is ruled out by #4 in combination with #8; it also violates #6. The solenoid which has become the standard magnetic field configuration at e$^+$e$^-$ colliders violates requirements #5, #7 and #9; therefore, it has to be ruled out. The only configuration that fulfills all requirements is the toroidal magnetic field. Since the ϕ-range for magnetic analysis is limited due to the coils, the detection efficiency for high multiplicity (> 4) final states will be low. However, in view of the present CEBAF program, it seems to be more important that the detector will be capable to complement the standard spectrometer set-up instead of trying to specialise it for high multiplicity reactions.

IV. The Large Acceptance Detector

The solution that has been proposed for the CEBAF *Large Acceptance Spectrometer (LAS)* is a superconducting toroidal magnet equipped with drift chambers, scintillation counters and shower counters. A description of the main features of the LAS will be given below.

1. Toroidal Magnet

The toroidal magnet consists of 8 coils arranged around the beam line to produce essentially a magnetic field in ϕ-direction. The size, field strength and coil shape were determined on the basis of the physics requirements (see table II for details). A perspective view of the magnet is shown in fig. 1, the coil shape is given in fig. 2. Each superconducting coil is embedded in a rigid coil case (about 4 meter long and 2 meter wide). Details of the coil layout, construction and protection have been worked out during the Workshop on CEBAF Spectrometer Magnet Design and Technology [10)]. The coils are housed in individual cryostats to facilitate manufacturing, assembly and testing. For the magnetic field calculations, the finite size of the coil was simulated by adding up the contributions of 4 discrete conductor loops (as indicated in fig. 2). The r-dependence of the magnetic field is given in fig. 3 for different z-positions. In a cylinder of 50 cm diameter around the axis the magnetic field is $\leq$10 Gauss. As demonstrated in fig. 4, the field lines are essentially circles (corresponding to a pure ϕ-field) with important deviations close to the coils. Figure 5 gives the integral over the ϕ-component of the field as a function of the particle emission angle θ. For forward going particles, the integral is about twice as high as for particles going sideways.

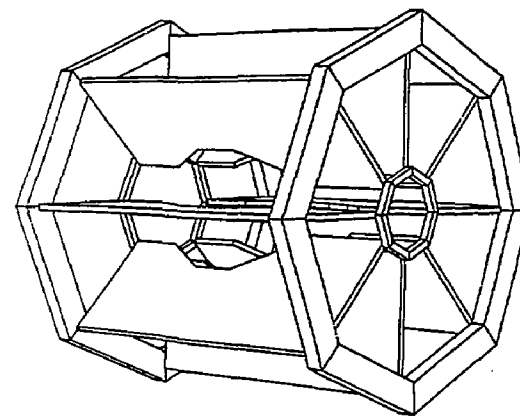

Figure 1 Perspective view of the toroidal magnet.

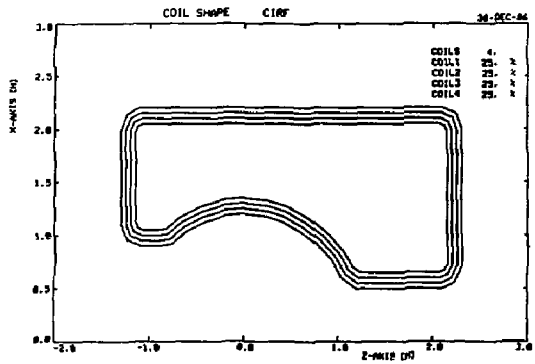

Figure 2 Coil shape. The superconductor is represented by 4 individual current loops.

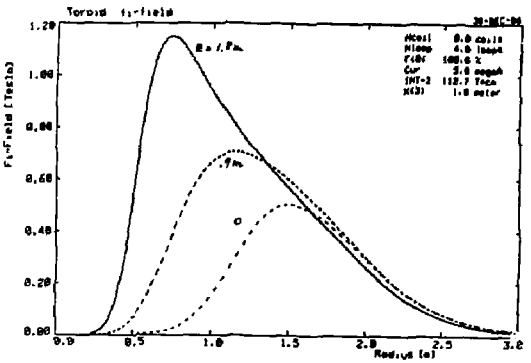

Figure 3 Radial dependence of B_ϕ for z=0, 0.9 m and 1.8 m (z=0 corresponds to the target position) and ϕ=0 (corresponding to the mid-plane between two coils).

The inner section of the coil is circular to avoid transverse (in ϕ-direction) motion of those outgoing particles that do not form a 90° angle with the conductor. This is demonstrated in fig. 6a for a rectangular coil shape (the current has been adjusted to make the total bend angle the same as for the circular coil). The transverse deflection depends on the angles θ (relative to the axis), ϕ (azimuthal angle) and on the particle momentum and polarity. The resulting loss of events will be difficult to correct. By using a circularly shaped coil, the angle of incidence can be kept normal to the coil, independent of θ. As shown in fig. 6b, the transverse particle motion is very much reduced.

2. Particle detection system

The proposed particle detection system consists of drift chambers to determine the track of charged particles, scintillation counters for the trigger and for time-of-flight, and shower counters to detect photons. A side view of the detection system is given in fig. 7, a cut in the target region in fig. 8. Note that all 8 segments are individually instrumented to form 8 independent magnetic spectrometers. This will facilitate track reconstruction in a large background environment.

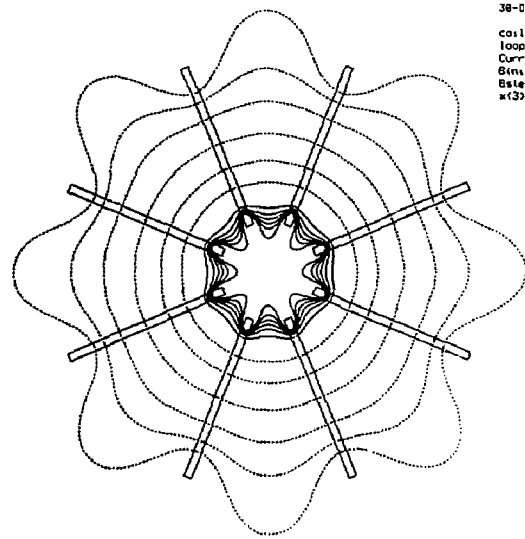

Figure 4 Field lines (giving the direction of the magnetic field) for z=1.8m (forward part of the magnet.

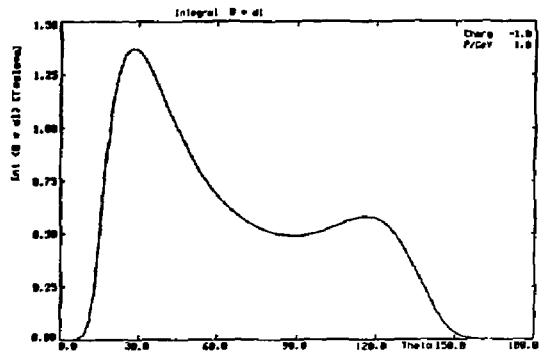

Figure 5 θ-dependence of the integral $\int B_\phi \cdot dr$. θ is the particle emission angle relative to the axis; the target has been assumed to be at z = 0 m. Particle momentum 1 GeV/c.

2.1 Tracking chambers

Charged particles are tracked by planar wire chambers. Each planar chamber consists of 4 layers of sense wires stretched in ϕ-direction. The position of the hit along the sense wire will be determined by charge division.

2.2 Scintillation Counters

The outer planar drift chambers are completely surrounded by scintillation counters. The barrel counters consist of 8*8 counters, each about 400 cm long, 20 cm wide, and 5 cm thick. The counters are viewed by 2" phototubes at both ends for improved timing and position resolution. The endcaps are covered by 8*4 pie-shaped counters, each viewed by one photomultiplier. Because of the high rate, the

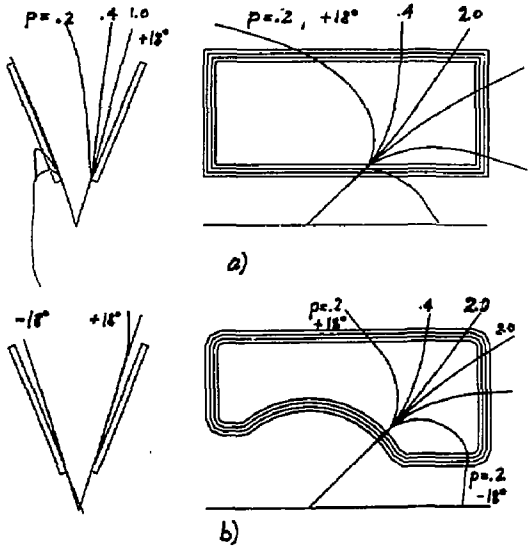

Figure 6 Transverse particle deflection in toroidal magnets for particles with θ=40°, p= 0.2, 0.4 and 2.0 GeV/c and ϕ=±18° (ϕ=0 corresponds to the mid-plane).
a) rectangular coil shape. Particles that are deflected away from the axis by the ϕ-component of the field are bent back to the mid-plane; particles that are deflected away towards the axis are bent towards the coils and are lost.
b) coil with a circular inner section. Note that there is no transverse motion at inner edge of the coil.

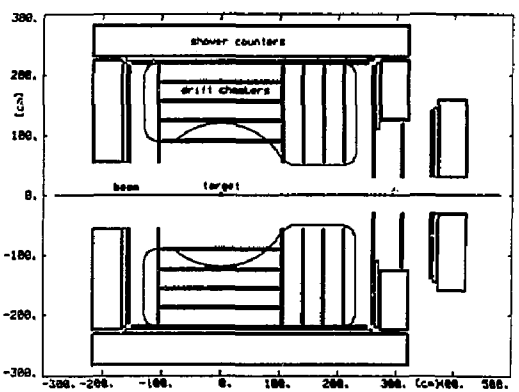

Figure 7 Transverse view of the particle detection system.

forward endcap counters are split into two rings: one ring at large and one at small angles. The scintillation counters serve the double purpose of providing the trigger and the time-of-flight information. Also, a fraction of the high energy neutrons (≃5%) will interact in the scintillation counters and will thus be detected.

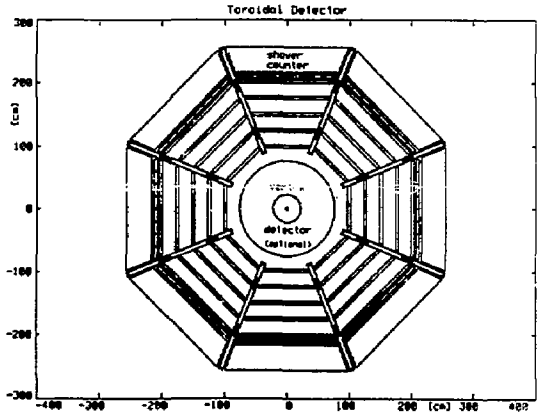

Figure 8 View of the detection system in the direction of the beam for z=0 (target position).

2.3 Shower Counter

The detector is surrounded by shower counters for the detection of showering particles like high energy photons from the decay of hadrons like π^0, η, η' etc. Due to the size and the weight of the counter (≃80 m², ≃100 tons), inexpensive materials and construction techniques have to be used (e.g., a sandwich of lead plates interleaved with active material like scintillators or gas detectors). The expected energy resolution is $\sigma/E_\gamma \leq .13/\sqrt{E_\gamma(\text{GeV})}$.

3. Maximum Luminosity

In an electron beam, the main background is caused by electron-electron scattering and wide angle bremsstrahlung. At a luminosity of $10^{33}cm^{-2}\cdot sec^{-1}$, the rate of Møller scattered electrons is estimated to be of the order of $5\cdot10^7 sr^{-1}\cdot sec^{-1}$. Since the energies are low, the electrons are bent back even by the small magnetic fringe field. A fraction of the electrons will, however, radiate photons that will subsequently generate spurious signals in the chambers. The total integrated flux of photons due to wide angle bremsstrahlung has been estimated to be of the order of $10^6 sr^{-1}\cdot sec^{-1}$ (luminosity $10^{33}cm^{-2}\cdot sec^{-1}$, E_e = 2 GeV, ^{12}C target, all photons above 10 keV). Compared to these electromagnetic background rates, the hadronic rates are nearly negligible. The total rate of electrons scattered into the angular range $15° \leq \theta \leq 150°$ due to hadronic processes is less than 1000/sec. The total hadron rate (mainly produced by by quasi-real photons) is ≃$5\cdot10^6$/sec. On the basis of these counting rate estimates and also due to past operating experience of a large acceptance detector at an electron accelerator[11], one can expect that the detector can be operated at a luminosity of ≃ $10^{33}cm^{-2}\cdot sec^{-1}$ (corresponding to a 1 μA electron beam on a 1 mg/cm^2 target).

There will be no difficulties to operate the detector at tagged photon beam intensity (≃10^7 γ/sec). (At this photon beam intensity, the hadronic production rate is about the same as in electron beam

with a luminosity of $10^{33}cm^{-2}sec^{-1}$; however, due to the lack of Møller scattered electrons the background rate is much lower.)

4. Track Resolution

The track resolution has been calculated taking the position resolution of the chambers and multiple scattering into account. The momentum resolution $\Delta p/p$ for known vertex position is shown in fig. 9 for 1 GeV/c particles as a function of the particle emission angle θ. The momentum resolution reaches 0.6 % in the forward direction; in the central part, it drops to 1.5 % due to the decreasing $\int B \cdot dl$. For known vertex position, $\Delta p/p$ is dominated by multiple scattering; therefore, it is nearly constant in the whole momentum range of interest. The initial angle can be determined with an uncertainty $\Delta\theta \leq 1$ mrad for 1 GeV/c particles (2 mrad for 0.2 GeV/c).

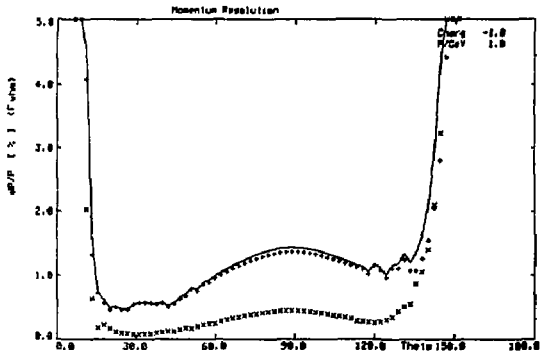

Figure 9 Momentum resolution $\Delta p/p$ (FWHM) as a function of the particle emission angle θ for $p = 1$ GeV/c. The vertex is assumed to be known.
- x contribution of the chamber position resolution
- + multiple scattering contribution
- — sum of both contributions.

5. Particle Identification

The combination of momentum and time-of-flight (a time resolution of $\Delta\tau \approx 200$ psec (sigma) was assumed) gives clean particle identification over a wide momentum range. In the forward direction, pions can be separated from kaons up to 1.5 GeV/c, the limit for kaon/proton separation is 2.5 GeV/c. π/e, π/μ and μ/e separation can be achieved by using the pulse height in the shower counter in addition.

6. Acceptance

Using a Monte Carlo technique, random multiple particle events were generated to determine the acceptance. Examples for single events as they would be reconstructed and displayed on-line by the detector single-event display are presented in figs. 10 and 11. For the calculation of the acceptance, the θ-range of the detector was taken to be $15° \leq \theta \leq 150°$, 20% of the ϕ-range was assumed to be obstructed by the coils. In addition, cuts in the kinetic energy of the emitted particles were applied to account for detection thresholds: $T_\pi \geq 40$ MeV and $T_p \geq 50$ MeV. For the process $\gamma + p \rightarrow F35(1975) \rightarrow \pi^- + \Delta^{++} \rightarrow \pi^- \pi^+ p$ about 60% of the all $\pi^- \pi^+ p$ events are accepted if only θ and T_{min} cuts are used. The addition of the ϕ-cuts reduces the total detection efficiency to 30%.

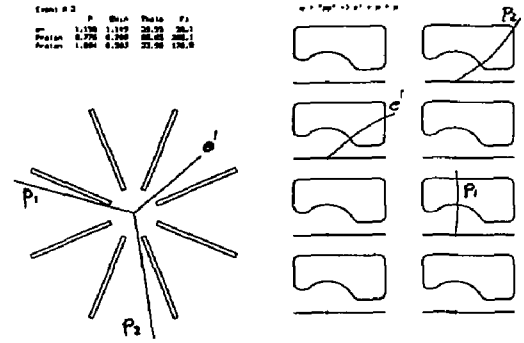

Figure 10 Single event display for a Monte Carlo generated event from the reaction (e,e'pp). $E = 2$ GeV, $\theta = 40°$. The left hand side of the display shows a view of the event in the direction of the beam, the r.h.s. presents the tracks in the 8 individual segments.

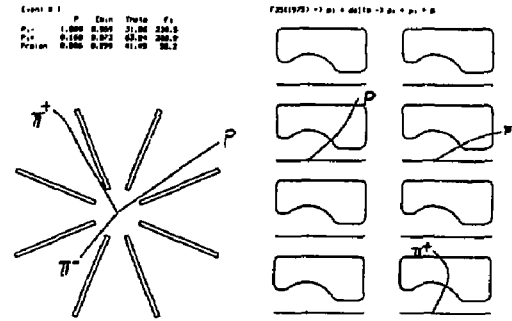

Figure 11 Single event display for a Monte Carlo generated event from the reaction $\gamma\ p \rightarrow N^* \rightarrow \pi^- \Delta^{++} \rightarrow \pi^- \pi^+ p$ induced by real photons. $E_\gamma = 1.8$ GeV.

7. Counting Rate Examples

a) (e,e'X)
The counting rate for have been estimated for $^{12}C(e,e')$ at $E = 2$ GeV and $\theta_e = 15°$. A luminosity of $10^{32}cm^{-2}sec^{-1}$ (per nucleon) and 80% ϕ-coverage have been assumed. The total rate of electrons scattered into the angular interval 14°-16° and the energy interval (1.3-2.0) GeV is ≈100/sec.

b) photon induced reactions
Combining a tagged photon beam with an intensity of 10^7 γ/sec and a hydrogen target of 0.5 g/cm² (≈7 cm liquid) results in a total hadronic production rate of ≈400 events/sec ($E_\gamma = 2$ GeV, $\sigma_{tot} = 140$ μb).

8. Layout of End Station B

The detector will be located in end station B. A possible layout of the end station is shown in fig. 12. End station and beam dump are fully shielded to allow for experiments using a high intensity beam on a thin gas target (also to allow for a second high

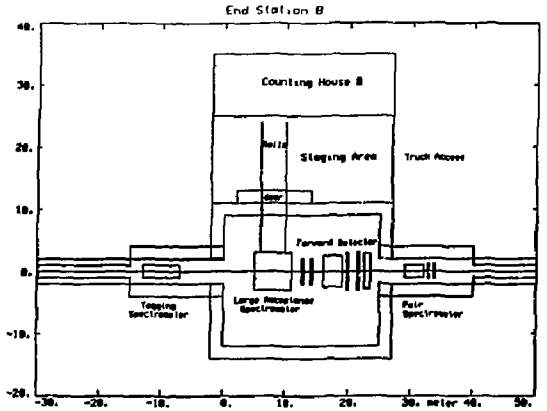

Figure 12 Proposed layout of the low intensity end station B.

intensity experiments in this area). The detector can be moved on rails into an adjacent staging area for extended service. For photon experiments, a vertically deflecting tagging spectrometer is located in an enlarged tunnel section.

V. Summary

A large acceptance magnetic spectrometer has been proposed for the investigation of electron- and photon-induced nuclear reactions at CEBAF. The magnetic field is generated by eight toroidal coils. Charged particles are tracked using scintillation counters and drift chambers; high energy photons are detected by shower counters. The spectrometer will be indispensable for the investigation of multiple particle final states from (e,e'X) reactions and from the decay of excited qq and qqq-states. In addition, it will provide the highest possible counting rate for experiments in which the luminosity is limited due to low target density or low beam intensity.

References

1) H.J. Pirner et al., Phys. Rev. Lett. 46 (1981) 1376.

2) N. Isgur, Proc. of the 1984 CEBAF Summer Workshop, Newport News, Virginia, ed. by F. Gross and R. R. Whitney, p. 199

3) T.H. Bauer et al., Rev. of Mod. Physics, 50 (1978) 261

4) M.E. Sainio, AIP Conf. Proc. 150 (1986) 886

5) M.P. Locher et al., Adv. in Nucl. Phys., Vol. 17 (1986) 47

6) I. Sick, Lecture Notes in Physics 260 (1986) 42

7) F. Lenz, Nucl. Phys. B279 (1987) 119

8) R.D. McKeown and R.G. Milner, 1985 CEBAF Summer Study, RPAC I, p. 12-45

9) R.G. Milner et al., private communication, submitted to Nucl. Instr. and Meth.

10) P.C. Marston: Report of the Working Group on the Large Acceptance Spectrometer, Proc. of the Workshop on CEBAF Spectrometer Magnet Design and Technology, Newport News, April 1988, ed. by J. Mougey and P. Brindza

11) L.A. Ahrens et al., Nucl. Instr. Meth. 173 (1980) 537.

Table I: Evaluation of magnetic field configurations for a large acceptance spectrometer to be used for electron- and photon-induced reactions

(+ denotes advantage, - drawback)

	Dipole	Solenoid	Toroid
Large solid angle	(+)	+ +	(+)
No transverse field	- -	+	+
No field at the target	- -	- -	+
Symmetric configuration	-	+ +	+
Open mechanical structure	(+)	-	+
Large $\int B \cdot dl$ at small angles	+	- -	+
High luminosity capability	-	+	+

Table II: Design considerations for the toroidal magnet

1) Size

time-of-flight path required for particle identification via momentum and β

$L \geq 2$ m for particles going sideways
$L \geq 3$ m for particles going forward
→ diameter $\simeq 4$ m, total length $\simeq 4$ m

2) Field level

a) small destabilizing forces
b) momentum resolution $\Delta p/p \simeq 1$ %
→ $\int B \cdot dl \simeq .5$ T·m → Amp·turns $\simeq 5 \cdot 10^5$

3) Number of coils

a) 4-fold symmetry for polarised target experiments
→ 4, 8, 12, ...

b) low obstruction of the ϕ-range due to the coils
→ 8 coils

4) Coil shape

a) no transverse focusing/defocusing effects due to r-and z-components of the field
→ circular inner coil shape

b) large $\int B \cdot dl$ in the forward direction
→ asymmetric coil shape with longer forward part

NUCLEAR PHYSICS AT PEP
RECENT RESULTS USING THE TIME PROJECTION CHAMBER

S. O. Melnikoff
Lawrence Livermore National Laboratory
University of California
P.O. Box 808 L-421
Livermore, Calif. 94550

Abstract

A preliminary result on Bose-Einstein correlations is reported using the *PEP-4* Time Projection Chamber facility. The data, from scattering 14.5 GeV electrons on nuclei, was taken at the Stanford Linear Accelerator Center positron-electron (*PEP*) storage ring. Bose-Einstein (BE) correlations were measured from events having identified like-sign pion pairs. The particle identification and tracking capability of the Time Projection Chamber (TPC) was used to select like-sign pion pair events. The resulting correlation function for the data was fitted to a gaussian form $R(q) = 1 + \lambda exp(-q^2\sigma^2)$ where q is the relative four-momentum difference of the pions. The fitted value to the chaoticity is $\lambda = 0.37 \pm 0.19$ and $\sigma = 1.37 \pm 0.41$ *fermi*. This result agrees with that from e^+e^- annihilation data taken with the TPC.

We explain the operation of the TPC and the analysis of the data used. The feasiblity of similiar detectors for doing high energy electron scattering on nuclei at *PEP* is briefly discussed.

Introduction

During the past year we have initiated a small program to study the feasibility of nuclear physics experiments at the PEP colliding beam facility[1] As part of this LLNL study small amounts of deuterium, or argon or xenon gas were infused into the PEP ring, in the vicinity of the TPC-2γ interaction region. The data from the dedicated gas-bleed and that as a result of electron scattering from residual gases already present in the ring (from previous run cycles) was analyzed to obtain a first look at possible physics topics that could be studied at a future nuclear physics facility. Such a facility could address the interest in looking at exclusive final states in inelastic electron scattering. Experiments at PEP can run at energies up to 14.5 GeV, well into the region of Bjorken scaling.

While our major concern is with the data from the TPC-2γ detector, for future experiments, a second important topic is in the area of detector design. The general feasibilty of any proposed detector facility must be addressed first, before a detailed design study based on the particulars of the physics. The advantage the nuclear physics community has at PEP is that a generation of working detectors have been in operation for more than five years. A study of these detectors, in particular the TPC-2γ facility, provides first answers to the questions of what works at PEP and what is unrealistic.

Our Bose-Einstein correlation result, which uses all the major components of the TPC-2γ facility, makes two important points. First that despite being optimized for high energy physics running, a TPC-like detector works well in a nuclear physics environment. Secondly the scale of any proposed future experiment will be closer to that of high energy physics than traditional nuclear physics experiments.

The Time Projection Chamber

All of our data and resulting measurements presented are from the *PEP-4* detector. We will summarize the design and operation of the detector facility with respect to those features relevent to our results. More complete reviews are available elsewhere[2-5], along with a good summary of the *PEP-9* or forward spectrometer[6].

Goal and Objectives

The *PEP-4* facility has been designed and built with three definite objectives:

1. Efficient charged particle detection and momentum measurement over a large fraction of the entire solid angle.
2. Identification of charged particles by means of energy loss measurements over the accepted momentum range.
3. Detection of energetic photons over a comparable solid angle with capabilities for reconstrution of neutral pions.

The forward detector system, or *PEP-9* , was design to observe or *tag* the outgoing electrons (positrons) in photon-photon or *two-gamma* interactions. These generally scatter at small angles with respect to the beam axis and are outside the *PEP-4* detector volume. We used the *PEP-9* system to tag the scattered electron from nuclei.

Geometry of the System

To achieve the design objectives listed above and to promote modularity during the construction phase of the facility, the *PEP-4* detector is divided into six subsystems. The entire central detector system is cylindrically symmetric about the e^+e^- beam axis; the forward spectrometer is symmetric about the interaction midplane perpendicular to the beam axis. Figure (1) is a schematic of the facility showing one arm of the forward spectrometer. Radially outward from the e^+e^- interaction point the six subsytems are:

1. An inner drift chamber (IDC) which wraps around the beam pipe, used as a fast pretrigger chamber.
2. The central detector, the *Time Projection Chamber* or *TPC* .
3. A solenoidal 13.25 KGauss superconducting magnet. The momentum resolution achieved was $(\sigma p/p)^2 = (1.5\%)^2 + (0.65\%p)^2$ $(p \text{ in } GeV)$.
4. A second cylindrical outer drift chamber (ODC) which encircles the magnet. The spatial resolution of the two drift chambers was 150–250 microns.
5. A set of electromagnetic calorimeters, surrounding and capping the magnet. These are follwed in radius by an iron superstructure forming the flux return yoke and hadron absorber layers for the muon detection system.

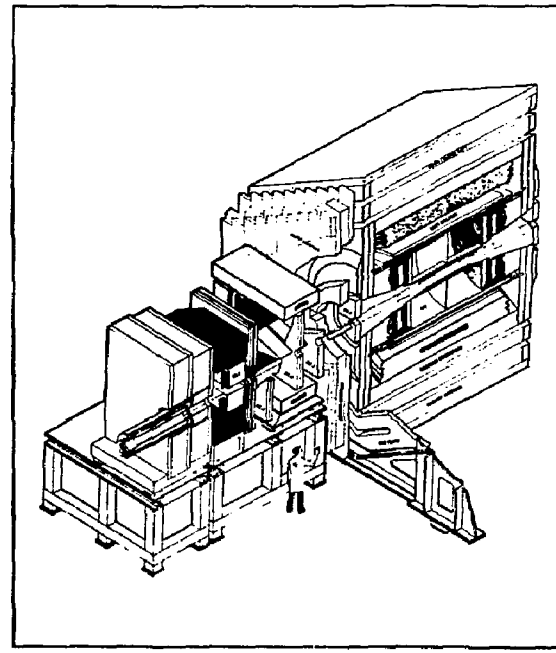

Fig. 1.1 Artist schematic view of the TPC-2γ facility. One arm of the forward spectrometer is shown here.

The rms energy resolution of the calorimeter using 14.5 GeV Bhabha events was $\sigma_E = 14\%\sqrt{E}$ $(E \text{ in } GeV)$.

6. A muon detection subsystem consisting of proportional drift tubes layered between sections of iron absorber material. The spatial resolution of the muon chambers was 700 microns.

Operation of the TPC

The central detector of the TPC-2γ system is the time projection chamber. The device is a large cylinder two meters long and two meters in diameter. The chamber is filled with a gas mixture of 80% Argon and 20% Methane and has operated at 8.5 atmospheres of pressure.

The volume is divided into symmetric halves by a conducting mesh membrane which is held at − 75 Kilovolts with the endplanes at ground voltage. A series of conductive rings at the inner and outer radii of the chamber are the components of the high-voltage *field cages* which produce a very uniform axial electric drift field, while a solenoidal magnet introduces a four kilogauss uniform magnetic field in the same direction. The ends of the cylindrical volume, the *endcaps*, are the detection planes for the *TPC* .

The uniform electric field in the drift volume is achieved by the field cages which step down the central membrane potential for a constant velocity drift field throughout the *TPC* volume. This is done by a set of $G-10$ fiberglass cylinders at the inner and outer radius on which $0.5mm$ wide conductive rings are etched. Design tolerances maintained a precision of better than 0.01% in the resulting electric field.

As pictured in Figure (2) each endcap is physically divided into six identical multiwire proportional chambers, the *sectors*. Each sector reads out information on a wedge of space formed by its boundaries in r and ϕ and the central membrane along the beam axis, a detection volume of approximately $0.51m^3$.

During operation, charged particles from an e^+e^- interaction will pass through the *TPC* volume. These particles will ionize the gas along their track length. On the average 200 primary ion pairs per $4mm$ of track are produced. The ionization electrons will drift in the direction of the electric field to the endplane detectors. The endplanes simultaneously do both the spatial tracking and energy loss measurement.

A sector detects incoming drift electrons with a set of 185 twenty micron diameter gold plated tungsten sense wires (of which 183 are read out). These are alternating with $75\mu m$ field shaping wires. Four millimeters underneath the sense wires, the copper clad endplane has been etched to form fifteen $7.5mm$ wide rows. The centers of the rows are spaced approximately equal distances apart, the first and last at 23.6 and $95.2cm$ from the interaction point. Each row is segmented into $7.5mm$ squares, called *pads*. These will see an induced signal from the sense wires. Figure (3) illustrates the layout of the wires and pads. An additional shielding plane of wires $7.5mm$ above the cathode plane is held at ground voltage.

Arriving clusters of ionization in the neighborhood of a wire will undergo charge avalanching which in turn induces a signal on some of the pads directly under the particular wire. Signal gains are typically 10^3 with sense wire voltages of $3.4kV$ and field wire voltages of +700 volts.

From the pads two coordinates, *xy* (in the sector frame), of tracking information are determined. The *xy* coordinates come from the center of a parabolic fit to the pads having signals. A third coordinate along the beam axis, Z, is determined by measuring the time it takes for the electrons to drift to a sense wire. Knowing this time and the constant drift velocity of the electrons in the uniform electric field in the gas mix allows us to *project* back in Z to find the original creation position of the electron-ion cluster. The term Time Projection Chamber originates from being able to use the available drift time information.

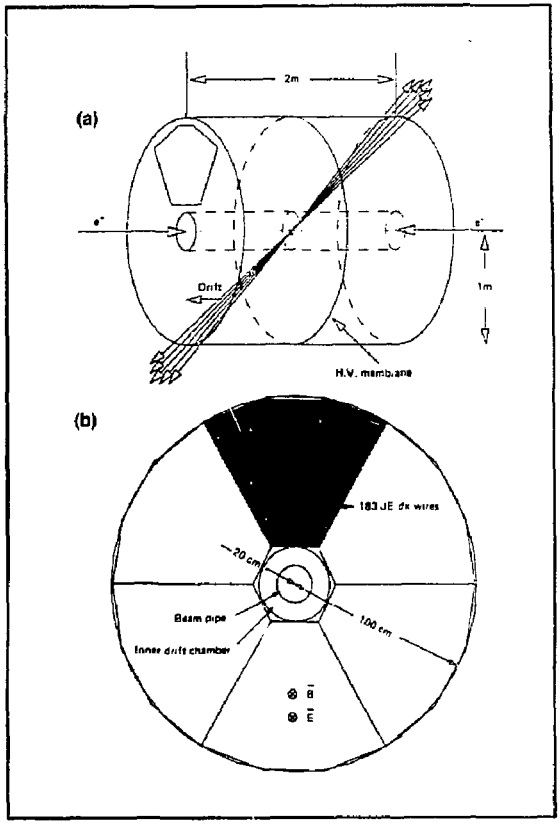

Fig. 1.2 *(a) Schematic of the TPC volume. (b) View of one TPC endcap showing the sectors and the dE/dx wires. The magnetic bending and electric drift fields are parallel (into the page).*

Particle Identification with the *TPC*

The *TPC* identifies a particle by measuring its ionization energy loss (proportional to the sense wire signal amplitude) through the gas volume and its momentum through the magnetic field's curvature of the track The average energy loss per unit length, dE/dx , is a well-defined function of a particle's velocity, given by the Bethe-Heitler relation[7]

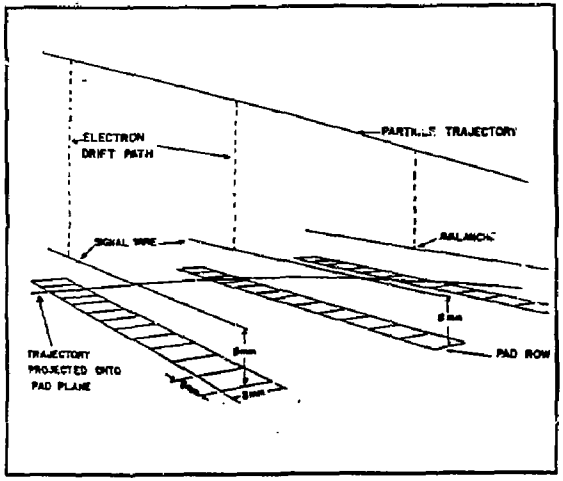

Fig. 1.3 *Detail of the TPC endcap wire/pad geometry showing placement of the cathode pads and the central wire over the pad rows. Pictured is one particle trajectory and its projection onto the pad plane.*

$$< dE/dx > \approx \frac{4\pi\eta Z^2 e^2}{m_e c^2 \beta^2} \left\{ ln\left(\frac{2m_e\beta^2\gamma^2}{I^2 + (\hbar\omega)^2\beta^2\gamma^2} \right) - 2\beta^2 \right\} \quad (01)$$

where

m_e is the mass of the electron

I is the effective ionization potential for the material

η is the electron density of the material

ω is the plasma frequency of the material.

For a $< dE/dx >$ resolution of better than 4% the TPC samples a track's ionization energy loss up to a maximum of 185 times. In practice a 'truncated mean' is used, being the mean for 65% of the sample having the smallest energy loss. Figure (4) shows the experimental energy loss curves as a function of momentum. The minimum of the curve is called minimum ionizing (and the momentum around this point the minimum ionizing region). Seen are the different mass bands corresponding to electrons, pions (and muons), kaons and protons along with ambiguous *crossover* regions between particle types. Pion and muon bands were not resolvable due to the momentum resolution obtained and their small (33.9 MeV) mass difference. The high and low momentum regions with respect to minimum ionizing are referred to as the one–over–beta–square and relativistic–rise regions respectively.

To quantify the probability of identifying a specific particle type, a dE/dx χ^2 is defined. For a measured track momentum P_x the χ^2_x is the distance squared between the measured dE/dx point and the theoretical curve for the x particle type. The lowest χ^2_x determines the identification of the particle.

Since TPC particle identification is dependent on conditions in the device that are time dependent (for example the Argon-Methane gas pressure) calibration plays an important part in the detector's performance. To calibrate the sectors, before final assembly a complete gain map of each was done. Later, run-time three point calibrations are used to correct it for any variations. Calibration of the absolute gain from the wires is done *in situ* at three points along a wire with Fe^{55} sources. These were located underneath the endplance and switchable, irradiating the wires through holes drilled in the endplanes.

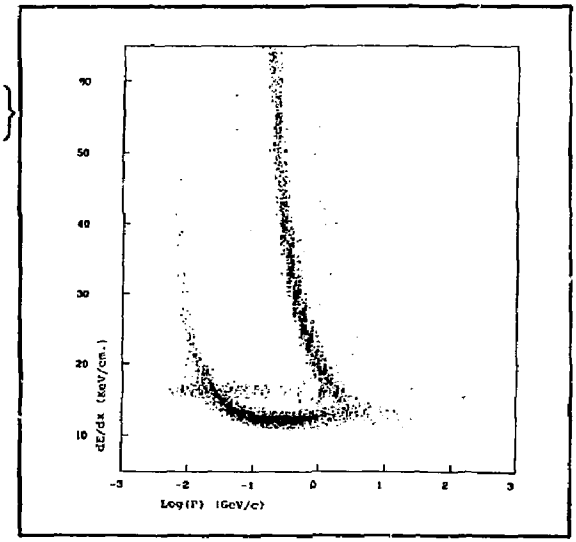

Fig. 1.4 *Plot of energy loss (dE/dx) vs. momentum for our data sample. Energy loss curves showing the presence of electrons, pions, kaons and protons are seen.*

First Test Run

Our first test of the gas-bleed system was done in March 1986. This was a live test of gas injection at PEP with beams and all detectors on. The first segment of the test was a 24 hour run with D_2, raising the pressure in the PEP beamline in the neighborhood of the TPC from 10^{-9} to $(3.0)10^{-7}$ *torr*. This was followed by a 16 hour run using Argon followed by an 8 hour run with Xenon. The neighborhood pressure in the ring for the two heavier gases was

raised to $(2.0) - (5.0)10^{-8}$ *torr*.

To trigger the detector during this test we required the following. An identified electron *tag* in the forward spectrometer along with a track in the IDC and a set of ionization clusters or *ripple* in the TPC forming a track. Lacking a charged track trigger in the TPC we also accepted as a trigger hits in the 2γ muon chambers or 2 *GeV* of energy deposited in the TPC poletip calorimeter. The event rate using this set of trigger configurations was $6-8$ sec^{-1}.

We collected approximately 30 tapes of raw data for further analysis or around 10^5 events. In addition to this data exists around 2000 tapes of raw data taken during past run cycles of high-energy e^+e^- physics running. About 10–20% of this data are events with electrons or positrons scattering from the residual gas in the PEP beamline. These tapes were separately analyzed from what we call the dedicated runs where gas was injected into the beampipe.

Data Analysis and Scanning

Data Selection

In order to filter out internal target (nuclear) physics from the e^+e^- or 2-γ processes also present in the data a set of offline selections were imposed:

1. The event had to have a associated $e^{\pm}$ tag
2. The event vertex had to be offset from the e^+e^- interaction point. We required $80.0 > Z_{vertex} > 6.0$ *cm*.
3. The tracks in the event had to cluster around the event vertex. This filtered out events that triggered the detector but had a second interaction occur shortly afterwards (during the TPC detector sensitivity time), where both were readout and written to tape as a single event.
4. Any event was also kept even if Z_{vertex} was inside the offsets when there were protons present in the event. These cuts left us with around $(3.0)10^4$ events for scanning and full analysis from the test run.

Event Scanning

As an introduction to the TPC-2γ data analysis system OASIS (originally OASYS for Offline Analysis SYStem), we did a selection and event-by-event hand scan of a selected sample. OASIS is a software interrupt driven program allowing for single event analysis/reanalysis applying different physics cuts to the data. A sampler of interesting events was compiled. This sampler included examples of quasielastic scattering, Δ production, associated strangeness production, deep-inelastic scattering and a unique example of massive target fragmentation from a Xenon nucleus.

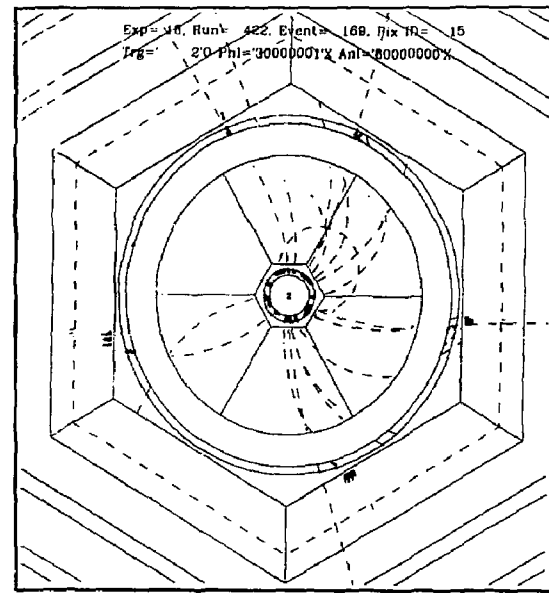

Fig. 1.5 *Example of an event as seen by the PEP-4 system. In this case, possible target fragmentation of an electron on a Xenon nucleus.*

Figure (5) shows an end-on and radial view of the high multiplicity xenon target fragmentation event. Figure (6) shows a plot of DeDx vs. momentum for the same event. In this figure each track is labeled by its track number and enclosed by a 2σ error ellipse. The theoretical DeDx curves for different particle masses are also plotted.

What is clear from this event is that to study such phenomena (*i.e.* looking at different exclusive final states) will require detectors capable of tracking and particle identification like a TPC.

Bose Einstein Correlations

The renewed interest in Bose-Einstein correlations has prompted recent investigations in e^+e^- an-

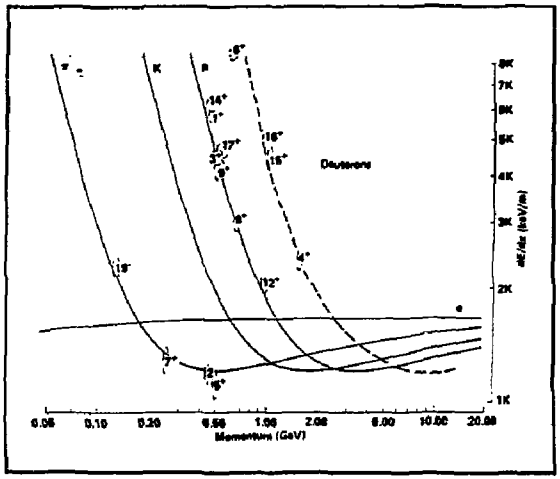

Fig. 1.6 *The dE/dx vs. Log(p) plot for the particles in the above Xenon event. Along with numerous protons, four deuterons are seen.*

nihilations and hadronic reactions[6-9]. The general ideas as applied to particle physics are an outgrowth of the formulation by Hanbury-Brown and Twiss (HBT) in radio astronomy. In high energy particle physics the acronym GGLP (Goldhaber-Goldhaber-Lee-Pais) is used to reference this correlation phenomena, along with the terms intensity interferometry or second-order interferometry.

BE correlation analysis is a tool to study the space-time development of particle emitting souces in high-energy interactions. Since boson wave functions are symmetrized according to Bose-Einstein statistics, a boson source (for instance emitting pions) will exhibit an enhancement for pions with small relative momenta. Quantitatively a two particle correlation function $R(p_1,p_2)$ is defined:

$$R(p_1,p_2) = \rho(p_1,p_2)/\rho_o(p_1,p_2)$$

where p_1 and p_2 are the pion four momenta and ρ, ρ_o are the pion densitiess for a correlated and uncorrelated (no BE statistics) sample respectively. The parameter $q = p_1 - p_2$ GeV, the relative four momenta of the pions, is defined so that $R(q)$ is proportional to the fourier transform of the emitting source's space time distribution. For sources that have a lifetime τ and have a gaussian distribution in space $S(\bar{r}) \propto exp(-r^2/2\sigma^2)$ then $R(\bar{q}) = 1 + exp(-\bar{q}^2\sigma^2)/[1 + (q_o\tau)^2]$. Here $\bar{q} = \bar{p}_1 - \bar{p}_2$ GeV/c is the pion three momenta difference and $q_o = |E_1 - E_2|$ GeV. In our analysis an exponential form $R(Q^2) = 1 + \lambda exp(-Q^2\sigma^2)$ where $Q^2 = \sqrt{p_1 - p_2)^2}$ GeV was used.

Analysis Procedure

For our study the higher statistics sample of beam-residual gas events was used. We required

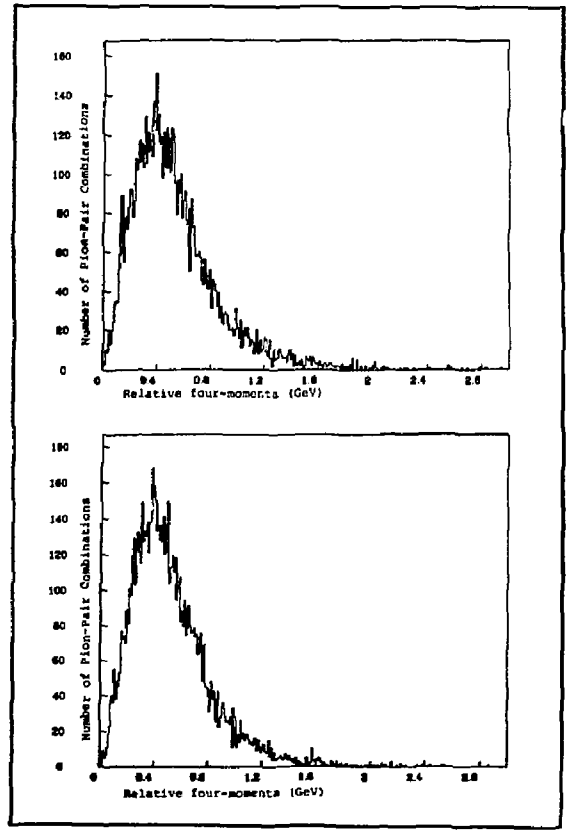

Fig. 1.7 *The pion density $\rho(p_1,p_2)$ as a function of Q^2 GeV. The top plot is for the correlated sample, the bottom for the uncorrelated sample.*

events having at least two like-sign pions identified in the TPC. A minimum momentum of 150 MeV/c was required, the cutoff for pions to track into the TPC volume. This helped filter out low momenta conversion pairs where an electron was misidentified as a pion. The sample thus obtained was scanned for failures in the track pattern recognition progam. Any *bad* events where, for example, a single track was divided into two (hence forming a pair of tracks having very small relative momenta and introducing a bias into our results) are rejected. Figure (7) is a plot of $\rho(\bar{p}_1,\bar{p}_2)$.

For $\rho_o(\bar{p}_1,\bar{p}_2)$ the pion density in the absence of BE correlations, event mixing was used. Event mix-

ing uses a pion from one event combined with a pion from a different (and independent) event, insuring no correlations between the pions. The correlation function $R(\bar{q})$ is then the ratio of the correlated to uncorrelated pion densities.

Results

Figure (8) is a plot of the correlation function $R(Q^2)$ An enhancement is seen at $Q^2 < 0.25$. Fitting to the exponential form above we get $\lambda = 0.37 \pm 0.19$ and $\sigma^2 = 1.37 \pm 0.41$ *fermi*. However even with our larger data sample this result is still statistics limited. We also looked at $R(Q^2)$ as a function of $P = |\bar{p}_1 + \bar{p}_2|$ GeV/c and as a function of the mediating virtual photon's momentum transfer $-q^2$ $(GeV/c)^2$. The results for both were consistant with no variations, again the statistics of our data sample limiting what we could do.

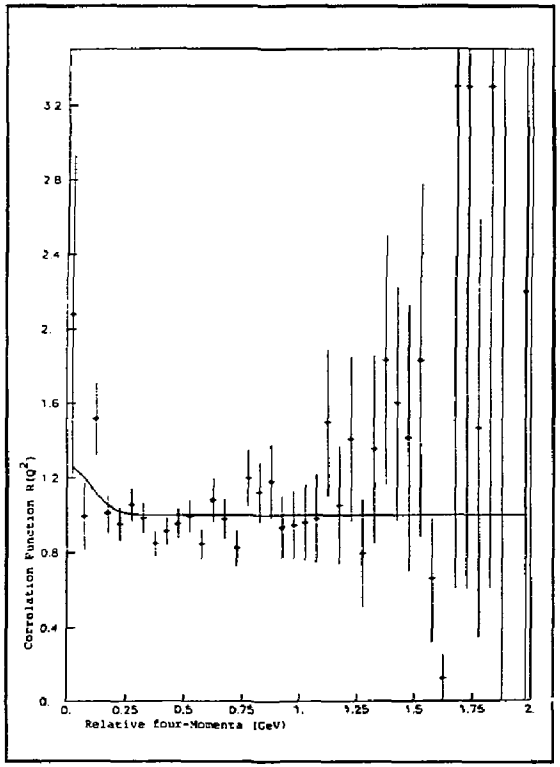

Fig. 1.8 *The fitted two-pion correlation function. The fitted data shows an enhancement at small relative four-momenta.*

Summary

We have briefly presented a preliminary result of a gas target test run at PEP. For this test and for subsequent data analysis the TPC-2γ facility was used. The combined three-dimensional tracking and particle identification capabilities of the TPC allow study of a number of processes of interest in nuclear physics. The success of the TPC at PEP indicates that a future nuclear physics facility at PEP should be of similiar capability. However the size and complexity of the TPC-2γ facility means that any future nuclear physics detector will be much larger that what has been traditional. In any case the feasibility of such a detector is very good.

REFERENCES

1. F.S. Dietrich *et. al.*, *An Exploratory Gas-Target Experiment at PEP using the TPC/2γ Facility;* Submitted to the 2nd conference on Intersections between Particle and Nuclear Physics Lake Louise, Canada (1986).
2. M.D. Shapiro, University of California Ph.D. Thesis, Berkeley (1985).
3. J. Marx and D. Nygren, *The Time Projection Chamber*, Physics Today, **46**, October (1978).
4. R. Madaras and P. Oddone, *Time-Projection Chambers*, Physics Today, **36**, August (1984).
5. H. Aihara, *et. al.*, IEEE Trans. Nucl. Sci. **NS-30**, a series of articles devoted to the different PEP-4 subsystems, (1983).
6. A. Buijs, University of Utrecht, Netherlands Ph.D. Thesis, Utrecht (1986).
7. D. Ritson, *Proceedings of the Summer Institute on Particle Physics*, edited by A. Mosher, SLAC Report **239**, 177, (1981).
8. H. Aihara, *et. al.*, Phys. Rev. **D31**, 996, (1985).
9. A. Breakstone *et. al.*, Phys. Lett. **162B**, 400 (1985).

A Nuclear Physics IR for PEP – Issues and Conceptual Design

K. Van Bibber
Lawrence Livermore National Laboratory
University of California
P.O. Box 808 L-421
Livermore, Calif. 94550

Abstract

A conceptual design for a nuclear physics interaction region at PEP is presented. The design is based on components of the 2γ (PEP-9) detector, configured as a large acceptance forward angle spectrometer suited for asymmetric fixed target kinematics. The system is evaluated with a prototype experiment in mind, namely pion production in quasielastic kinematics, $(e,e'\pi)$. Issues and open questions particular to internal target work are discussed.

Introduction

Most of the 'Work' of this Workshop has concerned identifying the unique physics potential of the MIT-Bates stretcher-storage ring and the PEP storage ring for nuclear physics, and rightly so. Nevertheless, the experimental conditions and beam parameters are sufficiently unlike those of fixed target operation that it is worthwhile giving some preliminary thought to the hardware – targetry and detectors – in order to realistically constrain physics proposals being developed for these facilities.

Presented here is a conceptual design of a small angle, large acceptance forward spectrometer for PEP. It is intended as a multiparticle spectrometer, which would record both the inelastically scattered electron, and resulting hadrons within $20^o - 25^o$ of the beam axis. As is, it is may be most suited for, among others: (*i*) inclusive electron scattering (*e.g.* from polarized targets); (*ii*) semi-exclusive measurements in hadronization studies (where the inelastically scattered electron and one or more hadrons normally will be detected); and (*iii*) vector meson production, *e.g.* $(e,e'\phi)$, $\rho \rightarrow K^+ + K^-$. The suitability as is for quasielastic scattering, *e.g.* $(e,e'p)$, $(e,e'2p)$ is less clear in view of the wide angle at which the struck nucleons normally go. Nevertheless, such a downstream spectrometer could be viewed as the first most essential piece of a comprehensive IR, with either a central tracker (solenoidal magnet, wire chambers, *etc.*), or a movable small solid angle spectrometer arm to cover wider angles.

A brief description of the IR environment will be given, followed by a discussion of how an existing detector, the PEP-9 2γ spectrometer could be reconfigured for fixed-target kinematics. Space does not permit a detailed description of all the components, but relevant parameters will be mentioned. Estimates of rates, resolution and acceptance will be presented. Finally, very preliminary considerations concerning data acquisition will be discussed. The gas jet target for unpolarized work will not be dealt with at all, as it will be described in detail in the paper of J. Molitoris[1] . However, the question of luminosity monitoring will be addressed, and a proposal to use Moller electrons (analogously to Bhabha scattering in e^+e^- physics) will be put forward.

The Interaction Region

A likely location for nuclear physics at PEP (at least initially) will be IR-8, shown in Figure 1. Four of six of the PEP interaction regions are nearly identical, and alternative siting would not change any important details. The beam line is 4 meters off the floor, and is 5.7 m and 9.9 m from the outer shielding wall and inner wall respectively. The distance from the $e^{\pm}$ interaction point to the first quadrupole magnet in either direction is approximately 6.4 m. The house for electronics and computer have been added to the figure. There is one interesting feature to be commented on in IR-8, which is the proton alcove downstream of the IR in the electron-going

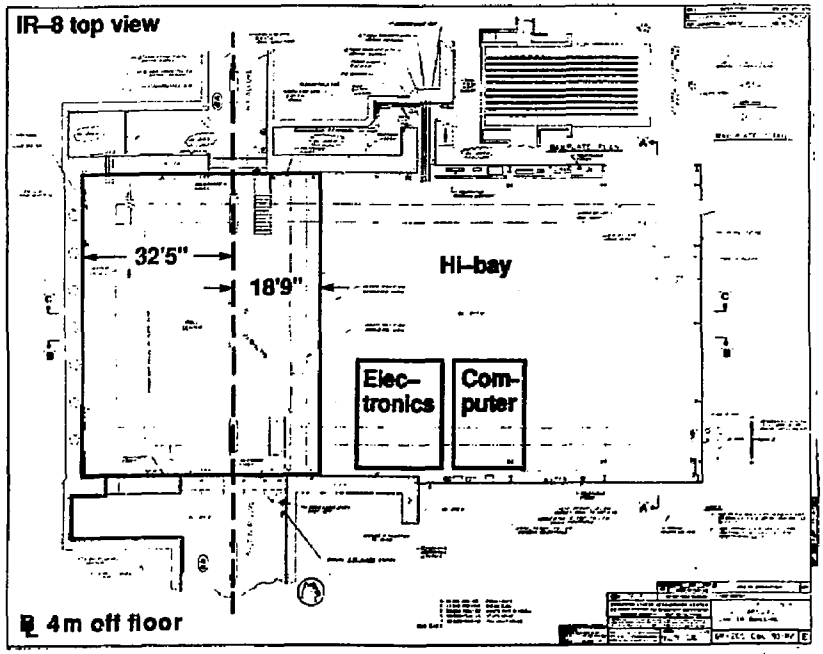

Fig. 1 *Top view of PEP Interaction Region 8. The electron direction is from top to bottom in the figure.*

direction. This feature was added to the design for PEP when it was anticipated that it might become an *ep* collider at some later date. Such an alcove would permit detectors at very small angles, should that be desirable in the future.

For fixed target physics, the gas target need not be located at the $e^{\pm}$ interaction point, and in any case the electron and positron beams will be separated everywhere except at IR-2 (this separation being $\approx 1\ cm$). Figure 2 shows the $10\sigma_{x,y}$ beam envelope and the horizontal and vertical 'beam stay clear' ($\equiv 10\sigma + 1\ cm$). Since it is anticipated that the gas jet target will be directed vertically, it is seen that even at $z = 4m$, a jet of radius $0.5 - 1\ cm$ will handily intercept the whole beam.

The PEP-9 2γ Spectrometer

The PEP-9 2γ Spectrometer is part of the TPC-2γ Detector, which is described in detail in the paper of S. Melnikoff[2] . The 2γ spectrometer actually consists of two symmetric low angle spectrometers at the 'North' and 'South' ends of the Time Projection Chamber (TPC). Each end is comprised of a Cerenkov detector, drift chambers, a magnetic volume, a time-of-flight hodoscope, calorimetry and muon identifiers. Subtending 20-200 msr, their chief function is to tag inelastically scattered $e^{\pm}$ in two-

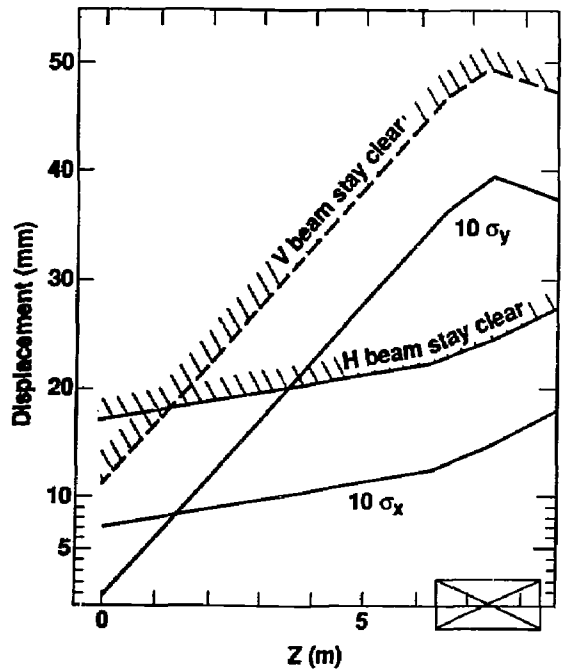

Fig. 2 *PEP beam profile for non-interacting IR's during high-luminosity era. Not final.*

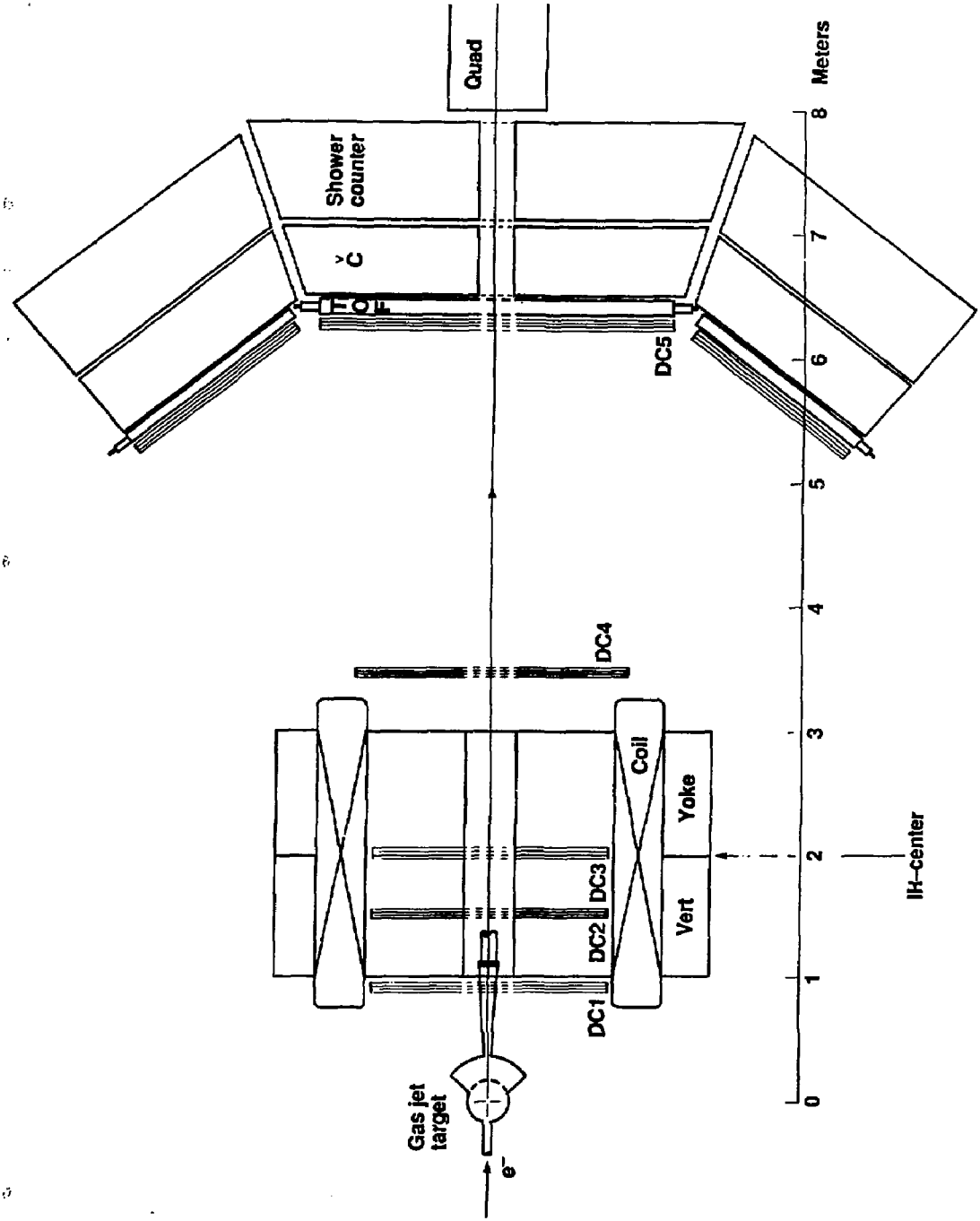

Fig. 3 *Conceptual design of a fixed target interaction region for PEP (top view).*

photon physics. Here the electron and positron do not annihilate, but rather each radiates a virtual photon which fuse to produce a hadronic or leptonic final state with the quantum numbers of two photons. It was the low-angle spectrometer system which made the TPC-2γ detector attractive for the nuclear physics test of 1986.

The development which permits us to think about PEP-9 for the future nuclear physics program at PEP is that the TPC-2γ collaboration has been approved for several years of high luminosity running at PEP. Under the high luminosity upgrade, the two final quadrupoles in IR-2 will be moved in much closer to the TPC, and most of the 2γ detector will need to be relinquished. Most of the collaborating institutions in PEP-9 have been extremely gracious in permitting us future use of their components.

A Spectrometer for Fixed Target Physics

The features of a spectrometer for nuclear physics generally desired for many of the experiments proposed at this Workshop are *(i)* large solid angle coverage for multiparticle final states; *(ii)* an angular range starting as close to the beam axis as possible; *(iii)* at least moderate momentum resolution ($\leq 10^{-2}$); and *(iv)* good particle identification (e, π, K, p, d) up to 5 GeV. Of particular importance is excellent $\pi - e$ discrimination for processes where the inclusive hadron production cross section in relation to the inelastic electron cross section may be severe.

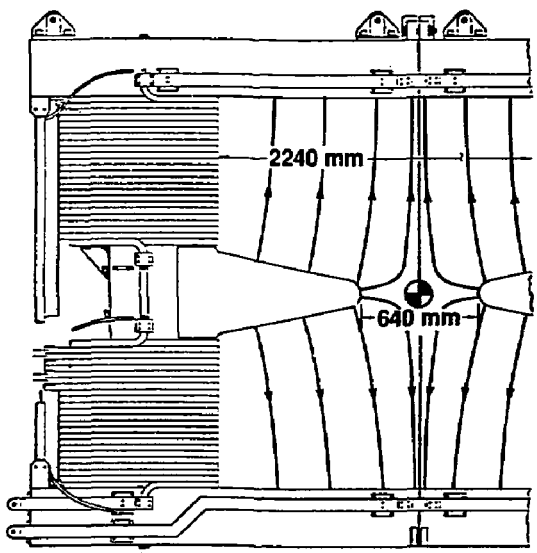

Fig. 4 *View from beam axis of existing PEP-9 Septum Magnet. Magnetic field lines are indicated.*

A conceptual design for a large acceptance forward spectrometer is shown in Figure 3, assembled partially from components of the PEP-9 spectrometer.

The Septum Magnet

Each half of the *PEP-9* spectrometer contains a septum magnet shown in Figure 4. The active area is approximately 2.2 m on a side, with a depth of 1 m. The coils around the vertical yoke are wound with the sense such that flux lines emerge from the septum or 'nose' of the magnet and are directed upwards in the top half and downwards in the lower half. The resulting field at the beam axis is zero as required; an air-core quadrupole cancels out higher multipoles to a large degree. An unfortunate characteristic of the magnets at present is that the $\int Bdl = 1.8\ kG - m$ only. The reason for this is twofold: *(i)* half of the amp-turns are outside of the vertical yoke and cause flux loss to the exterior region; and *(ii)* saturation of the iron, particularly in the nose. Our intention is to use the magnets back-to-back, but additionally to consider modifications that will increase the magnetic field strength. A study has been made using the two-dimensional code POISSON of various options involving addition of iron, and rewinding the coil. (Obviously as the coil will be rewound, the two yokes will be first joined before the mounting of the coil.) Figure 5 *top* shows the field lines for the magnet as is, where the maximum field strength is 4.9 kG. Figure 5 *bottom* shows the proposed modification. The equivalent number of amp-turns (762,000) is now wound around the nose, rather than the vertical yoke. The nose itself has been made wider, and the vertical and horizontal yoke-pieces have been moved outwards to preserve the active area of the spectrometer. The resulting maximum magnetic field is predicted to be 7.6 kG, and the average $\int Bdl \approx 12\ kG - m$. The three heavy lines indicate cuts along which the magnetic field is plotted in Figure 6.

Drift Chambers

The existing *PEP-9* detector consists of five drift chambers per arm termed DC1-5. The total number of planes per arm (*e.g.*, the North arm) is 15, as each DC basically consists of u, v, y stereo planes whose wire pitch is $\pm 5^o$ and 90^o from vertical respectively. Each plane consists of roughly 60 drift cells per plane, and each drift cell by itself resolves the 'left-right ambiguity' as instead of a single sense

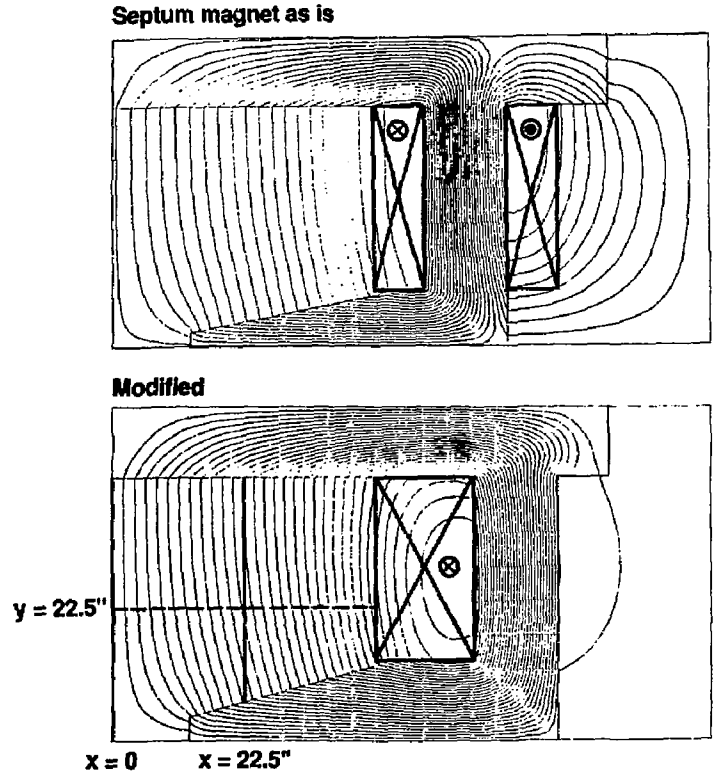

Fig. 5 *Quadrant field map for the present configuration of the septum magnet (top), and a possible modification (bottom). In the modified case, the coil return is made around the magnet nose. From 2-d code POISSON.*

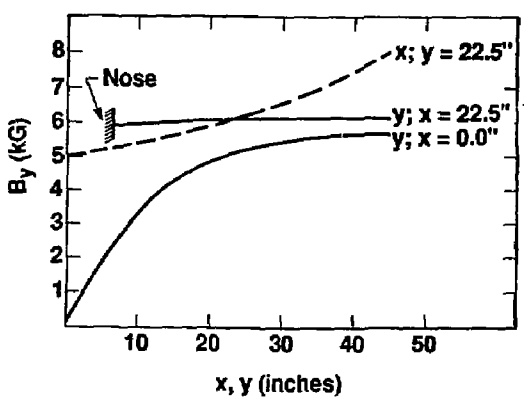

Fig. 6 *Profiles of vertical magnetic field component (B_y), vs. x, y. Cuts refer to dashed, and heavy solid lines in Figure 5.*

wire per cell, there is a double sense wire spaced by 250 μ.

The sense and cathode wires for DC2-5 are 38 μ and 250 μ respectively, and the gas mixture is $Ar - CO_2$ (16.4%) at one atmosphere. Windows for DC2-5 are aluminized mylar 25 μ thick. The typical resolution is $\sigma = 125$ μ. The most comprehensive document on the *PEP-9* drift cells is that of White[8].

The TOF Hodoscope

The TOF hodoscope of each arm of *PEP-9* is a lattice of 50 horizontal and 62 vertical scintillator strips, assembled in four quadrants. Each strip is 8.5 *cm* wide, and is read out by a single photomultiplier tube (PMT).

Corrections are made in analysis for time slewing due to amplitude variations (for which 15% improvements were reported in test beam measurements), and for propogation time through the scintillator ($\approx$ 14 *cm/nsec*). The resulting time resolu-

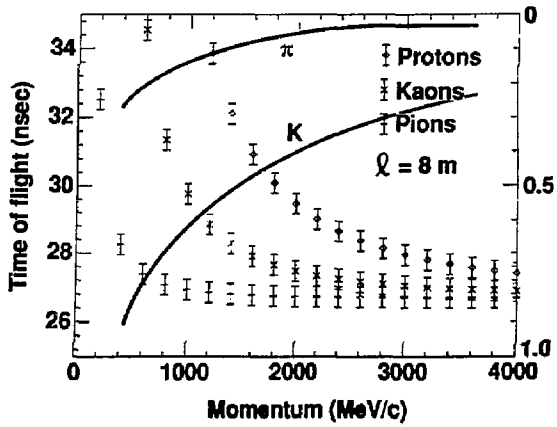

Fig. 7 *Time-of-Flight for π, K, p vs momentum left ordinate; π, K fraction surviving right ordinate.*

tion is found to be $\sigma = 0.47$ *nsec* for horizontal or vertical strips alone, and $\sigma = 0.30$ *nsec* where the average is taken between a coincident horizontal and vertical strip.

The particle identification by TOF that can be expected with this hodoscope in the spectrometer proposed is shown in Figure 7. (Note that the TOF wall in Figure 1 is actually at 6 *m* rather than at 8 *m* for which this calculation was performed.) Also included in the figure are the fraction of π, K surviving decay in flight for an 8 *m* flight path.

One intact TOF wall and electronics have been designated for future use in the nuclear physics interaction region, the other TOF wall was cut in half for use as a fast offline cosmic ray trigger for the TPC. When it has completed its function there, its use as lateral extensions to the downstream detector package could be negogiated.

The Calorimeter

The calorimeter is a critical component of the detector package as clean electron identification depends heavily on it. A suitable candidate appears to be the novel lead-liquid scintillator design of the Santa Barbara group used at FNAL[4] . Their detector consisted of 60 layers, each $1/3X_0$ thick. Each layer was made of an Al-Pb-Al laminate, plus a rectangularly corrugated teflon-coated aluminum sheet. The corrugations space the layers from one another, and are filled with liquid scintillator. Light emitted from the scintillator is thus confined to a strip of 3.17 *cm* width and is transmitted in either direction to its end. The layers are arranged to give *u, v, y* stereo views of $\pm 20.5^\circ$ and 90° respectively. Channels emerging on any side of the calorimeter with a common *(x,y)* coordinate are ganged together in the readout; a lightguide containing a wavelength shifter is mounted above the common ends with a small airgap and a single PMT reads out each lightguide. The resolution for the full scale detector $(2.44m \times 4.88m)$ was $12\%/\sqrt{E}$, and position resolution was about 3 *mm*. One practical difficulty which inhibited this group from adopting this design for the TPC was the difficulty of introducing a hole for the beam pipe through the device; this difficulty would obviously have to be countenanced in this spectrometer as well.

The Cherenkov Detector

The area where least progress has been made is the issue of Cherenkov detector(s). Cherekov detectors are possibly required for two purposes: to improve the π/e separation, and second, to improve the K/π separation. For the former case, the solution is straightforward. A threshold detector with atmospheric or sub-atmospheric pressure can be made handily with a range of gases to choose any threshold momentum p_t^π desired. The only complication is the very non-paraxial trajectories at the back end of the spectrometer that will result when the septum magnet is upgraded. The issue of K/π separation (indistinguishable above 1.5 *GeV/c* by time-of-flight alone) is more difficult. A combination of a heavy gas Cerenkov (*i.e.* neopentane) and silica-aerogel is certainly an option. Concerning aerogel, its range of index of refraction in manufacture is limited to $1.02 \leq n \leq 1.1$, and we are not aware of any commercial vendors at present. For $n = 1.02$, $p_t^\pi = 0.71$ *GeV/c*, whereas $p_t^K = 2.5$ *GeV/c*.

A ring imaging Cerenkov detector is also under study for particle identification, motivated by the design of Fermilab experiment E-665.

Performance of the System

Rates

In designing a large solid angle forward spectrometer, the inclusive rates must be well understood in order to select the appropriate instrumentation with the requisite granularity so the sytem will not be overwhelmed. Furthermore, it must be considered whether it will be possible to trigger on all of the categories of events of interest while minimizing useless triggers.

Rates have been estimated assuming a D_2 target, a luminosity $\mathcal{L} = 10^{32}$, and an effective coverage

in polar angle for the spectrometer of $4^o \leq \theta \leq 20^o$. Numbers below refer to incident energies of 14.5 (4) GeV.

Inclusive Electron Rate

The rate of inelastically scattered electrons from nuclei have been estimated using parameterized structure functions for deep inelastic scattering ($E_{min} = 0.1\ GeV$), and the assumption of y-scaling for the quasielastic part. This yields 40 Hz (400 Hz), the factor of 10 increase in going down in energy being due to quasielastic scattering.

Inclusive Hadron Rate

Useful parameterizations of inclusive hadron production at high energies are almost non-existent. Based on the data of Boyarski[6] using a 0.3 radiation length Be target at 18 GeV, the hadron singles rates should be less than 40 kHz.

Moller Electrons

The Moller electron spectrum diverges with increasing lab angle out to the maximum angle of 90^o, but the electron energy falls rapidly. (Wide angle electrons in the lab frame correspond to 'grazing' collisions in the center-of-mass frame.) Within the spectrometer's angular acceptance, the *total* Moller rate is 6×10^7 Hz (1.7×10^7 Hz); however the fringe field of the septum magnet should pin the softest part of the spectrum preventing these electrons from hitting the first plane of wire chambers. Cutting off the spectrum (somewhat arbitrarily) at $E_{min} = 30\ MeV$ results in a much lower rate: 8.5×10^5 Hz (2.3×10^5 Hz).

Resolution

The momentum resolution of the spectrometer is limited by multiple scattering of particles in the drift chambers and the air, the finite position resolution of the drift chambers, and the uncertainty of the exact trajectory through the magnet (as the field is inhomogeneous, particularly so at smaller angles). In the region where the field is fairly strong (and where the inhomogeneous nature of the field may be neglected), the resolution is estimated to be $\delta p/p = [(2.5 \times 10^{-5}) + 10^{-6}p^2]^{1/2}$ (see Figure 8). This resolution is predicated upon an average $\int Bdl = 10\ kG - m$, two sets of drift chambers (6 planes comprising 0.03 cm mylar for multiple scattering) separated by 1 meter before the magnet, and likewise after it, and a drift chamber resolution of $\sigma = 150\ \mu m$. (It is easy to see that only the inner two drift chamber planes contribute to the momentum uncertainty, and not the outer two.) It is a general property of non-focussing spectrometers that their low-momentum resolution is limited by multiple scattering, and it is difficult to achieve much better than 5×10^{-3}.

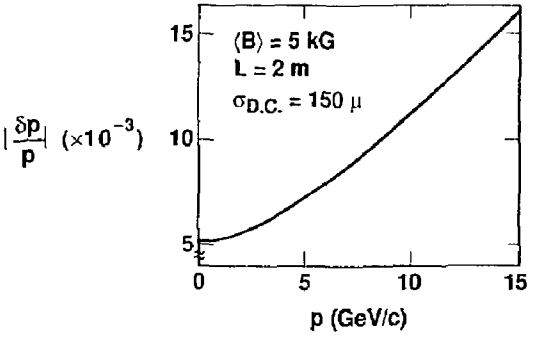

Fig. 8 *Estimated resolution of the septum spectrometer, not including effect of field inhomogeneity.*

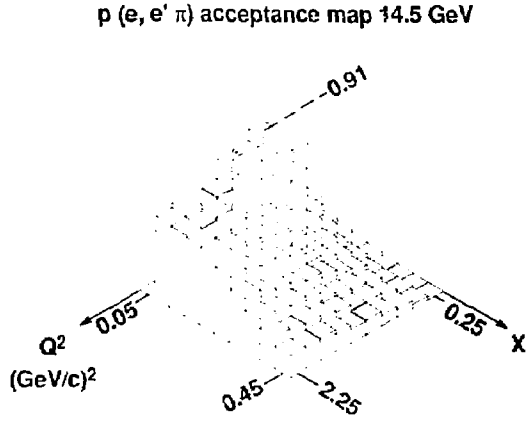

Fig. 9 *Acceptance map for the reaction $p(e,e'\pi)n$ at 14.5 GeV. The angular distribution for the pions was taken to be e^{10t}.*

Acceptance

The concept of a forward spectrometer is to detect the inelastically scattered electron, and at least part of the hadronic final state in the same detector. This will preferentially be the maximum rapidity part of the final state. With the gas jet target 100 cm in front of the septum magnet entrance, the magnet exit defines a square of $\theta_{x,y} = 18^o$. The acceptance surface for detecting both the electron and pion in the reaction $p(e,e'\pi)n$ at 14.5 GeV as a function of x, Q^2 has been calculated by Monte Carlo, and is shown in Figure 9. (The angular distribution of the pion about the momentum transfer vector **q** was taken to be e^{10t}, where $t = (p_\pi - q)^2$ in the usual

way). The acceptance is significant throughout x, and for all but the lowest Q^2. The corresponding map for quasielastic scattering from nucleons would be much worse, as the heavy mass of the nucleon implies a large momentum transfer angle, typically 50° or so. The dead solid angle that the vertical yoke represents is one of the most unsavory aspects of a spectrometer built around a septum magnet.

Data Acquisition

The total number of channels of data the spectrometer represents will be at least 3000, and could easily double if a conventional Cerenkov detector is forsaken in favor of a ring-imaging device. (The number of channels requiring readout with zero-suppression is estimated to be 50 per track, leading to a total of 100-250 per event typically.) The collaboration forming about such an interaction region for PEP (American / ANL / CalTech / LLNL / Massachusetts / RPI / SLAC / Virginia / Washington) has defined as a necessity a data acquisition rate of 30 Hz, and a realistic goal of 100 Hz. The former should be achievable within conventional VAX-based systems, the latter would require either multiple tape drives or the new WORM technology combined with a multiple processor system for data logging and analysis[9] . Nevertheless, at this stage it must be said that plans concerning computers and software are still at a fairly primitive level.

Luminosity Monitoring and Calibrations

Perhaps the chief unanswered issues for an internal target facility at PEP concern luminosity monitoring and calibration of the various detector components. The situation for e^+e^- physics is more felicitious in that Bhabha scattering provides both luminosity monitoring and monoenergetic (*e.g.* 14.5 GeV) electrons and positrons with a meaningful rate at wide angles (in spite of the Q^{-4} angular distribution) for running calibrations of calorimeters, TOF hodoscopes, DC's, *etc.*. The analog of Bhabha scattering for fixed target experiments, Moller scattering from atomic electrons in the gas target, holds out hope for luminosity monitoring. Figure 10 (a) and (b) shows that while the cross section rises steeply for larger angles, the energy drops precipitously; particles emitted at angles less than 5° will be occluded by the beam pipe within almost any spectrometer design. Nevertheless, electrons in the 100 MeV range should be cleanly identified with a combination of magnetic analysis and shower energy in a small NaI detector.

Calibration is a different matter; Moller scattering is of no use here to keep detectors calibrated even at small angles. Perhaps the only possibility is to intersperse actual data collection with periodic hydrogen target runs in order to collect sufficient ep elastic scattering pairs throughout the acceptance of the spectrometer.

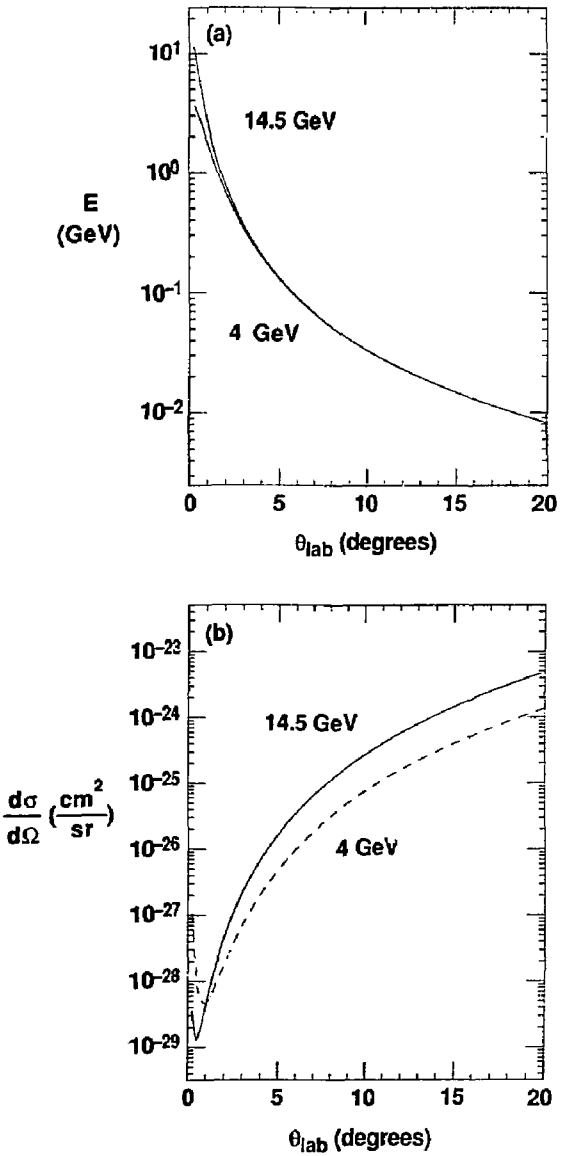

Fig. 10 *(a) Energy of Moller electrons vs. angle; (b) Differential cross section of Moller electrons vs. angle.*

Acknowledgements

The cooperation of S. Melnikoff and J. Molitoris has been invaluable in this work. I thank R. Early for assistance with the magnetic field calculations. We are very grateful to the member institutions of PEP-9 who have made their components of the 2π spectrometer and their counsel available to us freely.

REFERENCES

1. J.D. Molitoris, K. Van Bibber, *Development of a Warm Gas Jet Target for PEP*, Proceedings of this Workshop.
2. S.O. Melnikoff, *High Energy Nuclear Physics at PEP Recent Results using the Time Projection Chamber*, Proceedings of this Workshop.
3. J. White, *PEP-9 Drift Cells*; PEP-9 Technical Memo TG-311 DRF-015 (June 20, 1984).
4. V.K. Bharadwaj, Nucl. Instr. and Meth. **155**, 411 (1978) and Nucl. Instr. and Meth. in Phys. Res. **228**, 283 (1985).
5. A.M. Boyarski §C.2 *SLAC USERS MANUAL*, (1968).
6. W.J. Langeveld, *Optical Storage and its possible use in High Energy Physics*; Asilomar Conference on Computing in High Energy Physics (1986).

KAON ELECTROPRODUCTION FROM THE PROTON AND DEUTERON†

Stephen R. Cotanch and Shian S. Hsiao

Department of Physics, North Carolina State University
Raleigh, North Carolina 27695-8202

Abstract

Calculations for the electroproduction reactions $p(e,e'K)Y$ (Y=Λ,Σ) and $d(e,e'K)YN$ are reported to motivate future experiments using different facilities at SLAC. Study of the elementary production processes $p(e,e'K)\Lambda$ and $p(e,e'K)\Sigma$ will provide important information about KNY coupling constants, the kaon form factor, and possible differences between Quantum Hadrodynamic and Chromodynamic formulations. Inclusive measurements for $d(e,e'K)YN$ will permit unique investigations of YN interactions as well as a search for strange dibaryons which are predicted to occur at energies near the ΣN threshold.

Introduction

As evidenced by the Nuclear Physics at SLAC (NPAS) and Continuous Electron Beam Accelerator Facility (CEBAF) projects, as well as several other GeV electron accelerators under development outside of the U.S., interest in high energy electro-nuclear physics is clearly expanding. Much of this interest is motivated by the growing awareness that a complete understanding of the photon's electromagnetic coupling to hadrons provides an unique, theoretically "clean" handle for studying individual and composite hadron structure and hadronic interactions. Investigating kaon electromagnetic production is perhaps the most appropriate example of this philosophy since the K^+ meson has the simplest hadronic reaction mechanism. Further, photo, (γ,K), and electroproduction, $(e,e'K)$, studies directly address several fundamental issues in both nuclear and particle physics. These issues are detailed in the next two sections which describe kaon production from the proton and deuteron, respectively.

Production From The Proton

Unfortunately, the quantity of data for the elementary reaction is not significantly greater than it was twenty years ago. The quality of existing data also needs improvement as cross sections are only accurate to about 10% and polarizations are only determined to within 25 to 50%. Additional, more accurate, measurements will provide new information and insight into: the fundamental production mechanism; the quark structure of the participating hadrons (i.e. static properties, form factors, etc.); tests of various SU(N) symmetry predictions including the usefulness of kaon PCAC; the vector meson hypothesis; and the important issue of distinguishing between theoretical formulations based on Quantum Hadrodynamics (QHD, only baryons and mesons) and Quantum Chromodynamics (QCD, explicit color degrees of freedom).

Figure 1 shows a recently published[1] electroproduction calculation for the virtual photoproduction process $p(\gamma_V, K)\Lambda$. Complete details of the calculation are given in ref. 1. As indicated in the figure, the different curves correspond to various combinations of coupling constants (labeled set I and II, obtained from a phenomenological photoproduction analysis[2]) and kaon form factors. Notice that set I coupling constants provide a better description of the KΛ production data (asterists denotes experimental points). Enigmatically, however, set II coupling constants are favored for $K\Sigma^0$ production which is shown in Figure 2. It should be stressed that flavor SU(3) symmetry was assumed in transforming the coupling constants from Λ to Σ^0 production. Using vector dominance, the kaon form factor is represented by a simple monopole term, $(1 - Q^{**}2/M^{**}2)$, where M is the mass of the vector meson mediating the process. A detailed examination of both figures suggests that the phi meson (M = 1.02 GeV) generated form factor provides a slightly better description of the overall data than the rho which is more appropriate for π electroproduction (this conclusion appeared much more dramatic in ref. 1, however, the first figure in that work contained an error which is corrected in this paper). The dotted line in both figures represents the result using a kaon form factor computed within the quark model[3]. This form factor

†Supported in part by the U.S. Department of Energy and the Research Corporation.

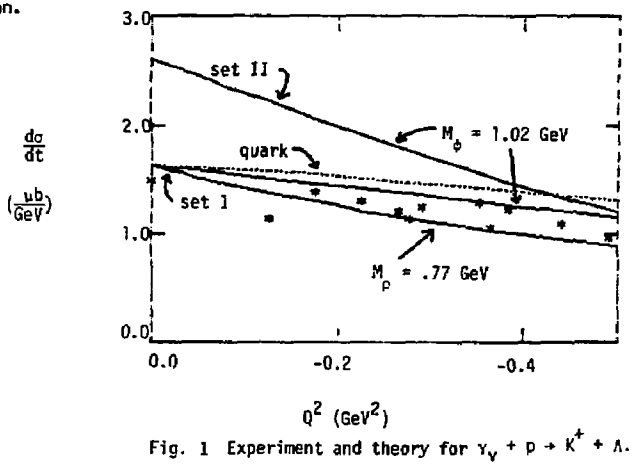

Fig. 1 Experiment and theory for $\gamma_V + p \rightarrow K^+ + \Lambda$.

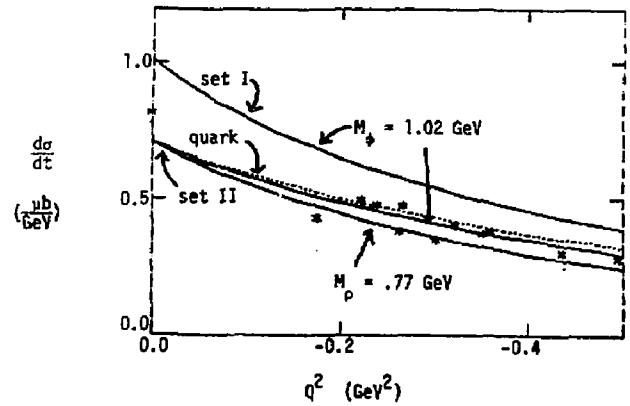

Fig. 2 Experiment and theory for $\gamma_v + p \to K^+ + \Sigma^\circ$.

seems to over predict the cross sections but when combined with the rho meson prediction does provide useful lower and upper theoretical cross section bounds. Because the current uncertainty in the data (error bars are shown in ref. 1) precludes extracting more detailed form factor information, more exacting theoretical constrains will have to await future precision measurements.

In addition to form factor studies and the determination of coupling constants, it is also of interest to understand the rapid Q**2 fall off of Σ° production relative to Λ production. Arguments have been given[4,5] which relate the Σ/Λ ratio decrease to the decrease of the neutron to proton structure function ratio which approaches .25 as the Bjorken scaling variable approaches 1. The implication is that the u and d quarks predominantly couple to isospin 0 which, with the addition of an isospin 0 s quark, favors Λ formation over the isospin 1 Σ production. Another related and important study is the high Q**2 behavior of kaon electroproduction. According to QHD the leading diagrams involve kaon exchange (t channel) and the cross section should scale like the kaon form factor squared (Q**-4 dependence). This prediction is completely different from the perturbative QCD results[6] which become more reliable at high Q**2. Accordingly, this may be a useful signature for delineating the two approaches as well as determining energy regions of applicability for each theory. Clearly, for these and the above reasons it is paramount that additional and more accurate KY electromagnetic production data be obtained.

Production From the Deuteron

The reactions $d(e,e'K)YN$ and $d(\gamma,K)YN$ afford an unique method for studying ΛN and ΣN interactions. This is of timely importance as the existing Λp data is both meager and imprecise and the future of Λ beams is not optimistic. The interesting physics centers around the cross section cusp region which is near the ΣN threshold and is displayed in Figure 3. This curve represents the Λn theoretical total elastic cross section generated by solving a coupled channels problem (see ref. 7 for full details) for the three mass partitions Λn, $\Sigma^\circ n$, and $\Sigma^- p$ using potential D provided by Nagels and de Swart[8]. This interaction, which contains hard core, tensor, and antisymmetric spin-orbit components, provides a reasonable comprehensive description of limited Λp elastic and inelastic, $\Lambda p \to \Sigma N$, data. This cusp is due to an enhancement in the triplet s wave sigma channel which is the strange analogue of the deuteron. Since Λn measurements are not possible the only direct way to investigate this system is through

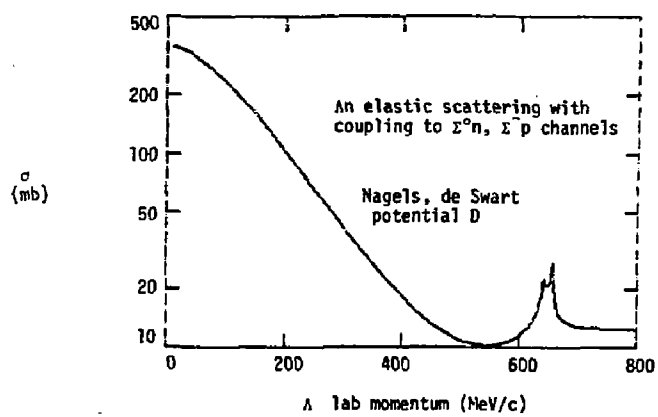

Fig. 3 Theoretical Λn total elastic cross section.

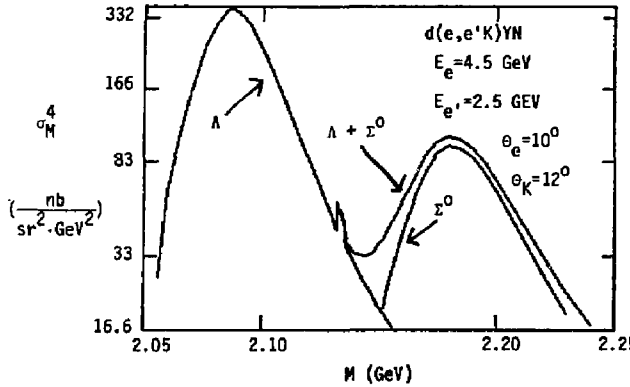

Fig. 4 Inclusive lab cross section for $d(e,e'K)(\Lambda h + \Sigma^0 n)$.

final state interaction studies of the reaction $d(e,e'K)\Lambda n$. In Figure 4 the predicted inclusive cross section (Λ is unobserved, only the three-momentum of the final electron and kaon are detected) is plotted versus the Λn invariant mass. Again notice the presence of the ΣN cusp near the sigma threshold (M = 2.13 GeV). Because this is an inclusive process it is not possible to resolve Λ and Σ^0 production hence, the upper curve represents the sum of the theoretical cross sections (the lower curves at low and high invariant masses represent pure Λ and Σ production, respectively). Accurate measurements of this reaction will provide firm constraints for YN potentials and will determine the unknown relative phase between Λ and Σ elementary production amplitudes (this calculation assumed +1 phase; a -1 phase generates a destructive dip instead of a peak in the cusp region). Further and of fundamental importance, such measurements would enable the search for strangeness -1 dibaryons which are predicted[9] to have mass values spanning the ΣN threshold (the singlet spin 0, D_0, has a calculated mass between 20 and 40 MeV below the cusp while the triplet spin 1, D_1, is expected to have a mass 20 to 40 MeV above the cusp). These six quark composite objects, which are distinct from a partial wave resonance between two three quark structures, have a predicted p wave internal configuration and also couple to p wave ΛN channels[10]. Consequently, the kaon angular distribution from $d(\gamma_v,K)YN$ should be markedly different for strange dibaryon formation than for the cusp excitation which is predominantly s wave. This is demonstrated, in part, in Figure 5 where the cusp in Figure 4 is isolated and decomposed into components. Note that the dominant contribution to the total cross section (top curve) is from including only the triplet s wave final state YN distortions (next curve from the top). Piekarz[11] has used this signature to argue for the formation of the triplet D_1 dibaryon using the reaction $d(\pi^-,K^-)\Lambda p$. He reports observing a maximum about 10 MeV above the ΣN threshold. Ideally, a search for the singlet D_0 should also be conducted since the experimental signature is clearer because at energies below the Σ threshold the inclusive measurement is free from the complexities of the sigma channel. This is illustrated in Figure 5 where the cross section for pure sigma production is shown to be relatively small at threshold (bottom curve is pure Σ^0 production). Unfortunately the (π^-,K^-) reaction is not effective in exciting the singlet state because the participating mesons have spin 0 and the elementary hadronic amplitudes have a small spin-flip component. However, the (γ_v,K) excites both spin states as shown in Figure 5. Kaon electromagnetic production is therefore not only an attractive, alternative process for triplet dibaryon

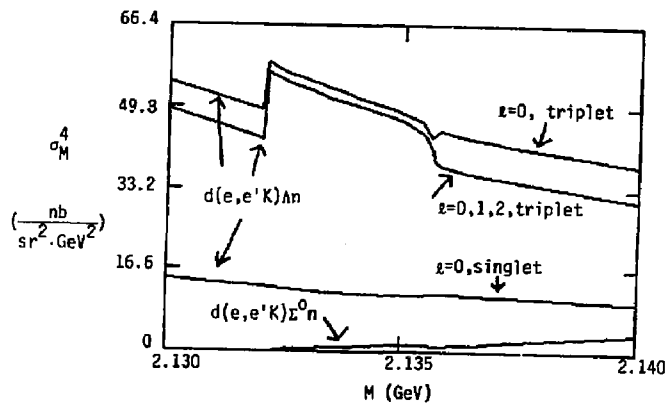

Fig. 5 Same as Fig. 4 for cusp region.

Λ

studies but also an unique way of searching for singlet dibaryon production from the deuteron.

Finally, it is also possible to study K^+n final state interactions using $d(\gamma_V,K)YN$. In contrast to K^+p the K^+n, or isospin 0, interaction is not well known. Improving our understanding of the KN amplitudes would further enhance the utility of the kaon as a scattering probe and provide important information concerning the exotic Z* strangeness +1 baryon resonances. Because the current experimental evidence is weak the existence of the Z* is highly controversial, however this resonance has also emerged from recent Skyrme model calculations[12].

Experimental Considerations At SLAC

The luminosity available to the Nuclear Physics Interaction Region project at PEP for proton and deuteron targets, 10**33/(cm**2·s), appears to be quite suitable for elementary production studies and, depending on spectrometer design, perhaps even adequate for Yn final state interaction investigations. For example, a conventional two arm coincidence experiment involving a kaon and electron spectrometer each have 50 and 10 msr solid angle acceptance, respectively, and ± 5% momentum acceptance could anticipate 2 counts per hour for $d(e,e'K)\Lambda N$. If a large acceptance 4π detector is used the count rate would be increased by at least an order of magnitude. These count rate predictions assume a 50% kaon detection efficiency and are based on the cross section value near the cusp regions of about 50 nb/(GeV·sr)**2. Because the background for this experiment is low it should be possible to obtain accurate cross sections even without a large number of counts. Even higher counting rates, however, could be obtained using the primary SLAC beam and end station A. Although these spectrometers have much smaller acceptances (use the 1.6 GeV detector for the kaon with $\Delta\Omega$ = 3 msr, $\Delta p/p$ = ±5%; use the 8 GeV spectrometer for the electron with $\Delta\Omega$ = .75 msr, $\Delta p/p$ = ± 2%) the effective luminosity is significantly higher, about 10**37. Predicted count rates for a double coincidence, inclusive measurement of $d(e,e'K)YN$ in the cusp region are about 1 every 2 minutes.

Conclusion

In summary, several important issues affecting both nuclear and particle physics could be resolved by performing more accurate measurements of the two reactions $p(e,e'K)Y$ and $d(e,e'K)YN$. More specifically, the elementary production studies would provide a decisive comparative test of QHD and asymptotic QCD while the final state interaction investigations would permit a clear search for strange dibaryons. Because much of the necessary equipment is already in place serious proposals to perform such experiments should receive high priority.

References

1. S. R. Cotanch and S. S. Hsiao, Nucl. Phys. A450, 419 (1986).
2. H. Thom, Phys. Rev. 151, 1322 (1966).
3. W. Polyzou and P. L. Chung, private communication.
4. O. Nachtmann, Nucl. Phys. B74, 422 (1974).
5. J. Cleymans and F. E. Close, Nucl. Phys. B85, 429 (1975).
6. S. J. Brodsky and C. R. Ji, SLAC-PUB-3745 (1985) and S. J. Brodsky private communication.
7. S. R. Cotanch and S. S. Hsiao, Proceedings of the International Symposium on Hypernuclear Physics, Tokyo (1986, in press).
8. M. M. Nagels, T. A. Rijken and J. J. de Swart, Phys. Rev. D15, 2547 (1977).
9. R. L. Jaffe, Phys. Rev. Lett. 38, 195 (1977).
10. C. B. Dover, Nucl. Phys. A450, 95 (1986).
11. H. Piekarz, Nucl. Phys. A450, 85 (1986).
12. D. O. Riska, private communication.

A

HOW GOOD IS VECTOR-MESON DOMINANCE IN THE DESCRIPTION OF E.M. FORM FACTORS OF HADRONS?

Manfred F. Gari

Institut für Theoretische Physik
Ruhr Universität Bochum
D-463 Bochum, W-G
and
Institut für Kernphysik
Kernforschungsanlage Jülich
D-5170 Jülich, W-G

Abstract

We discuss the quality of the vector-meson dominance approach in the description of electromagnetic form factors of nucleon and pion. A generalisation of this approach is given which includes the constraints at high Q^2 as obtained from perturbative quantum chromodynamics. An interesting possibility in the interpretation of the analysis is that nucleon and pion are very different in their quark-gluon structure. The importance for measurements of the electric form factors of neutron and proton as well as the pion form factor is emphasized.

The determination and understanding of the electromagnetic form factors of hadrons belongs to the fundamental problems in hadron physics. It is needless to say that with the knowledge of the form factors over a wide range of momentum transfer, important information on the underlying quark-gluon structure of the hadrons is obtained. As nucleon and pion are the simplest quark, resp. quark-antiquark systems they play a very special role. The simultaneous understanding of these bound states is of outstanding importance.

In the present discussion we investigate the quality of the vector-meson dominance (VMD) approach[1] in the description of the e.m. form factors of nucleon and pion. The connections to the quark-gluon description of the form factors is indicated together with the necessary modifications of the form factor description in view of the constraints obtained from perturbative QCD[2,3,4]. We follow the description of refs.5,6.

According to our understanding of a physical photon, the interaction of a virtual photon with a hadron consists of two different pieces: (i) a direct contribution which describes the interaction of the bare photon, and (ii) a contribution which is associated with the hadronic structure of the photon. This second part can be visualized by the interaction of the neutral vector mesons $\rho,\omega,\phi,J/\psi$ with the hadron.

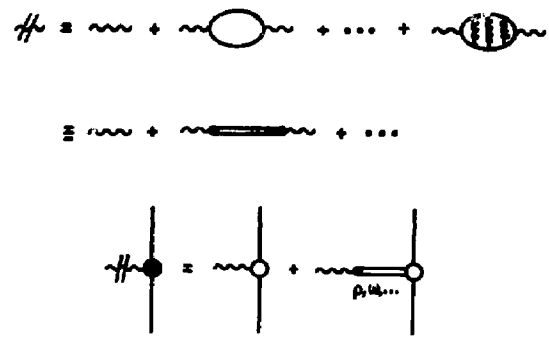

Fig.1

Hadronic (quark-gluon) structure of the photon and the interaction of a physical photon with a hadron.

Assuming that the vector meson contributions (Fig.1b) to the form factor, which dominate for momentum transfers close to the masses of the vector mesons, also dominate the form factor far away from these poles, the form factors can be described totally by the vector-meson contributions. *This is the origin of the vector-meson* dominance model. In the simplest version of this model, where one assumes a point-like interaction of the vector mesons with the hadron, the e.m. form factors are described completely by the vector meson propagators. For example, the nucleon isovector, as well as the pion e.m. form factor is given by the ρ-propagator:

$$F_\pi(Q^2) = m_\rho^2/(m_\rho^2+Q^2) = F_1^{IV}(Q^2) = G_M^p(Q^2)/G_M^p(0)$$

It is interesting to see the quality of such a simple description in the space-like region for the e.m. pion and nucleon magnetic form factor. A comparison with the available experimental information is shown in the following Fig.2.

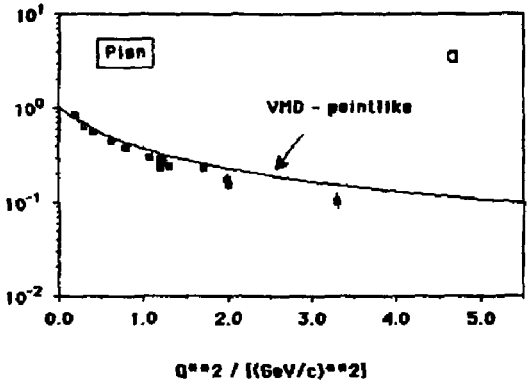

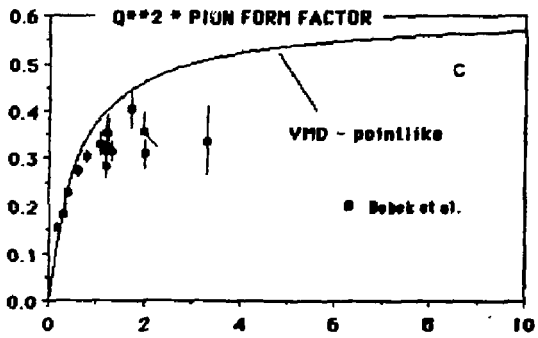

We realize that VMD, assuming point-like ρ - nucleon interaction, gives remarkable differences in the form factor description for nucleon and pion. While for the pion VMD gives a rough description of the data - showing very large deviation from the experiment only at high Q^2 - in the case of the nucleon the description is completely insufficient already at low Q^2.

How can we understand this difference? Does this finding already tell us that VMD is not a good way to describe hadron form factors?

Actually this is not the case as can be seen by considering structured particles. In a meson picture this seems to be rather an indication for a different importance of the meson cloud contribution of nucleon and pion. Consider the interaction of a photon with a hadron in the case of nucleon and pion. The emission probability for a virtual meson seems to be very different for nucleon and pion. The energy violation due to the uncertainty principle is very different in both cases. While ΔE is small for the nucleon, it is rather large for the pion, indicating a strong variation of the γ - nucleon interaction with momentum, while no such effect is expected for the pion. A similar effect is to be expected if we replace the photon by a ρ-meson. Compare Fig3 (V= γ , ρ, ω, φ, J/ψ).

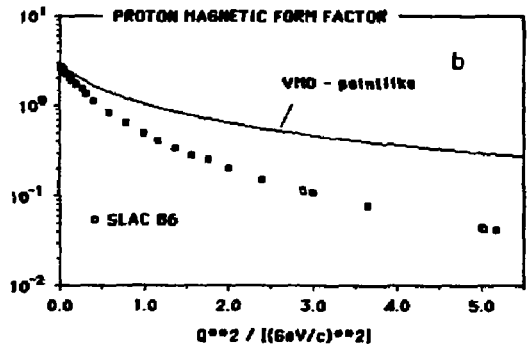

Fig.2

The e.m. form factors of pion and nucleon in the vector-meson dominance approach assuming point-like particles. Data are from refs.(7-10) for the nucleon and ref.(11) for the pion.

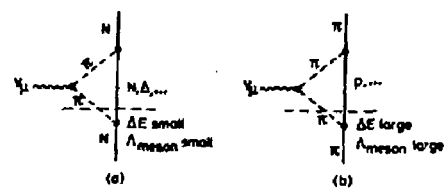

Fig.3

Illustration of the importance of meson cloud contributions to the interaction of the photon with nucleon and pion in a 'meson picture'.

This indicates that the strong disagreement of VMD with the data in the case of the nucleon disappears when we introduce a momentum dependence of the ρ - nucleon interaction:

$$G_M^p(Q^2)/\,G_M^p(0) = m_\rho^2/(m_\rho^2+Q^2) * \Lambda_1^2/(\Lambda_1^2+Q^2)$$

Here we denoted by Λ_1 a meson scale parameter giving the variation of the ρ - nucleon interaction with momentum transfer. This is the simplest possible assumption as long as we are only interested in the low Q^2 behavior. With $\Lambda_1 \sim m_\rho$ this corresponds roughly to the dipole form $F_D = [\Lambda^2/(\Lambda^2+Q^2)]^2$ with $\Lambda=\sqrt{0.71}$ GeV, which is the optimal one parameter fit to the nucleon data

For the pion we do not expect such a large effect according to the above discussion. Thus a small modification of the simple VMD picture gives a rough description of the experimental data - both for nucleon and pion - at least at low momentum transfer.

A closer look at the comparison of theory with experiment however shows that in order to obtain a satisfying description of the data several deficiencies have to be cured. First of all the parameter Λ in the best fit dipole form is not exactly the ρ-ω mass, a fact which is disturbing; Λ is slightly larger than 0.84 GeV.

A more severe point is the failure of this simple picture to describe the experiments for momentum transfer larger than 1 GeV/c - for all form factors under consideration.

In the following we will see that taking into account **(i) the direct interaction of the photon with the hadron - and (ii) the form factor predictions from perturbative QCD** - a satisfactory description of all available nucleon and pion experimental data is possible. For more details see also refs.(5,6).

Applying the factorization approach of Brodsky and Lepage, perturbative QCD predicts the following high Q^2 behaviour of pion and nucleon form factors:

Pion

$$Q^2 \to \infty: \qquad F_\pi(Q^2) \to 16\pi\alpha_s(Q^2) f_\pi^2/Q^2 \qquad (1)$$

Note that as the pion decay constant f_π=93 MeV is measured, the asymptotic form factor is known in form and magnitude[4].

Nucleon

Here we have different asymptotic forms for Dirac and Pauli form factors, namely:

$$\text{Dirac} \quad Q^2 \to \infty: \qquad F_1^N(Q^2) \to \alpha_s(Q^2)^2/Q^4$$

$$\text{Pauli} \quad Q^2 \to \infty: \qquad F_2^N(Q^2) \to F_1^N(Q^2)/Q^2 \sim Q^{-6} \qquad (2)$$

The Pauli form factor is power suppressed as compared to the Dirac form factor reflecting the suppression of helicity changing amplitudes in QCD.

Considering the vector mesons in a one-field approximation we can consider a universal vector-particle nucleon vertex function, which strongly simplifies the picture. We see that **VMD contradicts the high Q^2 prediction from perturbative QCD**. This is due to the additional power suppression originating from the vector-meson propagators and emphasizes the need for additional corrections to the form factors. The vector-meson contributions to the e.m. form factors die out with increasing Q^2 as compared to the direct interaction contribution.

Nucleon form factors

Using the known information on the vector meson nucleon interaction which we have from pion-nucleon scattering, $SU(3)_F$ and the Zweig rule ($g_{\varphi NN} \approx 0$), the nucleon isoscalar, isovector form factors are reduced to universal Dirac and Pauli vector-particle nucleon vertex functions $F_1(Q^2)$, $F_2(Q^2)$. Correspondingly, we have the following expressions for the isoscalar, isovector e.m. nucleon form factors:

$$F_1^{IV}(Q^2) = [\,\Delta_\rho\, c + (1-c)\,]\; F_1(Q^2)$$

$$\kappa_V F_2^{IV}(Q^2) = [\,\Delta_\rho\, c\kappa_\rho + (\kappa_V - c\kappa_\rho)\,]\; F_2(Q^2)\,, \qquad (3)$$

with $\Delta_\rho = m_\rho^2/(m_\rho^2+Q^2)$ and $c = g_{\rho NN}/f_\rho = g_{\omega NN}/f_\omega$. $m_{\rho(\omega)}^2/f_{\rho(\omega)}$ denotes the γ-$\rho(\omega)$ coupling constant. m_ρ=0.776 GeV, m_ω=0.784 GeV, κ_V=3.706, κ_S= -0.12.

The isoscalar form factors $F_1^{IS}(Q^2)$, $\kappa_S F_2^{IS}(Q^2)$ are obtained from eq.(3) for $\rho \to \omega$ and $\kappa_V \to \kappa_S$.

The crucial information on the meson, resp. quark-gluon dynamics is hidden in the universal intrinsic Dirac- and Pauli-vertex functions F_1 and F_2. These functions have also to fulfill the requirements from meson physics[12] at low Q^2 and PQCD at asymptotic Q^2, as illustrated in the following Fig.4.

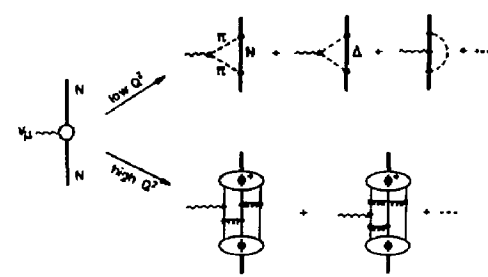

Fig.4

Illustration of the low Q^2 - high Q^2 constraints as incorporated in the present analysis. Low Q^2: meson dynamics; high Q^2: perturbative QCD. Some of the leading meson cloud contributions are shown, as well as the leading gluon exchanges.

Introducing meson and quark-gluon scale parameters Λ_1 and Λ_2 respectively, very simple forms for both F_1 and F_2, which fulfill the above requirements are:

$$F_1(Q^2) = \Lambda_1^2/(\Lambda_1^2 + \hat{Q}^2) * \Lambda_2^2/(\Lambda_2^2 + \hat{Q}^2)$$

$$F_2(Q^2) = F_1(Q^2) * \Lambda_2^2/(\Lambda_2^2 + \hat{Q}^2) \qquad (4)$$

with

$$\hat{Q}^2 = Q^2 \log((\Lambda_2^2 + Q^2)/\Lambda^2_{QCD}))/\log(\Lambda_2^2/\Lambda^2_{QCD})$$

Note that for $Q^2 \gg \Lambda_2^2$ the form factors have the asymptotic form required from PQCD. Thus Λ_2 tells us something about the range of applicability of PQCD.

The magnetic and electric form factors G_M, G_E are defined as usual by:

$$G_M^{p(n)} = F_1^{p(n)} + F_2^{p(n)}; \qquad G_E^{p(n)} = F_1^{p(n)} - Q^2/4M^2 F_2^{p(n)}$$

where $F_1^{p(n)}, F_2^{p(n)}$ denote Dirac and Pauli nucleon form factors:

$$F_1^{p(n)} = 1/2[F_1^{IS} + (-) F_1^{IV}]; \; F_2^{p(n)} = 1/2[\kappa_S F_2^{IS} + (-) \kappa_V F_2^{IV}$$

An analysis of the world nucleon cross section data in terms of the above form factor description yields with ε=0.342, κ_p=6.61 and κ_ω=0.32 the following scales: Λ_1=0.785 GeV, Λ_2=2.22 GeV and Λ_{QCD} = 0.267 GeV.

Interested in a precise determination of the scale Λ_{QCD} one has to take into account also the contributions from the anomalous dimensions of the three-quark component[6]. This we will not discuss here. The parametrization from above gives already a satisfactory description of the data. The inclusion of the anomalous dimensions in the analysis leads to Λ_{QCD} = 180 MeV and very small changes in the other parameters; see ref.(6) for details of this analysis.

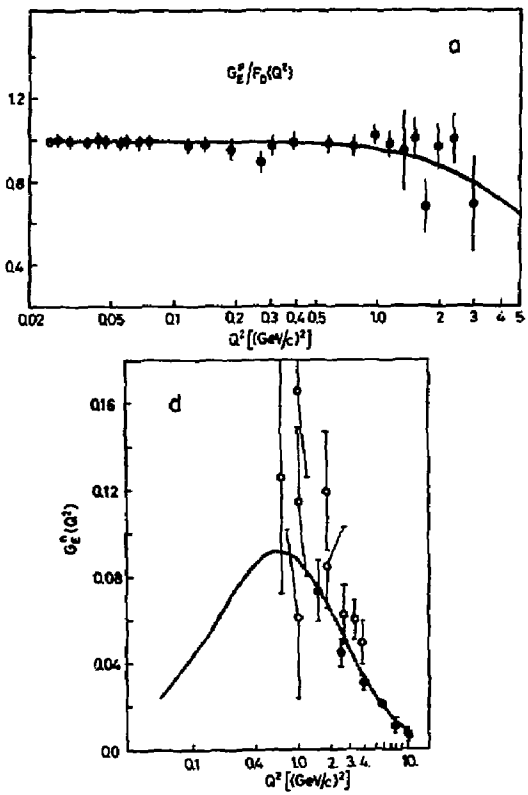

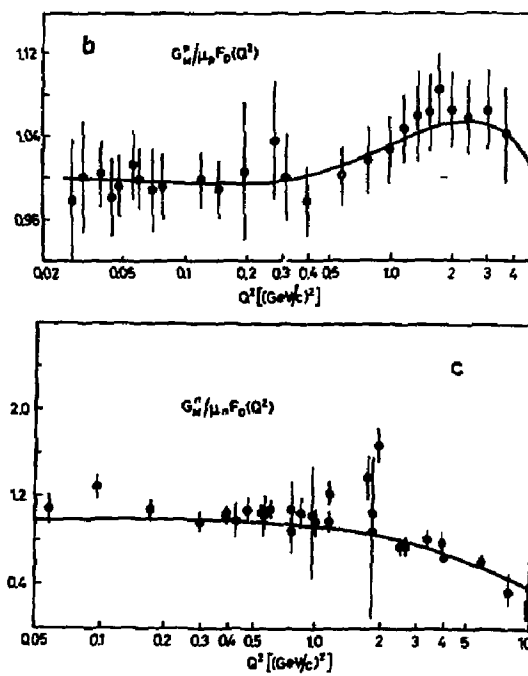

Figs. 5 a-d

Results of the form factor analysis in comparison with the analysed data. The deviation from the common dipole form $F_D(Q^2) = [1/(1+Q^2/0.71)]^2$ is shown, except for the electric neutron form factor G_E^n: a) G_E^p/F_D, b) $G_M^p/\mu_p F_D$, c) $G_M^n/\mu_n F_D$, d) G_E^n. Data points are from the analysis of the cross sections of refs.(7-10).

One has a clear splitting between meson and quark-gluon scale. While the meson scale is about the mass of the vector mesons (ρ,ω) as expected from meson physics, the quark-gluon scale is rather large $\Lambda_2 \approx 3\Lambda_1$. Note that Λ_2 is the only parameter in this picture where we have no information from other sources.

In view of the constraints on the model we realize a remarkable description of the data (χ^2/data $\approx$ 0.5). It is interesting to note that the proton data already determine the form factors. An interesting finding of the QCD-VM model is the fact that the electric neutron form factor turns out to be very large at high Q^2 in contrast to the general belief . It even exceeds the magnetic neutron form factor for $Q^2 > 4M^2$. In view of the fact that the neutron form factor turns out - in this model - to be dominated by the Pauli contribution, direct measurements of the electric and magnetic nucleon form factors are of great importance and will yield important information on the spin-flip parts of the form factor (see also refs.3,5,6 for details).

As can be seen from the above equations (3&4), the Pauli form factor- for both neutron and proton - is dominated by the isovector part. This means that the electric neutron form factor is strongly related to the Pauli form factor of the proton. Therefore measurements of the electric neutron form factor as well as the Pauli form factor of the proton will give us valuable information on the quark spin flip contributions. In the following Fig.6 we show the importance of the Pauli contribution to the magnetic form factor of the proton.

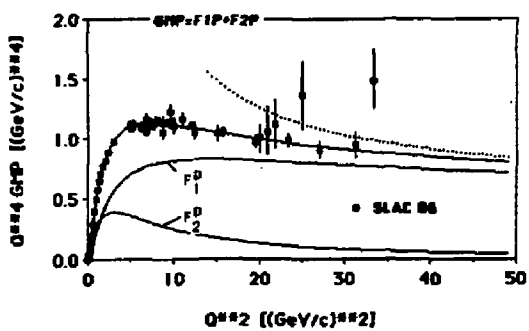

Fig.6

High Q^2 behavior of the proton magnetic form factor $Q^4 G_M^p$. The relative importance of Dirac and Pauli contribution is shown. The dotted line corresponds to the asymptotic form as obtained from PQCD .

Within the present model, which takes care of direct and vector-meson contributions to the form factor, we can now answer the question of importance of the vector-meson pole piece. A measure for this part at $Q^2 = 0$ is the constant c in eq.3. For the above given analysis we have c=0.342 showing that the vector meson contribution is rather small, 34 % at $Q^2 = 0$.

It is interesting to see what replaces the dipole form at low Q^2. For $Q^2 << \Lambda_2^2$ the isovector part has the following form:

$$F_1^{IV}(Q^2) = [\Delta_\rho c + (1-c)]\ \Lambda_1^2/(\Lambda_1^2+Q^2)$$

$$\sim [m_\rho^2/(m_\rho^2+Q^2)]^2 * 0.34 + 0.66\ m_\rho^2/(m_\rho^2+Q^2)$$

Instead of a moving of the rho-meson mass to higher values, a superposition of a monopole and dipole gives the desired structure.

Note that the presented formulas are only thought for a description of the space-like momentum transfer region! It is is only an effective form factor description and not suited for any continuation into time-like momentum transfer.

The vector-meson contribution to the magnetic form factor is shown in Fig.7.

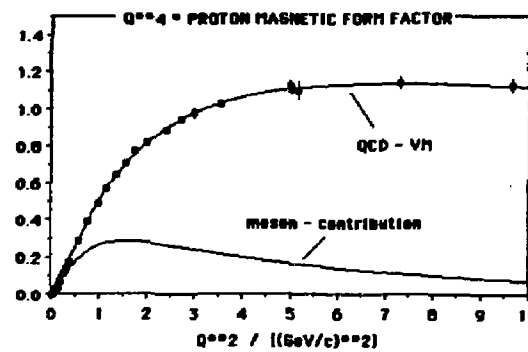

Fig.7

The magnetic form factor in the QCD-VM model. The part which originates from the ρ,ω contribution is indicated.

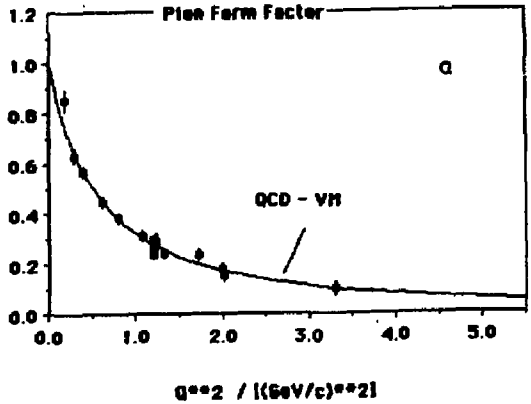

Fig.8

Pion form factor eq.(5), in comparison with the available experimental information. $F_\pi(Q^2)$ and $Q^2 F_\pi(Q^2)$ is shown. To stress the high momentum region, also the non-vector meson part, i.e. the part of the pion form factor which approaches the asymptotic form obtained in PQCD is shown (hard contribution).

Due to the additional power suppression originating from the vector-meson propagator, the vector-meson contribution dies out with increasing Q^2 and becomes less and less important. This is an important finding in connection with the reliability of perturbative QCD calculations of the magnetic form factor. Associating the vector meson contribution with the gluon part of the proton wavefunction it might give us some hint about the importance of the leading Fock states. We shall come back to this point later in connection with the pion form factor where just the opposite behavior is found.

Pion form factor

An analysis equivalent to the one for the nucleon, suggests a form factor for the pion of the type:

$$F_\pi(Q^2)=[\Delta_\rho c_\pi + (1-c_\pi)]\,\Lambda_2^2/(\Lambda_2^2+\hat{Q}^2)\,; \qquad c_\pi=g_{\rho\pi\pi}/f_\rho \qquad (5)$$

For $Q^2 \to \infty$: $F_\pi(Q^2) \to (1-c_\pi)\,\Lambda_2^2/\hat{Q}^2$

$\hat{Q}^2$ as defined in eq.4

An optimal description of the data is obtained for $c_\pi = 0.975$, $\Lambda_{QCD} = 180$ MeV and $\Lambda_2 = 2.19$ GeV.

The result of such an analysis is shown in Fig.8.

In contrast to the nucleon case, the analysis of the pion form factor data reveals a dominant contribution of the vector-meson part up to high momentum transfer. What is usually called the hard contribution and is very large in the case of the nucleon, plays here a minor role.

Fig.9

Interpretation of the vector meson part of the form factor as a gluon contribution of the pion wavefunction.

If the vector meson contribution can be associated with the part of the form factor connected with the gluon part of the wavefunction this might be a hint that in the case of the pion form factor the gluon part plays a dominant role, while for the nucleon the situation is reversed and the valence quarks dominate.

We note that the discussed analysis is the most simple one which actually can be performed. However because of the clear dominance of the vector-meson contribution, the situation in comparison with the nucleon is not likely to be changed qualitatively. In view of the importance of these questions, measurements of the pion form factor at high momentum transfer are highly desirable.

Kaon form factor

There are interesting consequences concerning the K^+ form factor. Using $SU(3)_F$ and a universality condition $c_\pi = c_\rho = c_\varphi$, we have according to the quark assignement of $K^+ = u\bar{s}$, the following prediction for the Kaon form factor:

$$F_{K^+}(Q^2) =$$

$$[(1/2\,\Delta_\rho + 1/6\,\Delta_\omega + 1/3\Delta_\varphi)c_\pi + (1-c_\pi)]\Lambda_2^2/(\Lambda_2^2+\hat{Q}^2)$$

Comparison with VMD form factor models

In the case of the nucleon there exist a variety of vector-meson dominance models. We have seen that the point-like vector meson dominance model including only the established mesons does not give a reasonable form factor description. Most of the models therefore used generalisations in the direction of including heavier vector mesons as $\rho', \rho'', \rho''', \omega', \omega'', \omega'''$ and Ψ', Ψ'', Ψ''', still with point-like meson nucleon interactions. Although the coupling constants of these hypothetical particles are determined by a fit to the nucleon data no satisfactory description could be obtained. Examples for these type of form factor descriptions are given in Figure 10 where we show the magnetic form factor of the proton, which is the most important form factor as it is best known experimentally.

It is noticeable that the strict point-like vector meson dominance pictures of KK and ZB are not able to give the magnetic form factor, not even at low Q^2. The model of Höhler et al. includes the information from pion nucleon scattering which gives additional information beyond VMD for the isovector case. The model of IJL includes a direct coupling of the photon to the nucleon as discussed above, however only in the case of the Dirac form factor. The Pauli form factor is treated in VMD. In addition, a parametrized ρ-propagator was necessary to explain G_M^p. Although both Höhler et al. and IJL give a good description of the proton magnetic and electric data at low momentum transfer, they fail at high Q^2 and in the description of the neutron form factors.

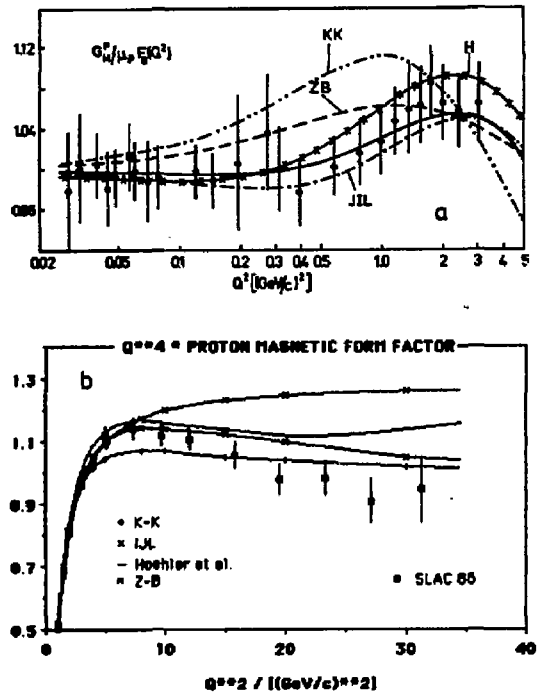

Fig.10

Comparison of different types of form factor descriptions in the case of the magnetic proton form factor ; a) low Q^2: $G_M^p/\mu_p F_D$ is shown: KK[13], IJL[14], Höhler et al.[15], ZB[16] and QCD-VM b) high Q^2: $Q^4 G_M^p$ for KK[13], IJL[14], Höhler et al.[15], ZB[16].

In summary we note that combining the information from meson physics at low Q^2 and the perturbative QCD predictions at high Q^2, a satisfactory description of the present experimental data is achieved. The vector-meson pole contributions dominate at low Q^2 only in the case of the pion. They play a minor role for the nucleon. Relating the vector-meson contributions to those arising from the higher Fock state contributions of the hadron wavefunction one would expect that nucleon and pion wavefunctions[17] are very different in their nontrivial structure. In view of the importance of these problems for the understanding of the hadronic interactions[18,19], extended measurements of the nucleon as well as of the pion form factors are necessary. Especially the measurement of the electric proton form factor, which is presently known only up to $Q^2 \sim 2\ GeV^2/c^2$, will give important insight into the underlying quark-gluon structure.

Thanks are due S.J. Brodsky and N.G. Stefanis for discussions.

REFERENCES

1. For a review see M. Gourdin , Phys. Rep. **11C**, 29 (1974); J.J. Sakurai, Currents and Mesons, The University of Chicago Press(1969).
2. G. P. Lepage and S.J. Brodsky, Phys. Rev. **D22**, 2157 (1980); S. J. Brodsky and G. P. Lepage, Phys. Scr. **23**, 945 (1981).
3. C.E. Carlson, in Proceedings of the NATO Advanced Study Institute on New Vistas in Electro-Nuclear Physiscs,Banff Canada, 22Aug. (1985).
4. S.J. Brodsky and G. Farrar, Phys. Rev. **D11**,1309 (1975).
5. M.F. Gari and W. Krümpelmann, Z. Phys. **A322**, 689 (1985); Phys.Lett. **B173** (1986)10.
   M.F. Gari, International Conference and Symposia on Unified Concepts in Many Body Problems, State University of New York at Stony Brook, Sept. 1986
6. M.F. Gari and N.G. Stefanis , RUB-TPII-86-21, Phys.Lett.B, to be published.
7. S Rock,R.G. Arnold,P. Bosted, B.T. Chertok, B.A. Mecking, I. Schmidt, Z.M. Szalata, R.C. York, R. Zdarko, Phys. Rev.Lett. **49**, 1139 (1982).
8. F. Borkowski, G.G. Simon, V.H. Walther, R.D. Wendeling, Z. Phys. **A275**, 29 (1975); Nucl. Phys. **B93**, 461 (1975). G.G. Simon, F. Borkowski, Ch. Schmitt,V.H. Walther,Z. Naturforsch. **35a**,1 (1980).
9. R. Arnold et al. Phys.Rev.Lett. **57** (1986) 174
10. W. Albrecht, H.J. Behrend, H. Dorner, W. Flauger, H.Hultschig, Phys. Lett. **26B**, 642 (1968).
11. C.J. Bebek et al., Phys.Rev. **D17** (1978) 1693.
12. U. Kaulfuß and M. Gari, Nucl. Phys. **A408**, 507 (1983) ; M. Gari and U. Kaulfuß, Phys. Lett. **136B**, 139 (1984)
13. J.G. Körner and M. Kuroda,Phys.Rev.D16,2165(1977)
14. F. Iachello, A.D. Jackson and A. Lande, Phys. Lett. **43B**,191 (1973).
15. G. Höhler et al.,Nucl.Phys.**B114** (1976) 505.
16. S. Blatnik and N. Zovko, Acta Physica Austr. **39**, 62 (1974).
17. S.J. Brodsky, "Quarks and Nuclear Forces", Springer Tracts Vol. 100 (1982).
    F.E. Close,R.G. Roberts and G.G. Ross, RAL-86-083.
18. V.L. Chernyak and I.R. Zhitnitsky, Nucl.Phys. **B246**(1984) 52 ;
    V.L. Chernyak and A.R. Zhitnitsky, Phys.Rep. **112**(1984) 173.
19. M.F. Gari and N. Stefanis, Phys. Lett.**157B** (1986) 462. and Phys.Rev.**D35** (1987) 1074.

BARYON RESONANCES WITHOUT QUARKS: A CHIRAL SOLITON PERSPECTIVE*

MAREK KARLINER

Stanford Linear Accelerator Center
Stanford University, Stanford, California, 94305

ABSTRACT

In many processes involving low momentum transfer it is fruitful to regard the nucleon as a soliton or "monopole-like" configuration of the pion field. In particular, within this framework it is possible to obtain detailed predictions for pion-nucleon scattering amplitudes and for properties of baryon resonances. One can also derive model-independent linear relations between scattering amplitudes, such as πN and $\overline{K}N$. A short survey of some recent results is given, including comparison with experimental data.

1. INTRODUCTION

This talk describes the application of chiral soliton ideas to the meson-baryon S-matrix. Most of the original work reported here was done in collaboration with Michael Mattis at SLAC.[1,2,3]

How can the chiral soliton picture of the nucleon be put to a quantitative test? The flow chart in Fig. 1 illustrates two potentially productive approaches to the problem. Both will be described in some detail in the course of this talk. For now, I will just summarize the two alternatives.

One possibility is to take the simplest realization of this picture, i.e. the simplest mesonic Lagrangian admitting soliton solutions with the right quantum numbers and then calculate the properties of baryons in that model. The simplest model satisfying such criteria is the Skyrme model. In that model the pion-nucleon scattering matrix can be computed explicitly and it is in good agreement with experiment. The Skyrme Lagrangian is of course only a very crude approximation to the true low-energy effective Lagrangian of QCD. In addition, the results obtained from the Skyrme model might therefore depend on the details of the action. Hence the second approach for testing the chiral soliton picture: it turns out that one can derive model independent predictions, valid for all models in which the baryon corresponds to a soliton of a hedgehog form. In all such models the static soliton is not an eigenstate of the isospin **I**, nor of the angular momentum **L**. Instead it is invariant under the action of $\mathbf{K} = \mathbf{I} + \mathbf{L}$. Therefore the meson-baryon S-matrix has well-defined transformation properties under **K**. This property of the S-matrix yields new and somewhat surprising relations between the various meson-baryon scattering matrix elements. Some of these model-independent relations are satisfied remarkably well in Nature. Let me now describe the two approaches in some detail, addressing first the Skyrme model calculation. I will begin with a very brief review of some basic results in Ref. 3. The Skyrme Lagrangian with a chiral-symmetry breaking mass-term is given by

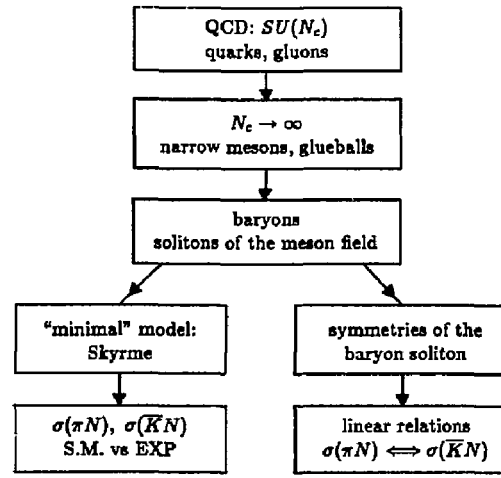

Fig. 1. Flow chart illustrating two possible ways of putting the chiral soliton ideas to a quantitative test: a model-dependent and a model-independent one.

$$\mathcal{L} = \frac{f_\pi^2}{16}\mathrm{Tr}\left(\partial_\mu U\,\partial_\mu U^\dagger\right) + \frac{1}{32e^2}\mathrm{Tr}\left[\left(\partial_\mu U\right)U^\dagger, \left(\partial_\nu U\right)U^\dagger\right]^2 + \frac{f_\pi^2 m_\pi^2}{8}\left(\mathrm{Tr}\,U - 2\right). \tag{1}$$

Here f_π is the pion decay constant (186 MeV in the real world), m_π is the pion mass, and e is a new, dimensionless coupling constant peculiar to the model. The "small parameter" $1/N$ enters the Lagrangian through f_π and e, which behave like $N^{\frac{1}{2}}$ and $N^{-\frac{1}{2}}$ in the large-N limit, respectively.

The chirally invariant vacuum is $U(x) \equiv 1$ and pions are usually thought of as small fluctuations around this state, hence the standard notation:

$$U = \exp\left[\frac{2i}{f_\pi}\vec{\pi}(\vec{x},t)\cdot\vec{\tau}\right]$$

For small $\vec{\pi}/f_\pi$ we have $U \approx 1 + 2i\vec{\pi}(\vec{x},t)\cdot\vec{\tau}/f_\pi$ and then the first term in Eq. (1) becomes just the kinetic term for free pions, as expected:

$$\frac{f_\pi^2}{16}\mathrm{Tr}\left(\partial_\mu U\,\partial_\mu U^\dagger\right) \;\to\; \frac{1}{2}\left(\partial_\mu\vec{\pi}\cdot\partial_\mu\vec{\pi}\right) \;+\; \ldots \tag{2}$$

In addition to the vacuum solution, (1) has static soliton solutions which break the chiral symmetry and carry one unit of baryon number. They can all be obtained by an isospin rotation from the canonical "hedgehog" solution:

$$U_0 = \exp\left[F(r)\hat{r}\cdot\vec{\tau}\right] \quad \text{and} \quad U_A = A\,U_0\,A^{-1} \tag{3}$$

* Work supported by the Department of Energy, contract DE-AC03-76SF00515.

where A is a constant $SU(2)$ matrix. When A is treated as a collective coordinate, one finds that the nucleon corresponds to a superposition of the U_A-s. Schematically we can write this as

$$|N\rangle = \int dA\, \chi(A)\, |A\rangle$$

where $\chi(A)$ is the wave-function in the space of collective coordinates. While $|A\rangle$ corresponds to a state pointing in a well-defined direction in the internal space, it has an ill-defined isospin and angular momentum. On the other hand, the state $|N\rangle$ has well-defined spin and isospin, but does not point in any specific direction in the internal space. The situation here is completely analogous to the problem of a particle constrained to move on a circular ring, as shown in Fig. 2.

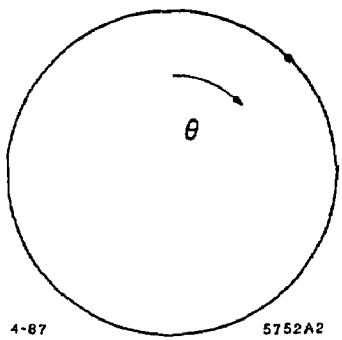

Fig. 2. A one-dimensional analogue of the collective coordinate A: particle constrained to move on a circular ring. Classical ground state corresponds to a particle at rest at some fixed angle θ. In quantum mechanics this is no longer true and we must have an eigenstate of the angular momentum operator $L_\theta = -i\frac{\partial}{\partial\theta}$.

Classically, a particle at rest at any angle θ is a ground state of the system. In quantum mechanics the eigenstates of the hamiltonian no longer are localized at a fixed angle θ. Instead, they are eigenstates of the angular momentum operator $L_\theta = -i\frac{\partial}{\partial\theta}$. Using this analogy, we see that a nucleon with a well-defined spin and isospin corresponds to a *rotating* soliton.

Static properties of the nucleon in the Skyrme model obtained in Ref. 3 were based on treating f_π and e as free parameters, to be adjusted for the best fit to nucleon and Δ masses. All other static quantities were obtained as functions of e and f_π. Some properties of the nucleon turned out very well, but some others were in serious disagreement with experiment. Most notably, the values of f_π and g_A had errors of about 30% and 50%, respectively. At this point it is worth reminding ourselves that the Skyrme Lagrangian is in principle an equally good approximation to an underlying $SU(N)$ gauge theory with $N = 3$ or $N = 5$, etc. In the real world $N = 3$ and it is therefore very unlikely that the Skyrme Lagrangian can reproduce experimental quantities which explicitly depend on N. Typically the most we can hope for is to reproduce experimental quantities which do not depend on N in the leading order of the $1/N$ expansion. For example, while $f_\pi \sim N^{\frac{1}{2}}$ and $g_A \sim N$, the ratio $f_\pi^2/g_A \sim N^0$ and in contrast to f_π and g_A taken separately, it reproduces experiment to 3%. As shown in Table I, similar statements can be made about some other N-independent ratios.

The purpose of this example is *not* to suggest that *all* N-independent quantities should agree well with experiment, for this is hardly the case. The results in Table I suggest however that the N-independent quantities stand a better chance of reproducing the real world data. If our guiding principle is to look for such quantities, it is natural to examine the pion-nucleon S-matrix, since meson-baryon scattering amplitudes are independent of N in the large-N limit.[1]

The first step towards the computation of the πN S-matrix is the realization that small fluctuations around the soliton can be identified with physical mesons. This is schematically illustrated in Fig. 3.*

Once that identification is made, it is clear that in order to obtain the pion-nucleon S-matrix, we should in principle find the eigenmodes of small fluctuations around a rotating soliton. This is a very difficult problem. Fortunately enough, in the large-N limit there is an important simplification: in that limit the soliton rotates very slowly, with angular velocity $\omega_s \sim 1/N$. The reason is as follows. The spin of the nucleon is $\frac{1}{2}\hbar$, independent of N. It is the product of the Skyrmion angular velocity ω_s and its moment of inertia I_s. The Skyrmion radius R_s is independent of N and its mass M_s scales like N.[3] Consequently

$$I_s \sim M_s R_s^2 \sim N \qquad \text{while} \qquad I_s\,\omega_s = \frac{1}{2}\hbar \sim N^0$$

therefore

$$\omega_s \sim 1/N$$

The characteristic time scale t_{rot} associated with the Skyrmion rotation is large, $t_{rot} \sim 1/\omega_s \sim N$. It is much greater than the time t_π that a pion moving with the speed of light spends in the vicinity of the nucleon:

$$R_s \sim N^0; \qquad R_s/c \sim N^0 \sim t_\pi \ll t_{rot} \sim N$$

A pion will therefore not observe the rotation, but rather will take a "snapshot" of the soliton in one of its possible orientations. The probability of any given orientation is proportional to $|\chi(A)|^2$. This justifies the impulse approximation: first obtaining the scattering amplitude for scattering of a pion by a soliton pointing in a *fixed orientation* and then superimposing such amplitudes, according to their weight in $\chi(A)$.

In addition to neglecting the rotation, as described above, we can neglect the nucleon recoil, since in the large-N limit the pion kinetic energy in the domain of interest is independent on N, while $M_s \sim N$. In order to obtain the Lagrangian describing scattering of mesons by a static soliton, we write the chiral field U in the form:

$$U = \exp\left[F(r)\hat{\tau}\cdot\vec{\pi} + \frac{2i\vec{\pi}}{f_\pi}\right]. \tag{4}$$

This form of U is then plugged back into the original

* This identification breaks down for fluctuations which do not change the energy of the system. Such fluctuations correspond to the translational and rotational zero modes of the soliton. In our treatment this subtlety is neglected, spoiling the agreement with experiment in the low partial waves.

TABLE I

STATIC PROPERTIES OF THE NUCLEON IN THE SKYRME MODEL AND THEIR DEPENDENCE ON N.

Quantity	N-dependence	Prediction	Experiment	Error
$\langle r^2\rangle^{1/2}_{I=0}$	$\sim N^0$	0.59 fm	0.72 fm	18%
$\langle r^2\rangle^{1/2}_{M,I=0}$	$\sim N^0$	0.92 fm	0.81 fm	14%
μ_p	$\sim N$	1.87	2.79	33%
μ_n	$\sim N$	-1.31	-1.91	31%
μ_p/μ_n	$\sim N^0$	1.43	1.46	2%
g_A	$\sim N$	0.61	1.23	50%
f_π	$\sim N^{\frac{1}{2}}$	129 MeV	186 MeV	31%
f_π^2/g_A	$\sim N^0$	27,280 MeV^2	28,127 MeV^2	3%
$g_{\pi NN}$	$\sim N^{\frac{3}{2}}$	8.9	13.5	34%
$g_{\pi N\Delta}$	$\sim N^{\frac{3}{2}}$	13.2	20.3	35%
$g_{\pi N\Delta}/g_{\pi NN}$	$\sim N^0$	1.5	1.5	$\lesssim 1\%$

The predictions are from Ref. 3. Skyrme model is *a priori* an equally good effective Lagrangian for $N_c = 3$ and $N_c = 5$. So it does not reproduce well the quantities which depend on N in the leading order of the $1/N$ expansion. On the other hand, as demonstrated by the table above, it typically does much better for ratios in which the N-dependence cancels out.

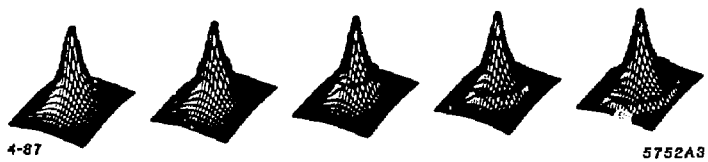

$$U_0 = \exp\left[F(r)\hat{\mathbf{r}}\cdot\vec{\tau}\right]$$

$$U = \exp\left[F(r)\hat{\mathbf{r}}\cdot\vec{\tau} + \frac{2i\vec{\pi}(\vec{x},t)}{f_\pi}\right]$$

Fig. 3. A two-dimensional example showing how fluctuations around the classical soliton profile should be identified with the physical mesons. Time flows from left to right and the fluctuation corresponds to an outgoing spherical wave.

Lagrangian (1) and the action is expanded in powers of $\vec{\pi}/f_\pi$:

$$\mathcal{L}(U) \quad \rightarrow \quad \mathcal{L}(\vec{\pi}) = \frac{1}{2}\vec{\pi}\,\Box\,\vec{\pi} + O\left(\vec{\pi}^3/f_\pi^3\right) \qquad (5)$$

where $\Box$ is a second-order linear differential operator depending on U_0. For $r \rightarrow \infty$, $U_0 \rightarrow 1$ and then $\Box$ becomes just the free four-Laplacian, as in (2). The term linear in $\vec{\pi}$ vanishes, since U_0 is an extremum of the classical action. In addition, in the $N \rightarrow \infty$ limit we can formally neglect the $O\left(\vec{\pi}^3/f_\pi^3\right)$ terms, since $f_\pi \sim N^{\frac{1}{2}}$, and such terms are suppressed relative to the quadratic one. We are left with a quadratic Lagrangian and therefore with linear equations of motion, which can be schematically written as:

$$\Box\,\vec{\pi} = 0$$

These equations describe the motion of a meson in a potential provided by the soliton background.* Since the potential is invariant under $\mathbf{K}$, K plays the role of the angular momentum in the usual partial wave decomposition. The equations can be explicitly solved for each value of K, yielding the eigenmodes of $\vec{\pi}$ as functions of energy. For $|\vec{x}| \gg R_s$, $F(r) \rightarrow 0$ (*cf.* Eq. (3)), the potential vanishes, and up to a phase, the $\vec{\pi}$ wave function is that of a free particle. This phase is just the scattering phase-shift defining the S-matrix element in a given pion-Skyrmion channel. We shall refer to the latter as *reduced* matrix elements. The reason for this name will become clear in a moment.

* The explicit expression for $\Box$ is rather complicated and will not be given here. Interested reader is referred to the original literature Refs. 4, 6, 8 and 9.

In order to obtain the pion-nucleon S-matrix from the pion-Skyrmion one, we need to project the Skyrmion onto states with well-defined isospin and spin. This projection is carried out as follows. First, given the T-matrix† T_{U_0} for scattering off U_0, the corresponding T-matrix for scattering off U_A (*cf.* Eq. (3)) is given by:

$$T_{U_A} = \hat{D}(A)\, T_{U_0}\, \hat{D}(A)^\dagger \tag{6}$$

where $\hat{D}$ is the adjoint representation of A. Next we superimpose the T_{U_A}-s according to their weight in the nucleon wave function $\chi(A)$. The complete expression for the physical T-matrix is then:

$$T_{PHYS} = \int_{SU(N_f)} dA\; \chi^\dagger_f(A)\, \hat{D}(A)\, T_{U_0}\, \hat{D}(A)^\dagger \chi_i(A) \tag{7}$$

where $SU(N_f)$ is the flavor group and $\chi_{i(f)}$ is the wavefunction of the baryon in the initial (final) state. Integration over the flavor group can be carried out in closed form (see Appendix B of Ref. 9 for details.) The final result has a very simple structure:

$$T_{PHYS} = \sum_i C_i \mathcal{T}^{\rm RED}_i \tag{8}$$

where $\mathcal{T}^{\rm RED}$ are the T-matrix elements in the pion-Skyrmion system and the C_i-s are group-theoretical factors. The structure of Eq. (8) explicitly demonstrates two ingredients on which the physical answer depends: symmetry and dynamics. C_i-s reflect only the symmetry and are independent of the details of the Lagrangian. They are determined by the flavor group and by the fact that the soliton is invariant under $\mathbf{K}$; all dynamics is contained in the reduced matrix elements. We are all familiar with this type of division into group theory and dynamics. For example, isospin conservation dictates that the T-matrix for $\pi N \to \pi N$ is given by

$$T_{\pi N} = C_{\frac{1}{2}} T_{\frac{1}{2}} + C_{\frac{3}{2}} T_{\frac{3}{2}} \tag{9}$$

where $C_{\frac{1}{2}(\frac{3}{2})}$ are $SU(2)$ Clebsch-Gordan coefficients and $T_{\frac{1}{2}(\frac{3}{2})}$ are the $I = \frac{1}{2}(\frac{3}{2})$ reduced matrix elements.

In the foregoing discussion we have focused on the 2-flavor Skyrme model. Extension to 3-flavors is in principle straightforward. The embedding of the $SU(2)$ hedgehog inside $SU(3)$ is done by setting

$$U_0 \to \left(\begin{array}{c|c} U_0 & \\ \hline & 1 \end{array}\right) \tag{10}$$

Technical details for $SU(3)$ are however much more complicated. The interested reader is again referred to the original literature, especially Ref. 9.

At this point we can summarize the prescription for computing the meson-baryon S-matrix in the Skyrme model:

- identify small fluctuations around the soliton with mesons
- meson wave function $\Longrightarrow$ phase shifts, $\mathcal{T}^{\rm RED}_i$
- K symmetry $\Longrightarrow T_{PHYS} = \sum_i C_i \mathcal{T}^{\rm RED}_i$
- Approximations:
  - ▷ $m_u = m_d = m_s = 0 \Longrightarrow$ massless pseudoscalar mesons, exact $SU(3)_f$
  - ▷ Large-$N \Longrightarrow$ no recoil, linear eq's of motions
  - ▷ Zero modes for $L = 0, 1, 2$; neglected

We are ready to compare the Skyrme model T-matrix with the experiment. It is customary to decompose the experimental data into channels with well-defined isospin I, angular momentum J and orbital angular momentum L. Such channels are denoted by $L_{2I,2J}$ where L is denoted by an appropriate letter: S, P, D, F, G, H, I, K for $L = 0, 1, 2, 3, 4, 5, 6, 7$, respectively. The T-matrix for each $L_{2I,2J}$ channel is plotted as a function of the energy, on the so-called Argand plots (*cf.* Fig. 4).

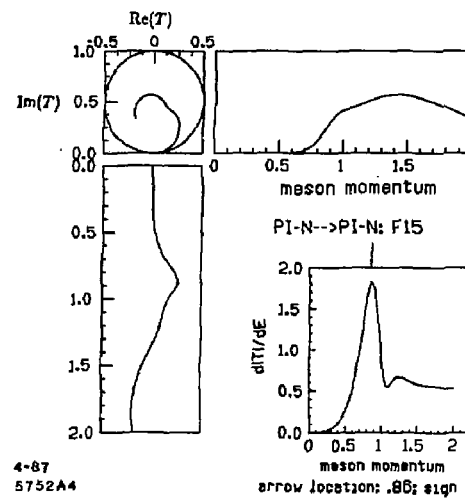

Fig. 4. Sample Argand diagram. A resonance corresponds to the maximum velocity of $d|T|/dE$ (here denoted by an arrow). In the Skyrme model the plot in the unitarity circle, ImT *vs.* ReT, is independent of e and f_π.

The part of the diagram bounded by the unitarity circle, ImT *vs.* ReT is independent of e and f_π and therefore provides the most stringent test of the model. Fig. 5 compares the experimental results for $\pi N \to \pi N$ S-matrix with those of the 3-flavor Skyrme model.

I'd like to stress again that the Skyrme model calculation as shown in Fig. 5 *contains no adjustable parameters*. The parameters of the model determine the energy scale, but not the *shape* of the Argand plots. Apart from the S, P and D partial waves, containing the spurious zero modes, overall agreement with experiment is quite good.

The most conspicuous feature of Fig. 5 is the fact that the $L_{I=1/2,J=L-1/2}$ channel is much larger than $L_{I=1/2,J=L+1/2}$ for all L's. This is true for both experiment and the Skyrme model. A similar, albeit less pronounced pattern holds for

† We interchange freely between the S-matrix and T-matrix, using the one which is the most convenient. The two are related by $T = (S - 1)/2i$.

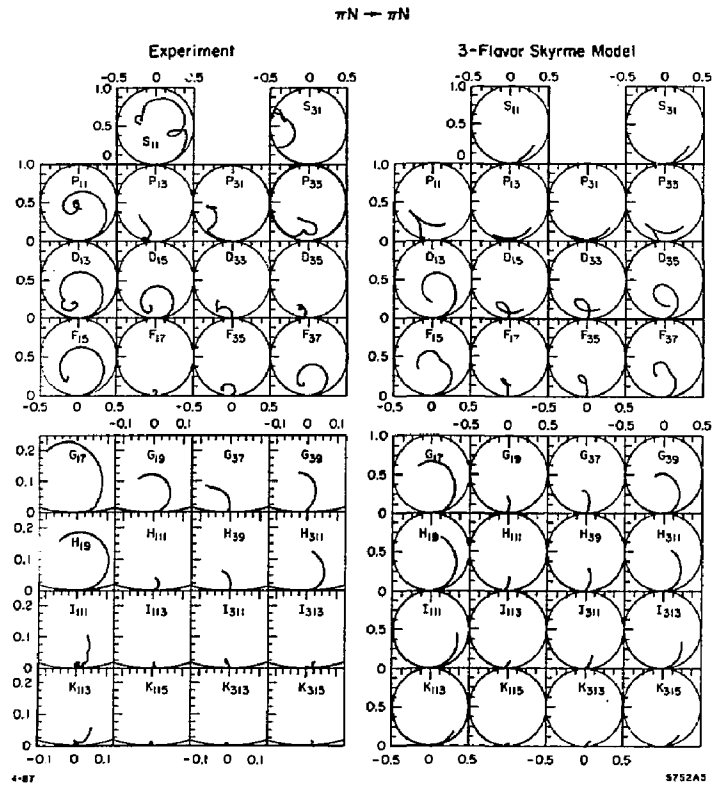

Fig. 5. $\pi N \to \pi N$: comparison between the 3-flavor Skyrme model and experiment (from Ref. 9). The plots show $\mathrm{Im}(T)$ *vs.* $\mathrm{Re}(T)$ for each channel. Channels are labeled by L_{2I2J}, where L is the pion orbital angular momentum, I is the total isospin and J the total angular momentum.

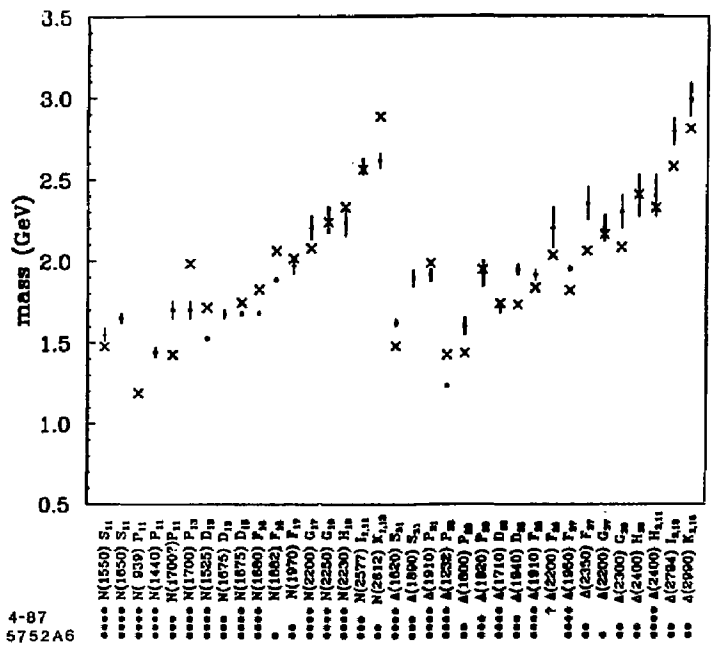

Fig. 6. Spectrum of N and Δ resonances: 3-flavor Skyrme model (crosses) *vs.* experiment (points with error bars) (from Ref. 9). Resonances are assigned stars according to the Particle Data Book. The Skyrme-model values for m_N and m_Δ are obtained from Eq. (9) of Ref. 3, using the "best fit" parameters of Ref. 9 (e =4.79, f_π =150 MeV.)

$L_{I=3/2,J=L+1/2}$ and $L_{I=3/2,J=L-1/2}$ channels. In the chiral soliton framework this phenomenon has a very simple explanation: there are eight reduced amplitudes entering Eq. (8) for $SU(3)_f$. Out of these, five turn out to be very small and only three are significant, with roughly the same magnitude. The magnitude of the *physical* amplitudes is therefore determined by group theory, *i.e.* the relative strength of the C_i-s multiplying the three principal reduced amplitudes.

Having obtained the complete set of partial-wave channels, we can compute the resonance masses from the maxima of $d|T|/dE$. The resulting spectrum of N and Δ resonances is displayed in Fig. 6. With over 30 resonances and two adjustable parameters, masses are predicted with an average of about 7%. While all of the 4-star resonances appear in the same place in 2- and 3-flavor calculation, the 1- and 2-star resonances in the F_{15} and F_{37} channels supply a surprise: as demonstrated by Fig. 7, these weak resonances appear only when the third flavor is introduced. It is somewhat puzzling that the appearance of non-strange resonances should be sensitive to the existence of the strange quark. A possible explanation is that they couple to the strange quark sea in the proton.

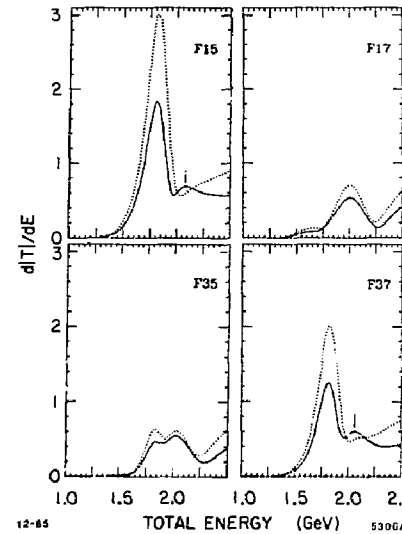

Fig. 7. Speed diagrams for the four F-wave amplitudes in the 2- and 3-flavor Skyrme models (dotted and solid lines, respectively).

Fig. 8. $\pi N \to \pi\Delta$: comparison between the 3-flavor Skyrme model and the experimental solution of Ref. 13 (from Ref. 9). Channels are labeled by $LL'_{2I,2J}$, with L and L' the incoming and outgoing pion angular momenta, respectively. An asterisk denotes amplitudes which were found to be small and/or poorly determined by the available data, and were therefore not included in the experimental solution. The partial-wave analysis of the experimental data is not as unambiguous as in $\pi N \to \pi N$, but in all cases the Skyrme model correctly reproduces the sign of $\mathrm{Im}(T)$, which is a crucial test for theory.

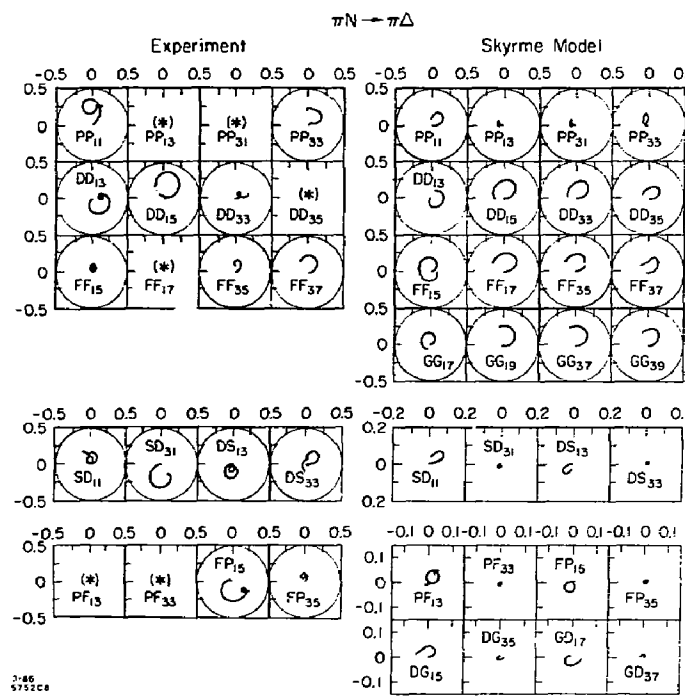

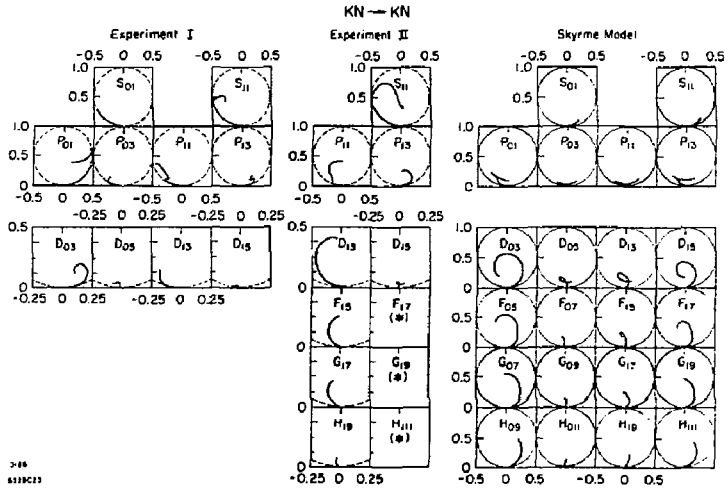

Fig. 9. $KN \to KN$: comparison between the Skyrme model and two experimental solutions (from Ref. 9): "Experiment I" from Ref. 14 and "Experiment II" from Ref. 15. Channels are labeled by $L_{I,2J}$. Note that experimental and Skyrme-model plots for $L \geq 2$ are shown on different scales. The resonance-like behavior in some of the experimental channels is evident.

In addition to the elastic $\pi N \to \pi N$ processes, we can also consider inelastic processes, such as $\pi N \to \pi\Delta$. The only change with respect to $\pi N \to \pi N$ is that χ_f stands now for the Δ, instead of the nucleon wavefunction. The results are shown in Fig. 8. The experimental partial-wave analysis of $\pi N \to \pi\Delta$ is somewhat less clear-cut than $\pi N \to \pi N$, since a $N\pi\pi$ final state may represent $N\rho$, as well as $\Delta\pi$. The sign of Im(T) is however unambiguous in most cases and wherever it is known experimentally, the Skyrme model yields the correct answer. This is highly non-trivial: the only other theoretical scheme which passes this test is the quark model.

The results discussed so far were obtained in the 3-flavor model, but did not involve strange particles. We will now review two processes with open strangeness, beginning with $KN \to KN$. That reaction is rather different from $\pi N \to \pi N$, because any resonances in the KN channels must be exotics, involving more than three quarks. The question whether such resonances exist experimentally has long been a controversial subject.* The Skyrme model has no built-in bias of this kind and therefore it is interesting to compare its predictions with experiment, as shown in Fig. 9. In general, the predictions contain *too many* resonances, compared to the data. Of particular interest are the F-waves, where the model typically works best. The theory predicts a clean resonance in the F_{05} channel, similar to the one observed in D_{03}. This channel has not yet been analyzed experimentally and thus provides an interesting prediction. Contrary to the KN channel, there is nothing exotic about $\overline{K}N \to \overline{K}N$. The partial-wave analysis of experimental data is of good quality, although not as precise as $\pi N \to \pi N$, especially in the higher partial waves. The theory reproduces most of the essential features of the experiment, as shown in Fig. 10. Since we work in the chiral limit, $m_K = 0$, there is no point in attempting to extract the spectrum of the strange resonances.

It is possible to study many more inelastic, strange and non-strange processes. Details may be found in Ref. 9. At this point I would however like to move on to the model-independent tests of the chiral soliton picture, as outlined at the beginning of this talk. Let me invoke the isospin analogue once more. If we consider elastic scattering of charged pions on nucleon, *a priori* there are *four* different amplitudes to consider: $T(\pi^+p)$, $T(\pi^-p)$, $T(\pi^+n)$ and $T(\pi^-n)$. From Eq. (9) we learn that they can all be obtained from *two* reduced amplitudes:

$$T_{\pi N} = C_{\frac{1}{2}} T_{\frac{1}{2}} + C_{\frac{3}{2}} T_{\frac{3}{2}}$$

Only two out of the four can be independent, and so there is a *linear relation* between any three of the four. This is a rather generic phenomenon, with an interesting counterpart in the chiral soliton framework, valid for all models in which the nucleon corresponds to a soliton invariant under the K symmetry: with three flavors any elastic meson-baryon T-matrix element is given by a linear superposition of the eight reduced amplitudes. In the Skyrme model five reduced amplitudes are negligible and the other three make the dominant and roughly equal contributions to the physical amplitudes. Even though we cannot compute the reduced amplitudes in Nature, it is natural to make the dynamical assumption that this hierarchy exists in the real world as well:

$$T_{PHYS} \approx \sum_{i=1}^{3} C_i T_i^{\mathrm{RED}} \qquad (11)$$

* Some of our colleagues even refuse to be confused by data, as is perhaps best illustrated by the 1984 Particle Data Book: "*... The general feeling, supported by prejudice against baryons not made up of three quarks, is that the suggestive counterclockwise movement in the Argand diagram of some of the partial waves is not real evidence for true Breit-Wigner resonances...*" (p. S243).

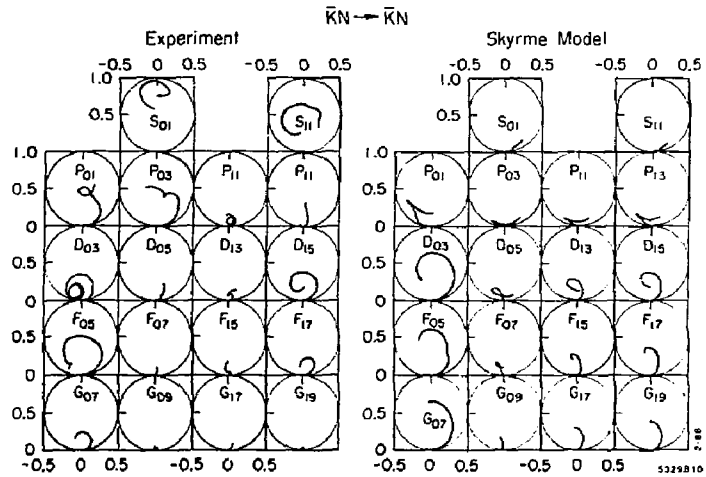

Fig. 10. $\overline{K}N \to \overline{K}N$ **: comparison between the Skyrme model and the experimental solution of Ref. 16 (from Ref. 9). Channels are labeled by** $L_{I,2J}$.

Such an assumption not only explains why for $\pi N \to \pi N$ $L_{I=1/2,J=L-1/2} \gtrsim L_{I=1/2,J=L-1/2}$, etc., but also yields some quite new and interesting predictions. For a given value of L there are many experimental amplitudes, all determined in terms of the three unknown reduced amplitudes. Consequently, there are linear relations among the experimental amplitudes. Such relations are almost model independent, relying only on the K-symmetry group theory and on the assumption that scattering is dominated by the three reduced amplitudes.

First, there are rather accurate linear relations between $\pi N \to \pi N$ and $\pi N \to \pi\Delta$. Very similar relations can be derived in the 2-flavor case, as was originally done in Ref. 5. In that case there are only 3 reduced amplitudes and no dynamical assumptions are necessary. In order to test the predictions inherent to 3-flavors, it is however necessary to consider relations between strange and non-strange amplitudes.[17] One such relation reads

$$a_1 F_{15}^{\pi N} + a_2 F_{37}^{\pi N} = b_1 F_{05}^{\overline{K}N} + b_2 F_{07}^{\overline{K}N} \qquad (12)$$

where a-s and b-s are purely group-theoretical coefficients obtained from C_i-s in Eq. (11), and $F_{15}^{\pi N}$, $F_{37}^{\pi N}$, $F_{05}^{\overline{K}N}$ and $F_{07}^{\overline{K}N}$ are the experimental partial-wave amplitudes.

As shown by Fig. 11, the prediction contained in Eq. (12) is satisfied with remarkable accuracy. It is also possible to derive similar predictions for G-waves. At present the partial wave analysis for the G-wave $\overline{K}N$ is not yet reliable enough. The G-wave linear relation is therefore a real prediction for what the $\overline{K}N$ G-waves should look like. I very much hope that this prediction will be put to a test sometime in the near future, perhaps with the advent of the K-factories. It is important to note that Eq. (12) *cannot* be obtained from $SU(3)_f$ by itself. While $SU(3)_f$ is part of the symmetry used to derive Eq. (12), it is clear that $SU(3)_f$ alone cannot produce such a relation, since it mixes amplitudes with different total angular momenta. A more detailed argument shows that even

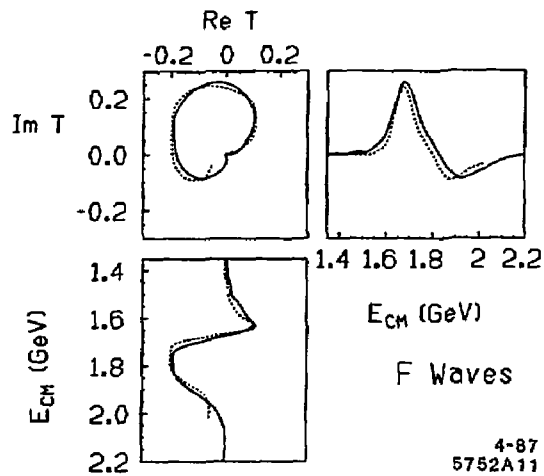

Fig. 11. Test of the prediction for a linear relation between $\pi N \to \pi N$ and $\overline{K}N \to \overline{K}N$, Eq. (12). The scattering matrix T is plotted both as function of energy and in $\mathrm{Im}(T)$ *vs.* $\mathrm{Re}(T)$ representation. Continuous lines: linear combination of the experimental F_{15} and F_{37} $\pi N \to \pi N$ amplitudes. Dotted lines: linear combination of the experimental F_{05} and F_{17} $\overline{K}N \to \overline{K}N$ amplitudes. $\overline{K}N$ amplitudes are shifted by the strange quark mass $\approx$ 150 MeV.

the more elaborate "conventional" symmetries, such as $SU(6)$ are also incapable of reproducing Eq. (12).[17] That being the case, the very precise experimental confirmation of the F-wave linear relations should be regarded as another strong testimony in favor of the view that the nucleon indeed can be regarded as a soliton of the meson field.

In closing, I would like to mention that the same ideas which make it possible to obtain the pion-nucleon S-matrix can be applied to the photoproduction of pions on nucleons. This is done by coupling the photon field to the chiral field U and then proceeding as in pion-nucleon scattering. An explicit calculation of the photoproduction helicity amplitudes was recently carried out along these lines in Siegen University.[18]

I hope that this brief review has convinced you that the chiral soliton picture of the nucleon is not only valid on a qualitative basis, but also can be used to study details of low energy hadronic phenomena in a way complementary to and on a par with the quark picture.

REFERENCES

1. E. Witten *Nucl. Phys.* **B160**, 57 (1979).
2. E. Witten, in Lewes Workshop Proc.; A. Chodos *et al.*, Eds; Singapore, World Scientific, 1984.
3. G. Adkins, C. Nappi, and E. Witten, *Nucl. Phys.* **B228**, 552 (1983).
4. M. P. Mattis and M. Karliner *Phys. Rev.* **D31**, 2833 (1985) and references therein.
5. M. P. Mattis and M. Peskin *Phys. Rev.* **D32**, 58 (1985).
6. A. Hayashi, G. Eckart, G. Holzwarth, and H. Walliser, *Phys. Lett.* **147B**, 5 (1984).
7. H. Walliser and G. Eckart, *Nucl. Phys.* **A429**, 514 (1984).
8. M. Karliner and M. P. Mattis, *Phys. Rev. Lett.* **56**, 428 (1986).
9. M. Karliner and M. P. Mattis, *Phys. Rev.* **D34**, 1991 (1986).
10. M. Karliner and M. P. Mattis, SLAC-PUB-3991, to be published in proceedings of the 2nd Conference on the Interaction Between Particles and Nuclear Physics, Lake Louise, Canada.
11. G. Höhler, F. Kaiser, R. Koch, and E. Pietarinen, *Handbook of Pion-Nucleon Scattering* (Fachinformationszentrum, Karlsruhe, 1979), Physik Daten No. 12-7. Reproduced in Review of Particle Properties, *Rev. Mod. Phys.* **56**, part II (1984). ($\pi N \to \pi N$)
12. R. E. Cutkosky *et al.*, in *Baryon* 1980 (conference proceedings), ed. N. Isgur; reproduced in Review of Particle Properties, *op. cit.* ($\pi N \to \pi N$)
13. D. M. Manley, R. A. Arndt, Y. Goradia, and V. L. Teplitz, *Phys. Rev.* **D30**, 904 (1984). ($\pi N \to \pi \Delta$)
14. K. Hashimoto, *Phys. Rev.* **C29**, 1377 (1984). ($KN \to KN$)
15. R. A. Arndt and L. D. Roper, *Phys. Rev.* **D31**, 2230 (1985). ($KN \to KN$)
16. G. P. Gopal *et al.*, *Nucl. Phys.* **B119**, 362 (1977). Reproduced in Review of Particle Properties, *op. cit.* ($\overline{K}N \to \overline{K}N$)
17. M. Karliner *Phys. Rev. Lett.* **57**, 523 (1986).
18. G. Eckart and B. Schwesinger, *Photoproduction of Baryon Resonances in the Skyrme Model;* Siegen University preprint, SI-86-3, Feb. 1986.

A H_2 GAS JET AS INTERNAL TARGET

R704 Collaboration at CERN, Geneva, Switzerland
J. Fay
IPN, Lyons, France
M. Macri
INFN, Genoa, Italy

Abstract: Experiment R704, the last to be performed at the CERN Intersecting Storage Rings, has successfully applied a new method to studying ($\bar{c}c$) states formed directly in antiproton-proton annihilations. The novelty of the method lies in the capability of building a highly performing annihilation source by letting a cold antiproton beam, coasting inside ring 2 at the ISR, continuously interact with a dense internal H_2 target. Details of the characteristics of the source are given in this paper.

1. Introduction

The possibilities offered by the availability of an intense antiproton source for the study of ($\bar{c}c$) states are now well established [1]. The scheme adopted for the R704 experiment required the use of an internal target (a molecular hydrogen jet) continuously intersecting a cold antiproton beam coasting inside the vacuum pipe of ring 2 at the CERN Intersecting Storage Rings (ISR).

The RF system and cooling equipment of ring 2 at the ISR provided great flexibility of beam-control operations, while the well-localized, high-density target permitted the small-size, high-luminosity source required for charmonium formation studies. The method allows for an absolute calibration in the centre-of-mass energy to a fraction of a MeV.

The luminosity of the annihilation source was continuously monitored by measuring, with a solid-state silicon telescope, the yield of protons from small-angle $\bar{p}p$ elastic scattering. The coupled measurement of energy and angle in the silicon detector provided an essentially background-free sample of elastic events.

2. The Beam-Target System

In a formation experiment with antiprotons interacting on a stationary hydrogen target, the energy of the beam is related to the value (m_r) of the mass of the resonance by the equation

$$E_{\bar{p}} = m_r^2/2m_p - m_p .$$

To study charmonium states we operated ring 2 at the ISR in the range of momentum from 3.5 to 6.5 GeV/c. The unbunched antiprotons coasted inside the ring with a revolution frequency of $\nu \approx 3.1 \times 10^5\ s^{-1}$, crossing, at each turn, an internal target mounted in the straight section upstream of the intersection region 17. The maximum beam current reached was 5.5 mA corresponding to $N = 1.1 \times 10^{11}$ circulating antiprotons. The target, a H_2 gas jet, had a density of $\varrho = 10^{14}$ atoms per cm^3 and a diameter, at the intersection with the beam, of $d \approx 0.9$ cm.

To summarize, the features of the source were:

i) High luminosity, up to a maximum value:

$$L_0 = \varrho_{H_2} d_{H_2} N \nu = 3 \times 10^{30}\ s^{-1} \cdot cm^{-2} .$$

ii) Long beam lifetime: $T_{beam} \approx 100$ h at the maximum jet density, almost entirely accounted for by beam losses caused by nuclear interactions in the jet.

iii) Small momentum bite, at best:

$$\Delta p/p = \pm 4 \times 10^{-4} ,$$

corresponding to an incertitude in the centre-of-mass energy of $\Delta\sqrt{s} \approx 0.5$ MeV/c^2.

iv) Small source volume:

height × width × depth = 0.5 × 0.8 × 0.9 cm^3 (for 90% containment).

v) No energy drift during data taking.

The techniques by which the required performance of the operation of ring 2 at the ISR was achieved are described elsewhere [1], while a description of the target system is given in the following section.

3. The Jet Target

The optimal thickness of the internal target for this type of experiment lies in the range of 1 to 3×10^{14} atoms per cm^2. A much thicker target would perturb the beam to an uncontrollable level, while a thinner one would, given the limited supply of antiprotons, lead to an unacceptably low luminosity. The target, intersecting an unbunched beam, must operate continuously to minimize the ratio of instantaneous rate on detectors to integrated luminosity, and have small transverse dimensions, with maximum beam overlap.

A target in the required density range and with the appropriate geometry can be built by letting molecular hydrogen at high pressure and low temperature expand through a narrow throat injector of suitable shape [2]. At a short distance from the nozzle throat, the flow field of the gas is similar to that from a point source (Fig. 1). Stream lines are almost straight with the stream core clustering in large agglomerates of molecules which can move at supersonic speed (hence the name 'jet') over long distances in high vacuum, without absorption or diffusion by the residual gas.

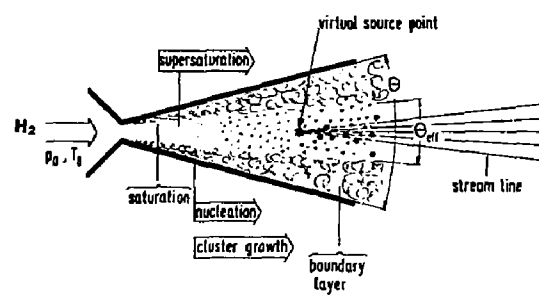

Fig. 1 Converging-diverging nozzle: schematic localization of phases in the gas expansion [2].

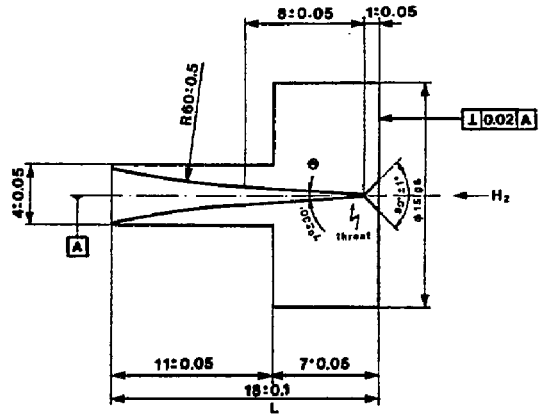

Fig. 2 Cross-section of the nozzle.

For experiment R704 we built a target with a trumpet-like injector (Fig. 2). This shape maximizes the density of the jet core [2]. The values of the nozzle parameters were: D = 30 μm, the throat diameter: θ = 3.5°, the angular half-acceptance; and L = 18 mm, the total length. It was manufactured from copper in the CERN workshop [3].

We choose to operate at liquid N_2 temperature to simplify the construction of the temperature-control system and for reliability of operation over long periods.

Figure 3 schematizes the target system. The expansion took place in chamber 1. Typical operating conditions were at p_0 = 10 bar and T_0 = 77 K. A three-collimators system (C_1, C_2, C_3) (Fig. 4) selected the central, denser part of the jet which, after crossing the ISR ring 2, was absorbed by the sink pumps.

The injector was mounted on a movable mechanism to allow for the possibility of optimizing its position relative to the collimation system.

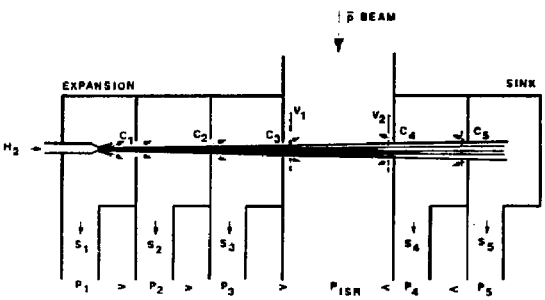

Stage	S (l/s)	C (l/s)
1	7000	0.7
2	4000	3.0
3	4000	7.0
ISR	2000	80.0
4	S4=8000	1100.0
5	S5=120000	

Fig. 3 Schematic of the target system: chambers 1, 2, and 3 constitute the production stage, and chambers 4 and 5 the sink stage. The gas jet intersects the antiproton beam at 90°. Listed are pumping speeds (S) for each stage and conductances (C) between chambers.

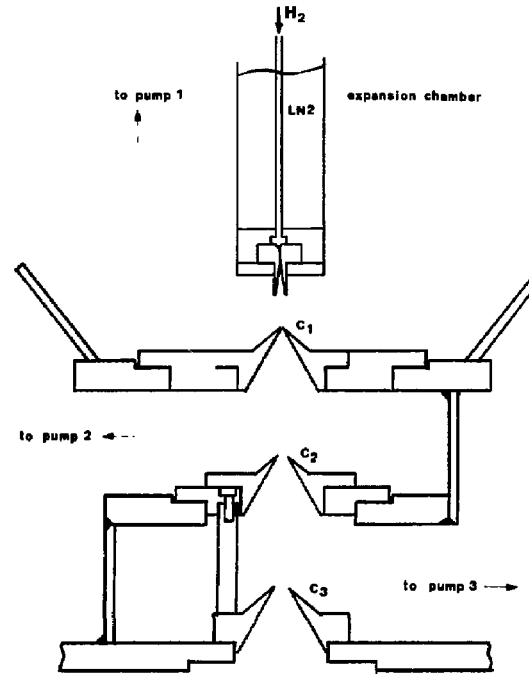

Fig. 4 System of collimators. The diameters are: 1.4 mm for C_1, 2.4 mm for C_2, 5.6 mm for C_3.

Out of a total flux of 10 Torr · l · s^{-1} expanding from the nozzle, the collimation system selected 0.15 Torr · l · s^{-1} = 10^{19} atoms per second. This corresponded to a density of 10^{14} atoms per cm^3, at the interaction point (26 cm downstream from the nozzle throat), as can be calculated from the speed of the clusters (1290 m · s^{-1}) and the dimensions of the jet (d = 9 mm).

A major concern in the target design arose from the need to limit the pressure increase in the ISR vacuum pipe to an acceptable level. As a consequence, both the expansion and the sink chambers were separated from the ISR vacuum pipe by the maximum number of pumping stages compatible with the available space.

On the production side, the collimators, C_1, C_2, C_3, which defined the dimensions of the jet at the intersection with the antiproton beam, connected three different chambers that were evacuated by the successive stages of a differential pumping system. The pumping speeds acting on each chamber and the conductances between chambers are listed in Fig. 3.

On the sink side the jet was dumped on a cryogenic pump of high speed (120,000 l · s^{-1}). A differential pumping system, formed by two cryogenic pumps of 4,000 l · s^{-1} each, separated the vacuum pipe from the dump.

A pressure rise to about 10^{-7} Torr in the vacuum pipe, around the target region, was mainly due to clusters which hit the edges of the last collimator on the production side and did not reach the sink system. Backstreaming gas from the sink accounted for a negligible fraction of the pressure increase in the vacuum pipe.

Two additional pumps, acting on the ISR ring section where the target was mounted, limited to 1.5 m the region where the pressure was larger than 10^{-9} Torr. The pressure rise in the vacuum pipe corresponded to only 1.5% of the target thickness spread over a length of a few metres.

In order to avoid machine vacuum contamination in the case of breakdown of the target system, two fast-acting ultra-high-vacuum valves were installed to separate the production and sink systems from the vacuum pipe of ISR ring 2.

To avoid blockage of the nozzle throat by impurities, high-purity H_2 was used and the injection line was provided with mechanical filters (2 μm), a condensation trap at liquid N_2 temperature, and an active charcoal trap.

A system to monitor the jet intensity was mounted in front of the large sink cryogenic pump. It consisted of a plate of stainless steel (6 × 100 mm^2) which could scan across the jet. A pressure rise was then produced by the gas backscattered from the plate. A typical profile of the jet is shown in Fig. 5; the measured pressure rise has been converted into thickness traversed by the antiproton beam.

The operations of the target were controlled by two microprocessor-based systems which performed all tasks related to start up, the jet on/off procedure, bookkeeping of the measurements, and safety checks.

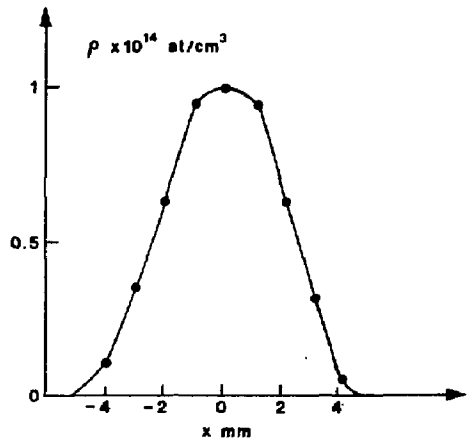

Fig. 5 Target-thickness profile as obtained from measurements with the monitor described in the text.

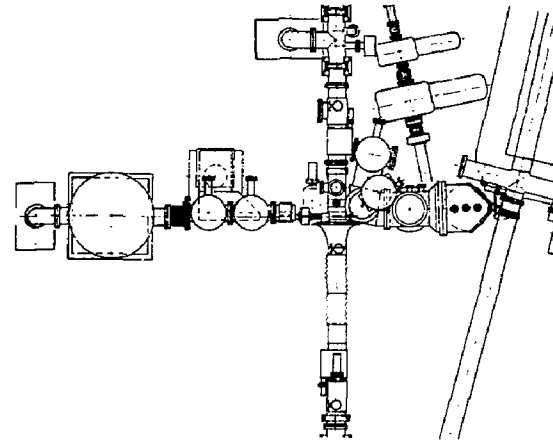

Fig. 6 Target system layout: top view.

A top view of the complete target system mounted on ring 2 at the ISR is shown in Fig. 6.

Conclusion

The H_2 internal target described in this contribution has been successfully operated in the R704 experiment.

The same novel technique will be used at the FERMILAB $\bar{p}$ Accumulator and at the CERN Low-Energy Antiproton Ring (LEAR).

References

1. C. Baglin et al., CERN-EP Internal Report 85-01 (1985)
   C. Baglin et al., Phys. Lett. **163B** (1985), 400.
   C. Baglin et al., Phys. Lett. **171B** (1986), 135.
   C. Baglin et al., Phys. Lett. **172B** (1986), 455.
2. W. Obert, Properties of cluster beams formed with supersonic nozzles, Proc. 11th Symposium on Rarefied gaz Dynamics, Cannes, 1978 (CEA, Paris, 1978), p. 118.
3. J.C. Brunet et al., CERN-ISR-GE/82-20 (1982), A different method has been developed at KfK Karlsruhe by W. Obert.

NUCLEAR EFFECTS IN ELECTROPRODUCTION OF HADRONS

A. Harindranath and J. P. Vary

W. K. Kellogg Radiation Laboratory
California Institute of Technology, Pasadena, CA 91125
and
Physics Department, Iowa State University, Ames, IA 50011

K. E. Lassila

Physics Department, Iowa State University, Ames, IA 50011

We evaluate the possibility of observing nuclear effects in semi-inclusive electroproduction of hadrons(h) from nuclei. We assume factorization and nuclear independence of fragmentation functions in the current fragmentation region. Hence it is shown that the production ratio of oppositely charged hadrons h^+/h^- for the same nucleus is quite insensitive to nuclear effects and the ratio of cross sections for the production of the same sign hadron from different nuclei exhibit the same behaviour as the inclusive ratio which is sensitive to nuclear effects.

I. INTRODUCTION

Recent inclusive electroproduction experiments on nuclear targets[1] have received considerable attention because of the evidence they provide for the importance of nuclear effects on quark distributions in nuclei. It is reasonable to examine other high energy lepton-nucleus and hadron-nucleus reactions for the consequences of nuclear effects. For example, nuclear effects in lepton pair production in hadron-nucleus interactions have received attention recently. In this work we consider the nuclear effects in electroproduction of hadrons from nuclei.

This paper is organized as follows. In Sec. II we review the conventional assumptions and resulting cross section expressions for the electroproduction of hadrons. Details regarding the fragmentation functions and quark distribution functions used in this work are given in Sec. III. In Sec. IV we evaluate the nuclear effects of quark distribution functions in various cross sections and cross section ratios. Sec. V contains our conclusions.

II. INCLUSIVE HADROPRODUCTION

First let us review the inclusive process e N $\rightarrow$ e' X. The cross section is given by[2]

$$\frac{d^2\sigma}{dxdy} = \frac{4\pi\alpha^2}{Q^4} 2M_N E[(1-y)F_2(x,Q^2) + xy^2 F_1(x,Q^2)]$$

where x is the usual Bjorken scaling variable, $y = \nu/E$ where ν is the energy transfer and E is the incident energy, M_N is the mass of the target and Q^2 is the negative of the four-momentum squared of the virtual photon. F_1 and F_2 are the inelastic structure functions. In the above expression we have neglected $\frac{M_N}{2E}xy$ with respect to $1-y$ in the coefficient of F_2. In the scaling region $F_{1,2}(x,Q^2) \rightarrow F_{1,2}(x)$ and further F_1 and F_2 are related by the Callan-Gross relation $2xF_1(x) = F_2(x)$. Thus we have,

$$\frac{d^2\sigma}{dxdy} = \frac{4\pi\alpha^2}{Q^4} 2M_N E \frac{1+(1-y)^2}{2} F_2(x).$$

In the quark parton model we have $F_2(x) = \sum_i e_i^2 q_i(x)$ where $q_i(x)$ is the quark distribution function and e_i is the charge of the quark i.

For the semi-inclusive process[3] e N $\rightarrow$ e' h... (see Fig. 1) we define the variables ϵ=h.p, κ=h.q, u=κ/p.q and z=ϵ/p.q. Here p, q and h are the 4-momenta of the target, virtual photon and the hadron respectively. The target fragmentation region is defined by ϵ finite, $\kappa \rightarrow +\infty$, u finite. The current fragmentation region is defined by ϵ finite, $\kappa \rightarrow -\infty$, u and z finite. In the lab frame current fragmentation corresponds to the detected hadron moving in the direction of the current (with allowance for a bounded transverse momentum h_t). In the lab frame $z = E_h/\nu$ where E_h is the energy of the hadron.

In the present work we restrict ourselves to the current fragmentation region and further neglect the transverse momentum of the hadron.

In the parton model, the cross section for inclusive hadron production is given by

$$\frac{d^2\sigma}{dxdydz} = \frac{4\pi\alpha^2}{Q^4} 2M_N E \frac{1+(1-y)^2}{2} \sum_i e_i^2 x q_i(x) D_i^h(z)$$

where the fragmentation function D_i^h represents the probability for the quark of flavor i to break up with the production of hadron h carrying momentum fraction z. Factorization (seperation of the cross section in x and z variables) and scaling (q_i(x)

FIG. 1

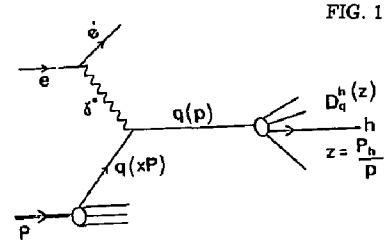

Inclusive hadron production in deep inelastic electron scattering with nuclear targets. Here thick lines represent hadrons, a wavy line represents the virtual photon and thin lines represent electrons or quarks.

and $D_i^h(z)$ do not depend on Q^2) are characteristic assumptions of the parton model. In reality both $q_i(x)$ and $D_i^h(z)$ depend on Q^2 due to QCD scaling violations. These scale breaking effects can be possibly seen by comparing the data at different values of Q^2. At low values of Q^2 we expect a breakdown of factorization, due to finite strong coupling corrections. Due to these complications that arise in the low Q^2 region we restrict ourselves to the deep inelastic region.

III. FRAGMENTATION FUNCTIONS AND QUARK DISTRIBUTION FUNCTIONS

For the calculation of cross section we need models for the quark distribution functions and fragmentation functions. For the fragmentation process there are hadronization models motivated by QCD. In the present work, however, we employ simple parametrizations deduced from experiment. For simplicity we further assume that the detected hadron is the lightest one, the pion.

Using isospin invariance, charge conjugation and the equality of unfavored functions, we need only two independent fragmentation functions $D_u^{\pi^+}(z)$ and $D_u^{\pi^-}(z)$. Neglecting sea quark distributions ($x \simeq .2$) and using an isoscalar target (deuteron), these functions have been extracted[4] recently up to z=0.8. A simple parametrization

$$zD_u^{\pi^+}(z) = 0.7(1-z)^{1.75},$$

$$zD_u^{\pi^-}(z) = \frac{1-z}{1+z} zD_u^{\pi^+}(z)$$

fits the data reasonably well. We use this parametrization in this work. It is worth noting that this parametrization tends to fall faster with z than that[5] of the data at lower Q^2 (See Fig. 2) which is consistent with QCD evolution of the valence fragmentation function.

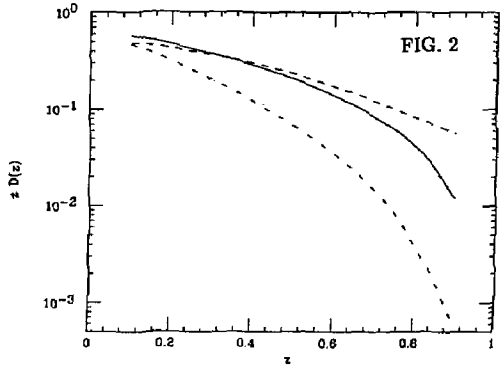

Fragmentation functions extracted from experiments. Solid line and dot-dash line represents $zD_u^{\pi^+}(z)$ and $zD_u^{\pi^-}(z)$ respectively (taken from Ref. 4). Dashed line and dotted line represents $zD_u^{\pi^+}(z)$ and $zD_u^{\pi^-}(z)$ respectively (taken from Ref. 5).

For the quark distribution functions we use the quark cluster model (QCM)[6-8] which was proposed to explain the deep inelastic ^3He scattering results from SLAC[9]. In the QCM one assumes the nucleus at all times is organized into color singlet clusters. The clusters are labelled by their leading Fock space component in the infinite momentum frame as three-quark (3-q), six-quark (6-q), etc., clusters. Larger clusters are assumed to form by the overlap of smaller clusters. As is customary in parton phenemenology, we assume that the participating quark or antiquark is quasifree. Second we assume that the cluster is also quasifree. We also neglect quark exchange processes between clusters. Since we are interested in qualitative behaviour of cross sections and cross section ratios we have further adopted the following simplifying assumptions in this work. All clusters larger than 6-q clusters are approximated as 6-q clusters and Fermi motion is neglected. The quark distribution function in a nucleus is $q_i(x) = p_3 n_{3_i}(x) + p_6 n_{6_i}(x)$ where p_3 and p_6 are 3-q and 6-q cluster probabilities. In this work we use the quark distribution functions $n_i(x)$ for various clusters from Ref. 7.

IV. NUCLEAR EFFECTS

From the expression for the cross section given in Sec. II we have,

$$\frac{1}{d\sigma/dx}\frac{d^2\sigma}{dxdz} = \frac{\sum_i e_i^2 q_i(x) D_i^h(z)}{\sum_i e_i^2 q_i(x)}.$$

Denoting the quantity on the r.h.s of the above equation by N^h we can form the charged particle ratio

$$\frac{N^{h^+}}{N^{h^-}} = \frac{\sum_i e_i^2 q_i(x) D_i^{h^+}(z)}{\sum_i e_i^2 q_i(x) D_i^{h^-}(z)}.$$

Explicitly we have,

$$\frac{N^{\pi^+}}{N^{\pi^-}} = \frac{4q_u(x)\eta(z) + q_d(x) + s(x)[7+5\eta(z)]}{4q_u(x) + q_d(x)\eta(z) + s(x)[7+5\eta(z)]}$$

where

$$\eta(z) = \frac{D_u^{\pi^+}(z)}{D_u^{\pi^-}(z)} = \frac{1+z}{1-z}.$$

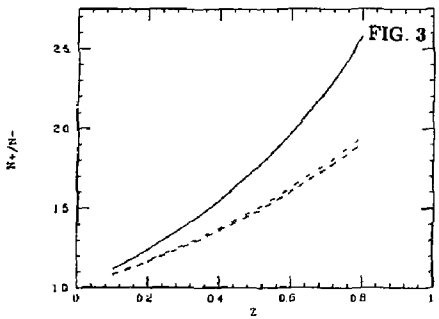

The ratio $\frac{N^{h^+}}{N^{h^-}}$ (for definition see text) plotted versus z for constant x (=0.1) for the nuclei, proton (solid line), ^{12}C (dot-dash line), ^{56}Fe [$p_6 = 0.0$] (dashed line) and ^{56}Fe [$p_6 = 0.3$] (dotted line).

In Fig. 3 we plot $\frac{N^{\pi^+}}{N^{\pi^-}}$ as a function of z (at x=0.1) for proton, ^{12}C and ^{56}Fe targets. Introduction of six quark clusters barely

changes the ratio for ^{12}C and ^{56}Fe since the same nucleus occurs in the numerator and the denominator. The difference between the proton and the ^{12}C curves, for example, comes simply from the presence of neutrons in ^{12}C. We expect similar predictions for other models proposed to explain the nuclear effects in deep inelastic lepton scattering.

Next let us examine what we can learn by studying the normalized cross section ratios for different nuclei. Let us define

$$R(x) = \frac{e_i^2(x) q_i^{Fe}(x) D_i^{\pi^-}(x)/56}{e_i^2(x) q_i^{D}(x) D_i^{\pi^-}(x)/2}.$$

In Fig. 4 we plot R(x) at z=0.1. It is readily seen that R(x) exhibits the same qualitative behaviour as the inclusive cross section ratio. Within the QCM the behavior of R in the region x greater than 1 will exhibit steps just as the inclusive cross section ratio[10].

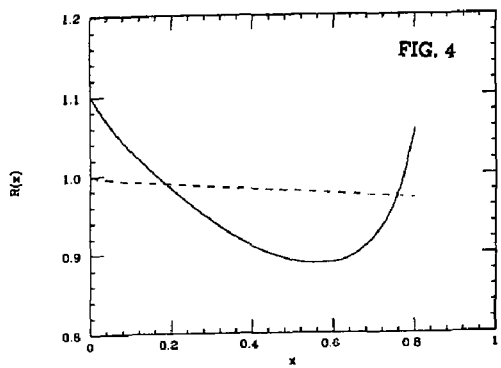

The ratio R (for definition see the text) calculated in the QCM plotted versus x for z=0.1. The dashed line corresponds to $p_6(D)$=0.0 and $p_6(Fe)$ =0.0. The solid line corresponds to $p_6(D)$=0.0 and $p_6(Fe)$=0.3. The small deviation from unity of the dashed line originates from the non-isoscalar nature of ^{56}Fe.

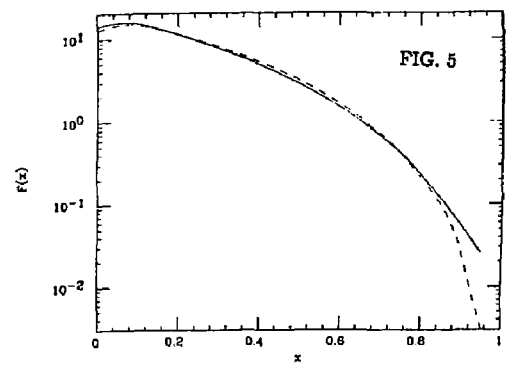

The quantity F (for definition see the text) plotted versus x for z=0.1. The target nucleus is ^{56}Fe. Dashed line and solid line correspond to p_6=0.0 and 0.3 respectively.

To get an estimate of the magnitude of the cross section to be expected let us write

$$\frac{d^2\sigma}{dxdydz}\Big|_z = \frac{4\pi\alpha^2}{Q^4} 2M_N E \frac{1+(1-y)^2}{2} F(x).$$

We plot F(x) in Fig. 5. As can be seen the presence of 6-q clusters produces an order of magnitude enhancement in the $x \to 1$ region over the result if there are no quark clusters.

V. CONCLUSION

Assuming factorization and nuclear target independence for fragmentation functions we have shown that the semi-inclusive hadron production cross section ratio for oppositely charged hadrons with the same target nucleus is quite insensitive to nuclear effects. On the other hand the ratio of cross sections for the *same* hadron produced off *different* nuclei is seen to exhibit the same striking behavior as the inclusive ratio.

ACKNOWLEDGEMENTS

This work is supported in part by the National Science Foundation grants PHY85-05692 and PHY-04197 and by the U.S.Department of Energy under contract Nos. DE-AC02-82ER40068 and W-7405-ENG-82, Division of High Energy and Nuclear Physics.

REFERENCES

1. J. J. Aubert *et al.*, Phys. Lett. **123B**, 275 (1983); A. Bodek *et al.*, Phys. Rev. Lett. **50**, 1431 (1983), **51**, 534 (1983); R. G. Arnold *et al.*, Phys. Rev. Lett. **52** 727 (1984); See also G. N. Taylor in *Intersection Between Particle and Nuclear Physics*, Lake Louise, Canada 1986, AIP Conference Proceedings 150, edited by D. F. Geesaman. For recent review of theoretical models see E. L. Berger, *ibid.*
2. F. E. Close, *An Introduction to Quarks and Partons*, (Academic, New York, 1979).
3. Ref. 2; M. Gronau, F. Ravndal and Y. Zarmi, Nucl. Phys. **B51**, 611 (1973); E. Reya in *Perturbative Quantum Chromodynamics*, edited by M. Jacob, Physics Reports reprint book series- Volume 5 (North Holland Publishing Company, Amsterdam, 1982); F. Janata in *1986 CEBAF Summer Workshop Proceedings*, June 23-27, 1986, CEBAF, Newport News, Virginia.
4. J. J. Aubert *et al.*, Phys. Lett. **160B**, (1985) 417.
5. L. M. Sehgal in *Proceedings of the VIII International Symposium on Lepton and Photon Interactions*, edited by F. Gutbrod (Hamburg, 1977).
6. H. J. Pirner and J. P. Vary, Phys. Rev. Lett. **46**, 1376 (1981); H. J. Pirner in *Progress in Particle and Nuclear Physics*, edited by A. Faessler (Pergamon, Oxford, 1985), p.361; J. P. Vary, Nucl. Phys. **A418**, 195c (1984).
7. C. E. Carlson and T. J. Havens, Phys. Rev. Lett. **51**, 261 (1983).
8. M. Sato, S. A. Coon, H. J. Pirner, and J. P. Vary, Phys. Rev. **C33**, 1062 (1986).
9. D. Day *et al.*, Phys. Rev. Lett. **43**, 1143 (1979).
10. J. P. Vary in *Proceedings of the VII International Seminar on High Energy Physics Problems, Multiquark Interactions, and Quantum Chromodynamics*, edited by V. V. Burov, Dubna pub. no. D-1, 2-84-599 (1984) p.186; J. P. Vary, Nucl. Phys., *op. cit.*.

CAN PION ELECTROPRODUCTION PLUMB THE PION SEA?

R.S. HICKS

Department of Physics and Astronomy
University of Massachusetts
Amherst, MA 01003

Abstract

An outline is given of the proposal that the nuclear pion field can be determined by coincidence electropion production. Experimental requirements for the measurement of $(e, e'\pi)$ cross sections are discussed, with particular regard to the properties of the PEP storage ring.

Introduction

The meson field representation of the nuclear force provides the basis for our most detailed, yet tractable, model for calculating nuclear properties. Although the roles of heavy and multiple meson exchanges remain open questions at present, there is some evidence to suggest that the principal process, involving one-pion exchange, is understood. The first such evidence came from calculations of the thermal np capture $(n + p \rightarrow d + \gamma)$ rate. When only the neutron and proton were considered the computed rates were about 10% lower than the observed value.[1]

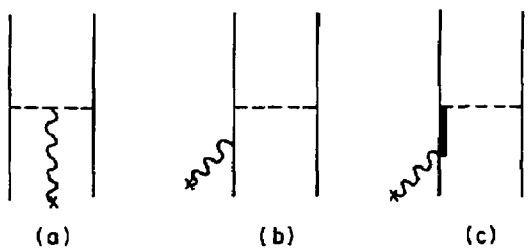

FIG. 1. One-pion exchange current diagrams: (a) pionic current, (b) pair current, and (c) nucleon resonance current.

This discrepancy was subsequently removed by the evaluation of the three one-pion exchange currents shown in Fig. 1, with the pion-nucleon coupling constants being taken from measured π-N scattering cross sections. More dramatic evidence for the contribution of one-pion exchange currents is found in the cross section for the electrodisintegration of the deuteron at threshold, shown in Fig. 2. Calculations for nucleons only produce a deep diffraction minimum near squared four-momentum transfer $Q^2 = 12$ fm^{-2}, in blatant disagreement with the data. Again, consideration of the three one-pion exchange currents of Fig. 1 is crucial for resolving this disagreement.[2] Compelling evidence for the role of pion exchange currents is also found in the cross sections measured for the break-up of the deuteron by 100 – 500 MeV photons,[3] as well as in the magnetic moments[4] and elastic M1 form factors[5] of ^{3}H and ^{3}He. There is, however, little evidence to confirm our understanding of the meson field in $A \geq 4$ nuclei, where the nuclear force is closer to saturation.

The lack of definitive data on the pionic content of heavy nuclei has impeded the understanding of the EMC effect, where a difference is observed between the cross sections per nucleon for deep inelastic lepton scattering from the deuteron and from heavier nuclei. Various theories, based on diverse ideas, purport to account for this observation. Some theories explain the difference by postulating an enhancement of the pion field in massive nuclei. Other theories do not. Without clear experimental information on the meson field in $A \geq 4$ nuclei, there exists no means of identifying the correct ideas. One experimental investigation that has been made is that of Carey *et al.*,[6] who measured the scattering of polarized 500 MeV protons from deuterium and lead targets in the quasielastic continuum. Since the

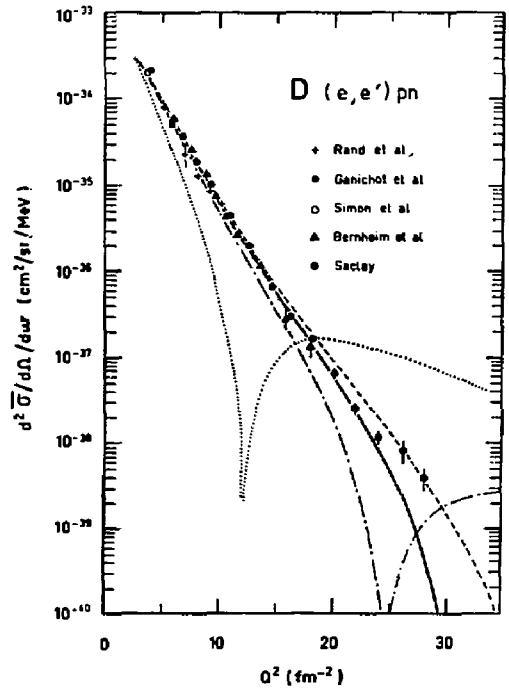

FIG. 2. Cross section for the electrodisintegration of the deuteron at threshold.[2] The dotted curve is for nucleons only, the dash-dotted curve includes one-pion exchange currents, and the dashed curve includes in addition ρ-meson exchange. The total result, indicated by the continuous curve, also takes into account the contribution of Δ-isobars.

π-N coupling is strong, such experiments should be sensitive to any A-dependence of the pion field. Carey *et al.* isolated the axial-longitudinal coupling of the proton to the pion field from other interactions by measuring a complete set of polarization transfer variables. Within experimental errors, the results show the axial-longitudinal response functions for d and Pb to be equal, suggesting that there is no enhancement of the pion field in massive nuclei. Notwithstanding the significance of this result, the question of the A-dependence of the pion field is one of such importance that it should be explored by any means possible.

It is unlikely that any single experimental study can resolve the issue. For example, the momentum distribution of the virtual pions in deuterium may be somewhat different from that in heavy nuclei, and hence measurements at a single momentum transfer value, such as that of Carey *et al.*, cannot be entirely conclusive. The interpretation of the proton scattering measurements is also compromised by the inherent complexity of the proton-nucleus interaction; for example, the understanding of polarization transfer asymmetries measured for discrete nuclear states in $(\vec{p},\vec{p})$ has presented considerable difficulty. The means of probing the pion field to be discussed in this paper, the $(e,e'\pi)$ reaction, is also subject to uncertainty, particularly from the large final-state interaction effects.[7] For both reactions, there is theoretical debate regarding the interpretability of the data in terms of the nuclear pion field. In fact, on an even more basic level, the range of applicability of the meson field representation has yet to be defined.

Pion Electroproduction in the Continuum

Güttner *et al.*[8] have suggested that the nuclear pion field can be investigated by longitudinal electroproduction of pions in the continuum region. Güttner *et al.* argue that if virtual pions can be interpreted as partons of nucleons and nuclei, the pion distribution function could be determined in a manner analogous to the determination of the quark distribution functions from deep inelastic scattering. For low squared momentum transfer $|t|$ onto the target nucleon, data for charged

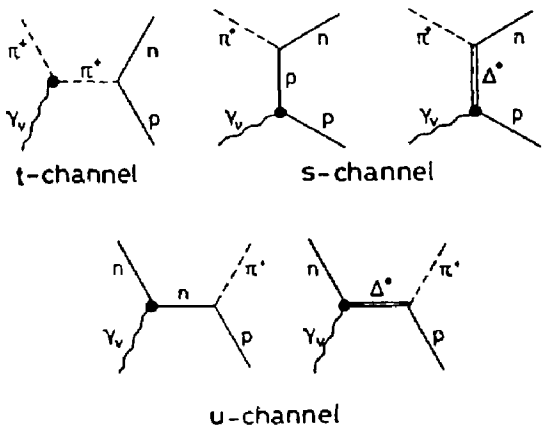

FIG. 3. Born term diagrams for the reaction $ep \rightarrow e'\pi^+ n$.

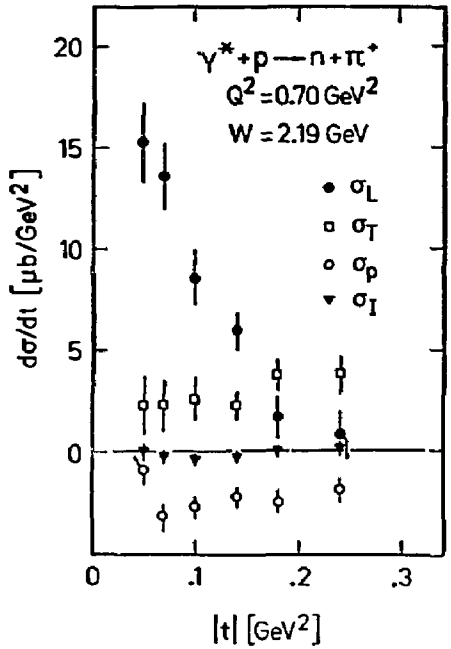

FIG. 4. Components of the cross section for $ep \rightarrow e'\pi^+ n$ as a function of the squared momentum transfer $|t|$ onto the target nucleon.[9]

pion electroproduction have been reasonably described by the Born term model, the reaction diagrams for which are shown in Fig. 3. It is the t-channel diagram which is of relevance for the investigation of the nuclear pion field.

Four separate terms contribute to the cross section obtained when the scattered electron and produced pion are measured in coincidence:[9]

$$2\pi\frac{d^2\sigma}{dtd\phi} = \frac{d\sigma_T}{dt} + \varepsilon\frac{d\sigma_L}{dt} + \varepsilon cos(2\phi)\frac{d\sigma_P}{dt} + \sqrt{2\varepsilon(\varepsilon+1)}cos\phi\frac{d\sigma_I}{dt}.$$

In this expression ϕ is the angle between the hadron production and electron scattering planes and ε measures the polarization of the virtual photon. Due to the $J^\pi = 0^-$ spin of the pion, the t-channel diagram contributes mainly to the longitudinal component of the cross section $d\sigma_L/dt$, shown in Fig. 4. In fact, a crucial element in the argument of Güttner *et al.* is that the strong peaking observed at low $|t|$ in the longitudinal cross section arises almosts solely from the t-channel. The objective of the experimental procedure is therefore to perform measurements throughout a sufficiently comprehensive range of photon polarization parameters ε and out-of-plane angles ϕ to permit the isolation of $d\sigma_L/dt$ from the transverse ($d\sigma_T/dt$ and $d\sigma_P/dt$) and interference ($d\sigma_I/dt$) components in the cross section.

Güttner *et al.* define the pion momentum distribution function $G_{\pi^*/N}(x,Q^2)$ to be the probability of finding a virtual pion π^* in the nucleon with momentum fraction $x = P(\pi^*)/P(N)$, the familiar Bjorken scaling parameter. The distribution func-

tion $G_{\pi^+/N}(x,Q^2)$ is then extracted from the longitudinal component of the cross section at small $|t|$ by means of

$$\frac{d^2\sigma_L(eN \to e'\pi X)}{dx dQ^2} = G_{\pi^+/N}(x,Q^2)\frac{d\sigma_{el}(e\pi^+ \to e'\pi)}{dQ^2},$$

with the elastic scattering $e\pi^+ \to e'\pi$ cross section being calculated using a dipole form for the electromagnetic form factor of the pion.

Due to the lack of available data, Güttner *et al.* were able only to analyze the case of the $ep \to e'\pi^+ n$ reaction, for which the deduced distribution function had to be defined as the probability of finding a virtual π^+ with momentum fraction x in state $\pi^+ n$. Values for $G_{\pi^+/p}$ were extracted for $x = 0.062, 0.123$, and 0.154, and, with an assumed functional dependence, the pion distribution function was integrated, yielding $(3.0 \pm 0.5)\%$ π^+ mesons in the proton. The unexpected smallness of this value has been attributed to various factors, some of which will be mentioned below. In practice, one would seek to assess the total pionic content of the nucleon by performing a semi-inclusive measurement for all possible final states X. Moreover, comprehensive measurements should be carried out for complex nuclei, to study the A-dependence of the number of virtual pions per nucleon.

Experimental Considerations

The objectives of the measurement, namely, to isolate the longitudinal term in the cross section and check that it is dominated at low $|t|$ by the t-channel reaction diagram, demand rather comprehensive experimental capabilities and procedures:

1. The spectrometer(s) should have large out-of-plane angular acceptances in order to exploit the ϕ-dependence of the cross section for separation of the $d\sigma_P/dt$ and $d\sigma_I/dt$ terms.

2. In order to separate $d\sigma_T/dt$ and $d\sigma_L/dt$ it is necessary to measure the cross section for different values of the virtual photon polarization parameter ϵ with the kinematic parameters Q^2, t, and s, the squared invariant mass of the $\gamma^* N$ system, held constant. If $d\sigma_T/dt$ and $d\sigma_L/dt$ are to be extracted with reasonable precision, a range of incident electron energies are required. The operating range of the PEP storage ring at the Stanford Linear Accelerator Center (SLAC), extending from 18 GeV down to perhaps 4 GeV, appears to be well-suited to the needs of the $(e,e'\pi)$ experiment. Particularly for the higher incident energies, it is essential that the apparatus be capable of detecting scattered electrons and electroproduced pions at small angles with respect to the beam direction. The scattered electrons of interest will be primarily in the range $\theta_e = 10° - 40°$, and the corresponding pions between $\theta_\pi = 10°$ and $20°$.

3. Because the experiment calls for a semi-inclusive measurement in the continuum region, fine resolution is not of primary importance.

4. The spectrometer(s) should have good particle identification capabilities. In particular, π^+, π^-, and π^0-mesons should be simultaneously detectable. Assuming a charge-symmetric nuclear force, and an isospin T=0 target, equality of the π^- and π^+ production cross sections provides assurance that the dominant reaction mechanism is the t-channel diagram, for in this case, the ratio of the production cross sections is equal to the ratio of the squared pion charges:

$$\frac{\sigma(\pi^-)}{\sigma(\pi^+)} = \frac{(-1)^2}{(+1)^2} = 1.$$

Data taken at DESY[9] and elsewhere on the deuteron show that this is the case for $|t| < 0.15$ (GeV/c)^2, as indicated in Fig. 5. For high $|t|$ the cross section ratio is closer to 1/4, consistent with the result expected for hadronization after scattering from valence quarks of charge $\frac{1}{3}$ (for π^- production) and $\frac{2}{3}$ (for π^+ production). Due to lack of charge for the π^0, neutral pions cannot be produced through the t-channel diagram. However, π^0 production does occur for the other diagrams, and hence measurement of the π^0 yield would provide information on the contribution from these background terms.

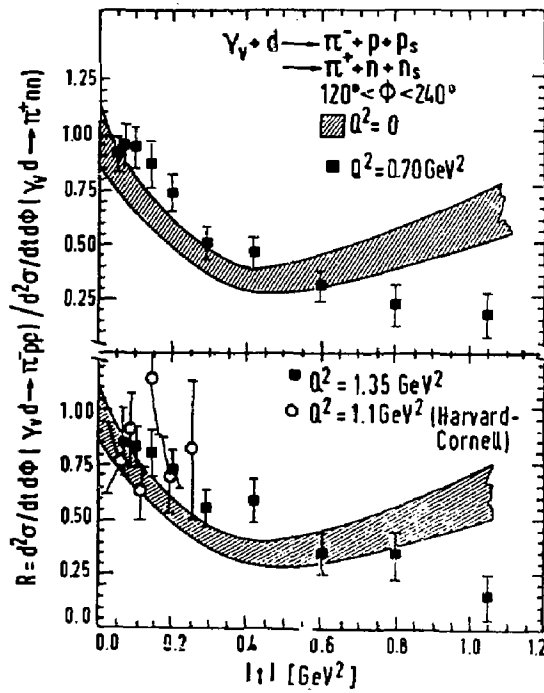

FIG. 5. Ratio of π^- and π^+ production cross sections for deuterium.[9]

5. If it is the longitudinal t-channel mechanism which is dominant at low $|t|$, the struck pion should be ejected close to the direction of the momentum transfer and should carry energy fraction $z = E_\pi/\nu$ close to unity, where ν is the electron energy loss $E - E'$. The acceptance of the spectrometer(s) should be optimized to study such events.

6. Due to the smaller pion production cross sections at high Q^2, useful data will likely be confined to $Q^2 \leq 2$ (GeV/c)^2. As Q^2 increases so does the spatial resolution of the virtual photon, and the experiment becomes more sensitive to closely-bound virtual pions in the nucleon: What appears at low-Q^2 to be a bare nucleon, at high-Q^2 may be resolved into a nucleon and virtual pion. (The situation is directly analogous to the evolution of the deep inelastic structure functions with increasing Q^2.) The $ep \rightarrow e'\pi^+n$ data analyzed by Güttner *et al.* had a maximum Q^2 of 0.70 (GeV/c)^2, inadequate to provide good sensitivity to these pions.[10] This, in part, explains the small π^+ admixture found in the proton. It should be noted, however, that as Q^2 increases the use of the Born term model represented in Fig. 3 becomes questionable as more and more reaction diagrams can contribute to pion electroproduction.

7. In order to avoid the strong final-state interaction between the nucleon and outgoing pion the energy transfer should be greater than 2.2 GeV, sufficient to put the pion above the resonance region. Nevertheless, even in this case, Monte Carlo calculations by Stoler[7] show that the cross sections measured for pion production from complex nuclei can be reduced by a factor of approximately 2 by final state interactions. Thus, even if one were to simply search for a possible A-dependence of the pion field, the conclusiveness of the results could well be obscured unless the large final-state interaction effects are understood. The neglect by Güttner *et al.* of rescattering of the pion from the nucleon also contributed to the small π^+ content found in the proton.[12]

8. The time structure of the incident beam should be consistent with low accidental-to-real coincidence count rate ratios. The standard 3-bunch mode of PEP, which provides a duty factor of less than 0.1%, is clearly far from optimum. The feasibility of performing $(e, e'\pi)$ studies at PEP would be greatly enhanced if future efforts to increase the number of stored bunches are successful.

Previous electroproduction measurements have utilized conventional magnetic spectrometers, one for the scattered electron, and the other to detect the pion ejected close to the momentum transfer direction. In the experiment of Brauel *et al.*,[9] for example, the two spectrometers each had an acceptance solid angle of 3.2 msr, with ± 100 mrad angular acceptance in the vertical direction. The good ~ 5% duty factor of the DESY synchrotron permitted Brauel *et al.* to use 10 cm long liquid hydrogen and deuterium targets and thereby achieve luminosities $\mathcal{L} \geq 10^{34}$ cm^{-2} s^{-1}, despite the poor synchrotron beam current. With the anticipated luminosity at PEP being no better than 10^{33} cm^{-2} s^{-1}, small acceptance spectrometers are out of the question.

One experimental possibility, proposed by van Bibber,[11] would be to use the septum magnets of the PEP-9 collaboration in a modified field configuration. In principle, such a spectrometer could provide acceptance angles close to ±20° in both the horizontal and vertical directions. Suitably instrumented with Čerenkov counters, time-of-flight hodoscopes, and a shower counter comprised of alternating layers of lead and liquid scintillator, the spectrometer could also have good particle identification properties. For this detector the estimated true electron-pion coincidence count rate is quite encouraging:[14] about 10 s^{-1} for $\mathcal{L} = 10^{33}$ cm^{-2} s^{-1}. The difficulty of using such a device in the standard low-duty factor PEP mode would be the high background singles rate from recoil hadrons, estimated to be about 4 per beam crossing.[15] Most of the recoil particles have momentum less than 2 GeV/c. Several measures may be taken to reject these particles, for example, the construction of highly-segmented detectors with multi-hit event processing capability, and the use of an event trigger which demands the production of a high-z pion. Nevertheless, the range of practicable luminosities will be unavoidably compromised unless the PEP duty factor can be raised.

Another concern of the septum magnet spectrometer is the relatively low field strength of ≤ 0.3 T existing close to the transmitted beam path. The smallness of this field, incurred as a consequence of the mandate not to interfere with the steering of the stored beam, results in relatively poor momentum resolution for particles emerging at small angles. An alternative system, previously developed at SLAC for the measurement of inclusive hadron production cross sections, utilized a large-aperture dipole magnet traversed by a superconducting transport tube to expel the magnetic field, thereby providing a field-free region for the beam emerging from the target.[16] In this

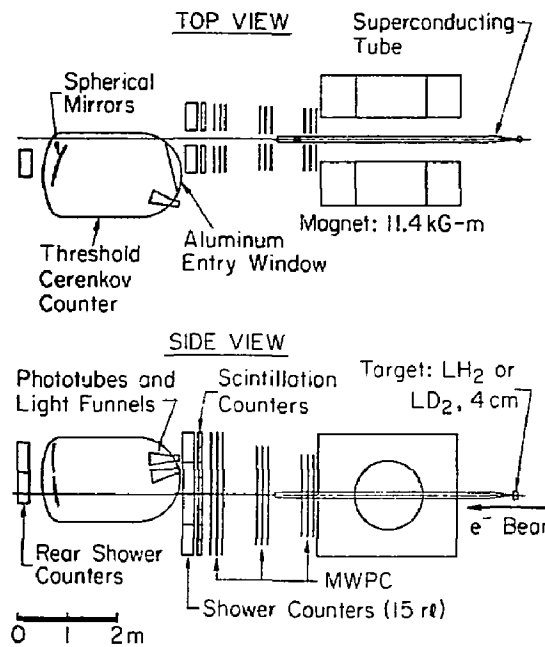

FIG. 6 Large-acceptance, forward-angle spectrometer used by Martin *et al.* for the measurement of inclusive hadron production cross sections.[16]

way, magnetic fields ≥ 1 T could be applied only a few cm from the stored beam. A schematic representation of this apparatus is presented in Fig. 6.

Summary

Preliminary studies indicate that the measurement of coincidence electropion production should be feasible at the PEP storage ring, especially if efforts to improve the duty factor by injecting more beam bunches are successful. The observation of peaking in the longitudinal cross section at small $|t|$, combined with a π^+ to π^- production ratio close to one, suggests a reaction mechanism in which the longitudinally-polarized photon couples directly to a virtual pion. Whether or not the nuclear pion sea can be quantitatively determined from such measurements is rendered uncertain by the possible importance of other reaction mechanisms, as well as by the large final-state interaction effects. Nevertheless, measurements of this type may well help to define the region of applicability of the meson field representation.

This work was supported by the U.S. Department of Energy.

References

1. D.O. Riska and G.E. Brown, Phys. Lett. 38B, 193 (1972).
2. S. Auffret *et al.*, Phys. Rev. Lett. 55, 1362 (1985).
3. J.M. Laget, Nucl. Phys. A312, 265 (1978).
4. E.L. Tomusiak *et al.*, Phys. Rev. C 32, 2075 (1985).
5. F.-P. Juster *et al.*, Phys. Rev. Lett. 55, 2261 (1985).
6. T.A. Carey *et al.*, Phys. Rev. Lett. 53, 144 (1984).
7. P. Stoler, Proceedings, this conference (1987).
8. F. Güttner *et al.*, Nucl. Phys. A429, 389 (1984).
9. P. Brauel *et al.*, Z. Physik C 3, 101 (1979).
10. E.L. Berger, A. Schafer, private communications (1987).
11. K. van Bibber, Proceedings, this conference (1987).
12. H.J. Pirner, private communication (1986).
13. J. Spencer, Proceedings, this conference (1987).
14. B. Fillipone, R. Milner, private communications (1987).
15. S. Rock, private communication (1987).
16. J.F. Martin *et al.*, Phys. Rev. D 20, 5 (1979).

(e,e'π) AND THE PION NUCLEON FORMFACTOR

Andreas Schäfer and Steven E. Koonin

W.K.Kellogg Radiation Laboratory, CALTECH, Pasadena, CA 91125, USA

It has been claimed[1] that the reaction

$$e + p \rightarrow e' + \pi^+ + n \qquad (1)$$

tests directly the 'pion content of the nucleon'. Such a measurement would be very interesting as it could test some of the models[2] proposed to explain the EMC effect. We will argue that this claim is invalid and that the only information one can extract from such an experiment is the pion nucleon formfactor $F_{\pi NN}$ (and the electromagnetic formfactor of the pion).

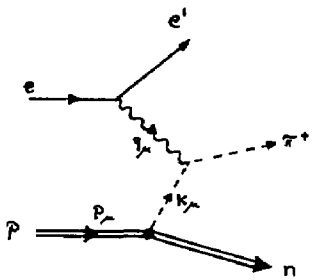

Fig.1 : The reaction (e p , e' π^+ n)

An experiment of the type (1) was carried out by Brauel et al.[3] in 1979 at DESY. One might consider repeating this experiment at PEP and comparing the results for different target nuclei, e.g. for hydrogen and a heavy nucleus. Such an experiment should show some characteristic differences due to nuclear binding, i.e. due to the exchange of virtual pions between the nucleons of a nucleus. Brauel et al. isolated the graph of Figure 1 by doing a Rosenbluth separation (which guarantees that the photon is scattered off a spin zero particle) and by imposing a cut on the total momentum squared of the outgoing baryon state (Figure 2).

$$(p - k)_\mu (p - k)^\mu \leq (1.2\,GeV)^2 \qquad (2)$$

For very large momenta $Q^2 = -q^2$ or, more precisely, for $x\sqrt{q^2} > 1\,GeV$ the longitudinal cross section can be simply written as

$$\frac{d^2\sigma_L(ep \rightarrow e'\pi^+n)}{dx\ dQ^2} = G_{\pi^+/p}(x)\ \frac{d\sigma_{elastic}(e\pi^+ \rightarrow e'\pi)}{dQ^2} \qquad (3)$$

where $G_{\pi^+/p}(x)$ is a Q^2 independent function, namely the probability to find a virtual π^+ with momentum fraction x associated with a proton. This interpretation holds only for large Q^2. For small values, i.e. for $x\sqrt{Q^2} \ll 1\,GeV$, the ratio of the two cross sections

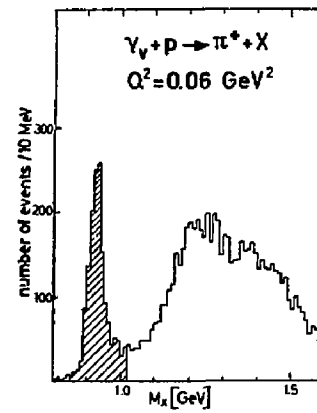

Fig.2 : The experimentally observed values for the square of the four-momentum of the outgoing baryon state. Only the shaded events were taken into account. The broad bump at 1.2 - 1.3 GeV is due to the reaction (e p , e' π Δ) . (From ref. 2)

$$\frac{d^2\sigma_L(ep \rightarrow e'\pi^+n)}{dx\ dQ^2} \Big/ \frac{d\sigma_{elastic}(e\pi^+ \rightarrow e'\pi)}{dQ^2} = G(x,Q^2) \qquad (4)$$

becomes a strongly Q^2 dependent function with no simple physical interpretation. This is illustrated in Figure 3. The nucleus emits virtual pions with a momentum squared $t = -k^2$. The further these pions are off mass shell, i.e. the larger the value of $|t|$, the sooner they will be reabsorbed. Thus, strongly off shell pions can only be found close to the nucleus. Due to the pion

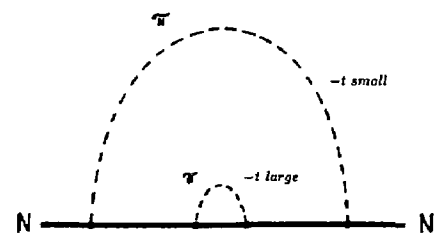

Fig.3 : The virtual pion cloud of a nucleon. Pions which are far off the mass shell are found close to the nucleus.

nucleon formfactor $F_{\pi NN}(t)$ there are no pions with arbitrarily large $|t|$. The strong decrease of $F_{\pi NN}$ with t renders the total number of virtual pions finite. If one probes the virtual pion cloud of a nucleus with photons the response one gets depends on the resolution, i.e. on Q^2. For small Q^2 virtual pions with large t cannot be resolved. Consequently $G(x,Q^2)$ decreases with decreasing Q^2.

Now the problem with the reaction (1) is that the Rosenbluth separation can only be done for small values of Q^2, typically smaller than 1 GeV^2, because the longitudional cross section drops to zero. The question is therefore whether for such a low Q^2 the function $G(x,Q^2)$ is still a good approximation to $G_{\pi^+/p}(x) = \lim_{Q^2\to\infty} G(x,Q^2)$. We interpret the results of reference 1 as a proof that this is not the case, in complete disagreement with the authors of that paper.

They analyzed the data of ref. 2 under the assumption

$$G(x,Q^2 = 0.7\ GeV^2) \approx G_{\pi^+/p}(x) \qquad (5)$$

and claimed that there would be far less virtual pions associated with a nucleon than is usually assumed. Furthermore they concluded that the proton radius is

$$R = 1.5 \pm 0.1\ fm \qquad (6).$$

The latter result they got from the relation[3]

$$G_{\pi^+/p}(x) = \frac{g^2}{8\pi^2} \int_{\frac{x^2M^2}{1-x}}^{\infty} \frac{t\, F_{\pi NN}(t)}{(t+m_\pi^2)^2}\, dt \qquad (7)$$

where the pion nucleon form factor is related to the nucleon radius by

$$F_{\pi NN}(t) = e^{-0.106\ (t+m_\pi^2)\ R^2}. \qquad (8)$$

Because they got from the data very small values for $G(x,Q^2 = 0.7\ GeV^2)$ they had to postulate such an extremely large nuclear radius. The value in Eq.(6), however, is completely unacceptable. In Figure 4 we show the formfactor for $R = 0.7\ fm$ and $0.8\ fm$ which is the physically reasonable range[4] (dashed lines).

The exponential form of the πNN formfactor (8) is motivated by the bag model. From a phenomenological point of view one can also advocate a dipole form[5]

$$F_{\pi NN}(t) = \left(\frac{\Lambda^2 - m_\pi^2}{\Lambda^2 + t}\right)^2, \qquad (9)$$

with $\Lambda = (4.8 - 7.0,\ fm^{-1}$ (dash-dotted lines) or even a monopole form[6] (dotted line)

$$F_{\pi NN}(t) = \frac{\Lambda^2 - m_\pi^2}{\Lambda^2 + t} \qquad (10)$$

with $\Lambda \approx 5\ fm^{-1}$.

In fact, $F_{\pi NN}$ is tested experimentally only for small values of t ($t \le 0.2\ GeV^2$), where all of these functions coincide more or less, whereas the formfactor used by Güttner et al. is definitely ruled out.

Besides being incompatible with other experiments the analysis of ref.1 is also inconsistent with the analysis by Brauel et al.. By fitting an exponential t dependence to their data Brauel et al. got $R = (1 \pm 0.2)\ fm$. We thus conclude

$$G(x,Q^2 = 0.7\ GeV^2) \ll G_{\pi/p}(x) \qquad (11)$$

in agreement with our crude argument sketched in Figure 2. It is therefore not possible to measure directly the 'pion content of a nucleus'. One can only extract $F_{\pi NN}(t)$ for some limited t range, as was done by Brauel et al.. The ratio in Eq.(3) becomes especially uninformative if the electrons are scattered off a nucleus instead of a proton. The final state interactions are important and they will blur the meaning of $G(x,Q^2)$ still further.

By doing an inclusive measurement as opposed to an exclusive one the problem that the Rosenbluth separation works only for too small values of Q^2 is not remedied. One just looses the possibility to extract $F_{\pi NN}$.

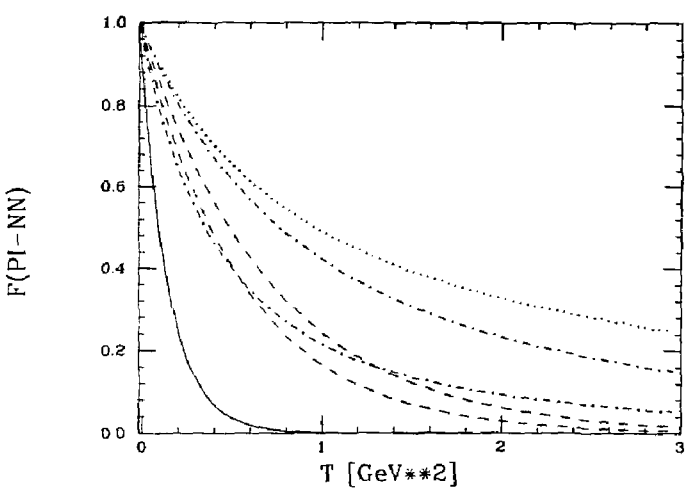

Fig.4 : Comparison of the different $F_{\pi NN}$ formfactors discussed in the literature. The two dashed lines sketch the range expected for an exponential formfactor (ref. 4). The dash-dotted line bounds the allowed range for a dipole formfactor according to ref. 5. The dotted line is the monopole formfactor used in ref. 6. The result of ref. 1 is the solid line.

REFERENCES :
[1] F. Güttner, G. Chanfray, H. J. Pirner, and B. Povh, Nucl.Phys. **A429** (1984) 389
[2] C. H. Llewellyn Smith, Phys.Lett. **128B** (1983) 107
M. Ericson and A.W.Thomas, Phys.Lett. **128B** (1983) 112
E. L. Berger, F. Coester, and R. B. Wiringa, Phys.Rev. **D29** (1984) 398
[3] P. Brauel et al., Z.Phys. **C3** (1979) 101
[4] A. W. Thomas in Advances in Nuclear Physics 13, eds. J. W. Negele and E. Vogt
[5] B. L. Friman, V. R. Pandharipande, and R. B. Wiringa, PRL 51 (1983) 763
[6] J. Cohen and J. M. Eisenberg, Phys.Rev. **C28** (1983) 1309

MODIFICATION OF NUCLEON PROPERTIES IN NUCLEI

Carl M. Shakin
Department of Physics, Brooklyn College of the City University of New York
Brooklyn, New York 11210

Abstract: We interpret various nuclear physics experiments as providing evidence for modification of QCD order parameters in nuclei.

Introduction

I would like to emphasize that three topics of current interest in nuclear physics: the EMC effect,[1] the quenching of the longitudinal response seen in inclusive (e,e') reactions,[2] and the use of the Dirac equation to describe nucleon motion in nuclei,[3-5] are all related to a single effect, the modification of the gluon condensate in nuclei.[6] We will argue that, in all three cases mentioned above, we are seeing the effects of a change of a QCD mass (or length) scale away from its vacuum value. The order parameter describing this scale change is an order parameter of the gluon condensate.[7] In the absence of current quark masses, there is only a single mass scale developed dynamically in QCD. It is possible to construct an effective Lagrangian for QCD[7] which only contains a single dimensional order parameter. A change in this parameter will lead to a corresponding change of all dimensional quantities. In particular, we have shown[6,7] how a length scale may be specified for QCD by making use of the gauge and Lorentz invariant parameter,

$$\langle \mathrm{vac} | \frac{g^2}{4\pi^2} G^a_{\mu\nu} G^{\mu\nu}_a | \mathrm{vac} \rangle = \frac{3}{32\pi^2} g^4 \phi_o^4 . \qquad (1)$$

Here g^2 is the QCD coupling constant renormalized at the mass scale, μ^2. (Equation (1) may be taken as a definition of the quantity $g^2\phi_o^2$.) We remark that a value of 0.012 $(\mathrm{GeV})^4$ has been obtained for the left-hand side of (1) in work on QCD sum rules. (Note that this quantity is a renormalization group invariant in a physical gauge.)

As we have seen in other works,[6,7] various dynamical masses are given in terms of the quantity, $g^2\phi_o^2$. We obtain a dynamical gluon mass,

$$m_G^2 = \frac{1}{4} g^2 \phi_o^2 , \qquad (2)$$

and a dynamical quark mass,

$$(m_q^{G\ell})^2 = \frac{1}{6} g^2 \phi_o^2 , \qquad (3)$$

as well as a number of other mass parameters, all of which are proportional to the same order parameter. The quark also obtains a dynamical mass via the formation of a chiral condensate, however, in our model the chiral condensate order parameters do not define an independent mass scale. Therefore, if we take the current quark mass to be zero for the up and down quarks, there is only a single mass scale in our effective Lagrangian, which we assume describes QCD at large length scales.[6,7]

Now the presence of quarks tends to break down the gluon condensate and in nuclear matter we claim that ϕ_o should be replaced by $\phi_{NM} < \phi_o$. Indeed, we want to show that if $\phi_o/\phi_{NM} \approx 1.25$, we can understand the various phenomena mentioned at the beginning of the introduction.

The EMC Effect

There have been a very large number of theoretical papers which deal with the EMC effect.[9] The rescaling model of Close, Ross, Roberts and Jaffe[10] is quite interesting, although the physical basis of this model is obscure. (It has also been noted that the model really does not fully address the effects arising from a mechanical change in the size of the nucleon.[11]) In this model moments of structure functions are assumed to exhibit "rescaling". With A specifying a nucleus of mass number A, and N denoting the nucleon, it is assumed that moments are related by the following expression,[10]

$$M_A(Q^2) = M_N(\zeta_{NA}(Q^2)Q^2), \qquad (4)$$

where the quantity $\zeta_{NA}(Q^2)$ evolves with Q^2 as follows,

$$\zeta_{NA}(Q^2) = \zeta_{NA}(Q_o^2)^{\alpha_s(Q_o^2)/\alpha_s(Q^2)} . \qquad (5)$$

Here $\alpha_s(Q^2)$ is the running coupling constant and Q_o^2 is the momentum scale for which a valence quark model (such as the bag model) is supposed to give a good description of the nucleon structure function ($Q_o^2 \lesssim 1\ \mathrm{GeV}^2$). The essential assumption is that $\zeta_{NA}(Q_o^2)$ is given by a length scale modification,

$$\zeta_{NA}(Q_o^2) = \left(\frac{\lambda_A}{\lambda_N} \right)^2 > 1. \qquad (6)$$

Here λ_N is a length scale appropriate to the nucleon in vacuum, and λ_A is the length scale appropriate for the nucleus. In the papers dealing with the rescaling model one finds calculations of the ration λ_A/λ_N based upon models of the nucleon-nucleon correlation functions.[10] We prefer to make the identification

$$\frac{\lambda_A}{\lambda_N} = \frac{\phi_o}{\langle \phi \rangle_A} , \qquad (7)$$

where the brackets denote the average value of $\phi(r)$ in the nucleus. For example, we can write, using a local-density approximation,

$$\phi(r) \approx \phi_o \left(1 - \frac{1}{5} \frac{\rho(r)}{\rho_{NM}} \right) , \qquad (8)$$

where $\rho(r)$ is the matter density of a nucleus and ρ_{NM} is the density of nuclear matter. Therefore, we have

$$\langle\phi\rangle_A \cong \phi_o\left(1 - \frac{1}{5}\frac{\langle\rho\rangle_A}{\rho_{NM}}\right) \qquad (9)$$

and

$$\frac{\lambda_A}{\lambda_N} \cong \frac{1}{\left(1 - \frac{1}{5}\frac{\langle\rho\rangle_A}{\rho_{NM}}\right)} . \qquad (10)$$

Thus, the A dependence of the ratio λ_A/λ_N is here related to the fact that nuclei of different mass number have different percentages of surface nucleons. (A naive extrapolation of (10) higher densities would indicate a deconfining phase transition of about five times nuclear matter density.)

We have noted that in the effective Lagrangian we have suggested to model QCD at large length scales there is only a single dimensional quantity, if we neglect the small current masses of the up and down quarks.[7] Dimensional quantities will then scale with the value of this order parameter. For example, the radius of a nucleon in nuclear matter will be given by,

$$\frac{R_{NM}}{R_{vac}} = \frac{\phi_o}{\phi_{NM}} , \qquad (11)$$

where R_{vac} is the nucleon radius in vacuum. The average radius of a nucleon in a nucleus is then given by,

$$\frac{\langle R\rangle_A}{R_{vac}} = \frac{\phi_o}{\langle\phi\rangle_A} . \qquad (12)$$

Thus, using (7), we can also identify

$$\frac{\lambda_A}{\lambda_N} = \frac{\langle R\rangle_A}{R_{vac}} . \qquad (13)$$

This result is consistent with the fact that in the rescaling model one "rescales" the moments (or the structure function) of the nucleon itself.

While the rescaling model has some attractive features, we believe that further study is required. In particular, one should actually calculate the structure function of a nucleon, either in vacuum or in a nucleus using an appropriate model of nucleon structure.

Modification of nucleon electromagnetic form factors in nuclei

Issues related to the effects of the nuclear medium in modifying nucleon properties have recently been reviewed by A. Gerard[12] and we refer the reader to that work for a more complete set of references.

We have published a number of papers on this topic and have shown that the momentum transfer dependence and the mass number dependence of the quenching of the longitudinal response in nuclei may be understood in terms of the medium-modified form factors we calculated in earlier work.[13] For example, consider the usual phenomenological expression for the electromagnetic form factor of the proton,

$$G_E^p(q^2) \cong \frac{1}{\left(1 - \frac{q^2}{a_{vac}^2}\right)^2} . \qquad (14)$$

Here $a_{vac}^2 = 0.71$ GeV^2 is the value of this quantity in vacuum. In nuclear matter we have

$$\frac{a_{vac}}{a_{NM}} = \frac{\phi_o}{\phi_{NM}} , \qquad (15)$$

or alternatively,

$$\frac{[r_p^2]^{\frac{1}{2}}_{NM}}{[r_p^2]^{\frac{1}{2}}_{vac}} = \frac{\phi_o}{\phi_{NM}} , \qquad (16)$$

where $[r_p^2]^{\frac{1}{2}}$ is the r.m.s. radius of the proton calculated from the slope of the form factor at $q^2=0$. We have shown in an earlier work[14] that the ratio

$$\frac{\langle[r_p^2]^{\frac{1}{2}}\rangle_A}{[r_p^2]^{\frac{1}{2}}_{vac}} = \frac{\phi_o}{\langle\phi\rangle_A} , \qquad (17)$$

which we have calculated using a soliton model of the nucleon,[13] reproduces the values of (λ_A/λ_N) which are required to fit the EMC effect. That is, the electromagnetic radius of the nucleon (calculated using a soliton model of the nucleon) scales with the inverse of the dynamical quark mass and that dynamical mass scales as the ratio ϕ/ϕ_o.[6,7]

The medium-modified form factors obtained earlier[13] have been used to explain a large body of data dealing with the longitudinal response in nuclei[15-17] and the charge distribution of ^{208}Pb.[18] The situation with respect to the transverse response is more complicated since there appears to be a large amplitude for two-nucleon processes which is important in the region of the quasi-elastic peak.[15] More theoretical and experimental work is needed to clarify the situation in the case of the transverse response.

Some attempts have been made to study the modification of nucleon properties in nuclei via y-scaling.[19] One can use the analysis of y-scaling to argue that there is little change of nucleon properties in nuclei[20]; however, we believe this conclusion is premature. For example, the analysis of y-scaling presupposes that one can use the impulse approximation to understand the data. However, as can be seen from the experimental data summarized in Ref. 12, the impulse approximation (with free-space nucleon form factors) cannot explain the data in the most recent (e,e') and (e,e'p) experiments.[21] Therefore, it is hard to understand why the impulse approximation should provide a satisfactory basis for the analysis of y-scaling. While y-scaling may be an experimental fact, it is not clear that one has identified the reaction mechanism correctly so that firm conclusions may be drawn. Again, further study is required.

Dirac phenomenology and the relativistic Brueckner-Hartree-Fock theory

In the work of Noble[22] one finds the first attempt to relate the quenching of the longitudinal response to a change of nucleon size. Noble uses the scaling relation,

$$\frac{R_{NM}}{R_{vac}} = \frac{m_N}{m^*_{eff}} \quad , \tag{18}$$

where

$$m^*_{eff} = m_N + U_s . \tag{19}$$

Here U_s is the scalar potential felt by a nucleon in nuclear matter. Dirac phenomenology[4,5] yields $U_s \approx 400$ MeV so that $R_{NM}/R_{vac} \approx 1.74$, or in ^{56}Fe $\langle R\rangle/R_{vac} \approx 1.4$. This represents an increase of the average nucleon radius in ^{56}Fe of about 40 percent, while to explain the EMC effect (or to explain the quenching of the longitudinal response) in iron, the radius increase needs to be only 15 percent.[10,16] At first sight there might appear to be a problem with the rescaling analysis; however, as we will discuss below, an understanding of the relativistic Brueckner-Hartree-Fock theory[3] allows us to clarify this situation and to see the applicability of the rescaling analysis.

The problem with the simple analysis of (18) and (19) is that U_s contains a number of effects which have nothing to do with the change of mass scale. In particular the various contributions to U_s include exchange (Fock) terms arising from the exchange of omega, rho and pi "mesons" between nucleons. We must remove these terms from U_s before we calculate a value for the modified mass parameter, $\tilde{m}$. In our analysis we found $U_s \approx -350$ MeV; however, only about 60 percent of this scalar potential was due to sigma exchange. (This may be seen from inspections of Figs. (2.8) - (2.12) of [3], for example.) Therefore, $\tilde{m} \approx 938-210 = 728$ MeV, and

$$\frac{R_{NM}}{R_{vac}} = \frac{m_N}{\tilde{m}} \approx 1.29 . \tag{20}$$

There is certainly some theoretical error to be associated with the estimate in (20), but the result is quite close to that obtained from our previous analysis.

More precisely, we can see that in the theory of covariant soliton dynamics,[11] the mass and radius of a nontopological soliton are given by,[23]

$$m^* = f(g_\chi, \eta)\, m_q^{dyn} , \tag{21}$$

$$R = \frac{h(g_\chi, \eta)}{m_q^{dyn}} , \tag{22}$$

where m_q^{dyn} is a dynamical quark mass arising from the coupling of the quark to the QCD condensates and f and h are dimensionless functions of a coupling constant, g_χ, and a mass ratio, η. The mass ratio does not change upon rescaling, so that

$$\frac{R_{NM}}{R_{vac}} = \frac{m_q^{dyn}}{\tilde{m}_q^{dyn}} , \tag{23}$$

$$= \frac{\phi_o}{\phi_{NM}} , \tag{24}$$

as noted earlier.

Summary

In summary, we can say that if we use the order parameter of the gluon condensate to set the mass and length scale both in vacuum and in nuclei, we can understand several interesting phenomena from a unified point of view. Either theoretical analysis or phenomenological considerations lead to the conclusion that the gluon consensate order parameter is reduced by about 25 percent in nuclear matter. This effect may be considered as a precursor of a deconfining phase transition.[24]

References

1. J.J. Aubert et al. (EMC collaboration) Phys. Lett. 123B, 275 (1981); A. Bodek et al., Phys. Rev. Lett. 50, 1431 (1984); 51, 534 (1984); R.D. Arnold et al., Phys. Rev. Lett. 52, 727 (1983). BCDMS Collaboration, Phys. Lett. 163B, 282 (1985).

2. Z.E. Meziani et al., Phys. Rev. Lett. 52, 2130 (1984).

3. M.R. Anastasio, L.S. Celenza, W.S. Pong, and C.M. Shakin, Phys. Rep. 100, 327 (1983).

4. L.S. Celenza and C.M. Shakin, Relativistic Nuclear Physics: Theories of Structure and Scattering (World Scientific, Singapore, 1986).

5. B.D. Serot and J.D. Walecka, in Advances in Nuclear Physics, Vol. 16, edited by J.W. Negele and E. Vogt (Plenum Press, New York, 1985).

6. L.S. Celenza and C.M. Shakin, Phys. Rev. D34, 1591 (1986).

7. L.S. Celenza and C.M. Shakin, Effective Lagrangian Methods in QCD, in Chiral Solitons, edited by K.F. Liu (World Scientific, Singapore, in press).

8. M.A. Shifman, Ann. Rev. Nucl. Part. Sci. 33, 199 (1983).

9. For a review see R.L. Jaffe, in Relativistic Dynamics and Quark-Nuclear Physics, edited by M.B. Johnson and A. Pickleseimer (Wiley, New York, 1985).

10. F.E. Close, R.J. Jaffe, R.G. Roberts and G.G. Ross, Phys. Rev. D31, 1004 (1985).

11. S. Brodsky, private communications.

12. A. Gerard, Saclay Report No. 2388 (Sept. 1986). To be published in the proceedings of the CEBAF Summer Workshop (Newport News, June 23-28, 1986).

13. L.S. Celenza, A. Rosenthal and C.M. Shakin, Phys. Rev. C32, 232 (1985).

14. L.S. Celenza, A. Rosenthal and C.M. Shakin, Phys. Rev. Lett. 53, 892 (1984).

15. L.S. Celenza, A. Harindranath and C.M. Shakin, Phys. Rev. C32, 248 (1985).

16. L.S. Celenza, A. Harindranath, C.M. Shakin and A. Rosenthal, Phys. Rev. C32, 650 (1985).

17. L.S. Celenza, A. Harindranath and C.M. Shakin, Phys. Rev. C33, 1012 (1986).

18. L.S. Celenza, A. Harindranath, C.M. Shakin and A. Rosenthal, Phys. Rev. C31, 1944 (1985).

19. G.B. West, Phys. Rep. 18C, 264 (1975).
I. Sick, Phys. Lett. 157B, 13 (1985).
R.D. McKeown, Phys. Rev. Lett. 56, 1452 (1986).

20. I. Sick, contribution to CEBAF Workshop - 1986 (to be published).

21. G. Van der Steerhoven et al., Phys. Rev. Lett. 57, 182 (1986).

22. J. Noble, Phys. Rev. Lett. 42, 412 (1981).

23. L.S. Celenza, V.K. Mishra, and C.M. Shakin, Mass scales in QCD and nuclear dynamics, Brooklyn College Report B.C.I.N.T. 86/051/155 (1986). Unpublished.

24. See for example, M. Satz, Ann. Rev. Nucl. Part. Sci. 35, 245 (1985).

INFLUENCE OF SIX-QUARK BAGS ON ELECTRON SCATTERING

Gerald A. Miller

Institute for Nuclear Theory
Department of Physics, FM-15
University of Washington
Seattle, Washington 98195

Abstract

Possible signatures of the presence of nuclear six-quark bags are discussed.

I. Introduction

In the past few years, many workers have tried to use quarks and their interactions to compute nuclear properties. One way to include quarks is to postulate the existence of nuclear six-quark bags[1], and then predict the influence of such objects on various nuclear reactions. Information about how QCD determines nuclear properties may be obtained if a given reaction turns out to be very sensitive to the presence (or lack) of such objects. The purpose of this communication is to discuss some electronuclear reactions that might yield information about six-quark bags.

Let me begin with an outline. First, I discuss my conception of the term "six-quark bag", and the properties of such objects. Simple estimates show that copious numbers of such objects might exist in nuclear matter. Suppose 40 or 50% of the baryons in a heavy nucleus were six-quark bags. One might expect that this would contradict many observations. Consider one spectacular piece of evidence for nucleonic degrees of freedom: the measurement of the charge density difference between Pb and Tl.[2] I found[3] that including (more than about 50% of) six-quark bags does not affect the predicted cross section very much. No strong disagreement is found![3] One may even claim that including six-quark bags improves the comparison between theory and experiment. Kisslinger and Hoodbhoy[4] and others have argued that recent measurements of the He and H charge densities provide evidence for the existence of six-quark bags at the 15% level. But the main message is that elastic scattering is not extremely sensitive to *the six-quark bag presence in nuclei.* (*I say this* because six-quark (6q) bags are generally one among many "second order" effects yielding similar contributions.) Thus, my purpose here is to instead consider inelastic electron scattering and to examine regions of the (Q^2,ν) plane where 6q bags might be found. P. Mulders[5] has already studied the role of 6q bags in the inclusive (e,e') process. He finds that six-quark bags could be responsible for the suppression of the longitudinal structure function and can fill in the "dip" region between the nucleon- and Δ- quasielastic peaks. Furthermore, in the Δ production region (ν = 300 MeV), the contributions of six-quark bags to the transverse structure function are about equal to those of the Δ. I reproduced Mulders' results and extended them to the case of a ^{4}He target. Six-quark bags are indeed important numerically. However, their largest contributions occur near the Δ region, so it is difficult to tell a Δ from a six-quark bag. In the hope of obtaining more definitive information, I suggest experimental studies of the energy dependence of the angular distribution of protons emitted in the (e,e'p) or (e,e'pp) reactions.

II. What and Why Six-quark Bags?

Learning how confinement works in nuclei is a fundamental issue. One way to make progress is to determine if quark effects (as opposed to nucleonic) effects) contribute to making the nucleus. Quarks may participate if they are confined occasionally in six-quark (6q) bags. To differentiate from "ordinary" effects we suppose that the 6q bag is orthogonal to simple product states of nucleonic wave functions. For present purposes we take the 6q bag to consist of six (antisymmetrized) quarks in the lowest (κ = -1, L = 0) state of the MIT bag. Eigenfunctions and energy eigenvalues have been obtained in Ref. 6. Some relevant features are shown in Table 1, taken from Ref. 5.

Table 1. Six-quark Bag Properties

I,S	Mass (GeV)
0,1	2.16
1,0	2.24
1,2	2.36
2,1	2.52

The numbers I,S represent the isospin and spin of the 6q system. These states are expected to have a width of about 150 MeV, which is a bit larger than that of the Δ. If one decomposes the 6q wave function into sums of products of baryon-baryon wave functions one finds that 80% of the probability is contained in components in which one of the "baryons" carry color. About 10% of the wavefunction occurs in nucleon-nucleon components, so there is some overcounting. However, this is smaller than other uncertainties.

One may view the six-quark bags as off-shell components in a generalized baryon-baryon wave function. From the table one sees that the typical energy denominators are about 0.3 to 0.6 GeV. One needs that amount of input energy to place these objects on the energy shell where they can be observed (under sufficiently lucky conditions).

Another property of six-quark bags is their size. In Ref. 6 the radius of a six-quark bag (R_6) is about $2^{1/3}$ times the radius of a nucleon. As discussed below, this assumption has a significant incluence on the location of the quasielastic peaks for 6q bag knockout. Lomon[7] assumes a smaller value of R_6.

III. How Many Nuclear 6-quark Bags Are There?

I would really like to know the answer to the above question. Estimates range from zero to very many. Here I present a very simple estimate based on geometry. One wants to use 6q bags instead of nucleons to represent the short-distance baryon-baryon wave function. Our procedure[1] has been to replace a two-nucleon wave function by a 6q bag whenever the motion of the pair brings their centers closer than a distance, r_0. Probability conservation is maintained by taking the probability for the 6q bag as equal to the removed probability for the nucleons to be closer than r_0. The value of r_0 is then an important number, and $r_0 \sim 1$ fm often leads to

results in good agreement with experiment.[1] This separation occurs when the edge of one nucleon is at the center of the other, provided the radius of the nucleon is taken as about 1 fm. Then the volume of the overlap region is large. The 6q probability per nucleon pair turns out to be between about 3 and 6%, depending on the state.

In heavy nuclei there are many possible pairs and (in this picture) many 6q bags. Consider, for example, a nucleon in infinite nuclear matter of density ρ_0 (= 0.166 Fm^{-3}). The probability that another nucleon lies within r_0 is $\frac{4\pi}{3} r_0^3 \rho_0 \approx 0.7$. Although Pauli principle effects multiply this number by 3/4, this seems excessively large. I don't insist that there really are that many 6q bags in nuclei, but it is likely there are some. The most irritating feature of this is that existing data cannot be used to rule out such an enormous percentage.

IV. ^{205}Pb - ^{205}Tl Charge Density Difference

This quantity is one of the best tests of the conventional nuclear picture. One observes the structure of the 3s proton wave function quite clearly.[2] Surely copious amounts of 6q bags should spoil this result. Calculation[3] shows that this is not so! The reason is that, in our treatment of elastic electron scattering, the dominant effect of 6q bags is that they are bigger than nucleons. But the difference between R_6 and a nucleon radius is very small compared to the size of the Pb nucleus. Thus no effect remains. The size is the only influence because six-quark bags are formed in the interior. There, the effective density of the center of mass of an NN pair is essentially the product of the 3s density by the approximately constant density of the nuclear interior.

V. Using (e,e') to See 6 Quark Bags

We want to ask what are the appropriate values of the momentum transfer ($Q^2 = -q^2$) and energy loss (ν) for 6q bags to be observable. Start with Q^2. We include processes in which the virtual photon knocks the 6q bag out of the nucleus. In this mechanism the 6q bag maintains its character. It is not blown to bits in the absorption of the virtual photon. In that case the 6q amplitude includes the appropriate form factor $G_6(Q^2)$. We follow Refs. 5 and 6 and assume that the six-quark bags are larger than nucleons. That means that the ratio of 6q to nucleon form factors:

$G_6(Q^2)/G_3(Q^2)$ approaches zero as the momentum transfer Q increases, and it becomes harder to find 6q bags at higher momentum transfers. This does not mean that it is harder to observe the influence of quarks at higher values of Q^2. It is just that the coherent effects of the 6q bag acting as one particle go away at high momentum transfer.

If the radius of the six-quark bag were equal to or smaller than that of the nucleon, as implied in Ref. 7, the opposite conclusion could be drawn. The calculations discussed below follow Refs. 5 and 6.

What about the photon energy loss, ν? The basic idea is that a 6q bag can be knocked out of the nucleus if it absorbs a photon of large enough energy ν. These excitation energies are the masses of the six-quark bag minus the mass of two bound nucleons. From Table 1, this is about 0.3 to 0.6 GeV. Considering the expected width of the 6q systems, these values of ν are contiguous with those needed for production of the Δ.

Thus 6q bags might be important at fairly low Q^2, but fairly high (by typical nuclear standards) values of ν.

VI. (e,e') Calculations

As mentioned in the introduction, I follow the work of Mulders.[5] The formulae necessary to make calculations of the cross sections are given in Mulders' paper.

It is necessary to discuss the basic assumptions of his model.

1. A photon strikes and knocks out either a three-quark (nucleon) (with probability P_3) or six-quark bag with probability P_6 given by $P_6 = 1 - P_3$. In this model, pionic components of nuclei do not contribute.

2. A plane wave approximation is used for all outgoing particles. The knocked out nucleons, 6q bags and produced Δ's are all on the mass-shell. Thus no final state interactions are included.

3. The final states are $|3q\rangle \times |A-1\rangle$ or $|6q\rangle \times |A-2\rangle$. These are treated as orthogonal states. Thus there is no interference between the two terms. This is a good approximation when Q^2 is large enough so that the one and two-baryon states are kinematically well-separated, but 6q bags have effects at values of $Q \lesssim 500$ MeV/c. Then (on average) each baryon of the 6q bag carries $\lesssim 250$ MeV/c, a value close to the Fermi momentum.

As Mulders remarks, the model is oversimplified but one can use it to determine the region of sensitivity to 6q effects in the (e,e') reaction. Furthermore, the model is consistent with data from Q = 400 to 500 MeV/c when natural values of the parameters ($P_6 \sim 0.4$) are used.

During the oral presentation I showed several figures from Ref. 5. These showed that the suppression of the longitudinal structure could be understood in terms of six-quark bags. This is because some 40% of the strength occurs at values of ν about .3 - .6 GeV ABOVE the quasi-elastic peak for nucleon knockout. There are also nice results for the transverse structure function. The six-quark bags fill in the dip region between the nucleon and delta peaks. In fact, the contributions of the six-quark bags are approximately equal to that of the delta. These results of Mulders are for the ^{12}C nucleus. I showed also calculations (but no data) for the ^4He nucleus. The values q and ν for which 6q bags are important are roughly the same as for the ^{12}C target.

The contributions of the individual six-quark bag states exhibit interesting peaks as a function of ν for fixed Q^2). However, these peaks are not directly observable since they occur in the Δ region.

The result of all of this is that there are large 6q bag effects seemingly in agreement with the data. However, we encounter the problem of too many competing mechanisms one more time.

VII. Better Identification of 6q Bags?

The six-quark bags of interest here are made of quarks in L = 0 states. Therefore, the angular distribution for the decay into two nucleons is isotropic, in the 6q rest frame. This is very different than the decay $\Delta \to N\pi$ ($3\cos^2\theta + 1$). I propose to use this idea to separate the contributions of 6q bags and delta decays.

Consider, for example, measurements of the angular distributions of protons emitted in the (e,e') reaction. One can look for a resonant enhancement of isotropic correlations. The isotropy is to be with

respect to the direction of the photon momentum. If the 6q bags I discuss are relevant there could be a 150 MeV wide region of energy ($\nu \approx 0.3$-0.6 GeV/c or higher depending on the model) in which the angular distributions of high energy protons are isotropic. The restriction to high energy protons enters since we want the products of the decay $6q \to NN$, not $6q \to \Delta N$ or $6q \to \Delta\Delta$.

One could apply the rapidity analysis of McKeown et al.[8] to identify the isotropic distribution. Ref. 8 dealt with pion absorption on a cluster of nucleons. After absorption, the cluster spews out nucleons. They[8] found the velocity (essentially the rapidity y) of the coordinate frame in which the emitted nucleons have an isotropic angular distribution. The same technique should work for the photon absorption under consideration here. In that case $y \sim \tanh^{-1}|\vec{q}|/M_{6q}$ is the rapidity of the 6q bag that absorbed the photon. In the frame of rapidity y, the nucleons from the $6q \to NN$ decay are emitted isotropically.

Another possibility is to look for a resonant enhancement of the isotropic angular distribution of two protons emitted in the (e,e'pp) reaction. This could be done with a 4π detector.

This hope for identifying the 6q effects lies in combining two distinct effects: an isotropic angular distribution (in the appropriate coordinate system) and a resonant energy behavior. Combining these two separate pieces of information may allow the separation of 6q bag effects from the background of ordinary two-nucleon processes which are not expected to have those two features.

VIII. Summary

The Summary is given in the Introduction.

References

1. G.A. Miller, Workshop on Nuclear Chromodynamics, ed. S. Brodsky and E. Moniz, World Scientific Publishing, Singapore, 1986, p. 343.
2. G.A. Miller, Int. Rev. of Nucl. Phys, ed. W. Weise, World Scientific Publications, Singapore (1984), p. 189.
3. G.A. Miller, Phys. Lett. 174B, 229 (1986).
4. P. Hoodbhoy and L.S. Kisslinger, Phys. Lett. 146B, 163 (1984).
5. P. Mulders, Nucl. Phys. 459A, 525 (1986).
6. R.L. Jaffe, Phys. Rev. Lett. 38, 195 (1972); A.T. Aerts et al., Phys. Rev. D 17, 260 (1978).
7. E.L. Lomon, AIP Conf. 97, 78 (1983).
8. R. McKeown, Phys. Rev. Lett. 49, 1033 (1980).

NUCLEAR FRAGMENTATION, PART I
PROTON-NUCLEUS COLLISIONS AT HIGH ENERGIES

Andrew S. Hirsch, Purdue University,
West Lafayette, IN 47907
John Molitoris, Lawrence Livermore National Laboratory
Livermore, CA 94550

Abstract: The features of p-nucleus collisions leading to the production of nuclear fragments are briefly reviewed. Emphasis is placed on what is known and what is unknown experimentally.

When a proton of incident energy exceeding about 1 GeV collides with a large target nucleus, such as xenon, nuclei of up to about 1/3 the target mass (A_T) become likely reaction products. This has been known for over three decades[1] and has been studied extensively using both emulsions[2] and radiochemical techniques.[3] Counter experiments have made detailed and comprehensive examinations of these nuclear fragments[5,6,7,8] although the vast majority of these have been inclusive in nature. It has been clearly established that fragmentation is a high energy process with a threshold of about 1 GeV for incident protons[8] (fig. 1), and a high charged particle multiplicity indicative of a central collision. Above about 10 GeV, the typical fragment cross section enters the limiting fragmentation region where it is independent of energy up to the highest energies studied, 350 GeV.[7] Despite the great body of experimental data that now exists, the production mechanism of nuclear fragments by high energy protons remains unclear. Processes such as evaporation[9], cold fracturing[10], and a phase transition (gas to liquid) near the critical point[7] have been proposed to account for the systematics of the data.

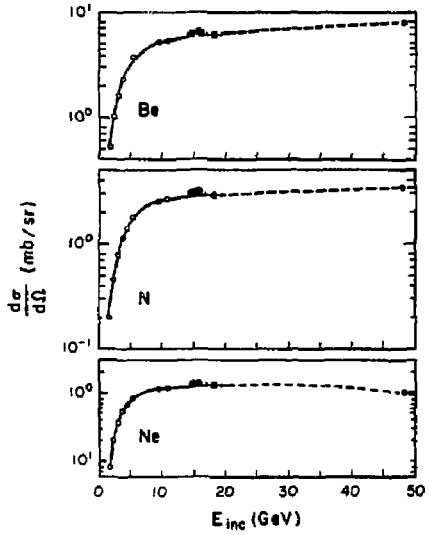

Fig. 1: Fragment cross section vs. incident energy. Solid curve is fit to the data from 1-20 GeV (AGS data). The point at 48 GeV was obtained at Fermilab, Ref. 7.

Fragment kinetic energy spectra are characterized by a Maxwell-Boltzmann like shape, although they tend to be broader than a single MB spectrum (fig. 2). The peak in the kinetic energy spectrum for a fragment such as carbon produced from p-xenon collisions occurs at about 2 MeV per nucleon, and thus a significant number of fragments emerge with very small kinetic energies. Studies of the spectra indicate that the Coulomb energies involved are small when compared to the tangent sphere value of the fragment and the target minus fragment system. A possible interpretation of this fact is that fragmentation is a multibody breakup involving the entire volume of the disassembling system. This is in contrast to a system undergoing sequential evaporation. We know from a recently completed experiment at the AGS[8] that the slope characterizing the high energy tail of the spectrum is independent of incident energy from 1 to 350 GeV, but the shape of the spectrum changes dramatically between 1 and 6 GeV. The high energy tails also indicate that all of the fragments come from a common system which has been reduced in nucleon number over the initial target.[6,7] For a xenon target, this 'remnant' sytem is some 20 nucleons lighter. By detecting fragments at both forward and backward scattering angles, the speed of the emitting system has been found to be very small, $\beta \sim .002$ for xenon. Thus, the remnant system is practically at rest in the laboratory.

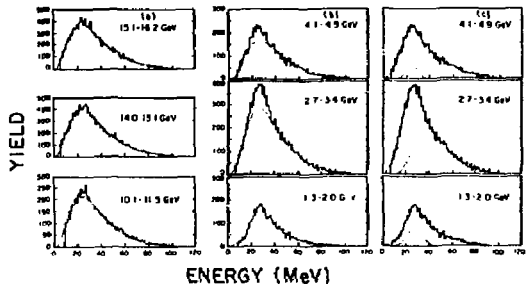

Fig. 2: Kinetic energy spectra obtained at the AGS.
a) Solid curve is the total fit
b) Fragmentation component
c) Gaussian component, Ref. 8.

The fragment mass yields have a power law fall off with fragment mass number (fig. 3). It has been shown that fragment multiplicities and cross sections for fragments in the range $2 \leq Z_f \leq 12$ are essentially the same whether these events are observed with a fragment trigger (A_f =20-40) or not.[11] Thus the inclusive and coincident data are evidently the same, reinforcing the notion of a multibody breakup. Assuming that fragmentation is a multibody breakup, we can estimate that the total energy in the remnant system must have been on the order of 1 GeV.[8]

The above paragraphs summarize some of the 'facts' concerning fragmentation. Experiments have also been performed with high energy protons incident on nuclear targets with the focus on the outgoing

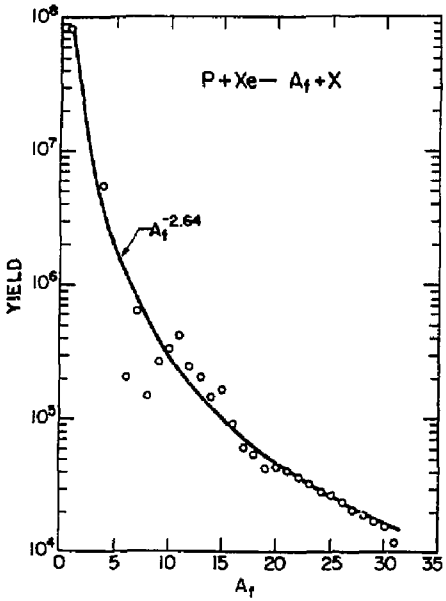

Fig. 3: Mass yield vs. fragment mass obtained at FNAL (Ref. 7).

nucleons.[12] These studies show that the incident proton produces a fast moving source of nucleons ($\beta \sim .1-.2$) which, when fully developed contains (3-5) x $A_T^{1/3}$ nucleons. We note that for a xenon nucleus, this is in good agreement with size of the remnant system. Thus, there is a hint that fragments may be produced when a moving source containing a substantial fraction of the nucleons in the original target is formed. A 4 GeV proton incident on a heavy target was found 30% of the time to produce a moving source which carried away about 75% of the incident energy. One might conjecture that the remaining 25% was left in the surviving nuclear system. This happens to agree with the estimate made above for the energy in the remnant.

A 4π experiment capable of measuring the kinetic energies of protons and heavy fragments, with charge and perhaps mass identification, could resolve many of the issues raised above. How much energy is in the remnant system? Is the decay sequential or simultaneous? Is fragment production correlated with the formation of a moving source of nucleons? These questions and many others may be addressed when exclusive experiments are performed with high energy probes on heavy nuclear targets.

References

1. N. A. Perfilov et al., Fiz. Nauk 60, 3 (1960) [Sov. Phys.-Usp. 3, 1 (1960)].
2. J. Hudis, Nuclear Chemistry, edited by L. Yaffe (Academic, New York, 1968), Vol. 1, Chap. 3.
3. R. Wolfgang et al., Phys. Rev. 103, 394 (1956); O. Scheidemann and N. T. Porile, Phys. Rev. C 14, 1534 (1976).
4. A. M. Poskanzer et al., Phys. Rev. C 3, 882 (1971).
5. G. D. Westfall et al., Phys. Rev. C 17, 1368 (1978).
6. J. A. Gaidos et al., Phys. Rev. Lett., 42, 82 (1979).
7. A. S. Hirsch et al., Phys. Rev. C 29, 508 (1984).
8. T. C. Sangster, Ph. D. thesis, Purdue University (1986); M. Mahi, Ph. D. thesis, Purdue University (1986).
9. W. A. Friedman and W. G. Lynch, Phys. Rev. C 28, 950 (1983).
10. J. Aichelin et al., Phys. Rev. C 30, 107 (1984).
11. A. I. Warwick et al., Phys. Rev. C 27, 1083 (1983).
12. K. Nakai et al., Phys. Lett. 121B, 373 (1983); T.-A. Shibata et al., University of Tokyo Report UTPN-195 (1983).

Nuclear Fragmentation, Part II
Electron-Nucleus Collisions at High Energies

John D. Molitoris
Lawrence Livermore National Laboratory
Livermore, CA 94550

Andrew S. Hirsch
Purdue University
West Lafayette, IN 47907

Some observed features of $e^{\pm}$-nucleus collisions are discussed and similiarities with high energy p-nucleus collisions are outlined. A search for massive nuclear fragments ($A \gtrsim 4$) produced in these $e^{\pm}$-nucleus collisions is proposed.

In February 1986 an exploratory experiment[1] was conducted at PEP using the TPC/2γ facility, where the Time Projection Chamber (TPC) provided the primary particle identification in electron-nucleus collisions. A small quantity of gas was bled into the beam pipe inside the TPC at the interaction region. This increased the pressure in the interaction region about two orders of magnitude and was sufficient to increase the incidence of target beam gas events well above that of the residual gas. Although deuterium, argon, and xenon were used, only some features of the $e^{\pm}$+Xe collisions will be discussed here. The analysis of this data is still in a very preliminary state.

The $e^{\pm}$+Xe data had a significant number of events with large proton and deuteron multiplicities. The energy deposition (ν) in these events typically ranges from about 6 to 10 GeV with $Q^2<0.1$ GeV^2 and $x<0.01$. Figure 1 shows one of the most spectacular events in the $e^{\pm}$+Xe data. The left hand side of the figure shows an end-cap projection of the charged particle tracks and the right hand side shows the same tracks folded in Φ. This event has 4 deuterons and 9 protons in the TPC and the highest deuteron and proton multiplicities of all the data. The kinematic variables take on the values: $Q^2=0.07$, $x=0.003$, and $\nu=10$ GeV. A plot of the rapidity (y) vs transverse momentum ($p_\perp$) is shown in figure 2, where $\langle y\rangle=0.146$ and $\langle p_\perp\rangle=0.55$.

These high multiplicity events leave such questions unanswered as the source of the deuteron production and the mechanism which produces the many fast protons. Such questions may be answered by further analysis of the TPC data, but that data cannot determine what happens to the remainder of the nucleus. The energetic protons and deuterons account for up to 13% of the target mass, which leaves most of the nucleus behind. A complete experiment should record the energetic protons and deuterons as well as the subsequent decay of the target remnant. This could not be done in the exploratory run at PEP as any massive nuclear fragments were stopped in the thick beam pipe and vertex detector of the TPC. In addition to the relationship between the remnant and the observed high energy nucleon and deuteron yields, it is important to understand how the energy deposited by the incident electron in the nucleus affects the target remnant. This requires that the incident electron also be detected.

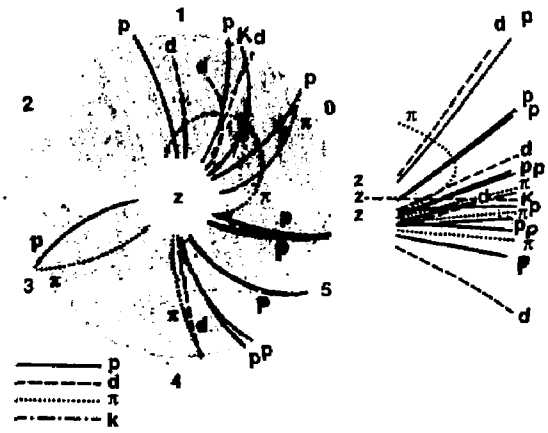

Figure 1. 14.5 GeV $e^{\pm}$ + Xe (run 422, event 169)

A situation similiar to the above has been noted in high energy p+A collisons. Here, Nakai et al[2] have observed energetic nucleon emission much like that

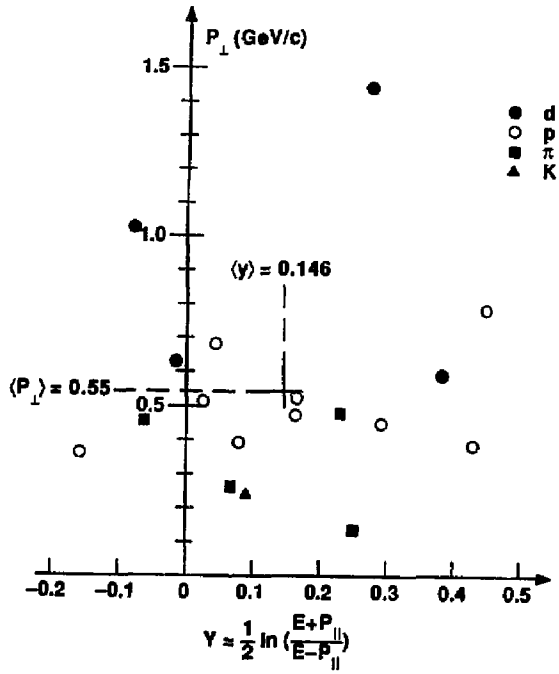

Figure 2. $e^{\pm}$ + Xe at 14.5 GeV

seen in the TPC data and estimate there to be about (3-5) x $A_T^{1/3}$ energetic nucleons produced per collision. This estimate is in agreement with the higher multiplicity proton events (proton multiplicity ≥ 7) in our $e^{\pm}$+Xe data assuming that the proton and neutron multiplicities are equal and summing in the nucleons bound up as deuterons. Furthermore, Hirsch et al[3] have studied massive fragment production in p+A collisions (see Part I of this presentation) and were able to estimate the mass loss between the initial target nucleus and the remnant from the kinetic energy spectra of the fragments. The mass difference determined by Hirsch et al is also in good agreement with the total mass of the fast nucleons observed by Nakai. This and other common features of the two p+A measurements allowed Hirsch to draw a connection between high multiplicity energetic nucleon emission and massive fragment production[3].

As Nakai et al[2] only measured the fast nucleon component and Hirsch et al[3] only measured the fragmentation of the remnant system, a definitive experiment detecting both processes in coincidence has yet to be performed. Furthermore, neither measurement detected the incident proton, so the energy deposited in the nucleus was not well known. Whether or not the energetic nucleons observed in $e^{\pm}$+Xe collisions at PEP are related to massive fragmentation of the remnant nucleus has yet to be determined. Presently, such a study would be unique to PEP due to the projectile and bombarding energy. Also, the proposed detector scheme at a PEP nuclear physics interaction region[4] would allow an exclusive measurement to be performed (described below).

Independent of any results in p+A collisions, one would like to study the behavior of the remnant nucleus in $e^{\pm}$+A collisions and its dependence on the various kinematic variables. Assuming that the remnant does break up into massive fragments, it would be interesting to determine fragment production as a function of ν for fixed values of Q^2. While it is most probable that the characteristics of target fragmentation are only functions of ν, one should keep an open mind concerning the dependence on other kinematic variables, i.e. Q^2. For example, one might conceive that the later stages of fragmentation might "remember" tne mode of initial energy deposition. Very low Q^2 events where the virtual photon appears hadron-like to the nucleus might be different from true deep-inelastic events ($Q^2>1$) where one pictures the formation of a string whose length scale may be comparable to nuclear dimensions.

We can make a rough estimate of the coincident counting rate by taking the deep inelastic cross section per nucleon $d^2\sigma/d\Omega_e dE'$ from the parametrized structure functions, and making the usual assumption that the nuclear cross section is the incoherent sum over the nucleons. This gives the inclusive cross section for a given energy deposition ν, and Q^2. To get the coincident cross section where one also measures a fragment with $A\geq 4$, we note that in the p+A work (ref. 3), the fragment cross section ($A\geq 4$) was ≈0.3 of the geometric cross section. Thus, taking the factor of 0.3, a total heavy-ion telescope coverage of 0.5 sr, and assuming isotropy of fragment emission, we find rates of >3Hz for $0.001\leq Q^2\leq 1$ and <1 Hz for $1\leq Q^2\leq 5$. This results from integrating over the electron scattering angle range $0°<\theta<11°$ (realizable with the proposed septum spectrometer for the nuclear physics region at PEP[4])and ν=5.5-14.5 GeV. We have assumed a luminosity of 1.5×10^{29} cm^2 sec^{-1} for Xe.

This is a multifaceted experiment and can be performed in three phases. Central to the experiment is the implementation of a warm gas jet target in PEP with the capability of using heavier gases (i.e. Ar, Kr and Xe). It is also important that the target allow solid state detector arrays to be placed in close

proximity to the gas jet with no obstructions. Solid state detector telescopes have excellent Z and energy resolution and have been used successfully by Hirsch et al[3] to detect heavy fragments from p+A collisions. It would be advantageous to have the solid state detector arrays subtend a reasonably large solid angle, as the fragmentation cross section is not known and difficult to estimate theoretically. With just the solid state detector telescopes, one could perform an inclusive measurement similiar to the one for p+A collisions.

A more interesting measurement and an improvement on the above would be to include a small angle spectrometer to tag the incident electron and determine ν and Q^2. Then any dependence of the fragment production on ν and Q^2 could be observed.

Finally, the addition of a 4π detector centered on the target would enable us to observe the energetic protons and deuterons seen at TPC and ascertain if there is a connection between these and fragment production.

Presently we are studying the feasibility of solid state detectors in the PEP environment. The electromagnetic field of the circulating beam is intense enough to render these detectors useless if they are placed too close to the beam or not shielded properly. Furthermore, they are susceptable to radiation damage which will continually degrade their energy resolution and (again) if not shielded properly, the signal can be swamped by synchrotron radiation. We hope to test some of these effects on the solid state detectors in fall 1987, when PEP will be operated for high energy physics. A simple apparatus could be incorporated into the beam line which could move the detector array toward and away from the beam. The effectiveness of various foils to block the electromagnetic field could also be investigated. Before this is done, a study of the solid state detectors' outgassing properties in high vacuum must be performed as they will be coupled directly to the PEP vacuum.

References

1. F. S. Dietrich, S. O. Melnikoff, and K. A. Van Bibber, "An Exploratory Gas-Target Experiment at PEP using the TPC/2γ Facility," UCRL preprint 94764, June 1986.

2. K. Nakai et al, Phys. Lett. 121B, 373 (1983); T.-A. Shibata et al., University of Tokyo Report UTPN-195 (1983).

3. A. S. Hirsch et al, Phys. Rev. C 29, 508 (1984)

4. K. A. Van Bibber, (contribution to this workshop).

A FRESH LOOK AT BOSE-EINSTEIN CORRELATIONS

Werner Hofmann
Lawrence Berkeley Laboratory, University of California, Berkeley, California

Recent experimental data on Bose-Einstein (BE) correlations between identical bosons are reviewed, and new results concerning the interpretation of the BE enhancement are discussed. In particular, it is emphasized that the classical interpretation of the correlation function in terms of the space-time distribution of particle sources cannot be directly applied to particle production in high energy reactions.

Bose-Einstein (BE) correlations between like-sign pions, also known as the GGLP effect, have first been observed over 25 years ago and have been of continued interest since[1]. In this paper, I will summarize recent progress in our understanding of the BE effect. First the "classical" BE effect and its interpretation is summarized. Next, I will show that the classical description is not appropriate for high-energy reactions, and will point out where modifications are required. Following is a review a experimental data and a discussion of experimental problems which complicate the study of BE correlations, and some concluding remarks.

The classical "setup" to study BE correlations is indicated in Fig. 1: given a (large) number of fixed, identical, incoherent ("chaotic") pion emitters with lifetime τ and a spatial distribution $\rho(r)$ (with a characteristic width R), plus two distant detectors looking for the simultaneous emission of two identical pions with four-momenta $p_1 = (E_1,p_1)$ and $p_2 = (E_2,p_2)$. For any pair of emitters, there are two ways for the particles to propagate to the detectors, and those two amplitudes interfere.

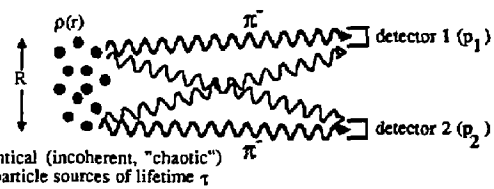

Fig. 1. Amplitudes interfering in the creation of the Bose-Einstein enhancement for identical bosons

Summing over all pairs of emitters, it is easy to show that the resulting two-particle correlation function C is essentially the square of the four-dimensional Fourier transform of the (normalized) distribution $\rho(r) = \rho(\mathbf{r},t)$ of emission points[2,3]:

$$C = \sigma^{(2)}(p_1,p_2) / \sigma_0^{(2)}(p_1,p_2) = 1 + |\int d^4r\, \rho(r) e^{iqr}|^2 \qquad (1)$$

with

$$q = p_1 - p_2 = (q_0,\mathbf{q})$$

Here $\sigma^{(2)}(p_1,p_2)$ denotes the measured two-particle cross section, and $\sigma_0^{(2)}(p_1,p_2)$ stands for the two-particle cross section in the absence of BE symmetrization. Since all sources are assumed to have identical lifetimes, the Fourier transform factors into a term depending only on $q_0 = E_1 - E_2$ and a term depending on three-momentum difference $\mathbf{q} = \mathbf{p}_1 - \mathbf{p}_2$: $C = 1 + |\tilde{\rho}(\mathbf{q})\tilde{g}(q_0)|^2$. For large $\mathbf{q}$ or q_0 the integral vanishes and we obtain $C = 1$; for small momentum differences C rises and reaches $C = 2$ for $\mathbf{q} = q_0 = 0$. In other words, BE statistics predict that identical bosons will be preferentially emitted in the same quantum state, i.e. $|q| R < 1$ and $q_0 \tau < 1$ (we use $\hbar = c = 1$ everywhere). Since the correlation function C(q) is rather insensitive to details of the distribution $\rho(r)$ — it is e.g. virtually impossible to distinguish a gaussian distribution in space from a group of emitters arranged on the surface of a sphere — experiments are typically limited to the determination of R and τ. In case the events exhibit a preferred axis, such as in e^+e^- annihilation into jets of hadrons, one can make futherstatements concerning the shape of the distribution of emitters ("spherical" or "cigar-like" or "pancake-like") by studying the effective size as a function of the angle between q and the event axis.

At a first glance, the interpretation given by eqn. (1) works extremely well: considering e.g. two rather different pion sources, namely heavy ion collisions at 1.8 GeV/nucleon[4] and e^+e^- annihilations at 29 GeV cms energy[5], we find in both cases a two-pion correlation function which is constant for large momentum transfers, and rises for small momentum differences (Fig. 2). For the heavy-ion system, the correlation length of about 70 MeV/c translates into a characteristic source size of ≈3 fm — just about the size of the composite nuclear system — whereas for e^+e^- annihilation the enhancement extends over a larger range in q, resulting in an effective source size of about 0.7 fm, consistent with the expected range of the confinement forces responsible for particle production.

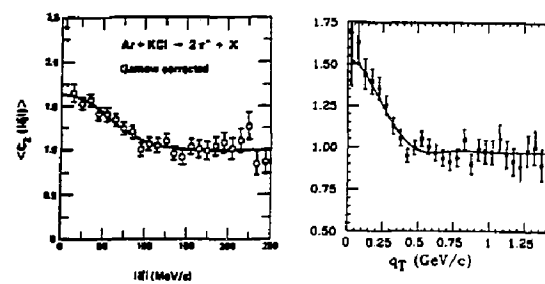

Fig. 2. (a) Two-pion correlation function measured in Ar + KCl collisions at 1.8 GeV/Nucl, as a function of the momentum difference |q| [4]. (b) Two-pion correlation function obtained in e^+e^- annihilation at 29 GeV cms energy[5], as a function of q_T, the component of q perpendicular to the total momentum of the pion pair.

However, several authors[2,6,7] have recently pointed out that eqn. (1) is not appropriate to describe BE correlations among particles produced in high energy reactions. As we shall see, several of the basic assumptions are violated: 1) particle sources are typically not

at rest, but move with high velocity with respect to each other; 2) because of this motion, the spectra of different emitters (as observed in a common frame, such as the lab frame) will not be identical; 3) for eqn. (1) to hold, the spectra should be approximately constant over a range $|q| \approx 1/R$; however momentum spectra in e^+e^- reactions, e.g., show strong variation over a range of a few 100 MeV. Finally one may question if the different emitters are actually incoherent.

In order motivate these statements and to show how the interpretation of BE correlations has to be modified to suit high-energy reactions, I need to discuss the present model of the space-time evolution of particle production in high-energy reactions[8], as it has evolved over the last decade or so. I will use e^+e^- annihilation as the simplest example. At t=0, a quark and an antiquark are created from a virtual photon (Fig. 3). They recede from each other at close to the speed of light, feeding energy into the color force field which builds up between them. At early times, corresponding to short gluon wavelengths, perturbative QCD can be used to describe the structure of this color field; at later times, large coupling constants cause any perturbative treatment to break down, and we have to resort to the phenomenological picture of a color flux tube ("string"[9]) spanned from quark to antiquark. Such a string provides a linear confinement potential, in agreement with measurements and consistent with results obtained using QCD on discrete space-time lattices. The energy stored in this color field is ultimately released through the production of new quark-antiquark pairs, which screen the color field and which recombine to form colorless hadrons. Since the decay of the color field will occur on a typical time scale τ_0 in the rest frame of the corresponding string segment, particle production points will scatter about the hyperbola $t^2 - z^2 = \tau_0^2$. On average, the primary quarks will propagate over a distance $\gamma\tau_0 = (\sqrt{s}/2m)\,\tau_0$ before they are confined to a hadron. We expect τ_0 to be of the order of typical hadron sizes; m is a typical hadronic mass scale, $O(m_p)$. At PEP energies — $\sqrt{s}$ = 29 GeV — this picture implies a longitudinal extent of the distribution of particle sources of about 30 fm, as compared to a transverse extent of order 1 fm (the diameter of a flux tube).

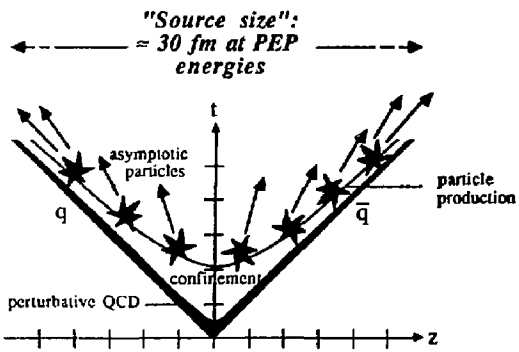

Fig. 3. Space-time evolution of particle production in e^+e^- annihilation into hadrons

Since this general model relies mainly on invariance arguments, and since all models with specific dynamics constructed so far agree with it[9,10], there is considerable confidence in this picture. Why, then, is this large source size not observed experimentally ?

The key to the answer lies in the observation that for such a space-time evolution source position in space and momentum of the emitted particles are highly correlated. A source moving along the z-axis with a velocity β will typically decay at a distance $z_{lab} \approx \beta\gamma c\tau_0$ from the origin, and the average z-component of momentum of one of its daughters will be $\langle p_{z\,lab}\rangle \approx \beta\gamma E_0$, where E_0 is its average energy in the rest frame of the emitter; hence $\langle p_{z\,lab}\rangle \propto z_{lab}$. This correlation implies the particles created at opposite "ends" of the event are never closeby in phase space. As a consequence, BE correlations will show no evidence of a large source size. This is most easily demonstrated in the example of two decaying "fireballs" of radius R and lifetime τ moving rapidly in opposite directions (Fig. 4). BE statistics enhances two-particle production near the diagonal $p_{z1} \approx p_{z2}$ (neglecting transverse momenta, for simplicity). We note that regions where the enhancement occurs are populated by particle pairs originating from the same fireball, never from opposite fireballs. The BE correlation length is therefore determined by the fireball size R/γ (as seen in the lab), and not by the two-fireball separation $D \approx \gamma\tau$!

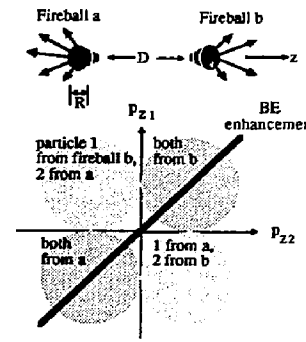

Fig. 4. Simple model to illustrate BE correlations for moving sources with $\beta \approx 1$. Lorentz boosts result in $p_z > 0$ for most particles emitted from 'b', and in $p_z < 0$ for most particles from 'a'. The lower plot indicates the resulting two-particle density. In the region of the BE enhancement, $p_{z1} \approx p_{z2}$ (indicated by the black band), both particles tend to stem from the same fireball.

For the more general case of e^+e^- jets, it is easy to show that each of the emitters indicated in Fig. 3 will spread particles over approximately ± 0.7 units in rapidity $y = (1/2)\log(1+\beta_z/1-\beta_z)$, centered at the rapidity of the emitter[11] (assuming isotropic emission in its rest frame). Particle distributions from different emitters will overlap in momentum space provided that the rapidity difference Δy of the emitters is of the order of one unit or less. In a comoving frame, this in turn implies a maximum separation of the emitters $\Delta z \approx \tau_0 \sinh(\Delta y) \approx \tau_0$. In such frame, the BE correlation length both in longitudinal momentum difference and in energy difference is therefore of order $1/\tau_0$. The equality of space and time scales is a natural consequence of the covariant description. The correlation length in transverse direction is determined by the flux tube diameter, which is of the same order as τ_0. Since the BE correlation length thus is similar for q-vectors parallel and

perpendicular to the jet (= z) axis, we would thus expect the distribution of particle sources to appear roughly spherical, and no cigarlike with a large ratio of major to minor axes, as one migh naively expect based on Fig. 3.

More detailed studies[2,6] confirm these features: one finds that

- the correlation function C depends mainly on the (invariant) square of the four-momentum transfer $Q^2 = -q^2 = (p_1-p_2)^2$, and hence cannot be represented in the form $C = 1 + |f(q)g(q_0)|^2$
- the apparent source size, determined from the correlation length in Q^2, is of order τ_0
- the source appears essentially spherical
- the measured source size is almost independent of the cms energy and the momentum of the pion pair

Let me briefly discuss one explicit implementation of BE effects - a modification of the Lund hadronization model[9] proposed first by Andersson and myself[6], and later studied in detail by Artru and Bowler[12]. The basic idea is simple: consider a typical space-time diagram à la Lund[9] for particle production via string decay into quark-antiquark pairs (top diagram in Fig. 5). In this scheme, break-up points of the string uniquely determine particle momenta; the energy of particle is proportional to the distance between the production points of its quarks, and its momentum is proportional to the difference in quark production times. It is plausible that the matrix element M describing the decay of the color string is given by $M \propto e^{i\xi A}$, where $\xi = \kappa + iP/2$. A denotes the (invariant) space-time area spanned by the string. The real part of ξA, κA, is essentially the classical string action (κ denotes the energy per unit length, $\kappa \approx 1$ GeV/fm). The imaginary part, PA/2, describes the breaking of the string by quark-antiquark production at a constant rate P per unit length. In order to properly symmetrize production amplitudes for final states containing several identical bosons, we need to sum over all diagrams corresponding to permutations of those particles. In the context of BE correlations between two given pions, let us consider the effect of exchanging those two pions. Swapping two particles will change the space-time area swept by the string, and hence both the amplitude and phase of $e^{i\xi A}$ (bottom diagram in Fig. 5). Given the known magnitudes of κ and P [9], it is easy to see that the interference pattern between the amplitudes corresponding to Fig. 5 is dominated by the phase change of order $\Delta\phi \approx Q^2/2\kappa$. As a result, amplitudes interfere constructively for $Q^2 < \kappa \approx (0.4\,\mathrm{GeV})^2$ and cause a BE enhancement at low Q^2, compared to an effectively incoherent superposition for larger Q^2. As in the classical case, C(q) reaches a limiting value $C = 2$ for $q = q_0 = 0$, indicative of complete chaoticity of the source. However, whereas in the classical case the chaoticity is built in via the assumption that emission phases vary randomly from emitter to emitter and from event to event, here the strong momentum dependence of the amplitude $e^{i\xi A}$ guarantees virtually random phases between amplitudes corresponding to different permutations of particles, unless the final state contains two pions with almost identical momenta.

I should point out here that much of our revived interest in BE correlations results from this point of view — BE correlations as a measure of multiparticle production amplitudes and their phases — as opposed to the classical geometrical interpretation, which suffers from conceptual difficulties for systems with dimensions of the order of the wavelength of the emitted particles.

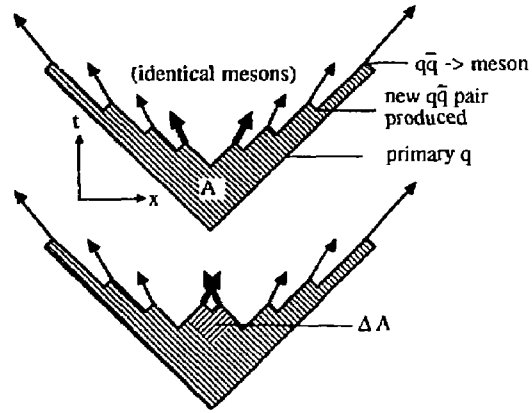

Fig. 5. Space-time structure of quark fragmentation in e^+e^- annihilation, as predicted in the Lund string model. The space-time area swept by the color field is denoted by A and gives rise to the production amplitude $M \propto e^{i\xi A}$. An exchange of the two central particles results in a change of that area by ΔA, with a corresponding change in amplitude and phase.

In the remainder of this paper, I will summarize relevant experimental data (with some emphasis on results from e^+e^- colliders) and discuss potential drawbacks in the experimental procedures. To begin, let us see if there is indeed evidence that BE correlations depend only on Q^2, and not on q and q_0 in a factorizable fashion.

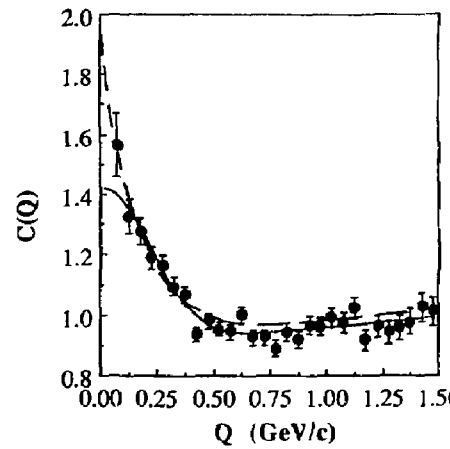

Fig. 6.Correlation coefficient C as a function of $Q = \sqrt{-q^2}$, measured in e^+e^- annihilation at 29 GeV cms energy[5]. Full line: fit to the data based on eqn. (3). Dashed line: prediction of the model of ref. 6. Possible dilution of the BE correlation due to long-lived resonances is not included in the model curves. Predictions of the model of ref. 2 exhibit a very similar shape.

Fig. 6 demonstrates the that BE enhancement is certainly seen in the variable $Q = \sqrt{Q^2}$. A clean distinction between the classical form

$$C = 1 + \alpha \exp(-R_j^2 q^2) \exp(-\tau^2 q_0^2) \quad (2)$$

(where we have for simplicity used a gaussian space-time distribution of emission points; the "fudge" factor α will be discussed later) and the relativistically invariant form (note the different sign of the q_0 term)

$$C = 1 + \alpha \exp(-R^2 q^2) = 1 + \alpha \exp(-R^2 q^2) \exp(+\tau^2 q_0^2) \quad (3)$$

however turns out to be rather difficult, since q and q_0 are of course highly correlated. Basically, the distinction boils down to the question of whether there is a positive correlation for large and approximately equal $|q|$ and q_0. Both the TASSO[13] and CLEO[14] groups claim evidence in favor of eqn.(3). For the TASSO data, the evidence is based on a global fit of the measured $C(q,q_0)$, which prefers eqn.(3) over eqn.(2). However, their statistical errors on the large $|q|$, large q_0 data are such that the evidence, though statistically significant, is by no means striking. In the CLEO paper, the main conclusion — absence of a $\exp(-\tau^2 q_0^2)$ dependence, as displayed in their Fig. 3 — depends strongly on the maximum q (or, to be specific, q_T) allowed; Fig. 6 of the same paper indicates a significant q_0 dependence. In any case, higher statistics data would certainly be welcomed!

An essential prediction of the new class of models is that the BE correlation length is virtually independent of the reaction energy, the dipion momentum, and the angle between q and the event axis. Fig. 7 shows a summary of effective radii R determined using eqn. (3) for different reaction types over a wide range of cms energies; given the systematic problems to be discussed later, the data are consistent with each other and point to an effective radius of about 0.7 - 1 fm. The source shape is consistent with approximate spherical symmetry[5,13,14] (Fig. 8) and independent of the γ-factor of the pion pair (Fig. 9).

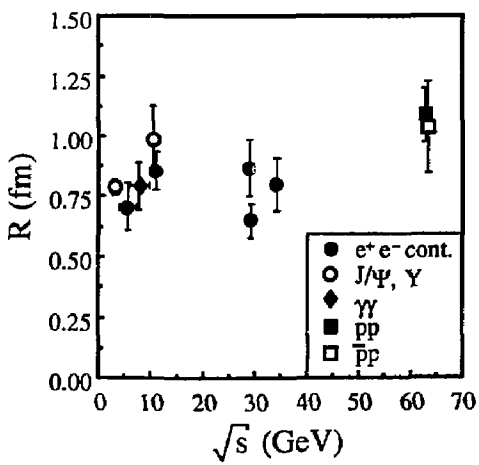

Fig. 7. Size parameter R of the pion source, determined according to eqn. (3) in various reactions, as a function of the cms energy[1,5,13,14,15].

Both in Figs. 2 and 6 we note that C does not seem to reach the predicted value C = 2 for vanishing momentum difference q of the two pions. Parameterization of the BE enhancement in terms of a gaussian (egn.(3)) typically yields $\alpha \approx 0.5$ - 0.6 instead of $\alpha \approx 1$ (after correction for particle misidentification, detection efficiency etc.); see Fig. 10. The two exceptions are BE correlations in J/Ψ decays and in two-photon collisions, for which α near 1 is measured. Several explanations have been put forward for the deviation of α from 1: BE correlations are absent for coherent particle sources[2,3], hence $\alpha < 1$ could be evidence for a partial coherence of the source.

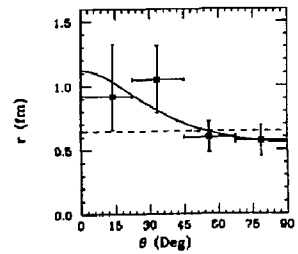

Fig. 8. Apparent size of the pion source in e^+e^- annihilation at 29 GeV, determined using eqn. 3, as a function of the viewing angle with respect to the jet axis[5]. Curves are based on the assumption the the pion emitting region is a three-dimensional ellipsoid, with a transverse size R_0 and a longitudinal extent cR_0, for c=1 (dashed), c=2 (solid) and c=3 (dotted).

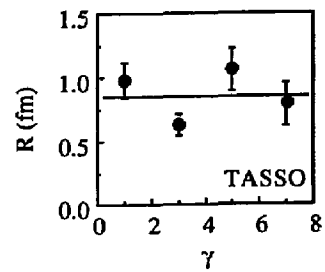

Fig. 9. Size parameter R of the pion source in high-energy e^+e^- annihilation, as a function of the boost $\gamma = E_{\pi\pi}/m_{\pi\pi}$ of the pion pair[13].

A much simpler explanation is that the measured value of α is usually obtained from an extrapolation of data at finite Q^2 to $Q^2 = 0$ and is therefore sensitive to the assumptions concerning the Q^2-dependence of the BE enhancement. The usual gaussian shape is used mainly for convenience and has no strong theoretical motivation. In fact, the recent models discussed above[2,6] predict shapes which are much more peaked for $Q \to 0$. As shown in Fig. 6, the models are in reasonable agreement with data in the range typically covered by experiments, $Q > 50$ MeV, and nevertheless extrapolate to $C \approx 2$ for $Q \to 0$. Another reason for a non-gaussian shape is pion production by long-lived resonances such as ω, η, and η'. For pions created in such decays, the effective source size is of the order $1/\Gamma_{\text{resonance}} > 20$ fm. Correspondingly, such pions contribute[16] to the BE enhancement only for small $Q < 10$ MeV/c - a region not covered by experimental data, resulting in an underestimate of α (Fig. 11). The absence of detectable BE

correlations for pion daughters from long-lived particles has been demonstrated experimentally using pions from K_0^s decays[5].

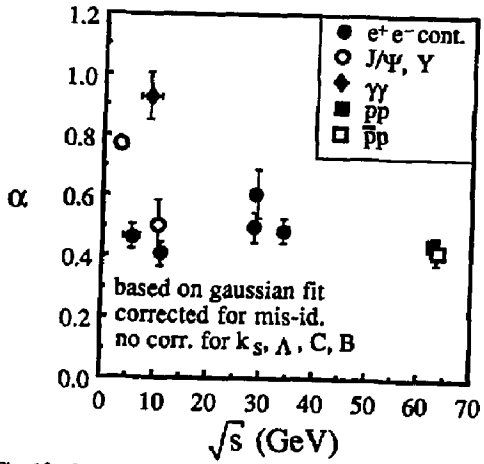

Fig. 10. Parameter a determined from fits of $C(Q^2)$ according to eqn. (3), for different reaction types as a function of cms energy[1,5,13,14,15]. Data points are corrected for particle misidentification (except for the ISR data), but are not corrected for the reduction in α due to pions from decays of long-lived particles.

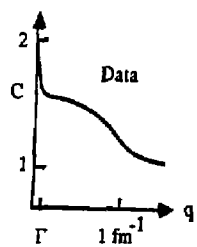

Fig. 11. Expected Q-dependence of the two-pion correlation function C, assuming that 50% of all pairs contain at least one decay product of a long-lived resonance of decay width Γ. The dotted region indicates the region typically covered by data points.

The CLEO group has attempted to correct their data for resonance effects and obtain $\alpha \approx 1$ after correction (Fig. 12). The problem there is, however, that the decrease in the effective α is very sensitive to the rates of η and η' production[17], which are not well measured and probably overestimated in current fragmentation models. It is therefore very difficult to draw any clear-cut conclusion at this point. Obviously, there are several mechanisms which explain $\alpha_{measured} < 1$ in a rather natural fashion; its seems premature to invoke partially coherent sources at this point. Clearly, more detailed data is needed.

However, major technical problems stand in the way of more precise measurements. Let us first consider the $\sigma^{(2)}(p_1,p_2)$ term in the definition of C (eqn. (1)): particle pairs in the interesting region $p_1 \approx p_2$ tend to overlap in the detector and create pattern recognition problems.

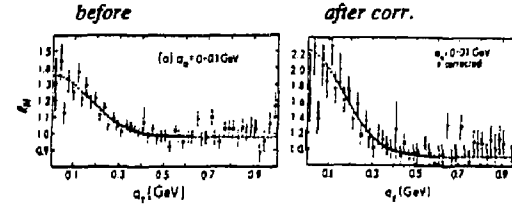

Fig. 12. Two-pion correlation function C as a function of q_T (see Fig. 2), for $q_0 < 0.1$ GeV. (a) uncorrected data, (b) corrected for the fraction of non-interfering pion pairs from decays of long-lived particles. From CLEO[14]

Furthermore, since the BE effects occurs only for identical particles, some particle identification is required, otherwise the data has to be corrected for a (typically 30%) contamination from other species. Finally, one needs to remove (or correct for) pions from very long-lived particles such as K_0^S or Λ, and ideally one would want to reject pions from particles with C or B quarks. These corrections introduce additional uncertainties. Finally, the rate of pairs at low Q decreases rapidly with Q, since the available phase space goes like Q^2. Even worse, however, are the problems caused by the $\sigma_0^{(2)}(p_1,p_2)$ term in eqn. (1). Obviously, BE effects cannot simply be "switched off" in the experiment in order to determine $\sigma_0^{(2)}$. One technique is to approximate $\sigma_0^{(2)}(p_1,p_2)$ by the product of single particle densities $\sigma^{(1)}(p_1)\sigma^{(1)}(p_2)$. This procedure removes the BE enhancement, but it also removes correlations caused e.g. by phase space constraints, superposition of different event types etc., and can result in a serious overestimate of C(q≈0). Another solution is to use unlike particles, i.e. unlike-sign pion pairs, to derive $\sigma_0^{(2)}$. The problem here is that while natural correlations due to phase space etc. are taken into account, the unlike-sign pion sample shows many additional correlations due to resonance decays and local charge conservation. Furthermore, acceptance corrections will usually not cancel when comparing like-sign to unlike-sign pion pairs. Even if great care is taken in handling all these problems, one is typically left with a O(10%) systematic uncertainty on the parameter R for "easy" data samples - such as global BE correlations in e+e- annihilation. For more difficult samples such as pions produced in νN reactions[18] (where event characteristics such as the hadronic mass W vary from event to event) or for specific phase space region in e^+e^- events, systematic errors due to the $\sigma_0^{(2)}$ determination can easily reach 50%; the systematic problems in the determination of α are even worse.

Let me summarize: I feel that BE correlations provide a rather interesting way to study multiparticle production dynamics; however, given our limited understanding of even the simplest cases (e^+e^-) and the experimental problems discussed above, I don't view BE correlations at this moment as a powerful diagnostic tool for such complicated processes as electron scattering off nuclei. Topics I would like to see studied (most likely in e^+e^-)

include: the precise shape at low Q^2, the detailed dependence on q and q_0 (or similar variables, see ref. 13), and the effect (and rates) of resonances. As to applications in nuclear physics, I feel that one first needs to understand results from simple (e^+e^-) systems in a quantitative way. Nevertheless, it is certainly interesting to see effective source radii measured in the current and target fragmentation region, and for different values of Bjorken x - there is always hope for a surprise!

This work was supported by the US Department of Energy under contract number DE-AC03-76SF00098. The author wants to thank M.G. Bowler and X. Artru for valuable correspondence, and acknowledges interesting and helpful discussions with G. Goldhaber, I. Juricic and M. Suzuki.

References

1. For recent reviews, see: G. Goldhaber, LESIP I Workshop, Bad Honnef, Germany (1984), and LBL-19417 (1985); G. Goldhaber and I. Juricic, LESIP II Workshop, Santa Fe, NM, 1986, and LBL-21531 (1986); and references given there.
2. M.G. Bowler, Z. Phys. C29, 617 (1985). This reference contains a very pedagogical introduction to theory of BE correlations; a more rigorous treatment is given in ref. 3.
3. M. Gyulassy at el., Phys. Rev. C20, 2267 (1979), and references given there.
4. W.A. Zajc et al., Phys. Rev. C29, 2173 (1984)
5. TPC Collaboration, H. Aihara et al., Phys. Rev. D31, 996 (1985)
6. B. Andersson and W. Hofmann, Phys. Lett. 169B, 364 (1986)
7. M. Gyulassy and K. Kolehmainen, Presented at Conf. on Ultrarelativistic Nucleus-Nucleus Collisions, Asilomar, Pacific Grove, CA, 1986
8. J.D. Bjorken, Int. Conf. on Physics in Collision, Stockholm, Sweden, 1982, and FERMILAB-Conf-82/42-THY (1982)
9. B. Andersson et al., Phys. Rep. 97, 33 (1983); X. Artru, Phys. Rep. 97, 1 (1983)
10. G. Marchesini et al., Nucl. Phys. B181, 335 (1981)
11. E.L. Berger, Nucl. Phys. B85, 61 (1975)
12. X. Artru, M.G. Bowler, Oxford-NP 79/86 (1986), submitted to Z. Phys. C
13. Tasso Collaboration, M. Althoff et al., Z. Phys. C30, 355 (1986)
14. CLEO Collaboration, P. Avery et al., Phys. Rev. D32, 2294 (1985)
15. AFM Collaboration, T. Akesson et al., Phys. Lett. 129B, 269 (1983)
16. P. Grassberger, Nucl. Phys. B120, 231 (1977)
17. M.G. Bowler, Phys. Lett. 180B, 299 (1986)
18. EMC Collaboration, M. Ameodo et al., Z. Phys. C32, 1 (1986)

Development of a Warm Gas Jet Target for PEP

John D. Molitoris and Karl A. Van Bibber
Lawrence Livermore National Laboratory
Livermore, CA 94550

Abstract

We are presently involved in a feasibility and design study of a warm gas jet target system for PEP. Our aim is to construct a low throughput system which will produce a target of dimensions less than 1 cm³ with areal densities in the range ≈ 10^{-8} - 10^{-10} g/cm².

Introduction

Warm gas jet targets (WGJT) have been used successfully in experiments at Fermi National Accelerator Laboratory (FNAL) and Brookhaven National Laboratory (BNL)[1,2] and have been found to be reliable for long periods of time. In fact, the implementation of a WGJT at FNAL was motivated by the previous use of an unreliable cold target system[2]. WGJT's work well for a wide range of gases and cost much less than a cold target system due to the lack of a liquid nitrogen handling mechanism. In view of this, we are using the Purdue WGJT system[1] as a model for an internal target for PEP.

The PEP base vacuum is typically ≈ 3 x 10^{-9} torr and is maintained by ion pumps built into the PEP beam line. Any internal target system implemented in PEP must be able to locally confine the gas to a high degree and recover the PEP base pressure in as short a distance as possible both upstream and downstream from the target. Such increases in the base pressure not only do not add to the effective target thickness, but serve to decrease the lifetime of the recirculating beam. A schematic of such a system is shown in fig. 1. Here the flow is directed through a nozzle into a receiver vessel which pumps out most of the gas. A well defined jet matched to a tight orifice on the receiver volume keeps backstreaming from the receiver into the target volume to a minimum. Most of the gas that does not make it into the receiver is pumped out by the first evacuation stage. This section is conductance limited from a second stage which incorporates more pumps and is further conductance limited from the main ring of PEP. Beyond the second pumping stage the PEP evacuation system must be able to maintain an acceptable vacuum.

Very stringent conditions are imposed on any target system coupled directly to the PEP beam line. One

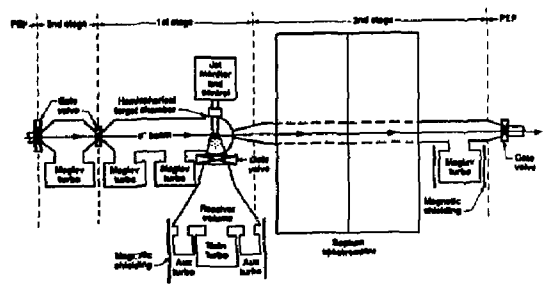

Figure 1. Schematic of a gas jet target system. The gas flows from some inlet volume through a nozzle and into the receiver. Most of the gas is pumped out through the reciever.

major criteria is that the outgassing of heavy hydrocarbons (A>50) be negligible. Figure 2 is a spectrum from our residual gas studies of the PEP vacuum which shows that for A>50 there are only three mass peaks (even on the most sensitive scale). These peaks represent benzene (C_6H_6) and two other trace gases (in the 50 to 60 a.m.u. mass region). For A<50 a.m.u. similiar scans show carbon monoxide (CO), carbon dioxide (CO_2), nitrogen (N_2), water vapor (H_2O), hydrogen (H_2) and argon (Ar) to be present in the ring. The condition on heavy hydrocarbons makes it difficult to use most conventional high throughput pumps in the target chamber, so we are presently investigating the possibility of using specially modified magnetically levitated turbomolecular pumps which are backed by a dry pumping system to maintain the vacuum in the target chamber. Pumps in the receiver volume (see fig. 1) are highly conductance limited from the PEP vacuum (by the receiver orifice) and can be sectioned off by two gate valves (one close to the orifice and one at the throat of each pump). Therefore these pumps may be

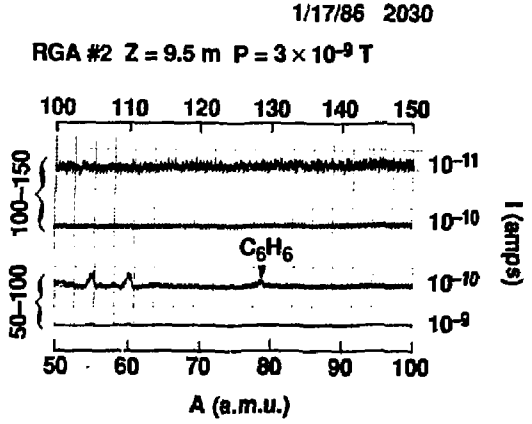

Figure 2. Mass spectrum of the PEP vacuum taken with a Residual Gas Analyzer (RGA). Scans are shown on two sensitivity scales for the mass ranges 50-100 a.m.u. and 100-150 a.m.u.

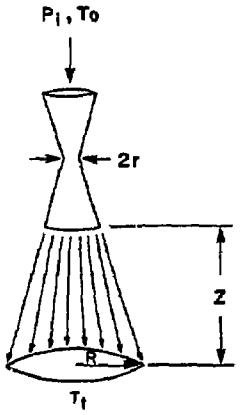

Figure 3. Schematic of a de Laval nozzle and jet. P_i and T_o are the input pressure and temperature in °K of the target gas. Z is the length of the jet and R is its radius at beam intersection. (From ref. 1).

conventional turbo molecular pumps, but with some modifications and a coldtrapped backing system.

Operation of a WGJT in PEP requires areal densities = 10^{-8} - 10^{-10} g/cm² with as low a throughput as is feasible. Low throughputs (<0.01 torr-l/sec) simplify the pumping scheme and reduce the overall cost of the system.

Although an actual WGJT system will incorporate the features of this schematic, it will probably look much different due to detector placement and other factors. Crucial to the design of any such system is the nozzle which produces the gas jet target.

Nozzle Considerations

A gas jet is usually produced by an axially symmetric converging-diverging nozzle, where the gas passes through a converging entry section and a diverging exhaust section (see figure 3). The constriction where these sections meet is the orifice which governs the throughput and density of the jet. This is a de Laval nozzle and its properties are well known[3]. In particular, for the correct conditions, a subsonic flow in the entry section on passing through the orifice will change into a supersonic flow in the exhaust section. Here the flow becomes sonic at the orifice. For this to occur the receiver pressure must be below a certain critical pressure[1], but this is always true for jets flowing into a high vacuum region. On the exhaust end of the nozzle there develop rarefaction waves tending to lower the pressure of the jet to that of the receiver. Somewhere on the outer border of these waves a shock front cuts across and intercepts them (see figure 4). If the receiver pressure remains lower than that of the exhaust, these shock fronts emanate from somewhere within the nozzle. The pressure decreases across the rarefaction wave towards the interior of the jet, consequently there is a pressure gradient acting from the boundary toward the interior which makes the jet boundary curve inward. The adjustment to receiver pressure occurs via this intercepting shock outside the nozzle and is the desirable regime for operation of the target system. Within the

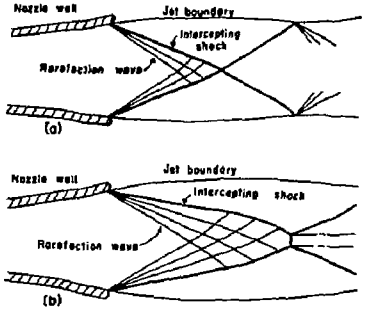

Figure 4. Shock patterns which may result in a diverging jet emitted with a pressure greater than the receiver pressure. (a) Here no shock disc is formed, while (b) illustrates the shock front being cut off by a disc perpendicular to the axis. (From ref. 3).

nozzle the boundary is defined by the diverging section. After the gas exits there is a free boundary due to the axially directed layer of subsonic gas and the low pressure region of the target vessel. As the boundary layer disperses into the target vessel, the jet gradually loses its structure and any pattern fades.

Figure 3 is a schematic of a converging-diverging nozzle and the jet it produces. Mantsch and Turkot[2] approximated the flow through such a nozzle by a one-dimensional gas-dynamics model assuming an ideal gas in steady state, isentropic flow. This model takes the actual shape of the gas jet to be known. Using the quantities defined in fig. 3, the density of gas (where the shock interfaces with the vacuum) is

$$\rho = \left(\frac{r}{R}\right)^2 \left(\frac{P_i M}{C T_0}\right) \left(\frac{2}{\gamma+1}\right)^{(1/(\gamma-1))} \left(\frac{\gamma-1}{\gamma+1}\right)^{1/2}$$

and the throughput of the nozzle is given by

$$Q = \pi r^2 P_i \left(\frac{2}{\gamma+1}\right)^{(1/(\gamma-1))} \left(\frac{2\gamma}{\gamma+1}\right)^{1/2} \left(\frac{C}{M T_0}\right)^{1/2} T_t,$$

where M is the molecular weight of the gas, C the molar gas constant (83 mbar- ℓ-mole^{-1} °K^{-1})and γ is the ratio of the specific heats ($\gamma_{monoatomic}$=5/3 and $\gamma_{diatomic}$=7/5). Here r is the radius of the throat, R the radius of the jet profile, P_i the inlet pressure of the gas, T_0 the inlet temperature, and T_t the temperature of the jet. Stringfellow et al have measured the throughput and density profile of jets produced with 0.004" and 0.006" orifice nozzles, they find agreement with the above equations to be quite good[1]. However, these workers were not able to obtain a narrow jet below inlet pressures of 25 psig, which implies that they may have approached the lower limit of viscous flow for their nozzles (small Reynolds numbers, before the onset of Stokes flow) or that other effects due to the nozzle construction set in. As both of the above equations are quadratic in r and linear in P_i, it is wise to reduce the orifice diameter and, if necessary, accept a smaller increase in the pressure to gain a net reduction in target density and throughput.

Figure 5 shows the He gas throughput as a function of inlet pressure for various orifice sizes <0.004". For a 0.000125" nozzle one can obtain throughputs less than 0.01 torr-ℓ/sec for P_i<40 psi. Here we have assumed that T_t is equal to T_0, and neglected the cooling which occurs in the exhaust region of the nozzle. As the increase of the Mach number from the throat to the exhaust port will lower T_t, the curves

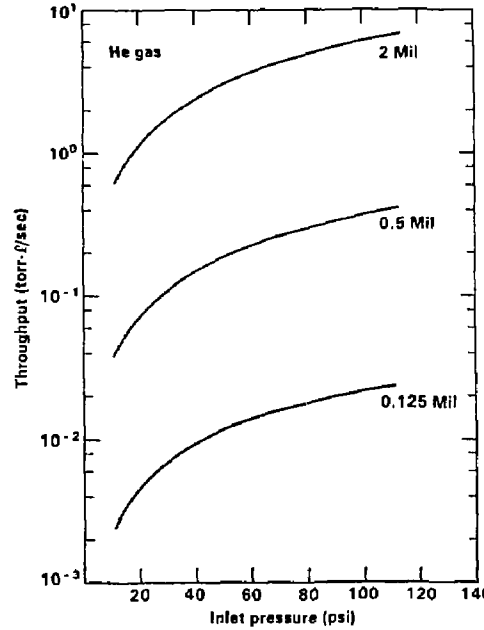

Figure 5. Throughput as a function of inlet pressure for small orifice nozzles.

in figure 5 represent upper limits on the throughput.

As figure 5 is only for He gas, fig. 6 shows how the throughput varies as a function of the mass for a fixed inlet pressure of two atmospheres. Here the throughput is shown to decrease with increasing target mass (A_{tgt}), so a target system which can handle the throughput of the lighter gases, should have enough pumping speed for the heavier gases. It should be noted that the pumping speed does decrease as A_{tgt} increases, which tends to make the design throughput a constant.

One is constrained to use a gas target in particle storage rings by the fact that the beam is recirculated. A thicker solid target will scatter the entire beam in a few fractions of a second, hence gas targets have been explored extensively for storage rings. The density of a target should be such that the beam has a reasonable lifetime in the ring. The solid curve in fig. 7 is the maximal density allowable in PEP for a two hour lifetime of a circulating 14.5 GeV e$^-$ beam. The dashed lines are the calculated target densities for gas jets produced by an inlet pressure of two atmospheres with various small diameter orifice nozzles. Only the 0.000125" nozzle is below the allowable densities for all target masses. One would like to increase the density of the lower mass targets so

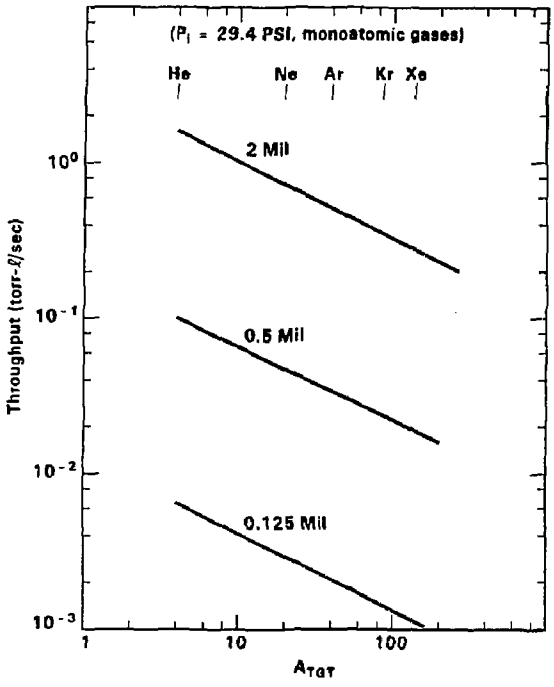

Figure 6. Throughput as a function of target mass for small orifice nozzles.

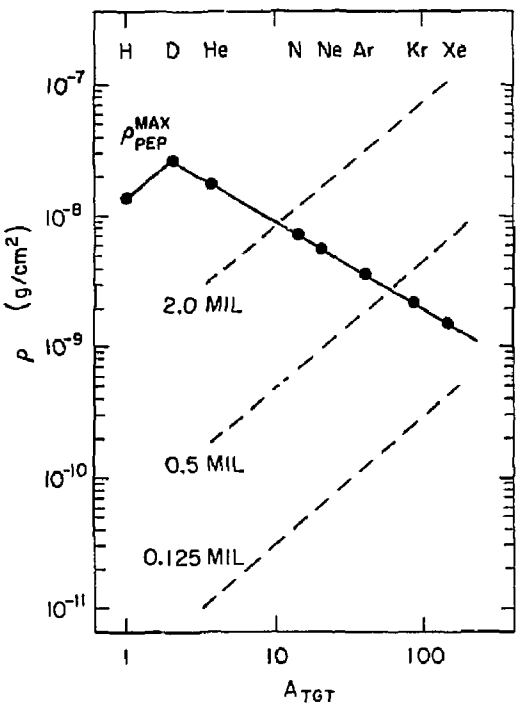

Figure 7. Allowable target densities in PEP as a function of target mass (solid line). The dotted lines are the densities provided by a fixed orifice nozzles under a constant inlet pressure of 29.4 psi.

that a higher luminosity could be obtained. This could be done by increasing the inlet pressure for low A_{tgt}, but for a fixed orifice P_i must be increased about three orders of magnitude to track the allowable density for PEP. If one could switch to a larger orifice nozzle, P_i could be varied within a more reasonable range. It must be kept in mind that by increasing the densities by either of these methods, one also increases the throughput.

Nozzle Design and Fabrication

In order to achieve the desired throughputs and densities a nozzle with an orifice = 0.000125" is required. It is not possible to bore such small diameter holes with conventional techniques, although holes as small as 0.001" can be obtained with special drills. For holes <0.001" one must use electron, ion or laser beam techniques. We are presently pursuing a laser method to obtain orifices of the desired diameter. Figure 8a shows a 0.00015" hole which was obtained with laser techniques. A cross sectional side view of the hole is shown in fig. 8b. This shape is actually ideal for a nozzle throat as it diverges smoothly after the minimum constriction.

There are various ways to construct the rest of the nozzle. One would like to guarantee the shape and surface finish of the final piece through the orifice. As it is not possible to inspect the interior of the nozzle down to the orifice, we are pursuing an electrodeposition method. Here a mandrel is carefully machined to the specifications of the interior of the nozzle. The mandrel is easily inspected and the quality of the mandrel's shape and surface finish guarantees that of the final piece ar long as the etching process is well known. The mandrel is electroplated with a thick layer of material and the exterior is machined to specifications. Finally the mandrel is etched out. As the converging section of the nozzle is typically less than a third the length of the diverging section and is less critical, it can be made by standard high precision machining techniques. Figure 9 shows conical mandrels which will be used to produce nozzle exhaust sections. These mandrels are aluminum and will be electrodeposited with nickel.

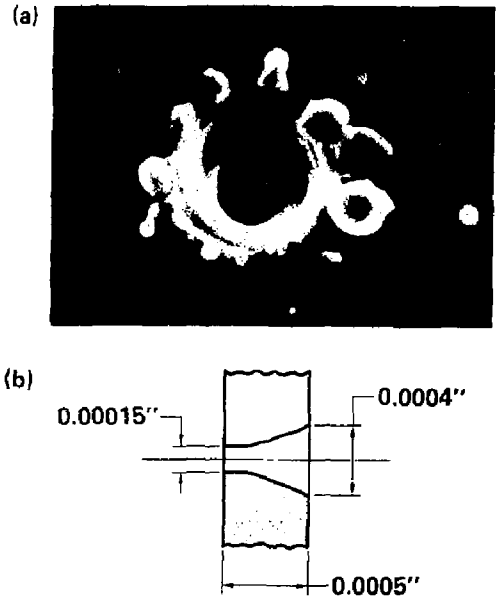

(a) Laser drilled 0.00015" diameter orifice. Detail in (b) shows shape of interior and dimensions.

Figure 8. (a) Photograph taken with a scanning electron microscope of a 0.00015" dia. hole bored with a Neodymium YAG laser. (b) Cross sectional view of hole.

By using the techniques described above, the converging and diverging sections of the nozzle are built separately and joined via a laser weld. The initial nozzles have orifice diameters down to 0.001". This configuration can be decoupled and smaller orifices inserted. An orifice of the type shown in figure 8a can be mated to the converging section via a circular laser weld of 0.004" to 0.005" dia and the sections rejoined. Ideally the orifice should join smoothly with the converging and diverging sections, but for these small constrictions that is not possible. This design will have a discontinuity where the orifice section mates to the converging and diverging sections of the nozzle. The effect that this 'step' will have on the flow through the nozzle should be small considering the dimensions involved to the overall length of the nozzle and exhaust port area (although this is still under study). The step should act to slightly increase the boundary layer (the subsonic flow layer which interacts with the wall of the nozzle exit) and perhaps create stream lines and a stable shock front within the nozzle itself. As the shock pattern repeats itself, the diverging section will act to control the expansion of the gas and reproduce the shock front outside the nozzle.

Finish is 1L down to 0.008" dia pin. Material is electro deposited on mandrel which is etched out.

Figure 9. Conical aluminum mandrels.

The other variables in the nozzle design are the overall length of the diverging section, the area of the exhaust duct and the shape of the diverging section. The length and the area define the geometric opening angle of the nozzle, which must be chosen as to not interfere with the flow from the orifice. The actual shape of the nozzle not only controls the expansion of the jet in a specific manner, but it should match the flow lines from the orifice and allow sufficient room for a boundary layer. Some of the shapes the diverging section can take on are shown in fig. 10. Although for axially symmetric flow a parabolic nozzle should be preferred, the conical and trumpet shapes are those mainly used in gas target systems[1,4,5,6]. In profiling studies of nozzles with the same orifice diameters and diverging section lengths, the trumpet shaped nozzle has been shown to have a slightly narrower density distribution than the conical one[4].

Profiling Studies

At LLNL we are presently constructing nozzles using the methods described above. Our first set of de Laval nozzles will have conical exhaust sections with throat diameters of 0.001" and 0.002". These nozzles will be evaluated by studying the jets they produce and their operation in a WGJT system on loan from Purdue University. The density profile of the gas jet will be measured by deuteron elastic scattering at the LLNL 30" cyclotron. In the present set up the beam

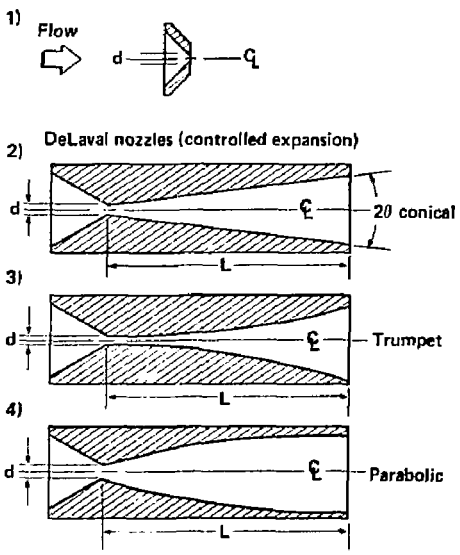

Figure 10. Axial cross sectional view of nozzles showing the various interior shapes.

and detector are kept fixed and the jet is moved perpendicular to the beam. We are interested in the density profile across the jet and how this profile changes as a function of the distance from the nozzle.

The effect of the P_i on the jet will also be studied. In principle one should be able to produce a jet at input pressures lower than that used by Stringfellow et al[1]. In practice other factors may be preventing this.

Using the above profiling studies we can attempt to match the jet to the receiver opening such that the amount of gas flowing into the target vessel is a minimum. Ideally one would like to direct all of the gas jet into the receiver and leave the target chamber vacuum unaffected, but in practice this is impossible as the boundary layer begins to diffuse as soon as the jet exits the nozzle. The Purdue WGJT only directed about 80% of its throughput into the receiver. This was due mainly to the distance between the nozzle and receiver opening and the fact that they pulsed their jet. Pulsing cuts down on the overall throughput, but the jet is not well formed at the beginning and end of the pulse. Consequently, less of the gas is directed into the receiver then.

Our goal is a continuous operation WGJT that meets the above density and throughput criteria and has a nozzle receiver mating which directs >95% of the throughput into the receiver. The above studies will enable us to model and ultimately design a WGJT system for PEP.

The authors would like to thank Prof. Daniel Burshader of Stanford University and Dr. Alfred Buckingham of LLNL for enlightening discussions. We are grateful to Prof. Andrew Hirsch of Purdue University for the loan of their WGJT system and to Norman Dean and the SLAC Vacuum Group for their help and advice.

REFERENCES

1. B. C. Stringfellow et al., Nucl. Inst. and Meth. A251, 242-253 (1986).

2. D. Gross, P. Mantsch and F. Turkot, FNAL Report TM-534-0710.000 (January 1975); P. Mantsch and F. Turkot, FNAL Report TM-582-0710.000 (June 1975); P. Mantsch and F. Turkot, FNAL Report TM-586-0710.000 (June 1975).

3. R. Courant and K.O. Friedrichs, "Supersonic Flow and Shock Waves (New York Interscience, New York, 1948).

4. W. Obert, "Properties of Cluster Beams Formed with Supersonic Nozzles", 11th Symposium on Rarified Gas Dynamics, Cannes, 1978 (CEA, Paris 1978), p 1181.

5. M. Macri, "A Clustered H_2 Beam", in Physics with Low Energy Cooled Antiprotons (Plenum, New York, 1983) p 432.

6. J. F. Brolley, IEEE Trans. Nucl. Sci. 20 (3), 475 (1973).

EXCLUSIVE AND INCLUSIVE REACTIONS WITH REAL AND VIRTUAL PHOTONS TO PROBE MULTI-QUARK EFFECTS

K. E. Lassila

Ames Laboratory-DOE and Physics Department, Iowa State University
Ames, Iowa 50011

and

A. Harindranath* and J. P. Vary*

Physics Department, California Institute of Technology, Pasadena CA 91125

Abstract

We have examined many exclusive and inclusive reactions to conclude it best to project real or virtual photons on partons in a nucleus to probe the mechanism responsible for the EMC effect. Such reactions could be triggered on particles produced beyond usual (nucleon target) kinematical limits from quarks in, e.g., multi-quark color singlet structures. We show that the multi-quark fragmentation function may be measurable in the quark (QCD or real) Compton effect.

Introduction

Deep inelastic scattering experiments on nucleons and nuclei have unambiguously established that the partons of QCD behave differently in nuclear matter than they do in an isolated nucleon.[1] To established what these differences are and the sources of these differences is an objective of future experiments for which predictions can only be made from model calculations at the present time. A specific model which has been remarkably successful in explaining this anomalous behavior is the quark cluster model (QCM).[2] In the QCM the quarks (q) in a nucleus are organized into multi-quark color singlet clusters involving groups of i = 3, 6, 9, etc., quarks. For a 3-q cluster, a critical radius R_c is assumed such that clusters of 6 or more quarks are defined by the number of 3-q clusters joined by the center of mass separations $d \leq 2R_c$. This definition allows one to calculate probabilities for cluster existence and to calculate the momentum fraction x distribution for quarks in a cluster with reasonable facility and reliability.[3] One of the striking and compelling features of the QCM is the prediction of x values beyond those possible for quarks in free nucleons, i.e., $0 \leq x \leq i/3$, for an i quark cluster. Calculations have yielded excellent descriptions of deep inelastic lepton scattering (DIS) data, of the EMC effect, and of the elastic charge form factor of ^{3}He.[2] Predictions have likewise been made for the Drell-Yan process and electroproduction on nuclei.[4,5] The high momentum components of quarks in clusters make unique contributions to these processes, and particularly in pre-threshold production of particles in high energy collisions with nuclear targets.[6]

From an experimental study viewpoint, the injection of nuclei into high energy electron beams or in some other way colliding nuclei with electrons and photons appears to be one of the best possible ways to study and to probe for partons with high momentum components within the nucleus. Though hadron reactions would yield larger statistics on events originating from $x \geq 1$ partons, the background problems would be horrendous. Of all reactions examined, the cleanest seems as if they will be those done with a real or virtual photon probe into the nuclear interior. Further DIS experiments are well worth doing but would, most likely, not shed new light on the source of the EMC effect. In Ref. 3, we pointed out that the QCM makes rather unique predictions for ratios of DIS experiments from different nuclear targets. If one takes the DIS cross section times the energy transfer ν divided by the Mott cross section to get the nuclear structure function νW_2 and takes data for two targets of nucleon number A and B, the ratio $V = [\nu W_2(A)/A]/[\nu W_2(B)/B]$ will show a sequence of unique steps in the $x > 1$ region. The size of these steps is predicted by the calculable probabilities for clusters, as mentioned above. Events in the region $1 < x < 2$ in the QCM will be most sensitive to 6-q clusters while events in the region $2 < x < 3$ will be most sensitive to 9-q clusters, etc. For each increase in x by unity, the ratio V will increase. Preliminary results of an experiment at SLAC apparently confirm this behavior.[7] This is the strongest possible motivation, then, for performing more sophisticated calculations for exclusive reactions to encourage more direct study of high momentum quarks in nuclei.

Multi-Quark Fragmentation

We shall pursue the possibility that (I) the QCD Compton process and (II) Compton scattering from quarks may be the best probes for location high momentum quarks besides providing information on an interesting, previously unmeasured physical quantity, the multi-quark fragmentation function.

In Fig. 1, we depict the collision between a photon (γ) and a nucleon, with the microscopic γ-q collision enlarged within the circle. In the head-on γ-q collision, as drawn in the center of momentum (cm) frame for (I) the QCD Compton process, the final state quark q_f and the gluon G go back-to-back and produce jets as

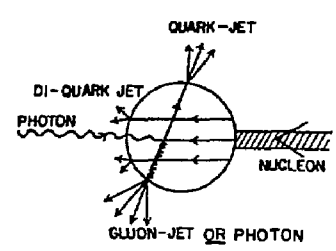

Fig. 1. The photon-nucleon (three quark cluster) collision. The photon-quark interaction is shown in the center of momentum frame with the final state quark, gluon, and diquark jets for the QCD Compton process. For the QED Compton process, the final state gluon is relabelled as the final state photon (with or without originating an EM shower).

labelled by the parent parton.[8] For (II), usual Compton scattering, as also indicated in the magnified region of Fig. 1, the final state gluon and its jet are replaced by a photon (and its resultant electromagnetic shower, if present). The dynamical part of the calculation is done in terms of the three basic QCD or QED diagrams for (I) or (II) which are shown in combined form in Fig. 2. Here, the label $\hat{s}$, $\hat{t}$, and $\hat{u}$ show the familiar s,t, and u Mandelstam channel for the γ-q interaction. With a nucleon, or 3-q cluster,

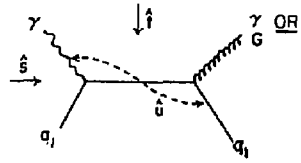

Fig. 2. The QCD Compton effect (I) for photon + quark → gluon + quark and the QED Compton effect (II) for photon + quark → photon + quark with the subprocess kinematical variables as labelled.

target the remainder of the event consists of two quarks, or a di-quark, breaking up in the target fragmentation region. The 'di-quark' (two quarks which need not be in a bound state) is still an interesting object for study because of the basic QCD information it contains. Its behavior when probed with different real and virtual photons will give Q^2 evolution data which is nonexistent to date.

The process in Fig. 1 is used to describe the photon-3 quark cluster interaction when the nucleon target is inside a nucleus. There is also a relatively large probability that the photon will interact with color singlet clusters of 6, 9, etc., quarks. The interaction of the photon with a 6-q cluster is depicted in Fig. 3 for (I) the QCD Compton process and (II) the QED Compton effect. Two main differences from the 3-q

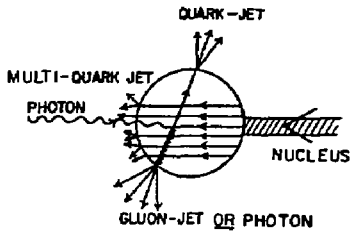

Fig. 3. The photon-nucleus collision with quark cluster structure in the nucleus. The enlarged interaction region sketched inside the circle shows the photon interacting with a six quark cluster. In (I), the QCD Compton effect, the quark and gluon go out back-to-back; in (II), the QED Compton process, the quark and photon go out back-to-back. The remainder of the six-quark cluster after the photon-quark reaction continues in the direction opposite to the incident photon and fragments as the multi-quark jet (in the case drawn, as a five-quark jet).

cluster target, as pictured in Fig. 1, stand out: The kinematic range of x is 0 to 2, and the diquark fragmentation region is replaced by five-quark break-up. This type of experiment , (I) and (II), thus offers the unique possibility of measuring multiquark fragmentation functions. Furthermore, backgrounds can be drastically reduced by selecting events coming from those quarks with large x. These events could have abnormally large total energy in the jets or a hadron in a jet with abnormally large momentum. Since the incident photon disappears completely, the projectile fragment region is very clean. Therefore, the back-to-back quark and gluon jets in (I) or quark jet with a recoil final photon in (II) can provide a trigger to tag photon-quark events with unusually high cm energy, indicating a reaction with a cluster. These events should provide a good sample of multi-quark fragmentation.

It may be possible in the future to obtain data relevant to the Q-squared evolution behavior of this multiquark fragmentation function. The five-quark recoiling object has many ways in which gluons might interact and be emitted so it is possible to have deviation from the most naive type of Altarelli-Parisi behavior.

Calculation

Detailed mathematical expressions will not be given here nor details of the Monte Carlo procedure used for the program, some of the output of which will be discussed. An effort to mainly sketch the physics involved will be done to aid experimenters with thoughts along these lines.

Calculations involving the multi-quark portion of this investigation are highly preliminary, but the results given on photon-3 quark cluster interactions are reliable. These were done by Monte Carlo methods to produce the complete QCD Compton event in the photon-nucleon cm frame. The QED Compton results follow by changing gluon variables into photon variables and removing the fragmentation aspect of the photon, gluon.

The dynamical input is described by the three diagrams in Fig. 2. This input is supplemented by the addition of fragmentation functions appropriate for the quark, gluon, and diquark in the final state. In typical, present day experiments, the photon energy will probably be so low that the jets overlap considerably. This is no real limitation on the use or validity of the calculation unless the cm energy is so low that there is less than about 2.5 GeV available for each jet. The photon-3q cluster calculation at any rate must be done to get a reliable estimate of the background with which photon-6q cluster reactions are to be compared.

To study three color systems in reaction (I) moving separately in the cm frame, we essentially use the Field-Feynman prescription for the fragmentation of each color system. The diquark, for present purposes, is approximated as a color anti-triplet system and treated accordingly. The radiated gluon is treated as a quark-antiquark pair of definite flavor. A cascade chain or string is generated via Monte Carlo between the quark of this pair and the diquark. Also, a string of primary mesons is created between the antiquark of this pair and the original final state quark labelled q_f in Fig. 2. The Q-squared dependent fractional momentum distributions for quarks in the nucleons in the target nucleus are those of Buras and Gaemers.[9] The momentum of partons created along the chain transverse to the fragmentation axis is taken as Gaussian with width 350 MeV/c. An appropriate suppression factor for strange quarks created along the chain is used. Then,

the final distributions in the lab system for the fully generated events are obtained by a Lorentz transformation along the photon direction to the laboratory system.

Probably the dominant effect of the large x parton component in the nucleus will show up in the increased cross section at large transverse momentum (p_t). The ratio of positive to negative pions will increase with p_t also. At high p_t, roughly bigger than 3.5 GeV/c, the processes under discussion should dominate the old fashioned vector meson dominance terms. In Fig. 4, we show plotted the invariant cross section as a function of the transverse momentum of the gluon jet for a number of photon energies. These curves are for real photons, but the general trend stays similar for virtual photons. The gluon is produced with low rapidity

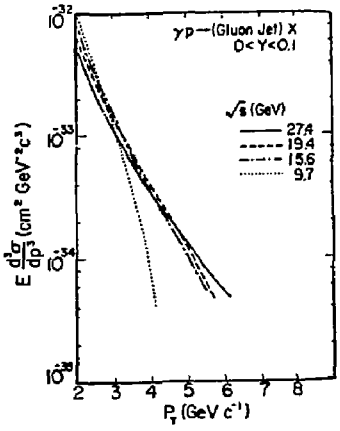

Fig. 4. Calculated invariant gluon jet production cross section as a function of transverse momentum for the QCD Compton effect on a three quark cluster. The curves are labelled by the cm energy 9.7, 15.6, 19.4, and 27.4 GeV in the photon-nucleon cm system and correspond to photon laboratory momentum values of 50, 150, 200, and 400 GeV/c, respectively.

$0 < Y < 0.1$ for each of photon energies as labelled by 9.7, 15.6, 19.4, and 27.4 GeV cm energy. These correspond to photon momentum of values 50, 150, 200, and 400 Gev/c, respectively, incident upon a nucleon. The curves can be reinterpreted in terms of expectations for collision of the photon with a six quark cluster, nine quark cluster, etc. Suppose the incident momentum is 50 GeV/c; the dotted curve will be produced in collisions with quarks that have $0 < x < 1$. The dot-dashed curve then gives the general p_t dependence for events produced from quarks with $2 < x < 3$, possible in 9-q clusters; the dashed curve for events produced from quarks with $3 < x < 4$, possible for quarks in 12-q clusters; and, the solid curve corresponds in trend to the result for $4 < x < 5$. The events produced off quarks in 6-q clusters with $1 < x < 2$ would lie intermediate betweer the dotted and the dot-dash curves. The relative normalization of these curves would fall as photon energy increases, but the general trend with a longer tail in p_t should be a reasonable result to expect from photon reactions with nuclei when clusters are present. The detailed calculations explicitly for these various big clusters should be completed soon because they now appear relevant since the recent SLAC NE3 experiment found events out to x values near 6.[7] For and incident photon beam of 25 GeV/c, the dotted curve gives the relative p_t dependence for reactions off 6-q clusters and the dot-dash curve correspondingly off 12-q clusters.

Discussion and Conclusions

The Quark Cluster Model has achieved considerable success in describing the ways that quarks seem to behave differently in nuclei than they do in free nucleons. Detailed comparisons and calculations now appear needed for significant further progress. To reach this goal we have begun complete Monte Carlo calculations of events expected to be produced by photons interacting with the quark clusters in nuclei. The QCM predicts more large transverse momentum events than could occur from a nucleus made of independent nucleons. We also find that the ratio of positive to negative pions will be larger if the photon is indeed interacting with clusters in a nuclear target. These predictions are a consequence of high momentum quarks in the clusters. This leads to the occurence of events well beyond the kinematic limits for photo reactions with free nucleons. Triggering an experiment on such events leads to the possibility of studying and measuring a new physical quantity, the multi-quark fragmentation function. On a free nucleon, a photon interaction with a quark leaves behind a diquark which is an interesting and legitimate object for QCD study.[10] The object left behind when a photon interacts with a quark in a six quark cluster will be five quarks rather than a diquark. An interesting reason for looking at the 5-q system is to find out to what extent it behaves as a single entity. If it does, then when it fragments as shown in Fig. 3, the QCD activity between quarks is complicated and one can enhance a sample for study by triggering on events from large x quarks. From the counting rules, then, one might expect to find a target fragmentation z distribution that is concentrated near $z = 0$ with a very high power of $(z - 1)$. Such a sample would contrast markedly with those from the diquark fragmenting when a free nucleon interacts.

Acknowledgment

This work was supported by the U.S. Department of Energy Contract No. W-7405-Eng-82, Office of Energy Research (KA-01-01), Division of High Energy and Nuclear Physics.

References

* On leave from Iowa State University, Ames, Iowa.

1. D. Day et al., Phys. Rev. Lett. 43, 1143 (1979); J. J. Aubert et al. (European Muon Collaboration abbreviated EMC) Phys. Lett. 123B, 275 (1983); A. Bodek et al., Phys. Rev. Lett. 50, 143 (1983).

2. H. Pirner and J. P. Vary, Phys. Rev. Lett. 46 1376 (1981); H. J. Pirner, Progress in Particle and Nuclear Physics Ed. A. Faessler (Pergamon, Oxford, 1985) p. 361; J. P. Vary, Nucl. Phys. A418, 195 (1984); C. E. Carlson and T. J. Havens, Phys. Rev. Lett., 51, 261 (1983); J. P. Vary, S. A. Coon and H. J. Pirner, Proceedings of the International Conference on Hadronic Probes and Nuclear Interactions (AIP, New York, 1985) p. 83.

3. J. P. Vary, A. Harindranath and K. E. Lassila, International Conference and Symposium on Unified Concepts of Many-Body Problems, Eds. Kuo and Speth (North-Holland, Amsterdam, 1987).

4. A. Harindranath and J. P. Vary, Phys. Rev. D, in press.

5. A. Harindranath, K. E. Lassila and J. P. Vary, "Electroproduction of hadrons from Nuclei," Phys. Rev. D, submitted for publication.

6. K. E. Lassila and J. P. Vary, "Pre-Threshold Production of the W Intermediate Boson," Proceedings of the International Conference on Neutrino Physics, Ed. E. Fowler (Purdue University, IN, 1978) p. 435.

7. University of Virginia-Cal Tech experiment, SLAC-NE3.

8. A. Ng, R. Orava and K. E. Lassila, Z. Phys. C 14 313 (1982).

9. A. J. Buras and K. J. F. Gaemers, Nucl. Phys. B 132 249 (1978).

10. U. P. Sukhatme, K. E. Lassila and R. Orava, Phys. Rev. D25 2975 (1982) and XII International Symposium on Multiparticle Dynamics, Ed. W. D. Shephard and V. P. Kenney (World Scientific, Singapore, 1982) p. 465.

PION ELECTROPRODUCTION FROM NUCLEI AND QUARK-PION NUCLEAR INTERACTIONS

Paul Stoler
Physics Department, Rensselaer Polytechnic Institute, Troy, NY 12181*

The theory of pion photo and electroproduction is closely related to our understanding of fundamental processes involving elementary particles. At excitations below 2 GeV these reactions have provided much of our information about baryon resonances (Do-78). At higher excitations, in the scaling region they are directly related to the processes by which quarks hadronize. The study of these reactions are interesting in nuclei where one would like to learn about the influence of the nuclear environment on the elementary processes.

In the past electro and photoproduction experiments on nuclei have been strongly limitated by the parameters of existing electron accelerators, the most important of which are low energy and duty factor. The new generation nuclear physics facilities at CEBAF and PEP will complement each other in making possible programs of pion electroproduction not previously possible. CEBAF, with an eventual maximum energy of ~ 6 GeV, will cover the nucleon resonance region, through the transition to x scaling. PEP with a maximum energy of ~ 14 GeV is well suited for experiments in the x scaling and higher Q^2 region.

The main features of both kinematic regions which can be addressed by CEBAF and PEP are seen in Figure 1, which shows inclusive electron scattering data from SLAC.

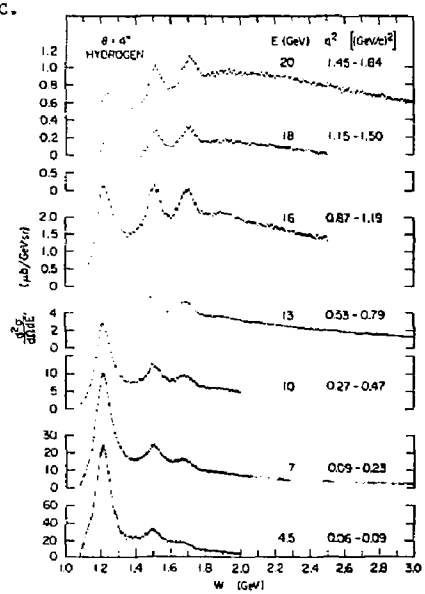

Figure 1 Inelastic electron scattering data obtained at SLAC (St-75) as a function of W for various values of Q.

In the resonance region only the delta is free from the interference of other resonances, whereas above the delta there are about 20 known resonances, all of which overlap strongly with each other. The properties of these resonances can be disentangled only from exclusive experiments involving pion electroproduction. An active program to study the properties of resonances is planned for CEBAF (Bu-87, Mu-87).

Photoproduction data on nuclei is sparse in comparison with that for the nucleon. In the resonance region nuclear programs have concentrated only on real photon experiments in the delta energy region (see e.g. St-87), and even in this energy region there have been no exclusive electroproduction experiments on nuclei. This situation will certainly change in the next several years with the arrival first of MAMI-III at Mainz, and later CW accelerators at Bates and Saclay. However only CEBAF and PEP will have enough energy to cover the entire resonance region.

Because the delta is the lowest energy nucleon excitation, is very strongly excited at low Q^2, and plays an important role in medium energy nuclear phenomena, one of the most actively studied subjects in nuclear physics during the past decade concerns the production and propagation of the delta in nuclei, including the absorption of the delta by the medium (Ge-83). The propagation of the pions in the nucleus is part of the problem of the propagation of the delta through the successive decay and formation of the delta due to the strong pion-nucleus final state interaction (FSI).

In the future there will be a strong interest in studying some of these problems for the higher excitation resonances. However, the problem of overlaping resonances will add to the complications in interpreting the data. A favorable energy to study may be in the region of excitation near W = 1520 MeV, where the S_{11} and D_{13} stand out clearly, and behave differently as a function of Q^2.

For example, it will be interesting to see how the width of this peak is affected by the nuclear medium as it is for the delta. Pion FSI play an important role at all excitation energies. This also will complicate the interpretation of experiments where the motivation is to learn about the initial interaction process in the nuclear medium. Examples at low and high energies respectively are the effects of medium polarization on the spin-isospin operators (Dy-86, Mu-79), and the modifications of the pion distribution involved in t-channel electroproduction in nuclei compared to the case of the nucleon (Hi-79).

Figure 2 shows the mean pion interaction length in a nucleus, obtained by a simple convolution of the elementary pion nucleon interaction with a uniform nucleon density. At the peak of the delta this length is about 0.5 fm, increasing to 2 to 3 fm at higher energies.

A more realistic picture emerges from experiments on pion nucleus scattering in the delta region performed at LAMPF (As-81). Figure 3 shows the various components of the pion-nucleus interaction which they obtained for ^{12}C. In addition to quasi-free scattering, nuclear effects such as coherent scattering and true absorption are important at the delta peak, but decreasc relative to quasi-free scattering at higher energies. It would be interesting to see how these effects evolve with increasing energy.

The effects of pion FSI in photo and electroduction are most important at the peak of the delta. They also depend upon the nuclear radius, being smallest for light nuclei. This is illustrated in Figures 4 and 5, which show the effect of final

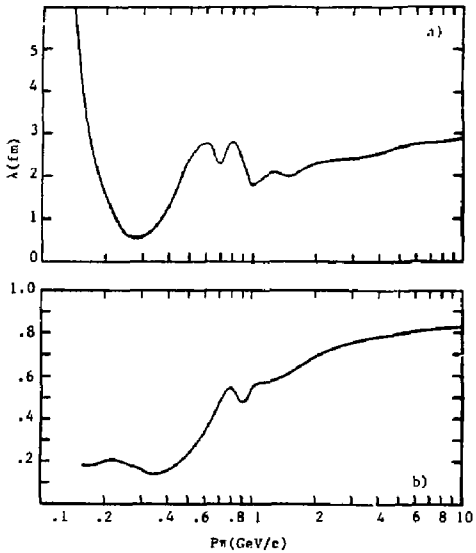

Figure 2 a) Charged pion mean path in nuclei obtained by convoluting the elementary pion nucleon interaction cross section with a uniform nuclear density. b) Fraction of pion nucleon interactions resulting in inelastic events.

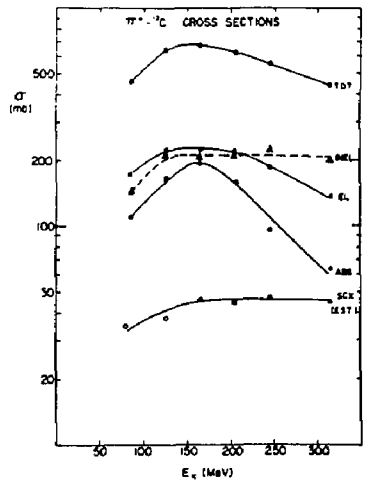

Figure 3 The various components of the pion nucleus interaction for ^{12}C from AS-81.

state interactions on charged pion photoproduction from ^{2}H, and ^{12}C at energies corresponding to the peak of the free nucleon delta. The ^{2}H data, taken at Saclay (Fa-84), show only a small effect of pion FSI. (There is a large enhancement at the highest momenta in the spectrum of Figure 4, due to the large interaction between the p-p pair emerging in a relative s state). The ^{12}C (Ar-82) data indicate a large reduction in the quasi free production peak, which can be explained by the cascading and true absorpiton of the pions interacting strongly with the other nucleons.

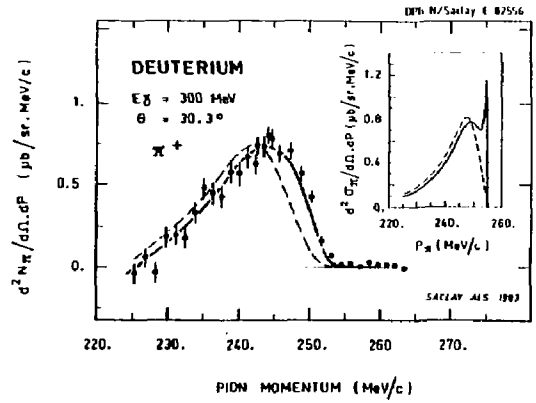

Figure 4 Momentum spectrum of positive pions due to the reaction $^{2}H(\gamma,\pi^{+})X$ for E = 300 MeV, obtained at Saclay (Fa-84). The dashed curve, due to a calculation by J.M. Laget, is a simple quasifree process with no pion FSI. The solid curve includes FSI. The enhancement at the high momentum part of the spectrum is due to scattering of two protons emerging in a relative s-state.

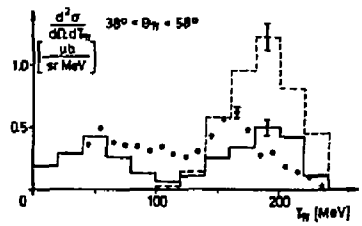

Figure 5 Energy spectrum of positive pions from the reaction $^{12}C(\gamma,\pi^{+})X$ obtained at Bonn (Ar-82). The dashed curve is due to a Monte-Carlo cascade simulation with no pion FSI. The full curve includes pion FSI.

At high energy, above the resonances, the cross section for the reaction $^{1}H(e,e'\pi^{+})n$ is much smaller than that for more inelastic processes. Also, pions may be the secondary result of the decay of primary hadrons. Within the framework of mesons and baryons, the pion electroproduction cross section at forward angles can be reproduced by the t channel Born diagram shown below.

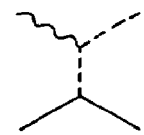

For unpolarized electrons the cross section can be written as follows:

$$\frac{d\sigma}{dE_e d\Omega_e d\Omega_\pi} = \Gamma \left\{ \frac{d\sigma_T}{d\Omega_\pi} + \varepsilon \frac{d\sigma_L}{d\Omega_\pi} + \varepsilon \frac{d\sigma_P}{d\Omega_\pi} \cos 2\phi_\pi \right. \quad (1)$$

$$\left. + \sqrt{2\varepsilon(\varepsilon+1)} \frac{d\sigma_I}{d\Omega_\pi} \cos \phi_\pi \right\}$$

Because of the longitudinal coupling of the photon to the pion, the longitudinal term σ_L dominates at forward angle, and approximately follows the form exp(At), which is characteristic of a high energy diffractive process. In fact at high energies the same function fits diverse high energy diffractive processes such as Compton scattering, vector meson production and proton scattering (Le-78). Figure 6 shows the result of an experiment separating the four cross sections of equation 1. The t dependence of σ_L is typical of t channel dominance.

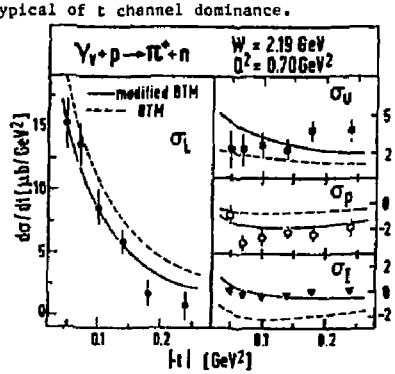

Figure 6 The separation of the various components of equation 1 for kinematics corresponding to Table Ia. The curves are the result of Lagrangian calculations based on Born term diagrams. Data and figure from Br-78.

From the quark-gluon point of view an interesting question is how to describe the evolution of the initial struck quark, which carries the virtual photon's energy and momentum, to the final hardronic state. This subject was discussed in ample detail in this workshop, and the reader is referred to other sources in these proceedings and elsewhere (e.g. Di-87). One of the most successful phenomenological approaches to this problem has been the Lund hadronization code (An-83), which is a Monte-Carlo simulation of the evolution of a string as it successively dissipates the initial quark energy by fragmenting into the final hadrons via the creation of quark-antiquark pairs. Figure 7 shows an example of the kind of results obtained by (Ch-87) using this code for charged pion production. The figure illustrates the distribution of charged pions as a function of the variable Z ($=E_\pi/\nu$), the fraction of the initial quark's energy carried by the pion. Here, ν is the virtual photon energy absorbed by the quark. Only near Z = 1 are the pions mainly primary, i.e., not the result of the decay of stable primary hadrons.

When this reaction is imbedded in a nucleus, in the simplest model the pions are produced on free nucleons having a Fermi momentum distribution. The emerging pion distribution will be strongly modified by strong FSI. For example, Figure 8 shows a Monte-Carlo simulation of the momentum distribution of pions due to the reaction $p(e,e'\pi^+)n$ from a uniform Fermi gas. The pion FSI consists of multiple elastic diffraction scattering, with inelastic events simply absorbed. At energies considered here, only about ten to fifteen percent of the high Z interacting pions are elastically scattered.

Due to the strong FSI, the modification of the primary electroproduction process by the nuclear environment is just one part of, and cannot be separated from the overall problem of electro-

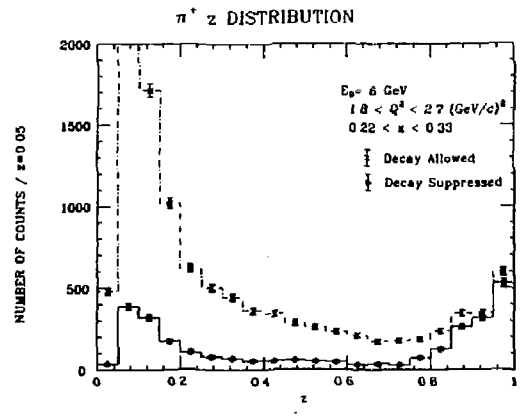

Figure 7 Spectrum of charged pions obtained by C.C. Chang using the Lund hadronization code (An-83). The lower curve is the spectrum of primary pions. The upper curve includes pions resulting from unstable primary hadrons.

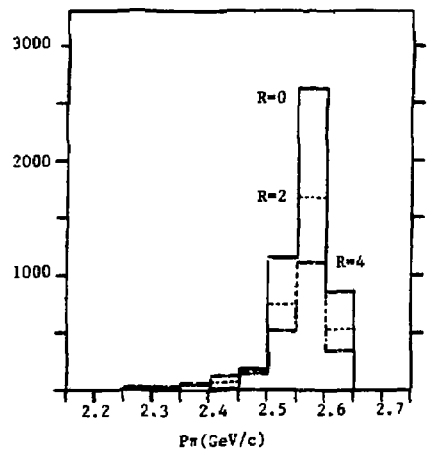

Figure 8 Simulated pion momentum spectra for the reaction $A(e,e'\pi^+)X$ corresponding to the quasifree kinematics and spectrometer acceptances of Table I-a. The three curves denote a)no FSI, b)R_A = 2.0 fm., c)R_A = 4.0 fm.

production from nuclei, in which the uncertainty of the FSI must be taken into account.

During the workshop, the utility of using the pion electroproduction reaction to learn about the pion distribution in nuclei was disucssed, with some

doubts expressed. However, some very interesting points were raised (Br-87) about the effect of the nuclear medium on the quark hadronization process and the pion FSI.

The distance over which the hadronization occurs in a nucleus is thought to be related to the momentum of the hadron through the uncertainty principle and relativistic time dilation effects (see Ar-84, Bj-76, Ni-81, Bi-80). The higher momentum hadrons, corresponding to $Z > 0.5$ are produced furthest from the initial interaction site, according to the approximate relationship $r = E/m^2$, where E is the hadron energy and m it's mass.

When the electroproduction reaction is imbedded in a nucleus an interesting question is how the quark interacts with the nuclear environment prior to hadronization, and the subsequent evolution into the final hadron state, including the FSI of the hadrons themselves. It may be that the cross sections in nuclear matter for the quarks is rather small (Bi-80), so that at high enough energies the high Z hadrons may actually be produced at the edge of the nucleus, and the final hadron spectrum may be relatively independent of nuclear radius.

This effect has also been predicted from QCD considerations (Be-81). From the QCD point of view the high energy probe selects closely spaced valence quark-antiquark pairs. The diffractive interaction of the produced high energy hadron with the nucleus results in a longer interaction length in nuclear matter than would be expected from ordinary multiple scattering of mesons from nucleons in the nucleus. This effect should also result in an altered jet transverse momentum spectrum Z.

The transparency effects are expected to become apparent when $E >> R_A m^2$, where R_A is the nuclear radius. They have been observed in moun scattering in the deep inelastic scaling region, by the EMC group (Ar-84), involving moun energy transfers of several tens of GeV. It was found that the production of hadrons with $Z > 0.5$ is independent of R_A. In electron scattering experiments at SLAC (Os-78) at lower energy transfer the number of hadrons per nucleon produced at high Z was observed to diminish with increasing nuclear radius indicating the presence of FSI. However, due to poor statistics the data were averaged over an energy transfer interval 3 -17 GeV, and a Z interval 0.5 - 1.0. From these two sets of results Ar-84 conclude that $r \sim 0.1$ fm/GeV within a broad statistical range. However, using $E > R_A m^2$ as a cutoff, one expects a hadronization length for pions on the order of several fm. Another possibility is that the quark FSI in nuclear matter is increasing at lower energy transfer.

Pion electroproduction on nuclei may be the best way to study the effects of nuclear matter on quark hadronization because of the $1/m^2$ dependence of the hadronization length. Experiments should be carried out at high Z, where the observed hadrons carry most of the virtual photon energy, and are not likely to be the result of more complicated or secondary processes. Also, at small t the nucleus is minimally disrupted, and the diffractive properties of the pion interaction are preserved.

Example of a Specific Experiment

An experimental measurement of the cross section for pion electroproduction from nuclei at small θ_π and large Z was simulated using the Monte-Carlo code mentioned above (St-87a). Two kinematic settings and kinematic conditions, given in Table I, were chosen to conform to parameters likely to be available at PEP.

Kinematics I

$W = 2.3$ GeV $Q^2 = 0.6$ GeV$^2/c^2$
$E = 6$ GeV $E' = 3.4$ GeV $\theta_e = 10°$ $P_\pi = 2.6$ GeV/c

Kinematics II

$W = 4.0$ GeV $Q^2 = 2.0$ GeV$^2/c^2$
$E = 17$ GeV $E' = 8.0$ GeV $\theta_e = 7°$ $P_\pi = 9.0$ GeV/c

Table I

The pion angular acceptance, $\Delta\theta_\pi = \Delta\phi = \pm 20°$ is in accordance with a possible design discussed at this workshop, and the pion momentum acceptance of 10% selects the highest interval of Z. The solid angle for electrons coincident with the detected pions was taken as 100 mr, with an energy acceptance of 1 GeV. The luminosity was taken as 1×10^{33}.

The resulting pion momentum spectra for the lower energy kinematics, for nuclei with $R_A = 2.0$ fm and $R_A = 4.0$ fm are shown in Figure 8. Also shown is the spectrum with no FSI. Although FSI are important, with considerable depletion in the quasi-free peak, the pions observed in the spectrometer would have undergone very little FSI, since those pions which would have interacted are either scattered elastically or inelastically out of the range of the spectrometer acceptance, or they are absorbed.

To estimate the effect of a finite hadronization length, a simple model was constructed, in which the hadronization length distribution is given by. $N(L) = N(0)\exp(-L/H)$, where $H = E \times H_0$. The hadronization parameter H_0 is in units of fm/GeV. The ratio of the simulated cross section relative to that for the proton as a function of nuclear radius, for two values of the parameter H_0; 0 fm and 1 fm is given in Figure 9.

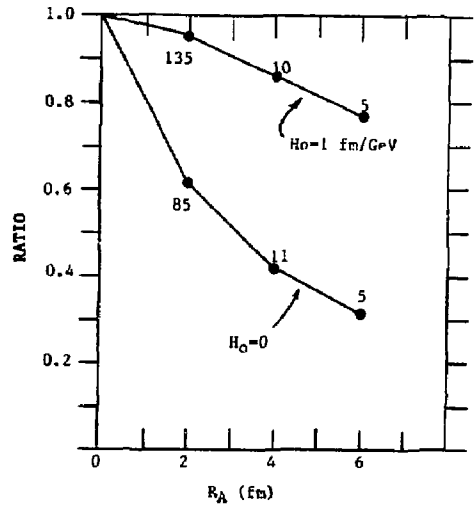

Figure 9 Stimulated ratio of high Z pions detected from nuclei as a function of R_A, for two values of the parameter H_0 defined in the text, corresponding to kinematics-b of Table I. The estimated number of hours of beam on target necessary to obtain the ratio to a statistical accuracy of 2% is shown for various points.

The elementary cross sections of Br-79 was used to estimate counting rates at the lower energy kinematics, and for the higher energy the extrapolation $1/(W^2-M^2)^2$ was used. Counting rates vary from about 30 per hr. to more than 1000 per hr., depending on atomic number and kinematic conditions. The number of hours with beam on target needed to obtain a statistical precision of 2% are also shown in Figure 9.

In conclusion, it seems that pion electroproduction from nuclei may be an excellent way of learning about the quark hadronization in nuclei, and that such experiments may be quite feasible at PEP with the appropriately designed experimental equipment.

*Work supported in part by the National Science Foundation, Grant no. PHY-8601006.

References

(An-83) B. Anderson et al., Physics Reports, 97, 31 (1983).
(As-81) D. Ashery et al., Phys. Rev. C 23, 2173 (1981).
(Ar-82) J. Arends et al., Z. Phys. A, 305, 205 (1982).
(Ar-84) A. Arvidson et al., Nucl. Phys. B246, 381 (1984).
(Be-81) G. Bertsch, S.J. Brodky, A.S. Goldhaber, Phys. Rev. Lett. 47, 297 (1981).
(Bi-80) A. Bialas and E. Bialas, Phys. Rev. D, 675 (1980).
(Bj-76) J.D. Bjorken, SLAC-PUB-1756 (1976).
(Br-79) P. Brauel et al., Z. Phys. C, 101 (1979).
(Br-87) S.J. Brodsky, comments during the present workshop and private communication.
(Bu-87) V. Burkert et al., Report of the CEBAF Steering Committee on Nucleon Resonances, CEBAF PAC Meeting Feb. 1987.
(Ch-87) C.C. Chang, private communication.
(Di-87) F. Dietrich and C. Johnson, Research Program at CEBAF (II), p. 389, SURA 1987.
(Do-78) 'Electromagnetic Interactions of Hadrons, Vol. I', A Donnachie and G. Shaw ed., Plenum, New York (1978).
(Dy-86) S. Dytman and F. Tabakin, Phys. Rev. C 33, 1699 (1986).
(Fa-84) J.L. Faure et al., Nucl. Phys. A424, 383 (1984).
(Ge-83) 'Proceedings of the Symposium of Delta-Nucleus Dynamics' D.F. Geesaman et al., eds. Argonne National Laboratory Report ANL-PHY-83-1,
(Hi-87) R. Hicks, Talk presented at this workshop.
(Le-78) 'Electromagnetic Interactions of Hadrons, Vol. I', A. Donnachie and G. Shaw eds., Plenum, New York (1978), p. 345.
(Mu-79) N. Mukhopadhyay, N. Toki and W. Weise, Phys. Lett., 84B, 35 (1979).
(Mu-87) N. Mukhopadhyay, Proceedings of the CEBAF Summer Workshop - 1986, SURA (1987) p. 451. p. 491.
(Ni-81) N.N. Nikolaev, Sov. Phys. Usp. 24, 531 (1981).
(Os-78) L.S. Osborne et al, Phys. Rev. Lett., 40, 1624 (1978).
(St-75) S. Stein et al., Phys. Rev. D 12, 1884 (1975).
(St-87) P. Stoler, Research Program at CEBAF (II), p. 261, SURA (1987).
(St-87a) P. Stoler, report circulated at PEP collaboration meeting Feb. 1987.

ELECTROMAGNETIC PHYSICS WITH A POLARIZED ^{3}HE INTERNAL TARGET

R.G. Milner
W.K. Kellogg Radiation Laboratory,
California Institute of Technology,
Pasadena,
California 91125

Polarization observables provide one method of extracting small components of wave-functions and reaction mechanisms. Examples are the measurements of the D-state admixture in the ground state wave-functions of ^{3}He [1] and ^{4}He [2] ; measurement of t_{20} in π-deuteron elastic scattering[3]; measurement of t_{20} in e-deuteron elastic scattering[4]; deep inelastic asymmetry measurements on the nucleon[5]; parity measurements in electron-deuteron elastic scattering[6]. A program of measurements of polarization observables on the proton, deuteron, and ^{3}He would provide a very strict constraint for any model of nucleons in the nucleus.

To date, the only targets of polarized nuclei considered in detail for polarization studies in electromagnetic physics have been the proton, the deuteron, and ^{165}Ho [7]. The targets require both cryogenics and intense magnetic fields to produce polarizations of order 50%. These intense magnetic fields are a likely source of systematic error for measurement of small asymmetries in that they will deflect both the incident and scattered beams. Also, the proton and deuteron targets are based on the method of dynamic nuclear polarization and hence the polarized nucleus is part of a large molecule, e.g. butanol, ammonia. This can dilute the measured asymmetry by typically an order of magnitude. Luminosities are limited to $\approx 10^{35}\text{cm}^{-2}\text{s}^{-1}$ by depolarization of the target.

A promising idea, which would eliminate many of the above problems, is to use an internal target of density $2 \times 10^{15}\text{cm}^{-2}$ of polarized atoms in an electron storage ring with a stored current of 100 mA. This would provide a luminosity of $10^{33}\text{cm}^{-2}\text{s}^{-1}$ and would use a new generation of polarized few-nucleon targets based on the method of optical pumping. These targets, if feasible, have the advantages of requiring only few gauss holding fields and do not give rise to any dilution of the measured asymmetry in that the polarized atoms are pure atomic species. At Argonne National Laboratory, Dr. Roy Holt is working on the development of a polarized deuterium target using direct optical pumping of an alkali followed by spin-exchange to a deuterium atom[8]. Such a technique would also work for a hydrogen atom. At Caltech, we have been working on the development of a polarized ^{3}He target. ^{3}He has the advantages that a direct optical pumping technique exists and also that its interaction with containment walls is very weak.

I. Target technology

It is important to note initially that in inclusive electron scattering from a spin-$\frac{1}{2}$ particle, it is necessary to have both beam and target polarized to obtain additional information beyond unpolarized measurements[9]. Thus, it is imperative for measurements on the nucleon or ^{3}He that there be the capability to deliver longitudinally polarized electrons at the interaction region in the ring.

The method used to polarize ^{3}He nuclei is an optical pumping technique developed by Colegrove, Schearer, and Walters[10]. Experimentally one requires a source of 1.083μm light to excite the $^3S_1$–$^3P_0$ transition. Until recently, one was limited to discharge lamps which because of Doppler broadening were not very efficient at pumping. A French group [11] has developed a high power infra-red laser which reliably emits 300mW of 1.083μm light. This laser yields polarizations of 70% in a sample of ^{3}He of density 10^{16}cm^{-3} and a feed rate of 3×10^{16} polarized ^{3}He per second. With higher power lasers now under development [12], feed rates of 10^{17} polarized ^{3}He per second look reasonable. It is important to note that the small holding magnetic field ($\approx$ 5 gauss) required to maintain the polarization of the ^{3}He, allows easy orientation of the target spins. As will be evident below, this is very important for maximizing sensitivity to particular interesting pieces of the cross-section.

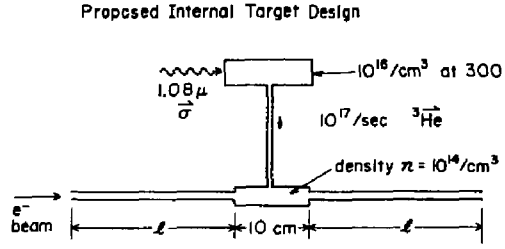

Fig.1 This figure is a schematic diagram of the proposed internal target design.

A schematic diagram of the proposed polarized ^{3}He internal target is shown in Fig. 1. A high power infra-red laser optically pumps a sample of ^{3}He at a density of 10^{16}atoms cm^{-3} contained in a pyrex cell. This cell is connected through a narrow tube to a 10 cm long "bottle". This "bottle" has a long narrow tube of length 30 cm and i.d. 7 mm at each end to act as an impedance for the gas flow. It may be necessary to arrange the end tubes in a clam-shell configuration so that they have a large i.d. when tuning the electron beam and collapse to a 7 mm i.d. when running the internal target. A few gauss holding magnetic field is required for the optical pumping process.

However, a possible problem is depolarization of the target by the intense beam. At Caltech, we have investigated the depolarization mechanism in the region of a few torr and for beams of several microamperes of 3 MeV protons[13]. The depolarization rate due to the charged particle beam is found to be consistent with a model based on the formation of the He_2^+ diatomic molecule. This molecule is formed in 3 body collisions and so the formation rate increases as the square of the pressure. Extrapolation of this model to the low pressures and high currents of an internal target indicate that target depolarization is a problem for luminosities in excess of $10^{34}\text{cm}^{-2}\text{s}^{-1}$.

I shall consider two interesting experiments that become possible with such a target. One is a measurement of the neutron electric form factor up to $Q^2 = 0.8$ (GeV/c)^2 with the proposed 1 GeV pulse stretcher ring at the Bates laboratory at MIT. The second is a measurement of the deep inelastic spin structure function for the neutron at the PEP storage ring at SLAC. In both experiments I shall assume a luminosity

of $10^{33}cm^{-2}s^{-1}$ and a longitudinally polarized electron beam of polarization 0.4.

II. Quasielastic electron scattering

An impulse approximation calculation [14] with a wave function obtained by solving the Faddeev equation with the Reid soft-core potential, has been performed in the quasi-elastic region for longitudinally polarized electrons incident on a polarized ^{3}He target. It is found that near the quasi-elastic peak the contribution of the two protons to the asymmetry is small, and so a polarization measurement can extract the contribution from elastically scattering from the neutron in ^{3}He. As one moves out into the tail of the quasi-elastic peak, the contribution of the two protons to the asymmetry increases. For example, at incident energies of a few hundred MeV and at low energy transfer, the asymmetry is large, and mainly due to D-state admixture in the wave function. It is clear one needs more realistic calculations that include effects like distortion and meson-exchange currents, but it is certain that measurement of the asymmetry in the tail of the quasi-elastic peak would provide a direct test of the small components of the ^{3}He wave function.

Consider the measurement of the asymmetry on the quasi-elastic peak as a measurement of the electric form-factor of the neutron (G_E^n) in ^{3}He. Our present knowledge of G_E^n [15], extracted from e-d elastic measurements, is quite poor. Clearly it is important to improve our knowledge of this fundamental quantity. The existing data has been parametrized as

$$G_E^n(Q^2) = \frac{-\tau\mu_n}{(1+\eta\tau)(1+Q^2/B)^2}$$

where $B = 0.71\ GeV/c^2$, μ_n is the neutron magnetic moment and $\tau = Q^2/4M^2$. Present indications are that $1 \leq \eta \leq 10$; however, the entire range $0 \leq \eta \leq \infty$ cannot really be excluded. We have taken $\eta = 5$.

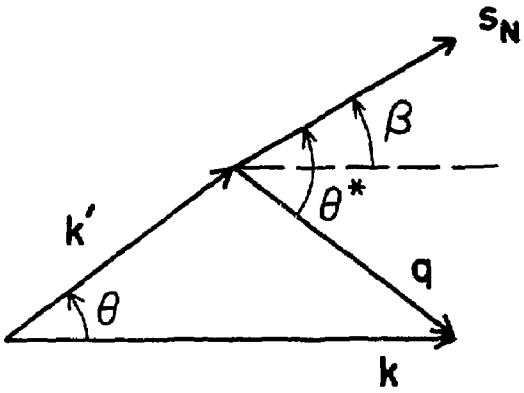

Fig.2 This defines the angles β, which is the angle between the nuclear spin vector, $\mathbf{S}_N$, and the incident electron momentum, k ; and θ^*, which is the angle between $\mathbf{S}_N$ and q, the 3-momentum transfer.

The measurement of G_E^n is basically a measurement of the asymmetry

$$A = \frac{\sigma(\theta,\theta^*,+) - \sigma(\theta,\theta^*,-)}{\sigma(\theta,\theta^*,+) + \sigma(\theta,\theta^*,-)} \qquad (1)$$

where $\sigma(\theta,\theta^*,+)$ is the cross section for quasielastic scattering of longitudinally polarized electrons with positive helicity off a polarized ^{3}He target whose polarization lies in the scattering plane and where the angle θ^* is defined in Fig. 2.

In the case of a free neutron the asymmetry is[6]

$$A_{en} = \frac{2\tau G_M^{n\,2}\cos\theta^* v'_T + 2\sqrt{2\tau(1+\tau)}G_M^n G_E^n \sin\theta^* \cos\phi^* v'_{TL}}{v_L(1+\tau)G_E^{n\,2} + v_T 2\tau G_M^{n\,2}}$$

where

$$v_L = (\frac{Q^2}{q^2})^2$$

$$v_T = \frac{Q^2}{2q^2} + \tan^2\frac{\theta}{2}$$

$$v'_T = \tan\frac{\theta}{2}\sqrt{\tan^2\frac{\theta}{2} + \frac{Q^2}{q^2}}$$

$$v'_{TL} = \frac{Q^2}{q^2}\frac{\tan\frac{\theta}{2}}{\sqrt{2}}$$

Here $q^2 = Q^2 + \nu^2$ in conventional notation .

To a good approximation the asymmetry due to quasielastic scattering off polarized ^{3}He is given by

$$A = \frac{A_{en}\sigma_n}{\sigma_n + 2\sigma_p}$$

where A_{en} is the asymmetry for the free neutron. The validity of this approximation was demonstrated by Blankleider and Woloshyn in their Faddeev calculation. One can see that by varying θ^*, i.e. the angle between the nuclear spin and the direction of momentum transfer, it is possible to pick out the longitudinal and transverse pieces of the quasielastic spin-dependent cross-section. In particular, if $\theta^* = \frac{\pi}{2}$, then the asymmetry is proportional to G_E^n; if $\theta^* = 0$, it is sensitive only to G_M^n. Also note that for a given Q^2, the asymmetry on the quasielastic peak vanishes at a value of θ_0^* given by

$$\frac{G_E^n}{G_M^n} = -\frac{\cot\theta_0^*}{\cos\phi^*}\sqrt{\tau + \tau(1+\tau)\tan^2\frac{\theta}{2}}$$

In what follows we assume that $\phi^* = 0 \pm 8°$, and so $\cos\phi^*$ is always within 1% of unity. This provides an elegant way of determining the ratio of $\frac{G_E^n}{G_M^n}$ as a function of Q^2, independent of the beam and target polarizations. The cross-section is obtained from a y-scaling model of quasielastic scattering from ^{3}He. This model is in excellent agreement with existing unpolarized data.

Running times for a $\pm 20\%$ measurement of G_E^n are then calculated using the following experimental parameters. We assume a luminosity of $L = 10^{33}cm^{-2}s^{-1}$. The polarizations of the ^{3}He target and incident electron beam are taken to be $p_T = 50\%$ and $p_e = 40\%$ respectively. We assume a solid angle of $d\Omega = 25$ msr for the spectrometer and take half the total yield of $(d\sigma/dE')\Delta E'$ over the quasielastic peak. All measured asymmetries are greater than 10^{-3}. The running time in terms of these parameters is then

$$t = \left[\frac{d^2\sigma}{d\Omega dE'}\Delta E'\Delta\Omega L(p_e p_T \Delta A)^2\right]^{-1} \qquad (2)$$

where ΔA is the required statistical uncertainty in the asymmetry.

The resulting running times for a ±20% measurement of G_E^n and a 1 GeV incident electron beam for $Q^2 = 0.2, 0.4, 0.6, 0.8$ $(GeV/c)^2$ are shown in Table 1. It is to be noted that the direction of q varies as a function of energy loss and θ and so θ^* will vary over the spectrometer acceptance. A large acceptance spectrometer would allow simultaneous measurement of the θ^* and ϕ^* dependence of the asymmetry. Measurements with $\theta^* = \frac{\pi}{2}$ provide information on G_M^n.

Table 1. Running times for a ±20% measurement of G_E^n

incident energy = 1 GeV
luminosity = $10^{33}\,cm^{-2}s^{-1}$
$P_T = 0.5$
$P_e = 0.4$
$d\Omega = 25$ msr

$\frac{Q^2}{(GeV/c)^2}$	$\frac{\theta}{deg.}$	A_{meas}	$\frac{T}{days}$
0.2	27.4	1.9×10^{-5}	4.5
0.4	41.8	6.8×10^{-3}	4
0.6	56.0	1.3×10^{-2}	6
0.8	72.4	2.1×10^{-2}	12

III. Deep inelastic electron scattering

In the deep inelastic region, it is possible to measure the spin- dependent structure functions of the neutron in the ^{3}He nucleus[16]. The internal spin structure of the nucleon is important as a constraint on the development and testing of theories and models of nucleon structure. For a comprehensive review of this subject, see reference 5.

One considers the case of deep inelastic scattering of parallel and antiparallel spins for the polarized electron and polarized nucleon. Then one measures the asymmetry of eqn. (1) with $\beta = 0$, where

$$\frac{d^2\sigma}{d\Omega dE'} = \frac{\alpha^2 \cos^2\frac{\theta}{2}}{4E^2 \sin^4\frac{\theta}{2}}\Big[W_2 + 2W_1 \tan^2\frac{\theta}{2}$$

$$\pm 2\tan^2\frac{\theta}{2}(E + E'\cos\theta)MG_1 \pm 8EE'\tan^2\frac{\theta}{2}\sin^2\frac{\theta}{2}G_2\Big].$$

W_1 and W_2 are the well-known unpolarized structure functions and G_1 and G_2 are two new spin-dependent structure functions. From considerations of the total photoabsorbtion cross-sections, it is found convenient to write A as follows:

$$A = D(A_1 + \eta A_2)$$

where

$$A_1 = \frac{M\nu G_1 - Q^2 G_2}{W_1}\ ; A_2 = \frac{\sqrt{Q^2}}{W_1}(MG_1 + \nu G_2)$$

$$D = \frac{1 - E'/E\epsilon}{1 + \epsilon R}\ ; \eta = \frac{\epsilon\sqrt{Q^2}}{E - \epsilon E'}$$

$$\epsilon = \left[1 + 2(1 + \frac{\nu^2}{Q^2})\tan^2\theta/2\right]^{-1}.$$

Here E and E' are respectively the incident and final electron energies; Q^2 is the four-momentum transfer squared; ν is the energy transfer; R is the ratio of longitudinal to transverse cross-sections.

In the Bjorken scaling limit

$$M^2\nu G_1(Q^2,\nu) \to g_1(x)\ ; M\nu^2 G_2(Q^2,\nu) \to g_2(x)$$

i.e., the spin-dependent structure functions scale. A_1 and A_2 can be readily expressed in terms of the quark spin distribution functions. It can be shown that the asymmetry A_2 vanishes for massless quarks. The asymmetry A_1 is the dominant term in deep inelastic scattering with longitudinal polarization.

Bjorken has derived[18] a sum rule for spin-dependent deep inelastic electron-nucleon scattering. This sum rule may be written as

$$\int_0^1 [g_1^p(x) - g_1^n(x)]dx = \frac{1}{6}\left|\frac{g_A}{g_V}\right| = 0.209 \pm 0.001$$

where g_A/g_V is the ratio of axial to vector weak coupling constants in nuclear beta-decay. This may also be written in the scaling limit as

$$\int_0^1 \frac{dx}{x}\left[\frac{A_1^p(x)F_2^p(x)}{1 + R^p} - \frac{A_1^n(x)F_2^n(x)}{1 + R^n}\right] = \frac{1}{3}\left|\frac{g_A}{g_V}\right|.$$

This form is convenient for experimental comparison. The scaling function $F_2(x)$ is the scaling limit of νW_2. Separate sum rules for the neutron and proton have been derived[17] using quark light-cone algebra and under the additional assumption that the net spin polarization of strange sea quarks is zero. These are

$$\int_0^1 g_1^p(x)dx = \int_0^1 \frac{dx}{x}\frac{A_1^p(x)F_2^p(x)}{1 + R^p} \approx \left|\frac{g_A}{g_V}\right|\frac{1.78}{12}$$

and

$$\int_0^1 g_1^n(x)dx = \int_0^1 \frac{dx}{x}\frac{A_1^n(x)F_2^n(x)}{1 + R^n} = \left|\frac{g_A}{g_V}\right|\frac{-0.22}{12}.$$

Recently, Jaffe has reconsidered these sum rules in light of the non-conservation of the U(1) axial current in QCD[19]. He derives inequalities at large Q^2

$$\int_0^1 g_1^p(x)dx = \int_0^1 \frac{dx}{x}\frac{A_1^p(x)F_2^p(x)}{1 + R^p} \le \left|\frac{g_A}{g_V}\right|\frac{1.18}{12}\left(1 - \frac{\alpha_s(Q^2)}{\pi}\right)$$

and

$$\int_0^1 g_1^n(x)dx = \int_0^1 \frac{dx}{x}\frac{A_1^n(x)F_2^n(x)}{1 + R^n} \le \left|\frac{g_A}{g_V}\right|\frac{-0.82}{12}\left(1 - \frac{\alpha_s(Q^2)}{\pi}\right).$$

These are derived assuming the validity of the Bjorken sum-rule and imply that the neutron sum-rule is bigger than the SU(3) picture by of order a factor of four.

Data has been obtained on polarized $e-p$ scattering. In a series of measurements performed at SLAC by the Yale-SLAC collaboration in the late seventies[5], the spin-dependent asymmetry A_1 has been measured for the proton over the deep

inelastic kinematic range $0.1 \leq x \leq 0.7$ and $1 \leq Q^2 \leq 10$ $(GeV/c)^2$ with an accuracy of 15-30%. The experimental data confirm the Bjorken polarization sum rule under the assumption that the neutron contribution is zero. The quality of the SLAC data on the proton is not sufficient to distinguish between the SU(3) and QCD sum-rules for each nucleon isospin state. New, as yet unpublished, data from EMC should have sufficient precision to do this[20]. The SLAC data also verify the scaling behaviour of A_1^p within their limited accuracy. Furthermore, the data successfully distinguished the phenomenological models of the spin structure of the proton and support the prediction of perturbative QCD that $A_1(x) \to 1$ as $x \to 1$ for the nucleon.

The prediction for $A_1^n(x)$ of the unsymmetrical quark model[5], which fits well the measured A_1^p data, is shown in Fig.3. We see that $A_1^n(x) \to 1$ as $x \to 1$ and that it is negative at small x. The bulk of the contribution to the sum-rule comes from the low x region. Thus, a sensitive test of the QCD model of the nucleon would be a measurement of $A_1^n(x)$ at low x as a function of Q^2. Fig.4 shows the statistical precision with which one can measure A_1^n as a function of x and Q^2 with a 15 GeV polarized electron beam incident on a polarized ^{3}He target at PEP. In the above notation I assume $p_t = 0.4$, $p_T = 0.5$, and luminosity $= 10^{33}cm^{-2}s^{-1}$. Also I take $R(x,Q^2) = 0.25$, an assumption which may be modified by the results of experiment E140 at SLAC. The statistical precision obtained in a 16 day run in a bin $\Delta\theta = 10$ mrad and $\Delta\nu = 200$ MeV is shown in the Q^2 vs. ν plane. The cross-section is taken from the Bodek fit

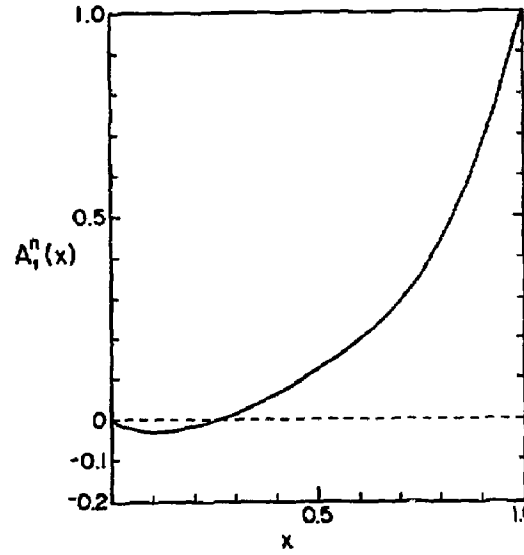

Fig.3 This figure shows the prediction of the unsymmetrical quark model for $A_1^n(x)$. It is taken from reference 5.

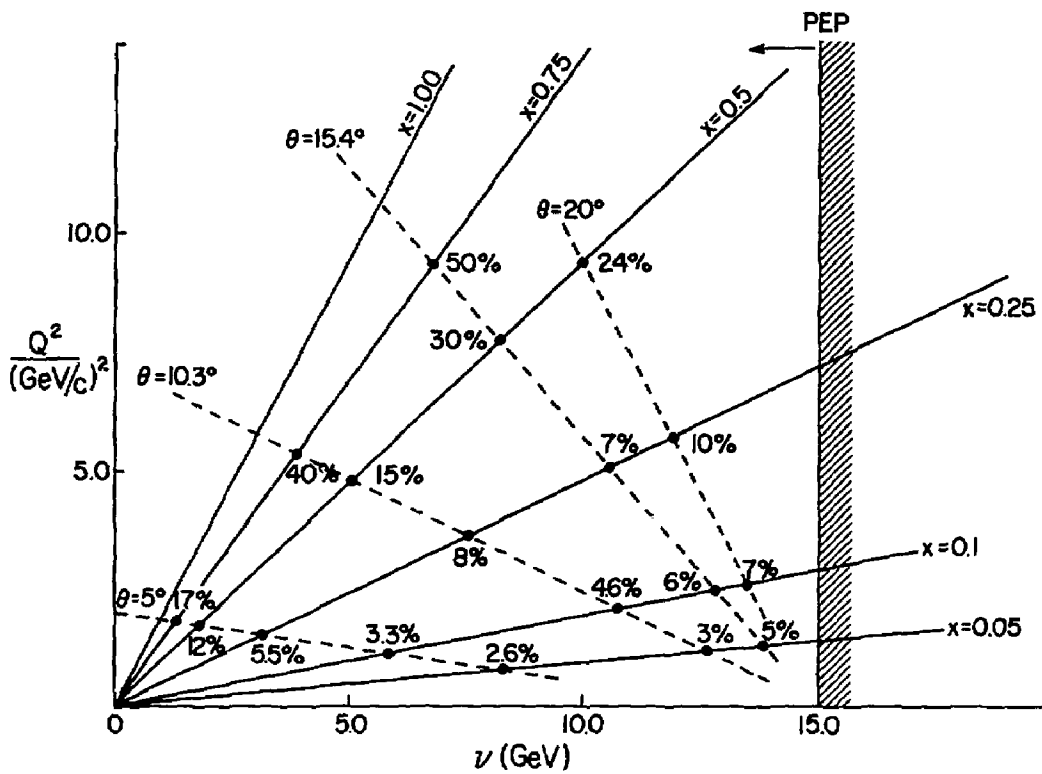

Fig.4 This figure shows the statistical precision with which one can measure $A_1^n(x)$ as a function of x and Q^2 in bins of $\Delta\theta = 10$ mrad and $\Delta\nu = 200$ MeV in a 16 day run with a 100 mA beam of 15 GeV 40% longitudinally polarized electrons incident on a $2 \times 10^{15}cm^{-2}s^{-1}$ 50% polarized ^{3}He target.

to the deep-inelastic region and no Fermi-motion is included. The dilution of the asymmetry because of the two protons in ^{3}He is included.

V. Summary

With a luminosity of $10^{33}\mathrm{cm}^{-2}\mathrm{s}^{-1}$ of polarized electrons incident on a polarized ^{3}He internal target, one could undertake very fundamental measurements on the neutron in ^{3}He. In the quasielastic region, one could measure the charge distribution of the neutron up to Q^2 of 0.8 $(\mathrm{GeV/c})^2$ at the proposed 1 GeV pulse stretcher ring at MIT. In the deep inelastic region, measurements on the spin structure of the neutron become possible at PEP if longitudinally polarized electrons become available at one of the interaction regions . It is strongly urged that a design study be carried out to determine feasibility and cost of implementing this. Using a reasonable choice of running parameters, the running time for an interesting series of measurements in each of these kinematic regions is of the order of 30 days. At Caltech an effort is underway to construct high density, high polarization targets of polarized ^{3}He which would permit these measurements.

This research was supported by the National Science Foundation under Grants PHY85-05682 and PHY-8351737.

References

[1] J.Jourdan *et al.*, Phys. Lett. **162B**, 269 (1985)
[2] B.C.Karp *et al.*, Phys. Rev. Lett. **53**, 1619 (1984)
[3] E.Ungricht *et al.*, Phys. Rev. Lett. **52**, 333 (1984)
[4] M.E.Schulze *et al.*, Phys. Rev. Lett., **52**, 597 (1984)
[5] V.W.Hughes and Julius Kuti, Ann. Rev. Nucl. Sc. **33**, 611 (1983)
[6] C.Y.Prescott *et al.*, Phys. Lett. **77B**, 347 (1978)
[7] F.J.Uhrhane, J.S.McCarthy, and M.R.Yearian, Phys. Rev. Lett. **26**, 578 (1971)
[8] R.J.Holt, Proceedings of Workshop on Polarized Targets in Storage Rings, Argonne National Laboratory (ANL-84-50), p.103 (May 1984)
[9] T.W.Donnelly and A.S.Raskin, Annals of Physics **169**, 247 (1986)
[10] F.D.Colegrove, L.D.Schearer, and G.K.Walters, Phys. Rev. **132**, 2561 (1963)
[11] M.Leduc *et al.*, "A new infra-red tunable laser (LNA) for optical pumping of helium", contribution to CLEO, June 1986, San Francisco
[12] L.D.Schearer *et al.*, IEEE **QE-22**, No. 5, 713 (1986)
[13] R.G.Milner, R.D.McKeown, and C.E.Woodward, Nucl. Instr. and Meth. *in press*
[14] B.Blankleider and R.M.Woloshyn, Phys. Rev. **C29**, 538 (1984)
[15] S.Galster *et al.*, Nucl. Phys. **B32**, 221 (1971)
[16] R.G.Milner, Proceedings of Workshop on Polarized ^{3}He Beams and Targets, Princeton NJ, October 1984 p. 186 (AIP Conference Proceedings No. 131)
[17] J.D.Bjorken, Phys. Rev. **148**, 1467 (1966)
[18] J.Ellis and R.Jaffe, Phys. Rev. **D9**, 1444 (1974)
[19] R.L.Jaffe, MIT CTP preprint No. 1445, submitted to Phys. Rev. Lett. Jan. 1987
[20] Private communication, T.Sloan

(e,e'N) REACTIONS WITH POLARIZED BEAMS AND POLARIZED TARGETS

S.Boffi, C.Giusti and F.D.Pacati

Dipartimento di Fisica Nucleare e Teorica dell'Universita', Pavia,
Istituto Nazionale di Fisica Nucleare, Sezione di Pavia, Italy

Abstract: The quasi-free nucleon knockout by the electron is studied in the general case of both polarized beams and polarized targets. The general formalism provides nine structure functions, four of which appear only when the target nucleus is polarized. Results obtained in a nonrelativistic DWIA framework on ^{7}Li and ^{39}K for cross sections, asymmetries and electron polarization ratios are presented. The particular case is also considered of a nucleon ejected along the direction of the momentum transfer from a target with spin oriented in the same direction where only three structure functions survive and can be simply separated.

In the one-photon exchange approximation and neglecting the electron mass and the nuclear recoil factor, the six-fold differential coincidence cross section for quasi-free nucleon knockout from a polarized target nucleus by an incident polarized electron may be written as follows [1]

$$\frac{d\sigma^h}{d\vec{p}'_o\, d\vec{p}'} = \alpha^2 \frac{1}{q_\nu^2\, p_o\, p'_o\, (\epsilon-1)} (\Sigma + h\,\Delta) \quad , \qquad (1)$$

where $\alpha = e^2/4\pi = 1/137$ is the fine structure constant and the ultrarelativistic electron with initial helicity h and momentum $\vec{p}_o$ is scattered to a final momentum $\vec{p}'_o$ while a nucleon is knocked out with final momentum $\vec{p}'$. Then, the four-momentum transfer is $q_\nu^2 = \omega^2 - q^2$, with $\omega = p_o - p'_o$ and $\vec{q} = \vec{p}_o - \vec{p}'_o$. In eq. (1)

$$\Sigma = 2\,\epsilon_L\, F_{oo} + F_{11} + [\epsilon_L\,(1+\epsilon)]^{1/2}\, F_{o1} - \epsilon\, F_{1-1} \quad , \qquad (2)$$

$$\Delta = (1-\epsilon^2)^{1/2}\, F'_{11} + [\epsilon_L\,(1-\epsilon)]^{1/2}\, F'_{o1} \qquad (3)$$

The quantity

$$\epsilon = [1 - 2\,(q^2/q_\nu^2)\,\tan^2\theta/2]^{-1} \qquad (4)$$

measures the transverse linear polarization of the virtual photon exchanged by the electron scattered at an angle θ, and

$$\epsilon_L = (-q_\nu^2/q^2)\,\epsilon \quad . \qquad (5)$$

In the laboratory frame, where the nucleon is ejected at an angle $\gamma \neq 0$ with respect to the momentum transfer $\vec{q}$ and the initial nucleus is assumed to be at rest and with a polarization direction specified by the zenithal angle θ^* and the azimuthal angle ϕ^*, the six structure functions in eqs. (2) and (3) depend on the seven variables (ω, q, p', γ, α, θ^*, ϕ^*), where α is the angle between the hadron and the electron planes. One has

$$\begin{aligned}
F_{oo} &= f_{oo} \quad , \\
F_{11} &= f_{11} \quad , \\
F_{o1} &= f_{o1} \cos\alpha + \bar{f}_{o1} \sin\alpha \quad , \\
F_{1-1} &= f_{1-1} \cos 2\alpha + \bar{f}_{1-1} \sin 2\alpha \quad , \\
F'_{11} &= f'_{11} \quad , \\
F'_{o1} &= f'_{o1} \sin\alpha + \bar{f}'_{o1} \cos\alpha \quad .
\end{aligned} \qquad (6)$$

where

$$\begin{aligned}
f_{oo} &= |J_o|^2 \quad , \\
f_{11} &= |J_1|^2 + |J_{-1}|^2 \quad , \\
f_{o1} &= 2\,\mathrm{Re}\,(J_1\, J_o^* - J_o\, J_{-1}^*) \quad , \\
f_{1-1} &= 2\,\mathrm{Re}\,(J_1\, J_{-1}^*) \quad , \\
f'_{11} &= |J_1|^2 - |J_{-1}|^2 \quad , \\
f'_{o1} &= -2\,\mathrm{Im}\,(J_1\, J_o^* + J_o\, J_{-1}^*) \quad , \\
\bar{f}_{o1} &= -2\,\mathrm{Im}\,(J_1\, J_o^* - J_o\, J_{-1}^*) \quad , \\
\bar{f}_{1-1} &= -2\,\mathrm{Im}\,(J_1\, J_{-1}^*) \quad , \\
\bar{f}'_{o1} &= 2\,\mathrm{Re}\,(J_1\, J_o^* + J_o\, J_{-1}^*) \quad .
\end{aligned} \qquad (7)$$

In eq. (7) an average over initial states and a sum over final undetected states of products of matrix elements J_μ are understood, where

$$J_\mu = \int d\vec{r}\, e^{i\vec{q}\vec{r}} \langle \Psi_f |\; j_\mu(\vec{r})\; | \Psi_i \rangle \qquad (8)$$

are matrix elements of the nuclear charge-current operator j_μ taken between the initial ($|\Psi_i\rangle$) and final ($|\Psi_f\rangle$) nuclear states.

For an unpolarized target nucleus the barred structure functions $\bar{f}_{o1}$, $\bar{f}_{1-1}$ and $\bar{f}'_{o1}$ vanish identically. In addition, $|J_1|^2 = |J_{-1}|^2$, i.e. $f'_{11} = 0$. Therefore, in this case one recovers the expression of the cross section in terms of five structure functions already studied in ref. 2 with incident polarized

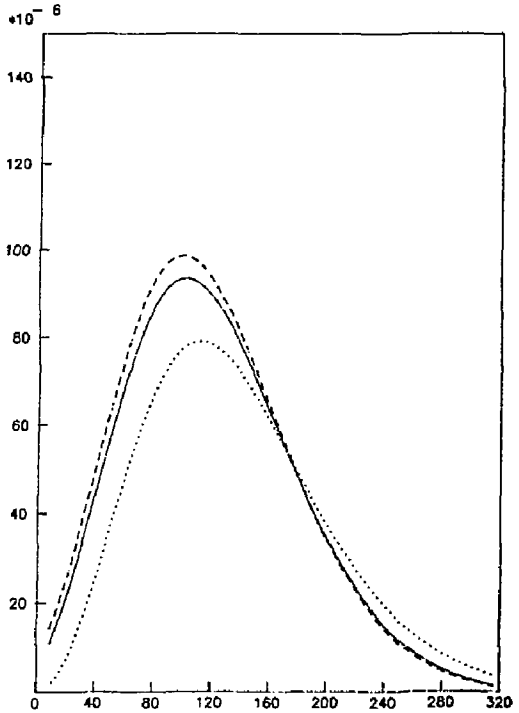

Fig. 1. Cross section (fm^3 sr^{-2}) vs. recoil momentum (MeV/c) for $p_{3/2}$ proton knockout from N-polarized ^{7}Li by unpolarized electrons of 700 MeV energy. The final proton energy is 144 MeV and q=2.6 fm^{-1}. Bound state from ref. 7, optical model from ref. 5 (solid line) and from ref. 6 (dashed line); dotted line for PWIA.

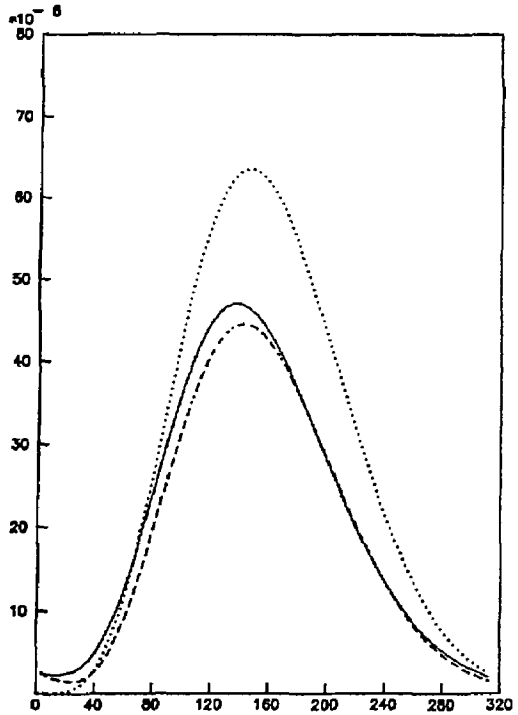

Fig. 2. Cross section (fm^3 sr^{-2}) vs. recoil momentum (MeV/c) for $d_{3/2}$ proton knockout from N-polarized ^{39}K by unpolarized electron of 500 MeV energy. The final proton energy is 100 MeV and q=2.2 fm^{-1}. Bound state from ref. 7 and optical model from ref. 8 for the solid line, bound and scattering states with the hamiltonian of ref. 9 for the dashed line; PWIA for the dotted line.

electrons. The same situation occurs when the target polarization is perpendicular to the hadron plane, because in this case $J_{-\lambda}\, J^{z}_{\lambda'} = (-)^{\lambda+\lambda'}\, J_{\lambda}\, J^{z}_{\lambda'}$.

The primed structure functions f'_{11}, f'_{01} and $\overline{f}'_{01}$ contribute only in the presence of polarized electrons. If in addition to an unpolarized electron beam also an unpolarized target is used, the familiar form in terms of only four structure functions, $f_{\lambda\lambda'}$, is obtained.[3]

When $y = 0$, the decomposition (6) in terms of nine structure functions is not possible because the angle α is no more defined. However, Σ and Δ can still be expressed in the form of eqs. (2) and (3) in terms of six F-responses. This means that in the socalled parallel kinematics ($y = 0$) six responses enter in the cross section contrary to what happens in the case with unpolarized targets where only two structure functions survive.

In the particular case of parallel kinematics and orientation of the target polarization along $\vec{q}$, i.e. of what can be called a superparallel kinematics, for symmetry reasons only F_{00}, F_{11} and F'_{11} survive in general, whereas the interference responses F_{01}, F_{1-1} and F'_{01} vanish.

The relevant quantity containing all the necessary ingredients for describing the knockout process is the matrix element in eq. (8).

The results presented in this paper are obtained with the nonrelativistic charge-current operator along the lines of previous work.[2,3]

The general formalism is here applied to the case of proton knockout by an electron of positive helicity from a polarized target. For each target polarization the nine structure functions depend on ω, q, p' and γ. Specific cases can be studied with 100% target

polarization ($m = j$) oriented longitudinally (L), normally (N) and sideways (S) with respect to the incident electron direction.[4] For symmetry reasons the N-polarization reduces the number of nonvanishing structure functions to five: only f_{00}, f_{11}, f_{01}, f_{1-1} and f'_{01} survive. Without final state interactions $f'_{01} = \overline{f}_{01} = \overline{f}_{1-1} = 0$ for L- and S-polarization of the target.

In ref. 1 figures are given for the different structure functions in ^{7}Li and ^{39}K under standard kinematical conditions. Their separation requires out-of-plane experiments with a high degree of precision.

As a first step one can measure cross sections which do not necessarily require out-of-plane kinematics nor such a high precision as do structure functions. In fact a measurement of the cross section with coplanar kinematics either with or without polarized incident electrons would be extremely useful to give access to new information. The numerical calculations indicate that peak values are obtained of the same order of magnitude as the ones with unpolarized targets. As an example to set the scale and to show the sensitivity to final state interactions in figs. 1 and 2 the cross section obtained with unpolarized electrons for N-polarized ^{7}Li and ^{39}K is reported.

With coplanar kinematics one can also measure asymmetries, i.e.

$$(\Sigma^N - \Sigma^S)/\Sigma_0 \ , \ (\Sigma^L - \Sigma^N)/\Sigma_0 \ , \ (\Sigma^S - \Sigma^L)/\Sigma_0 \ , \qquad (9)$$

where Σ_0 is the cross section with unpolarized target and unpolarized electron. These asymmetries are determined by the behaviour of the usual four structure functions f_{00}, f_{11}, f_{01} and f_{1-1} with different orientations of the target polarization. Only two of them are independent. In fig. 3 the N-S and the L-N asymmetries are given for $p_{3/2}$ hole in ^{39}K as a function of the recoil momentum p_R under the same kinematic conditions of fig. 2. These asymmetries are not vanishing as an indication that different results are expected for different orientation of the target polarization. Moreover, the size of the asymmetry is measurable and is increased by final state interactions.

Another measurable quantity with coplanar kinematics is the electron polarization ratio Δ/Σ with L- and S-polarization of the target. For N-polarization, $\Delta/\Sigma = 0$ as already noticed in ref. 4. In fig. 4 $(\Delta/\Sigma)_L$ is plotted for the $p_{3/2}$ hole in ^{7}Li. This result shows that the electron polarization ratio is large and can be measured, e.g., on top of the $p_{3/2}$ momentum distribution (p_R = 100 MeV/c) with a weak dependence on final state distortion.

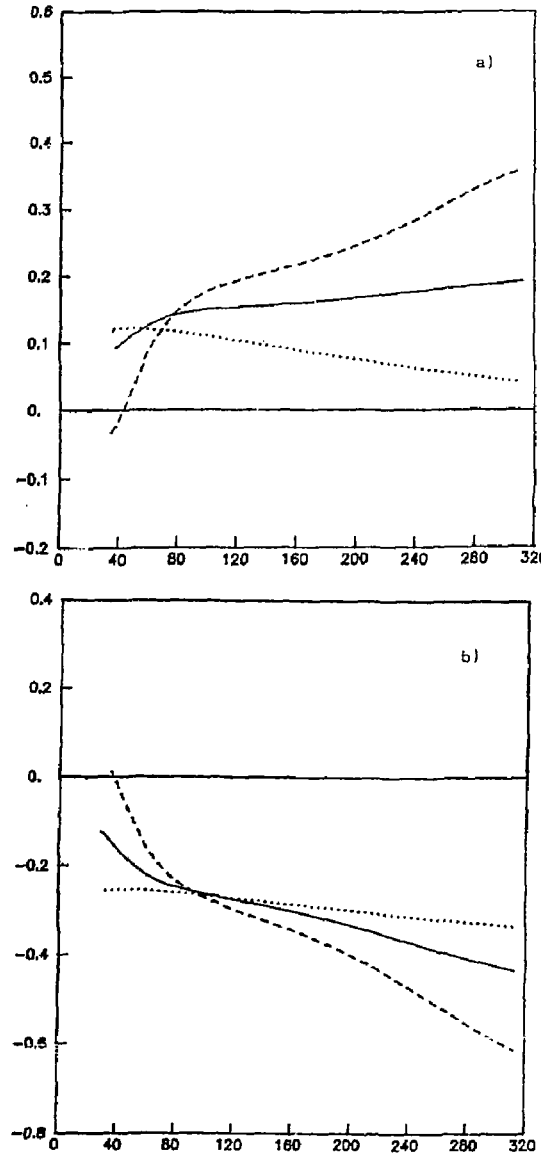

Fig. 3. Asymmetries a) $(\Sigma^N-\Sigma^S)/\Sigma_0$ and b) $(\Sigma^L-\Sigma^N)/\Sigma_0$ vs. recoil momentum (MeV/c) for $d_{3/2}$ hole in ^{39}K under the same conditions as in fig. 2.

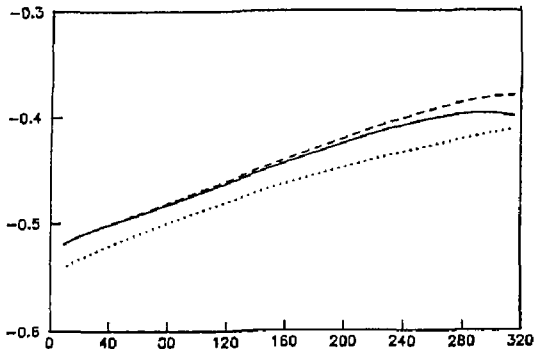

Fig. 4. The electron polarization ratio Δ/Σ vs. recoil momentum (MeV/c) with L-polarization of the ^{7}Li target nucleus for $p_{3/2}$ hole under the same conditions as in fig. 1.

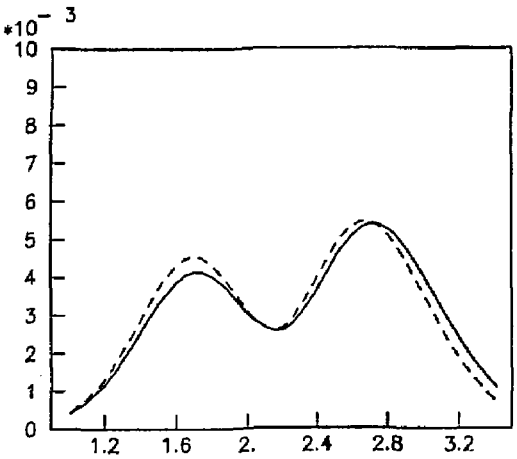

Fig. 5. The response F_{11} (fm^3) vs. momentum transfer q (fm^{-1}) for $d_{3/2}$ hole in ^{39}K polarized along $\vec{q}$ under parallel kinematic conditions. The other conditions are as in fig. 2.

The superparallel kinematics a priori involving only three nuclear responses is in principle interesting in order to achieve their separation. In fact, F'_{11} is simply determined by flipping the electron helicity. Then a Rosenbluth separation determines F_{oo} and F_{11}. In addition, in the present model based on the impulse approximation, F_{oo} vanishes for a target spin $j \geq 3/2$ ($m = j$) and $F_{11} = \pm F'_{11}$.

In fig. 5 F_{11} is plotted for the $d_{3/2}$ hole in ^{39}K. It appears that the maximum corresponding to $p'<q$ is higher by $\sim$ 20% than the one corresponding to $p'>q$. This large asymmetry as well as the whole response itself is entirely due to the final state interaction because in PWIA $F_{11} = 0$.

References

1. S.Boffi, C.Giusti and F.D.Pacati, to be published; S.Boffi, C.Giusti, F.D.Pacati and M.Radici, Proc. of CEBAF 1986 Summer Workshop, eds. F.Gross and J. Mougey (to be published).
2. S.Boffi, C.Giusti and F.D.Pacati, Nucl. Phys. A435, 697 (1985).
3. S.Boffi, C.Giusti and F.D.Pacati, Nucl. Phys. A386, 599 (1982).
4. T.W.Donnelly, in Perspectives in Nuclear Physics at Intermediate Energies, ed. S.Boffi, C.Ciofi degli Atti and M.M.Giannini (World Scientific, Singapore, 1984) p. 244; T.W.Donnelly and A.S.Raskin, Ann. of Phys. 169, 247 (1986).
5. A.K.Kerman, H.McManus and R.M.Thaler, Ann. of Phys. 8, 551 (1959).
6. O.N.Jarvis, C.Whitehead and M.Shal, Nucl. Phys. A184, 615 (1972).
7. L.R.B.Elton and A.Swift, Nucl. Phys. A94, 52 (1967).
8. P.Schwandt, H.O.Meyer, W.W.Jacobs, A.D.Bacher, S.E. Vigdor, M.D.Kaitchuck and T.R.Donoghue, Phys. Rev. C 26, 55 (1982).
9. M.M.Giannini and G.Ricco, Ann. of Phys. 102, 458 (1976).

SPIN DEGREES OF FREEDOM IN ELECTRON NUCLEON SCATTERING IN THE RESONANCE REGION

Volker D. Burkert
CEBAF
12070 Jefferson Avenue
Newport News, VA 23606, USA

Abstract

Some aspects of using polarized electrons and/or polarized targets in electron-nucleon scattering experiments are discussed. Polarization measurements can be used to extend the knowledge of nucleon formfactor measurements to higher Q^2 and are indispensable for a model-independent extraction of the helicity amplitudes of exclusive meson production. Measurements of polarization asymmetries may also help in revealing the excitation of weaker resonances.

I. Introduction

The study of the electromagnetic couplings of the ground state nucleon and its excited states should be an essential part of any research program to investigate electroweak interactions with nuclei. The ultimate goal in studying the 'elementary' process is to obtain information on the $\gamma^* NN^*$ vertex. Detailed knowledge of this transition provides the data base which is necessary for the interpretation of electron nucleus scattering at high momentum and high energy transfer. The understanding of nucleon-nucleon correlation, e.g., will depend essentially upon our understanding of the role played by nucleon resonances in nuclei. Studying nucleon resonance transition is, on the other hand, very important in itself. The knowledge of the Q^2 dependence of the $\gamma^* NN^*$ transition appears crucial for the development of more realistic, QCD based, interquark potentials for light quarks, and finally for the definite implementation of QCD to hadrons at intermediate distances where non perturbative effects have to be taken into account.

II. The Electric Formfactor of the Neutron and the Proton

The hadronic current in elastic electron nucleon scattering is specified by the electric and magnetic formfactors $G_E(Q^2)$ and $G_M(Q^2)$. The knowledge of these quantities up to the highest possible Q^2 is not only of fundamental importance for testing microscopic models of the nucleon and its electromagnetic coupling, but has strong impact on the interpretation of electron nucleus scattering in general. Our present knowledge is practically limited to the magnetic formfactors $|G_{M_p}|$ and $|G_{M_n}|$ which have been measured for Q^2 up to 30 and 20 GeV^2, respectively. G_{E_p} has been measured up to 3GeV^2 with uncertainties between 10% and 30% at Q^2>1GeV^2. Little is known about the electric formfactor of the neutron. In fact, our only solid knowledge comes from scattering of thermal neutrons off electrons from atoms, showing that $dG_{E_n}/dQ^2 > 0$. at $Q^2 \to 0$. There is some information on G_{E_n} at $Q^2 < 1.$GeV^2, extracted from elastic eD scattering[1]. These results, however, are necessarily model dependent in that they depend on the specific deuteron wavefunction assumed in the analysis. Attempts to measure $|G_{E_n}|$ from quasielastic eD scattering have not yielded satisfactory results[2]. A model independent measurement of G_{E_n} is urgently needed. Studying quark effects in nuclei at large Q^2 will bear heavily on the knowledge of the nucleon formfactors, since new effects will reveal themselves as deviations from the "conventional" picture of the nucleus.

Several ways of measuring this fundamental quantity have been proposed. One way is to measure G_{E_n} in scattering of polarized electrons from unpolarized neutrons and to study the neutron recoil polarization in a second scattering experiment[3]. An alternative method is to use quasielastic scattering of polarized electrons from vector polarized deuterium[4]. I will briefly discuss this latter method which may be of interest not only for use in storage rings but for external beam experiments at Bates and CEBAF as well.

For an orientation of the neutron spin in the electron scattering plane perpendicular to the direction of γ^*, the elastic electron neutron cross section is given by:

$$\frac{d\sigma}{d\Omega} = \left(\frac{d\sigma}{d\Omega}\right)_0 \left[1 + P_e P_n A^n(Q^2)\right]$$

(P_e=electron polarization, P_n=effective neutron polarization, $(d\sigma/d\Omega)_0$=unpolarized cross section).
The asymmetry is given by:

$$A^n(Q^2) = \frac{2\, G_{E_n}\, G_{M_n} \sqrt{\tau(1+\tau)}\, \operatorname{tg}\frac{\theta_e}{2}}{G_{E_n}^2 + \tau G_{M_n}^2 + 2\tau^2(1+\tau) G_{M_n}^2 \operatorname{tg}^2\frac{\theta_e}{2}} \; ; \; \tau = \frac{Q^2}{4M_n^2}$$

The appearance of the interference term allows the measurement of G_{E_n} if G_{M_n} is known, without Rosenbluth separation. This is advantageous in determining the electric formfactor because G_{E_n} is expected to be small[5], and its contribution to the elastic cross section at large Q^2 is negligible. Fig. 1 shows the expected asymmetry for $G_{E_n}=0$ and $G_{E_n}=-\tau G_{M_n}/\mu$, both of which are consistent with present data at not too small Q^2.

1. An Experiment to Measure G_{E_n} in $\vec{d}(\vec{e},e')p$

Using a polarized ND_3 solid state target with an approximately 20mW cooling power at a temperature of ≈270mK, luminosities of ≈$0.6\cdot10^{32}$ cm^{-2}sec^{-1} have been obtained (only neutrons in deuterium are counted)[6]. A cooling power of ≈500mW was achieved at ≈270mK in a dilution refrigerator[7]. This would allow measurements to be performed with effective luminosities in excess of 10^{33} cm^{-2}sec^{-1}. Neutron polarizations of ≈45% were obtained in a 3.5T magnetic field[8]. With a 5T field, neutron polarizations of 60% can be anticipated. Using appropriate kinematical cuts on the scattered electron and the recoil neutron angle, background contributions from neutrons in the nitrogen nucleus can largely be suppressed, and effective polarizations of ≈40% should be achievable[9]. The expected running time of a measurement of G_{E_n} is shown in Fig. 2 for a specific experimental setup. It is perhaps worthwhile noting that the use of polarized deuterium as target material has the advantage of allowing the same measurement to be carried out with protons (from the deuterons). A comparison of proton measurements with ND_3 and NH_3 as target materials would allow the testing of effects which may result from the binding of the proton in the deuteron. This information provides a sensitive mean in correcting the neutron data for nuclear effects.

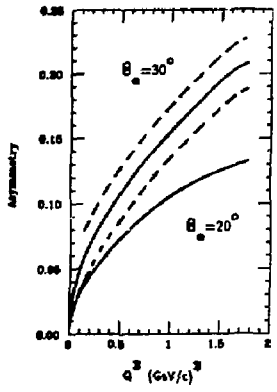

Fig. 1 Polarisation asymmetry $\vec{n}(\vec{e},en)$ for electron scattering angles. $G_{Ea}=-\tau G_{Ma}/\mu_n$ has been assumed. $A_n=0$ if $G_{Ea}=0$. The dashed lines indicate an uncertainty $\delta A=\pm 0.02$.

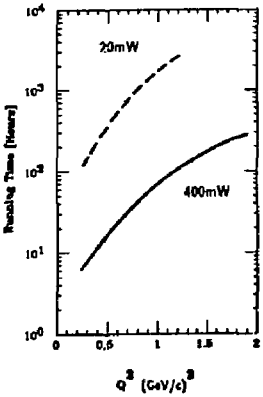

Fig. 2 Running time for an experiment to measure the neutron asymmetry with $\delta A = \pm 0.02$, for polarised target cryostats with different cooling power.

2. An Experiment to Measure G_{Ep} in $\vec{p}(\vec{e},e'p)$

The method outlined above can also be used to measure the polarised proton asymmetry using NH_3 as polarised target material. Hence the electric formfactor G_{Ep} of the proton can be measured. Since protons can be polarised to a higher degree than deuterons at higher temperatures, polarised proton targets can be operated at much higher cooling powers and therefore can be used with higher electron currents. With a ^{4}He cryostate of ≈10 Watts of cooling power at 1 Kelvin, luminosities of $5\cdot10^{34}$ cm^{-2}sec^{-1} (only free protons count) can be achieved[14]. The polarisation asymmetry as predicted by QCD sum rule calculations[5] is shown in Fig. 3. The expected running time of an experiment to measure G_{Ep} is displayed in Fig. 4. Measurements of G_{Ep} for Q^2 up to 6 GeV^2 appear feasible using existing polarised target technology.

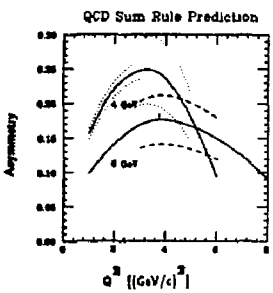

Fig. 3 QCD sum rule prediction of the polarised $\vec{p}(\vec{e},ep)$ asymmetry.

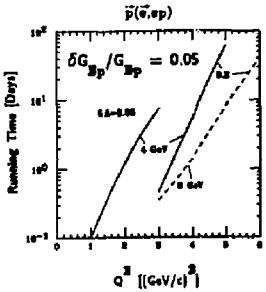

Fig. 4 Expected running time for an experiment to measure G_{Ep} with ±5% and ±20%, respectively.

In summary, it appears that with presently available polarised solid state target technology, considerably higher Q^2 values can be reached in measuring the electric proton and neutron formfactors than has been possible with the usual Rosenbluth separation.

III. Electroproduction of Nucleon Resonances

Studying the Q^2 dependence of the γ NN* transition for the nucleon resonances gives us many details of the wavefunction of the excited states. This knowledge is essential in developing more realistic interquark potentials which are based on the fundamentals of QCD[11]. It appears important to obtain as much information as possible to probe the full electromagnetic structure of the transition, including its spin structure. Before discussing exclusive measurements in some detail, it is perhaps instructive to recall some features of the inclusive cross section in the resonance region.

1. The Inclusive Cross Section p(e,e')X

It is widely assumed that the cross section for electroproduction of nucleon resonances would decrease faster with increasing Q^2 than the nonresonant part does. This, however, turns out not to be the case, as can be inferred from Fig. 5, where the total photoabsorption cross section in the mass region up to W=2GeV is shown for small and large values of Q^2[12]. I want to point out several interesting features in the Q^2 dependence of the cross section:

- -- The strong enhancement in the region of the Δ(1232) disappears quickly at large Q^2.
- -- The enhancements near W≈1.5GeV and W≈1.7GeV remain prominent up to the highest Q^2. The signal/background ratio does not appear to decrease at all over the entire Q^2 range.
- -- The shoulder near W≈1.45GeV in the Q^2=0 data, which is generally attributed to the excitation of the Roper P_{11}(1440), disappears very quickly with Q^2. Already at Q^2=0.1GeV^2 there are no indications of an excitation of this resonance any more.
- -- At Q^2>3GeV^2 a resonant structure near W=1.4 GeV seems to emerge which may even become dominant over the Δ(1232) at the highest Q^2.

In conclusion, the total photoabsorption cross section indicates very different Q^2 dependences for the various resonant parts of the cross section. The fast decrease of the Δ(1232) excitation strength offers the possibility to study the lower mass region at large Q^2 in detail, where the cross section is no longer dominated by the higher mass tail of the Δ(1232). This may prove especially important for studying the excitation of the P_{11}(1440) and possible other P_{11} partners nearby.

It is obvious that due to the large widths and large number of resonances (approximately 20 with masses below 2 GeV) individual resonances can in general not be isolated[13]. A program to separate and study details of single resonances requires studying spin and isospin structure of the intermediate state which can only be done by measuring the resonance decay products in exclusive experiments.

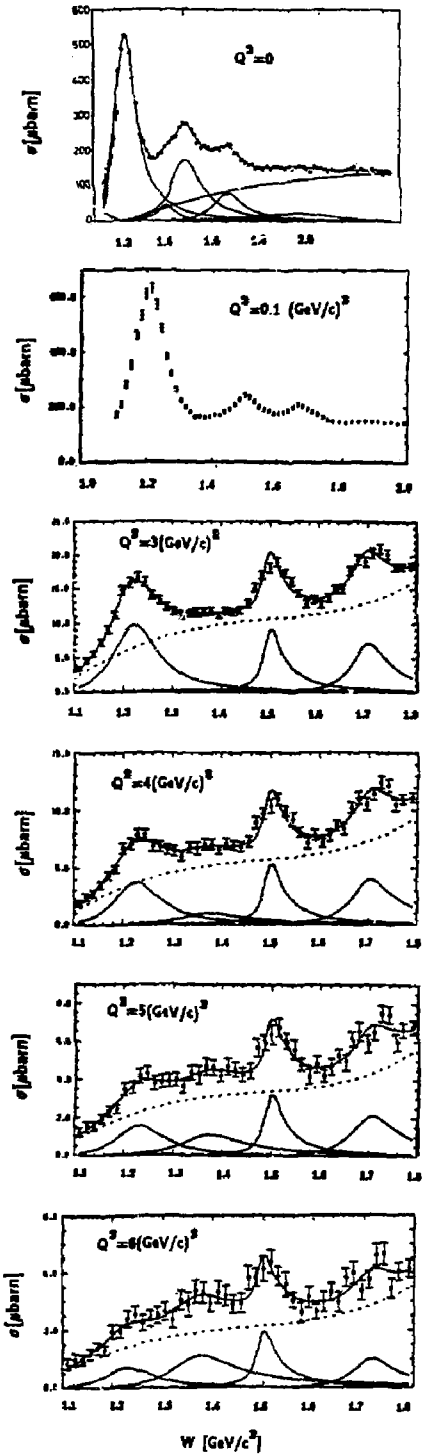

Fig. 5 Inclusive cross section for p(e,e')x at fixed Q^2.

2. Exclusive Reactions for Resonance Studies

Many of the lower lying resonances have a strong single π or η decay channel. The reactions $p(e,e'p)\pi^0(\eta)$, $p(e,e'\pi^+)n$ and $n(e,e'\pi^-)p$ are therefore most suitable for studying resonance properties. The unpolarised coincidence cross section is given by

$$\frac{d\sigma}{dE_e d\Omega_e d\Omega_\pi} = \Gamma_T\left\{\sigma_T + \varepsilon\sigma_L + \varepsilon\sigma_{TT}\cos 2\phi + \sqrt{\varepsilon(1+\varepsilon)/2}\,\sigma_{TL}\cos\phi\right\}$$

The first and third term depend on the transverse unpolarised and polarised coupling of the photon, the second term depends on the the longitudinal part and the last term is a transverse/longitudinal interference term. These quantities are functions of Q^2, W, θ^* and can be expressed in terms of 6 complex, parity conserving helicity amplitudes[10]:

$$\sigma_T = P/2K\left[|H_1|^2 + |H_2|^2 + |H_3|^2 + |H_4|^2\right]$$
$$\sigma_L = P/2K\left[|H_5|^2 + |H_6|^2\right]$$
$$\sigma_{TT} = P/K\ \mathrm{Re}\left[H_2 H_3^* - H_1 H_4^*\right]$$
$$\sigma_{TL} = 2P/K\ \mathrm{Re}\left[H_5^*(H_1 - H_4) + H_6^*(H_2 + H_3)\right]$$

A complete and model independent determination of these amplitudes requires at least 11 independent measurements at each kinematical point. Unpolarised experiments allow four independent measurements only. With a polarised beam one additional combination of these amplitudes can be measured. A polarised nucleon target allows eight sensible measurements, and experiments with polarised beams and polarised target allow measurement of five more combinations of amplitudes[10]. If one can measure the recoil polarisation, e.g., if the final state nucleon is a proton, one can obtain the same number of combinations as with a polarised target, four of which are different from the polarised target case[10].

A separation of the various terms requires detailed out-of-plane measurements. In addition to the $\cos\phi$ and $\cos 2\phi$ terms of the unpolarised cross section $\sin\phi$ and $\sin 2\phi$ terms appear in the polarisation dependent terms. Also, measurements with different orientations of the target spin will be necessary.

3. Existing Data

Although such a detailed experimental program has not been conducted so far, some information, in particular on the most prominent resonances, has been obtained from measuring the angular dependence of the unpolarised coincidence cross section. From experiments performed at the BONN, DESY, NINA synchrotrons[12,9] we have limited information on the transverse helicity amplitudes $A_{1/2}$ and $A_{3/2}$ for the $P_{33}(1232)$, $S_{11}(1535)$, $D_{13}(1520)$ and the $F_{15}(1688)$ proton resonances. It is well known that the $\gamma_v pP_{33}(1232)$ transition amplitudes drop faster with Q^2 than the elastic formfactor. As can be inferred from Fig. 6, the other resonances show quite a different behaviour.

The $S_{11}(1535)$ which can only be excited by helicity 1/2 in the $\gamma_v p$ initial state exhibits a strikingly weak Q^2 dependence. At Q^2=3 GeV^2, the $A_{1/2}$ has decreased by only 50% of its value at Q^2=0. For the $D_{13}(1520)$ and the $F_{15}(1688)$ the helicity-3/2 dominance at Q^2=0 switches to a helicity-1/2 dominance at large Q^2, a behaviour that is qualitatively in accordance with quark model predictions[11], as well as with expectations

from helicity conservation in perturbative QCD[17]. The transition to helicity 1/2 dominance seems to be a general feature at high Q^2. It is the details, however, of how this transition occurs that would give us insight into the dynamics of the multiquark-gluon system. Very little information is available for resonances other than the ones mentioned above, and practically no data exist for neutron resonances.

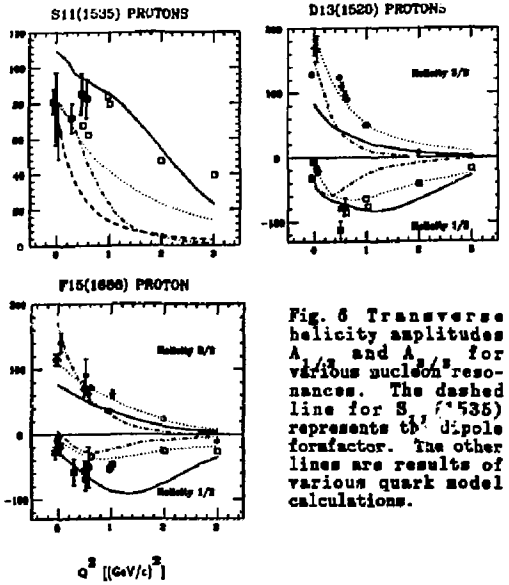

Fig. 6 Transverse helicity amplitudes $A_{1/2}$ and $A_{3/2}$ for various nucleon resonances. The dashed line for $S_{11}(1535)$ represents the dipole formfactor. The other lines are results of various quark model calculations.

It should be noted that the data points in Fig. 6 are subject to systematic uncertainties, largely due to the limited experimental information that could be used in the data analysis. Also, there are uncertainties in the description of the nonresonant part of the cross section[18].

An experimental program to study electroproduction of nucleon resonances should be able to combine very high statistics unpolarised cross section measurements and detailed polarisation measurements of the relevant asymmetries, going up to the highest possible Q^2. Polarisation asymmetries contain interference terms of amplitudes. They are therefore especially sensitive to small amplitudes and to relative phases between amplitudes. Already information of limited statistical accuracy will prove extremely sensitive in determining signs and absolute values of the less prominent amplitudes. In the following chapter we give two examples to illustrate the sensitivity of polarisation asymmetries to small amplitudes.

4. The Scalar Amplitude S_{1+} in the $\gamma_v p\Delta(1232)$ Transition

Quark models with SU(6) symmetry yield $S_{1+}=0$ for the scalar (longitudinal) multipole as a consequence of the assumed pure magnetic dipole transition between two states with angular momentum $L_q=0$ of the 3 quark system. The inclusion of a hyperfine color magnetic interaction arising from the QCD motivated one gluon exchange between the valence quarks[18] leads to a finite longitudinal coupling, reflecting the (SU(6) forbidden) L=2 state of the multiquark wavefunction[19]. Our present knowledge on S_{1+} for the $\Delta(1232)$ comes from studying $p(e,e'p)\pi^0$. Assuming s and p wave contributions only, and M_{1+} dominance (only terms with M_{1+} are retained), the unpolarised cross section can be written as:

$$\frac{d\sigma}{d\Omega^*_\pi} \simeq \left[\frac{5}{2}|M_{1+}|^2 - 3\,\mathrm{Re}\{M_{1+}E^*_{1+}\} + \mathrm{Re}\{M_{1+}M^*_{1-}\}\right]$$
$$+ \cos\theta^*_\pi\left[2\mathrm{Re}\{E_{0+}M^*_{1+}\}\right]$$
$$+ \cos^2\theta^*_\pi\left[-\frac{3}{2}|M_{1+}|^2 + 9\mathrm{Re}\{M_{1+}E^*_{1+}\} - 3\mathrm{Re}\{M_{1-}M^*_{1+}\}\right]$$
$$+ \varepsilon\cdot\sin^2\theta^*_\pi\cdot\cos 2\phi\left[-\frac{3}{2}|M_{1+}|^2 - 3\mathrm{Re}\{M_{1+}E^*_{1+}\}\right]$$
$$+ \sqrt{2\varepsilon(1+\varepsilon)}\cdot\sin\theta^*_\pi\cdot\cos\phi\left[-\mathrm{Re}\{S_{0+}M^*_{1+}\} - 6\cos\theta^*_\pi\cdot\mathrm{Re}\{S_{1+}M^*_{1+}\}\right]$$

From studying the ϕ and θ^*_π dependence of the cross section one can separate the term $\mathrm{Re}(S_{1+}M^*_{1+})$, which is most sensitive to S_{1+}. Fig. 7 shows results of previous measurements[14]. The accuracy of existing data is clearly not sufficient to separate resonant and nonresonant parts. Note that the quantity $\mathrm{Re}(S_{1+}M^*_{1+})/|M_{1+}|^2$ is displayed. A resonance-like behaviour of S_{1+} would result in a flat distribution in this quantity. The Q^2=1GeV^2 data show some W dependance which may indicate that the measured quantity contains nonresonant contributions. In order to enable a full determination of the resonant and nonresonant contribution to $(S_{1+}M^*_{1+})$, a measurement of the term $\mathrm{Im}(S_{1+}M^*_{1+})$ is required as well. This term is particularly sensitive to nonresonant contributions. If only S_{1+} and M_{1+} amplitudes of the resonance contribute, having the same phases, the term $\mathrm{Im}(S_{1+}M^*_{1+})$ would vanish identically. According to fixed and dispersion relation calculations the nonresonant contribution $\mathrm{Re}S_{1+}(I=1/2)$ may be of the same order of magnitude as $\mathrm{Re}S_{1+}(I=3/2)$. This would result in quite different phases for M_{1+} and S_{1+}, which consequently give rise to a sizeable polarisation asymmetry in the vicinity of the resonance.

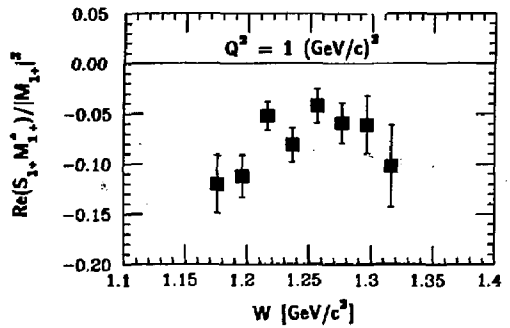

Fig. 7 The quantity $\mathrm{Re}(S_{1+}M^*_{1+})/|M_{1+}|^2$ in the $\Delta(1232)$ region. Data from DESY[14].

The quantity $\mathrm{Im}(S_{1+}M^*_{1+})$ can be measured by using a longitudinally polarised electron beam and measuring the cross section asymmetry[20].

$$A_e \simeq \sqrt{2\varepsilon(1-\varepsilon)}\cdot\sin\phi\cdot\sin\theta^*_\pi\left[\mathrm{Im}\{S_{0+}M^*_{1+}\} + 6\cos\theta^*_\pi\mathrm{Im}\{S_{1+}M^*_{1+}\}\right]$$

In this expression the same approximation as in the unpolarised cross section has been assumed. This experiment requires a measurement of the θ^*_π distribution of one of the outgoing hadrons at large ϕ (out of the scattering plane). Measuring the θ^*_π dependence of A_e at fixed $\sin\phi$ enables a separation of $\mathrm{Im}(S_{0+}M^*_{1+})$ and $\mathrm{Im}(S_{1+}M^*_{1+})$. Asymmetries of 5 to 10% can be expected[18].

5. Polarised Target Asymmetry in the Region of the $P_{11}(1440)$

There is an ongoing controversy as to whether or not the $P_{11}(1440)$ is actually composed of two P_{11} resonances as a recent analysis indicates[24]. In electroproduction, however, only weak indications of a resonant structure in this particular mass region have been seen in unpolarised electroproduction experiments. Single pion photoproduction data have on the other hand revealed a rather strong resonance excitation[25]. Pion electroproduction may help solve the above controversy because of the additional kinematical degree of freedom given by Q^2. The various resonances may exhibit very different Q^2 dependence.

Measurements of asymmetries with polarised targets appear quite sensitive to the strength of the $P_{11}(1440)$ excitation. Fig. 8 shows the sensitivity of the target asymmetry in π^0 production to the excitation of the $P_{11}(1440)$. By choosing a suitable orientation of the target polarisation and by carefully selecting the kinematics of the decay particles, interference effects may become large and exhibit sizable effects even from weak resonances. In this example the amplitudes which have been obtained in an analysis[23] of the world data at $Q^2=1$ GeV^2 were used. In the analysis, a sizable longitudinal amplitude S_{1-} was found for the $P_{11}(1440)$. This gives rise to strong effects in T_x which contains transverse-longitudinal interference terms.

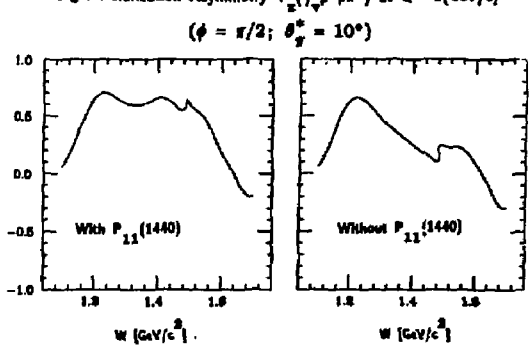

Fig. 8 Polarised target asymmetry $T_x(\gamma_v p\to p\pi^0)$ for a specific kinematical situation. The target protons are polarised perpendicular to the virtual photon direction, in the electron scattering plane. Results of a recent analysis[23] have been used to predict the asymmetry (l.h.s.). To illustrate the sensitivity to the longitudinal coupling of the P_{11}, the expected asymmetry is shown if the P_{11} were not excited (r.h.s.).

6. Double Polarisation Asymmetry

With a polarised beam and a polarised nucleon target, one can measure double polarisation asymmetries which require flipping the spin of the electron as well as of the target nucleons. Of particular interest is the asymmetry D_z

$$D_z = \frac{\sigma(P_e=1,P_z=1)-\sigma(P_e=1,P_z=-1)-\sigma(P_e=-1,P_z=1)+\sigma(P_e=-1,P_z=-1)}{\sigma(P_e=1,P_z=1)+\sigma(P_e=1,P_z=-1)+\sigma(P_e=-1,P_z=1)+\sigma(P_e=-1,P_z=-1)}$$

where the nucleon spin is aligned parallel and antiparallel to the direction of the virtual photon. Fig. 9 shows that this asymmetry can be large. D_z measures directly the helicity asymmetry

$$\frac{1}{2\pi}\int D_z\left(Q^2,W,\theta^*_\pi,\phi\right)d\phi = \frac{\sigma^T_{1/2}-\sigma^T_{3/2}}{2\sigma_0}$$

for the transverse cross section. The partial wave analysis of this quantity at fixed Q^2 and W yields the helicity asymmetry for single partial waves. Unpolarised measurements allow the determination of $\sigma^T_{1/2} + \sigma^T_{3/2}$ for single partial waves. The two measurements combined allow determination of $\sigma^T_{1/2} \sim |\sigma A_{1/2}|^2$ and $\sigma^T_{3/2} \sim |A_{3/2}|^2$ for specific resonances (after subtracting the nonresonant background). $A_{1/2}$ and $A_{3/2}$ have been predicted by microscopic models of the nucleon and provide tests of the helicity structure of the resonance transition. In view of the quark model and QCD predictions, e.g., that $\sigma_{1/2}$ should vanish at large Q^2, measurements of this type provide immediate tests of essential aspects of theoretical approaches in the nonperturbative regime. In Fig. 9 examples of predictions for D_z are shown.

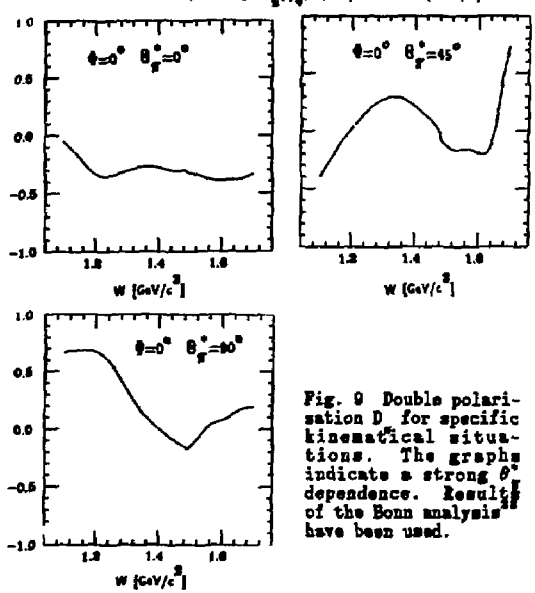

Fig. 9 Double polarisation D_z for specific kinematical situations. The graphs indicate a strong θ^*_π dependence. Results[23] of the Bonn analysis have been used.

IV. Parity Violation Measurement in the Δ(1232) Region

In low energy ($Q^2 \ll M_Z^2$) neutral current interactions, the parity violating contribution arises from the interference between the one-photon exchange and the neutral weak boson (Z^0) exchange graphs. In electron scattering, the interaction contains an isoscalar as well as an isovector piece in both the vector (V_μ) and axial vector (A_μ) coupling. The effective Lagrangian which describes the parity non-conserving (PNC) part of the interaction for electron hadron scattering is given by[26]

$$L^{PNC}_{eff} = -\frac{G_F}{\sqrt{2}}\cdot\left[\bar e\gamma_\mu\gamma_5 e\left(\tilde\alpha V^3_\mu+\tilde\gamma V^0_\mu\right) + \bar e\gamma_\mu e\left(\tilde\beta A^3_\mu+\tilde\delta A^0_\mu\right)\right]$$

The $\tilde\alpha$, $\tilde\beta$, $\tilde\delta$, $\tilde\gamma$ denote the respective coupling constants which have to be determined experimentally. In the

Glashow-Salam-Weinberg Model (GSW) of electroweak interaction, these coupling constants can be expressed in terms of a single parameter, the weak mixing angle θ_W. By choosing appropriate kinematical conditions for electron scattering from nucleons and nuclear targets, one can determine the couplings by a set of four linearly independent measurements.

The SLAC/Yale $D(\vec{e},e')X$ scattering experiment[25], in conjunction with atomic physics experiments[26], enabled a model independent determination of α, γ. The Mainz experiment[27] measures a different combination of the four coupling constants and allows the extraction of a combination of β and δ, using the previously obtained results as an input. It should, however, be noted that this experiment measures quasielastic electron scattering from ^9Be rather than elastic electron nucleon scattering. This fact could be of importance if the data are used for a determination of the weak angle. The Bates experiment[28], which has recently become operational, simply measures γ.

From this brief survey of existing measurements it is obvious that for a complete determination of the coupling constants additional measurements are needed. One should also attempt to measure a possible Q^2 dependence of these couplings. Deviations from the GSW model may occur at the level of one percent[29]. High precision measurements are therefore needed.

Various arguments have been made for measureing parity violation in elastic electron-proton scattering[30,31]. A precise measurement of the Δ-excitation seems equally important. We summarize here some arguments for measuring this process.

- $\Delta(1232)$ excitation separates the isovector part (α, β).
- It is an almost pure magnetic resonance with a dominant magnetic dipole (M_{1+}) excitation. The scalar coupling (S_{1+}) and the electric coupling (E_{1+}) are both small.
- At low Q^2 (<0.6 GeV^2) the nonresonant background is small. Its effects on the PNC asymmetry should be reliably calculable[32]. In order to understand the PNC effects of the nonresonant part at the one percent level, more precise electroproduction data in different isospin channels will presumably be needed as well.
- The asymmetry is predicted to be large in the GSW model[31,32].

$$A_{\Delta(1232)} = \left(\frac{G_F}{\sqrt{2}}\right)\left(\frac{Q^2}{2\pi\alpha}\right)\left[\tilde{\alpha} + F(Q^2,E)\tilde{\beta}\right]$$

and has a strong sensitivity to $\sin^2\theta_W$.

The factor $F(Q^2,E)$ in the above formula is close to 1 in the energy range of interest. Assuming a weak angle of $\sin^2\theta_W = 0.225$, one obtains $A_{\Delta(1232)} \approx -1.17\times10^{-4}Q^2$.

V. Conclusions

Polarisation experiments open up a large variety of possibilities to study electromagnetic properties of the nucleon and its excited states with increased sensitivity compared to unpolarised measurements. The numerical examples chosen assumed an external target situation at CEBAF energies. Most of the experiments can, of course, be done with gas targets in storage rings, if high enough luminosities can be achieved. "High enough" translates as $\geq 10^{31}$ cm^{-2} sec^{-1} for the measurement of the neutron electric formfactor and $\geq 10^{34}$ cm^{-2} sec^{-1} for the proton electric formfactor. The nucleon resonance program would also need luminosities in excess of 10^{34} cm^{-2} sec^{-1} for a substantial improvement of previous work, if full solid angle coverage is provided.

Precision experiments for studying parity violation in electron scattering require measurements with very high luminosity ($L>10^{38}$cm^{-2}sec^{-1}) and large acceptance detectors[25,28]. Because of the luminosity requirements, these experiments will have to employ thick targets in an external beam line.

References

1) S. Galster et al., Nucl. Phys. B32 (1971) 221.
2) W. Bartel et al., Nucl. Phys. B58 (1973) 429.
3) R. Arnold, C. Carlson, F. Gross, Phys. Rev. C23 (1981) 363.
4) V. Burkert, Lect. Notes in Phys. 234 (1984) 228.
5) W. A. Nesterenko, A. V. Radyushkin, Phys. Lett. 115B (1982) 410.
6) K. H. Althoff et al., Europhysics Conf. on Nuclear Physics with Electromagnetic probes, Paris (1985).
7) T. O. Niinikoski, Proc. 4th Workshop on Polarised Target Materials and Techniques, ed. W. Meyer, Bonn (1984).
8) W. Meyer et al., Nucl. Instr. Methods A244 (1986) 574.
9) V. Burkert, CEBAF Reports CR-86-002, CR-86-003, CR-86-011.
10) U. Hartfiel et al., Proc. 4th Workshop on Polarised Target Materials and Techniques, Bonn (1984).
11) W. Pfeil, Report of the 1986 Summer Study Group, CEBAF, Newport News, Virginia, 219.
12) F. Foster and G. Hughes, Rep. Prog. Phys. 46 (1983) 1445.
13) D. Walecka, Acta Physica Polonica B3 (1972) 117.
14) R. Walker, Phys. Rev. 182 (1969) 1729.
15) A. Bartl, W. Majerotto, Nucl. Phys., B62 (1973) 267.
16) E. Funsten, Report of the 1986 Summer Study Group, CEBAF, Newport News, Virginia, 183.
17) C. Carlson, Phys. Rev. D34 (1986) 2704.
18) N. Isgur, G. Karl, Phys. Rev. D19 (1979) 7853; Phys. Rev. D23 (1981) 817.
19) M. Bourdeau, N. C. Mukhopadhyay, Phys. Rev. Lett. 58 (1987) 976.
20) G. V. Gehlen, Nucl. Phys. B26 (1971) 141.
21) R. Arndt, J. Ford, D. Roper, Phys. Rev. D32 (1985) 1085.
22) R. L. Crawford, W. T. Morton, Nucl. Phys. B211 (1983) 1.
23) B. Boden and G. Kroesen, Report of the 1986 Summer Study Group, CEBAF, Newport News, Virginia.
24) P. Q. Hung, J. J. Sakurai, Phys. Lett. 63B (1976) 295.
25) C. Y. Prescott et al., Phys. Lett. 77B (1978) 347; Phys. Lett., 84B (1979) 524.
26) P. Q. Hung, J. J. Sakurai, Annual Rev. of Nucl. & Part. Science 31.
27) W. Achenbach et al., Presented at the Int. Symp. on High Energy Spin Physics, Protvino, Sept. 1986.
28) Proceedings of CEBAF Workshop on Parity Violation, Newport News, VA, Dec. 1986, ed. R. Siegel.
29) S. Kowalski, in (28).
30) P. Langacker, in (28).
31) D. Walecka, in (28); see also D. Walecka, Argonne Lecture Notes ANL-83-50 (1983).
32) S. Pollock, in (28).
33) S. Pollock, private communications.
34) D. Jones, S. Petcov, Phys. Lett. 91B (1980) 137.
35) V. Burkert, in (28).
36) B. Mecking, in (28).
37) J. C. Alder et al., Nucl. Phys. B46 (1972) 573.

A TAGGED PHOTON BEAM FROM BREMSSTRAHLUNG ON AN ARGON JET TARGET

M. Anghinolfi[2], A. Bertocchi[3], N. Bianchi[1], G.P. Capitani[1], P. Corvisiero[2], E. De Sanctis[1], S. Frullani[3], F. Garibaldi[3], C. Guaraldo[1], P. Levi Sandri[1], V. Lucherini[1], L. Mattera[2], V. Muccifora[1], E. Polli[1], A.R. Reolon[1], G. Ricco[2], P. Rossi[1], M. Sanzone[2], M. Taiuti[2], G.M. Urciuoli[3], U. Valbusa[2] and A. Zucchiatti[2]

(1) I.N.F.N. - Laboratori Nazionali di Frascati, P.O.Box 13, I-00044 Frascati, Italy.

(2) Dipartimento di Fisica dell'Università di Genova e I.N.F.N. - Sezione di Genova, I-16146, Genova, Italy.

(3) Laboratorio di Fisica dell'Istituto Superiore di Sanità and I.N.F.N. - Sezione Sanità, I-00185, Roma, Italy.

Abstract. A proposed monochromatic photon beam produced by the tagging technique is described. The radiator is a condensed molecular beam of argon (thickness 10^{-8} g/cm^2) installed in a straight section of the Adone storage ring. The recoil electron counters are placed in the magnetic field of the next dipole ring. The tagging system defines 80 channels (each 1% resolution) covering the photon energy range (0.4 - 0.8 E_0. The total photon intensity is about 10^8 sec^{-1}.

In view of the great interest in nuclear physics studies with electromagnetic probes, at Frascati it is foreseen to install an internal jet target on the electron storage ring Adone to produce a monochromatic high energy (up to 1.2 GeV) photon beam by the tagging technique.

The use of internal target in circulating beams antedates the availability of external beam from circular machines. In recent years, with improved understanding of beam dynamics and the contruction of high energy synchrotron and storage rings, there have been a renewed interest in this option and growing activity in the development of suitable targets. The target which gives the largest luminosity is a type of condensed molecular beam[1] which provides a flow of gas at supersonic speed (hence the name of gas "jet" target) due to the expansion of gas from a vessel at high pressure and low temperature into the vacuum through a nozzle of very small aperture (10 ÷ 150 μm) and special geometry. The molecular jet flies forward along the axis of expansion and it is absorbed after having crossed the accelerator vacuum pipe. Only the core of the jet reaches the ultra-high vacuum of the ring via several differential pumping stages where almost all the uncondensed residual gas is pumped off.

Fig. 1 shows the schematic view of the jet target proposed for Adone. The argon jet is produced in the chamber 1 (installed on top of the Adone vacuum pipe) where the gas expansion take place. The injector is a converging-diverging nozzle with special trumpet-shaped end part. Then the jet moves across the machine vacuum pipe to the sink system, installed below the storage ring.

We have interposed three differential pumping stages (each equipped with a 360 l/sec turbo-pump) to separate both the expansion and the sink chambers from the vacuum pipe in order to minimize the pressure rise in the interaction region ($\lesssim 10^{-8}$ torr). An additional

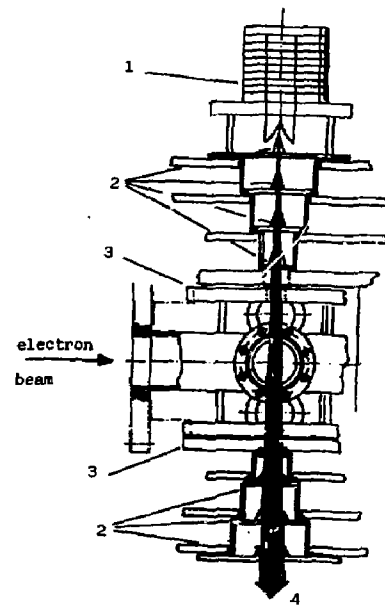

Fig. 1 - Side view of the argon jet target proposed for Adone: 1 gas expansion chamber; 2 collimators; 3 valves; 4 sink chamber.

pumping system (two 1000 l/sec turbo-pumps) is acting on the straight section of the ring where the jet target will be mounted, in order to reduce this rise pressure and limit the length of the region where the pressure is $\lesssim 10^{-8}$ torr. Two fast acting UHV valves separate the production and sink chambers from the Adone vacuum pipe to easy the jet on/off operations and to prevent the possible contamination of the ring in case of a large pressure bump due to breakdown of the target system. The operating conditions are inlet pressure and temperature 6 bar and 150 °K respectively, nozzle throat diameter 87 μm and semiaperture 3.5°.

From a total flux of 10^{20} Ar-atoms/sec expanding from

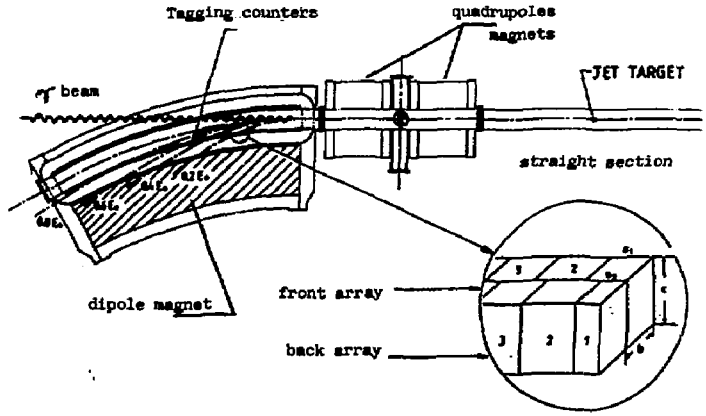

Fig. 2 - Schematic view of the tagging system

the nozzle the collimator system selects 5 10^{18} atoms/s, which corresponds to a target thickness of $\simeq 10^{-6}$ g/cm^2 ($\emptyset$ = 1 cm) on the path of the electron beam (that is a distance of $\simeq$25 cm from the nozzle).

The circumference of the Adone ring is approximately 105 m, so that a bunch of ultrarelativistic electrons takes about T_0 = 351 nsec to make a round. The ring is divided into twelve identical lattice elements each consisting of a straight section, a bending magnet (dipole) and a couple of defocusing-focusing magnets (quadrupoles).

Electrons are injected into the storage ring at an energy of 300 MeV (a few-turn injection will result in about 100 mA current circulating in the ring) and then accelerated to the desired energy by rising the magnetic field of the guiding magnets (this operation requires about 20 sec). The 51.4 MHz RF-cavity groups the circulating electrons into 18 bunches, each 1 nsec wide and 20 nsec apart.

After the rise in energy the argon jet will be fired into the vacuum pipe and the electron beam lifetime $\tau = T_0/(\sigma_R' x)$ cut down to about 130 sec (T_0 is the revolution period, σ_R' the removal cross section and x the jet target thickness). Then the cycle is ended by lowering the field of the magnets to the injection value. The removal cross section involves only that process of bremsstrahlung in which the energy loss places the electron outside the acceptance band-width of the ring (ξ=0.01 E_0, E_0 being the machine energy). In fact the target thickness is so small that neither the multiple scattering nor the ionization losses contribute to the lifetime, being the RF-cavity able to compensate for both the growth in divergency and the mean energy losses.

In fig. 2 is sketched a lay-out of the apparatus: the argon jet will be placed in a straight section (2.58 m long) between consecutive lattice elements and the recoil electron is bended by the dipole magnet and detected by a two-array scintillator counter hodoscope. This hodoscope will be placed between the ring vacuum pipe and the dipole magnet flux return joke. The scintillators have different sizes to give the same photon energy resolution ($\simeq$ 1% at E_0 = 1.5 GeV and $\simeq$ 2.7% at E_0 = 500 MeV) over the whole tagging range. The complete tagging system defines 80 energy channels covering the photon energy range $k = (0.4 \div 0.8)E_0$. This implies an extensive array of tagger detectors covering a side 1 m long of the bending magnet pole.

Since the determination of the photon energy relies on a coincidence between the tagging counters and the detector for the photoejected particles, the tagging method is limited by the random coincidences. In the normal operating mode the facility produce $\simeq 10^8$ photons/sec in the whole tagging range. To use the tagged photon beam at the maximum intensity it is foreseen the installation of a new 350 MHz RF-cavity which makes the beam almost continuous in time (126 bunches 2.86 nsec apart).

To compensate for the relatively low intensity of the tagged photon beam, the detection apparatus for photoejected particles has to cover a large solid angle and energy range simultaneously. In our case this apparatus will be a 4π BGO crystal ball (whose design is presently going on), consisting of 300 ÷ 400 crystals, each coupled to a photomultiplier. A 20 cm bore along a diameter of the sphere will allow the passage of the beam.

A partial list of experiments which will be carried out with this beam are:

- measurement of the total hadronic cross section through both the transmission method and the uranium photofission;
- deuteron photodisintegration;
- photo-exitation of nucleon resonances;
- particle correlation and resonance propagation in nuclei.

References

1. O.F. Hagena and W. Obert, J.Chem.Phys. 56,1793(1972)

SCATTERING OF POLARIZED ELECTRONS FROM ORIENTED ROTATIONAL NUCLEI

E. MOYA DE GUERRA

and

P. SARRIGUREN

I.E.M., C.S.I.C., Serrano 123. 28006-MADRID. (Spain)

ABSTRACT

The interest of using polarized beam and target to extract information on current distributions in rotational nuclei is pointed out. The differential cross section for elastic and inelastic scattering of longitudinally polarized electrons from oriented nuclei is analyzed in detail focusing on the case of K=½ ground state bands.

1. Introduction

The study of nuclear ground state rotational bands by means of electron scattering experiments has been a subject of interest for many years. So far, a substantial amount of experimental information is available concerning longitudinal form factors for transitions within the ground state band of many deformed nuclei[1]. However, little is known yet about the more interesting transverse form factors[2] that carry the information on the nuclear current distribution, and hence, on the nature of the rotational mode. This is mainly due to the fact that in ordinary electron scattering on deformed nuclei (i.e., with unpolarized beam and target) the differential cross section is dominated by the longitudinal form factor and, therefore, extracting information on transverse multipoles is hard, specially at low q values. In this brief communication we wish to point out that the best way to obtain information on transverse multipoles is to use oriented targets and, or polarized beam and target.

The differential cross section for scattering of linearly polarized electrons from an oriented nuclear target is given in first Born approximation by[3,4]

$$\frac{d\sigma}{d\Omega} = \frac{4\pi\,\sigma_M}{f_{rec.}}\,\sigma(h;\,\theta',\,\varphi') \qquad (1)$$

where σ_M and $f_{rec.}$ are the standard[5] Mott cross section and recoil factor, respectively, h is the incoming electron helicity and (θ',φ') is the target polarization direction with respect to the direction of the momentum transfer. The dependence on h and (θ',φ') in eq. (1) can be written as

$$\sigma(h;\,\theta',\,\varphi') = \sigma_o + \sigma_{al.}(\theta',\varphi') + h\,\sigma_{pol.}(\theta',\varphi') \qquad (2)$$

where σ_o is the usual combination of longitudinal and transverse form factors occurring in ordinary electron scattering, and $\sigma_{al.}$, $\sigma_{pol.}$ are, respectively, the alignment and polarization cross section that depend on the target polarization direction. While in ordinary scattering the different multipoles occurring in a given transition within the band appear allways in the combination[5]

$$\sigma_o = v_L|F_L|^2 + v_T|F_T|^2 \qquad (3)$$

with

$$|F_L|^2 = \sum_{A=even\geq 0} |F^{CA}|^2,$$

$$|F_T|^2 = \sum_{A=odd} |F^{MA}|^2 + \sum_{A=even\geq 2} |F^{EA}|^2, \qquad (4)$$

$\sigma_{al.}$ and $\sigma_{pol.}$ contain in general many different combinations of the longitudinal and transverse multipoles, some of which are interference terms between coulomb and transverse multipoles. Each of these combinations can be separeted by appropriate choices of the target polarization direction, as well as using the dependence on the target

orientation along a fixed polarization direction, on the electron helicity and on the scattering angle.

To make this presentation as short as possible only a specific case, that bears many interesting physical features, will be discussed in detail. This is the case of K=½ bands with level sequence I=½, $\frac{3}{2}$, $\frac{5}{2}$, $\frac{7}{2}$, ... In this case aligment of the target is not possible (ground state spin is I=½) and to get additional information to that contained in σ_o, experiments with polarized projectile and target have to be done.

2. Application to K=½ ground state bands

As it is well known[6] the level sequence of K=½ bands depends on the value of the decoupling parameter a. For $-1<a<1$ the spin sequence is I=½, 3/2, 5/2, ... this is for instance the case of the ground state bands of ^{29}Si, ^{183}W and ^{239}Pu. Polarization considerations are greatly simplified for spin ½ targets and the discusion here will be restricted to this kind of K=½ bands. When the target is prepared with its magnetic subatates M=±½ propulated with different probabilities, P(M), the polarization cross section for transition to any state within the band is given by[4]

$$\sigma_{pol.}=\alpha_1^{½}(\sin\theta'\cos\varphi' V'_{TL}F^1_{TL}+\cos\theta' V'_T F^1_T) \qquad (5)$$

where $\alpha_1^{½} = \frac{1}{\sqrt{3}}(1-2P(M=-½))$, V'_{TL}, V'_T are electron kinematic factors and F^1_{TL}, F^1_T are the q-dependent form factors that carry the information on the nuclear structure. F^1_{TL} contains interference terms between longitudinal (CΛ) and transverse (EΛ,MΛ) multipoles, while F^1_T contains only transverse multipoles.

In ordinary scattering $|F_T|$ can be separated from $|F_L|$ by the usual Rosenbluth sparation method and usually scattering at 180° is required. As said before, if $|F_T|^2 << |F_L|^2$ it is hard to extract information on $|F_T|$ from ordinary electron scattering.

With polarized beam and target the different terms in $\sigma_{pol.}$ can be easily separated, since for instance one has that

$$F^1_{TL} \propto ½(\sigma(h;\theta'=\tfrac{\pi}{2},\varphi'=0) - \sigma(h;\theta'=\tfrac{\pi}{2},\varphi'=\pi)) =$$

$$= ½(\sigma(h;\theta'=\tfrac{\pi}{2},\varphi'=0) - \sigma(-h;\theta'=\tfrac{\pi}{2},\varphi'=0)$$

$$F^1_T \propto ½(\sigma(h,\theta'=0) - \sigma(h,\theta'=\pi)) =$$

$$= ½(\sigma(h,\theta'=0) - \sigma(-h,\theta'=0))$$

Restricting ourselves to elastic and inelastic scattering to the two first excited states, the measurable form factors $|F_{L_{I_f}}|^2$, $|F_{T_{I_f}}|^2$, $F^1_{TL_{I_f}}$, $F^1_{T_{I_f}}$ are given in terms of the transition multipoles $F^{\sigma\Lambda}_{I_f}$ by the following relations[4] (where σ = C,E,M.; the index I_f is used to distinguish transitions to different states in the band, and a convention is used in which the $F^{\sigma\Lambda}$'s are real).

For elastic scattering (I_f=½):

$$|F_{L_{½}}|^2 = |F^{CO}_{½}|^2,\ |F^{T}_{½}|^2 = |F^{M1}_{½}|^2,\ F^1_{TL_{½}} =$$

$$= \sqrt{3/2}\, F^{CO}_{½} F^{M1}_{½},\ F^1_T = -\sqrt{3}\,|F_{T_{½}}|^2 \qquad (6)$$

For scattering to the first excited state (I_f=3/2):

$$|F_{L_{3/2}}|^2 = |F^{C2}_{3/2}|^2,\ |F_{T_{3/2}}|^2 = |F^{M1}_{3/2}|^2 + |F^{E2}_{3/2}|^2$$

$$F^1_{TL_{3/2}} = \sqrt{3/8}\, F^{C2}_{3/2}\,(\sqrt{3}\, F^{E2}_{3/2} - F^{M1}_{3/2}) \qquad (7)$$

$$F^1_{T_{3/2}} = \sqrt{3}/2(|F^{M1}_{3/2}|^2 - |F^{E2}_{3/2}|^2 + 2\sqrt{3}\, F^{M1}_{3/2} F^{E2}_{3/2})$$

For scattering to the second excited state (I_f=5/2):

$$|F_{L_{5/2}}|^2 = |F^{C2}_{5/2}|^2,\ |F_{T_{5/2}}|^2 = |F^{E2}_{5/2}|^2 + |F^{M3}_{5/2}|^2$$

$$F^1_{TL_{5/2}} = F^{C2}_{5/2}\,(F^{M3}_{5/2} - 1/\sqrt{2}\, F^{E2}_{5/2}) \qquad (8)$$

$$F^1_{T_{5/2}} = 1/\sqrt{3}(|F^{E2}_{5/2}|^2 - |F^{M3}_{5/2}|^2 + 4\sqrt{2}\, F^{M3}_{5/2} F^{E2}_{5/2})$$

Then, for every transition, one has four measurable form factors to determine at most three independent transition multipoles. Furthermore, in the q-regions where transverse multipoles are much smaller than longitudinal ones, the combined information on $|F_{L_{I_f}}|$ and $F^{l}_{TL_{I_f}}$ can be used to extract information on the transverse multipoles.

On the other hand, since the transition multipoles can be parametrized in terms of intrinsic multipoles that are common to all the transitions[4,7] (i.e., that are independent of inicital and final spins), the information on multipoles corresponding to different transitions can be combined to extract information on the intrinsic structure of the rotational band and on the nature of the rotational mode. For instance, the M1 multipoles of the intrinsic single particle ($\zeta^{M1}_{k}, \zeta^{M1}_{2K}$) and collective ($\zeta^{M1}_{R}$) currents can be obtained from[4,7]:

$$\zeta^{M1}_{k} = 1/\sqrt{3}\,(F^{M1}_{1/2} + \sqrt{2}\,F^{M1}_{3/2})$$

$$(\zeta^{M1}_{R} - \sqrt{2}\zeta^{M1}_{2K}) = 2/\sqrt{3}\,(F^{M1}_{1/2} - 1/\sqrt{2}\,F^{M1}_{3/2}) \qquad (9)$$

Similarly the E2 multipoles of the intrinsic single particle (ζ^{E2}_{2K}) and collective (ζ^{E2}_{R}) currents can be obtained from

$$\zeta^{E2}_{R} = (1/6\sqrt{5})(\sqrt{2}\,F^{E2}_{3/2} + \sqrt{3}\,F^{E2}_{5/2})$$

$$\zeta^{E2}_{2K} = 1/\sqrt{30}\,(\sqrt{3}\,F^{E2}_{5/2} - 4\sqrt{2}\,F^{E2}_{3/2}) \qquad (10)$$

Also, the C2 multipole of the intrinsic charge distribution (ζ^{C2}) is obtained, to lowest order in angular momentum, from

$$|\zeta^{C2}| = \sqrt{5/2}\,|F_{L_{3/2}}| \approx \sqrt{5/3}\,|F_{L_{5/2}}| \qquad (11)$$

Note that relation (11) is characteristic of the K=½ bands considered here, and provides the most direct test of band mixing effects in the charge distribution of rotational states. Departures from this relation in measured longitudinal form factors would give a direct measure of the above mentioned band mixing effects.

References

1. W. Bertozzi: Nucl. Phys. A374 (1982) 109c.
2. T.W. Donnelly and I. Sick: Rev. of Mod. Phys., 56 (1984) 461.
3. L.J. Weigert and M.E. Rose: Nucl. Phys., 51 (1964) 529.
   T.W. Donnelly and A.S. Raskin: An. Phys. (N.Y.) 169 (1986) 247.
4. E. Moya de Guerra: Phys. Rep. 138 (1986) No. 6, 293.
5. T. de Forest, Jr. and J.D. Walecka: Adv. in Phys., 15 (1966) 1.
   H. Uberall: "Electron Scattering from complex Nuclei", Parts A and B (Academic Press, 1971).
6. A. Bohr and B. Mottelson; "Nuclear Structure", v. II (Benjamin Inc., 1975).
7. E. Moya de Guerra: Ann. Phys. (N.Y.) 128 (1980) 286.

LIST OF PARTICIPANTS

Gary S. Adams
Rensselaer Polytechnic Institute
Department of Physics
Troy, NY 12180
(518)266-8406

Raymond G. Arnold
SLAC
Bin 43
P.O. Box 4349
Stanford, CA 94305
(415) 854-3300 X2755
ARNOLD at SLACVM

Peter D. Barnes
Carnegie Mellon Univ.
Physics Department
Pittsburg, PA 15213
(412) 268-2745
BARNES at CMPVS

Doug Beck
Cal Tech
Kellogg Radiation Lab
106-38
Pasadena, CA 91125
(818) 356-4238
BECK at CALTECH

Donald Benton
SLAC
Bin 43
P.O. Box 4349
Stanford, CA 94305
(415)854-3300 x3454
BENTON at SLACVM

Edmond L. Berger
Argonne National Lab.
9700 South Cass Ave.
Argonne, IL 60439
(312)972-6211
ELB at ANLHEP

Aron M. Bernstein
MIT - Bates
Department of Physics
Bldg. 26-433
Cambridge, MA 02139
(617) 253-2386
BERNSTEIN at MITLNS

Sigfrido Boffi
Istituto Naz. Fiz. Nucleare
Via Bassi, 6
I-27100 Pavia, Italy
(382) 392434
BOFFI at VAXPV.INFNET

Edward C. Booth
Boston University
Department of Physics
Boston, MA 02215
(617)353-2611
BOOTH at BUPHYA

Peter Bosted
SLAC
BIN 43
P.O. Box 4349
Stanford, CA 94305
(415) 854-3300 X2319
PYBRA at SLACVM

Harold C. Britt
LLNL
L280, E Division
Livermore, CA 94550
(415)422-0684
BRITT at LLL

Stanley J. Brodsky
SLAC
P.O. Box 4349
Bin 81
Stanford, CA 94305
(415)854-3300 x2644
SJBTH at SLACVM

Virginia R. Brown
LLNL
P.O. Box 808 L-297
Livermore, CA 94550
(415) 422-4092

Warren W. Buck
Department of Physics
Hampton University
Hampton, Virginia 23668
(804) 727-5277

Volker Burkert
CEBAF
12070 Jefferson Avenue
Newport News, VA 23606
(804)875-7840
BURKERT AT CEBAFVAX

Linda M. Burress
Lawrence Livermore National Lab.
P.O. Box 808, L-280
Livermore, CA 94550
(415) 422-9673

J.R. Calarco
Univ. of New Hampshire
Department of Physics
209AA Demeritt Hall
Durham, NH 03824
(603) 862-2088

C. E. Carlson
College of William & Mary
Department of Physics
Williamsburg, VA 23185
(804) 253-4471

Chia-Cheh Chang
University of Maryland
Department of Physics
College Park, MD 20742
(301) 454-5779
CHANGCC at UMCINCOM

Jian-ping Chen
SLAC
Bin 43
P.O. Box 4349
Stanford, CA 94305
(415)854-3300 x3646
JCHEN AT SLACVM

C. Ciofi degli Atti
INFN. - Rome
Sezione Sanita
Vale Regina Elena 299
I-00161 Roma ITALY
6-4993383

Lisa Clogher
SLAC
Bin 43
P.O. Box 4347
Stanford, CA 94305 ZIP = 94305
(415)854-3300 X3647

Sidney A. Coon
Department of Physics
Bldg. 81
University of Arizona
Tucson, AZ 85721
(602) 621-2950
COON at ARIZJVAX

Stephen R. Cotanch
North Carolina State Univ.
Department of Physics
Raleigh, NC 27612-8202
(919) 737-3316 X2512
COTANCH at NCSUPHYS

Frank. Dietrich
LLNL - L-405
P.O. Box 808
Livermore, CA 94550
(415) 422-4521

T. W. Donnelly
MIT - 6-300
Center for Theoretical Physics
Cambridge, MA 02139
(617)253-4847

Timothy R. Donoghue
Department of Physics
Ohio State University
Columbus, OH 43210
(614) 297-4775

John F. Dubach
Univ. of Massachusetts
Nuclear Physics/Lederle B422
Amherst, MA 01003
(413) 545-2548
DUBACH at UMASS

Bradley Filippone
Cal Tech
Kellogg Lab, 106-38
Pasadena, CA 91125
(818) 356-4517
BWF at CALTECH

John M. Finn
Department of Physics
College of William and Mary
Williamsburg, VA 23185
(804) 253-4471

J. Flanz
Bates Linear Accelerator
Department of Physics
P.O. Box 846
Middleton, MA 01949
(617) 774-2370

Salvatore Frullani
Physics Department
INSTITUTO SUPERIORE DI SANITA
Viale Regina Elena 299
00161 Roma, Italy
SANTEO at ICNUCEVM

David Fryberger
SLAC
Bin 20
P.O. Box 4347
Stanford, CA 94305
(415) 854-3300 x2768
DAFRA at SLACVM

Manfred Gari
Ruhr-Universitat Bochum
Agr. Mittelenergiephysik
Univer. 150, Geb.NP6/152
D-4630, Bochum 1,
W.GERMANY
02341-700-3707

Franco Garibaldi
Laboratorio Di Fisica
Ist. Sup. Di Sanita
Viale Regina Elena 299
00161 Roma, Italy
SANTEO at ICNUCEVM

Roger Gearhart
SLAC
Bin 20
P.O. Box 4349
Stanford, CA 94305
(415) 854-3300 X2709
GEARHART at SLACVM

David R. Gill
TRIUMF
4004 Westbrook Mall
Vancouver, BC V6T 2A3
Canada
(604) 222-1047
DRGILL at TRIUMFCL

Kevin Giovanetti
University of Virginia
Physics Department
Charlottesville, VA 22901
(804) 924-7481
KG6V at VIRGINIA

Peter A.M. Gram
Los Alamos National Lab.
MP-4 MS H846
Los Alamos, NM 87545
(505) 672-5562

A. Harindranath
Cal Tech
Kellogg Lab 106-38
Pasadena, CA 91125
(818) 356-4584
HARI at CALTECH

Ross S. Hicks
U. of Massachusetts
Department of Physics
Amherst, MA 01003
(413) 545-2480
RHICKS at UMASS

Andrew S. Hirsch
Purdue University
Department of Physics
W. Lafayette, IN 47907
(317) 494-5192

Werner Hofmann
Lawrence Berkeley Lab
Bldg. 50B, Room 6208
One Cyclotron Road
Berkeley, CA 94720
(415) 486-7177
WHP04 at LBL

J. Barrie Hughes
Stanford University
Hansen Laboratory
Stanford, CA 94305
(415) 723-0135

Ed Hungerford
Physics Department
University of Houston
Houston, TX 77004
(713) 749-3843
MEP0 at UHRCC

Kohei Itoh
University of
Saskatchewan
Department of Physics
Saskatoon, Saskatchewan
CANADA S7N OWO
(306) 699-6436 X6393

Ken Jacobs
MIT - Bates Linac
P.O. Box 846
Middleton, MA 01949
(617) 245-6600
KJACOBS at MITLNS

Robert L. Jaffe
MIT
Cambridge, MA 02139
(617) 253-4858
JAFFE at MITLNS

Calvin W. Johnson
University of Washington
Department of Physics
FM-15
Seattle, WA 98195
(916) 971-1128
CALVIN AT UWAPHAST

Juerg Jourdan
Cal Tech
Kellog Radiation Lab
106-38
Pasadena, CA 91125
(818) 356-4295
JOURDAN at CALTECH

Marek Karliner
SLAC
Bin 81
P.O. Box 4349
Stanford, CA 94305
(415)854-3300 x2266
MAREK at SLACVM

Lewis P. Keller
SLAC
Bin 20
P.O. Box 4349
Stanford, CA 94305
(415) 854-3300 X2725
KELLER at SLACVM

Arthur A. Kerman
MIT
Department of Physics
Cambridge, MA 02139
(617) 253-2361

Karl-Tasso Knopfle
MPI Kernphysik
Postfach 103980
D 6900 Heidelberg 1
Federal Republic of
Germany
(06221)516509
KTKNO at DHDMP15

Steven Koonin
Cal Tech
106-38
Pasadena, CA 91125
(818) 356-4586
KOONIN at CALTECH

Stanley Kowalski
MIT
Bldg. 26-427
Cambridge, MA 02139
(617) 253-4288
SK at MITLNS

Sebastian Kuhn
Lawrence Berkeley Lab
Building 88
1 Cyclotron Road
Berkeley, CA 94720
(415) 486-5088
KUHN AT LBL

James M. Lambert
Georgetown University
Department of Physics
Washington, DC 20057
(202)625-4144
PHYSL at GUVAX

Kenneth Lassila
Iowa State University
Department of Physics
Ames, IA 50011
(515) 294-1283

Jechiel Lichtenstadt
Tel-Aviv University
Department of Physics
Tel-Aviv, ISRAEL, 69978
(3) 420 667
JECH AT TAUPHY

Dick Louis
CERN
EP Division
1211 Geneva 23
SWITZERLAND
(22) 832-661

Robert Lourie
MIT
MIT/LNS Room 20D-004
Cambridge, MA 02139
(617) 253-5163
LOURIE at MITLNS

Allison Lung
SLAC
Bin 43
P.O. Box 4349
Stanford, CA 94305
(415)854-3300 X3647
LUNG at SLACVM

Mario Macri
CERN
EP Division
Instituto Nazionale
Fisica Nucleare
7223 Geneve SWITZERLAND
004122 833447

James S. McCarthy
University of Virginia
Department of Physics
Charlottesvile, VA 22901
(804) 924-6783

Edward K. McIntyre
Department of Physics
Boston University
590 Commonwealth Avenue
Boston, MA 02215
(617) 353-3425
EKM at BUPHYC

Robert D. McKeown
Cal Tech
106-38, Phys. & Astom.
Pasadena, CA 91125
(818)356-4270
BMCK at CALTECH

Bernhard Mecking
CEBAF
12070 Jefferson Ave.
Newport News, VA 23606
(804)875-7861
MECKING at CEBAFVAX

Steven O. Melnikoff
SLAC
Bin 35
P.O. Box 4349
Stanford, CA 94305
(415) 423-0450
SHINTAI at SLACTWGM

Hans-Otto Meyer
Indiana University
Physics Department
Swain Hall West
Bloomington, IN 47405
(812) 335-2883
MEYER at IUCF

Gerald A. Miller
University of Washington
Department of Physics,
FM-15
Inst. for Nuclear Theory
Seattle, WA 98195
(206) 543-2995
MILLER at UWAPHAST

Richard Milner
Cal Tech
106-38, Kellogg Lab
Pasadena, CA 91125
(818) 356-4587
RGM at CALTECH

Ralph Minehart
SLAC
Bin 43
P.O. Box 4349
Stanford, CA 94305
(415)854-3300 x2319
MINEHART at SLACVM

Rory A. Miskimen
Univ. of Massachusetts
Nuclear Physics Group
Graduate Research Center
Tower B Rm 417-C
Amherst, MA 01003
(413)545-2480
RORY at UMASS

John D. Molitoris
Lawrence Livermore Nat'l
Lab
High Energy Physics Group
L-421, PO Box 808
Livermore, CA 94550
(415) 423-3496

E.J. Moniz
MIT
Center for Theoretical
Physics
Cambridge, MA 02139
(617)253-7515

Jorge G. Morfin
Fermilab
Mail Stop 220
P.O. Box 500
Batavia, IL 60510
(312)840-4561
JORGE at FNAL

Jean Y. Mougey
CEBAF
12070 Jefferson Ave.
Newport News, VA 23606
(804)875-7844
MOUGEY at CEBAFVM

B. E. Norum
University of Virginia
Department of Physics
Charlottesville, VA 22901
(804)924-6789
BEN at VIRGINIA

C. N. Papanicolas
University of Illinois
Nuclear Physics Lab
23 Stadium Drive
Champaign, Illinois 61820
(217) 333-3190
COSTAS at UIUCNPL

G. A. Peterson
Univ. of Massachusetts
Nuclear Physics Group
417 GRC Tower B
Amherst, MA 01003
(413)545-2008
GPETE at UMASS

G.G. Petratos
SLAC
Bin 43
P.O. Box 4349
Stanford, CA 94305
(415)854-3300 x3646
GGP at SLACVM

Fred L. Petrovich
Florida State University
Department of Physics
Tallahassee, FL 32306
(904) 644-1576

G. Ricco
University of Genova
Dipartimento di Fisico
Via Dodecanesco 33
Genova, 16146, ITALY
39 10 5993 230

E.M. Riordan
SLAC
Bin 43
P.O. Box 4349
Stanford, CA 94305
Stanford, CA 94305
(415)854-3300 x3454
EMR at SLACVM

Stephen E. Rock
SLAC
Bin 43
P.O. Box 4349
Stanford, CA 94305
(415) 854-3300 X3454
SER at SLACVM

Sayed H. Rokni
SLAC
Bin 43
P.O. 4349
Stanford, CA 94305
(415)854-3300 x3315
MP4SHR at SLACVM

Andreas Schafer
Cal Tech
106-38, Kellogg Lab
Pasadena, CA 91125
(818) 356-4584
AXS at CALTECH

Ortwin Schwentker
Technische Universitat
Muenchen
Physik Department, E18
James-Franck-Stasse
D-8046 Garching bei
Munchen
Federal Republic of
Germany
89-3209-2586

Richard Sealock
University of Virginia
Physics Department
Charlottesville, VA 22901
(804) 924-3781
RMS6F at VIRGINIA

Carl M. Shakin
Brooklyn College
Department of Physics
Brooklyn, NY 11210
(718) 780-5813

Terry Sloan
University of Lancaster
Department of Physics
Lancaster, UK LA1 4YB
524-625201 X4114
TS at LAVA

Richard D. Smith
LLNL
L-405
Livermore, CA 94550
(415) 423-8228

James. Spencer
SLAC
Bin 26
P.O. Box 4349
Stanford, CA 94305
(415) 854-3300 X2960
JUS AT SLACVM

Paul Stoler
Rensselaer Polytech.
Inst.
Department of Physics
Troy, NY 12181
(518) 266-8388

Zen Szalata
SLAC
Bin 43
P.O. Box 4349
Stanford, CA 94305
(415) 854-3300 X3363
ZMSAMU at SLACESA

M. Taiuti
INFN - Genova
Via Dodecaneso 33
Genova 16146, ITALY
3910 - 5993 - 336

Tadaaki Tamae
Tohoku University
Lab. of Nuclear Science
Makamine, Sendai 982
JAPAN
022 - 245 - 2151

Gabriel Tamas
Institute de Recherche
Fondamentale
DPhN-HE - CEN Saclay
91191 Gif sur Yvette
Cedex
France
(1) 69077528

Stephen T. Thornton
University of Virginia
Department of Physics
Charlottesville, VA 22903
(804) 924-6808
STT at VIRGINIA

William Turchinetz
MIT/Bates Linear
Accelerator Center
P.O. Box 846
Middleton, MASS
01949-2846
(617) 245-6600

Karl A. Van Bibber
LLNL
Dept. of Physics
Livermore, CA 94550
(415)423-8949
SHINTAI at SLACTWGM

James Vary
Cal Tech
106-38, Kellogg Lab
Pasadena, CA 91125
(818) 354-4582
VARY at CALTECH

Robert Walker
Cal Tech
Kellog Radiation Lab
106-38
Pasadena, CA 91125
(818) 356-4296
RCW at CALTECH

Kebin Wang
Stanford University
Varian 306, Physics
Stanford, CA 94305
(415)725-2362

M. Weiss
LLNL
P.O. Box 808
Livermore, CA 94550
(415) 422-4094

Claude F. Williamson
Bates Linear Accelerator
Center
P.O. Box 846
Middleton, MA 01949-2846
(667) 245-6600
CFW at MITLNS

Granddon D. Yen
Cal Tech 106-38
Kellogg Lab
Pasadena, CA 91125
(818) 356-4513

Han Yin
Univ. of Massachusetts
Nuclear Physics
Lederle GRC Tower B, Rm.
417B
Amherst, MA 01003
(415)545-2008
GPETE at UMASS

Abbasli Zolfaghari
MIT
P.O. Box 846
Middleton, MA 01949
(617)245-6600
AWRI at MIT

★U.S. GOVERNMENT PRINTING OFFICE: 1987 788 019/ 79181
REGION NO. 4